New approaches in understanding layered intrusions: Field-based and analytical evidence from the Bushveld and Monchegorsk complexes

PhD thesis

Bartosz T. Karykowski

Cardiff University

School of Earth and Ocean Sciences

Submitted in fulfilment of the requirements for the degree of PhD

July 2017

Declaration

This work has not been submitted in substance for any other degree or award at this or any other university or place of learning, nor is being submitted concurrently in candidature for any degree or other award.

Signed ..... (candidate)

Date ..... (candidate)

Statement 1

This thesis is being submitted in partial fulfilment of the requirements for the degree of PhD.

Signed ..... (candidate)

Date ..... (candidate)

Statement 2

The thesis is the result of my own independent work/investigation, except where otherwise stated. Other sources are acknowledged by explicit references.

Signed ..... (candidate)

Date ..... (candidate)

Statement 3

I hereby give consent for my thesis, if accepted, to be available online in the University's Open Access repository and for inter-library loan, and for the title and summary to be made available to outside organisations.

Signed ..... (candidate)

Date ..... (candidate)

Statement 4

I hereby give consent for my thesis, if accepted, to be available online in the University's Open Access repository and for inter-library loans after expiry of a bar on access previously approved by the Academic Standards & Quality Committee.

Signed ..... (candidate)

Date ..... (candidate)

Acknowledgements

First of all, I would like to thank my supervisors Prof. Dr. Wolfgang D. Maier and Dr. C. Johan Lissenberg for their constant guidance throughout the past three years. I am particularly thankful for the many enlightening discussions with you, Wolf, on essentially every aspect of layered intrusion formation. I truly enjoyed the numerous field trips to Finland, Russia, South Africa and Germany over the past three years with Kate and you.

Furthermore, I would like to thank Dr. Pavel V. Pripachkin and Dr. Nikolay Y. Groshev from the Kola Science Centre in Apatity for their guidance and assistance in Russia. It would not have been possible to carry out this project without your help. I really enjoyed my time in Monchegorsk and Apatity - I will never forget the outstanding пироги, чай и водка in the field.

Dr. Duncan Muir and Dr. Matthew Loocke, thank you for your assistance in the scanning electron microscope lab. Moreover, Dr. Iain McDonald, Prof. Dr. Sarah-Jane Barnes and Dany Savard deserve special thanks for their help with lithophile and chalcophile element analysis. I would also like to thank Anthony Oldroyd for preparing so many thin sections for me, always considering all my peculiar requests.

I am particularly grateful for several grants from the Society of Economic Geologists Foundation (SEGF) and the Mineralogical Society of Great Britain and Ireland for fieldwork and analytical costs associated with the project. Special thanks also go to Eurasia Mining PLC and JSC Central Kola Expedition, in particular to Oleg Kazanov, for providing access to drill core. In addition, the project was supported by funds from the Canada Research Chair of Prof. Dr. Sarah-Jane Barnes.

Finally, I would like to acknowledge my family's constant moral support and encouragement along the way. Most importantly, I need to thank my girlfriend Inken for putting up with me, moving to Wales for me and being my best friend. I would have never been able to do this without your support; I dedicate this thesis to you.

Cardiff, July 2017

Abstract

The formation of layered intrusions remains one of the most important, yet unresolved issues in the study of mafic-ultramafic systems, although they are of major economic significance, hosting more than 80 % of the world's platinum-group element (PGE) resource.

In many layered intrusions, PGE mineralisation is associated with stratigraphic intervals that are characterised by pronounced igneous layering. Thus, the origin of layering and the emplacement mechanism of individual layers are closely related to the formation of PGE deposits. In this study, field-based and analytical evidence from the Bushveld Complex of South Africa and the Monchegorsk Complex in Russia is used to gain a better understanding of the small- and large-scale processes associated with the emplacement of layered intrusions.

Detailed examination of drill core and field exposures suggest that sill-like intrusions of crystal mushes play an important role in the formation of layered intrusions, especially in the lower ultramafic portions of large complexes. In contrast, the *in situ* Sr isotope analysis of plagioclase from the upper portion of the Bushveld Complex indicates that the more mafic portions may also crystallise *in situ* from crystal-poor magmas, which can also undergo mixing. Moreover, mineralogical and microtextural work based on high-resolution elemental mapping highlights the importance of melt migration at different stages of cumulate solidification as a consequence of displacement by convecting interstitial liquids and compaction.

Further, broadly stratiform PGE mineralisation in the Monchegorsk Complex cannot always be explained by a classic PGE reef model, in which the mineralised horizon marks the transition from sulfide-undersaturated to sulfide-saturated conditions. It is more likely that pre-formed sulfides were entrained in crystal mushes and emplaced into a semi-consolidated cumulate pile at different levels of the layered intrusion. Ultimately, thermal modelling shows that a multi-stage emplacement history of a complex should be regarded as highly prospective with respect to PGE-Ni-Cu mineralisation.

Contents

List of Figures

List of Tables

Chapter 1

Introduction

1.1 Project rationale

Large layered intrusions are of major economic importance as they host more than 80 % of the world's platinum-group element (PGE) resource (cf. Naldrett 2004). Deposits associated with layered intrusions are typically sulfide-poor and gain their value primarily from PGE with minor credits from Ni and Cu. The most important layered intrusion in this regard is the Bushveld Complex of South Africa, which accounts for roughly two-thirds of the global PGE resource. Almost all economic PGE deposits are hosted in laterally extensive, but narrow reefs in the central portions of intrusions with two exceptions, the Platreef and Lac des Iles. Despite the enormous economic significance of these mafic-ultramafic systems, the origin and formation of large layered intrusions and their PGE deposits is not entirely understood so far.

In particular, the origin of layering and the associated PGE enrichment in some of these layers remains one of the most fundamental, yet unanswered questions in layered intrusion research. Most of the models to explain the pronounced layering are essentially based on one of the following two principal mechanisms: (1) crystal settling and sorting (e.g., Wager & Brown 1967) or (2) *in situ* crystallisation (e.g., Campbell 1978). In the former model, crystals are believed to have nucleated in cotectic proportions and settled in a magma chamber, producing a relatively homogeneous succession. Episodically, the crystallisation was interrupted by crystal-charged slurries that swept down the walls and floor of the magma chamber. Upon loss of momentum, these slurries deposited their crystal load according to their density to produce the graded cumulate layers, characteristic of layered intrusions. Further developments of this model were presented by Emeleus (1986), Irvine et al. (1998), Eales (2002) and Maier et al. (2013). In contrast, the formation of igneous layering through *in situ* crystallisation is considered to result from progressively fractionating liquids that migrate inward from the crystallisation front. This implies that each layer (e.g., pyroxenite, norite, anorthosite) crystallised in cotectic proportions from a distinct fractionating liquid (see Campbell 1978, for a review).

Furthermore, the origin of igneous layering and the emplacement mechanism of layered intrusions are closely related to the formation of PGE deposits. Although

some researchers argue that PGE in layered intrusions were concentrated by chloride-rich, aqueous fluids (e.g., Boudreau & McCallum 1992), most authors favour a model, in which the mixing of two compositionally distinct magmas led to a supersaturation in sulfide liquid, thus producing the laterally extensive PGE reefs (e.g., Cameron 1980, Campbell et al. 1983, Naldrett et al. 2009). In contrast, Maier et al. (2013) argued that hydrodynamic sorting of slurries led to a basal concentration of dense minerals, such as sulfides and oxides, which had previously crystallised in cotectic proportions. *In situ* Sr isotope disequilibrium of plagioclase in samples from the PGE reefs was interpreted to be consistent with this model (Yang et al. 2013). Alternatively, it has been suggested that sulfide saturation may have occurred in a staging chamber at depth and that these sulfides were entrained by subsequent magma pulses (e.g., Lee & Butcher 1990, McDonald & Holwell 2011). Whether these processes represent end-members of a continuum is still completely unresolved.

Another extensively mineralised layered intrusion is the Paleoproterozoic Monchegorsk Complex in north-west Russia (e.g., Kozlov 1973). It is particularly interesting because most parts of the complex are well exposed over several kilometres along strike. Moreover, PGE mineralisation occurs at various stratigraphic levels, representing virtually all deposit types associated with layered intrusions in a single complex (cf. Dedeev et al. 2002). The origin of the complex and the PGE mineralisation, however, are rather poorly constrained.

The principal aim of the project is to gain a better understanding of the small- and large-scale processes associated with the emplacement of layered intrusions, and the mechanisms leading to PGE enrichment in distinct portions of the igneous succession. In the first part of the thesis, modern *in situ* Sr isotope analyses of plagioclase from the Bushveld Complex were coupled with mineral chemistry and state-of-the-art elemental mapping to constrain key petrogenetic processes, such as magma mixing, melt migration and compaction in cumulate rocks. In addition, mineralogical and microtextural evidence provides an insight into the emplacement mechanism of individual layers (crystal mush vs. liquid) and its bearing on sulfide mineralisation. The second part of the thesis is concerned with the origin of different styles of PGE mineralisation in the Monchegorsk Complex. For this, a thorough geo-

chemical characterisation of two mineralisation styles was coupled with field evidence from well exposed mineralised intervals and historic drilling data. This combination of data provides a unique opportunity to investigate critical controls on the formation of PGE mineralisation not only in the Monchegorsk Complex, but also in other large layered intrusions across the world. Moreover, the origin of PGE mineralisation has important implications for the emplacement mode of layered intrusions in general.

1.2 Fieldwork location and access

Samples from the Bushveld Complex were obtained from W. D. Maier's personal collection of historic drill core, intersecting the entire stratigraphy of the complex. Moreover, a field trip to the Bushveld in November 2015 provided a thorough introduction to the geology of the complex.

Samples from the Monchegorsk Complex were collected during two field seasons in August/September 2015 and 2016, respectively. The complex is located some 900 km north of St. Petersburg in the Kola Region of north-west Russia. Access to the area is provided by the *R21* highway ("Kola Motorway"), connecting St. Petersburg and Murmansk, which is part of the European route *E105* from northern Norway to Crimea. Additionally, the local Kirovsk-Apatity airport can be reached in just over an hour and provides daily services to Moscow and St. Petersburg. Although the region is situated north of the Arctic Circle ($\approx 68^\circ$ N), it is characterised by a warm-summer humid continental climate (Dfb), following the Köppen-Geiger climate classification system. The mean annual rainfall is approximately 561 mm, whereas the mean annual temperature is - 0.8 °C (Kozlov et al. 2009). The vegetation is typical of the *taiga*, comprising pine trees and firs.

The Monchegorsk Complex is very well exposed due to intense pollution from Norilsk Nickel's *Severonikel* smelter in the centre of the complex (Fig. 1). The smelter was built together with the town of Monchegorsk in the mid-1930s on previously unpopulated land after the discovery of Ni-Cu ores close-by (Bruno 2016). The population of the town grew rapidly from about 200 in 1933 to almost 35,000 in

Fig. 1. Norilsk Nickel's *Severonikel* smelter in the centre of the Monchegorsk Complex. Note the lack of vegetation.

1938. After the collapse of the Soviet Union, the population has steadily decreased from almost 70,000 to 45,000 in 2010 (Kozlov et al. 2009).

Local amenities and accommodation are sufficiently available in Monchegorsk, thus facilitating fieldwork logistics in the area.

1.3 Thesis outline

The main body of the thesis includes eight chapters in total. Following this introduction, Chapter 2 provides a geological overview of the Bushveld and Monchegorsk complexes to establish the relevant background knowledge for the subsequent chapters. Chapter 3 summarises the different analytical methodologies used for this study. Chapter 4 presents *in situ* Sr isotope data of plagioclase combined with the corresponding mineral chemistry from a continuous profile across the Rustenburg Layered Suite (RLS) of the Bushveld Complex, emphasising the importance of melt migration and magma mixing in cumulates. Chapter 5 explores the emplacement

mechanisms and intra-cumulate processes associated with the Lower Zone of the RLS. Chapter 6 aims to constrain critical controls on the formation of contact-style PGE-Ni-Cu mineralisation in the Monchegorsk Complex and how this relates to the emplacement of layered intrusions in general. Chapter 7 documents different examples of reef-style PGE mineralisation in the Monchegorsk Complex to demonstrate the diversity of petrogenetic processes, resulting in stratiform PGE enrichment in layered intrusions. Chapter 8 summarises key findings of this study and provides a brief synthesis of the complex processes involved in the formation of layered intrusions and the local enrichment in PGE. Chapters 4 to 7 represent parts of four manuscripts, which are either in preparation, in review or fully published.

Chapter 2

Geological setting and previous work

2.1 Geological overview of the Bushveld Complex

The 2.06 Ga Bushveld Complex of South Africa is located close to the centre of the Kaapvaal Craton and covers an area of approximately 450 km x 350 km, for a total areal extent of > 65,000 km^2 (Fig. 2). It comprises four different rock suites (Eales & Cawthorn 1996):

1. felsic volcanic rocks of the *Rooiberg Group*,
2. granites and granophyres of the *Rashoop Granophyre Suite*,
3. granitic rocks of the *Lebowa Granite Suite*,
4. layered mafic-ultramafic rocks of the *Rustenburg Layered Suite* (RLS), as the most voluminous group.

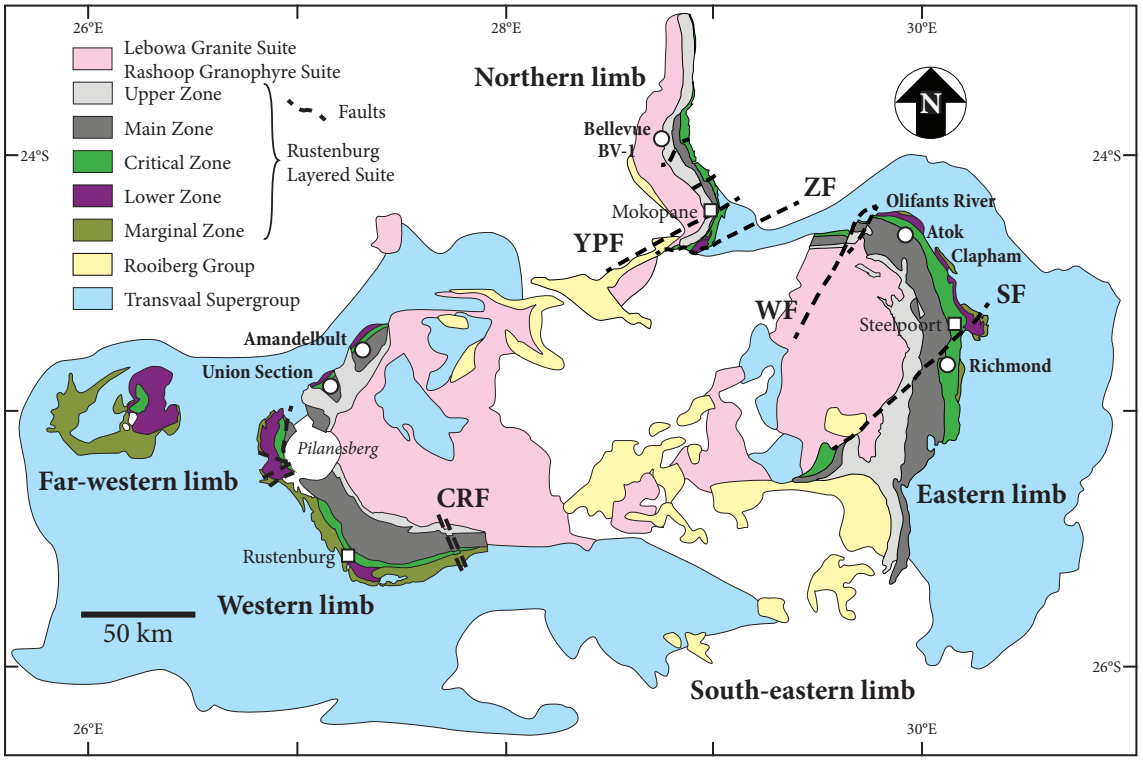

Fig. 2. Simplified geological map of the Bushveld Complex. Samples for this study were taken from the Union Section and drill core BV-1. Modified after Yudovskaya et al. (2013). YPF = Ysterberg-Planknek Fault; ZF = Zebadiela Fault; WF = Wonderkop Fault; SF = Steelpoort Fault; CRF = Crocodile River Fault.

2.1.1 Local geology

The layered mafic-ultramafic sequence of the Bushveld Complex crops out in four different areas, known as limbs, with a fifth under younger sedimentary cover. These include the far-western, the western, the northern, the eastern and the covered south-eastern or *Bethal* limbs (Fig. 2). According to Cawthorn & Webb (2001), gravity modelling suggests a connection between the eastern and western limbs, but the relationship to the other limbs remains debatable. Moreover, the connectivity between these two limbs was confirmed by seismic and magnetic modelling (Webb et al. 2004, Cole et al. 2013).

Notably, some layers can be traced across the complex for more than 150 km along strike. In general, they show a low-angle dip towards the intrusion centre; however, paleomagnetic data indicate that the layers were initially subhorizontal (e.g., Letts et al. 2009).

2.1.2 Stratigraphy

A standard zonal subdivision into five distinct major units has been traditionally accepted for the RLS after Hall (1932). The noritic *Marginal Zone* is present at the bottom, followed by the ultramafic *Lower Zone*, the mafic-ultramafic *Critical Zone*, the gabbronoritic *Main Zone* and the ferrogabbroic *Upper Zone* at the top, for a cumulative thickness of up to 8.1 km in the eastern limb, whereas the western part is slightly thinner with approximately 7.2 km (Fig. 3). The exact stratigraphic position of several zone boundaries, however, remains contentious (e.g., Kruger 1990, Mitchell 1990). The complete succession from the Lower to the Upper Zone is rarely exposed; only the area north of Steelpoort hosts the full sequence (Fig. 2). In most other areas, the Lower, the Critical and the Main zones successively abut against the floor rocks. In contrast, the Upper Zone locally cuts downwards into the underlying parts of the complex, terminating in the floor sequence (van der Merwe 1976, Wilson et al. 1994). These areas are known as *gap areas* and are present north of the Pilanesberg, i.e., Northern Gap, and in the northern limb (Coertze & Schumann 1962, van der Merwe 1976, Wilson et al. 1994).

Marginal Zone

The Marginal Zone has a highly variable thickness, ranging from 0 to 800 m, and is believed to consist of multiple intrusions of magma (Eales & Cawthorn 1996).

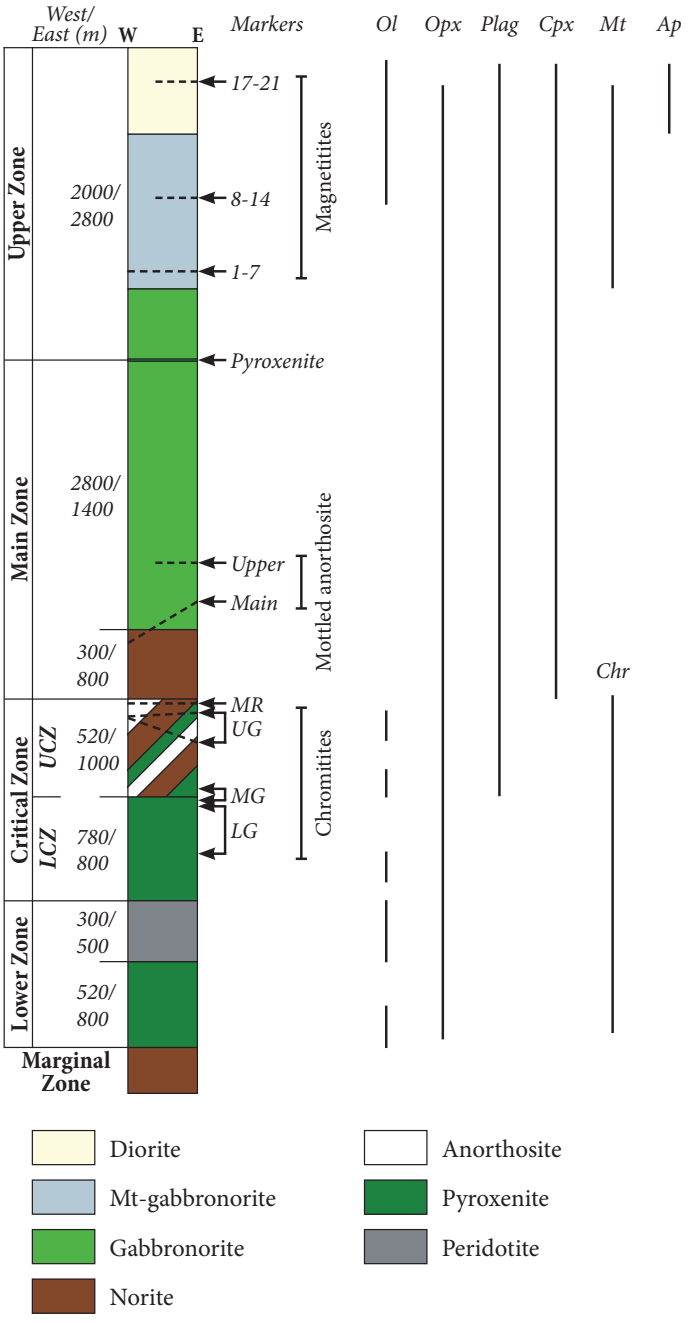

Fig. 3. Simplified stratigraphy of the RLS. Modified after Cawthorn et al. (2006). Abbreviations: LCZ = Lower Critical Zone; UCZ = Upper Critical Zone; MR = Merensky Reef; UG = Upper Group; MG = Middle Group; LG = Lower Group; ol = olivine; opx = orthopyroxene; plag = plagioclase; cpx = clinopyroxene; mt = magnetite; chr = chromite; ap = apatite.

The zone is characterised by the frequent occurrence of quartzitic and dolomitic xenoliths within fine-grained, unlayered norite, gabbronorite and minor pyroxenite, which is generally attributed to the assimilation of sedimentary lithologies from the *Transvaal Supergroup*. According to Cawthorn et al. (2006), these rocks are unlikely to represent the true chilled margins of the intrusion, but rather variably contaminated magmas that crystallised relatively quickly, prior to the emplacement of the more voluminous layered suite of rocks.

Lower Zone

The Lower Zone (LZ) is predominantly composed of harzburgite and pyroxenite with less than 1 vol % chromite, reaching up to 2,000 m in thickness (Fig. 3) (Cawthorn 2015). It shows a greater variability in thickness and lateral continuity relative to all other zones. The distribution of the LZ is mainly controlled by

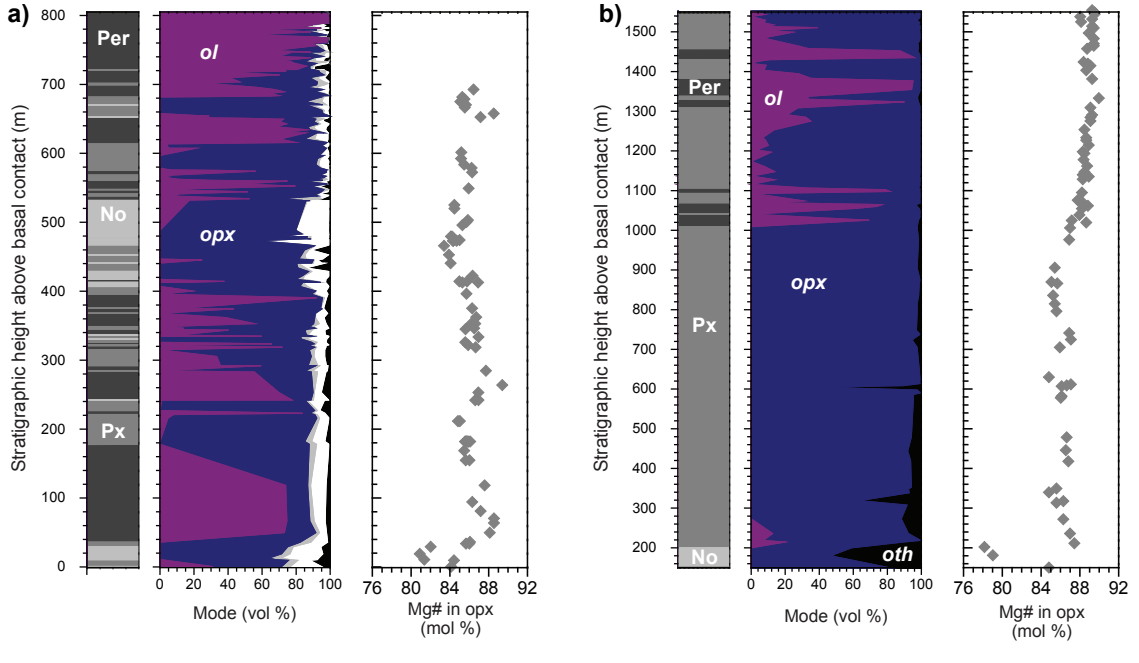

Fig. 4. Lithostratigraphy of the Lower Zone together with the corresponding Mg# in orthopyroxene as a fractionation index. a) Union Section in the western limb. Grey = clinopyroxene; white = plagioclase; black = other minerals. b) Olifants River Trough in the eastern limb. Data were taken from Teigler (1990) and Cameron (1978*b*), respectively. Abbreviations: Per = peridotite; Px = pyroxenite; No = norite; ol = olivine; opx = orthopyroxene; oth = other minerals.

the floor rock topography, as it generally occurs in local floor rock depressions or troughs, such as in the *Olifants River Trough* in the eastern limb of the Bushveld Complex (Cameron 1978*b*). The succession becomes thinner in the areas between these troughs, locally forming separated bodies (e.g., Scoon & Teigler 1995, Wilson 2015). In the far-western limb, the LZ attains a thickness of about 1,000 m, thinning towards the east, where it reaches approximately 800 m in the western limb at the Union Section (Engelbrecht 1985, Teigler 1990). In contrast, the LZ in the eastern limb may reach a thickness of more than 1,500 m in the Olifants River and Clapham troughs (Cameron 1978*b*, Wilson 2015). Both limbs, however, show a decreasing LZ thickness from north to south until it disappears east of Rustenburg and south of the Steelpoort Fault, respectively (Fig. 2). The distribution and thickness of the LZ in the northern limb are rather erratic. It mostly occurs in isolated sill-like bodies with considerable changes in thickness, ranging from $<$ 800 m to 1,700 m over short distances (de Villiers 1970, van der Merwe 1976), and is commonly separated from the overlying igneous succession by a distinct layer, rich in floor rock xenoliths (Maier et al. 2008, Yudovskaya et al. 2013).

The stratigraphy of the LZ is exceptional at the Union Section as it features the first example of a chilled margin at the base of the LZ, consisting of a ca. 90-cm-thick chill sequence, comprising Mg-rich basaltic andesite and komatiite (Maier et al. 2016a). This is overlain by a ca. 200-m-thick succession of interlayered fine-grained phlogopite-rich pyroxenite, locally enriched in Pd and medium-grained peridotite (Maier et al. 2013). Above this, an approximately 180-m-thick succession of interlayered medium-grained pyroxenite and peridotite is present, followed by approximately 140 m of slightly plagioclase-enriched rock types, ranging from pyroxenite to melanorite. The uppermost portion of the LZ is dominated by peridotite with minor pyroxenite (Fig. 4 a).

Detailed work by Teigler (1990), Cameron (1978*b*) and Wilson (2015) demonstrates several significant differences between the LZ in the western and eastern limbs (Fig. 4). Besides great thickness variations, the stratigraphy is also rather dissimilar, with an olivine-dominated LZ in the west and a more orthopyroxene-rich LZ in the east. More recently, Wilson (2015) described a previously unknown 750-

m-thick succession of highly magnesian peridotites and pyroxenites, termed Basal Ultramafic Sequence (BUS), which underlies the LZ and the Marginal Zone in the Clapham area of the eastern limb. The author argued that the emplacement of the BUS predated the intrusion of the LZ. Hence, the BUS is interpreted to represent the earliest stage of filling several compartments of the proto-Bushveld magma chamber, especially in the eastern limb of the complex.

With respect to the the LZ, a comparison between the Olifants River and the Clapham troughs shows that the intra-limb stratigraphy of the eastern limb is broadly consistent, but thicknesses of units vary considerably (Cameron 1978*b*, Wilson 2015). Moreover, the thick pyroxenitic portion in the lower part of the LZ is absent in the western limb. The Mg# (100 x molar Mg/(Mg+Fe)) of orthopyroxene mostly ranges from 84 to 90, and shows relatively little variability across both limbs with no clear fractionation trend. This apparent lack of fractionation led to the conclusion that the LZ crystallised from a very large volume of magma (e.g., Eales & Cawthorn 1996). The upper boundary of the LZ is variably defined; however, Teigler & Eales (1996) proposed to place the boundary at the top of the uppermost olivine-rich unit.

Critical Zone

The Critical Zone is subdivided into two subzones, the Lower Critical Zone (LCZ) and the Upper Critical Zone (UCZ). Up to 90 % of the LCZ are composed of orthopyroxenite, whereas harzburgite and minor olivine-orthopyroxenite constitute the rest of the zone, for a total vertical thickness of up to 800 m (Fig. 3) (Teigler & Eales 1996). Moreover, the LCZ contains nine major chromite layers with a thickness of up 1 m, termed LG1-7 (Lower Group) and MG1-2 (Middle Group). Detailed field studies indicate that these layers can be correlated across most of the Bushveld Complex, south of the Thabazimbi-Murchison Lineament (Teigler & Eales 1996, Cousins & Feringa 1964). In contrast, the LCZ appears to be absent in the northern limb (van der Merwe 1976, Ashwal et al. 2005, Tanner et al. 2014).

The appearance of cumulus plagioclase defines the base of the UCZ, which occurs in between the four MG chromite layers (MG2/3). In the eastern and western

limbs, this level is defined by an up to 3-m-thick layer of anorthosite. In contrast, the UCZ in the northern limb overlies a thick sequence of harzburgite, likely representing the LZ, which has been interpreted to reflect the absence of the LCZ in this part of the complex (Maier et al. 2008, Hulbert 1983). The up to 1-km-thick UCZ is characterised by eight cyclic zones that consist of ultramafic rocks, norites and anorthosites with sharp bottom contacts. Additionally, two to three chromite layers occur towards the top of the UCZ, namely the UG1-3 (Upper Group). Moreover, several thin basal chromite layers are present in the uppermost two cyclic units, which are known as the *Merensky* and *Bastard Cyclic Units*, respectively.

The frequent occurrence of chromite layers in the Critical Zone, in particular the LG6 in the LCZ, makes the Bushveld Complex the largest chrome reserve on Earth (Crowson 2001). Furthermore, the Merensky Reef and the UG2 chromitite represent the world's largest PGE resource, both of which will be discussed in section 2.1.7 (Naldrett 2011).

Main Zone

The Main Zone (MZ) comprises an up to 3-km-thick succession of norite and gabbronorite with minor anorthosite and pyroxenite (e.g., Ashwal et al. 2005, Klemm et al. 1985, van der Merwe 1976, Mitchell 1986, 1990, Roelofse & Ashwal 2012). As opposed to most other zones of the RLS, the MZ lithologies are largely unlayered. The definition of the base of the zone is rather difficult; however, it is commonly placed at the top of the Bastard Cyclic Unit, overlying the Merensky Reef (e.g., Mitchell 1990). In contrast, Kruger (1990) argued for a lower boundary at the level of the Merensky Reef, as Sr isotope compositions change significantly at the this stratigraphic level. A further division of the MZ was proposed by Kruger (1990), who defined two subzones based on the principal formation processes for each subzone: (1) the lower Main Zone (LMZ) and (2) the upper Main Zone (UMZ). The author envisaged that the formation of the LMZ was characterised by frequent influxes of fresh magma (*Integration Stage*), whereas the UMZ represented an episode of undisturbed fractionation of the magma chamber (*Differentiation Stage*).

An important interval in the MZ is the so-called *Pyroxenite Marker* (PM),

which consists of one or more pyroxenite layers of less than 1 m in thickness (e.g., Klemm et al. 1985). Sharpe (1985) reported a gradual reversal in mineral compositions and whole rock Sr isotope ratios at this level, which he interpreted to represent an addition of magma. Locally, the PM may also contain minor PGE mineralisation (e.g., Maier et al. 2001). Apart from the PM, the MZ appears to be barren south of the Thabazimbi-Murchison Lineament. In the northern limb, however, sulfide mineralisation has been described at several stratigraphic levels. Maier & Barnes (2010) and Holwell et al. (2013) studied mineralised pyroxenitic to gabbronoritic lithologies from the UMZ at Moorddrift. Furthermore, the UMZ hosts sulfide mineralisation at Aurora and in the *T Zone* of the Waterberg project, both of which are located in a far northern extension of the northern limb (Huthmann et al. 2016, 2018, Kinnaird et al. 2017, Maier et al. 2008, McDonald et al. 2017).

The upper boundary of the MZ has traditionally been taken at the first appearance of magnetite as a cumulus phase (e.g., Eales & Cawthorn 1996), although some workers prefer to place this boundary at the level of the PM, which is some 600 to 700 m below the first appearance of cumulus magnetite (e.g., Kruger 1990). In this study, the shift in Sr isotope ratios associated with the PM will be used to define the upper boundary of the MZ (Fig. 3).

With respect to the origin of the MZ, Kruger (2005) suggested that the parental magma to the MZ intruded the Bushveld magma chamber in the northern limb before it flowed south into the eastern and western limbs of the complex, where it interacted with the CZ parental magma. According to Kruger & Marsh (1982) and Kruger (1994), the MZ parental magma was of gabbronoritic rather than noritic lineage and highly radiogenic in terms of Sr isotope composition with Sr_i ratios well above 0.71 (Kruger 2005). In contrast, Maier & Barnes (1998) and Roelofse & Ashwal (2012) argued that the MZ was emplaced as a crystal mush, containing a small melt component.

Upper Zone

The Upper Zone (UZ) is the laterally most extensive zone among all zones of the RLS. It reaches a thickness of up to 2.8 km and hosts up to 26 magnetite layers, rang-

ing from a few centimetres to > 10 m in thickness (e.g., Barnes et al. 2004, Cawthorn & Molyneux 1986, von Gruenewaldt 1973, Tegner et al. 2006). In most cases, these layers have sharp bottom contacts, whereas the upper contacts are commonly gradational. The up to 2-m-thick *Main Magnetite Layer* (MML) is the fourth layer from the bottom and represents a major resource of vanadium (Fig. 3). According to Crowson (2001), the MML accounts for more than 50 % of the global vanadium production. Compositionally, the zone consists of gabbronorite, anorthosite, magnetitite as well as ferrodiorite with variable amounts of pyroxene, olivine, magnetite, ilmenite and apatite (e.g., Ashwal et al. 2005, Cawthorn & Molyneux 1986, von Gruenewaldt 1971, 1973, Molyneux 1970). On the basis of whole rock Sr isotope data, Kruger et al. (1987) and Kruger (2005) argued that the UZ crystallised from a well-blended mixture between 60 vol % fractionated MZ magma with $Sr_i \approx 0.7084$ and 40 vol % fresh magma with $Sr_i \approx 0.7055$ to produce the typical Sr isotope composition of 0.7073 for the UZ. The only exception is the UZ in the Bethal limb, where it has a significantly less radiogenic composition with $Sr_i \approx 0.7055$ compared to elsewhere in the Bushveld Complex (Kruger 2005). The author interpreted the Bethal limb to represent an isolated intrusion of the magma that was added to the residual MZ magma in all other limbs of the complex, thus confirming previous work by Buchanan (1977). Hence, the UZ in the Bethal limb is considered to have crystallised from the unradiogenic end-member prior to mixing. Consequently, Kruger (2005) proposed that the Bushveld chamber was fed from the Bethal limb before it flowed into the eastern, western and northern limbs, where it thoroughly mixed with the resident MZ magma. Although numerous compositional reversal in the mineral and bulk geochemistry have been described across the UZ (e.g., Ashwal et al. 2005, von Gruenewaldt 1973, Scoon & Mitchell 2012, Tanner et al. 2014), the consistent Sr isotope composition is generally interpreted to reflect relatively undisturbed differentiation of the UZ (e.g., Kruger 1994, Mangwegape et al. 2016).

2.1.3 Tectonic environment

Most of the economically significant layered intrusions in the world are located in the central portions of stabilised cratons, such as the Bushveld Complex and the

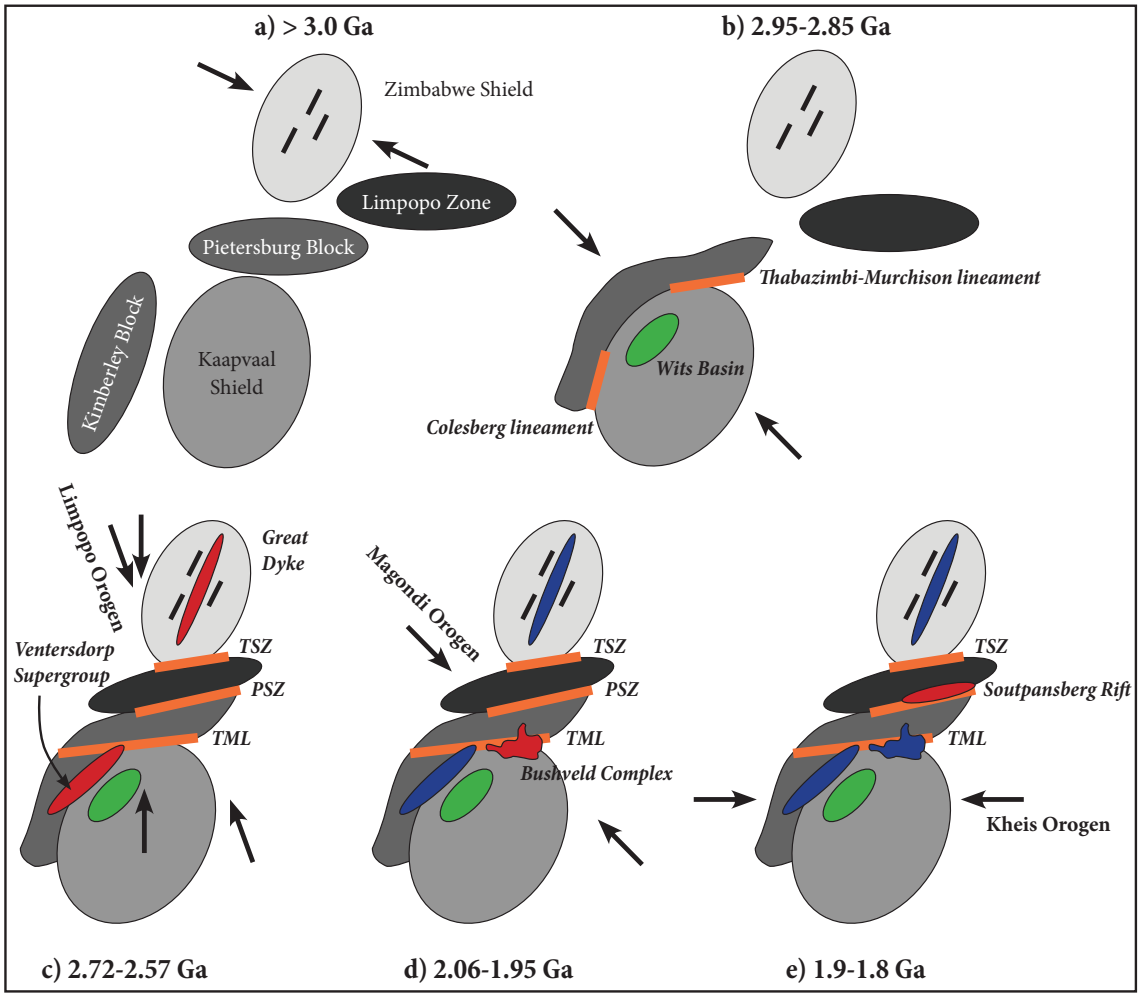

Fig. 5. Tectonomagmatic evolution of southern Africa. a) Tectonic setting in southern Africa before ca. 3.0 Ga. b) Collisional accretion of terranes along the margins of the Kaapvaal Craton between 2.95 and 2.85 Ga. Note the development of the Thabazimbi-Murchison lineament (TML) and the Colesberg lineament. c) Collision of the Kaapvaal and Zimbabwe cratons, leading to the development of the ca. 2.7 Ga Limpopo Belt and the intrusion of the Great Dyke and the Ventersdorp Supergroup. d) Reactivation of pre-existing structures by the Magondi Orogen and emplacement of the ca. 2.06 Ga Bushveld Complex, as a consequence of a collisional rift. e) The ca. 1.88 Ga Kheis Orogen produced the collisional Soutpansberg Rift along the Palala Shear Zone (PSA). Modified after Silver et al. (2004). Abbreviations: TSZ = Tiangle Shear Zone.

Great Dyke in the Kaapvaal Craton, and the Stillwater Complex in the Wyoming Craton (Groves et al. 1987). The emplacement of the Bushveld Complex is generally considered to be associated with the Thabazimbi-Murchison Lineament (TML), separating the northern limb from the rest of the complex (Fig. 2). This major trans-lithospheric suture zone is believed to represent an important pathway for dense primitive magma into the upper crust. According to Holzer et al. (1999), the

collision between the Kaapvaal and the Zimbabwe cratons resulted in localised transpressional extension along the TML or potentially other faults in the area, such as the Crocodile River and Steelport faults (e.g., McCouri & Vearncombe 1987, Good & De Wit 1997, Silver et al. 2004, Cawthorn et al. 2002). This regional tectonic regime allowed for the intrusion of large volumes of mantle-derived magma (Fig. 5). In contrast, Clarke et al. (2009) suggested that the Bushveld Complex was emplaced in a back-arc environment, in which the TML was used by ascending primitive magmas. Recent high-precision age dating, however, suggested a relatively short duration of mafic-ultramafic magmatism ($<$ 1 million years (m.y.); Zeh et al. 2015), which is inconsistent with a subduction-related model.

The TML developed at around 2.9 Ga as part of a major suture zone during the collision of three distinct terranes, the Pietersburg Block in the north, the Kimberley Block in the west and the Kaapvaal Shield in the south (Fig. 5 a, b) (Silver et al. 2004). Afterwards, the collision between the Kaapvaal and Zimbabwe cratons, which also included the Limpopo Zone, led to the intrusion of the Ventersdorp Supergroup (ca. 2.71 Ga) and the Great Dyke (ca. 2.57 Ga) along collisional rifts (Fig. 5 c). The subsequent Magondi Orogen at ca. 2.05 Ga reactivated shear zones in the Limpopo Zone, which resulted in the intrusion of the Bushveld Complex along the TML (Fig. 5 d). During the Kheis Orogen from ca. 1.8 to 1.9 Ga, another collisional rift, known as the *Soutpansberg Rift*, developed along the Palala Shear Zone (PSZ) in the Limpopo (Fig. 5 e).

2.1.4 Age

The age and duration of magmatism in the Bushveld Complex is currently a much-debated issue. The upper age limit for the mafic-ultramafic RLS is defined by a thick sequence of basaltic andesites to rhyolites of the 2,061 $\pm$ 2 Ma Rooiberg Group (Walraven 1997, Buchanan et al. 2002). Cross-cutting relationships indicate that the 2,054.4 $\pm$ 1.8 Ma Lebowa Granite Suite postdates the intrusion of the RLS (Walraven & Hattingh 1993). Hence, the time bracket for the intrusion of the RLS ranges from ca. 2,061 to 2,054 Ma.

Scoates & Friedman (2008) obtained the first high-precision chemical abrasion isotope dilution (CA-ID) TIMS U-Pb age for the intrusion of the Merensky Reef in the western limb (2,054.4 ± 1.3 Ma), whereas Zeh et al. (2015) dated the Merensky Reef in the eastern limb at 2,055.09 ± 0.36 Ma. Additionally, Scoates & Wall (2015) presented updated CA-ID-TIMS U-Pb zircon ages for the Merensky Reef in the eastern (2,056.88 ± 0.41 Ma) and the western limbs (2,057.04 ± 0.55 Ma), thus establishing synchronous crystallisation of this horizon in both limbs. The age offset between the data from Zeh et al. (2015) and Scoates & Wall (2015) has been attributed to a combination of different reference values and data reduction protocols (Wall 2016).

In terms of the duration of magmatism, Zeh et al. (2015) argued on the basis of high-precision CA-ID-TIMS U-Pb dating that the RLS was emplaced and cooled in less than 1 m.y. (1.02 ± 0.63 Ma), whereas Wall (2016) concluded that magmatic activity associated with the RLS lasted for at least 4 m.y. from 2,060 Ma onwards. The oldest succession of rocks in the RLS was shown to be the UG2 interval (2,060.12 ± 0.89 Ma) and the Bastard Reef (2,059.34 ± 0.55 Ma). Wall (2016) interpreted the UCZ to represent a stack of amalgamated sills, produced by out-of-sequence magma injections between 2,060 and 2,057 Ma, largely in accordance with the model proposed by Mungall et al. (2016). Moreover, data from Wall (2016) suggest that the youngest rocks are preserved in the UZ and in the LZ, close to the base of the intrusion.

2.1.5 Parental magma composition

Historically, the zonal subdivision of the RLS was mainly based on obvious changes in mineralogy, and subsequent whole rock Sr isotopic studies have shown that changes in isotope compositions broadly correspond to the mineralogical changes.

Kruger (1994) interpreted the RLS to have formed during two principle stages: (1) the *Integration Stage*, represented by the lower part of the complex (LZ, CZ and the lower part of the MZ), was characterised by open system conditions with multiple isotopically distinct influxes of magma and (2) the *Differentiation Stage*, which proceeded mainly under closed system conditions, was dominated by large-

scale fractional crystallisation and limited additions of new magma (upper part of the MZ and the UZ). In this study, we use major shifts in Sr isotopes to define zone boundaries, as initially proposed by Kruger (1990).

Evidence for the addition of geochemically distinct pulses of magma led to several detailed studies on the parental magma composition of the RLS. The main focus of these studies have been quenched marginal rocks and related fine-grained sills exposed in the floor of the intrusion (Davies et al. 1980, Cawthorn et al. 1981, Sharpe 1981, Harmer & Sharpe 1985, Barnes et al. 2010); however, more recently, drill cores, intersecting the lower contact of the igneous succession, demonstrated the presence of relatively fresh chilled margins (Wilson 2012, Maier et al. 2016a).

Sharpe (1981) established the widely accepted classification of RLS parental magmas in three suites: (i) Bushveld 1 (B1) magma underlying the LZ, (ii) B2 magma underlying the UCZ and (iii) B3 magma underlying the MZ. Recent studies by Wilson (2012) and Maier et al. (2016a) suggested that the B1 magma represented a komatiitic magma with 18 to 19 wt % MgO, derived from the asthenosphere, which has been contaminated by crustal lithologies underlying the Bushveld Complex, whereas the B2 and B3 magmas are interpreted to represent tholeiitic basalts with approximately 8 wt % MgO (Sharpe 1985).

2.1.6 Host rocks of the Bushveld Complex

The Bushveld Complex was emplaced discordantly into Neoarchean to Paleoproterozoic sedimentary rocks of the Transvaal Supergroup and Archean basement granites and gneisses. The former includes a variety of chemical and siliciclastic sedimentary rocks, which were deposited from ca. 2.642 to 2.056 Ga (Walraven & Martini 1995, Scoates & Wall 2015). The lower part of the Transvaal Supergroup is known as the *Chuniespoort Group* and consists of an approximately 2-km-thick succession of carbonate rocks. The upper part of the Transvaal Supergroup marks the transition from predominantly chemical sedimentation in the *Chuniespoort Group* to siliciclastic sedimentation in the 6 to 7-km-thick *Pretoria Group* (Eriksson et al. 2006).

The lowermost part of the *Chuniespoort Group* in the vicinity of the Bushveld

Complex is represented by a less than 30-m-thick sequence of mature, cross-bedded quartzite, basal conglomerate, intertidal pelite and carbonate, known as the *Black Reef Formation* (Button et al. 1981, Els et al. 1995). The sequence is overlain by marine dolomites, subordinate limestones, cherts and minor shales of the *Malmani Subgroup* (Button 1973b). The author subdivided the carbonate platform into different formations based on the presence of distinct stromatolite types, cherts and shales. These formations are from the base to the top: *Oaktree*, *Monte Christo*, *Lyttelton*, *Eccles* and *Frisco*. Notably, the iron content increases across the Malmani carbonate platform, which culminates in the approximately 600-m-thick *Penge Iron Formation*, overlying the Malmani Subgroup (e.g., Eriksson et al. 1975). The iron formation comprises macro-, meso- and micro-banded sediment, containing quartz, magnetite, hematite and different carbonates (Beukes 1973).

After the deposition of banded iron formation in the Transvaal Basin, the depositional environment changed from chemical to siliciclastic sedimentation in the *Pretoria Group*. The lowermost sedimentary sequence of the *Pretoria Group* is the *Duitschland Formation*, which is characterised by a basal angular unconformity with the underlying *Penge Iron Formation*, representing a major hiatus (Eriksson & Altermann 1998). It consists of shales, limestones and dolomites with subordinate diamictites, conglomerates and lavas (Button 1973a, Clendenin 1989, Bekker et al. 2001). The remainder of the *Pretoria Group* comprises alternating shale, quartzite and quartz-arenite with subordinate conglomerate, diamictites and carbonate rocks (e.g., Button 1973a, Eriksson et al. 2006). Moreover, three major volcanic deposits, predating the intrusion of the Bushveld Complex, occur across the sequence (*Timeball Hill Formation*, *Hekpoort Formation* and the *Machadodorp Volcanic Member* of the *Silverton Formation*) (Lenhardt et al. 2012). The tectonic environment during the deposition of the *Pretoria Group* has been suggested to represent a fault-controlled or graben basin, especially related to Archean tectonic features, such as the Thabazimbi-Murchison Lineament (Eriksson et al. 1991, 1993).

Even though the western and eastern limbs of the Bushveld Complex were emplaced into siliciclastic *Pretoria Group* lithologies, providing no direct evidence for the interaction between Bushveld parental magmas and the underlying *Chuniespoort*

Group, the magmas must have passed through the laterally extensive Malmani carbonate platform before final emplacement (Beukes 1987, Eriksson et al. 2006). In fact, the northern limb cuts across the Transvaal Supergroup from south to north. The floor rocks in the southern portion of the limb consist of *Pretoria Group* siliciclastic lithologies, whereas the central portion is dominated by dolomitic lithologies of the *Chuniespoort Group*, which give way to the underlying Archean basement granites and gneisses further north (van der Merwe 1976, Buchanan et al. 1981). It is worth noting that these lithologies did not only represent the floor, but also the roof to some intrusions or zones as noted by Holwell et al. (2007).

2.1.7 Platinum-group element mineralisation

Economic PGE deposits in the Bushveld Complex include the Merensky Reef, the UG2 chromitite and the Platreef (e.g., Lee 1996). Other reefs, such as the Bastard and the Pseudo reefs, closely resemble the Merensky Reef; however, they are discontinuous along strike and PGE concentrations do not reach commercially exploitable grades (Naldrett et al. 1986). The formation of reef-style mineralisation (Merensky Reef, UG2) is a strongly debated issue in layered intrusion research (see Mungall & Naldrett 2008, for a review). Traditionally, two principal models have been proposed for the concentration of PGE in laterally extensive reefs: (1) the concentration of PGE by ascending, volatile-rich fluids from the underlying cumulate (e.g., Ballhaus et al. 1988, Boudreau et al. 1986*a*,*b*, Boudreau & McCallum 1992, Mathez 1995, Mathez et al. 1997, Willmore et al. 2000); or (2) scavenging of PGE from the overlying magma column by dense sulfide melt (e.g., Campbell et al. 1983, Naldrett 1989, Naldrett et al. 2008, Barnes & Maier 2002, Cawthorn 2005). According to the latter model, sulfide saturation was reached in response to either magma mixing (e.g., Campbell et al. 1983) or pressure changes in the magma chamber (e.g., Cawthorn 2005). The dense sulfide droplets then settled through the magma column to the floor of the chamber, which resulted in the equilibration with large volumes of silicate magma to account for the high R factor, typical of sulfides in PGE reefs (R factor: magma/sulfide ratio). Alternatively, it was suggested that volatile-rich fluids dissolved small amounts of sulfur and PGE from the footwall cumulates, while

migrating upwards through the cumulus pile (e.g., Boudreau & McCallum 1992, Mathez 1995, Mathez et al. 1997, Willmore et al. 2000). These fluids mixed with the resident magma in the chamber and triggered local sulfide saturation, which allowed for further PGE scavenging from the resident magma.

It has been noted, however, that none of these models can account for the presence of autoliths or roughly circular depressions in the reef interval, known as *potholes* (e.g., Carr et al. 1994, 1999, Latypov et al. 2015, Maier et al. 2013, 2016b, Roberts et al. 2007). More recently, detailed underground observations of the Merensky Reef led to the suggestion that reef-style PGE mineralisation formed through *in situ* crystallisation (e.g., Latypov et al. 2015, 2017). These authors proposed that magma mixing along the floor of the magma chamber resulted in the formation of a superheated sheet of hybrid magma that, upon cooling, crystallised chromite and sulfide *in situ*. The PGE are envisaged to have been scavenged from the continuously intruding magma at the base of the chamber, which led to vigorous thermal or compositional convection, producing high R factors (Latypov et al. 2015). In contrast, Maier et al. (2013) suggested that slumping of semi-consolidated cumulate slurries resulted in hydrodynamic sorting and the formation of density-sorted layers, some of which are enriched in sulfides and oxides. Hence, the high PGE concentrations in these reefs depend on the efficient collection of interstitial sulfide.

Merensky Reef

The Merensky Reef, as one of the most important PGE reefs in the Bushveld Complex, has been mined since 1928 in the Rustenburg area of the western limb (Cawthorn et al. 2002). The reef can be traced for more than 280 km across the western and eastern limbs with most of the mining activity concentrated in the western limb, although several projects in the eastern limb are under evaluation (e.g., Booysendal, Marula).

The term *Merensky Reef* is a mining term and refers to the mineralised zone of the Merensky Cyclic Unit (MCU) (Lee 1996). The reef interval includes from the base to the top: a footwall anorthosite, norite or pyroxenite that is overlain by a lower chromitite, ranging from 1 to 10 cm in thickness. In most places, the chromitite

is overlain by an up to 14-m-thick unit of pegmatoidal feldspathic pyroxenite or feldspathic harzburgite and dunite (e.g., Cousins 1969, Naldrett et al. 2009, Viljoen 1999). This succession is normally capped by a 2 to 10-cm-thick chromitite, although the number of chromitites can vary depending on the location (Barnes & Maier 2002). The olivine-rich reef-facies is mostly confined to the northwestern portion of the Bushveld Complex, but it also occurs sporadically in the southwestern portion (Naldrett et al. 2009). Typically, the dip of the reef ranges from 9° to 27° towards the centre of the complex.

The Merensky Reef is characterised by interstitial sulfide mineralisation, accounting for up to 3 vol % of the mineral mode (Lee 1996, Vermaak & Hendriks 1976). The sulfide assemblage is dominated by pyrrhotite, pentlandite, chalcopyrite, pyrite, cubanite and mackinawite (Vermaak & Hendriks 1976). Economic PGE mineralisation is generally associated with the pegmatoidal pyroxenite, but sulfides are also present up to 1 m below the lower chromitite in the immediate footwall anorthosite, norite or pyroxenite, and up to several tens of centimetres above the upper chromitite in the hanging wall (Barnes & Maier 2002, Kinloch 1982). The separation of the two chromitites is highly variable across the complex, ranging from zero to several metres (e.g., Maier & Eales 1997, Naldrett et al. 1986, 2009, Seabrook et al. 2005, Vermaak 1976). Transitions from thin ($<$ 10 cm) to thick reefs ($>$ 30 cm) may occur over lateral distances of less than a kilometre.

Typical average precious metal grades in the Merensky Reef reach up to 7.3 ppm Pt + Pd + Rh + Au in the western limb and 6.1 ppm Pt + Pd + Rh + Au in the eastern limb, respectively, with Pt/Pd ratios mostly above 2 (Buchanan 1988). The Merensky chromitites, below and above the pegmatoidal pyroxenite, are especially highly enriched in PGE, reaching up to 37 ppm Pt and 4 ppm Pd (Barnes & Maier 2002). Viljoen (1999) noted that the grade of the ore is inversely proportional to the reef thickness. Hence, thicker reef sections are not necessarily more economic to mine.

Locally, the reef is not conformable with the underlying cumulates, but transgresses into the footwall for up to 15 m. According to Viljoen (1999), 15 to 30 % of the Merensky Reef in the southern part of the western limb is affected by this phe-

nomenon, which is known as *potholing*. Especially the olivine-rich reef-facies seems to have been favourable for this process. Detailed descriptions of potholes associated with the Merensky Reef have been provided by Latypov et al. (2015, 2017).

UG2 chromitite

The UG2 chromitite is considered to represent the largest PGE resource on Earth (Vermaak 1985). The mineralised chromitite defines the base of the of the *UG2 Cyclic Unit*, which is situated between 15 and 400 m below the MCU (Lee 1996). Generally, the greatest vertical separation between the UG2 and the MCU occurs the in eastern limb of the Bushveld Complex.

The cyclic unit is essentially composed of a 3 to 10-m-thick, coarse-grained ultramafic layer, which ranges in composition from harzburgite to pyroxenite (e.g., Barnes & Maier 2002, Cousins & Feringa 1964, De Klerk 1982, Hiemstra 1985, 1986, Mondal & Mathez 2006). Most importantly, it contains several thin chromite layers of up to 10 cm in thickness, as well as the mineralised UG2 chromitite, which can be traced for more than 280 km across the complex. It is commonly underlain by a pegmatitic pyroxenite; however, anorthosite is also locally present (Cawthorn et al. 2002). The thickness of the chromite layer ranges from 70 cm in the area north-west of Rustenburg to 130 cm in the eastern part of the western limb, although section up to 2.5-m-thick have also been described (Fig. 2) (Cawthorn et al. 2002, Schouwstra et al. 2000, Vermaak 1985). In addition, lateral variations are very pronounced. Locally, the UG2 chromitite is composed of up to 9 subseams, such as in the Dwars River area of the eastern Bushveld (Voordouw et al. 2010).

The mineralogy of the UG2 chromitite is rather simple with 60 to 90 vol % chromite, 10 to 35 vol % poikilitic orthopyroxene and minor interstitial plagioclase (e.g., Barnes & Maier 2002, Junge et al. 2014, Mathez & Mey 2005). The sulfide abundance is generally very low with less than 0.1 vol % in the western limb, 0.2 vol % in the eastern limb and slightly higher in the northern limb with up to 1 vol % (e.g., Penberthy & Merkle 1999, Gain 1985, Von Gruenewaldt et al. 1989).

The UG2 reef in the western limb contains on average 5.6 ppm Pt + Pd + Rh + Au, whereas average precious metal concentrations are somewhat higher in

the eastern limb with 6.8 ppm Pt + Pd + Rh + Au (Hiemstra 1985, 1986, Lee 1996). Moreover, the distribution of PGE across the UG2 reef is not homogeneous as distinct peaks in concentration were described at the bottom and the top of the chromitite (e.g., Von Gruenewaldt et al. 1986, Maier & Barnes 2008). Pt/Pd ratios appear to be rather variable among the different limbs. According to data summarised by Barnes & Maier (2002), the UG2 chromitite in the western limb has considerably higher Pt/Pd ratios compared to the eastern and northern limbs (Pt/Pd: 2.3 vs. 1.2 and 1.4, respectively).

The occurrence of potholes is also a common feature of the UG2 chromtitite, largely similar to those in the Merensky Reef, although no spatial correlation has been observed between potholes in the Merensky Reef and the UG2 (Cawthorn & Barry 1992). They range in diameter from less than 20 cm to more than 100 m with a vertical extend of up to 40 m (Carr et al. 1994, 1999, Viljoen 1999).

Platreef

In contrast to the stratiform PGE reef mineralisation associated with the Merensky Reef and the UG2 chromitite, the Platreef is a complex, pyroxenite-hosted Ni-Cu-PGE deposit, located at the base of the Bushveld Complex (e.g., Holwell & McDonald 2006, Kinnaird et al. 2005, Manyeruke et al. 2005, van der Merwe 1976). The presence of the Platreef is restricted to the northern limb of the complex – it does not occur south of the TML (Fig. 2). Merensky (1925) subdivided the Platreef into three distinct sectors based on common footwall lithologies: (1) Archean granite and gneiss in the northern sector; (2) dolomite of the Malmani Subgroup in the central sector; (3) shale, banded ironstone and calcsilicates of the Transvaal Supergroup in the southern sector (Kinnaird et al. 2005). The thickness of the Platreef appears to be strongly controlled by the floor rock topography: in footwall synforms, the mineralised sequence reaches up to 400 m, whereas above antiforms the thickness decreases to less than 20 m (e.g., Holwell et al. 2005, Kinnaird et al. 2005, Kinnaird 2005). Locally, the sulfide mineralisation also continues into the footwall gneisses (Holwell & McDonald 2006). Particularly sulfide-rich Platreef intervals are generally associated with floor rock synforms and embayments as noted by Nex (2005) in the

central sector of the northern limb. Unlike in the CZ of the Bushveld Complex south of the TML, chromitites in the Platreef are rare and generally discontinuous with a traceable strike length of a few tens of metres at most (Holwell & Jordaan 2006). From south to north, the mineralised Platreef transgresses downwards into progressively older sedimentary rocks of the Transvaal Supergroup, until it rests on Archean basement granites and gneisses (north of the farm Zwartfontein) (e.g., van der Merwe 1976, Buchanan et al. 1981). Large xenoliths of different footwall lithologies are also common in the Platreef (e.g., Von Gruenewaldt et al. 1989, Holwell et al. 2005).

Average precious metal concentrations in the Platreef rarely reach more than 5 ppm Pt + Pd + Au (cf. McDonald & Holwell 2011, and references therein). In comparison to the Merensky Reef and the UG2, the Platreef is also characterised by much higher base metal concentrations, considerably lower average Pt/Pd ratios (< 1) and greater fractionation between PPGE (Rh, Pt, Pd) and IPGE (Os, Ir, Ru) (e.g., Vermaak 1995, Holwell & McDonald 2006, Maier et al. 2008, McDonald et al. 2005, Kinnaird 2005, Kinnaird et al. 2005).

Despite numerous studies on the Platreef, the origin of the mineralised sequence remains under debate (see McDonald & Holwell 2011, for a detailed review). Following McDonald & Holwell (2011), the available models for the formation of the Platreef can be divided into three principal groups.

Early researchers argued that the Platreef mineralisation formed through the *in situ* contamination of the magma with country rocks, which led to sulfide saturation (e.g., Buchanan et al. 1981). Although many studies have shown highly variable sulfur isotope compositions at different Platreef localities in the northern limb, suggesting *in situ* contamination of the magma (e.g., Holwell et al. 2007, Manyeruke et al. 2005, Sharman-Harris et al. 2005), Holwell et al. (2007) demonstrated that early sulfides in the Platreef have a mantle source and that the addition of external sulfide did not trigger sulfide saturation. These results were also confirmed by Penniston-Dorland et al. (2008), Sharman et al. (2013) and Smith et al. (2016).

The second group of models envisaged that sulfide saturation occurred at depth, prior to the final emplacement of the Bushveld Complex, and that these sulfides were transported to form the Platreef. In this regard, one subgroup of studies

suggested that the Platreef represented a marginal facies of the UCZ elsewhere in the Bushveld Complex (e.g., Cawthorn et al. 2002, Kruger 2005, Maier et al. 2008, Naldrett et al. 2008, Pronost et al. 2008), whereas another group of researchers interpreted the Platreef to have formed independently from the mineralised UCZ units as a set of geochemically distinct sills that entrained pre-formed sulfide (e.g., Holwell & McDonald 2007, Holwell et al. 2011, McDonald et al. 2005, McDonald & Holwell 2007). One of the main arguments of the latter authors against a direct link between the UCZ south of the TML and the Platreef is a hiatus between the intrusion of the Platreef and the MZ as the mineralised UCZ units are generally interpreted to have formed in response to mixing with MZ magma (see above). Prior to the seminal work by Holwell et al. (2005) on the field relationships between the Platreef and the overlying MZ gabbronorites, it has been assumed that the MZ was comagmatic with the Platreef (e.g., van der Merwe 1976, Kruger 2005). A distinct chill zone at the base of the MZ gabbronorites, however, established that the MZ unequivocally postdated the emplacement of the Platreef. Moreover, Holwell & Jordaan (2006) showed that the MZ gabbronorites intruded the Platreef. Hence, it is difficult to argue that mixing between MZ magma and the resident CZ magma resulted in the formation of the mineralised UCZ units south of the TML as well as the Platreef.

On the basis of phase sorting and unmixing in crystal slurries, Maier et al. (2013) proposed that the Platreef represented a marginal facies of the Merensky Reef, where hydrodynamic sorting was less efficient due to higher cooling rates close to the intrusion contact. According to these authors, this process resulted in less pronounced layering and generally lower PGE grades in comparison to the Merensky Reef. The viability of this model, however, remains difficult to test.

Despite lower grades and less favourable Pt/Pd ratios, large-scale open-pit mining of the Platreef has proved to be much more cost-efficient than underground mining of the narrow, higher-grade reefs elsewhere in the Bushveld Complex.

2.2 Geological overview of the Monchegorsk Complex

2.2.1 Regional geology

The Monchegorsk Complex is located along the Pechenga–Imandra–Varzuga rift on the Fennoscandian Shield in the centre of the Kola Peninsula (Fig. 6). The Fennoscandian Shield comprises four distinct geological entities: the (i) Norrbotten, (ii) Karelian, (iii) Belomorian and (iv) Kola cratons or provinces (Lahtinen et al. 2008). The shield is composed of approximately 80 % tonalite-trondhjemite-granodiorite (TTG) with minor granulite complexes, greenstone belts and amphibolites.

Terrane accretion from ca. 2.9 to 2.7 Ga resulted in the assembly of the Kola Craton, which collided with the Karelian Craton at ca. 2.72 Ga, thus producing the Fennoscandian Shield of northern Europe (Hölttä et al. 2008). In the Paleoproterozoic, the area was affected by one of the most significant periods of global mafic-ultramafic magmatism, which led to the formation of voluminous layered intrusions, volcanic suites and dyke swarms across both cratons (e.g., Vogel et al. 1998). Comparable expressions of this igneous event were also recorded across the Canadian Shield, which were interpreted to reflect the spatial proximity of the two shields at the end of the Archean (Bleeker & Ernst 2006). Subsequently, the region was overprinted by the Svecofennian orogeny, lasting from ca. 2.0 to 1.8 Ga. Detailed reviews of the Archean and Paleoproterozoic evolution of the Fennoscandian Shield were compiled by Hölttä et al. (2008) and Lahtinen et al. (2008), respectively.

The Fennoscandian layered intrusions can be broadly subdivided into two groups based on their age (Fig. 6). The older group of Paleoproterozoic intrusions is confined to the Kola Craton and includes the 2.5 Ga Mt. General'skaya, the Monchegorsk Complex and Fedorova-Pana (Amelin et al. 1995, Balashov et al. 1993, Bayanova et al. 2009, 2010, Serov et al. 2007). In contrast, the second group of intrusions occurs throughout the entire shield and comprises the 2.44 Ga Tornio-Näränkävaara Belt in Finland and Sweden (e.g., Kemi, Penikat, Portimo) as well

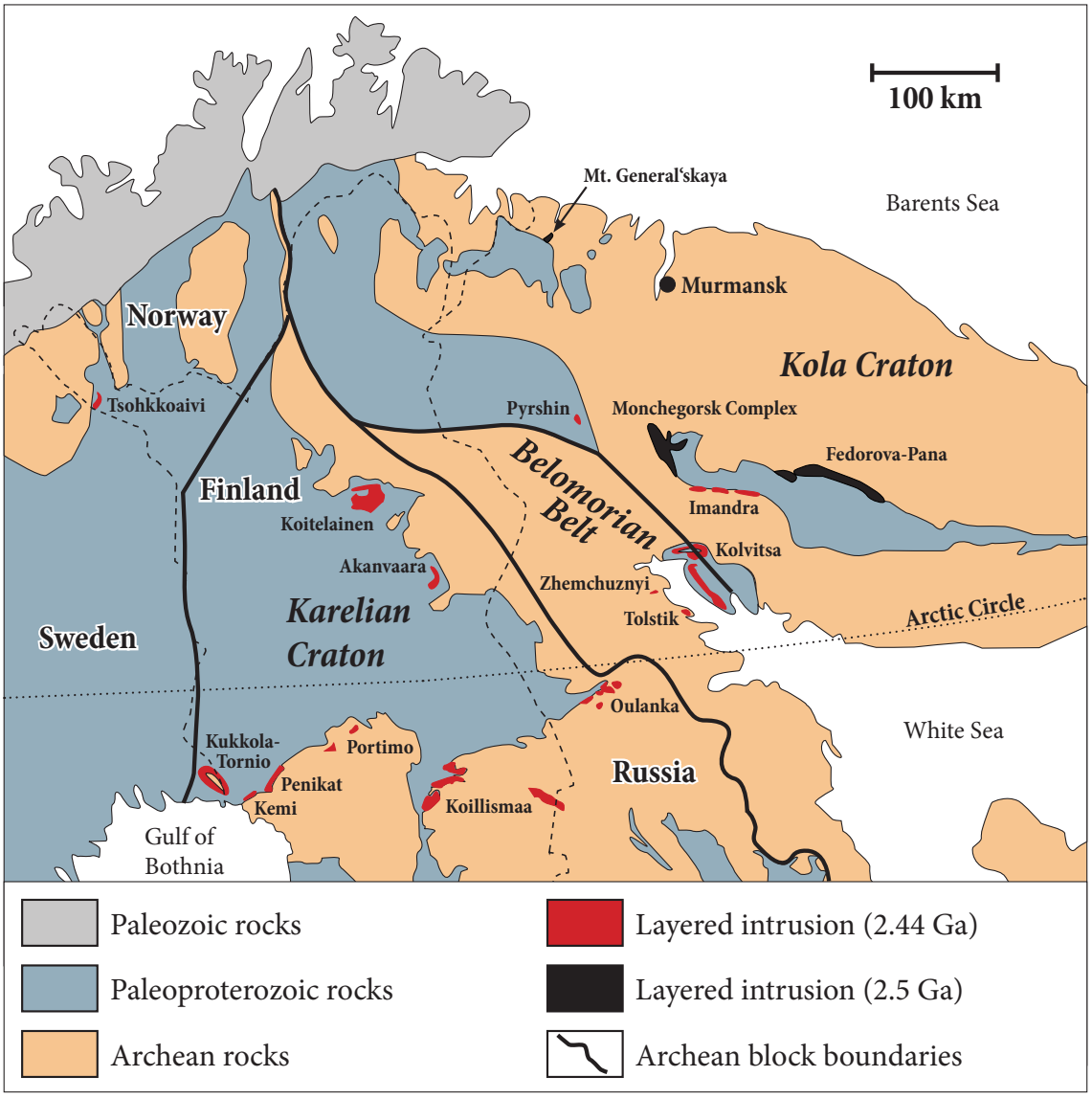

Fig. 6. Simplified geological map of the north-eastern part of the Fennoscandian Shield, showing the location of Paleoproterozoic layered intrusions. Modified after Alapieti et al. (1990).

as a number of other coeval intrusions in Russia, such as Oulanka, Imandra and Burakovsky (e.g., Alapieti et al. 1990).

Most importantly, these intrusions host a variety of distinct styles of PGE, Ni, Cu, Cr and V mineralisation, ranging from stratiform chromitites and basal contact-style PGE-Ni-Cu mineralisation to different types of reef-style mineralisation (Alapieti et al. 1990, Chashchin et al. 1999, Chistyakova et al. 2015, Huhtelin 2015, Iljina et al. 1992, Kozlov 1973, Mutanen 1997, Schissel et al. 2002, Sharkov &

Chistyakov 2012). The mafic-ultramafic Monchegorsk Complex is particularly notable in this regard, as it hosts virtually all deposits types typically associated with layered intrusions in a single complex (Karykowski et al. 2016).

2.2.2 Local geology

The Monchegorsk Complex was emplaced into Archean high-grade metamorphic basement of the *Kola Group*, comprising metapelites, quartzites, banded iron formation and minor dioritic gneisses (Rundqvist & Mitrofanov 1993). The depth of emplacement is estimated to be around 10 to 15 km based on the presence of kelyphitic rims around olivine (Pechersky et al. 2004). The complex is overlain by volcanic and sedimentary rocks of the *Strel'na Group*, which represent the lowermost unit of the *Imandra-Varzuga Greenstone Belt* (Melezhik & Sturt 1994, Vrevskii et al. 2010, Zagorodny et al. 1982). Although the region reached amphibolite-facies conditions during the Svecofennian orogeny, the Monchegorsk Complex remained largely well-preserved because of the relatively deep level of emplacement and the high metamorphic conditions (Pechersky et al. 2004).

The complex comprises two spatially separate intrusions, covering an area of approximately 550 km^2: the predominantly ultramafic *Moncheplutonn* ($\approx$ 65 km^2) and the mafic *Main Ridge* ($\approx$ 485 km^2), which are separated by the *Monchetundra Fault*, trending north-west (Fig. 7 inset).

The Moncheplutonn is crescent-shaped and consists of six distinct mountains, arranged in two branches. The NNE-trending branch with a length of approximately 7 km is ultramafic in composition. It is referred to as *NKT Massif* and includes Mts. Nittis, Kumuzhya and Travyanaya (Fig. 7). The W-trending branch is mafic-ultramafic in composition and slightly longer with 9 km, consisting of Mts. Sopcha, Nyud and Poaz. The intersection of the two branches is occupied by a dunitic body, hosting several massive chromite layers, known as the *Dunite Block*, which is considered to belong to the Moncheplutonn (Smolkin et al. 2004). The total thickness of the Moncheplutonn is more than 2,700 m, but a continuous stratigraphic profile across the intrusion is difficult to obtain due to tectonic fragmentation of the complex. A composite profile across the Moncheplutonn can be subdivided into five major zones

(Fig. 8): (1) the *Peridotite Zone* at the base of the complex, reaching ≈ 500 m in thickness, including the Dunite Block; (2) the *Interlayered Peridotite-Pyroxenite*

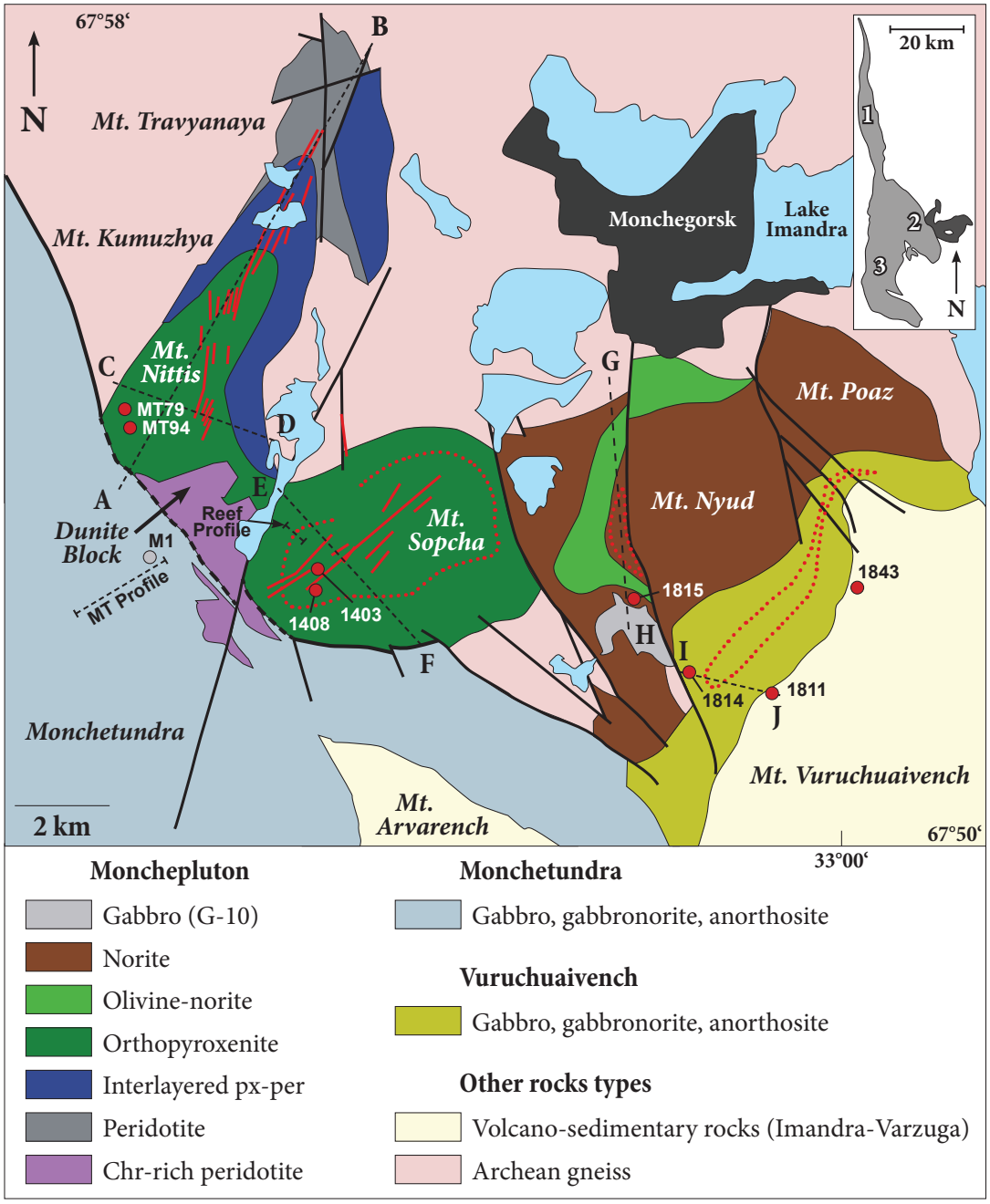

Fig. 7. Simplified geological map of the Monchegorsk Complex. The location of diamond drill cores used in this study are shown as red circles. Solid and dashed red lines indicate Ni-Cu-PGE mineralisation. The inset shows the full extent of the complex. The dark grey crescent-shaped body is the Monchepluton and the light grey body is the Main Ridge. 1: Volchetundra; 2: Monchetundra; 3: Chunatundra. Abbreviations: per = peridotite; px = pyroxenite; chr = chromite.

Zone, reaching ca. 300 m in thickness; (3) the *Pyroxenite Zone* with a thickness of more than 750 m; (4) the *Noritic Zone* in the upper portion of the intrusion with a thickness of at least 450 m and (5) the *Gabbroic Zone* with a thickness of more

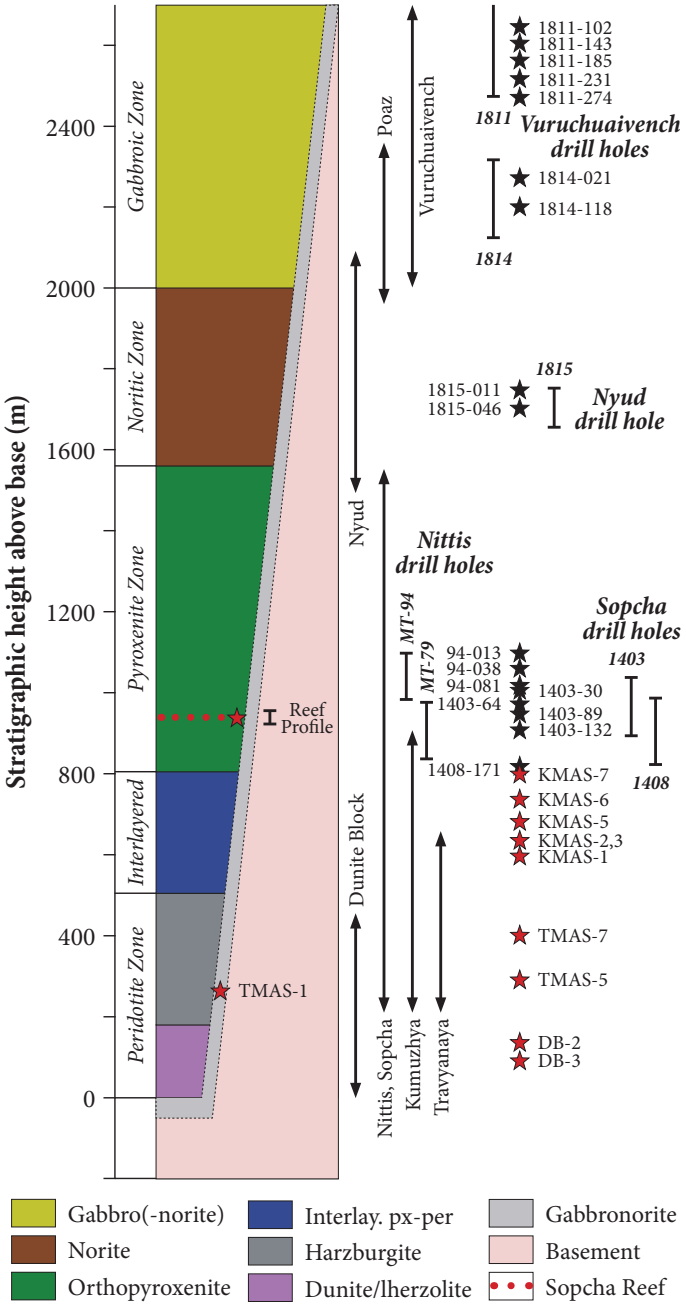

Fig. 8. Simplified stratigraphic column across the Monchepluton together with outcrop and drill core sample locations and numbers. Red stars indicate outcrop samples, whereas black stars show drill core samples. Note that not all samples are shown for every drill core. Modified after Sharkov & Chistyakov (2012).

than 700 m (the uppermost portion of the intrusion has been eroded), comprising the Vuruchuaivench intrusion, which has been shown to represent the continuation of the underlying Noritic Zone (Rundkvist & Sokolova 1978, Sharkov & Chistyakov 2012, Rundkvist et al. 2014).

Dunite Block

The Dunite Block is generally considered to represent the lowermost portion of the *Peridotite Zone* (Fig. 8) (e.g., Smolkin et al. 2004). It covers an area of about 1,500 x 3,000 m and consists of dunite, lherzolite and minor olivine-orthopyroxenite with abundant chromite. The thickness of the igneous body reaches up to 700 m (Chashchin et al. 1999). Moreover, several massive chromite layers occur in the central portions of the Dunite Block.

NKT Massif

The NKT Massif forms a 7-km-long and more than 3-km-wide elongated igneous body. From south to north, the NKT Massif exposes progressively deeper portions of the ultramafic sequence of the Monchepluton (Fig. 9 A-B). The Nittis intrusion, at the southern end of the NKT Massif, reaches a cumulative thickness of more than 1,500 m, which gradually decreases to approximately 500 m at Travyanaya (e.g., Sharkov & Chistyakov 2014). The *Peridotite Zone* attains a thickness up to 400 m in the NKT Massif and is composed of harzburgite and minor dunite (e.g., Kozlov 1973). The overlying *Interlayered Peridotite-Pyroxenite Zone* reaches up to 300 in thickness, whereas the *Pyroxenite Zone* has a thickness of at least 700 m and is only exposed at Nittis (Fig. 9 C-D). Typically, pyroxenitic lithologies in the Monchegorsk Complex are represented by orthopyroxenite with variable amounts of olivine (Kozlov 1973). The contact zone between the ultramafic NKT Massif and the underlying Archean basement gneisses is characterised by an up to 50-m-thick zone of relatively fine-grained gabbronorites and norites, which is often referred to as the *Marginal*, *Bottom* or *Basal Zone* (e.g., Chashchin et al. 2016, Dedeev et al. 2002, Latypov 2003, Sharkov & Chistyakov 2012).

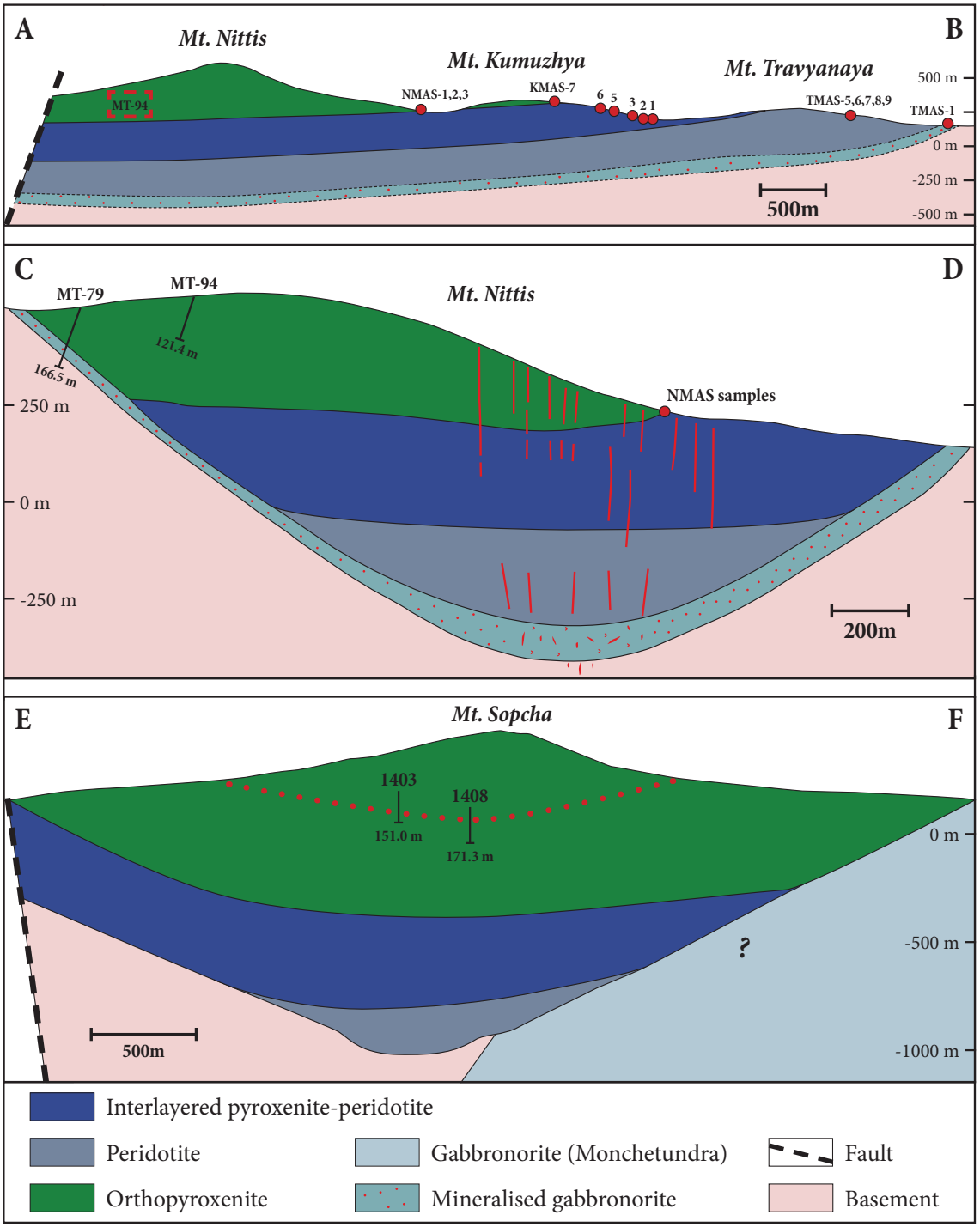

Fig. 9. Schematic geological cross-sections, corresponding to profiles A-B (NKT Massif), C-D (Nittis), E-F (Sopcha), G-H (Nyud) and I-J (Vuruchuaivench) in Fig. 7. Red dots show sample locations together with sample numbers corresponding to those in Fig. 8. Solid red lines indicate vertical massive sulfide veins (C-D). Red dotted line indicates disseminated sulfide mineralisation of the Sopcha Reef (E-F). Modified after Dokuchaeva & Yakovlev (1994): A-B, G-H; Chashchin & Mitrofanov (2014): C-D; Sharkov & Chistyakov (2014): E-F; Pripachkin et al. (2005) and Sharkov & Chistyakov (2012): I-J.

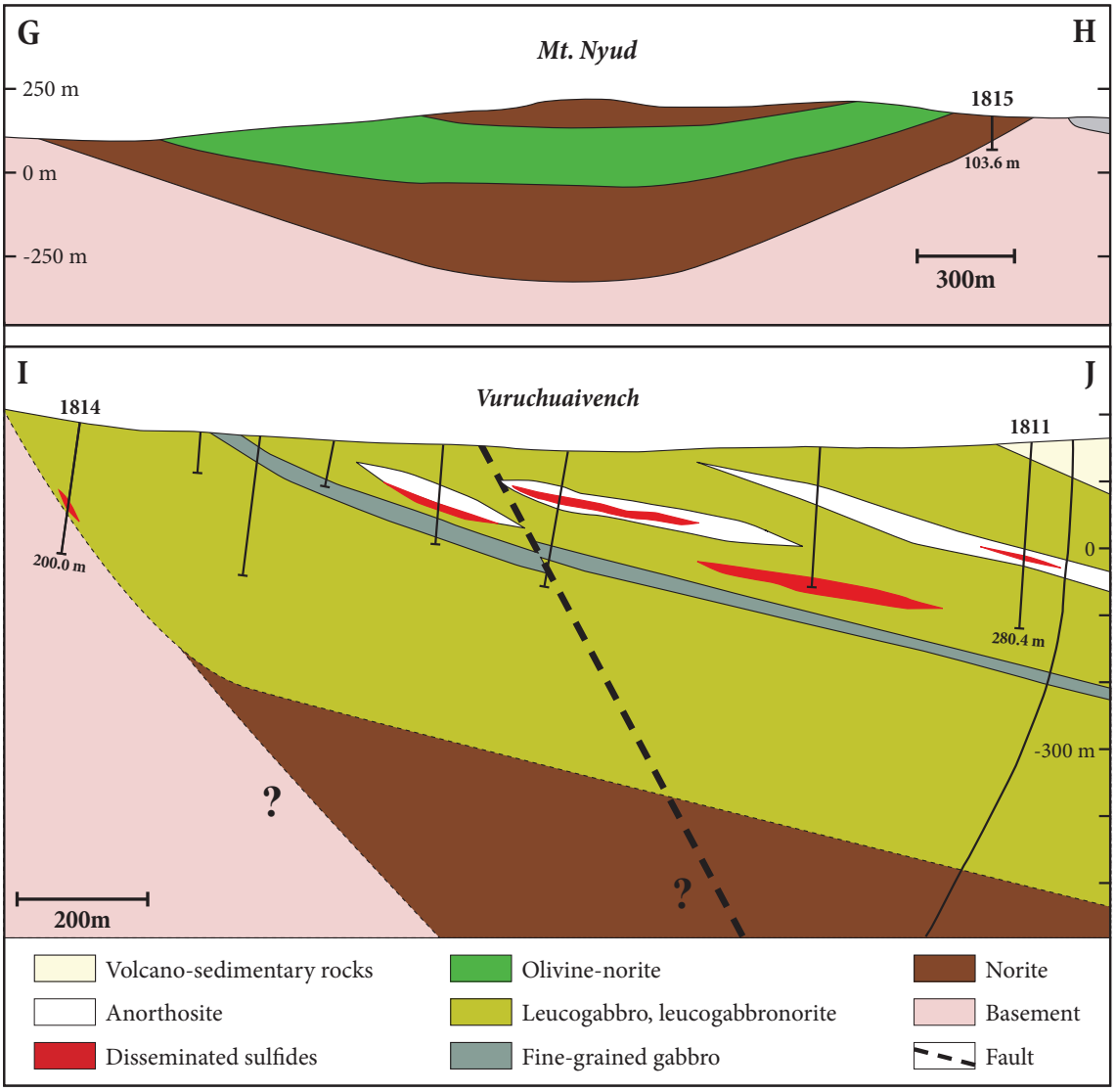

Fig. 9 (cont.)

Sopcha intrusion

The lithostratigraphy of the Sopcha intrusion is broadly similar to that of the NKT Massif. The former is dominated by medium-grained ultramafic rock types, which range from dunite to orthopyroxenite with variable amounts of olivine. According to Sharkov & Chistyakov (2014), the Sopcha intrusion comprises all three ultramafic zones of the Moncheplutonː the *Peridotite Zone* ($>$ 400 m), the *Interlayered Peridotite-Pyroxenite Zone* ($\approx$ 300 m) and the *Pyroxenite Zone* ($>$ 750 m), for a total thickness of approximately 1500 m (Fig. 8, 9 E-F).

Nyud intrusion

The Nyud intrusion reaches a thickness of approximately 600 m and includes mafic lithologies of the *Noritic Zone*, ranging from melanorite to leuconorite with minor olivine-norite in its central portion (Figs. 7, 8, 9 G-H) (e.g., Kozlov 1973, Dedeev et al. 2002, Sharkov & Chistyakov 2012). Locally, the contact zone between the Nyud intrusion and the Archean basement is marked by a relatively thin *Marginal Zone*, similar to that underlying the NKT Massif. The mafic Nyud intrusion is considered to represent the continuation of the ultramafic NKT Massif.

Poaz intrusion

The Poaz intrusion is composed of an approximately 400-m-thick succession of medium-grained leuconorites and leucogabbronorites, overlying the Nyud intrusion (e.g., Kozlov 1973, Chashchin et al. 2016). It represents the transition between the *Noritic Zone* and the *Gabbroic Zone* of the Monchepluton (Fig. 8).

Vuruchuaivench intrusion

The Vuruchuaivench intrusion consists of medium-grained leucogabbronorite and minor anorthosite, both of which are pervasively altered, although primary textures are preserved. The intrusion is believed to represent the uppermost portion of the Monchepluton, overlying noritic to gabbronoritic lithologies of Mts. Poaz and Nyud (Fig. 7, 8, 9 I-J). According to Pripachkin et al. (2005), the lower part of the intrusion consists of massive gabbronorite, whereas the upper part is dominated by layered gabbronorite, reaching a total thickness of up to 700 m. Moreover, these authors argued that the contact between the upper and lower part is defined by a fine-grained gabbro, which they interpreted as a chill zone.

Main Ridge Massif

In comparison to the Monchepluton, only limited geological information is available on the Main Ridge, which comprises the Volchetundra, Monchetundra and Chunatundra intrusions (Fig. 7 inset). These intrusions represent three tectonic blocks

of an originally continuous intrusion with a thickness of more than 2,500 m (e.g., Sharkov & Chistyakov 2012). They are largely leucogabbronoritic to anorthositic in composition and relatively homogeneous along strike (e.g., Sharkov & Chistyakov 2012). It is likely that the Main Ridge forms the upper part of the Monchepluton and therefore the continuation of the *Gabbroic Zone* (Rundkvist & Sokolova 1978). These authors suggested that the complex was tectonically fragmented and that the Main Ridge was subsequently thrust into its current position west of the Monchepluton. This is supported by the presence of a relatively thick blastomylonitic zone between the Monchepluton and the Monchetundra intrusion (Smolkin et al. 2004). However, the Main Ridge has received rather little scientific attention, in part due to the scarcity of PGE mineralisation, difficult field conditions outside of the Monchetundra intrusion and access restriction to areas that belong to the *Lapland Biosphere Reserve*.

2.2.3 Age

Conventional U-Pb thermal ionisation mass spectrometry (TIMS) data on zircon and baddeleyite from the Monchegorsk Complex, comprising the Monchepluton and Main Ridge intrusions, indicate that the complex has been emplaced continuously over a period spanning more than 60 m.y. from 2,506 ± 10 to 2,445 ± 11 Ma (Bayanova et al. 2009). A compilation of existing U-Pb ages for the Monchegorsk Complex are compiled in Figure 10. The prolonged duration has been suggested to arise either from long-lived mantle plume magmatism, exploiting deep crustal structures, or non-plume related magmatism, triggered by delamination of subcontinental lithospheric mantle (Bayanova et al. 2009, Richardson & Shirey 2008). In contrast, U-Pb TIMS data for the 2.44 Ga layered intrusions in Finland suggest their formation over a short period of time (< 5 m.y.). Therefore, the current paradigm of relatively short-lived mantle plume magmatism and rapid formation of layered intrusions does not seem to be applicable to the Russian intrusions of the Fennoscandian Shield (e.g., Zeh et al. 2015, Wall 2016).

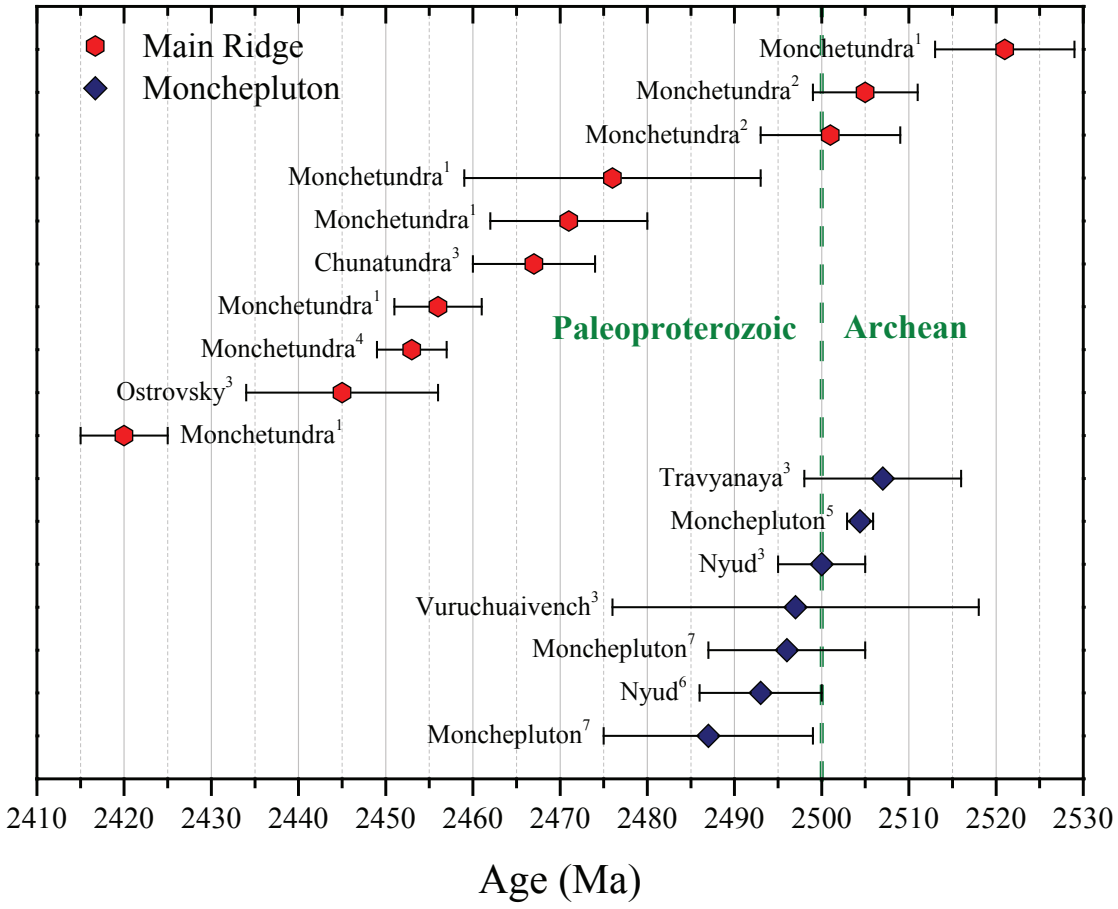

Fig. 10. U-Pb TIMS ages on zircon and baddeleyite together with their error bars for different rocks from the Monchegorsk Complex, comprising the Monchepluton and Main Ridge. [1]Bayanova et al. (2010); [2]Bayanova & Mitrofanov (2005); [3]Bayanova et al. (2009); [4]Mitrofanov et al. (1995); [5]Amelin et al. (1995); [6]Balashov et al. (1993); [7]Smolkin et al. (2004).

2.2.4 Types of mineralisation

Mining activity in the Monchegorsk area dates back to the 1930s, when massive sulfide veins were discovered in the NKT Massif and subsequently exploited until 1970 (e.g., Dedeev et al. 2002, Kozlov 1973). Moreover, several other occurrences of PGE(-Ni-Cu) mineralisation were explored throughout the complex. Traditionally, four different styles of mineralisation have been recognised in the Monchegorsk Complex (Dedeev et al. 2002, Pripachkin & Rundkvist 2008):

1. Massive sulfide veins at Sopcha and the NKT Massif

2. Disseminated sulfide mineralisation at Nyud, Sopcha and the NKT Massif

3. PGE-rich chromite layers in the Dunite Block

4. Stratiform PGE mineralisation at Vuruchuaivench

Despite extensive drilling in the area, the formation of the complex and its mineralisation remain poorly understood. Scientific research over the past 20 years has been mainly focused on the detailed mineralogical characterisation of the PGE mineralisation (e.g., the platinum-group minerals), and on the geochronology of the complex together with the analysis of Sr and Nd isotope compositions (e.g., Bayanova et al. 2009, 2010, Chashchin et al. 2012, Chashchin & Petrov 2013, Chashchin et al. 2016, Grokhovskaya et al. 2000, 2009, Sharkov & Chistyakov 2014). A systematic geological and geochemical characterisation of the entire complex, beyond the mineralised intervals, has not been carried out so far. For this reason, the following section is intended to give a brief overview of the current state of research with respect to the origin of the sulfide mineralisation in the Monchegorsk Complex.

Massive sulfide veins

The lower portions of the NKT Massif and the Sopcha intrusion host several vertical to sub-vertical, massive sulfide veins, which cross-cut layered peridotites and orthopyroxenites (Fig. 9 C-D). The contacts between the veins and the silicate host lithologies are generally sharp, although a cm-thick halo of disseminated sulfide mineralisation occurs in the contact zone (Dedeev et al. 2002). These veins can be traced over 6 km along strike and attain a thickness of up to 2 m (cf. Chapter 6) (Dedeev et al. 2002). The vertical extent of these veins may be as much as 400 m (Kozlov 1973). Notably, the sulfide veins are closely associated with dioritic to gabbronoritic pegmatites, which gradually replace the sulfide mineralisation in the upper parts of the vein system (Sharkov & Chistyakov 2014). Two types of massive sulfide veins have been documented: Ni-rich and Cu-rich veins. The Ni-rich veins are dominated by pyrrhotite and pentlandite with minor chalcopyrite, reaching up to 5.1 wt % Ni, 2.6 wt % Cu and 5.8 ppm Pt + Pd (Yakovlev et al. 1999). In contrast, the Cu-rich veins consist predominantly of chalcopyrite with minor pyrrhotite and pentlandite. Disseminated sulfide mineralisation is commonly associated with the

immediate host rocks. The Cu-rich veins have average metal concentrations of 1.1 wt % Ni, 9.4 wt % Cu, 8.54 ppm Pt and 20.45 ppm Pd (Yakovlev et al. 1999). Individual samples may reach up to 12.1 wt % Cu and 78 ppm PGE.

According to Sharkov & Chistyakov (2014), these veins represent cooling joints that were filled with interstitial silicate melt and sulfide liquid from the ultramafic cumulates. These authors argued that upon opening of the cooling joints, the liquid components of the cumulate were sucked into these joints. Subsequently, the dense sulfide liquid collected at the bottom of the joint, whereas the silicate melt crystallised above.

Disseminated sulfide mineralisation

The relatively unaltered NKT Massif and the Nyud intrusion host the so-called *basal deposit*, which occurs in the contact zone between the intrusion and the basement gneisses. The sulfide mineralisation is largely disseminated and the thickest mineralised intersections reach 40 to 50 m with sulfide contents as high as 20 vol % (Dedeev et al. 2002). The sulfide mineralisation mainly comprises pyrrhotite, pentlandite, chalcopyrite and pyrite with minor bornite, cubanite, violarite and sphalerite. The sulfides generally occur interstitial to silicates and as irregular blebs and droplets of up to 30 mm in diameter. Limited geochemical analyses of NKT Massif samples yielded metal concentrations of up to 0.55 wt % Ni, 0.14 wt % Cu and 4.2 ppm Pt + Pd (Dedeev & Kozyrev 2000). The origin of this type of mineralisation, however, remains unknown.

Another significant occurrence of disseminated sulfide mineralisation is associated with the central part of Mt. Sopcha. Orthopyroxenites from the *Pyroxenite Zone* host an up to 6-m-thick interval of coarse- to medium-grained, mineralised dunite, harzburgite and olivine-orthopyroxenite, known as the *Horizon 330*, the *Peridotite Layer* or simply the *Sopcha Reef* (Fig. 7). The mineralised interval can be traced around the exposed portions of Sopcha and drilling confirmed its lateral continuity across the intrusion, although it is locally offset by faulting (Smolkin & Neradovsky 2006). The lower contact of the reef is sharp with an *autobreccia* at the bottom, whereas the upper contact appears to be gradational into typical Sopcha

orthopyroxenites (Konnikov & Orsoev 1991). The sulfide mineralisation consists of chalcopyrite, pyrrhotite and pentlandite with minor millerite, bornite and pyrite. Typical metal concentrations in the ores average at 0.5 wt % Ni, 0.17 wt % Cu and 0.9 ppm Pt + Pd (Dedeev et al. 2002, Yakovlev et al. 1999). Grokhovskaya et al. (2003) reported somewhat higher precious metal concentrations, ranging from 1.8 to 8.0 ppm PGE. The origin of the reef is not fully understood; however, one of the current models envisages that the crystallisation of the Sopcha intrusion was interrupted by an injection of a sulfide-undersaturated primitive melt into semi-consolidated Sopcha orthopyroxenites. Subsequently, sulfide saturation was triggered in response to *in situ* fractionation of this primitive melt batch, which resulted in the concentration of the chalcophile metals (e.g., Smolkin & Neradovsky 2006). In contrast, Sharkov & Bogatikov (1998) suggested that the primitive melt injection was enriched in volatiles and fluids, derived from crustal rocks, which concentrated the PGE. Upon cooling of the PGE- and fluid-rich primitive melt, platinum-group minerals (PGM) crystallised at physical barriers, such as in the colder contact zone between the injected melt and the underlying orthopyroxenites.

The laterally discontinuous *Critical Horizon*, located in the central portions of the Nyud intrusion, also contains significant sulfide mineralisation. Sharkov & Chistyakov (2014) reported that the mineralisation is hosted by numerous micronoritic bodies that cut across the layered noritic lithologies of the Nyud intrusion. In addition, these micronorites commonly host abundant hornfels xenoliths from the Archean basement. Most of the sulfide mineralisation occurs finely disseminated, although massive lens-like bodies are also present (Kozlov 1973). Individual samples may reach up to 2.37 wt % Ni, 0.73 wt % Cu and 1.48 ppm Pt + Pd (Dedeev et al. 2002). Sharkov & Chistyakov (2014) suggested that the Critical Horizon also formed in response to the opening of cooling joints, which were subsequently filled with interstitial silicate melt and sulfide liquid, similar to the massive sulfide veins in the NKT Massif and the Sopcha intrusion.

Chromite layers in the Dunite Block

The Dunite Block, representing the lowermost portion of the Monchepluton, hosts stratiform chromite mineralisation, known as the *Sopcha Lake* deposit (Russian: *Sopcheozero*). The chromite mineralisation ranges from 3 to 32.5 m in thickness and has a footprint of approximately 280 x 1,400 m (Dedeev et al. 2002). The ore body is characterised by commonly occurring schlieren of massive chromite, although disseminated chromite is also present. The central portions of the layers have the highest Cr_2O_3 concentrations, reaching up to 52 wt %, but the grades decrease towards the margins of the block; Chashchin et al. (1999) reported up to 2.7 ppm PGE in the chromitites.

Reef-style PGE mineralisation in the Vuruchuaivench Massif

In the late 1990s, stratiform PGE mineralisation has been discovered in the upper portion of the Vuruchuaivench intrusion, represented by leucogabbronorites and minor anorthosites (e.g., Grokhovskaya et al. 2000, Pripachkin & Rundkvist 2008). The mineralised reef has been confirmed for approximately 5 km along strike (Fig. 7). The thickness generally varies from a few decimeters to 25 m (Grebnev et al. 2014). The sulfide mineralisation occurs finely disseminated in sheet- and lens-like bodies and comprises millerite, chalcopyrite, pyrrhotite, pyrite and minor pentlandite (Grokhovskaya et al. 2000). The entire intrusion is pervasively altered to actinolite and sericite, although primary rock textures are preserved. Based on rare earth element variations across the intrusion, Grebnev et al. (2014) argued that the PGE reef formed in response to sulfide saturation, triggered by extensive fractionation in a large magma chamber. In contrast, Grokhovskaya et al. (2000) suggested on the basis of the presence of Pd-arsenides and -bismuthotellurides as the principal PGE hosts that a late-stage magmatic fluid exsolved from the magma and concentrated the PGE together with other elements, such as S, As, Te, Se, and Hg.

2.2.5 Outstanding problems

Although a number of geological and geochemical studies have been published on different issues associated with the formation of the Monchegorsk Complex, one of the most important unresolved question is the timing and duration of magmatism in the Monchegorsk area, and by extension, the Fennoscandian Shield as a whole (e.g., Bayanova et al. 2009). Notably, there appears to be a distinct correlation between the development of macroscopic layering and the occurrence of sulfide mineralisation in layered intervals of the Monchegorsk Complex (e.g., Sopcha Reef, Vuruchuaivench). This observed correlation requires further examination in order to establish whether layering can be directly linked to the presence of sulfide mineralisation. Furthermore, the mechanisms leading to the pronounced layering in layered intrusions are not well understood either. Moreover, the origin of the different disseminated sulfide occurrences in the Monchegorsk Complex and their genetic relationships to each other remain poorly understood. Especially the formation and the timing of emplacement of the massive sulfide veins are essentially unknown. As most studies focused on the description of the mineralisation, a thorough geological and geochemical analysis to determine the mineralisation style has never been carried out. Hence, it remains debatable whether the reefs in the Monchegorsk Complex can be compared to those in other well-studied layered intrusions, such as the Bushveld or Stillwater complexes.

The subsequent chapters on the Monchegorsk Complex are aimed at exploring the geological and geochemical characteristics of disseminated sulfide mineralisation in various parts of the complex to allow for a classification of the different mineralisation style in relation to known sulfide occurrences in other layered intrusions. Additionally, first-order field observations will be coupled with geochemical data to constrain the origin of the mineralisation, including the cross-cutting massive sulfide veins. Ultimately, determining key controls for the formation of the different mineralisation styles will have important implications for the emplacement of the Monchegorsk Complex and the development of layering in large layered intrusions in general.

Chapter 3

Methodology

3.1 *In situ* Sr isotope analysis of plagioclase

The analysis of *in situ* Sr isotope compositions of plagioclase was conducted on a Photo Machine Analyte G2 laser microprobe coupled to a Nu Plasma HR multicollector inductively coupled mass spectrometer (LA-MC-ICP-MS) at the Geological Survey of Finland in Espoo. The analytical conditions were largely similar to those reported by Yang et al. (2013), who used a slightly modified methodology from that described by Ramos et al. (2004, 2005). The analyses were produced in static ablation mode using a beam diameter of 145 to 200 μm, a pulse frequency of 10 Hz and a beam intensity of 2.07 J/cm^2. The beam diameter, however, is generally too large to resolve small-scale zonation of interstitial plagioclase in thin section. Since the depth to diameter ratio of the ablation pits was typically well below 1, defocusing and element fractionation were not an issue (e.g., Mank & Mason 1999). The samples were ablated in a HelEx ablation cell with a He gas flow of 0.4 and 0.1 l/min. The multicollector ICP-MS is fitted with 9 Faraday detectors and amplifiers with $10^{11}\Omega$ resistors and it was set up to measure the following isotopes ^{84}Sr-Kr,

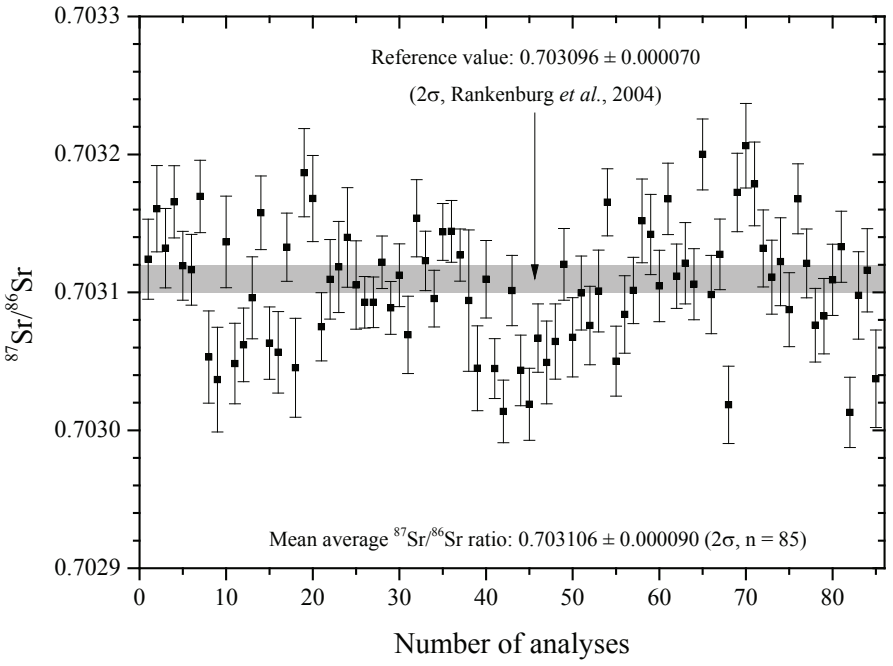

Fig. 11. Measured *in situ* Sr isotope compositions of the in-house standard MIR a. The error bar represents 2σ.

^{85}Rb, ^{86}Sr-Kr, ^{87}Rb-Sr and ^{88}Sr in static mode. A review of potential factors affecting the data quality of Sr isotope analysis by LA-MC-ICP-MS were summarised in great detail by Vroon et al. (2008). According to these authors, one of the main problems with the method is the instrumental mass discrimination and the laser-induced elemental and isotopic fractionation. Correction of these two factors was performed using an exponential correction and a $^{86}Sr/^{88}Sr$ ratio of 0.1194. Moreover, the isobaric interference of ^{87}Rb on ^{87}Sr was corrected with the ^{85}Rb signal and a $^{87}Rb/^{85}Rb$ ratio of 0.38571. Waight et al. (2002) also noted that Ca argides could interfere with the masses of the different Sr isotopes in samples with high Ca/Sr ratios, such as plagioclase. This interference, however, can be corrected by monitoring the $^{42}Ca^{40}Ar/^{42}Ca^{40}Ca$ peak on mass 82, although Ramos et al. (2004) did not observe this interference in a Ca/Sr ratio range between 50 and 500. The Ca/Sr ratio for the samples used in this study were generally < 250. Prior to each ablation, a background measurement of 30 s allowed for the correction of the isobaric interference of ^{86}Kr on ^{86}Sr. The measured isotope ratios were then age-corrected to 2,055 Ma using the $^{87}Rb/^{86}Sr$ ratio and a ^{87}Rb decay constant of 1.393 x 10^{-11} y^{-1} (Nebel et al. 2011). The average total Sr signal obtained for plagioclase samples was 0.4 V. Under these conditions, 120 s of ablation were needed to obtain an internal precision of $\leq \pm$ 0.000070 (1σ). The repeated analysis of an in-house plagioclase standard after approximately every ten measurements on the sample verified the accuracy of the LA-MC-ICP-MS protocol (Fig. 11). The in-house plagioclase standard (MIR a) is an isotopically homogeneous plagioclase megacryst from a lava of the Dutsin Miringa Hill volcano (Northern Cameroon Line) and has a reference $^{87}Sr/^{86}Sr$ ratio of 0.703096 $\pm$ 0.000070 (2σ, Rankenburg et al. 2004), determined by thermal ionisation mass spectrometry (TIMS). The measurement of the standard throughout the entire analytical session yielded an average $^{87}Sr/^{86}Sr$ ratio of 0.703106 $\pm$ 0.000090 (2σ, n = 85), which is in accordance with the reference ratio of the standard. Multiple analyses of the USGS Microanalytical Reference Material *BHVO-2G* ($^{87}Rb/^{86}Sr = 0.065$) gave an average $^{87}Sr/^{86}Sr$ ratio of 0.703476 $\pm$ 0.000139 (2σ, n = 10), which agrees with the GeoREM preferred value of 0.703469 $\pm$ 0.000014 (2σ, Elburg et al. 2005). Since the Rb/Sr ratio of the reference material BHVO-2G is

an order of magnitude higher than that of the analysed plagioclase crystals and the in-house plagioclase standard (MIR a), the Rb interference correction within the Rb/Sr range of the samples is validated.

3.2 Mineral chemistry

Major element compositions of rock-forming minerals were determined, using a Zeiss Sigma HD Analytical Field Emission Gun SEM equipped with two Oxford Instruments 150 mm^2 EDS detectors at Cardiff University. Analyses were carried out using an accelerating voltage of 20 kV, 2.5 nA beam current, a spot size of 10 µm and a counting time of 30 s. Natural minerals and synthetic metals from *Astimex Ltd.* were used for calibration. Diopside, olivine and plagioclase from the same supplier were measured during the analytical runs to monitor instrumental drift.

3.3 Elemental mapping

High-resolution element maps of entire thin sections were collected, using a Zeiss Sigma HD Analytical Field Emission Gun Scanning Electron Microscope (SEM) equipped with two Oxford Instruments 150 mm^2 EDS detectors at Cardiff University. Mapping was performed using an accelerating voltage of 20 kV, 2.5 nA beam current, a pixel size of 8.6 µm and a dwell time of 3 ms per pixel. Natural minerals and synthetic metals from *Astimex Ltd.* were used for calibration. Diopside, olivine and plagioclase from the same supplier were measured during the analytical runs to monitor instrumental drift. The modal mineralogy was determined using computed phase images, which are based on X-ray spectra collected for each pixel of the thin section. Binning of the spectra was followed by a manual phase classification of each characteristic X-ray spectrum for all phases > 0.1 vol %.

3.4 Lithophile element analysis

Whole rock major and trace elements were analysed at Cardiff University using a JY Horiba Ultima 2 inductively coupled plasma optical emission spectrometer (ICP-OES) and a Thermo Elemental X7 Series inductively coupled plasma mass spectrometer (ICP-MS). After heating approximately 2 g of each sample for two hours in a muffle furnace at 900 °C, the Loss on Ignition (LOI) was determined gravimetrically. A mass of 0.100 g of the ignited residue was mixed with 0.400 g of Li metaborate flux (Alfa Aesar Spectroflux 100B) in a Pt-Rh crucible. Approximately 0.5 ml of a lithium iodide solution was added to the mixture as a non-wetting agent. After fusing the mixture in a Claisse Fluxy automated fusion system, the melt was dissolved in 50 ml of dilute HNO_3 in a teflon beaker with a magnetic stirrer on a hot plate. Subsequently, the solution was spiked with 1 ml of 100 ppm Rh spike solution as an internal standard and diluted to a total volume of 100 ml with de-ionised water. A detailed description of the methodology can be found in McDonald & Viljoen (2006).

3.5 Chalcophile metal analysis

The PGE concentrations were determined by nickel-sulfur fire assay at Lab-MaTer, Université du Québec at Chicoutimi in Canada, following the analytical protocol outlined by Savard et al. (2010). For this, 15 g of same sample powder that was used for the lithophile element analysis, were thoroughly mixed in a ceramic crucible with 10 g sodium carbonate, 15 g sodium tetraborate, 5 g nickel, 5 g silica and 3 g sulfur. The mixture was covered by a further 15 g of sodium tetraborate, before it was fused in a muffle furnace for 90 min at 1050 °C.

Table 1. Comparison of results obtained at LabMaTer and the accepted values for international standards

	KPT				**LK-NIP**		
	LabMaTer (n = 8)		*LabMaTer*		*LabMaTer (n = 7)*		*Geolabs*
	This run	1 σ	working value[a]	1 σ	This run	1 σ	Certificate
Os (ppb)	2.08	0.43	2.80	0.19	0.01	0.02	n.v.
Ir	5.98	0.91	6.62	0.74	0.17	0.01	0.19
Ru	15.93	0.59	16.85	0.93	0.45	0.04	0.44
Rh	14.09	1.51	15.35	1.24	0.85	0.06	0.90
Pt	103.91	28.68	97.40	20.99	12.79	0.76	13.43
Pd	121.51	18.95	123.40	18.60	16.18	1.44	17.96
Au	40.71	8.49	37.33	11.55	4.26	1.05	4.63

	WMS-1a						**Blank**	
	LabMaTer (n = 2)		*LabMaTer*		*CANMET*		*LabMaTer (n = 36)*	
	This run	1 σ	working value[a]	1 σ	Certificate	1 σ	This run	1 σ
Os (ppb)	120.00	1.94	135.40	4.60	150.00	n.v.	0.18	0.06
Ir	337.01	3.08	338.50	4.50	322.00	10.00	0.01	0.01
Ru	143.98	2.35	147.10	1.30	145.00	7.00	0.03	0.01
Rh	254.30	3.51	254.60	2.90	222.00	15.00	0.02	0.01
Pt	1962.89	35.18	2032.00	45.40	1910.00	70.00	0.12	0.06
Pd	1572.23	24.49	1534.30	36.12	1450.00	50.00	0.51	0.19
Au	220.65	1.92	311.60	30.80	300.00	43.00	1.23	0.16

KPT = Quartz diorite (in-house LabMaTer)
LK-NIP = Nipigon Diabase (Geolabs)
WMS-1a = Wellgreen massive sulfide (CANMET)
[a] = Savard et al. (2010)
n.v. = no value

After cooling, the NiS bead was separated from the slag and fully dissolved in 180 ml of concentrated HCl in a closed PFA jar, which was placed in a vented oven at 110 °C. Subsequently, 10 ml of a stannous chloride solution and 4 ml of a tellurium solution were added to the dissolved bead to co-precipitate all noble metals. After another 24 hours in the vented oven, the black precipitate was vacuum-filtered through a cellulose membrane filter and rinsed with ca. 50 ml dilute HCl. The filter was then dissolved in a mixture of 2 ml HCl and 2 ml HNO_3 in the PFA jar and placed on a hot plate for 12 hours. Lastly, the digested filter was diluted with de-ionised water to a volume of 25 ml. Gold and PGE were analysed using a Thermo Elemental X7 Series ICP-MS. The instrumental drift was monitored with a thallium spike and a multiple PGE-Au and Re stock solution was used for external calibration

of the instrument. Under these conditions, the limits of detection were 0.024 ppb Ru, 0.027 ppb Rh, 0.573 Pd, 0.192 Os, 0.020 Ir, 0.174 Pt and 0.490 Au (three times the standard deviation of 36 analysed blanks based on the IUPAC definition; Long & Winefordner 1983). Analytical precision and accuracy are given in Table 1.

3.6 Sulfur analysis

Sulfur concentrations were measured by infrared spectrometry using a HORIBA EMIA 220-V at LabMaTer, Université du Québec at Chicoutimi in Canada, following the methodology outlined by Bédard et al. (2008). Typically, 0.1 to 0.3 g sample powder were covered with 1 g iron, 2 g tungsten and 0.3 g tin, all of which acted as accelerators. The sample was then heated in an O_2 flux by an induction furnace and the volatilised gases were analysed by an infrared detector. The detection limit under these conditions was 22 ppm (Bédard et al. 2008).

Chapter 4

In situ Sr isotope compositions of plagioclase from a complete stratigraphic profile of the Bushveld Complex

Parts of this chapter were submitted as:
Karykowski, B. T., Yang, S.-H., Maier, W. D., Lahaye, Y., Lissenberg, C. J., O'Brien, H. (minor revision). In situ Sr isotope compositions of plagioclase from a complete stratigraphic profile of the Bushveld Complex, South Africa: Evidence for extensive magma mixing and percolation. *Journal of Petrology*.

Co-author contributions:
W. D. Maier, C. J. Lissenberg and S.-H. Yang were involved in discussions during the writing of the manuscript. Y. Lahaye and H. O'Brien supervised LA-MC-ICP-MS analyses.

Abstract

The cumulates of the Bushveld Complex, forming the largest known layered intrusion on Earth, are known to have crystallised from several isotopically distinct magma pulses. Here, we present *in situ* Sr isotope compositions combined with the corresponding mineral chemistry of plagioclase from all lithological zones, covering $>$ 6 km of stratigraphy to constrain the petrogenesis of the complex.

The *in situ* data coupled with high-resolution elemental maps of individual plagioclase grains reveal complex zonation patterns with respect to mineral chemistry and Sr isotope composition. This suggests that interstitial plagioclase in the Bushveld Complex crystallised from multiple isotopically distinct influxes of melt, percolating through a mafic cumulate framework and displacing the resident melt. Similarly, cumulus plagioclase grains are the result of continual ingress of distinct magma, which picked up previously formed plagioclase crystals.

Sr isotope compositions across the layered sequence seem to be largely decoupled from fractionation indices, such as Mg#, anorthite content or trace element ratios. As these observations cannot be explained by bulk assimilation, we propose that the elevated Sr isotopic signature of the Bushveld cumulates may have resulted from the interaction of the parental magma with a fluid derived from the up to 2-km-thick dolomitic footwall, which caused a major shift in Sr isotope composition without significantly affecting the degree of fractionation or trace element signature.

The decarbonation and/or assimilation of dolomite during the intrusion of the Bushveld Complex may be of major importance not only for the petrogenesis, but also for the emplacement of the layered intrusion as devolatilisation is directly linked to space creation due to volume loss, thus producing a lopolith.

4.1 Introduction

Recent technical developments in the analysis of radiogenic isotope ratios allowed for the progression from powdered whole rock-based isotope measurements to the *in situ* isotope analysis at the single-crystal and sub-grain scale (e.g., Ramos et al. 2004, 2005, Charlier et al. 2006, Müller et al. 2000, 2002). A number of *in situ* isotope studies on magmatic rock samples have shown that single grains may exhibit primary isotopic heterogeneity, even at the sub-grain scale (e.g., Charlier et al. 2007, Davidson et al. 1998, Chadwick et al. 2007). As radiogenic isotope ratios remain unaffected by melting and crystallisation, they can be used as a powerful petrogenetic tool for tracing source contributions in a given magmatic succession (e.g., Faure 1986). This provides a unique opportunity to study magmatic processes operational during an open system magma chamber evolution (e.g., Gagnevin et al. 2005, Davidson et al. 2007, Gao et al. 2015, Ginibre & Davidson 2014). For example, Sr-Nd isotope disequilibrium between clinopyroxene and plagioclase in samples from the Xiaohaizi layered intrusion in NW China suggests the crystallisation of these minerals from geochemically distinct magmas (Wei et al. 2014). Moreover, disequilibrium Sr isotope compositions of plagioclase within single thin sections from the Baima layered intrusion in SW China were interpreted to result from the co-accumulation of cumulus plagioclase that had crystallised from different magmas (Liu et al. 2014). On the basis of Sr isotopic zoning in single plagioclase crystals from the Rum layered intrusion in Scotland, Tepley & Davidson (2003) were able to elucidate the events during crystal growth in a magma undergoing contamination.

As the largest known layered intrusion on Earth, the Bushveld Complex has traditionally received considerable attention from the isotope community (Cawthorn 2015, and references therein). Early Sr isotope studies on powdered whole rock samples and mineral separates by Eales et al. (1990b), Kruger & Marsh (1982), Kruger (1990), Lee & Butcher (1990) and Sharpe (1985) have provided a large body of isotope data across the Bushveld Complex, which have been complemented and synthesised by Kruger (1994). Distinct shifts in Sr isotope compositions have been identified across the layered sequence of the complex. These variations subsequently

served as a basis for the subdivision of the Bushveld Complex into several zones, broadly reflecting distinct parental magma compositions (Kruger 1994). These zonal subdivisions, however, are not necessarily unambiguous: Sr isotope compositions of Upper Zone lithologies from the Bethal limb are significantly less radiogenic compared to Upper Zone samples from the other limbs (Kruger 2005). The author interpreted this as evidence for the crystallisation of the Upper Zone from a mixed magma, whereas the Bethal limb recorded the Sr isotope composition of the less radiogenic end-member before mixing.

Moreover, Eales et al. (1990a) recognised Sr isotope disequilibrium between plagioclase and coexisting orthopyroxene in some samples from the Upper Critical Zone of the western Bushveld. Similar results were also reported by Roelofse & Ashwal (2012) for the lower Main Zone of the northern Bushveld. Further, Sr isotope compositions of plagioclase separates from the Merensky and Bastard Cyclic Units in the eastern Bushveld, analysed by Seabrook et al. (2005), show typical Main Zone Sr isotopic signatures. Harmer et al. (1995) conducted the first systematic Pb isotope study across the Bushveld Complex, concluding that Pb isotopes vary systematically in a similar manner to Sr isotope ratios. However, later studies by Mathez & Waight (2003) and Mathez & Kent (2007) also showed Pb isotope disequilibrium between different plagioclase populations as well as between coexisting plagioclase and sulfide. Further, Schoenberg et al. (1999) demonstrated Os isotope disequilibrium between cumulus chromite and interstitial material in different chromitites from the Bushveld Complex. In addition, disequilibrium Nd isotope compositions between plagioclase and orthopyroxene have been reported by Prevec et al. (2005). These authors argued that orthopyroxene crystallised early on from a contaminated magma, whereas plagioclase was subsequently derived from a relatively uncontaminated magma.

The first *in situ* study of Sr isotope compositions in the Bushveld Complex was conducted by Chutas et al. (2012), using a microdrilling technique. This method confirmed previous results of Sr isotope disequilibrium between coexisting plagioclase and orthopyroxene in the Critical Zone of the eastern Bushveld. Moreover, the authors recognised disequilibrium between orthopyroxenes from the Lower Zone.

Yang et al. (2013) were the first to produce *in situ* Sr isotope data for Bushveld plagioclase using LA-MC-ICP-MS. Their study focused on samples from the Upper Critical Zone of the western Bushveld. Disequilibrium between plagioclase rims and cores, and between cores of different plagioclase grains in a single sample was reported. These results were interpreted to reflect the co-accumulation of plagioclase grains from different parental magmas followed by further crystal growth in a residual liquid, infiltrating from other portions of the cumulate pile. The study demonstrated that the method is capable of effectively tracing the lineage of individual plagioclase crystals in a sample. More recently, Roelofse et al. (2015) and Mangwegape et al. (2016) produced *in situ* plagioclase Sr isotope data for the Main and Upper zones of the northern Bushveld. The latter authors followed the two-stage model by Kruger (1994), arguing that the upper part of the Main Zone and the Upper Zone formed primarily in response to normal fractionation, whereas the lower part of the Main Zone originated from the repeated influx of magmas. Based on isotope disequilibrium between and within co-existing cumulus minerals, Roelofse et al. (2015) suggested that these influxes were essentially variably contaminated crystal mushes.

The observation of Sr isotope disequilibrium has important implications for the formation of the sampled lithology, and, by extension, for the complex as a whole. Particularly in samples from stratigraphic levels where influxes of geochemically distinct magma are known, mineral-scale isotope analyses have the potential to shed light upon changes in isotope composition of a magma during crystal growth, e.g., magma mixing and/or interaction with crustal lithologies. In this study, we present coupled major element and *in situ* Sr isotope data of plagioclase from a composite profile at the Union Section and Bellevue, covering the entire stratigraphy of the Bushveld Complex with the aim of constraining key petrogenetic aspects of the largest known layered intrusion on Earth.

4.2 Samples

The thirty-seven samples used for this study are from the western and northern limbs of the Bushveld Complex. The Marginal, Lower and Critical zones were sampled from drill cores NG1, NG2 and NG3, respectively, whereas the Main Zone samples were taken from the exploration drill core SK-2. All these boreholes were drilled at the Union Section of the western Bushveld Complex (Fig. 2). The Upper Zone samples are from the Bellevue drill core BV-1, drilled in the northern limb of the intrusion. The Union Section samples were previously described in detail by Teigler (1990) and Mitchell (1990), whereas Barnes et al. (2004) and Ashwal et al. (2005) provided petrographic descriptions and geochemical data for the Upper Zone samples from the Bellevue core.

A major reversal in mineral compositions coupled with a shift in Sr isotopic signature at the level of the Pyroxenite Marker is taken to represent the boundary between the Main Zone and the Upper Zone (Fig. 3). This transition can be clearly pinpointed in the eastern and western limbs, whereas in the northern limb the boundary has not been defined so far. Ashwal et al. (2005) described two pyroxene-rich layers and a thick troctolitic horizon in the BV-1 drill core. However, the authors argued that neither of these represent the equivalent of the Pyroxenite Marker from the eastern or western limbs. A common stratigraphic feature among all three limbs is the first appearance of cumulus magnetite in the Upper Zone, which we use in the present study to correlate both drill sections (cf. Ashwal et al. 2005). This marker horizon occurs some 550 m above the Pyroxenite Marker at the Union Section, whereas in drill core BV-1 from the northern limb this level corresponds to a depth of 1575.8 m (Ashwal et al. 2005, Mitchell 1990). The uppermost Main Zone sample was collected 250 m below the Pyroxenite Marker at the Union Section. To ensure sample coverage between the uppermost Main Zone sample and the first appearance of cumulus magnetite, the lowermost sample from the northern limb was collected about 400 m below the first appearance of cumulus magnetite. Therefore, the entire profile of the Bushveld Complex should be represented in the studied sample set, covering some 6.4 km of igneous stratigraphy. On the one hand,

the sample selection was intended to represent typical rock types from each zone, covering cumulus as well as intercumulus plagioclase in zone that host both (Critical Zone, Main Zone). It is worth noting that the entire Lower Zone is characterised by interstitial plagioclase, except for a 2.9-m-thick norite interval in the central part of the zone. The distinction between isotopic heterogeneity in cumulus and intercumulus plagioclase, respectively, has important implications as these two may record processes at different stages of cumulate formation. On the other hand, the aim of the sampling was to ensure complete coverage of the Bushveld stratigraphy at a relatively consistent spacing. Additionally, drill core samples were selected that exhibited the least degree of macroscopic alteration.

4.3 Results

While the *in situ* analyses of Sr isotopes in plagioclase broadly reproduces the whole rock Sr isotopic variation across all zones of the Bushveld Complex, certain differences were also revealed. The error-weighted average *in situ* Sr isotopic variation, together with the corresponding anorthite contents and its FeO concentrations, are shown in Figure 12 and Table 2. Additionally, Figure 13 shows the individual *in situ* analyses coupled with anorthite contents for every sample. The full dataset of the analyses is provided in Appendix C.

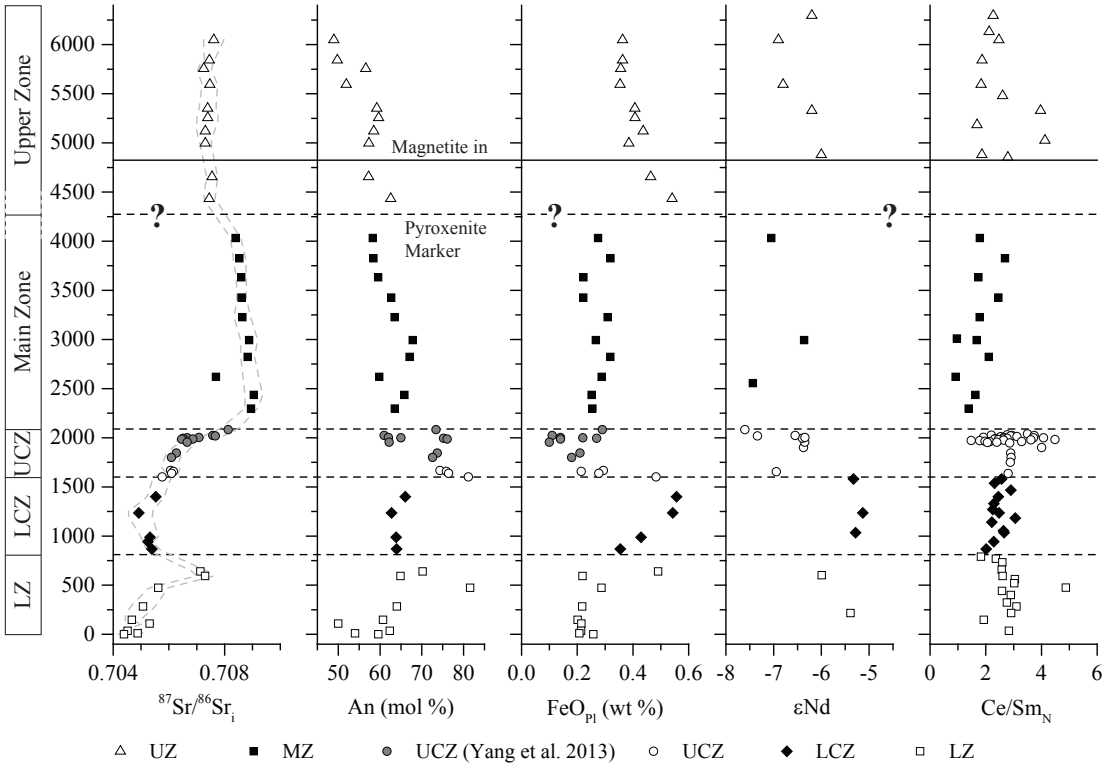

Fig. 12. Plot of error-weighted average *in situ* $^{87}Sr/^{86}Sr_i$ ratios together with the average anorthite contents, the average FeO concentrations in plagioclase, εNd values from Maier et al. (2001, 2013) and chondrite-normalised Ce/Sm ratios against stratigraphic height. Trace element data were taken from Maier et al. (2013). Normalisation values were taken from McDonough & Sun (1995). Abbreviations: UZ = Upper Zone; MZ = Main Zone; UCZ = Upper Critical Zone; LCZ = Lower Critical Zone; LZ = Lower Zone.

4.3.1 Lower Zone

The analysed samples from the ultramafic Lower Zone (LZ) mainly comprise dunite, harzburgite, pyroxenite, norite and gabbronorite. Generally, norites are

Table 2. Error-weighted average *in situ* Sr isotope compositions, anorthite contents and FeO concentrations of plagioclase, Union Section, western Bushveld Complex. Initial $^{87}Sr/^{86}Sr_i$ is re-calculated to 2,055 Ma (Zeh et al. 2015). The number of analyses per sample is given as "n"

Sample	Height (m)	Unit	Rock	$^{87}Sr/^{86}Sr_i$	2σ	An	FeO (wt %)	n
351.70A	6049	UZ	Mt	0.70761	0.00015	48.9	0.36	21
559	5842	UZ	Mt-G	0.70745	0.00010	49.8	0.36	15
644.8	5756	UZ	Mt	0.70725	0.00014	56.6	0.36	14
806.02	5595	UZ	Mt-G	0.70747	0.00015	51.9	0.35	16
1049.26b	5352	UZ	Mt-G	0.70739	0.00018	59.2	0.41	12
1144.8	5256	UZ	Mt-G	0.70740	0.00026	59.7	0.41	12
1279.93	5121	UZ	Mt-G	0.70731	0.00017	58.5	0.44	16
1404.35	4996	UZ	Mt-G	0.70731	0.00012	57.3	0.39	12
1745.45A	4655	UZ	G	0.70755	0.00012	57.3	0.46	12
1967.1	4434	UZ	G	0.70745	0.00011	62.6	0.54	16
A1	4032	MZ	GN	0.70840	0.00010	58.3	0.28	16
A35	3826	MZ	GN	0.70853	0.00013	58.4	0.32	14
A65	3633	MZ	GN	0.70860	0.00011	59.6	0.22	13
A106	3426	MZ	GN	0.70861	0.00009	62.7	0.22	14
A141	3227	MZ	GN	0.70864	0.00014	63.5	0.31	19
A168	2994	MZ	GN	0.70888	0.00017	67.8	0.27	15
A206	2822	MZ	GN	0.70883	0.00014	67.1	0.32	13
A238	2620	MZ	GN	0.70769	0.00014	59.8	0.29	15
A271	2436	MZ	GN	0.70905	0.00020	65.8	0.25	14
A297	2297	MZ	Px	0.70895	0.00014	63.6	0.25	13
NG3-146.5	1667	UCZ	Px	0.70606	0.00018	74.4	0.29	15
NG3-156.16	1657	UCZ	An	0.70616	0.00014	75.9	0.21	15
NG3-175.56	1638	UCZ	N	0.70610	0.00014	76.4	0.28	17
NG3-212.93	1601	UCZ	An	0.70576	0.00018	81.1	0.48	15
NG1-163.27	1400	LCZ	Px	0.70553	0.00017	66.0	0.56	15
NG1-327.45	1236	LCZ	Px	0.70492	0.00025	62.8	0.54	14
NG1-575.35	988	LCZ	Px	0.70532	0.00015	63.8	0.43	16
NG1-695.5	868	LCZ	Px	0.70539	0.00013	64.0	0.35	14
NG2-134.4	639	LZ	Dun	0.70713	0.00012	70.2	0.49	15
NG2-180.55	593	LZ	Px	0.70730	0.00019	64.9	0.22	12
NG2-300	474	LZ	Px	0.70562	0.00018	81.6	0.29	16
NG2-490.05	283	LZ	Hz	0.70507	0.00018	64.0	0.22	10
NG2-626.17	147	LZ	Ol-Px	0.70467	0.00018	60.7	0.20	13
NG2-664.35	109	LZ	Hz	0.70531	0.00014	50.0	0.22	12
NG2-737	36	LZ	N	0.70452	0.00015	62.3	0.21	14
NG2-762.27	11	LZ	GN	0.70488	0.00016	54.0	0.21	13
NG2-772.98	0	LZ	GN	0.70439	0.00020	59.6	0.26	12

UZ = Upper Zone, MZ = Main Zone, UCZ = Upper Critical Zone, LCZ = Lower Critical Zone, LZ = Lower Zone
Lithologies: Mt = magnetitite, Mt-G = magnetitite-gabbro, G = Gabbro, GN = gabbronorite, N = norite, A = anorthosite, Px = pyroxenite, Ol-Px = olivine-pyroxenite, Hz = harzburgite; Dun = dunite

rather unusual in the LZ and their origin remains elusive. According to Teigler (1990), norite occurs as a thin interval of 2.9 m in thickness hosted by typical LZ pyroxenite. The initial *in situ* $^{87}Sr/^{86}Sr$ ratio of plagioclase at 2,055 Ma (Sr_i) in the LZ covers a relatively wide range from 0.7037 to 0.7077 (Figs. 12, 13 a). Variations in anorthite content are even more pronounced, ranging from 38.2 to 79.0 mol %, excluding the norite sample, which contains cumulus plagioclase (NG2-300). This sample has an error-weighted average *in situ* Sr_i ratio of 0.7056 ± 0.0002 and an anorthite content of 83.8 ± 0.9 mol %. The error-weighted average *in situ* Sr_i ratios show a relatively small, yet gradual upward increase from 0.7044 at the base to 0.7056 at 474 m (Fig. 14). The next two samples, analysed at 593 and 639 m, have a much higher average Sr isotope composition, reaching 0.7073 and 0.7071, respectively. Notably, this excursion in Sr_i ratios does not correlate with any variation in trace element ratios or Mg# (100 x molar Mg/(Mg+Fe)), even though the anorthite content of these two samples are in line with the general upward increase (Fig. 14, 15).

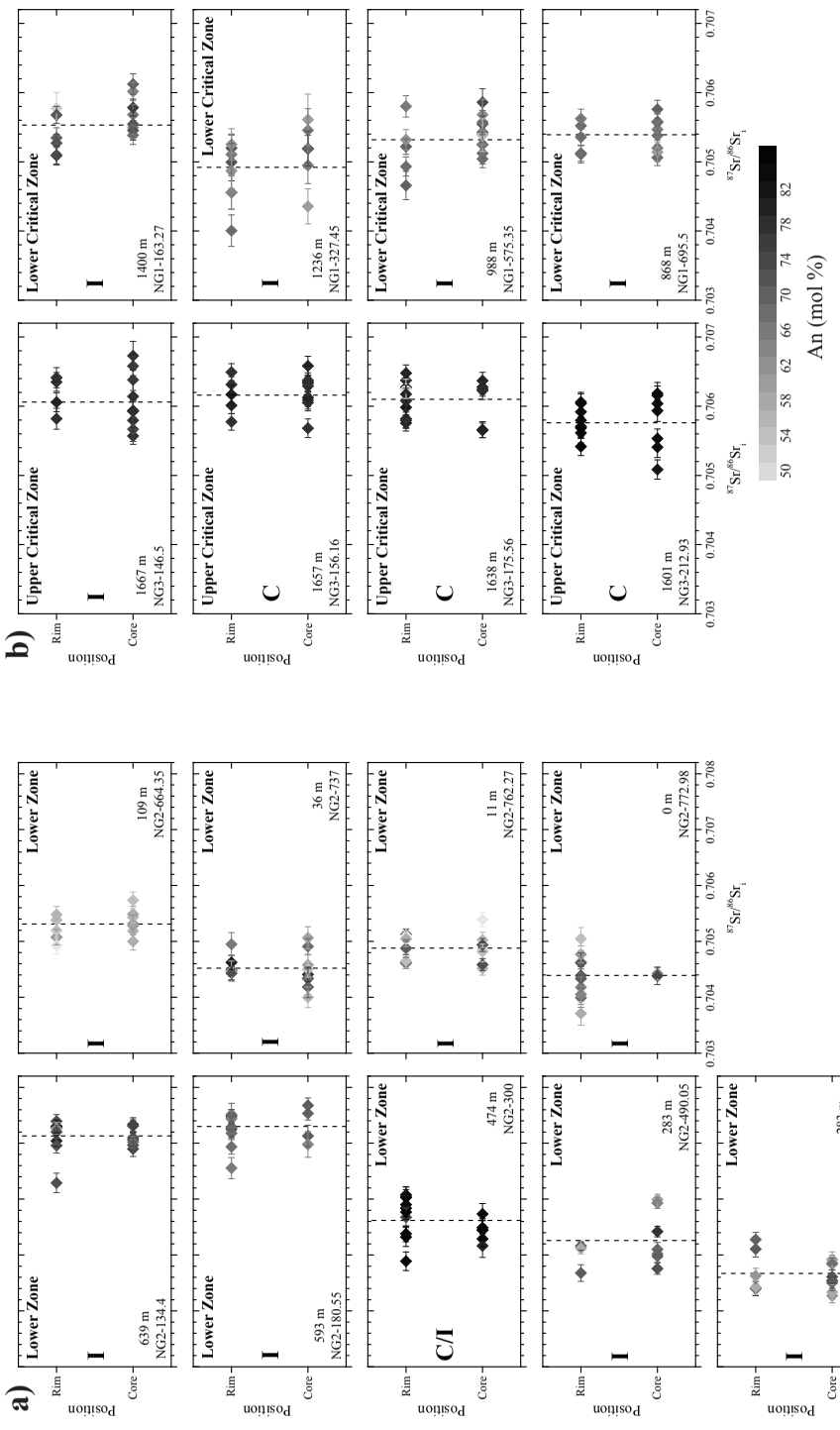

Fig. 13. Intra-sample *in situ* Sr isotope variation coupled with anorthite contents. a) Lower Zone. b) Critical Zone. c) Main Zone. d) Upper Zone. Abbreviations: C = cumulus; I = intercumulus.

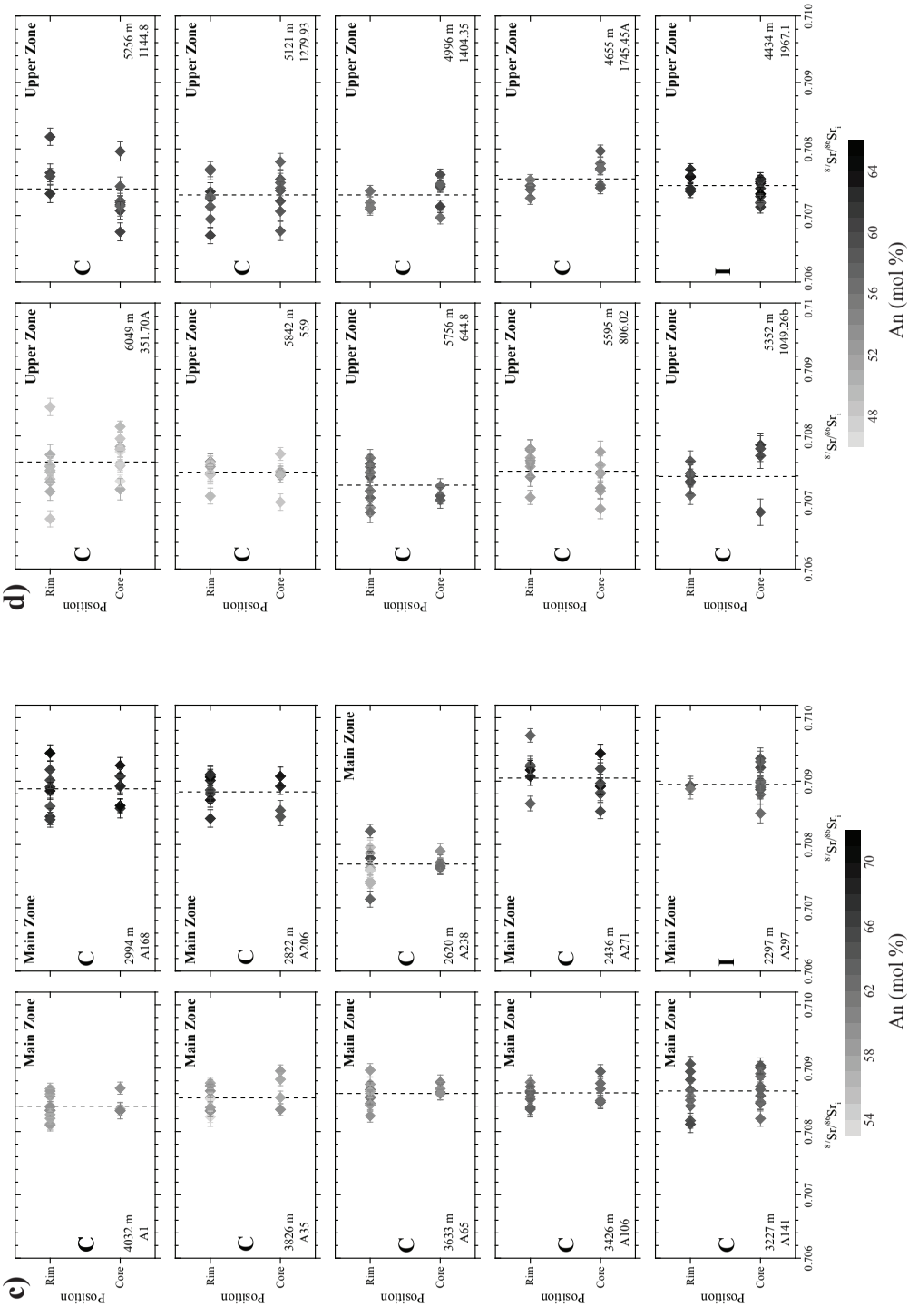
d)
Upper Zone
C
I
Rim
Core
Position
6049 m
351.70A
5842 m
559
5756 m
644.8
5595 m
806.02
5352 m
1049.26b
5256 m
1144.8
5121 m
1279.93
4996 m
1404.35
4655 m
1745.45A
4434 m
1967.1
0.706
0.707
0.708
0.709
0.710
0.71
$^{87}Sr/^{86}Sr_i$
48
52
56
60
64
An (mol %)
c)
Main Zone
4032 m
A1
3826 m
A35
3633 m
A65
3426 m
A106
3227 m
A141
2994 m
A168
2822 m
A206
2620 m
A238
2436 m
A271
2297 m
A297
54
58
62
66
70

Fig. 13 (cont.)

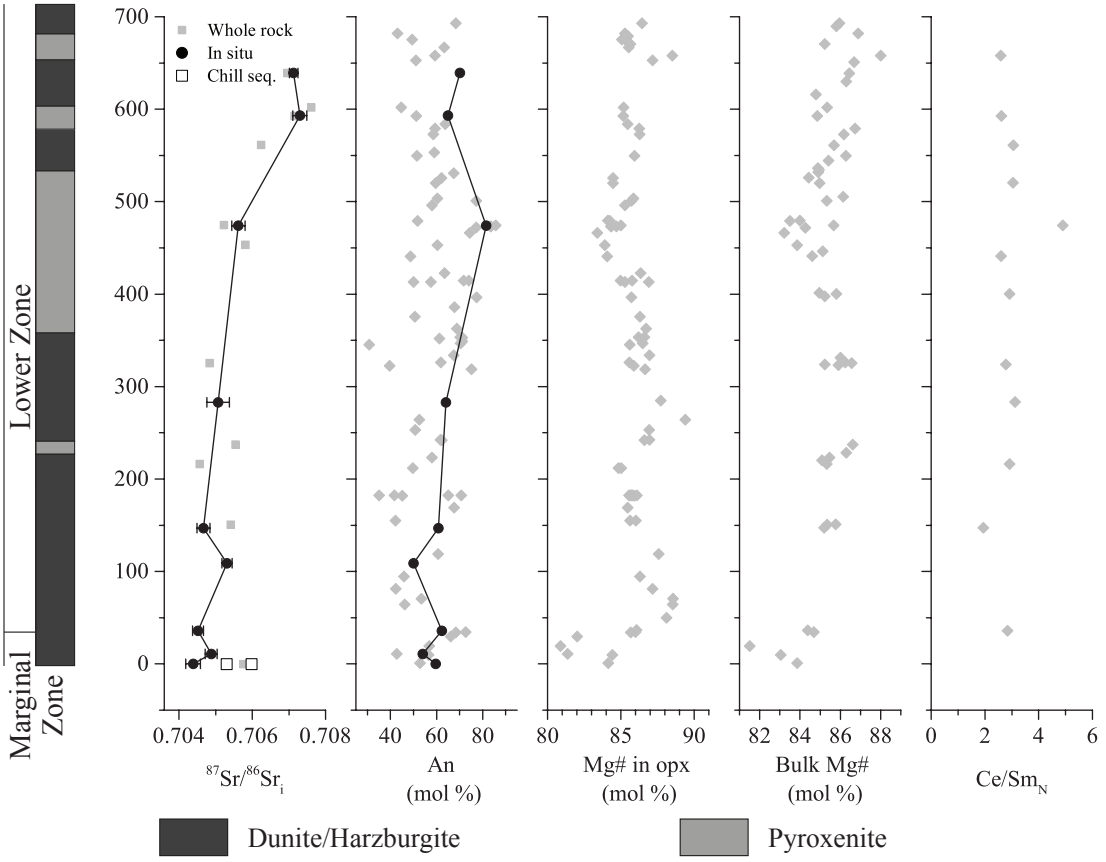

Fig. 14. Plot of error-weighted average *in situ* and whole rock $^{87}Sr/^{86}Sr_i$ ratios together with average anorthite contents, Mg# in orthopyroxene, whole rock Mg# and chondrite-normalised Ce/Sm ratios for the Lower Zone. The standard deviation is represented by the error bar. Whole rock data and mineral compositions were taken from Teigler (1990). Trace element data were taken from Maier et al. (2013). *In situ* Sr isotope data for the chill sequence (Chill seq.) were taken from Maier et al. (2016a). Normalisation values were taken from McDonough & Sun (1995).

4.3.2 Critical Zone

All the analysed samples from the Lower Critical Zone (LCZ) are pyroxenites with interstitial plagioclase, showing *in situ* Sr_i ratios from 0.7040 to 0.7061 (Fig. 13 b). The An content of the analysed grains show considerable variation, ranging from 48.8 to 73.6 mol %. The error-weighted average *in situ* Sr_i ratios cover a relatively narrow range, varying from 0.7049 to 0.7055, showing little change with stratigraphic height (Fig. 16).

The transition from the Lower to the Upper Critical Zone (UCZ) is defined by

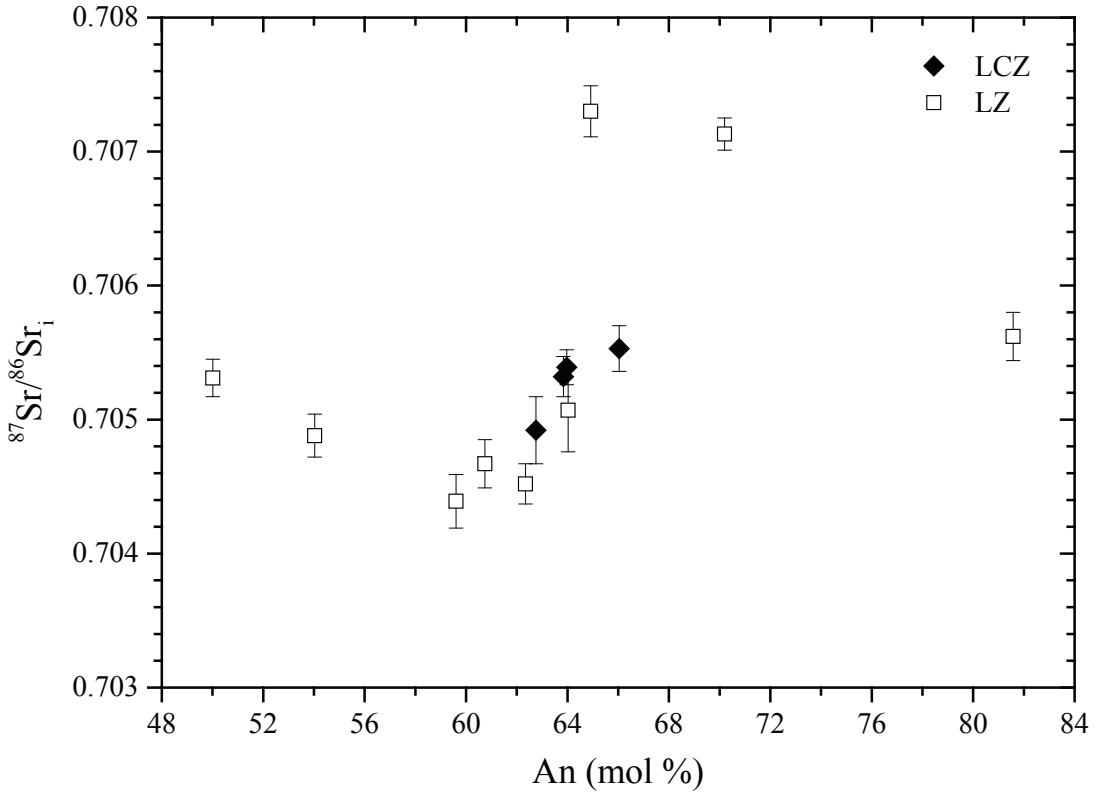

Fig. 15. Plot of error-weighted average *in situ* $^{87}Sr/^{86}Sr_i$ ratios vs. anorthite content for samples from the Lower Zone (LZ) and the Lower Critical Zone (LCZ).

the first appearance of cumulus plagioclase. The analysed UCZ samples comprise two anorthosites, a norite and a pyroxenite with variable amounts of chromite. The *in situ* Sr isotope composition of cumulus plagioclase ranges from 0.7051 to 0.7066 (Fig. 13 b), whereas anorthite contents vary from 74.0 to 82.8 mol %. The error-weighted average *in situ* Sr_i ratios exhibit a more limited variation, ranging from 0.7058 to 0.7062. They show a sharp upward increase and no clear correlation with the anorthite contents or trace element ratios (Fig. 16, 17). The Sr_i ratio of intercumulus plagioclase from the pyroxenite ranges from 0.7056 to 0.7067 with an average of 0.7061 $\pm$ 0.0003, which is similar to the Sr isotopic signature of cumulus plagioclase from this zone. The anorthite content is generally lower with 74.7 $\pm$ 1.5 mol %.

4.3.3 Main Zone

The principle rock types in the Main Zone (MZ) are layered olivine-free (leuco)-gabbronorite and minor norite, containing at least 50 vol % subhedral to euhedral plagioclase laths of up to 5 mm in length. The lowermost sample from this zone (A297) is a pyroxenite with $<$ 5 vol % interstitial plagioclase. Sample A238 has a much larger grain size compared to the other analysed MZ samples. Petrographically, it is a gabbronorite, but the plagioclase grains are mostly anhedral to subhedral, showing strong zonation. The *in situ* Sr isotope composition of all samples from the MZ, except for sample A238, ranges from 0.7081 to 0.7097, whereas the anorthite

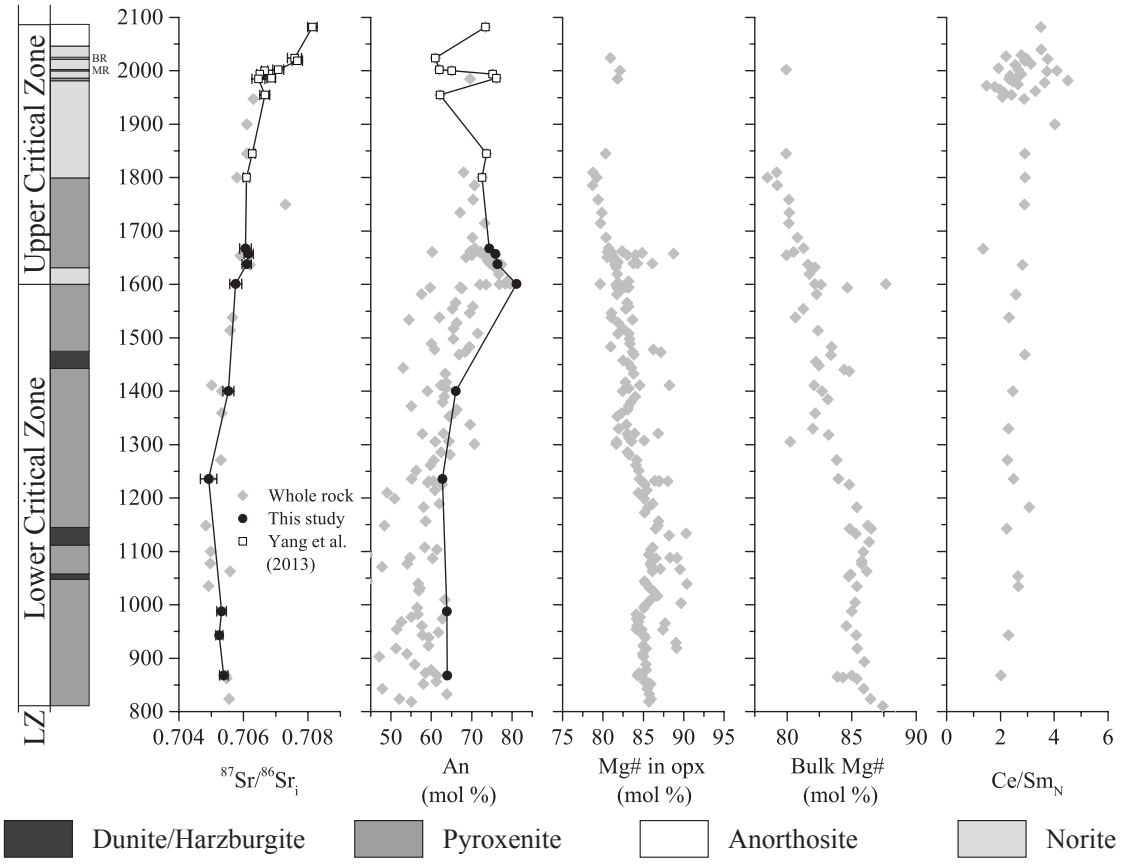

Fig. 16. Plot of error-weighted average *in situ* and whole rock $^{87}Sr/^{86}Sr_i$ ratios together with average anorthite contents, Mg# in orthopyroxene, whole rock Mg# and chondrite-normalised Ce/Sm ratios for the Lower and Upper Critical Zone. The standard deviation is represented by the error bar. Whole rock data and mineral compositions were taken from Teigler (1990) and De Klerk (1991), respectively. Trace element data were taken from Maier et al. (2013). Normalisation values were taken from McDonough & Sun (1995).

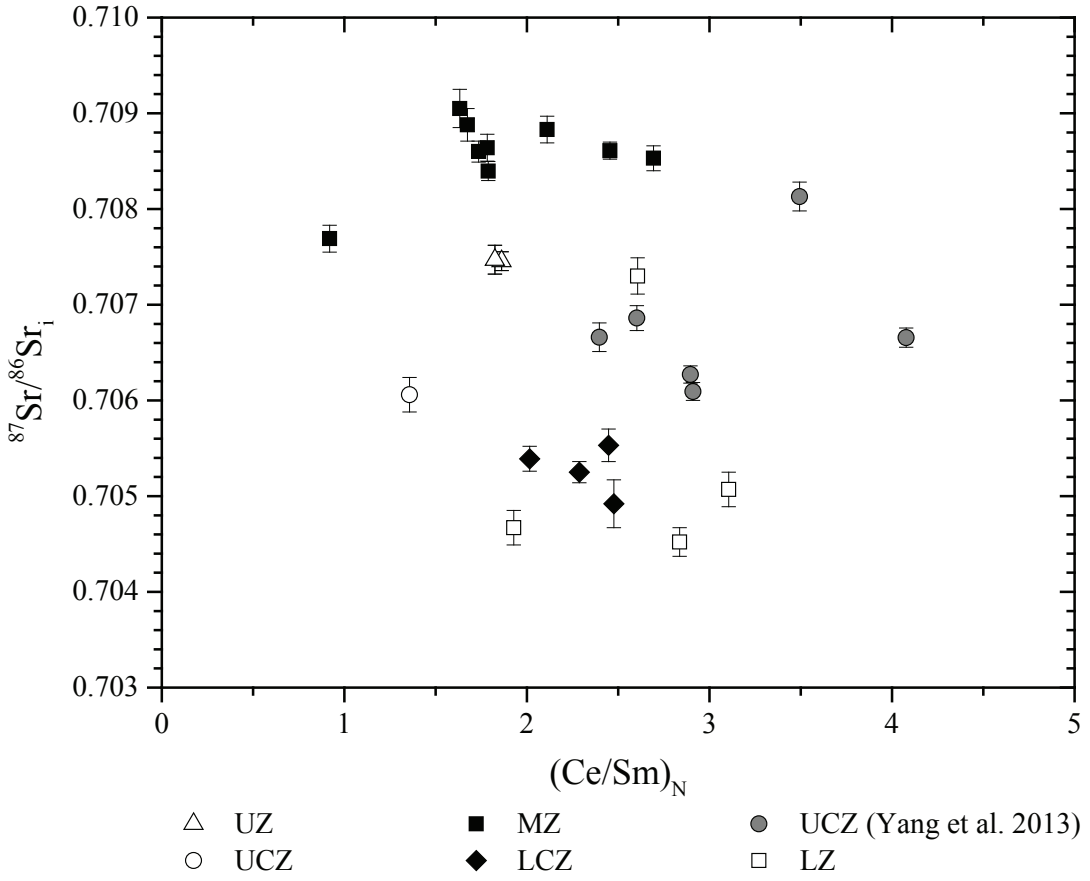

Fig. 17. Plot of error-weighted average *in situ* $^{87}Sr/^{86}Sr_i$ ratios vs. chondrite-normalised Ce/Sm ratios for samples from all zones of the Bushveld Complex. Trace element data were taken from Maier et al. (2013). Normalisation values were taken from McDonough & Sun (1995).

content varies from 56.8 to 71.5 mol % (Fig. 13 c, 18). In contrast, sample A238 shows considerably lower Sr_i ratios of 0.7071 to 0.7082 with anorthite contents from 54.5 to 65.9 mol %. The error-weighted average *in situ* Sr_i ratios within the MZ broadly decrease upwards, showing a positive correlation between anorthite content, trace element ratios and *in situ* Sr isotopes, except for sample A238 (Fig. 17). The lowermost sample from the MZ (A297) has a slightly lower anorthite content due to intercumulus plagioclase in the pyroxenite.

4.3.4 Upper Zone

The analysed Upper Zone (UZ) samples are represented by (magnetite-)gabbroic rocks with minor magnetitite. The variation of the *in situ* Sr isotope composition

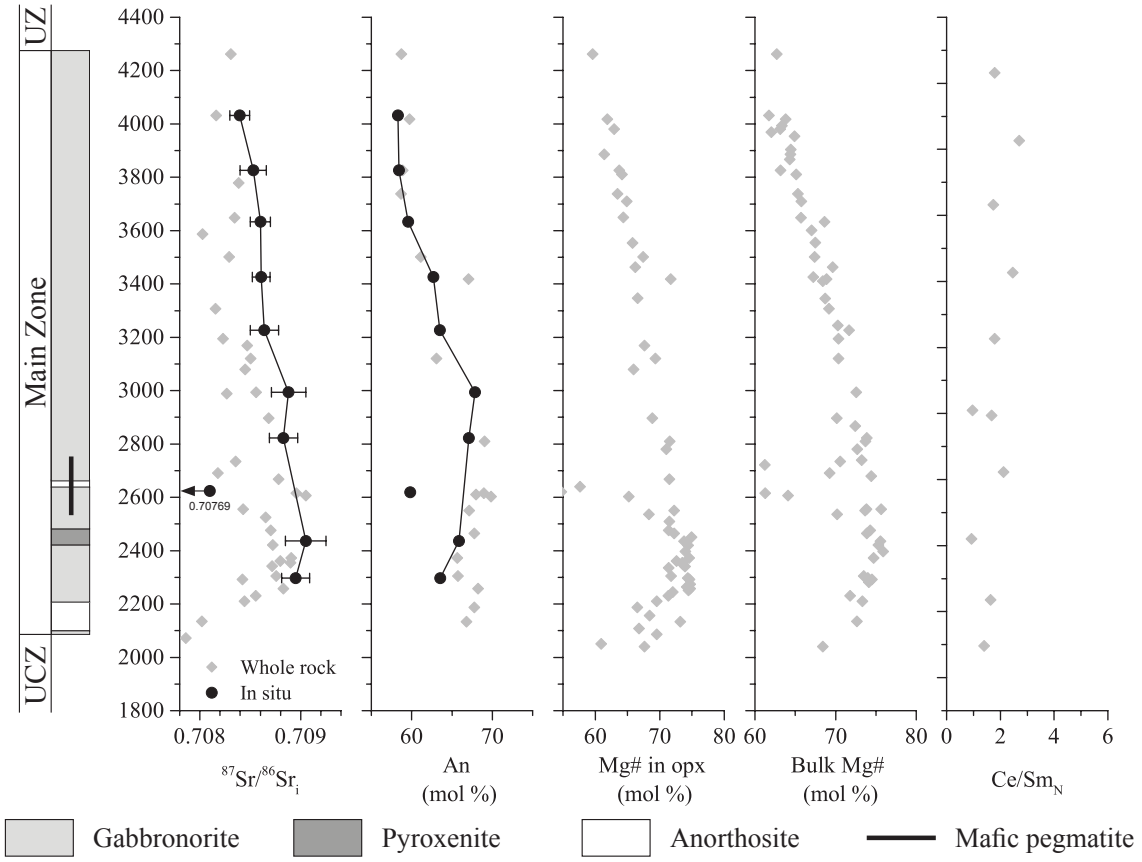

Fig. 18. Plot of error-weighted average *in situ* and whole rock $^{87}Sr/^{86}Sr_i$ ratios together with average anorthite contents, Mg# in orthopyroxene, whole rock Mg# and chondrite-normalised Ce/Sm ratios for the Main Zone. The standard deviation is represented by the error bar. Whole rock data and mineral compositions were taken from Mitchell (1986). Trace element data were taken from Maier et al. (2013). Normalisation values were taken from McDonough & Sun (1995).

of plagioclase is relatively small, ranging from 0.7067 to 0.7084 (Fig. 13 d). The average anorthite contents cover a range from 46.4 to 66.0 mol %, showing a general upward decrease, whereas the error-weighted average *in situ* Sr isotope composition of plagioclase varies only slightly from 0.7073 to 0.7076 (Fig. 19). There is no clearly distinguishable stratigraphic trend in the *in situ* Sr isotopes across the UZ as all Sr_i ratios fall within error of the mean value of ≈ 0.7074. Whole rock Sr isotope data for UZ samples from the western limb, analysed by Kruger et al. (1987), are only marginally lower with ≈ 0.7073.

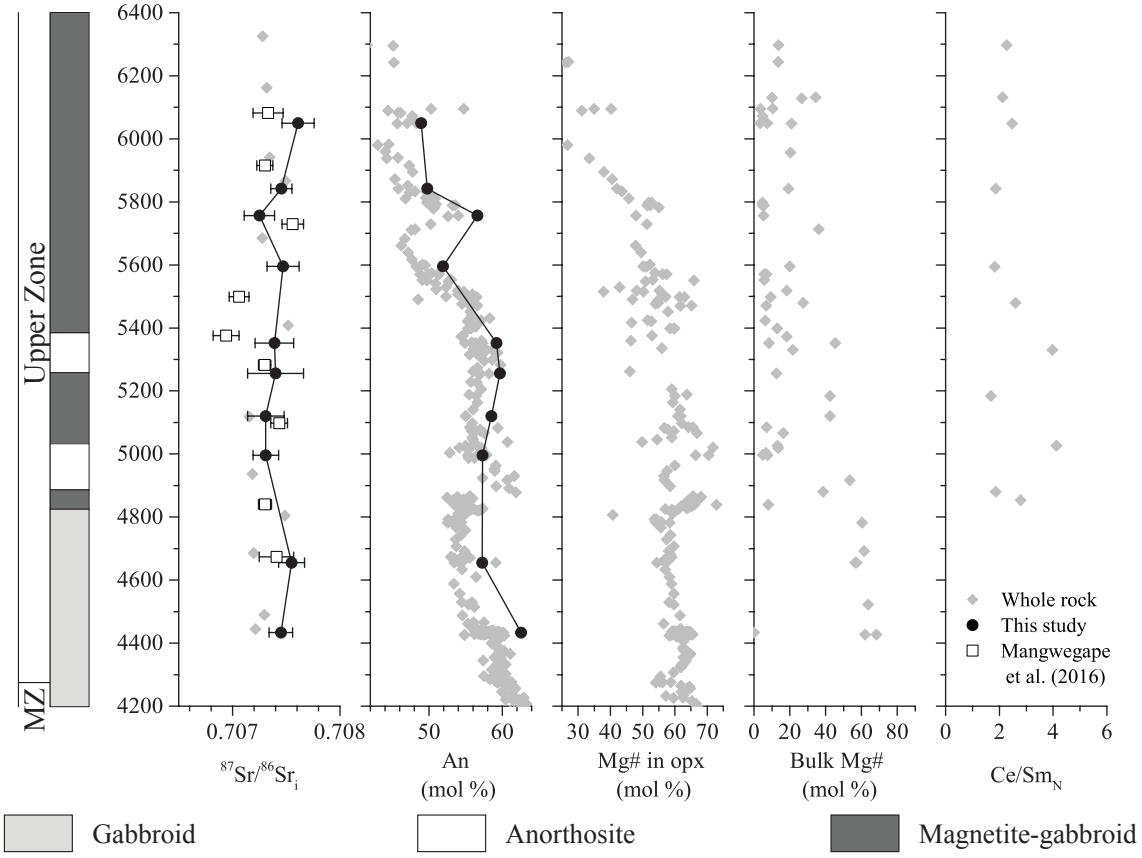

Fig. 19. Plot of error-weighted average *in situ* and whole rock $^{87}Sr/^{86}Sr_i$ ratios together with average anorthite contents, Mg# in orthopyroxene, whole rock Mg# and chondrite-normalised Ce/Sm ratios for the Upper Zone. The standard deviation is represented by the error bar. Sr isotope data from the northern limb were taken from Mangwegape et al. (2016). Whole rock data and mineral compositions were taken from Barnes et al. (2004) and Ashwal et al. (2005), respectively. Note that the whole rock $^{87}Sr/^{86}Sr_i$ ratios shown for comparison are not from the Bellevue drill core, but from the western limb analysed by Kruger et al. (1987). Trace element data were taken from Maier et al. (2013). Normalisation values were taken from McDonough & Sun (1995).

4.3.5 Summary

Distinct changes in Sr_i ratios are evident across the different zones of the Bushveld Complex (Fig. 12). Intercumulus plagioclase from the LZ is characterised by relatively constant Sr_i ratios and FeO concentrations in plagioclase, except for the uppermost sample of the LZ. The anorthite contents show no clear stratigraphic trend, resulting in a lack of correlation between Sr_i ratios and anorthite content or trace element ratios (Fig. 14, 15, 17). In the LCZ, the Sr_i ratio shows a reversal to ratios typical for the lower part of the LZ and then shows a slight upward increase.

The FeO concentrations in plagioclase exhibit a gradual increase towards the top of the LCZ. Variation in anorthite contents is rather limited, although they seem to correlate with Sr_i ratios (Fig. 15). A sharp decrease in FeO concentrations in plagioclase occurs at the base of the UCZ, which correlates with a reversal towards lower anorthite contents. However, anorthite contents are generally much higher than in the LCZ. The Sr_i ratios increase slightly from the base to the middle of the zone before they increase significantly at the top of the UCZ. Accordingly, a correlation between Sr_i ratios and anorthite contents is not evident (Fig. 20). The lower part of

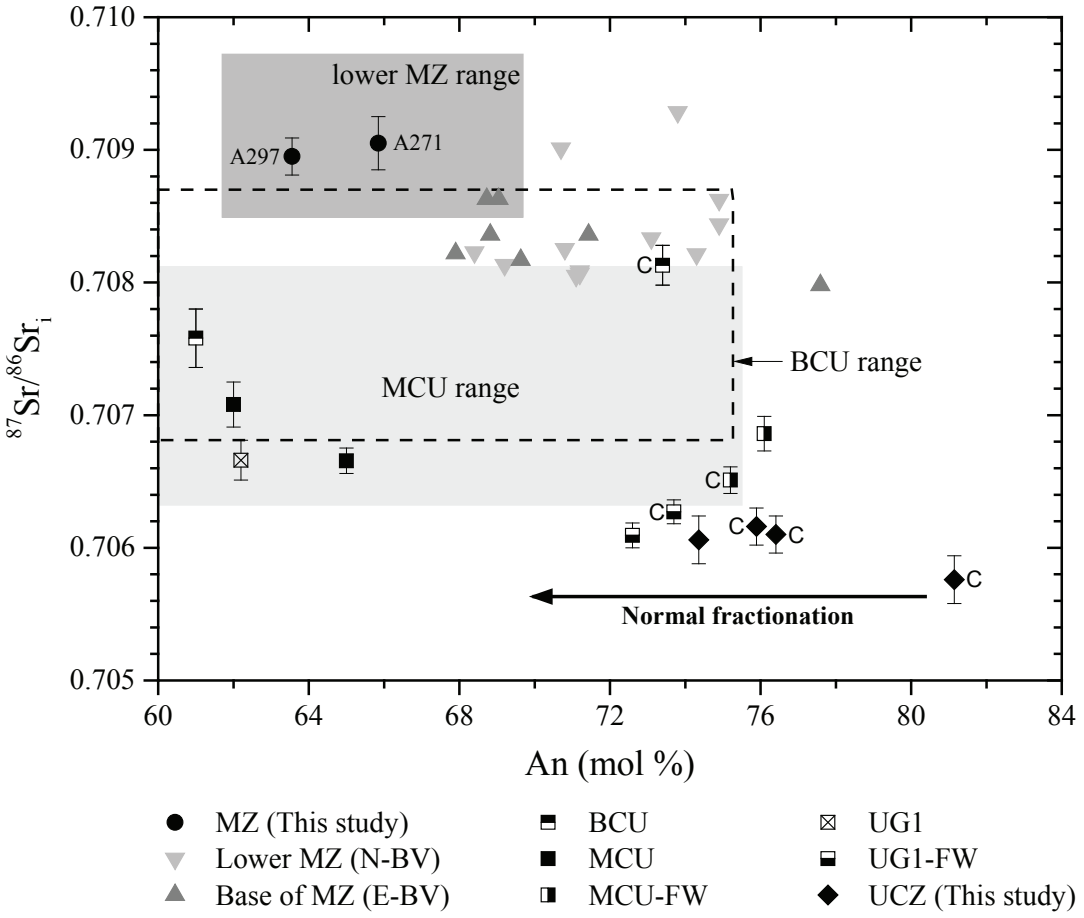

Fig. 20. Plot of anorthite contents against error-weighted average *in situ* $^{87}Sr/^{86}Sr_i$ ratios for different samples from the Upper Critical Zone. Data for the squares were taken from Yang et al. (2013). Data for the base of the Main Zone were taken from Seabrook et al. (2005). Data for the lower Main Zone were taken from Roelofse (2010). The standard deviation is represented by the error bar. Abbreviations: MZ = Main Zone; UCZ = Upper Critical Zone; BCU = Bastard Cyclic Unit; MCU = Merensky Cyclic Unit; UG1 = Upper Group 1 chromite layer; FW = footwall. Symbols marked with a "C" are samples with cumulus plagioclase.

the MZ has the highest Sr_i ratios of the complex, whereas the overlying rocks show a progressive upward decrease in Sr_i ratios. The FeO concentrations in plagioclase remain relatively constant across the MZ, whereas the anorthite contents increase slightly from the base upwards before they gradually decrease in the upper part of the MZ, resulting in a broad correlation between anorthite contents and Sr_i ratios (Fig. 18, 24). An exception is sample A238 from the lower part of the MZ, which has much lower Sr_i ratios and anorthite contents than the other MZ samples, even though the FeO concentrations in plagioclase are within the range of the other MZ samples. The Upper Zone is characterised by lower Sr_i ratios compared to the MZ, exhibiting a sharp increase in anorthite contents and FeO concentrations in plagioclase, both of which gradually decrease towards the top of the zone. Ce/Sm has proven to be a useful trace element ratio in the discrimination of different Bushveld lithologies. Maier & Barnes (1998) showed that LZ and LCZ lithologies are characterised by Ce/Sm_N ratios of about 3.65, whereas MZ lithologies have considerably lower Ce/Sm_N ratios of about 2. This is also evident in the present dataset as Ce/Sm_N ratios across the LZ and CZ are generally well above 2, whereas the MZ is characterised by Ce/Sm_N ratios around 2 (Fig. 12). Even though the MZ has the least fractionated Ce/Sm_N ratios, it features the highest Sr_i ratios. The UZ shows the highest variation in Ce/Sm_N, ranging from 1 to 4.

4.4 Discussion

4.4.1 Sr isotope disequilibrium between coexisting minerals

The *in situ* Sr isotope composition of plagioclase frequently shows more radiogenic Sr signatures than the respective whole rock analysis. This becomes especially apparent in the MZ as the gabbronorites contain high amounts of plagioclase in contrast to ultramafic rocks from the LZ or CZ, which have only limited amounts of plagioclase ($<$ 10 vol %). Several studies attributed this to disequilibrium between coexisting minerals, where pyroxene would have a different Sr isotope composition than plagioclase in the same sample (e.g., Eales et al. 1990a, Roelofse & Ashwal 2012, Seabrook et al. 2005, Yang et al. 2013). Only Chutas et al. (2012) reported *in situ* Sr isotope data of both plagioclase and orthopyroxene, confirming the existence of disequilibrium. Another possible reason for the difference between whole rock and *in situ* Sr isotope data could be the excessive effect of age-correction on whole rock samples, containing K-rich minerals with relatively high Rb/Sr ratios like alkali feldspar, amphibole and mica, as the Rb/Sr ratio is directly included in the correction.

A mass balance calculation for a typical MZ gabbronorite (sample A1), using its mineral mode from Mitchell (1986), the *in situ* Sr isotope composition of plagioclase and Sr concentrations in the respective mineral shows that the Sr_i ratio of pyroxene would have to be unrealistically low ($Sr_i \approx 0.6969$) in order to reproduce the whole rock Sr isotope composition (Table 3). Accordingly, a model envisaging Sr isotope disequilibrium between plagioclase and coexisting pyroxene based on whole rock Sr analyses appears rather implausible because of the extremely small Sr contribution

Table 3. Calculated Sr_i of pyroxene from sample A1 based on mineral mode, Sr concentrations, whole rock Sr data and the *in situ* Sr_i ratio of plagioclase

Mineral	**[1]Mode (vol %)**	**[2]Sr_{Min} (ppm)**	**In situ Sr_i**	**Calculated Sr_i**
Plagioclase	65.4	365	0.70839	-
Orthopyroxene	24.4	9	-	0.69689
Clinopyroxene	10.2	27	-	

**Whole rock Sr isotope composition of MZ sample A1: 0.70816*
[1]Data from Mitchell (1986)
[2]Average Sr concentration based on MZ mineral separates from Roelofse (2010)

from pyroxene to the whole rock Sr budget ($\approx$ 350 ppm Sr in plagioclase vs. $<$ 30 ppm Sr in pyroxene).

Regarding the presence of minerals with high Rb/Sr ratios, Roelofse (2010) reported $\approx$ 4 vol % biotite and up to 12 vol % amphibole associated with pyroxene alteration in samples from the MZ. Furthermore, De Klerk (1982, 1991) and Teigler (1990) provided mineralogical modes of CZ and LZ samples, indicating similar modal abundances of mica.

On the basis of mass balance calculations and the consistent gap between *in situ* and whole rock Sr analyses in the MZ, we suggest that the gap partly results from an excessive age-correction of the whole rock data due to the presence of variable amounts of secondary mica and amphibole in the samples. We envisage that the alteration occurred in response to the introduction of small amounts of fluid along cracks, fissures and grain boundaries, which had an effect on the mineralogy, resulting in the formation of minerals with high Rb/Sr ratios as well as Rb concentrations, which significantly increase the amount of ^{87}Sr being subtracted during age-correction of the whole rock sample as shown in Table 3. In addition, these secondary minerals may also have a different isotope composition, reflecting that of the fluid. In contrast to whole rock analyses, these altered areas can be largely avoided with *in situ* analyses by focusing on clean and pristine areas of each analysed grain. Thus, the effect of this heavily depends on the modal mineralogy of the analysed sample: high amounts of plagioclase will result in a larger offset compared to samples with little plagioclase.

4.4.2 Intra-sample Sr isotope variations

Figure 21 shows the standard deviation of the *in situ* Sr_i ratios across the analysed profile of the Bushveld Complex. They are highly variable and largely independent of plagioclase textures, i.e., cumulus (UCZ, MZ, UZ) vs. intercumulus (LZ, LCZ) plagioclase as shown in Figure 13. Mineral-scale Sr isotope heterogeneity has also been documented for the Rum intrusion in Scotland (Tepley & Davidson 2003). These authors described isotope disequilibrium between cores and rims in certain plagioclase grains. In this case, crystal rims are generally characterised by

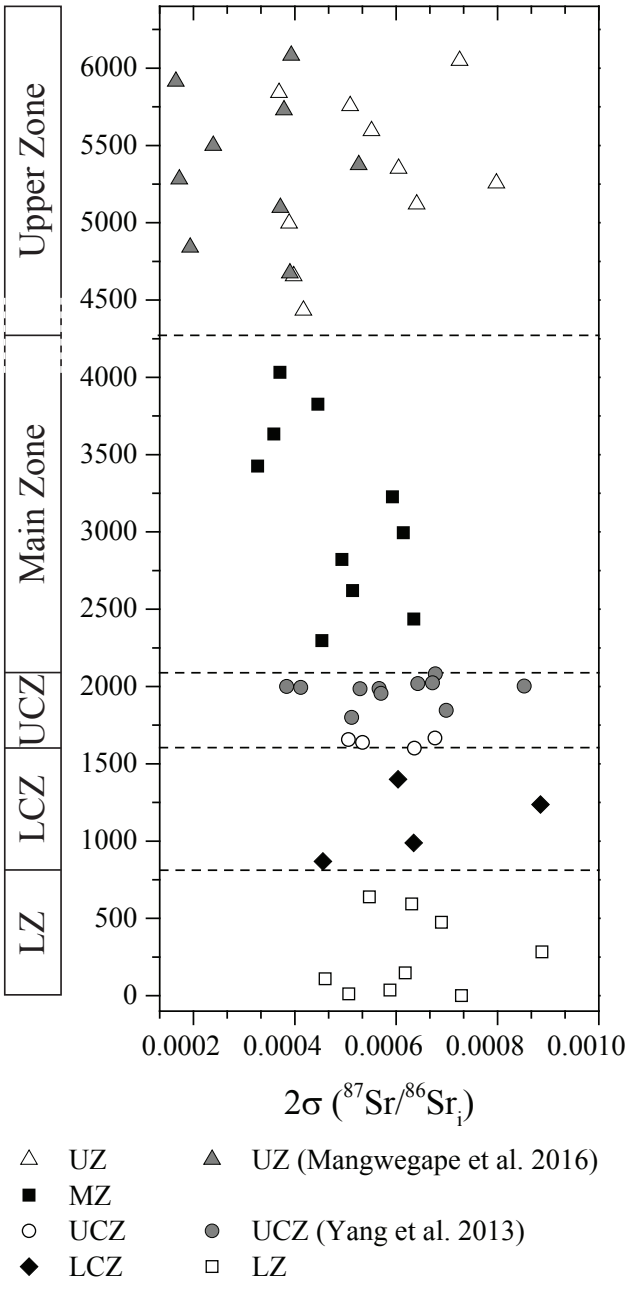

Fig. 21. Plot of the *in situ* $^{87}Sr/^{86}Sr_i$ ratio standard deviation (2σ) against stratigraphic height. Data for the Upper Zone and Upper Critical Zone (grey symbols) were taken from Mangwegape et al. (2016) and Yang et al. (2013), respectively. Abbreviations: UCZ = Upper Critical Zone; LCZ = Lower Critical Zone; LZ = Lower Zone.

more radiogenic compositions relative to the cores. Similar results were reported by Chutas et al. (2012) and Yang et al. (2013) for the LZ and CZ, respectively.

Tepley & Davidson (2003) interpreted this to reflect *in situ* crystal growth of plagioclase in a magma that was undergoing progressive wall-rock contamination. In contrast, Chutas et al. (2012) argued that the Sr isotope disequilibrium was produced by late-stage infiltration of relatively radiogenic melt through the cumulate, whereas Yang et al. (2013) suggested that less radiogenic proto-plagioclase grains were picked up by more radiogenic magma during mixing or mingling. Due to the size of the Bushveld Complex, it is unlikely that progressive wall-rock contamination affected the entire magmatic system in a way that can account for the observed Sr isotope disequilibrium. This may be a feasible mechanism for the much smaller Rum intrusion, in which the rate of crystallisation is lower than the rate of crustal contamination (Yang et al. 2013). The observed Sr isotope disequilibrium in single interstitial plagioclase crystals from the LZ that show distinctly euhedral domains (Figs. 13 a, 22 a, b) suggests that late-stage infiltration of radiogenic melt does not exclude growth of plagioclase crystals in different isotopically distinct batches of magma. Therefore, it is more likely that both processes contributed to the Sr isotope heterogeneity in cumulus as well as intercumulus plagioclase.

On the basis of Sr isotope disequilibrium between different UCZ plagioclase grains in a single thin section, Yang et al. (2013) concluded that the co-accumulation of plagioclase crystals from two isotopically distinct reservoirs was of key importance. The presence of more than one isotopically distinct plagioclase population would require that the standard deviations in certain zones are significantly elevated relative to zones that are characterised by a single plagioclase population. A correlation between specific zones and systematically more pronounced intra-sample variations, however, is not evident from the dataset, which argues strongly against the co-accumulation model (Fig. 13). Although the Sr isotope data are mostly averaged for each sample, the error bar essentially records the extend of the Sr disequilibrium. Moreover, these averages can be readily compared with existing whole rock Sr analyses from Bushveld Complex.

Our data show compositional variations between cores and rims of individual plagioclase grains, but these compositional trends are rather erratic and many grains show somewhat ambiguous primary core-rim variations (Fig. 13). Due to the ab-

sence of clear visual plagioclase zonation, it is difficult to determine whether the rim was actually formed after the core, especially in samples with interstitial plagioclase. Back-scatter electron imaging does not always allow for an unambiguous determination of growth zones, whereas high-resolution EDS-based elemental mapping reveals complex zonation patterns in cumulus and intercumulus plagioclase.

4.4.3 Formation of the Lower Zone

Teigler (1990) reported plagioclase and orthopyroxene compositions as well as bulk geochemistry for the LZ. The anorthite contents are highly erratic throughout the LZ, showing no distinct trend (Fig. 14). In contrast, the Mg# of orthopyroxene shows more subdued variation, except for the basal 50 m of the LZ, where the Mg# varies from 80.9 to 86.1. Between 50 to 210 m, the Mg# gradually decreases from 88.5 to 84.8, followed by a sharp increase to 89.4 at 265 m. Subsequently, the Mg# in orthopyroxene gradually decreases with a number of minor reversals. The bulk Mg# shows relatively little variation across the LZ, though there are fewer data in comparison to Mg# in orthopyroxene. The Sr_i ratios show relatively large variations over narrow stratigraphic intervals (Fig. 14). Nevertheless, a general upward increase in Sr_i ratios is evident together with a sharp rise in the uppermost two LZ samples. The more radiogenic signature of these samples could potentially be attributed to a local disturbance of the Sr isotope composition of plagioclase by external fluids. However, whole rock Nd isotope data of the radiogenic interval (Maier et al. 2000) also show a deviation towards slightly more enriched compositions (i.e. lower εNd) from the typical LZ and LCZ εNd value of - 5.3 (Fig. 12). Due to the more limited mobility of Sm relative to Rb, it is rather unlikely that an external fluid was capable of changing not only the Sr isotope composition, but also the Nd isotope composition of the magma. Instead, the *in situ* assimilation of either host rock lithologies or the intrusion of more radiogenic magma, as proposed by Kruger (1994), could account for the deflection in Sr_i ratios. The *in situ* assimilation of relatively evolved host rocks (e.g., felsic volcanic rock of the Rooiberg Group) would have strongly affected the trace element signature of the radiogenic samples, but trace element data from Maier et al. (2013) indicate that the LZ has a fairly homogeneous

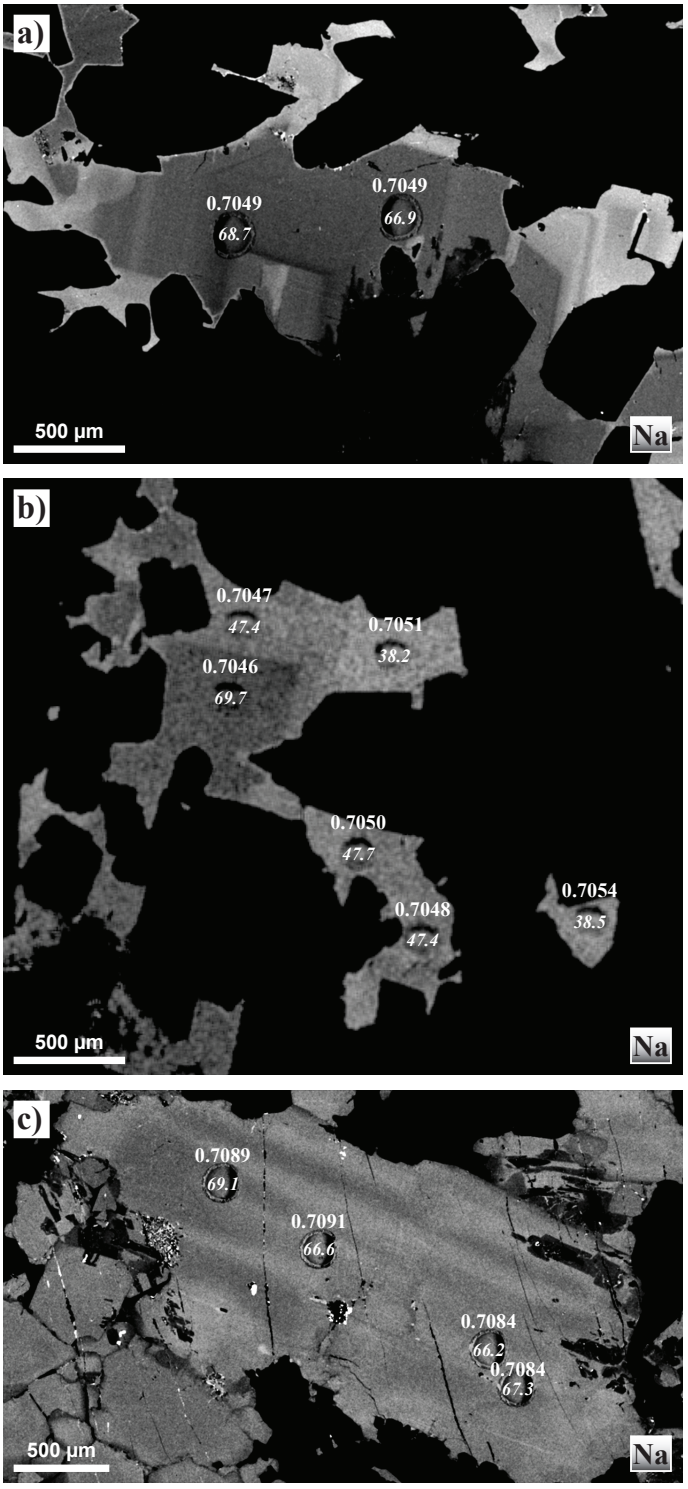

Fig. 22. Elemental maps showing the variation of Na in plagioclase. a) Interstitial plagioclase from the Lower Zone in sample NG2-762.27. b) Interstitial plagioclase from the Lower Zone in sample NG2-762.27. c) Zoned cumulus plagioclase from the Main Zone in sample A168.

trace element signature (Fig. 14). Figure 17 shows no correlation between Ce/Sm and Sr_i ratios, thus confirming that bulk contamination is unlikely to account for the shift in Sr_i ratios in the upper part of the LZ. In contrast, the influx of a more radiogenic mafic magma would not necessarily have a significant effect on the trace elements, although the Sr isotope composition would be affected. This model is consistent with the fact that the trace element signature and mineral compositions of the LZ lithologies show no geochemical difference between less and more radiogenic pyroxenites. Eales et al. (1990b) argued on the basis of Sr isotopes and reversals in mineral compositions that the LZ and CZ were subjected to repeated incursions of primitive mafic magma. Our results are largely in agreement with this model; however, based on our *in situ* Sr isotope work coupled with detailed elemental maps of interstitial plagioclase, we propose a two stage formation for the LZ cumulates.

We envisage the formation of a proto-cumulate, predominantly consisting of mafic minerals, i.e. olivine and/or orthopyroxene, that was either emplaced in a series of crystal mushes or possibly crystallised *in situ* from repeated incursions of primitive magma (Karykowski & Maier 2017). After the formation of the mafic framework, interstitial plagioclase crystallisation commenced, reflecting the Sr isotope composition of the magma from which it crystallised. However, the large variations in Sr isotope compositions and the distinct zonation patterns of interstitial plagioclase (Fig. 22 a, b) strongly argue against undisturbed crystallisation of plagioclase from a trapped interstitial liquid.

The complex zonation patterns suggest multiple influxes of melt into the mafic framework, mixing with and displacing some of the resident interstitial melt as a consequence of either compaction or displacement by convecting interstitial liquids (e.g., Boorman et al. 2004, Karykowski & Maier 2017). Each of these influxes produced an isotopically distinct rim around earlier plagioclase crystals (Fig. 22 a). Therefore, some interstitial plagioclase did not crystallise from the same melt that produced the mafic framework, explaining the large intra-sample variation in Sr isotope compositions (Fig. 13 a). The error-weighted average Sr isotope composition provides an insight into the proportions of less radiogenic to more radiogenic magma involved in the formation of interstitial plagioclase.

The relatively primitive, yet radiogenic signature of the magma, from which the interstitial plagioclase crystallised, may have been acquired from the interaction with the 2-km-thick Chuniespoort Group carbonate platform (Transvaal Supergroup), while the magma ascended through the crust (Fig. 23 a, b). Swart (1999) reported highly variable Sr concentrations for these carbonate rocks, ranging from 10 to 629 ppm at relatively low REE concentrations (La $<$ 10 ppm). Despite limited available Sr isotope data from these carbonates, data from Swart (1999) indicate that Transvaal Supergroup dolomite has a relatively radiogenic Sr isotope composition of 0.719 $\pm$ 0.012 (n = 7). These values are generally in agreement with Malmani data from Veizer et al. (1992), who reported Sr isotope compositions of 0.717 $\pm$

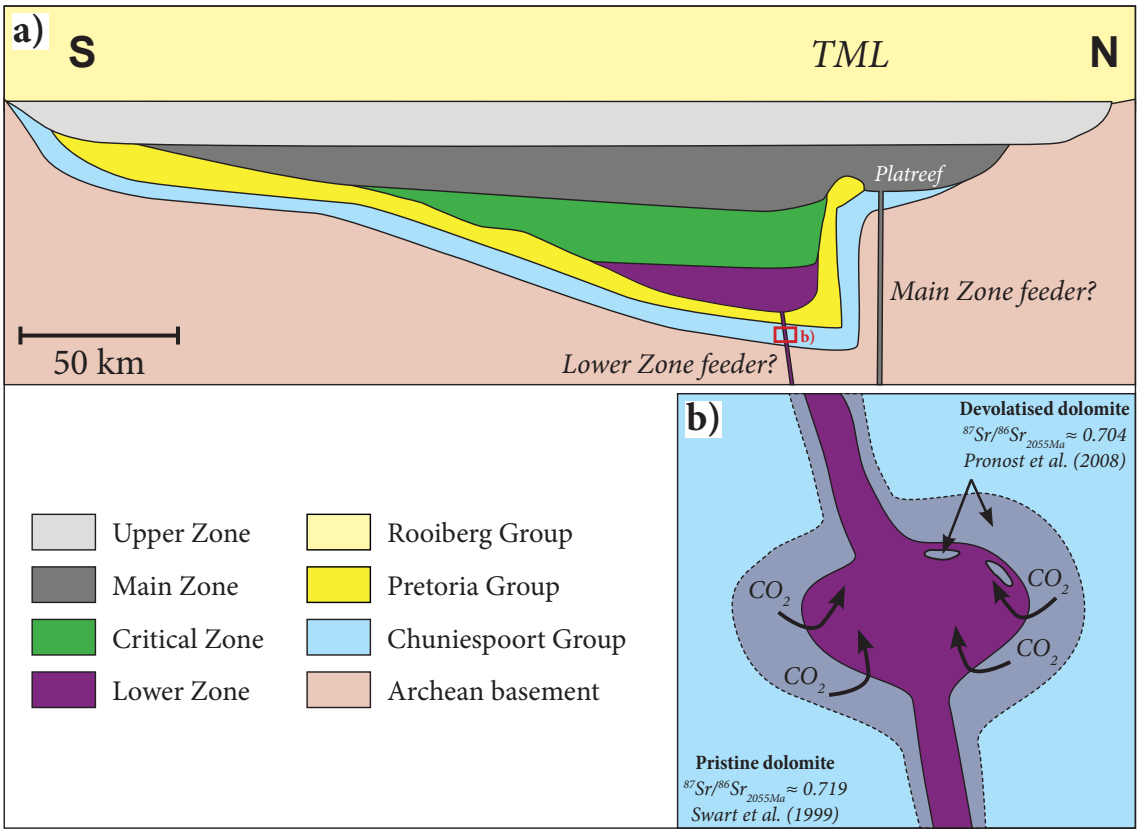

Fig. 23. Model for the interaction of ascending magma with the extensive carbonate platform of the Chuniespoort Group, underlying the Bushveld Complex. a) Schematic cross-section of the Bushveld Complex. b) Decarbonation of dolomite-rich Chuniespoort Group lithologies and introduction of radiogenic Sr into the magma. Sr isotope compositions for "pristine" and "devolatised" dolomite were taken from Swart (1999) and Pronost et al. (2008), respetively. The vertical exaggeration is about 8 x. Modified after Kruger (2005). Abbreviations: TML = Thabazimbi-Murchison-Lineament.

0.005 (n = 10). The contamination of a B1-type parental magma with 175 ppm Sr and Sr_i = 0.703 (Harmer & Sharpe 1985) by dolomite with 200 ppm Sr and Sr_i = 0.718 (average Sr concentration of Transvaal Supergroup carbonate rocks in the Transvaal Basin, as reported by Swart 1999), shows that relatively high degrees of bulk contamination ($\approx$ 37 %) are required to produce the most radiogenic Bushveld cumulates (Sample A271 from the MZ with Sr_i = 0.7091). For the most radiogenic LZ sample, the degree of contamination would still be as high as 26 %. Therefore, such degree of bulk contamination appears rather unrealistic and it would have probably affected the trace element signature, which is not observed.

Alternatively, the addition of a CO_2- and Sr-rich fluid released during the decarbonation of dolomite, as proposed by Ganino et al. (2008, 2013b), may have also produced the geochemical characteristics of the staging magma without the necessity of bulk assimilation or partial melting (Fig. 23 b). As the CO_2 solubility in mafic magma is generally low, the CO_2 component would have probably degassed, whereas Sr may have dissolved in the magma. According to Phinney (1992), the two main factors influencing the FeO concentrations in plagioclase are (1) oxygen fugacity and (2) polymerisation of the magma (Lundgaard & Tegner 2004). Hence, it seems plausible that the magma, responsible for the excursion in Sr isotopes and FeO concentrations in plagioclase, was characterised by a higher oxygen fugacity (Fig. 12). Ganino et al. (2008) showed that the interaction between a mafic magma and a fluid derived from the decarbonation of a sedimentary floor rock caused a significant increase in oxygen fugacity. Therefore, it is conceivable that the melt, percolating through parts of the mafic LZ framework, may have interacted with a fluid derived from dolomite-rich Chuniespoort Group, which resulted in a high oxygen fugacity and possibly an elevated Sr isotope composition of the magma. This model remains difficult to verify as fluid compositions are not very well constrained to date, but Pronost et al. (2008) reported unradiogenic Sr isotope compositions of $\approx$ 0.704 for a thermally-overprinted Malmani dolomite sample from the Sandsloot pit ("devolatised dolomite" in Figure 23 b). In comparison to the considerably more radiogenic Sr isotope composition of "pristine dolomite" from Swart (1999), this suggests that decarbonation may lead to a significant fractionation of Sr iso-

topes. Moreover, the fluid may potentially be somewhat similar in composition to slab-derived fluids related to subduction zones, which are enriched in elements considered to be mobile (LILE, Ba, Pb, Sr) during slab-wedge transfer (e.g., Hoogewerff et al. 1997). Notably, many back-arc basalts have a distinct slab signature, such as relatively radiogenic Sr isotope compositions and elevated incompatible element concentrations in comparison to magmatic rocks associated with mantle melting (e.g., Hawkesworth et al. 1993, Spandler & Pirard 2013). Regardless of the exact mechanism, varying volumes of more radiogenic melt, percolating through the mafic LZ framework, controlled the Sr isotope composition of interstitial plagioclase.

4.4.4 Formation of the Lower Critical Zone

Mineral composition and whole rock data for the LCZ from Teigler (1990) show an erratic, but gradual increase in anorthite contents from the base upwards (Fig. 16). Conversely, the Mg# of orthopyroxene remains constant from the base of the LCZ to 1,140 m, but the Mg# gradually decreases across the upper part of the LCZ. The bulk Mg# shows a similar trend compared to the Mg# of orthopyroxene. As the LCZ has a relatively unradiogenic Sr isotope composition compared to the uppermost portion of the LZ, interstitial plagioclase in the LCZ mostly formed from less radiogenic magma. However, the intra-sample range in Sr isotope compositions indicates that multiple isotopically distinct influxes of melt percolated through the mafic framework of the LCZ (Fig. 13 b). In fact, the intra-sample variation in Sr isotope compositions suggests a two end-member magma mixing trend between two relatively unradiogenic magmas across the LCZ, ranging from 0.705 to 0.706. In addition, the central part of the LCZ (samples NG1-327 and NG1-575) shows evidence for another later episode of melt percolation by even less radiogenic, yet relatively evolved magma with $Sr_i \approx 0.704$.

4.4.5 Implications for the formation of the Upper Critical Zone

All the UCZ samples from this study have a very narrow range in average *in situ* Sr_i ratios. The Sr_i ratios and An contents of cumulus plagioclase broadly overlap with those of Yang et al. (2013) from the footwall of the UG1 chromitite (Fig. 20). The overlying UG1 and Merensky footwall samples have slightly higher average Sr_i ratios, which increase even further through the Merensky Cyclic Unit (MCU) to the Bastard Cyclic Unit (BCU). The uppermost sample from the BCU, the Bastard anorthosite, has a similar average Sr_i ratio to plagioclase separates from the MZ analysed by Seabrook et al. (2005) and Roelofse (2010), respectively. When considering Sr_i ratio ranges, representing all *in situ* Sr analyses of a particular zone, it is worth noting that these ranges shift from lower to higher Sr_i ratios with height, e.g., the MCU range is considerably lower than the BCU range, which shows some overlap with the lowermost two MZ samples from this study. Regarding the formation of the UCZ, Barnes & Maier (2002) as well as Wilson & Chunnett (2006) argued on the basis of trace element patterns that the MCU and BCU crystallised from a mixture between CZ and MZ magmas. In contrast, Seabrook et al. (2005) and Yang et al. (2013) suggested that these units were formed by the co-accumulation of plagioclase from two isotopically distinct reservoirs, i.e., CZ and MZ parental magmas.

In the case of the latter model, the result would be a binary distribution of Sr_i ratios, where modal abundances of plagioclase from each reservoir are the main factor, controlling the average Sr_i ratio of the sample. Hence, we would expect to see similar *in situ* Sr_i ranges in the MCU and BCU with varying average Sr_i ratios, depending on the modal abundances of plagioclase from each parental magma. Moreover, samples containing plagioclase from two distinct reservoirs would have much larger Sr_i standard deviations compared to samples containing plagioclase from a single source. The UCZ data from this study together with data from Yang et al. (2013) show that there is no systematic difference in standard deviations (2σ) between the lower part of the UCZ and the upper part, which has been proposed to

contain two isotopically distinct plagioclase populations (Fig. 21). A broad overall decrease in standard deviations is evident across the analysed profile, which may reflect the upward increase of Sr concentrations in plagioclase, resulting in greater analytical precision (e.g., Cawthorn 2007).

Our data suggest that the *in situ* Sr isotope composition of plagioclase from the MCU and BCU resulted from the crystallisation of plagioclase from a mixed magma of alternating composition rather than from the co-accumulation of plagioclase from two distinct reservoirs. The lower part of the UCZ shows little evidence for magma addition and mixing, although the average Sr_i ratios increase slightly from the LCZ to the bottom of the UCZ. The first significant increase in Sr_i ratio occurs at the level of the UG1 chromitite. All overlying samples have gradually increasing Sr_i ratios, which is consistent with progressively increasing proportions of more radiogenic magma to the CZ parental magma, as proposed by Barnes & Maier (2002) as well as Wilson & Chunnett (2006). The gradual increase in average Sr_i ratios further suggests relatively protracted mixing or a slow addition of magma. Intra-sample Sr isotope variations in UCZ sample with cumulus plagioclase, however, show strong heterogeneity in their Sr isotope composition, which may indicate continual ingress of geochemically distinct magma that picked up previously formed plagioclase crystals (Fig. 13 b).

4.4.6 Petrogenesis of the Main and Upper Zones

The orthopyroxene composition and the bulk Mg#, determined by Mitchell (1986) for MZ samples from the same drill core, show a similar trend to the *in situ* Sr isotope compositions with a progressive upward and downward decrease in Mg#, starting at approximately 2,400 m (Fig. 18). Whole rock samples, located stratigraphically below the lowermost sample analysed in this study (sample A297), show a dramatic downward decrease in whole rock Sr_i ratios, whereas anorthite contents remain relatively high. Although these observations have not been confirmed by *in situ* analyses, Sr isotope data of plagioclase separates from the base of the MZ in the eastern limb analysed by Seabrook et al. (2005) largely confirm the low Sr_i ratios and relatively high anorthite contents (Fig. 24). Accordingly, these results suggest

that the lower portion of the MZ was still affected by the above mentioned mixing between CZ and MZ magma. Hence, this part of the MZ represents the continuation of the UCZ mixing trend with a strong contribution from the MZ magma. Based on Sr isotopic evidence, the entire mixing zone extends from 1,850 to 2,450 m, covering some 600 m in stratigraphy.

The *in situ* Sr isotope data from this study show a broadly positive correlation between anorthite contents and Sr_i ratios in the remainder of the MZ, suggesting a binary mixing between a relatively primitive, yet highly radiogenic component and a more evolved and less radiogenic component (Fig. 24). The gradual upward

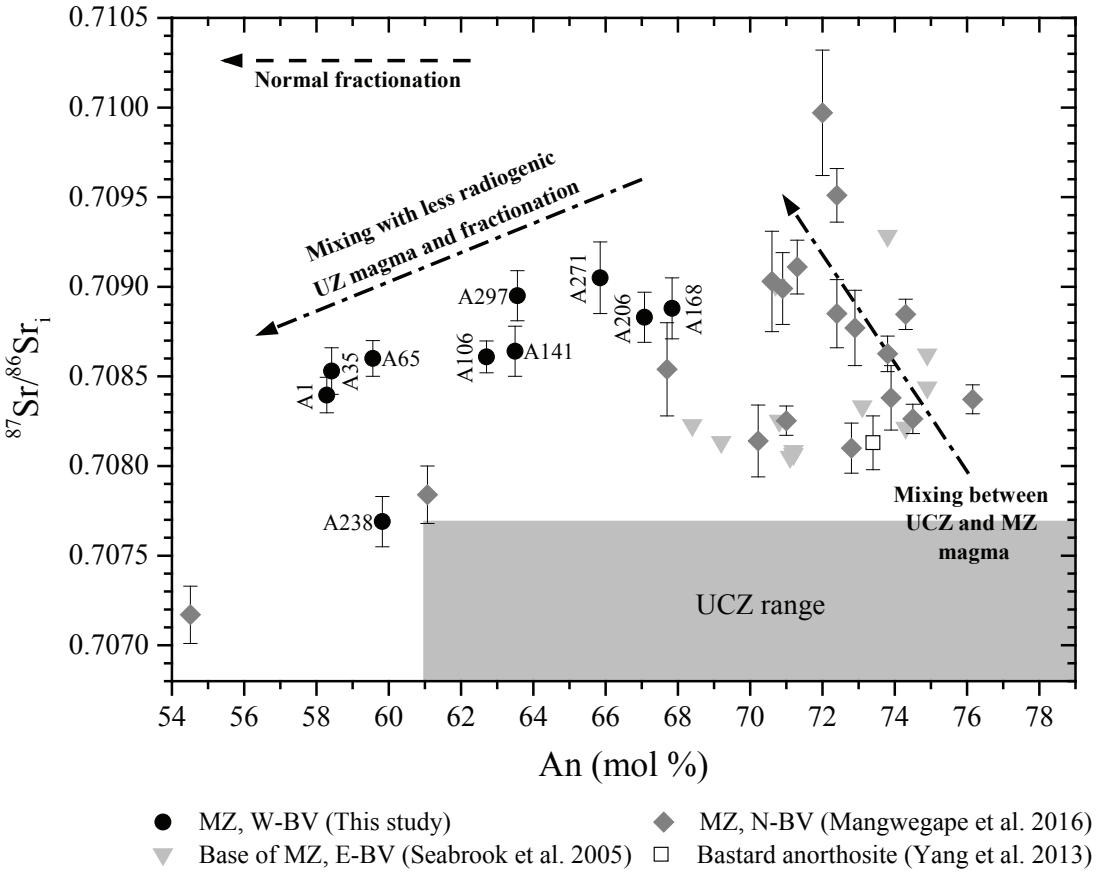

Fig. 24. Plot of anorthite contents against error-weighted average *in situ* $^{87}Sr/^{86}Sr_i$ ratios for different samples from the Main Zone. The standard deviation is represented by the error bar. Data for the base of the MZ and the northern limb MZ were taken from Seabrook (2005) and Mangwegape et al. (2016), respectively. Abbreviations: MZ = Main Zone; UCZ = Upper Critical Zone; E-BV = Eastern limb of the Bushveld Complex; N-BV = Northern limb of the Bushveld Complex.

decrease in Sr_i ratios above sample A271 can thus be explained by progressive mixing between these two components. The primitive, highly radiogenic end-member would be the parental magma to the MZ, whereas the less radiogenic counterpart could be either UZ or CZ magma. The combination of "primitive" and "highly radiogenic" magma is rather atypical for classic crustal contamination models, as magmas generally become more fractionated with contamination, which also affects the Sr isotopic signature. Trace element ratios strongly argue against extensive upper crustal contamination of the MZ parental magma as Ce/Sm ratios in the MZ are generally lower than in the CZ and LZ (cf. Fig. 14, 16, 17, 18). Alternatively, it could be argued that the magma was contaminated by mid- to lower crustal lithologies. Granulite- and amphibolite-facies gneisses from the Vredefort Dome (ca. 3.5 Ga), located about 150 km southwest of the Bushveld Complex, have Sr isotope composition at 2,055 Ma in the range of the MZ lithologies; however, Ce/Sm_N ratios of mostly well above 3 are clearly too high to explain those of the MZ (Hart et al. 1981, 1990).

Despite the lack of indicators for crustal contamination, the Sr isotope composition of the MZ parental magma is highly elevated. This observation may be consistent with the contamination of the magma with a fluid, derived from dolomite, which may have increased the Sr isotope composition of the magma, while leaving the trace element budget largely unaffected.

VanTongeren & Mathez (2013) showed that the parental magma to the UZ was compositionally similar to the tholeiitic B2-type sills described by Harmer & Sharpe (1985) and therefore also to the CZ magma. Sharpe (1985) suggested that the MZ was emplaced on top of the CZ cumulate pile, leading to an upward displacement of the fractionated resident magma, which subsequently crystallised the UZ. In contrast, Sr isotope data for UZ samples from the Bethal limb, reported by Kruger (2005), show significantly less radiogenic compositions (≈ 0.7055) compared to those in the UCZ, which provides strong evidence against an upward displacement. The model could explain the upward decrease in Sr_i ratios by mixing, but Kruger et al. (1987) and Cawthorn et al. (1991) argued that mixing between the residual CZ magma (eventually forming the UZ) and the relatively primitive MZ magma would

not have preserved the isotopic discontinuity at the level of the Pyroxenite Marker, which also defines the base of the UZ in this study (Fig. 12). Instead, these authors suggested that the UZ crystallised from a new batch of magma, emplaced close to the top of the MZ cumulates, which mixed with resident magma from the MZ. Maier & Barnes (1998) proposed that the MZ magma intruded as a highly viscous crystal mush into semi-consolidated UCZ and UZ cumulate. This model, however, does not account for the gradual upward decrease in Sr isotope composition, which requires magma mixing within the MZ.

In light of the evidence, we propose that progressive mixing between MZ magma and either overlying resident CZ magma or fresh UZ magma occurred already from the lower portion of the MZ to the Pyroxenite Marker. Regardless of the exact derivation of the added magma, the observed variation in Sr_i ratios across the MZ can be explained by an incremental addition of tholeiitic B2-type magma to the resident MZ magma. Consequently, early cumulus plagioclase grains, characterised by relatively radiogenic compositions, were overgrown by less radiogenic plagioclase as indicated by Figure 22 c. This interpretation is further supported by the distinct correlation between most of the MZ samples and the UZ samples in Figure 17. In order to preserve the isotopic discontinuity at the level of the Pyroxenite Marker, we agree that the UZ is likely to be the product of a separate pulse of B2-type magma with little to no addition of MZ magma. Evidence for the injection of UZ magma on top of the MZ cumulate pile is provided by the undulating contact between the MZ anorthosite and the Pyroxenite Marker with typical flame-like protrusions of anorthosite into the overlying gabbroids, described in the eastern limb of the Bushveld Complex (Fig. 2, Maier et al. 2001). In the sedimentological research community, these structures are unequivocally interpreted to result from density contrasts between unlithified layers, where the underlying less dense layer pushes up into the overlying denser layer (e.g., Anketell et al. 1970). This inversion in density is also present in the observed lithologies associated with the flame structures. Thus, we interpret these structures as an indication that the UZ was emplaced on top of a semi-consolidated MZ cumulate.

4.4.7 Comparison between the western and northern limb Main Zones

In comparison to the MZ from the northern limb studied by Mangwegape et al. (2016), the samples from this study have considerably lower anorthite contents, whereas Sr isotopic signatures are comparable (Fig. 24). One explanation for the higher anorthite contents in the northern limb may be the contamination of the MZ magma by carbonate-rich lithologies from the Chuniespoort Group, such as the Malmani dolomite. Evidence for the assimilation of Transvaal Supergroup lithologies has been documented in various parts of the northern limb (e.g., van der Merwe 1976, Gain & Mostert 1982, Kinnaird 2005, Kinnaird et al. 2005). Especially the Platreef is commonly characterised by the presence of different metasedimentary xenoliths, including dolomite (e.g., van der Merwe 1976, Armitage et al. 2002, McDonald & Holwell 2011), but the Main Zone has also been reported to contain carbonate-rich xenoliths (Kinnaird et al. 2005). These xenoliths range in size from a few centimetres to 90 m across (Gain & Mostert 1982).

The assimilation of dolomite or a partial melt thereof would have considerably increased the CaO concentrations in the magma, producing plagioclase with elevated anorthite contents relative to less contaminated portions of the magma chamber. Wenzel et al. (2002) proposed that a low viscosity calcite melt could be easily extracted at relatively low temperatures from a dolomitic protolith, whereas much of the MgO remained in the restite as periclase. This is further supported by the Mg# of pyroxene from the MZ, which shows very little variation among the three limbs of the Bushveld, suggesting nearly similar MgO concentrations in the magma.

Ganino et al. (2013a) showed that a partial melt derived from a dolomitic protolith can be highly enriched in REE. Such a process would have also changed the trace element ratios of the MZ magma. Trace element data from Roelofse (2010), however, indicate that there is no apparent difference in trace element signatures between the northern and western limb MZ. Hence, it is considered unlikely that the assimilation of a partial dolomitic melt in the northern limb led to an increase in

CaO and therefore anorthite contents. In contrast, the interaction between a CO_2-rich fluid, released from dolomite during decarbonation, would probably not have been capable of introducing high amounts of CaO into the melt without changing its Sr isotopic signature.

Alternatively, the Sr isotope variation in the northern limb MZ could be explained by variable contamination of the MZ magma with different Transvaal Supergroup lithologies, but again the trace element signature, such as the limited range of the Ce/Sm ratios, provides little evidence for the importance of this process.

Another explanation could be that most of the northern limb MZ represents a thick mixing zone between MZ and UCZ magma, similar to the eastern and western limbs of the Bushveld, but on a much larger scale. Figure 24 clearly suggests mixing between a potential end-member MZ magma and typical UCZ magma compositions. Notably, the Bastard anorthosite sample from the UCZ of the western limb analysed by Yang et al. (2013) plots well within the northern limb MZ range, suggesting that many of the northern limb MZ samples have an UCZ affinity in terms of Sr isotopic signature as well as anorthite contents. Some northern limb samples have even higher Sr isotope compositions than the proposed MZ magma (≈ 0.7091), but this could be explained by local contamination of the magma by the granitic footwall. The zone of mixing essentially comprises lithologies close to the UCZ-MZ boundary with Sr_i ratios, ranging from ≈ 0.7080 to ≈ 0.7090. In the western limb, this zone is approximately 300-m-thick, whereas in the northern limb this zone covers more than 1,000 m in stratigraphy. In the northern limb, the upward decrease in Sr_i ratios begins at a much higher stratigraphic level compared to the western limb, i.e., probably just below the troctolite horizon (cf. Fig. 13, Mangwegape et al. 2016). This may be the result of the increased thickness of the UCZ-MZ mixing zone. A potential issue with the model is that the MZ crystallised after the solidification of the Platreef (Holwell et al. 2005, Holwell & Jordaan 2006), although it is not entirely clear whether the Platreef crystallised simultaneously with the Upper Critical Zone (e.g., McDonald et al. 2005).

4.4.8 Implications for intrusion emplacement

The interaction between the large volumes of magma that produced the Bushveld Complex and the 2-km-thick carbonate platform of the Transvaal Supergroup could also be considered as a possible mechanism to create space in the crust since the devolatilisation and dissociation of chemical sediments is directly linked to volume loss, i.e. the thermal decomposition of dolomite results in lower molar volumes, larger surface areas and greater porosities (e.g., Olszak-Humienik & Jablonski 2014). Hence, the vertical inflation of the Bushveld Complex, or parts thereof, may have been accommodated by floor depression in response to volume loss, thus producing a lopolith (e.g., Cruden 1998).

4.4.9 Regional isotopic variation in the UCZ of the Bushveld Complex

Several authors have reported contrasting Sr isotope compositions for MCU and BCU cumulates in different parts of the Bushveld Complex. The MCU at the Rustenburg and Union sections in the western limb (Eales et al. 1986, Kruger & Marsh 1982) as well as at Richmond and Atok in the eastern limb (Seabrook et al. 2005, Lee & Butcher 1990) have Sr isotope compositions typical of the CZ ($Sr_i \approx 0.7064$), whereas the MCU at Amandelbult (Kruger 1992) in the western limb has a more MZ-like signature ($Sr_i \approx 0.7075$). Similar discrepancies were also reported for the BCU (Seabrook et al. 2005, Lee & Butcher 1990). The Sr isotope data presented in this study indicate that the UCZ crystallised from a magma with a Sr_i ratio of ≈ 0.7061, if not lower. Our data further suggest that the lower part of the MZ was still affected by mixing between CZ and MZ. Therefore, the initial influx of MZ magma before mixing would have had a Sr_i ratio of ≈ 0.7091, if not higher (MZ sample A271). Thus, the proposed Sr isotope composition of the MZ magma differs dramatically from previously assumed ratios (Eales et al. 1986, Kruger & Marsh 1982, Lee & Butcher 1990, Seabrook et al. 2005), except for Kruger & Mitchell (1985) who suggested a Sr_i ratio of 0.7090 for the MZ. Consequently, we interpret the regional differences in Sr_i ratios to represent varying degrees of mixing in different

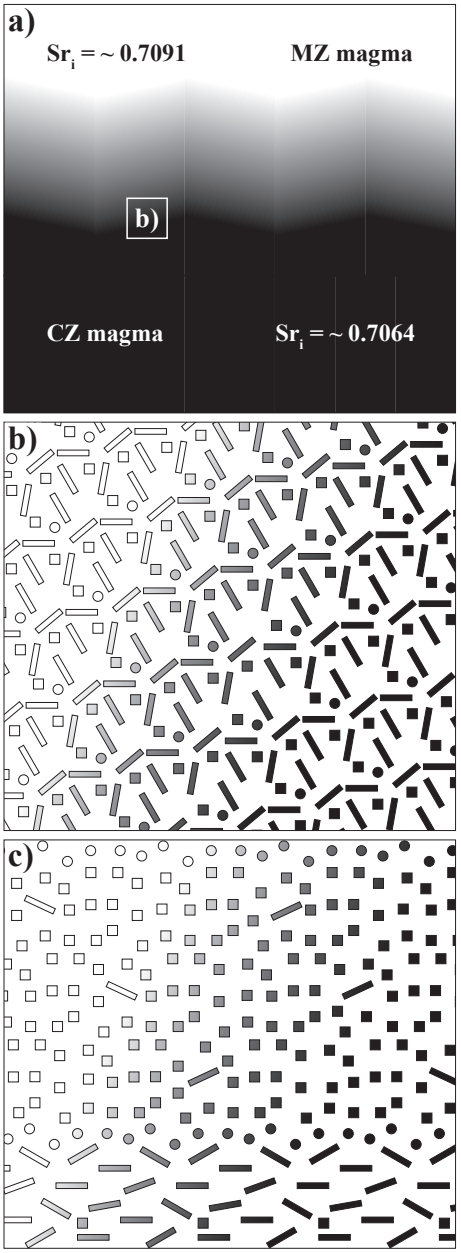

Fig. 25. Model for the observed regional variations in $^{87}Sr/^{86}Sr_i$ ratios among MCU profiles from different areas of the Bushveld Complex. a) Regionally non-uniform mixing between isotopically distinct MZ and CZ magma. b) Crystallisation of a proto-cumulate that reflects the different degrees in mixing. c) After the mobilisation of the proto-cumulate in a crystal slurry and associated density sorting, the variations in $^{87}Sr/^{86}Sr_i$ ratios are still present across individual continuous layers. Rectangles: plagioclase; squares: pyroxene; circles = chromite. Abbreviations: MZ = Main Zone; CZ = Critical Zone; MCU = Merensky Cyclic Unit.

portions of this very large magma chamber. The fact that none of the marginal sills from the Bushveld Complex (Harmer & Sharpe 1985) provide evidence for the

existence of a radiogenic MZ parental magma may simply reflect that the MZ is not represented in the suite of marginal rocks.

Regionally non-uniform mixing of magmas and the crystallisation of minerals in presumably cotectic proportions essentially produced a semi-consolidated cumulate pile with different isotopic signatures along the same stratigraphic level (Fig. 25 a, b). As proposed by Maier et al. (2013), these proto-cumulates may have been episodically mobilised by major slumping events associated with magma chamber subsidence, resulting in density-sorted crystal slurries. As a consequence, regional variations in the Sr isotope composition related to different degrees of magma mixing, before slumping and sorting, were preserved in the layered UCZ units (Fig. 25 c).

4.4.10 On iron-rich ultramafic pegmatites

One of the analysed samples from the MZ (sample A238) is an unusually coarse-grained gabbronorite, reaching up to 10 mm in grain size with an average *in situ* Sr_i ratio of ≈ 0.7077, which is much lower than the average *in situ* Sr_i ratios of all other samples from the MZ (Fig. 18). The chondrite-normalised rare earth element (REE) diagram in Figure 26 shows that this sample has a distinct REE pattern in comparison to typical MZ lithologies. Instead, the REE pattern is similar to that of iron-rich ultramafic pegmatites (IRUP) from the UCZ, described by Reid & Basson (2002). These authors also reported whole rock Sr isotope data for two samples, averaging at $Sr_i \approx 0.7074$. In addition, Scoon & Mitchell (2004) analysed IRUPs from the MZ for whole rock Sr isotope compositions. Their data confirm the lower range in Sr_i ratios, averaging at ≈ 0.7076 (n = 10). Based on the similarities in terms of REE patterns and Sr isotopes, we conclude that sample A238 belongs to the IRUP group. Notably, the sample also shows a considerable incursion in anorthite contents and Mg# (Fig. 18), which Scoon & Mitchell (2004) interpreted to result from a trapped liquid shift. This proposed reaction between trapped liquid and cumulus minerals, cannot account for the observed shift in Sr_i ratios between MZ cumulates and IRUP sample A238.

Based on our limited data on this single IRUP sample, it is impossible to present a conclusive petrogenetic model, but the coarse grain size, the evolved mineral chem-

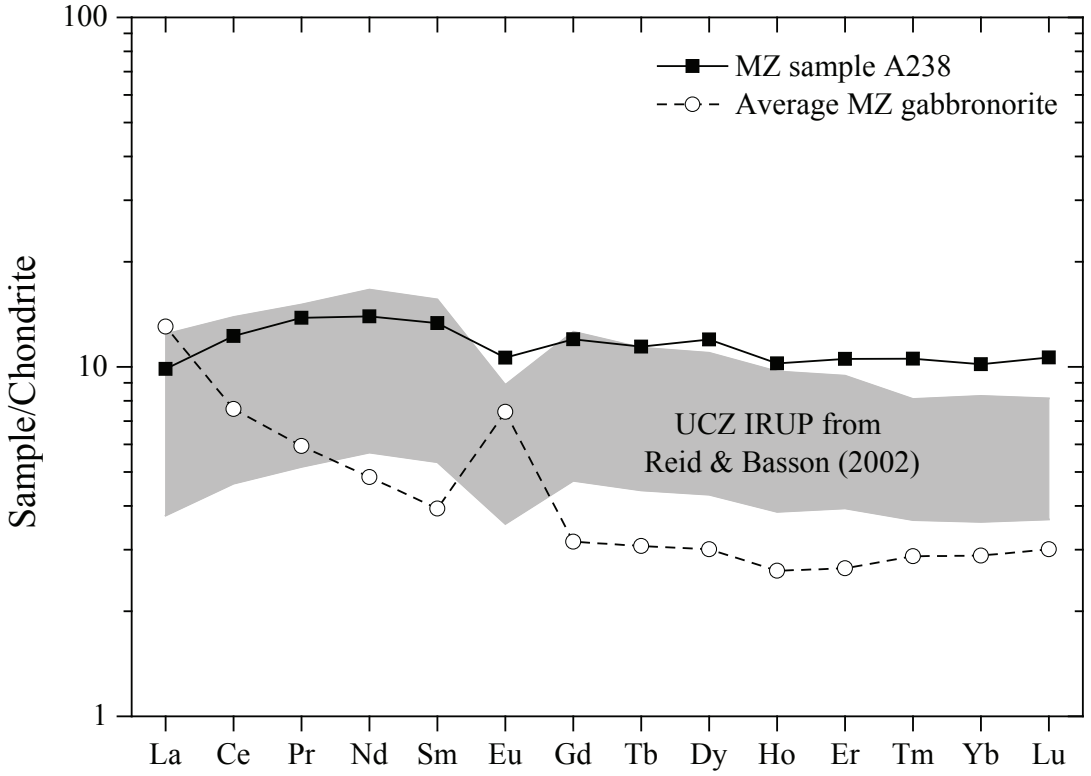

Fig. 26. Chondrite-normalised rare earth element (REE) pattern for sample A238 from the Main Zone. The average MZ gabbronorite REE pattern and the range of iron-rich ultramafic pegmatites (IRUP) are shown for comparison. Whole rock data for MZ and UCZ IRUP samples were taken from Barnes et al. (2004) and Reid & Basson (2002), respectively. Normalisation values were taken from McDonough & Sun (1995). Abbreviations: MZ = Main Zone; UCZ = Upper Critical Zone.

istry, the pronounced zonation of plagioclase and the distinct shift in Sr_i ratios indicate that the IRUP did not form from the same magma that crystallised the MZ, even though the sample is characterised by variable *in situ* Sr_i ratios (Fig. 13 c).

4.5 Summary

(1) Detailed variations in Sr_i ratios across the layered sequence of the Bushveld Complex reveal subtle, yet important differences between whole rock and *in situ* Sr isotope data. The latter commonly show more radiogenic compositions compared to the whole rock analysis, especially in the Main Zone. Our data indicate that this is not due to isotope disequilibrium between the rock-forming minerals, but due to an excessive age-correction, owing to the presence of secondary minerals with distinct Sr isotope compositions and high Rb/Sr ratios like mica and amphibole. Hence, age-corrected whole rock Sr isotope data may not always record the true Sr isotope composition of the sample.

(2) Complex zonation patterns in interstitial plagioclase from the Lower Zone, together with large variations in Sr isotope composition, suggest multiple incursions of primitive magma with varying Sr_i ratios into a mafic proto-cumulate. Each of these influxes produced an isotopically distinct rim around earlier plagioclase crystals. The initial Lower Zone magma likely had a relatively unradiogenic Sr isotope composition of < 0.7046. Pulses of more radiogenic magma may have acquired its isotopic signature from the interaction with the carbonate-rich floor rocks. Decoupling of anorthite contents from *in situ* Sr_i ratios as well as constant trace element ratios across the Lower Zone do not support bulk assimilation of crustal lithologies to explain the more radiogenic composition. However, a fluid phase, released from the decarbonation of the carbonates, may have changed the Sr isotopic signature of the magma without affecting trace element ratios.

(3) The Lower Critical Zone is slightly more radiogenic with Sr_i ratios of ≈ 0.7054 compared to the majority of the Lower Zone cumulates. The intra-sample range in Sr isotope compositions indicates that multiple isotopically distinct influxes of melt percolated through the mafic proto-cumulate, similar to the Lower Zone.

(4) The Upper Critical Zone shows a progressive increase in Sr_i ratios from the

bottom to the top. *In situ* analyses indicate that the zone crystallised from a Critical Zone magma mixed with progressively increasing proportions of Main Zone magma. Regional Sr isotopic variations in the Merensky Cyclic Unit and the Bastard Cyclic Unit are interpreted to be the result of non-uniform mixing between the two end-members.

(5) The lowermost part of the Main Zone represents the continuation of the Upper Critical Zone mixing trend, but the mixed magma at this level was already dominated by the Main Zone end-member. The highest Sr_i ratio in this zone is also likely to be the initial Sr isotope composition of the Main Zone magma before mixing ($Sr_i > 0.7091$). Trace element ratios suggest no crustal contamination. The progressive addition of a less radiogenic magma towards the top of the zone is evident in the gradual upward decrease in Sr_i ratios, e.g., Upper Zone magma. The enigma of a highly radiogenic Main Zone magma, which shows no evidence for crustal contamination, suggests an unusual mechanism of contamination. These observations can be explained by contamination of the Main Zone magma with a carbonate-derived fluid in a feeder conduit or a small staging chamber, similar to the upper part of the Lower Zone.

(6) The Upper Zone crystallised from a distinct pulse of magma with a Sr isotope composition of ≈ 0.7074 emplaced at the level of the Pyroxenite Marker. Fractional crystallisation proceeded with relatively limited disturbance, showing little evidence for the addition of an isotopically distinct magma.

(7) The interaction between devolatising sedimentary rocks and magma may also be an important petrogenetic process in other mafic-ultramafic intrusions – not only as a control on magma composition, but also regarding magma emplacement mechanisms as devolatilisation is directly linked to space creation due to volume loss.

Chapter 5

Microtextural characterisation of the Lower Zone of the Bushveld Complex

Parts of this chapter were submitted as:
Karykowski, B. T., Maier, W. D. (2017). Microtextural characterisation of the Lower Zone in the western limb of the Bushveld Complex, South Africa: Evidence for extensive melt migration within a sill complex. *Contributions to Mineralogy and Petrology* 172:60.

Co-author contributions:
W. D. Maier was involved in discussions during the writing of the manuscript.

Abstract

The Lower Zone of the Bushveld Complex comprises an up to 2-km-thick package of different ultramafic rock types with an approximately 90-cm-thick, sulfide-bearing noritic interval that occurs in the western and eastern limbs. The distribution and geometry of the zone are highly variable across the complex, showing pronounced, yet laterally discontinuous layering on different scales. Together with the distinct contact relations between rock types, the ubiquitous lack of large-scale fractionation in the Mg# of orthopyroxene, the variable Sr isotope compositions and the erratic Pt/Pd ratios, these observations strongly suggest an emplacement of the Lower Zone as a sill complex, as these contrasting geochemical characteristics are difficult to account for in a large Bushveld magma chamber, as previously suggested. It is more likely that these sills were episodically fed from a sub-Bushveld staging chamber, and variably contaminated, while passing through the crust before their final emplacement in the Lower Zone.

Detailed mineralogical and microtextural work based on high-resolution elemental mapping of a set of samples covering the entire Lower Zone stratigraphy of the western Bushveld shows that the variations in the late crystallising interstitial mineral mode are different from what would be expected, if all phases crystallised from a fixed initial mass of interstitial liquid. The interstitial mineral mode, represented by plagioclase, clinopyroxene and other late stage phases, shows variable ratios of these minerals, ranging from ca. 21:15:64 to 75:17:8. In comparison to modelled expected ratios, most of the analysed rocks have higher amounts of early crystallising interstitial phases (e.g., plagioclase, clinopyroxene), relative to late crystallising phases (e.g., quartz, alkali feldspar). Therefore, interstitial melt must have migrated at different stages of fractionation during cumulate solidification, as a consequence of either compaction or displacement by convecting interstitial liquids. Two samples, however, show the opposite: late phases are relatively more abundant than early ones, which is consistent with a convection-driven replacement of primitive interstitial liquid by more evolved liquid.

These results have important implications for the interpretation of the Lower

Zone and, by extension, for layered intrusions in general:

(1) interstitial sulfide mineralisation may be introduced into a cumulate through infiltrating melts, i.e., the liquid components of a sulfide-saturated crystal mush are not withheld from further migration, upon interaction with a cumulate pile;

(2) most importantly, late-stage minerals, such as zircon, rarely crystallise from trapped liquid that was initially in equilibrium with the cumulate.

Therefore, dating of interstitial zircon from cumulates is unlikely to record the actual timing of emplacement, but merely the crystallisation of a later episode of residual melt that migrated through the cumulate.

5.1 Introduction

The Bushveld Complex of South Africa, forming the world's largest known layered intrusion, hosts the most important platinum-group element (PGE), chromite and vanadiferous magnetite repository on Earth. The spectacular metal endowment of the Critical Zone led to a range of detailed studies focusing on this part of the intrusion, whereas the Lower Zone has traditionally received little scientific attention, in part due to the lack of economic PGE mineralisation and limited exposure. The up to 2-km-thick ultramafic unit is characterised by intricate discontinuous layering on all scales, comprising chromite-poor pyroxenite and olivine-bearing rocks with interstitial plagioclase, clinopyroxene and minor phlogopite, amphibole, quartz and sulfide (Cameron 1978*b*, Teigler & Eales 1996, Yudovskaya et al. 2013, Fig. 4 of present study). These interstitial phases are commonly interpreted to have crystallised as oikocrysts from trapped melt, which was in equilibrium with the surrounding cumulus crystals (e.g., Barnes 1986a). However, several studies have demonstrated the significance of residual melt migration in cumulates (Irvine 1980, Tait & Jaupart 1992, Bédard et al. 1992, Meurer & Meurer 2006), whereby an interstitial melt is expelled from a framework of cumulus phases or a "crystal mush". For example, Boorman et al. (2004) suggested a compaction-driven melt migration model to explain the modest increase in plagioclase abundance, associated with the transition from the Lower Zone to the Critical Zone of the Bushveld Complex.

This process may play a critical role when it comes to the origin of interstitial sulfide mineralisation, potential isotope disequilibrium between cumulus and intercumulus minerals and more importantly geochronology (e.g., Eales et al. 1990a, Prevec et al. 2005, Chutas et al. 2012, Yang et al. 2013). Modern high-precision dating of layered intrusions relies on the availability of zircon in cumulates. However, experimental studies show that zircon does not crystallise until the very late stages of fractionation (see Scoates & Wall 2015, for a detailed review). Therefore, melt migration has the potential to obscure crystallisation ages of cumulates, especially due to the fact that slow cooling of cumulate frameworks in layered intrusions facilitates enhanced porosity and permeability (e.g., Jerram et al. 2003). Moreover, the

origin and nature of the conspicuous interlayering in the Lower Zone remain under debate. Models range from gravity-controlled crystal settling and density sorting of minerals in crystal slurries on top of the cumulate pile, to repeated intrusions of sills to form a sill complex (see Naslund & McBirney 1996, for a detailed review of formation models).

In this study, we present detailed information on rock textures and mineralogy based on high-resolution X-ray elemental mapping of thin sections covering the entire stratigraphy of the Lower Zone. These element maps provide an excellent resource for a detailed two-dimensional visualisation of mineralogical and chemical variations as well as microtextures across a given sample, which can help elucidate physicochemical processes active during the formation of a cumulate body, i.e. melt migration recorded by interstitial material.

5.2 Layering in the Lower Zone

Detailed examination of drill core, intersecting the LZ at the Union Section, shows mostly sharp contacts on the macroscopic scale between different lithologies, which are primarily controlled by varying modal abundances of cumulus olivine and orthopyroxene (Fig. 27 a). A selection of photomicrographs highlighting the variability in rock types and textures across the LZ can be found in Appendix F. Layering is also prominent on a smaller scale, as shown in Figure 27 b, where alternating bands of dunite and pyroxenite define the layering on the sub-cm scale, but it may locally be disrupted by abundant schlieren or fragments of pyroxenite hosted in dunite (Fig. 27 a). However, gradational contacts may also be present, and are characterised by transitions from poikilitic harzburgite to more olivine-dominated dunite, and vice versa (Fig. 27 c). In places, we observe rock types that host abundant fragments from the pyroxenitic footwall in an ultramafic matrix, but contact relationships show gradual transitions from massive pyroxenite to seemingly poikilitic harzburgite, which may be interpreted to represent a magmatic breccia (Fig. 27 d). Conversely, altered olivine at the contact between peridotite and pyroxenite indicates that olivine-rich lithologies do not always postdate the orthopyroxene-rich

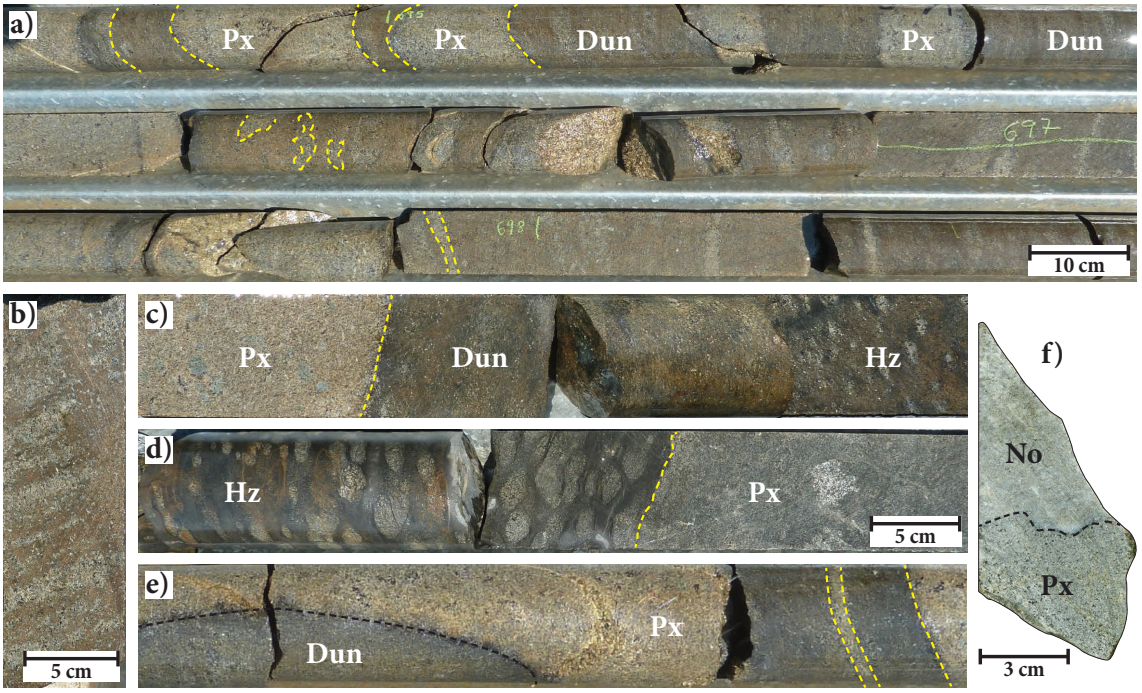

Fig. 27. Types of layering in the Lower Zone as intersected in drill core NG2 in the western Bushveld Complex. a) Complex interlayering between pyroxenite and dunite. Note the small schlieren of pyroxenite in dunite, core depth: 698 m. b) Small-scale layering between peridotite (brown) and pyroxenite (grey). Note the dunite cutting vertically across the layered succession, core depth: 237 m. c) Gradual transition between poikilitic harzburgite and dunite in contact with pyroxenite, core depth: 376 m. d) Contact between massive pyroxenite and poikilitic harzburgite. Note that the latter represents a breccia of massive pyroxenite in an olivine-dominated matrix (black), core depth: 328 m. e) Dunitic layer terminating half-way across the drill core, core depth: 694 m. f) Noritic interval hosted by pyroxenite. The basal contact is associated with sulfide mineralisation, core depth: 300 m. The core diameter is 63.5 mm (HQ).

ones (Appendix, Fig. F.3 b).

Even though detailed inspection of drill core demonstrates the pronounced interlayering of different mafic-ultramafic rock types, lateral variations along strike cannot be adequately evaluated without continuous outcrop or closely spaced drill holes. As a consequence of limited exposure and drill hole coverage of the LZ, the variability of individual layers along strike remains rather vaguely known in comparison to the Upper CZ. Cawthorn (2015) argued that LZ olivine-rich layers in the Olifants River Trough cannot be traced for more than a few hundred metres along strike. Furthermore, certain layers in the drill core we studied terminate half-way across the drill intersection, which strongly indicates discontinuous layering (Fig. 27

e). However, a rather conspicuous norite layer of ca. 90 cm in thickness has been delineated in the western as well as the eastern limbs of the Bushveld Complex (Fig. 27 f) (Lee & Tredoux 1986, Teigler 1990).

In summary, the LZ litho- and chemostratigraphy across the western and the eastern limbs reveal considerable lithological disparities (Fig. 4). In fact, they share very few characteristics, especially with respect to thickness and the presence of olivine-rich lithologies — only the mineral chemistry appears to be somewhat comparable. In addition, taking into account the marked variability of the LZ in the northern limb, it must be concluded that the zone is highly erratic along strike in terms of distribution, thickness, lateral continuity and lithostratigraphy (Scoon & Teigler 1995, Yudovskaya et al. 2013, Wilson 2015).

5.3 Results

A set of 9 samples covering the Lower Zone was collected from drill core NG2, which was collared at the Union Section of the western Bushveld Complex (Figs. 2, 28). The sample selection was intended to cover all rock types that are present in the Lower Zone, ranging from dunite and harzbugite to pyroxenite and gabbroic lithologies. Moreover, samples, showing as little evidence for alteration as possible, were selected. The mineralogy of the analysed samples is dominated by varying proportions of euhedral olivine and orthopyroxene, whereas all other minerals occur as interstitial phases within the euhedral framework (Fig. 29, Table 4).

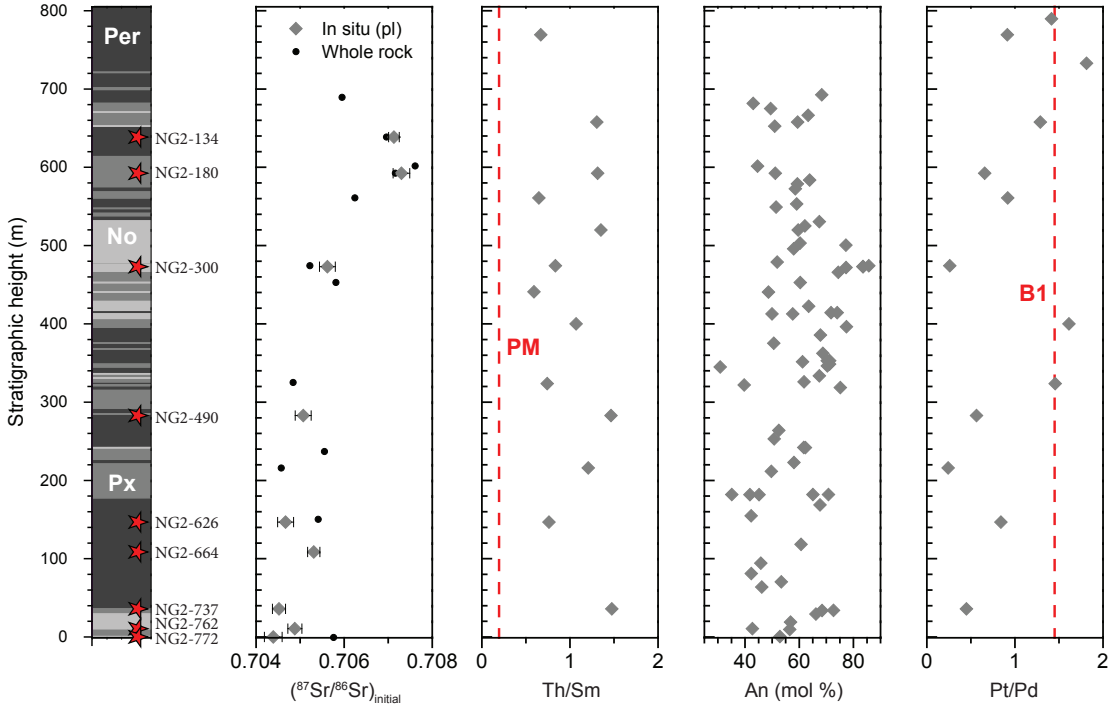

Fig. 28. Stratigraphic column of the Lower Zone together with a plot of average *in situ* plagioclase (pl) and whole rock Sr isotope compositions, whole rock Th/Sm ratios, average anorthite contents and Pt/Pd ratios. Red stars indicate samples used for this study. *In situ* Sr isotope data were taken from Chapter 4 and whole rock Sr isotope data were taken from Teigler (1990) and Maier et al. (2000), respectively. Trace element data and mineral chemistry were taken from Maier et al. (2013) and Teigler (1990), respectively. The primtive mantle (PM) Th/Sm ratio was taken from McDonough & Sun (1995). The Pt/Pd ratio for B1 was taken from Barnes et al. (2010).

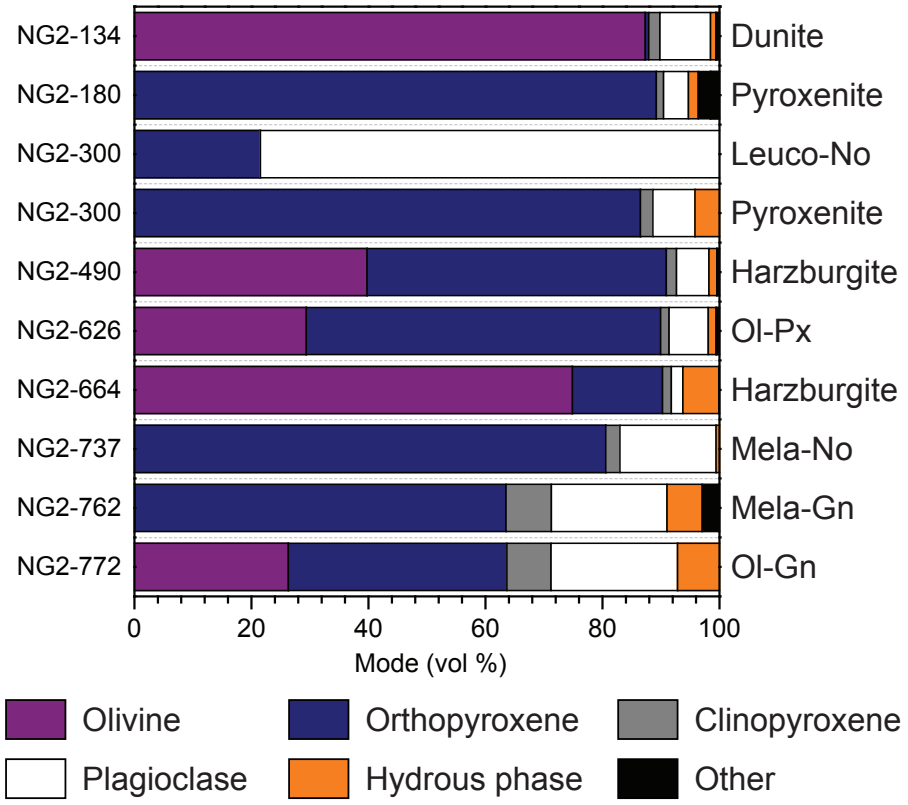

Fig. 29. Calculated mineral mode on the basis of elemental mapping. Note the gradual increase in hydrous phases within the lowermost three samples. Abbreviations: No = norite; Px = pyroxenite; Gn = gabbronorite; ol = olivine.

5.3.1 Sample NG2-134

Sample NG2-134 is a coarse-grained dunite with ca. 87 vol % euhedral olivine and ca. 9 vol % intercumulus plagioclase, whereas ortho- and clinopyroxene are minor intercumulus phases accounting for less than 1 vol % and ca. 2 vol %, respectively. Plagioclase shows strong compositional zonation with dramatic changes in anorthite contents from An_{78} to An_{45} over short distances — distinct subhedral anorthite-rich cores are overgrown by more albitic rims in the interstitial space (Appendix, Fig. G.1). Apatite is relatively abundant as small anhedral crystals reaching 100 µm at most. Phlogopite occurs as an accessory interstitial phase constituting less than 1 vol %. It is closely associated with sulfide, albite-rich plagioclase and to a lesser extent clinopyroxene.

Table 4. Mineral modes of the analysed Lower Zone samples on the basis of elemental mapping

Sample	NG2-134	NG2-180	NG2-300	NG2-300	NG2-490	NG2-626	NG2-664	NG2-737	NG2-762	NG2-772
Rock type	Dun	Opx	Leuco-No	Opx	Hz	Ol-Opx	Hz	Mela-No	Mela-Gn	Ol-Gn
Strat. height (m)	639	593	473	473	283	147	109	36	11	1
Opx (vol %)	0.6	89.2	21.5	86.5	51.2	60.5	15.4	80.6	63.5	37.3
Ol	87.3	-	-	-	39.8	29.4	74.9	-	0.1	26.3
Cpx	1.9	1.2	-	2.1	1.7	1.5	1.5	2.4	7.7	7.6
Pl	8.6	4.2	78.5	7.2	5.5	6.7	2	16.4	19.8	21.6
Chr	0.6	-	-	-	0.4	0.6	0.1	-	0.1	-
Qtz	-	2.1	-	-	-	-	-	-	2.9	-
Kfs	-	1.5	-	< 0.1	-	-	-	-	-	-
Phl	0.8	1.4	< 0.1	0.5	0.9	0.9	5.6	0.4	5.8	5
Amph	0.1	0.3	< 0.1	3.7	0.4	0.4	0.6	0.2	0.2	2.1
Total	100.0	100.0	100.0	100.0	100.0	100.0	100.0	100.0	100.0	100.0
Ap	++	++	+	+	++	++	++	+++	+++	+++
Lov	-	+	-	-	-	-	-	+	+	-
Zrc	-	+	-	-	-	-	-	-	-	-

Lithologies: Dun = dunite; Hz = harzburgite; Opx = orthopyroxenite; No = norite; Gn = gabbronorite; Ol = olivine. *Minerals*: Opx = orthopyroxene; Ol = olivine; Cpx = clinopyroxene; Pl = plagioclase; Chr = chromite; Qtz = quartz; Kfs = alkali feldspar; Phl = phlogopite; Amph = amphibole; Qtz = quartz; Kfs = alkali feldspar; Phl = phlogopite; Amph = amphibole; Ap = apatite; Lov = loveringite; Zrc = zircon

5.3.2 Sample NG2-180

Sample NG2-180 is a medium-grained orthopyroxenite with randomly oriented orthopyroxene accounting for ca. 89 vol %, whereas poikilitic plagioclase and clinopyroxene reach ca. 4 and 1 vol %, respectively. Additional interstitial phases comprise ca. 2.1 vol % quartz, 1.5 vol % alkali feldspar, 1.4 vol % phlogopite and minor amphibole (Fig. 30). These interstitial minerals show a strong spatial association with each other, and with albitic plagioclase, whereas more anorthite-rich plagioclase is more abundant towards the crystal edges. Subhedral apatite is relatively abundant reaching up to 250 µm across. Moreover, a fairly large subhedral zircon crystal measuring ca. 350 µm occurs in association with interstitial alkali feldspar. Another accessory mineral present is loveringite, which is a Ce-Zr-Ti-Cr-rich oxide mineral belonging to the crichtonite group (Gatehouse et al. 1978). It is present as a rather small, subhedral grain reaching up to 200 µm across (Fig. 36 a).

5.3.3 Sample NG2-300

Sample NG2-300 represents the lower contact between a medium-grained leuconorite and the medium-grained pyroxenitic footwall. The latter consists of ca. 87 vol % euhedral orthopyroxene, 7 vol % plagioclase and 2 vol % clinopyroxene. Other interstitial phases include ca. 4 vol % amphibole, less than 1 vol % phlogopite and accessory alkali feldspar. Plagioclase shows a relatively strong chemical zonation from the immediate contact into the footwall, where phlogopite is also more abundant (Fig. 31). Apatite crystals are generally rare, reaching 450 µm at most. Notably, the pyroxenite also hosts abundant sulfide mineralisation, occurring as fine disseminations throughout the rock. The contact between the two rock types is marked by a sub-mm-thick band of chromite, which follows the undulating contact. The thickness of the chromite band shows considerable lateral variation across the thin section, locally splicing into two sub-bands. The overlying leuconorite is weakly layered and composed of ca. 78 vol % subhedral to euhedral plagioclase and ca. 21 vol % anhedral to euhedral orthopyroxene. Accessory minerals include clinopyroxene and sulfide, which is generally less abundant in comparison to the underlying

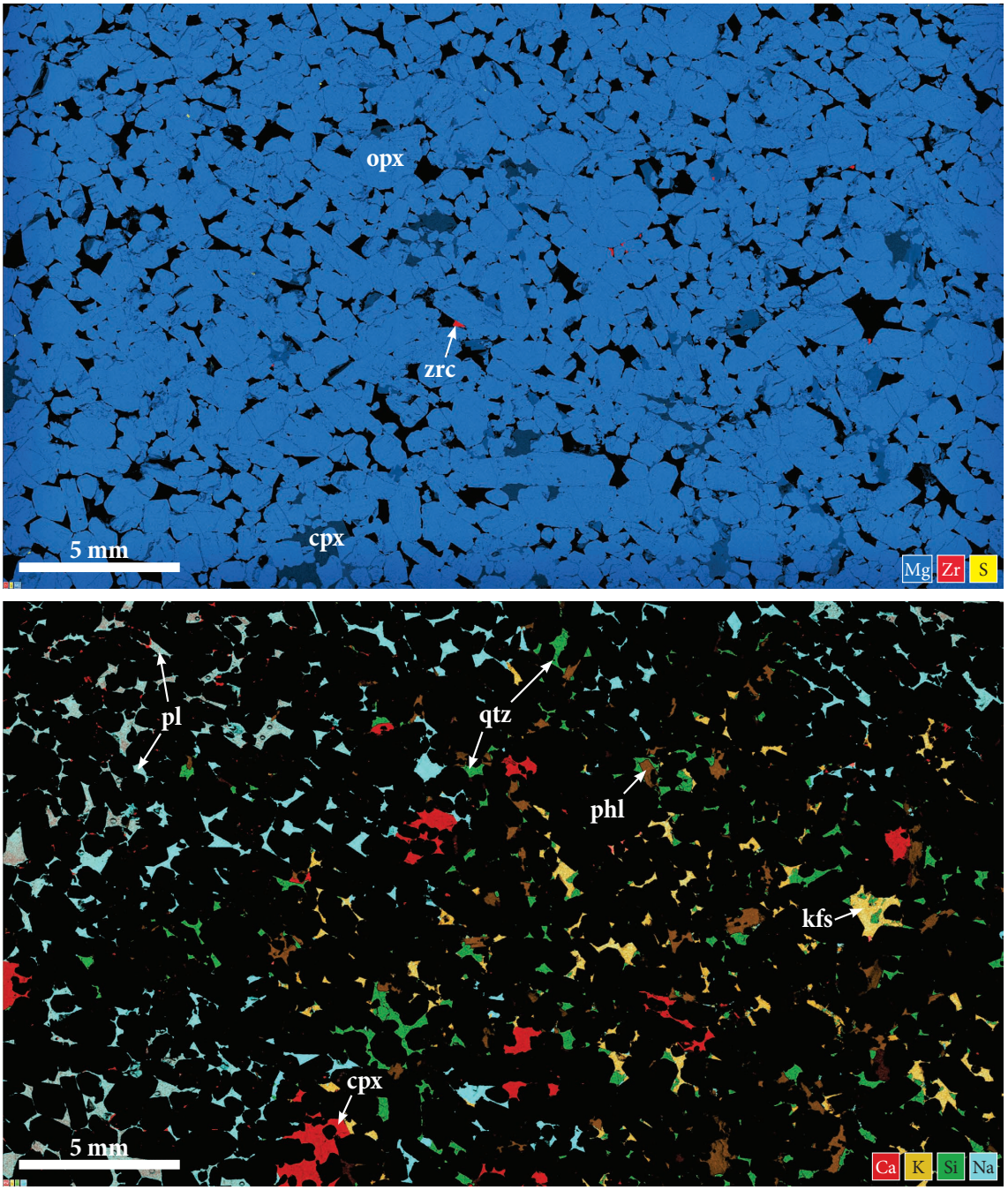

Fig. 30. Elemental map of orthopyroxenite NG2-180. Abbreviations: opx = orthopyroxene; cpx = clinopyroxene; qtz = quartz; pl = plagioclase; phl = phlogopite; kfs = alkali feldspar; zrc = zircon.

pyroxenite. The fabric of the leuconorite follows broadly the undulating contact marked by the chromite band.

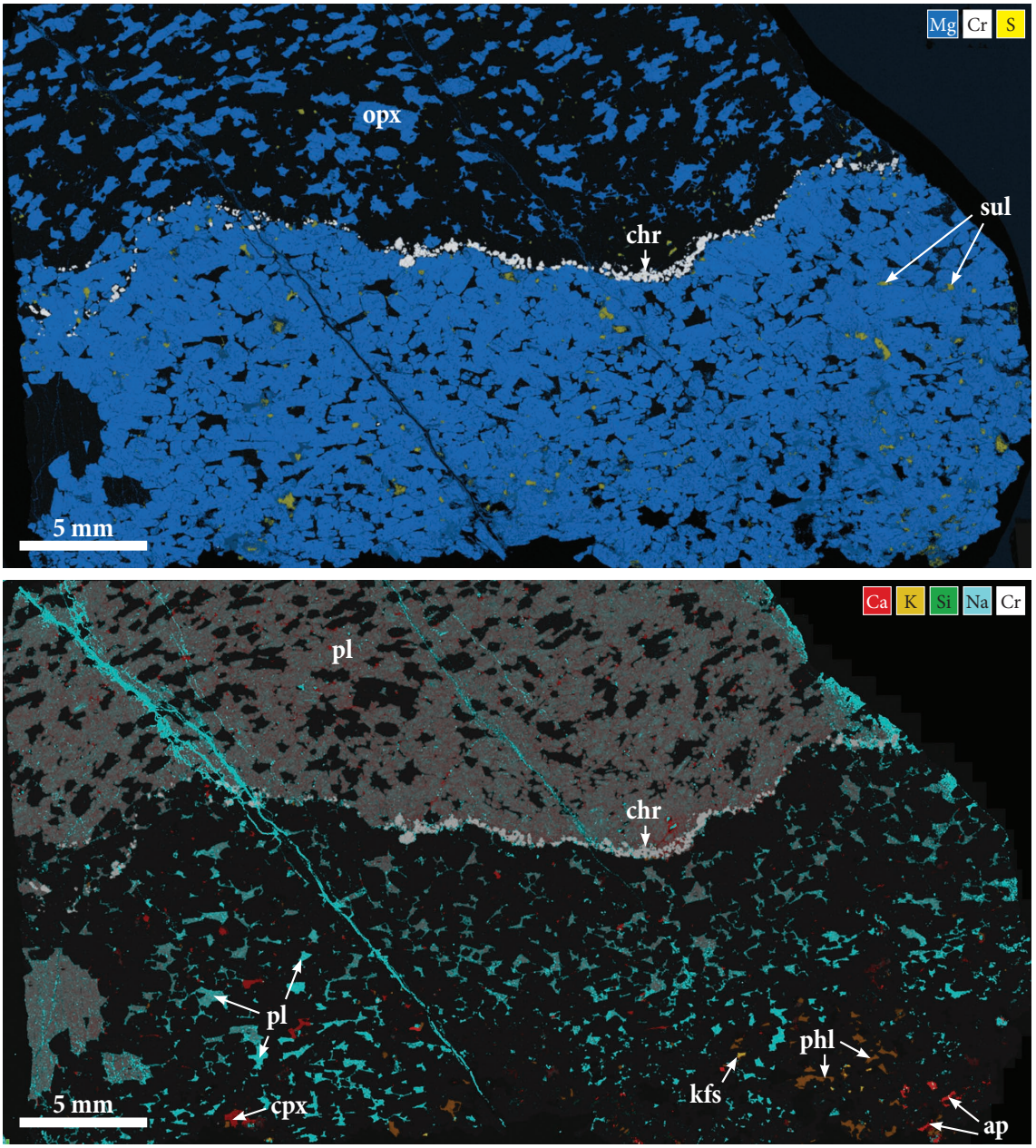

Fig. 31. Elemental map of sample NG2-300 showing a sharp contact between leuconorite and orthopyroxenite. The top of the image indicates stratigraphic up. Abbreviations: opx = orthopyroxene; cpx = clinopyroxene; chr = chromite; pl = plagioclase; kfs = alkali feldspar; phl = phlogopite; ap = apatite; sul = sulfide.

5.3.4 Sample NG2-490

Sample NG2-490 is a massive harzburgite, consisting of ca. 51 vol % orthopyroxene and 40 vol % olivine, with accessory chromite and sulfide. Clinopyroxene is

present as patchy oikocrysts throughout the thin section, accounting for less than 2 vol %. Plagioclase is more abundant, constituting ca. 6 vol %, and shows considerable chemical variation, although distinct core-rim compositional relationships are not evident (Appendix, Fig. G.4). Phlogopite occurs in a relatively confined area of the thin section, reaching up to 1 vol %, together with abundant interstitial anhedral to subhedral apatite of up to 300 µm in length. Notably, the sample contains a tabular megacryst of inclusion-poor orthopyroxene, which is similar in composition to smaller orthopyroxene grains surrounding it.

5.3.5 Sample NG2-626

Sample NG2-626 is a weakly layered olivine-orthopyroxenite with ca. 61 vol % orthopyroxene and 29 vol % olivine; minor patches of poikilitic clinopyroxene constitute less than 2 vol % (Appendix, Fig. G.5). Plagioclase occurs as an interstitial phase and accounts for ca. 7 vol %. It shows relatively pronounced compositional zonation with anorthite-rich subhedral cores and more albitic anhedral rims. Apatite is relatively abundant; it occurs as small anhedral grains, reaching up to 200 µm, and is closely associated with phlogopite and amphibole, which account for less than 1 vol % combined.

5.3.6 Sample NG2-664

Sample NG2-664 is a harzburgite, containing ca. 75 vol % euhedral olivine, 15 vol % intercumulus orthopyroxene, less than 4 % plagioclase plus clinopyroxene, as well as minor chromite and amphibole. Phlogopite is relatively abundant, reaching almost 6 vol %, and anhedral to subhedral apatite occurs as an accessory phase of up to 250 µm in length, commonly enclosed by orthopyroxene (Appendix, Fig. G.6). All the interstitial phases are concentrated in distinct pod-like areas of the thin section, rather than being homogeneously distributed throughout the sample.

5.3.7 Sample NG2-737

Sample NG2-737 is a melanorite with ca. 81 vol % euhedral orthopyroxene, 16 vol % plagioclase and minor clinopyroxene. Accessory phases are phlogopite and amphibole, accounting for less than 1 vol % combined. Interstitial plagioclase shows considerable chemical zonation with anorthite-rich cores and more albitic rims (Appendix, Fig. G.7). The sample also contains significant amounts of subhedral apatite, reaching up to 320 µm across, and less commonly loveringite of up to 250 µm.

5.3.8 Sample NG2-762

Sample NG2-762 is a fine- to medium-grained melagabbronorite with a predominance of prismatic orthopyroxene over clinopyroxene, and with accessory olivine and chromite. Clinopyroxene occurs as randomly distributed oikocrysts together with strongly zoned plagioclase. Despite the interstitial texture of the latter, the compositional variation commonly shows distinct euhedral anorthite-rich plagioclase cores, which are overgrown by more albitic rims (Fig. 32). Another striking feature is the abundance of phlogopite, constituting up to 6 vol %. It occurs in large interstitial patches spatially associated with subhedral to euhedral prismatic apatite grains of up to 800 µm in length, as well as anhedral quartz, which accounts for ca. 3 vol %. The sample also contains subhedral loveringite grains of up to 200 µm in length, as well as small amounts of sulfide (Fig. 36 b).

5.3.9 Sample NG2-772

Sample NG2-772 is a fine-grained olivine-gabbronorite situated ca. 1.4 m away from the floor rock contact of the intrusion. Olivine and plagioclase account for ca. 26 and 22 vol %, respectively, whereas orthopyroxene is slightly more abundant with 37 vol %. Phlogopite and amphibole reach ca. 5 and 2 vol %, respectively. The latter is closely associated with clinopyroxene rims, whereas phlogopite occurs as irregular patches throughout the rock. Moreover, the sample contains minor anhedral apatite and minor sulfide, both of which are confined to the interstices (Appendix, Figs. G.9,

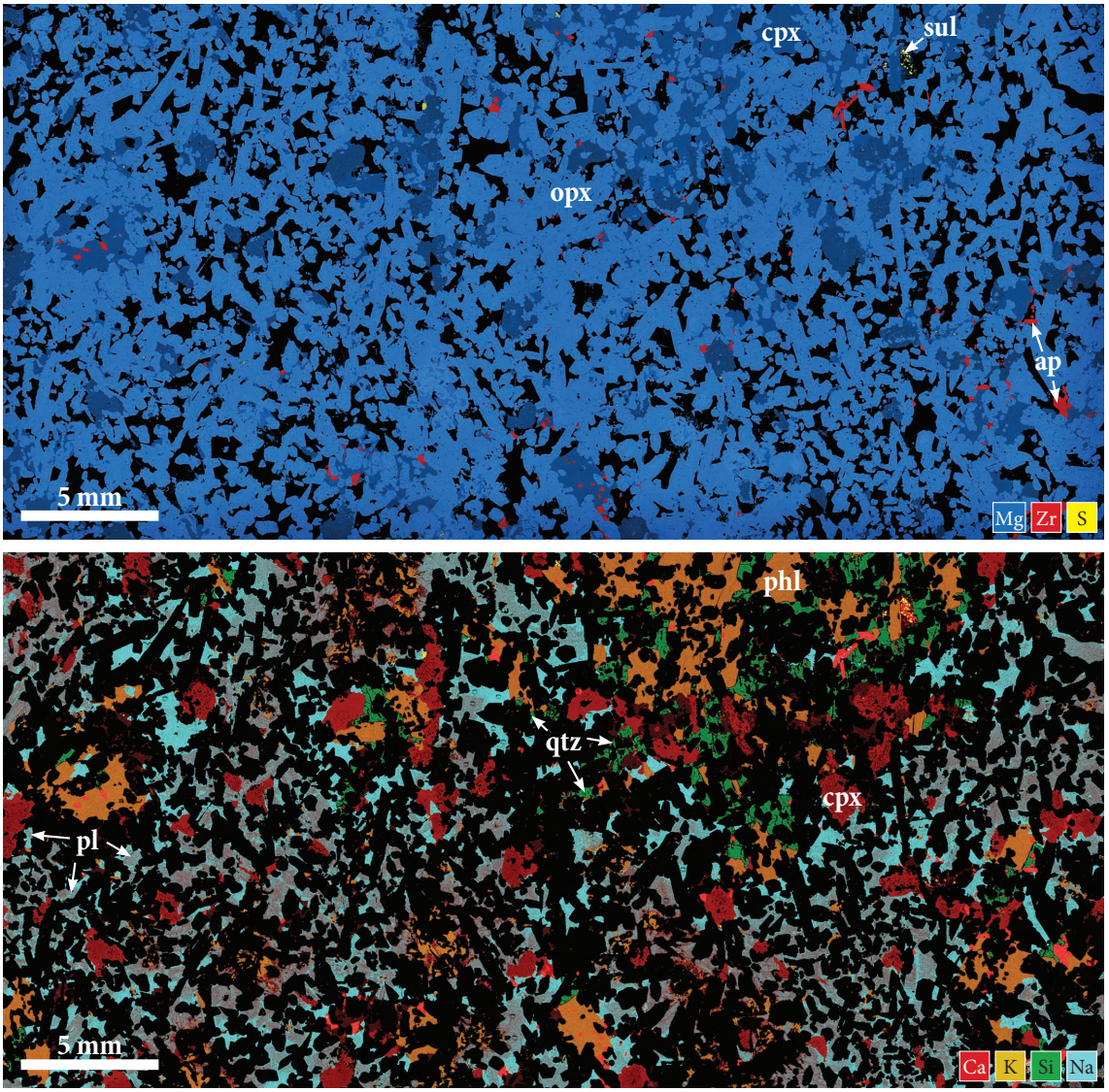

Fig. 32. Elemental map of melagabbronorite sample NG2-762. Abbreviations: opx = orthopyroxene; cpx = clinopyroxene; pl = plagioclase; qtz = quartz; phl = phlogopite; ap = apatite ; sul = sulfide.

G.10). Compositional zonation in plagioclase is fairly pronounced, mostly showing anorthite-rich cores and more albitic rims.

The analysed LZ sample set covers a wide lithological range from ultramafic to mafic compositions, i.e., dunite, harzburgite, orthopyroxenite, leuco- and melanorite and melagabbronorite. The total modal amount of interstitial phases is highly variable across the LZ and the relative proportions of clinopyroxene, plagioclase, alkali feldspar and hydrous phases, comprising the interstitial mineral assemblage, also

change dramatically irrespective of the host cumulate. Some ultramafic rocks are essentially barren of evolved or hydrous minerals, whereas others host significant amounts of these phases.

5.4 Discussion

5.4.1 Melt migration

In order to estimate the mineral proportions expected to crystallise from a patch of trapped liquid in equilibrium with cumulus orthopyroxene in a typical LZ pyroxenite, we conducted fractional crystallisation modelling, assuming a Bushveld B1 magma from Barnes et al. (2010), which has undergone fractional crystallisation up to the point where orthopyroxene compositions match the ones observed in the LZ. Subsequently, the residual liquid trapped in the interstitial space of the cumulus mineral framework crystallised in local equilibrium between phases under closed system conditions. PELE (Boudreau 1999) modelling shows that fractional crystallisation of a slightly hydrous B1 magma with ca. 12 wt % MgO (0.05 wt % H_2O) at 1,200 bar produces orthopyroxene compositions similar to the ones in the LZ (Mg# $\approx$ 83) after ca. 35 % crystallisation, which would be in equilibrium with a residual liquid of ca. 5.4 wt % MgO. Trapping of this liquid and subsequent closed system equilibrium crystallisation would result in an interstitial mineral assemblage, comprising ca. 49 vol % plagioclase, 13 vol % clinopyroxene, 17 vol % quartz and 21 vol % of other minerals including alkali feldspar and phlogopite, assuming that orthopyroxene crystallised as a relatively evolved overgrowth or rim on pre-existing cumulus grains (Table 5). The initial water content of the magma does not play a significant role in the calculations, as it primarily controls the ratio between phlogopite and alkali feldspar; this has a negligible effect on the model, due to the small

Table 5. Results of equilibrium crystallisation of trapped melt using PELE

Mineral	Equilibrium mineral mode	Interstitial mineral mode[1]
Orthopyroxene (vol %)	12.1	-
Clinopyroxene	11.1	12.6
Plagioclase	43.2	49.1
Quartz	14.9	17.0
Other minerals	18.7	21.3
Total	100.0	100.0

[1]Assuming that orthopyroxene crystallised as an overgrowth on cumulus orthopyroxene.
Melt composition: B1 magma from Barnes et al. (2010), which has undergone fractional crystallisation up to the point where orthopyroxene compositions match the ones observed in the LZ (En_{85}).
Conditions: 1.2 kbar; fO_2 = QFM.

difference in density of less than 10 %. However, the most realistic ratio between phlogopite and alkali feldspar based on the observed mineral proportions of the analysed LZ samples resulted from modelling with an initial water content of < 0.1 wt % H_2O. Above this value, phlogopite dominates significantly over alkali feldspar, which is inconsistent with our observations.

Using the relative mineral proportions that are expected to crystallise from trapped liquid under closed system equilibrium (plagioclase : clinopyroxene : all other late stage minerals = 49:13:38), the trapped liquid fraction can be estimated on the basis of measured plagioclase and clinopyroxene modes, respectively. For example, orthopyroxenite sample NG2-300 features an interstitial mineral assemblage of 7.2 vol % plagioclase, 2.1 vol % clinopyroxene and 4.2 vol % other late stage minerals (Table 3). Based on the plagioclase mode of this sample, the estimated trapped liquid fraction would be 41 vol %, while the clinopyroxene mode would suggest a slightly higher trapped liquid fraction of 46 vol %. In comparison to that, the late stage phases account for only 31 vol % of the interstitial mineral mode.

The results of this calculation for all other analysed LZ samples are shown in Table 6. The dataset shows that the trapped liquid estimates, derived from plagioclase and clinopyroxene modes, are generally higher compared to what the late stage mineral mode would suggest, except for two unusually phlogopite-rich samples (orthopyroxenite NG2-180, harzburgite NG2-664). Similar trapped liquid estimates based on plagioclase and clinopyroxene modes would be somewhat expected, as they are close to each other along the liquid line of descent, whereas the other phases, especially the hydrous minerals, crystallise very late. The disparity between these estimates cannot be explained by closed system fractionation, but requires a substantial loss of evolved trapped liquid from the cumulate after the crystallisation of plagioclase and clinopyroxene. A feasible mechanism to allow for trapped liquid to be lost during late stages of cumulate solidification could be compaction-driven melt migration as shown for the Lower Zone by (Meurer & Boudreau 1996, Boorman et al. 2004).

Table 6. Trapped liquid estimates

Sample	Rock type	*Interstitial mineral mode*			*Normalised mineral mode*			*Estimated trapped liquid*[1]		
		Pl	**Cpx**	**Oth**	**Pl**	**Cpx**	**Oth**	**Pl**	**Cpx**	**Oth**
NG2-134	Dun	8.6	1.9	0.9	75.4	16.7	7.9	58.5	48.7	7.9
NG2-180	Opx	4.2	1.2	5.3	39.3	11.2	49.5	30.4	32.8	49.5
NG2-300	Opx	7.2	2.1	4.2	53.3	15.6	31.1	41.4	45.5	31.1
NG2-490	Hz	5.5	1.7	1.3	64.7	20.0	15.3	50.2	58.5	15.3
NG2-626	Ol-Opx	6.7	1.5	1.3	70.5	15.8	13.7	54.7	46.2	13.7
NG2-664	Hz	2.0	1.5	6.2	20.6	15.5	63.9	16.0	45.2	63.9
NG2-737	Mela-No	16.4	2.4	0.6	84.5	12.4	3.1	65.6	36.2	3.1
NG2-762	Mela-Gn	19.8	7.7	8.9	54.4	21.2	24.5	42.2	61.8	24.5
NG2-772	Ol-Gn	21.6	7.6	7.1	59.5	20.9	19.6	46.1	61.2	19.6

[1]Assuming a ratio of pl : cpx : all other late stage minerals = 49 : 13 : 38 (modelled equilibrium assemblage).
Lithologies: Dun = dunite; Hz = harzburgite; Opx = orthopyroxenite; No = norite; Gn = gabbronorite; Ol = olivine.
Mineral: Pl = plagioclase; Cpx = clinopyroxene; Oth = other minerals.

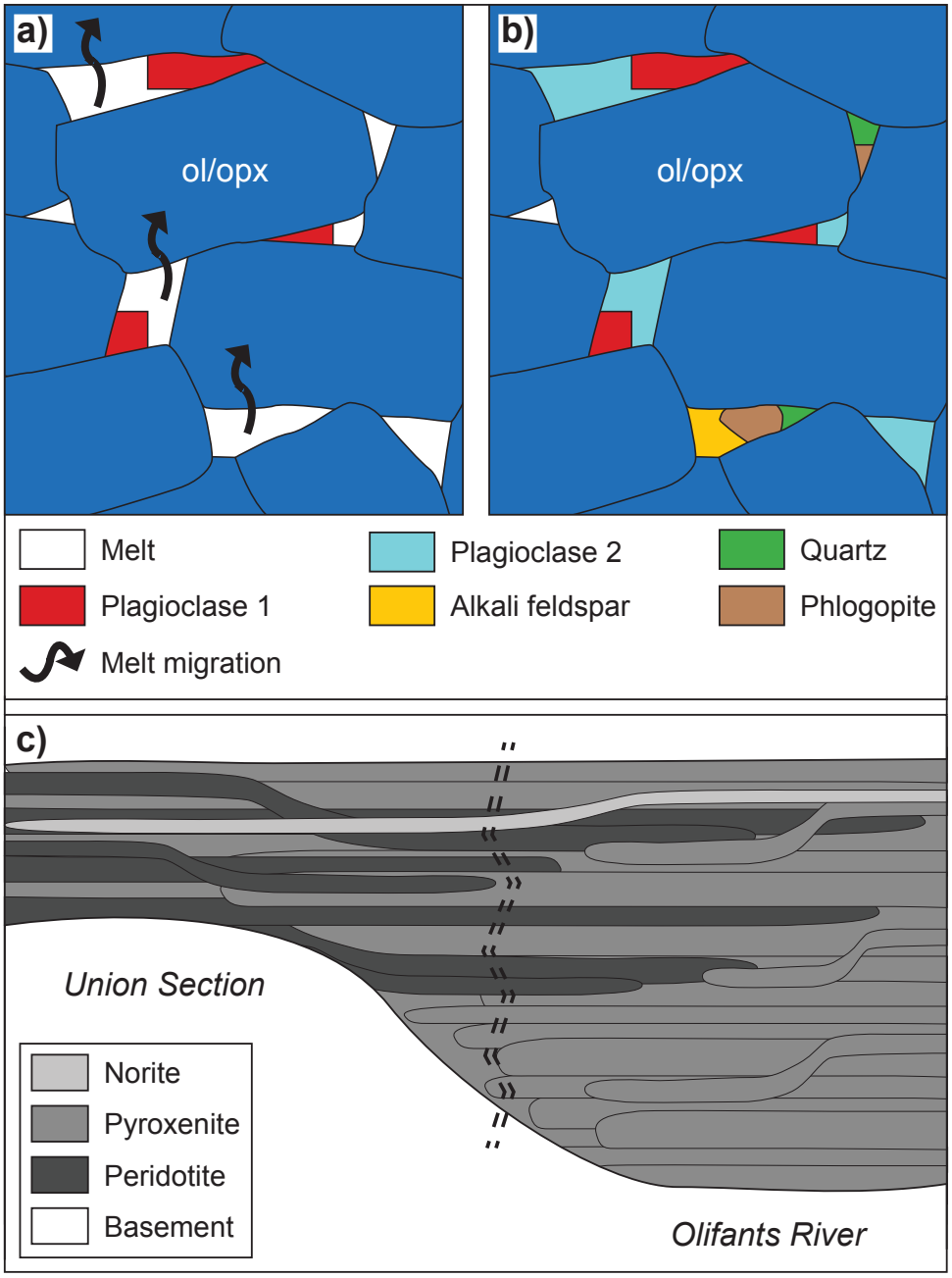

Fig. 33. a) Formation of intercumulus minerals from trapped liquid. Euhedral to subhedral plagioclase crystallises with a distinct geochemical and isotopic signature in the interstitial space. The residual liquid may be forced upwards as a consequence of compaction or displacement by a different migrating liquid. b) Infiltration of the cumulate by a geochemically and isotopically distinct batch of liquid from elsewhere in the crystal pile results in distinct overgrowths on pre-existing plagioclase grains. Upon further fractionation of the interstitial liquid, evolved phases, such as quartz, phlogopite, alkali feldspar, start crystallising. c) Schematic diagram illustrating the effect of floor rock topography on the geometry of the Lower Zone. The spatial distribution of geochemically distinct sills is controlled by bulges and troughs in the floor rock, i.e., the lowermost pyroxenite unit is only present in the Olifants River Trough. Note that the noritic interval cross-cuts the ultramafic succession in the western and eastern limbs.

The two phlogopite-rich samples, however, demonstrate that evolved trapped liquid in these systems can also be gained and not only lost: trapped liquid estimations derived from plagioclase and clinopyroxene modes in orthopyroxenite sample NG2-180 suggest 30 and 33 vol % trapped liquid, respectively, whereas late stage minerals account for 50 vol % of the mode. Compared with this, plagioclase and clinopyroxene modes in harzburgite sample NG2-664 suggest highly dissimilar estimates of trapped liquid with 16 and 45 vol %, respectively. Thus, it is more likely that the trapped liquid was removed from its original location within the cumulate at different stages of crystallisation through expulsion as a consequence of either compaction or displacement by convecting interstitial liquids (Fig. 33 a, b). Expelled melts that migrated through the cumulate, were characterised by variable degrees of fractionation, implying that evolved melts can be replaced by relatively primitive melts and vice versa.

It may be argued that orthopyroxenite sample NG2-180 has an unusually *felsic* interstitial mineral assemblage, as it is also characterised by a more radiogenic Sr isotope composition of plagioclase (Fig. 28), potentially reflecting interstitial melt compositions that were not derived from a mafic-ultramafic parental magma, but from felsic partial melts. On the other hand, sample NG2-134 also features an enriched Sr isotope signature, despite a typical *mafic* interstitial mineral assemblage (Table 4, Appendix, Fig. G.1). Hence, radiogenic Sr isotope compositions are not exclusive to a felsic interstitial mineral assemblage, which supports a mafic-ultramafic origin of the interstitial material in sample NG2-180. In addition, these more radiogenic samples show no evidence for a larger crustal component, as indicated by their Th/Sm ratios, which are largely in line with those of the other samples (Fig. 28).

Further support for commonly occurring melt convection is provided by the highly variable incompatible trace element abundances across the LZ (Fig. 34). A plot of whole rock La concentrations vs. the amount of trapped liquid indicates that most of the LZ samples have either lost or gained residual liquid relative to what would be expected from trapped liquid crystallisation of B1 magma under closed system conditions.

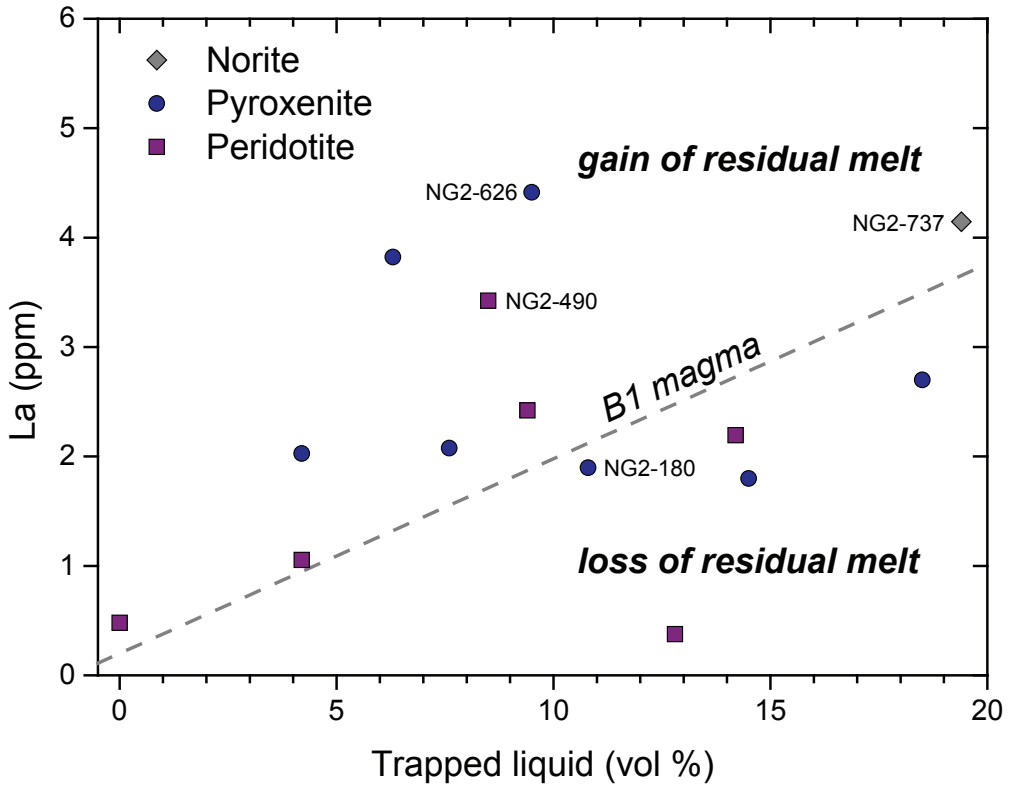

Fig. 34. Plot of whole rock La concentrations vs. trapped liquid. The trapped liquid component was estimated on the basis of the intercumulus mineral abundance in each sample. Note that most samples plot away from the dashed orthopyroxene-B1 magma tie-line. Data were taken from Teigler (1990), Maier et al. (2013) and this study. The La concentrations of B1 magma and LZ orthopyroxene were taken from Barnes et al. (2010) and Godel et al. (2011), respectively.

5.4.2 Emplacement of the Lower Zone as a sill complex

The presence of discontinuous layering in the LZ, together with the major lateral variations along strike in terms of distribution, thickness and lithotypes as well as the heterogeneous Sr isotope compositions and the erratic Pt/Pd ratios across the sequence, argue strongly against a classical closed system fractionation model of a large magma chamber (Fig. 27, 28) (Cameron 1978*b*, Teigler 1990, Yudovskaya et al. 2013, Chapter 4). Additionally, the lack of progressive fractionation, as indicated by the near-constant Mg# of orthopyroxene across an interval of up to 1,500 m, is also inconsistent with closed system crystallisation (Fig. 4). Despite potential rheological concerns about the ability of a crystal mush to move, the above described characteristics of the LZ as well as the cross-cutting relationships and textures observed in drill core (Fig. 27) cannot be explained by the intrusion of crystal-poor magma. Lay-

ers that terminate half-way across the drill intersection as well as evenly distributed fragments of pyroxenite in a olivine-dominated matrix argue strongly against the intrusion of crystal-poor magmas as some sort of density-driven accumulation of autoliths would be expected. Notably, several geochemical characteristics of the uppermost LZ peridotites provide further arguments against normal fractionation of a crystal-poor magma (Fig. 28). Olivines from these samples have the highest forsterite contents of all LZ lithologies, implying that they crystallised from the most primitive magma (Teigler 1990). Additionally, these peridotites are characterised by much lower PGE and Cu concentrations compared to the rest of the LZ (Maier et al. 2013). This has also been noted by Lee & Tredoux (1986) for olivine-rich lithologies in the upper portion of the Lower Zone in the eastern limb. Together with mantle-like Cu/Pd ratios and Cu/Zr ratios close to unity throughout the peridotic unit, this suggests a crystallisation from a sulfide-undersaturated magma, even though all other LZ lithologies, including the footwall, show evidence for cumulus sulfide, and thus for a crystallisation from a sulfide-saturated parental magma (Maier et al. 2013).

The contact relationship between the LZ pyroxenite and the ca. 90-cm-thick noritic interval sampled in NG2-300 provides an insight into the processes associated with the formation of this rather unusual noritic package. The sharp undulating contact shown in Figure 31 is broadly parallel to the fabric defined by the orthopyroxene crystals in the leuconorite. Moreover, the contact is marked by a thin chromite seam, which may be interpreted as a reaction product resulting from the partial melting of the footwall pyroxenite in a process similar to the petrogenetic model for the Merensky Reef proposed by Nicholson & Mathez (1991). Interstitial sulfide mineralisation associated with the lower rather than the upper contact of the noritic interval indicates that these sulfides were introduced as part of the leuconorite. These observations are best explained by a sill model in which the leuconorite intruded as a sulfide-saturated crystal mush with cumulus plagioclase and minor orthopyroxene, which led to local dissolution of the pyroxenite to form the chromite band. Residual melt and dense sulfide liquid locally percolated downwards into the footwall pyroxenite, as evidenced by the relatively high abundance of sulfides. The diverse

geochemical character of the LZ lithologies likely resulted from the crystallisation of cumulus minerals in a sub-Bushveld staging chamber that episodically fed variably contaminated crystal mushes into the LZ, as suggested by Ashwal et al. (2005). This staging chamber would have been large enough to allow for the crystallisation of considerable amounts of orthopyroxene, showing limited variability in Mg#.

A number of studies have previously suggested an intrusive sill-like emplacement of other parts of the Bushveld Complex, based mainly on the presence of large floor rock xenoliths between the LZ and the UCZ (Hulbert 1983, Maier et al. 2008, Yudovskaya et al. 2013). Furthermore, transgressive anorthosite seams in the Upper CZ were also interpreted to have injected in a sill-like manner (Maier et al. 2016b). The well-exposed Monchegorsk Complex in Arctic Russia may represent an analogue to what can be observed in other layered intrusions. The ultramafic Sopcha intrusion shows distinct macroscopic interlayering between two pyroxenitic lithologies of contrasting colour. In most places, the greenish upper layer defines a sharp undulating contact similar to layering in other intrusions (Fig. 35 a). However, further along

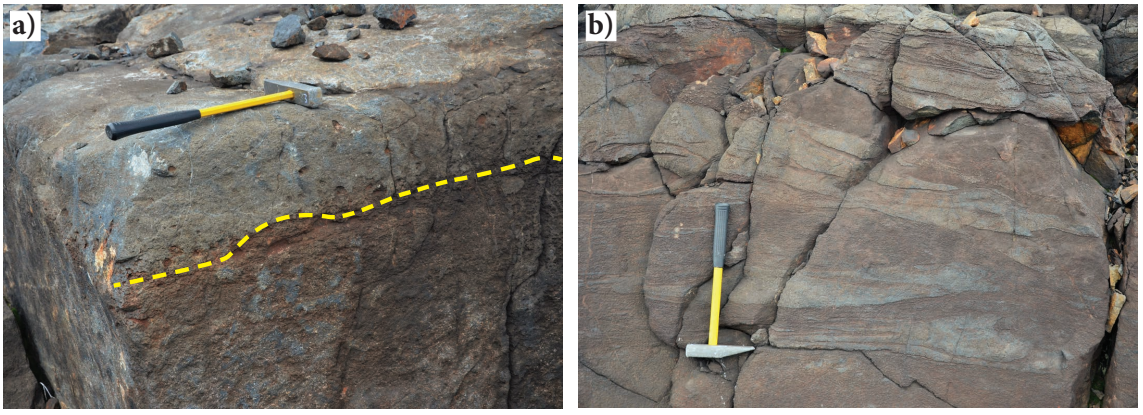

Fig. 35. Exposure of layered pyroxenite in the Monchegorsk Complex, NW Russia. a) Sharp boundary between greenish pyroxenite and the underlying mineralised brownish pyroxenite. b) Splicing of the greenish pyroxenite results in complex interlayering between the two rock types.

strike, this layer has bifurcated into a complex set of sub-layers that interfinger with the host pyroxenite (Fig. 35 b). Notably, these two lithologies are geochemically very similar, but the brownish host pyroxenite is extensively mineralised, accounting for why it can be visually discerned relative to the greenish one, whereas in most other cases this highly revealing feature is absent (cf. Chapter 7 for more details).

As a consequence, we suggest that bifurcation is a ubiquitous process at least within the LZ, accounting for the observed discontinuous layering, and allowing for the presence of sulfide-undersaturated lithologies above sulfide-saturated ones with distinct Pt/Pd ratios, possibly even across the entire Bushveld Complex. It is only apparent in successions characterised by visually distinctive and contrasting lithologies, i.e. xenolith-rich intervals, anorthosite/chromite seams, unusual noritic or sulfidic intervals. The lateral variations across the different limbs are thus strongly controlled by floor rock topography, which affected the spatial distribution and propagation of individual sills (Fig. 33 c).

5.4.3 Accessory minerals in the Lower Zone

According to Webster & Piccoli (2015), magmatic apatite occurs predominantly in two different crystal habits, either as equant to sub-equant or as acicular grains. Moreover, Tollari et al. (2008) showed that the most important controls on apatite saturation in mafic systems are SiO_2 and CaO concentrations, together with temperature, as the apatite solubility strongly increases with decreasing silica contents or degrees of polymerisation, and with increasing temperature (Piccoli & Candela 2002). In most mafic-ultramafic layered intrusions, apatite only becomes a cumulus phase relatively late in the crystallisation history. For example in the Upper Zone of the Bushveld Complex, in the Jameson Range of the Giles Complex and at Skaergaard, apatite saturation occurs together with Fe-Ti oxides in evolved ferrogabbros, locally producing nelsonite, which primarily consists apatite and ilmenite (Wager 1960, Tegner et al. 2006, Karykowski et al. 2017). The occurrence of acicular apatite, together with quartz, phlogopite and albitic plagioclase in a melagabbronorite close to the basal contact of the intrusion (sample NG2-762) suggests a magmatic origin under rapid cooling conditions (Fig. 36 c) (Webster & Piccoli 2015). In contrast, subhedral to euhedral apatite from melanorite sample NG2-737, together with non-cotectic proportions of evolved phases, such as quartz, phlogopite and alkali feldspar, provides little evidence for its late stage crystallisation from trapped liquid (Fig. 36 d). It is more likely that the apatite initially grew more or less freely in the interstitial space, but the most fractionated portion of the melt was expelled after

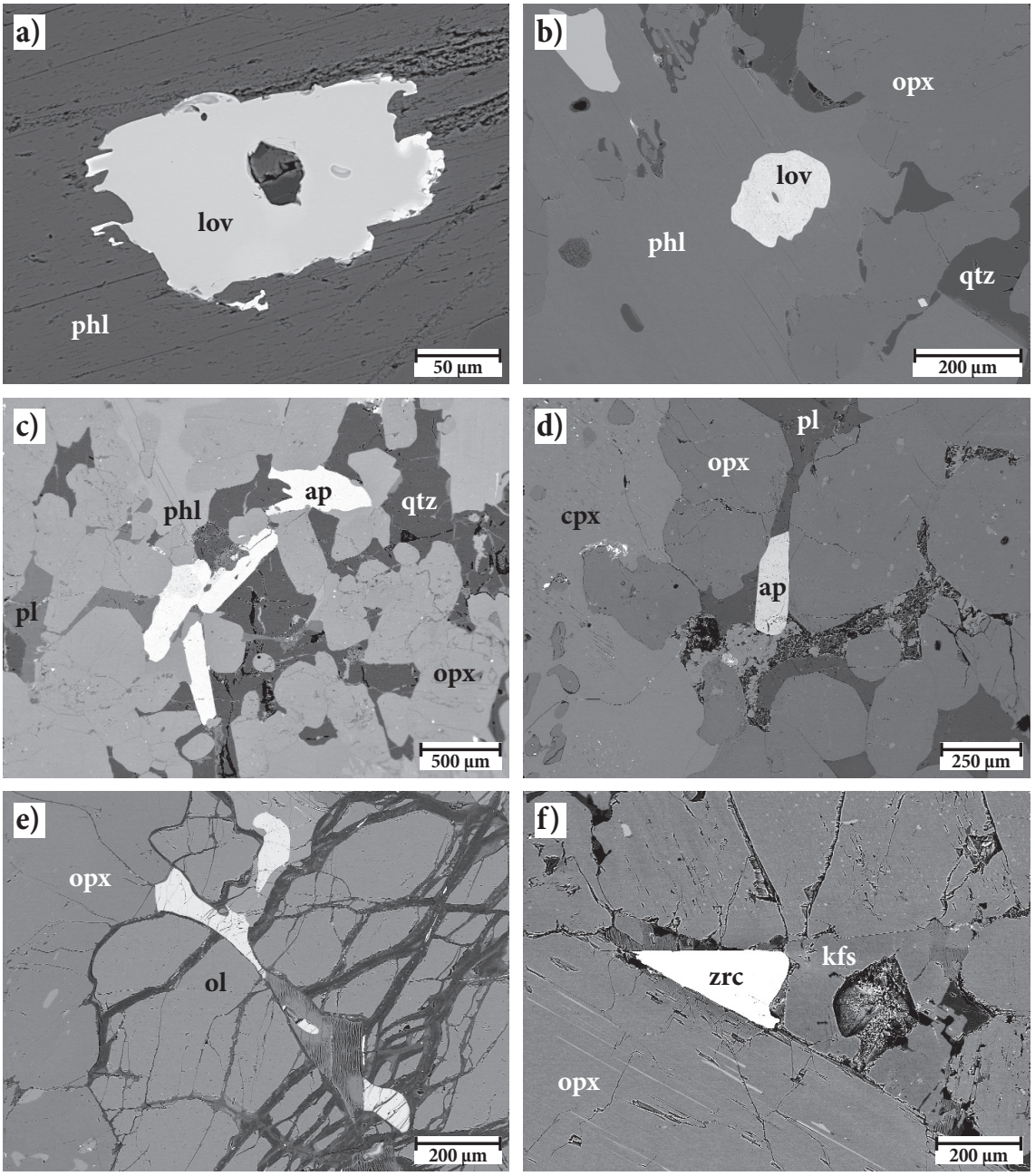

Fig. 36. Back-scatter electron images of accessory mineral phases in the analysed Lower Zone lithologies. a) Subhedral loveringite in phlogopite (NG2-180). b) Subhedral loveringite in association with interstitial phlogopite and quartz (NG2-762). c) Euhedral prismatic apatite in association with quartz, phlogopite and minor plagioclase (NG2-762). d) Euhedral prismatic apatite in association with relatively anorthite-rich plagioclase. Note the absence of quartz, phlogopite and other evolved minerals (NG2-737). e) Partially resorbed apatite next to plagioclase (NG2-490). f) Subhedral interstitial zircon together with alkali feldspar (NG2-180). See text for further explanation. Abbreviations: ol = olivine; opx = orthopyroxene; cpx = clinopyroxene; pl = plagioclase; qtz = quartz; phl = phlogopite; zrc = zircon.

apatite crystallisation, possibly due to compaction. Genetic and temporal relationships may even be more complicated, as some equant apatite crystals coexist with irregular-shaped ones, which may be interpreted as resorbed relicts of early apatite generations that interacted with pulses of apatite-undersaturated interstitial melt that migrated through the crystal pile (Fig. 36 e). Loveringite is a rather unusual REE-rich oxide mineral with the chemical formula $(Ca,Ce)(Ti,Fe,Cr,Mg)_{21}O_{38}$, belonging to the crichtonite group, and has been reported in a number of layered intrusions, e.g., Bushveld, Laouni and the Paleoproterozoic Penikat, Koitelainen, Burakovsky and Last-Yavr (Cameron 1979, Alapieti & Lahtinen 1986, Lorand et al. 1987, Tarkian & Mutanen 1987, Barkov et al. 1994, 1996). Due to its enrichment in Zr and REE, Tarkian & Mutanen (1987) envisaged loveringite to have crystallised from a crustally contaminated mafic magma in the Koitelainen intrusion in northern Finland. In contrast, Lorand et al. (1987) proposed that loveringite in the Laouni Complex in Algeria crystallised from highly evolved liquids that migrated through the cumulus pile as a result of compaction, essentially following Irvine's (1980) seminal work on *infiltration metasomatism*.

The only reported occurrence of loveringite in the Bushveld Complex so far, has been in the CZ by Cameron (1978*a*). In our LZ sample set, loveringite occurs in two of the three lowermost samples located close to the basal contact (melagabbronorite NG2-762, melanorite NG2-737), and in an orthopyroxenite sample in the upper third of the LZ (orthopyroxenite NG2-180). The presence of loveringite at the base of the intrusion may be consistent with local crustal contamination of the magma, as proposed by Tarkian & Mutanen (1987), based on a correlation between the occurrence of loveringite and crustal anatectic melts, but this does not hold for the sample further up in the sequence. Therefore, the main control on loveringite crystallisation seems to be the degree of interstitial melt fractionation, rather than crustal contamination, as loveringite is generally associated with the most fractionated mineral assemblage, not only in samples close to the base of the intrusion, but also higher up in the sequence (orthopyroxenite NG2-180). A possible explanation for the occurrence of loveringite together with a nearly-cotectic interstitial mineral mode at this stratigraphic level, may be that the orthopyroxenite represents a sill,

which has been emplaced relatively late, when permeability across most parts of the LZ was already low, thus hampering effective melt migration.

5.4.4 Implications for layered intrusions

Several studies have shown that isotope disequilibrium between rock-forming cumulus and intercumulus minerals is a ubiquitous feature throughout the entire succession of the Bushveld Complex and other layered intrusions. Disequilibrium Sr isotope compositions between plagioclase and coexisting orthopyroxene have been shown for the CZ and lower MZ (Eales et al. 1990a, Seabrook et al. 2005, Chutas et al. 2012, Roelofse & Ashwal 2012, Yang et al. 2013, Mangwegape et al. 2016). These results were further confirmed by Prevec et al. (2005), who measured Nd isotope compositions of the same two minerals in Merensky Reef samples. These findings are consistent with extensive multiphase melt migration, whereby cumulus minerals crystallised from a geochemically distinct magma in comparison to the intercumulus phases (Fig. 33 a, b).

Moreover, Pb isotope disequilibrium between plagioclase and sulfide has been reported for a number of CZ samples (Mathez & Waight 2003, Mathez & Kent 2007). Considering the results of our study, the observed isotope disequilibrium may be explained by a post-cumulus migration event of a sulfide-saturated melt through the crystal pile, as the sulfide texture indicate previous sulfide collection rather than *in situ* sulfide saturation. Additionally, melt migration may represent a potential mechanism to introduce sulfide mineralisation elsewhere in the cumulus pile. Maier et al. (2008) and McDonald & Holwell (2011) suggested that the Platreef comprised a number of mineralised sills, which intruded as sulfide-saturated crystal mushes. Therefore, it is conceivable that these mushes did not only form discrete sills, but also interacted with the existing cumulate, which resulted in further migration of the liquid components of the mush, i.e., liquid sulfide and residual melt (e.g., Hayes et al. 2017). Subsequently, these liquids crystallised in zones of low flow velocity, possibly similar to what can be observed in sample NG2-300 (Fig. 31).

Another important aspect of melt migration is its bearing on the origin and formation of datable minerals, such as zircon. In light of the evidence presented

in our study, it is rather unlikely that zircon and baddeleyite crystallised from the same magma as that which produced the cumulus minerals. Instead, migration of compositionally diverse residual melts through the crystal pile, and associated mixing, seems to be a common feature in parts of the Bushveld Complex, and thus is further substantiated by common isotope disequilibrium between cumulus and intercumulus minerals (Eales et al. 1990a, Mathez & Waight 2003, Seabrook et al. 2005, Prevec et al. 2005, Mathez & Kent 2007, Chutas et al. 2012, Roelofse & Ashwal 2012). As a consequence, interstitial zircon may have crystallised from any pulse of residual melt that migrated through the cumulus crystal framework, and potentially mixed with resident melt. Most importantly, calculations of trapped liquid estimates suggest that melt expulsion occurred at variable degrees of fractionation, which is why evolved residual melt may have been replaced with more primitive melt from elsewhere, thus delaying zircon saturation. Recent high-precision U-Pb isotopic dating of zircon and baddeleyite from the CZ of the western Bushveld Complex has been used to argue that the complex comprises discrete sheet-like intrusions, which were not emplaced sequentially, but were intruded beneath older layers (Wall 2016, Mungall et al. 2016). Our study, however, prompts the question as to what interstitial zircon records: the actual timing of emplacement of a layer or merely the crystallisation of zircon from a later, separate and unrelated episode of residual melt that migrated through the cumulate.

This problem has been discussed by Zeh et al. (2015) and can be particularly well demonstrated in the Upper CZ of the Bushveld Complex, for which recent high-precision geochronology suggested that the Merensky Reef was at least 2 m.y. younger than the overlying Bastard Reef (Wall 2016). However, field evidence from the western Bushveld clearly shows the opposite: the Bastard Reef cross-cuts the Merensky Reef (De Klerk 1982, Carr et al. 1994). Hence, this salient inconsistency highlights that precise U-Pb zircon ages may not record the actual timing of emplacement of the reefs, but may represent a later phase of residual melt migration from elsewhere in the crystal pile. A possible explanation for the Merensky paradox, relating to the inconsistency of field evidence and zircon age dating, may be that the Merensky pyroxenite, with its pegmatoidal texture, remained permeable for a

longer time than the Bastard pyroxenite.

Ultimately, this study demonstrates the importance of large-scale elemental mapping for an objective assessment of the compositional variation exhibited by the interstitial minerals. Therefore, a limited number of point analyses on interstitial phases may not always record the full range in chemical variability; this may explain the erratic trend in anorthite contents across the LZ (Fig. 28).

5.5 Summary

The Lower Zone of the Bushveld Complex is a highly variable succession of ultramafic lithologies, with minor mafic intervals. Igneous layering is generally complex, showing sharp contacts between pyroxenite and peridotite, although gradual transitions may also be present. The lateral continuity of individual layers is limited, as they commonly taper off over short distances. Together with the lack of fractionation in Mg# of orthopyroxene, variable whole rock as well as *in situ* Sr isotope compositions and erratic Pt/Pd ratios, these observations strongly suggest an emplacement of the Lower Zone as a sill complex rather than its crystallisation from a large magma chamber. The presence of a relatively thin sulfide-bearing interval of noritic composition provides further support for a sill-like origin of the zone.

Our detailed mineralogical and microtextural study shows that most samples from the Lower Zone show little evidence for a *truly* trapped liquid component in the cumulates. Melt migration may be a commonly occurring process in cumulate rocks, as indicated by the non-cotectic proportions of evolved mineral phases, such as quartz, phlogopite and alkali feldspar in most samples.

This has important implications for the formation of the Lower Zone and by extension for layered intrusions in general: (1) interstitial sulfide mineralisation may be introduced into a cumulate via migrating melts; (2) most importantly, late stage minerals, such as zircon, rarely crystallise from *truly* trapped liquid. Therefore, dating of interstitial zircon from cumulates is unlikely to record the actual timing of emplacement, but merely the crystallisation of a later unrelated episode of residual melt migrating through the cumulate.

Chapter 6

Origin of contact-style PGE-Ni-Cu mineralisation in the Monchegorsk Complex and its implications for the formation of layered intrusions

Parts of this chapter were submitted as:
Karykowski, B. T., Maier, W. D., Groshev, N. Y., Pripachkin, P. V., Barnes, S.-J., McDonald, I., Savard, D. (in review). Critical controls on the formation of contact-style PGE-Ni-Cu mineralisation: Evidence from the Paleoproterozoic Monchegorsk Complex, Kola Region, Russia. *Economic Geology*.

Co-author contributions:
W. D. Maier, S.-J. Barnes, N. Y. Groshev and P. V. Pripachkin were involved in discussions during the writing of the manuscript. I. McDonald and D. Savard supervised lithophile and chalcophile element analyses.

Abstract

The Paleoproterozoic Monchegorsk Complex, located in the Russian part of the Fennoscandian Shield, constitutes one of the largest mafic-ultramafic layered intrusions in Europe. The complex hosts extensive contact-style PGE-Ni-Cu sulfide mineralisation along its margin, irrespective of the host lithology, which ranges from peridotite to pyroxenite and gabbronorite. The mineralised intervals reach up to 3 ppm Pt + Pd and attain a thickness of up to 50 m in the central portions of the intrusion, thinning towards the periphery.

Our study shows that the key process, controlling the size and grade of a contact-style deposit in the Monchegorsk Complex, is the efficiency of sulfide collection in distinct zones of the intrusion. Strongly mineralised basal contacts are always associated with intense brecciation and the presence of large amounts of felsic pegmatite, suggesting a multi-stage emplacement of the mafic-ultramafic succession. Thermal modelling demonstrates that multiple episodes of magma influx are required to allow for significant partial melting of the basement. Moreover, the interaction between magma and basement leads to the local addition of water and potentially carbon dioxide to the magma, resulting in small-scale dissolution of cumulus phases and a reduction in viscosity of the interstitial melt. This increases the porosity of the mush in the vicinity of the lower intrusion contact, which promotes preferential sulfide liquid accumulation at the base, while the local decrease in magma viscosity facilitates gravitational settling of sulfide droplets. These factors lead to an efficient collection of sulfide liquid, especially in the centre of the complex, where permeability can be maintained the longest due to slower cooling relative to more peripheral parts.

6.1 Introduction

Layered intrusions around the world are a major target for metal exploration, as they host the bulk of global platinum-group element (PGE), Cr and V resources. Almost all economic PGE deposits are hosted in laterally extensive, but narrow reefs in the central portions of intrusions, such as in the Bushveld Complex (South Africa), the Great Dyke (Zimbabwe) and the Stillwater Complex (USA). The only economic non-reef-hosted PGE deposits are the *Platreef* in the Bushveld Complex and the *Roby Zone* of the Lac des Iles Complex (Canada). As opposed to reef-style mineralisation, the Platreef comprises a relatively thick succession of a variety of mineralised mafic-ultramafic rock types along the basal contact of the complex (cf. section 2.1.7), which is why this deposit type is termed *contact-style* (e.g., Zientek 2012). In fact, most large layered intrusions globally host contact-style mineralisation of variable thickness and metal concentration, notably the Portimo Complex (Finland), the East Bull Lake Complex (Canada) and the Fedorova-Pana intrusion (Russia), but none of them are exploitable under current market conditions (Iljina 1994, Schissel et al. 2002, Peck et al. 2001).

Genetic aspects of contact-style mineralisation, especially concerning the Platreef, are still under debate. In particular the timing of sulfide saturation relative to the final emplacement has been intensively discussed: some authors argued that the mineralisation formed in response to *in situ* contamination by country rocks in spatial proximity to the final emplacement (e.g., Buchanan et al. 1981, Gain & Mostert 1982), whereas more recent studies suggested that the *in situ* contamination did not play a critical role in triggering sulfide saturation, as several lines of evidence indicate that the magma was sulfide-saturated before final emplacement (Holwell et al. 2014, Kinnaird et al. 2005, Lee 1996, Maier et al. 2008, Manyeruke et al. 2005, McDonald & Holwell 2011, Peck et al. 2001).

Critical factors controlling the size and distribution of these deposits in relation to the unmineralised igneous succession are not fully understood yet. Notably, the stratigraphically lowermost portions of a layered complex, mostly represented by a thick peridotitic cumulate, commonly lack contact-style mineralisation at the base –

only higher up in the sequence do these deposits occur, e.g., Konttijärvi/Ahmavaara, Platreef.

This characteristic also applies to one of Europe's largest known layered intrusions, namely the Monchegorsk Complex. It is located approx. 120 km south of Murmansk on the Kola Peninsula of Russia and hosts extensive contact-style PGE-Ni-Cu mineralisation. The complex belongs to a group of Paleoproterozoic layered intrusions, occurring across the Fennoscandian Shield, which also includes the Portimo Complex in Finland. Recent exploration in the area, targeting the mineralised contact between the intrusion and the floor rocks, yielded intersections of up to 10.9 ppm Pt + Pd over 5.9 m (Eurasia Mining PLC 2010), for a total of 27.8 Mt of category C_1 + C_2 mineral reserves at 0.6 ppm Pt and 1.1 ppm Pd, respectively (Eurasia Mining PLC 2017).

In this study, we provide a new perspective on the formation of contact-style PGE mineralisation based on a thorough analysis of a range of mineralised basal contacts at different stratigraphic levels of the complex. The detailed compositional and lithological characterisation of the mineralisation, using mineral chemistry as well as lithophile and chalcophile element geochemistry in conjunction with thermal modelling, allows us to improve our understanding of ore-forming processes associated with the formation of mineralised basal intrusion contacts. Furthermore, these results have important implications for exploration targeting contact-style sulfide mineralisation.

6.2 Nature of mineralisation

As summarised in section 2.2.2, the stratigraphy of the NKT Massif and Nyud is rather simple lithologically, but highly complex in terms of texture (Figs. 9, 37). The Nittis intrusion, as intersected by drill holes MT79 and MT94, comprises a more than 300-m-thick succession of strongly layered orthopyroxenite. The lowermost 10 m of the intrusion constitute a diffuse contact zone characterised by a change in texture from strongly layered to distinctly ophitic orthopyroxenite (Figs. 37 a, 38). Additionally, several lenses, schlieren and patches of felsic pegmatite interlayered with different metasedimentary rocks occur in the lower part of the contact zone (Fig. 37 a, b). Hence, a distinct boundary between the ultramafic intrusion and the Archean basement cannot be defined. The contact zone is further associated with dolerite dykes and veins cross-cutting the complex unit. The bulk of the sulfide mineralisation is hosted by both types of orthopyroxenite, covering some 30 m at the base of the intrusion. Moreover, several thin sulfide-rich veinlets occur above the basal mineralised zone (Fig. 37 c, d). In addition to the basal sulfide mineralisation, steeply dipping massive sulfide veins, ranging from 5 cm to 3 m in thickness, occur mainly in the central parts of the intrusions, which were not intersected by drill holes MT79 and MT94 (Figs. 9, 37 e). They may reach a vertical thickness of more than 150 m and can be traced for up to 1.5 km, before they pinch out (cf. section 2.2.4) (Kozlov 1973).

Stratigraphically deeper portions of Nittis were sampled close to the contact between the *Pyroxenite Zone* and the underlying *Interlayered Pyroxenite-Peridotite Zone* (Fig. 9 A-B). A continuous sample set across the latter was collected at Mt. Kumuzhya and comprises olivine-rich lithologies, ranging from harzburgite to orthopyroxenite. Samples from the *Peridotite Zone*, located at the base of the NKT Massif, were recovered from an abandoned sulfide mine dump at Mt. Travyanaya, exploiting the contact zone between the intrusion and the floor rocks, which is represented by mineralised gabbronorite from the intrusion margin as well as different peridotitic rock types, mainly comprising harzburgite. Additional samples from the *Peridotite Zone* were collected from an abandoned chromite mine in the Dunite

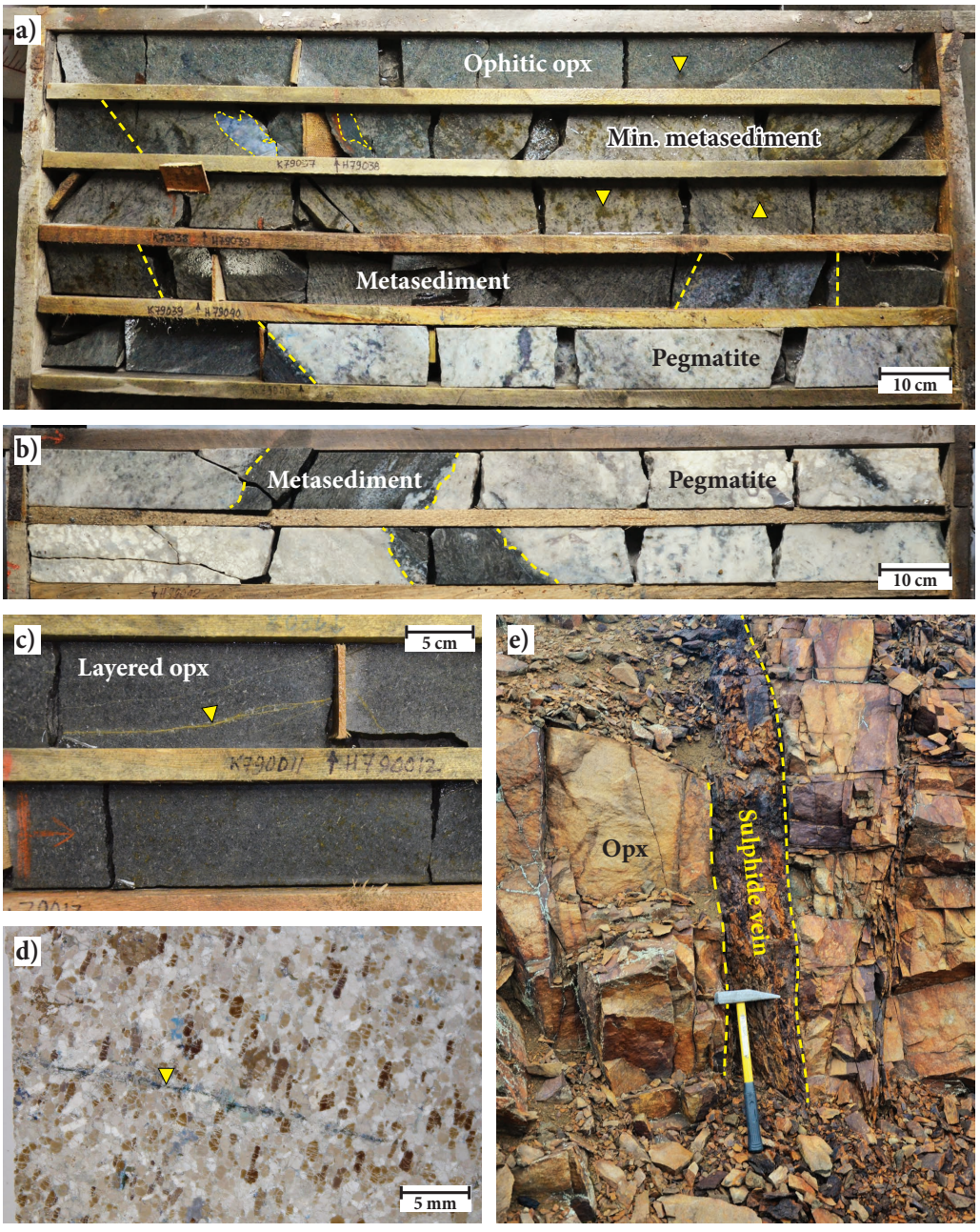

Fig. 37. Typical lithologies of the ultramafic Nittis intrusion. a, b) Mineralised contact zone between ophitic orthopyroxenite and the underlying basement lithologies with a ca. 2-m-thick interval of mineralised metasediment. Note the complex interlayering between metasediment and pegmatite (drill hole MT79: 146.5 - 153.2 m depth). c) Layered orthopyroxenite with abundant mm-sized sulfide veins (MT79: 120.8 m depth), overlying finely disseminated interstitial sulfide mineralisation (MT79: 121.6 m depth). d) Dark sub-mm-thick PGE-rich sulfide vein in layered orthopyroxenite. Note that this sample contains ≈ 30 ppm Pt + Pd (sample 79-39). e) Steeply dipping massive Ni-Cu sulfide vein hosted by orthopyroxenite close to the centre of the Nittis intrusion. Abbreviations: opx = orthopyroxenite.

Block (cf. section 2.2.4). The minimum cumulative thickness of the NKT Massif at the current erosional level is > 1,100 m.

On the basis of historic drilling, Kozlov (1973) reported that the basal mineralised zone generally follows the lower intrusion contact marked by gabbronorite, extending across the entire NKT Massif and Mt. Sopcha (Fig. 9 A-B). Its thickness increases from the peripheral parts of the intrusion towards the centre, reaching up to 50 m, with average sulfide contents of 3 to 5 vol % (Dedeev et al. 2002). The mineralised gabbronorite described by Kozlov (1973) is absent in the studied section at Nittis. However, the mineralised gabbronorite from the basal contact of the Travyanaya intrusion may be a representative analogue in terms of texture and composition. Drill holes MT79 and MT94, used for this study, intersected the western part of the Nittis intrusion, thus representing a more peripheral segment of the mineralised interval (Fig. 7).

Moreover, a basal mineralised contact zone has been intersected by drill hole 1815 collared in the peripheral part of the Nyud intrusion (Fig. 9 G-H). The mineralised horizon at Nyud comprises an approximately 20-m-thick unit of sulfide-bearing melanorite, overlying interlayered tonalite with abundant felsic pegmatite veins and schlieren similar to Nittis (FIG. LOGS). The mineralised melanorite gives way to barren melanorite up-section without a significant change in texture. The visible sulfide abundance is very similar to that at Nittis with approximately 3 vol %. The sulfides mostly occur as relatively small interstitial patches, reaching about 10 mm in diameter, together with minor sulfide-rich veinlets, in particular close to the intrusion contact.

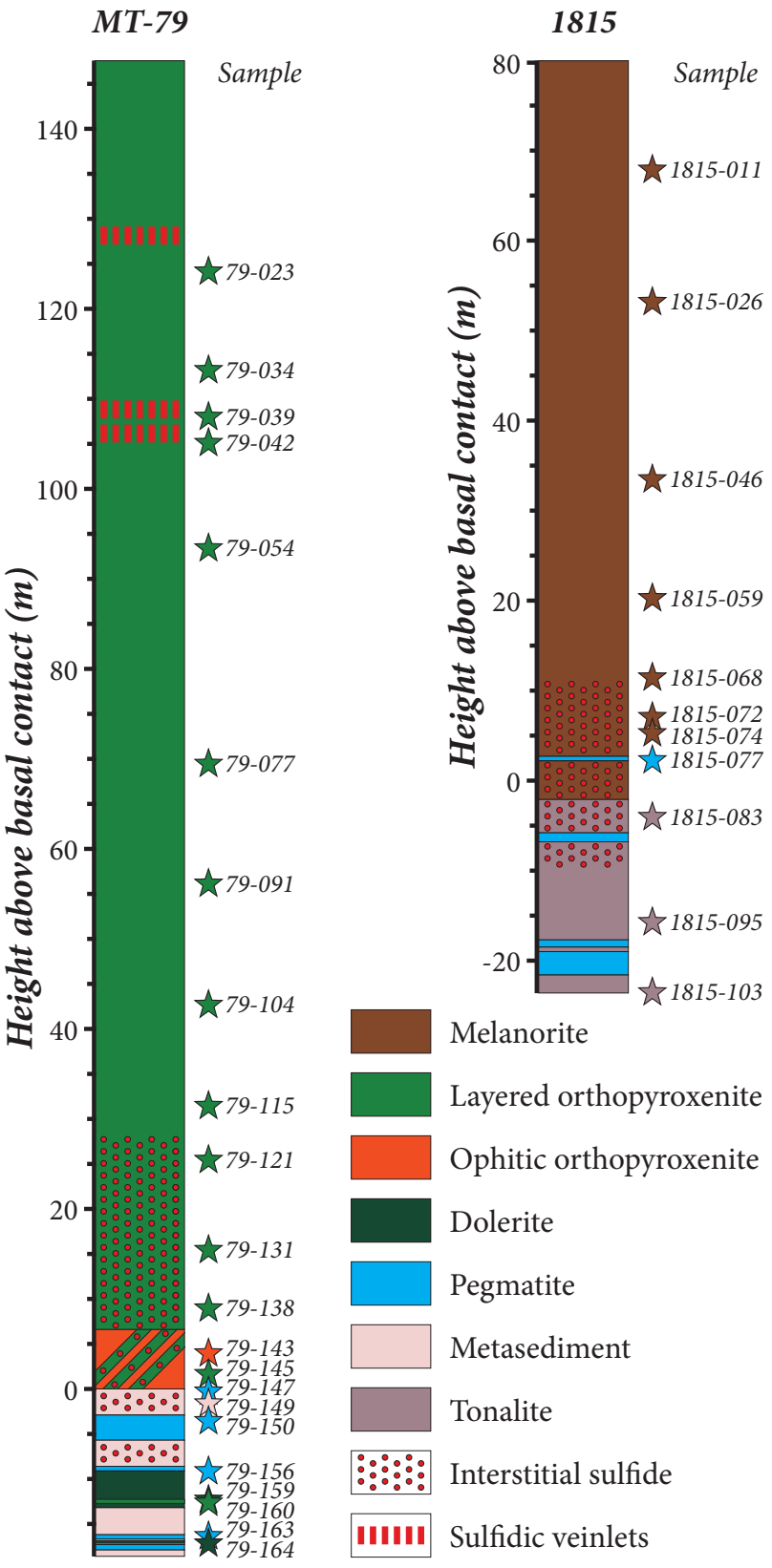

Fig. 38. Lithological logs and sample numbers for drill cores MT79 and 1815, intersecting the basal intrusion contact at Nittis and Nyud, respectively.

6.3 Results

The following section addresses the petrography, mineral chemistry and whole rock geochemistry of the analysed samples from the Moncheplutonic.

6.3.1 Petrography

The studied sample set from the Dunite Block, the NKT Massif and the Nyud intrusion comprises 45 samples, representing lherzolite, harzburgite, olivine-websterite, (olivine-)orthopyroxenite, melanorite, mineralised gabbronorite, felsic pegmatite and basement lithologies, as shown in Figure 38.

Lherzolite

The lherzolite is a coarse-grained mesocumulate with 60 to 65 vol % olivine, 25 to 30 vol % orthopyroxene and 10 to 15 vol % poikilitic clinopyroxene. In addition to approximately 1 vol % chromite, the rock also contains minor interstitial plagioclase, whereas sulfides are completely absent. The only occurrence of this rock type is in the Dunite Block, representing the lowermost portion of the *Peridotite Zone* (Fig. 39).

Harzburgite

The harzburgite is a fine- to medium-grained mesocumulate with 50 to 85 vol % olivine, 10 to 45 vol % orthopyroxene and minor clinopyroxene as well as plagioclase. The rock type is only present in the *Interlayered Pyroxenite-Peridotite Zone* at Kumuzhya and in the *Peridotite Zone* exposed at Travyanaya (Fig. 9 A-B). Harzburgite from the latter hosts disseminated interstitial sulfide mineralisation and thin sulfide veinlets, cross-cutting the rock (Fig. 40 a). The total amount of sulfide reaches about 2 vol %.

Olivine-websterite

The olivine-websterite is a medium- to coarse-grained orthocumulate with approximately 65 vol % orthopyroxene, 15 vol % olivine, 7 vol % clinopyroxene and

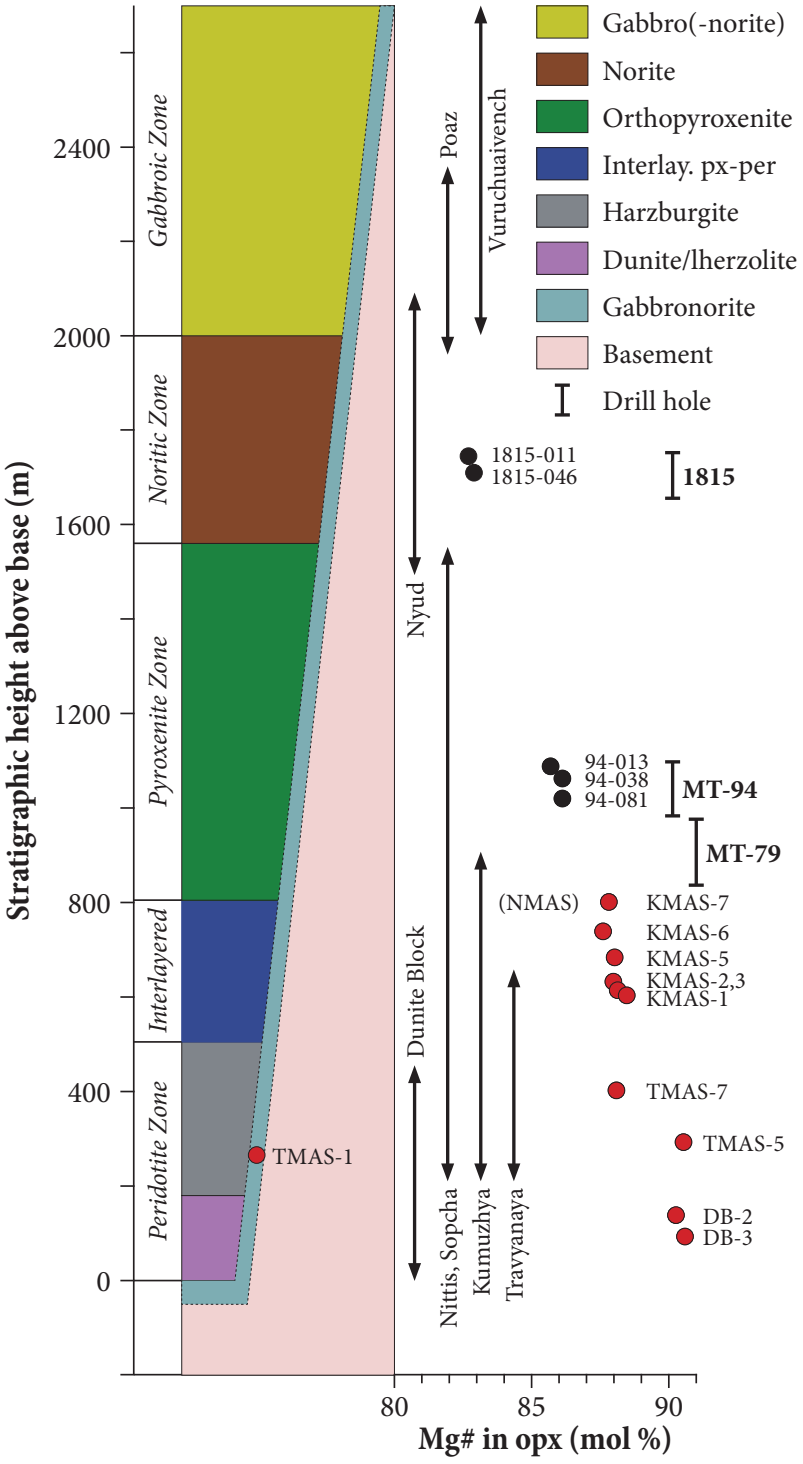

Fig. 39. Simplified stratigraphic column across the Moncheplutonn together with the Mg# of orthopyroxene from the Dunite Block, the NKT Massif and Nyud (this study). Red circles show outcrop samples, whereas black circle represent drill core samples. Abbreviations: interlay. = interlayered; px = pyroxenite; per = peridotite.

8 vol % plagioclase. It only occurs in the lowermost portion of the NKT Massif exposed at Travyanaya. The analysed sample is also characterised by abundant disseminated interstitial sulfide blebs, which reach up to 5 mm across and account for ≈ 5 vol %.

(Olivine-)orthopyroxenite

Two texturally distinct types of orthopyroxenite were intersected. The *layered orthopyroxenite* is an adcumulate with 70 to 90 vol % orthopyroxene and is only present at Nittis and Kumuzhya. Orthopyroxene occurs as highly elongated crystals

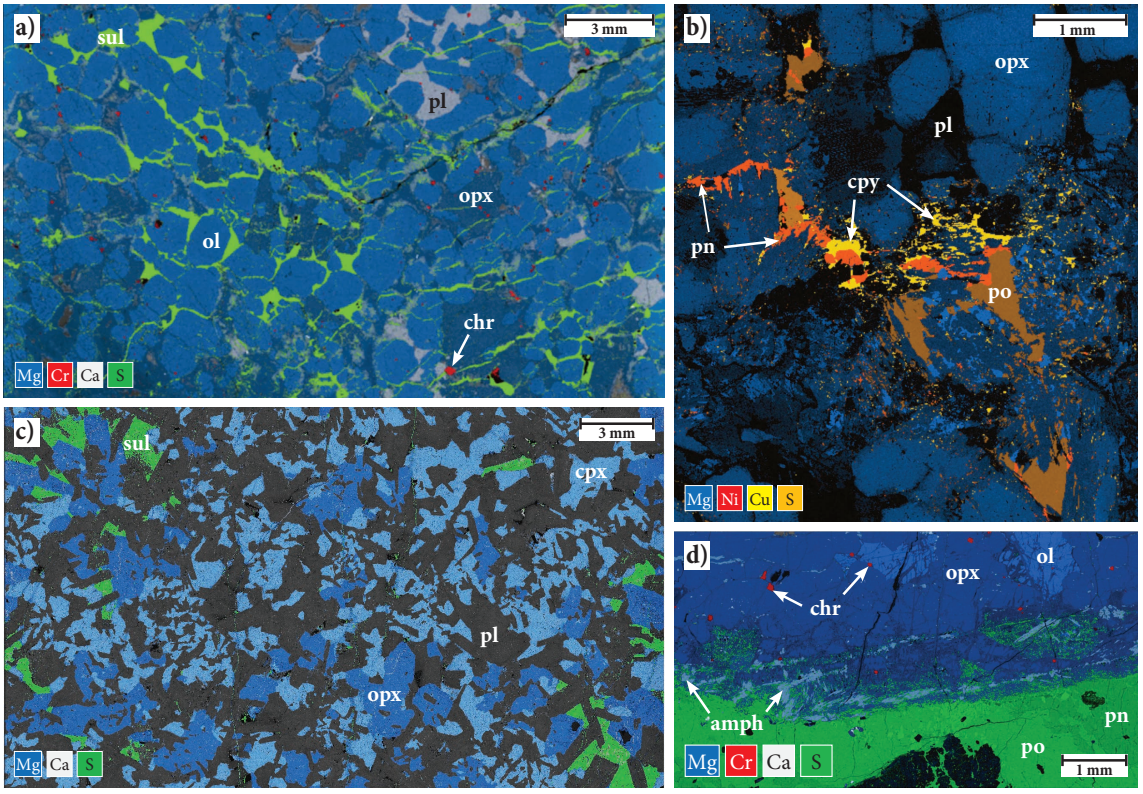

Fig. 40. Elemental maps of different types of sulfide mineralisation associated with the NKT Massif. a) Thin sulfide veinlets cross-cutting harzburgite from Travyanaya (sample 15TMAS-5). b) Interstitial sulfide mineralisation in orthopyroxenite from the basal contact zone at Nittis (sample 79-138). c) Interstitial sulfide in ophitic gabbronorite from the base of Travyanaya (sample 15TMAS-1). d) Contact between olivine-orthopyroxenite and vein-hosted massive sulfide mineralisation from the central part of the Nittis intrusion (sample 15NMAS-1). Note the local injection of sulfide into the immediate host rock. Abbreviations: opx = orthopyroxene; pl = plagioclase; amph = amphibole; chr = chromite; sul = sulfide; cpy = chalcopyrite; pn = pentlandite; po = pyrrhotite.

of up to 10 mm with an aspect ratio of up to 9:1 (Appendix H). Additionally, much smaller equant cumulus orthopyroxene is present in between the elongated ones, reaching 1 mm in diameter (Fig. 41 a). Anhedral plagioclase accounts for $<$ 10 vol % and occurs interstitial to the orthopyroxene. Clinopyroxene reaches up to 5 vol % and mostly forms small blebs within or along the margins of orthopyroxene. Moreover, large poikilitic grains interstitial to orthopyroxene are present. Olivine occurs only in a few samples, especially in those from Kumuzhya and the lower portions of the Nittis intrusion, where it accounts for up to 30 vol %. It is mostly subhedral, reaching up to 1 mm across. Most of the samples contain minor amounts of subhedral chromite. Sulfides generally occur in relatively large interstitial patches of up to 10 mm, comprising pyrrhotite, pentlandite and chalcopyrite with minor

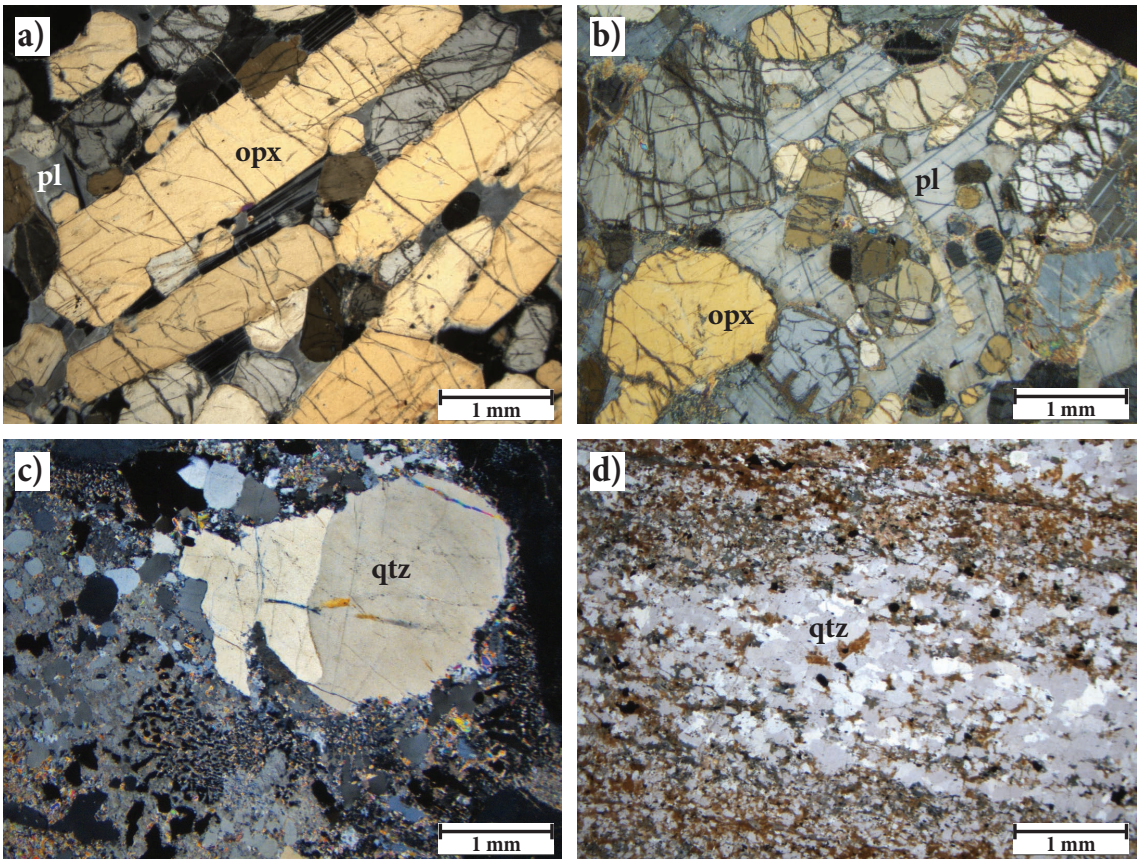

Fig. 41. Photomicrographs of major rock types in the Nittis and Nyud intrusions. a) Strongly layered orthopyroxenite from Nittis; crossed polarised light (XPL) (sample 94-118). b) Melanorite from Nyud; XPL (sample 1815-11). c) Pegmatite from the contact zone at Nittis; XPL (sample 79-150). d) Xenolith of banded mica schist from the contact zone at Nittis; plane polarised light (sample 79-156).

pyrite (Fig. 40 b).

The *ophitic orthopyroxenite* is mineralogically similar to the layered orthopyroxenite described above. Its texture, however, is distinctly ophitic, defined by randomly oriented lath-shaped orthopyroxene crystals with interstitial plagioclase. This rock type is commonly brecciated and intruded by mineralised layered orthopyroxenite, but it is not mineralised itself and only present in the basal contact zone of the Nittis intrusion.

Melanorite

The melanorite occurs exclusively at Nyud and shares many similarities with the layered orthopyroxenite from Nittis; however, the former is characterised by a higher modal abundance of mostly poikilitic plagioclase, ranging from 10 to 25 vol % (Fig. 41 b). Additionally, the mineral lamination is not as strongly developed as in the orthopyroxenite due to lower aspect ratios of the orthopyroxene crystals. Clinopyroxene is generally present as patchy oikocrysts, accounting for less than 5 vol %. Olivine is absent, whereas chromite occurs only as an accessory phase.

Mineralised gabbronorite

The mineralised gabbronorite is a medium-grained rock type with a distinctly ophitic texture defined by up to 4-mm-long plagioclase laths, accounting for $\approx$ 55 vol %, whereas poikilitic clino- and orthopyroxene comprise $\approx$ 30 and 12 vol %, respectively. Interstitial sulfide mineralisation is spatially associated with pyroxene and reaches up to 2 vol % (Fig. 40 c).

Felsic pegmatite

The felsic pegmatite is always associated with the contact between the mafic-ultramafic rocks and the basement. It is a highly variable rock type in terms of grain size as it ranges from very coarse- to fine-grained over short distances (Fig. 41 c). It generally consists of anhedral quartz and feldspar with minor amounts of mica. Locally, these minerals may form symplectites.

Basement lithologies

The country rock at the base of the NKT Massif is a relatively variable metasediment, consisting of different proportions of mica, chlorite, staurolite, quartz and feldspar, which form a strongly banded mica schist (Fig. 41 d). Fragments of this rock type frequently occur within orthopyroxenite close to the basal contact of the Nittis intrusion. In addition, these metasediments may contain up to 7 vol % sulfide over an interval of 2 m close to the intrusion contact, primarily comprising pyrrhotite with minor chalcopyrite and pentlandite. The same sulfide assemblage also occurs in grey tonalite, where it is in direct contact with the Nyud intrusion.

6.3.2 Mineral chemistry

The mineral chemistry of rock-forming minerals was determined in a set of 34 samples from the Dunite Block, the NKT Massif and the Nyud intrusion. The full dataset of mineral compositions is available in Appendix D.

As a result of the ubiquitous presence of cumulus orthopyroxene, the most suitable proxy for tracing the degree of fractionation is the Mg# of orthopyroxene (100 x molar Mg/(Mg+Fe)). A corresponding stratigraphic profile across the Monchepluton is shown in Figure 39. The Mg# of orthopyroxene covers a relatively small range at Nittis, varying from 84 in orthopyroxenite to 89 in the most primitive olivine-orthopyroxenite (NMAS-1) with Cr concentrations from 4,000 to 4,800 ppm (Fig. 42). The Kumuzhya intrusion features slightly more magnesian orthopyroxene with Mg#, ranging from 88 to 89 and up to 4,600 ppm Cr. The most primitive orthopyroxene compositions were measured in a harzburgite from Travyanaya, reaching Mg# = 91 with up to 5,000 ppm Cr. The Nyud intrusion is generally characterised by lower Mg# with an average of 83 and 3,400 to 3,900 ppm

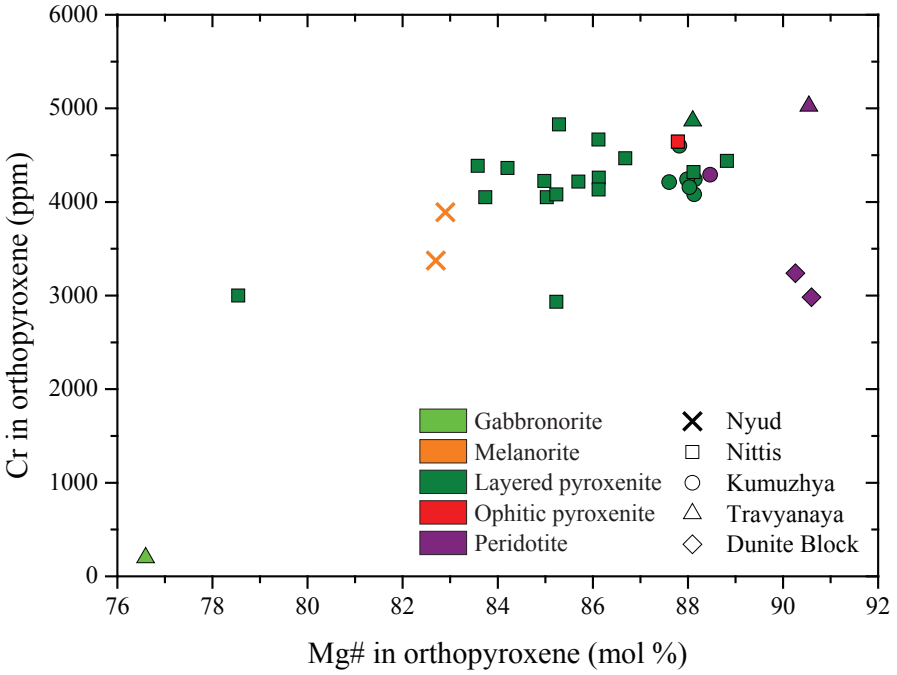

Fig. 42. Plot of Cr concentrations vs. Mg# in orthopyroxene from the Dunite Block, the NKT Massif and the Nyud intrusion.

Cr. The Mg# of clinopyroxene from the NKT Massif varies from 84 to 91, whereas clinopyroxene from the Nyud intrusion has an Mg# of 85. Olivine from the NKT Massif covers a range in forsterite contents from Fo_{82} to Fo_{87}. Only chromite-rich dunite and lherzolite from the Dunite Block have even more magnesian olivine with Fo_{92} and Fo_{89}, respectively. The stratigraphic variation in mineral chemistry across the Nittis intrusion shows a distinct ca. 200-m-thick basal compositional reversal in orthopyroxene composition (Fig. 45), which is also evident in clinopyroxene and olivine compositions (not shown).

6.3.3 Lithophile element geochemistry

A total of 57 samples, covering the Dunite Block, the NKT Massif and Nyud, were analysed for lithophile elements. The full dataset of whole rock geochemical analyses can be found in Appendix E.

The major element composition of the analysed samples is primarily controlled by variations in the modal proportion of rock-forming minerals. Peridotites from Kumuzhya, Travyanaya and the Dunite Block are mainly characterised by high modal proportions of olivine with varying amounts of ortho- and clinopyroxene, as reflected in the high MgO concentrations of more than 40 wt % (Fig. 43 a, b). Notably, the peridotites show a bimodal distribution in terms of Cr concentrations, reflecting distinct differences in chromite abundance (Fig. 43 c). Kumuzhya orthopyroxenites generally feature higher modal proportions of orthopyroxene relative to olivine, resulting in slightly lower MgO concentrations, ranging from 33 to 38 wt %. Nittis orthopyroxenites have distinctly lower MgO contents of 17 to 28 wt %, as they are mainly composed of orthopyroxene with varying proportions of plagioclase, whereas clinopyroxene and olivine are minor components. The analysed melanorites from Nyud have 16 to 25 wt % MgO due to slightly higher modal proportions of plagioclase compared to Nittis orthopyroxenites. Chromium concentrations are also slightly lower at Nyud. The mineralised gabbronorite from Travyanaya has the lowest MgO and Cr concentrations with 8 wt % and < 300 ppm, respectively. Notably, the analysed samples from Nittis and Nyud show considerable overlap with mafic-ultramafic rocks from the Fedorova-Pana intrusion (Schissel et al. 2002); how-

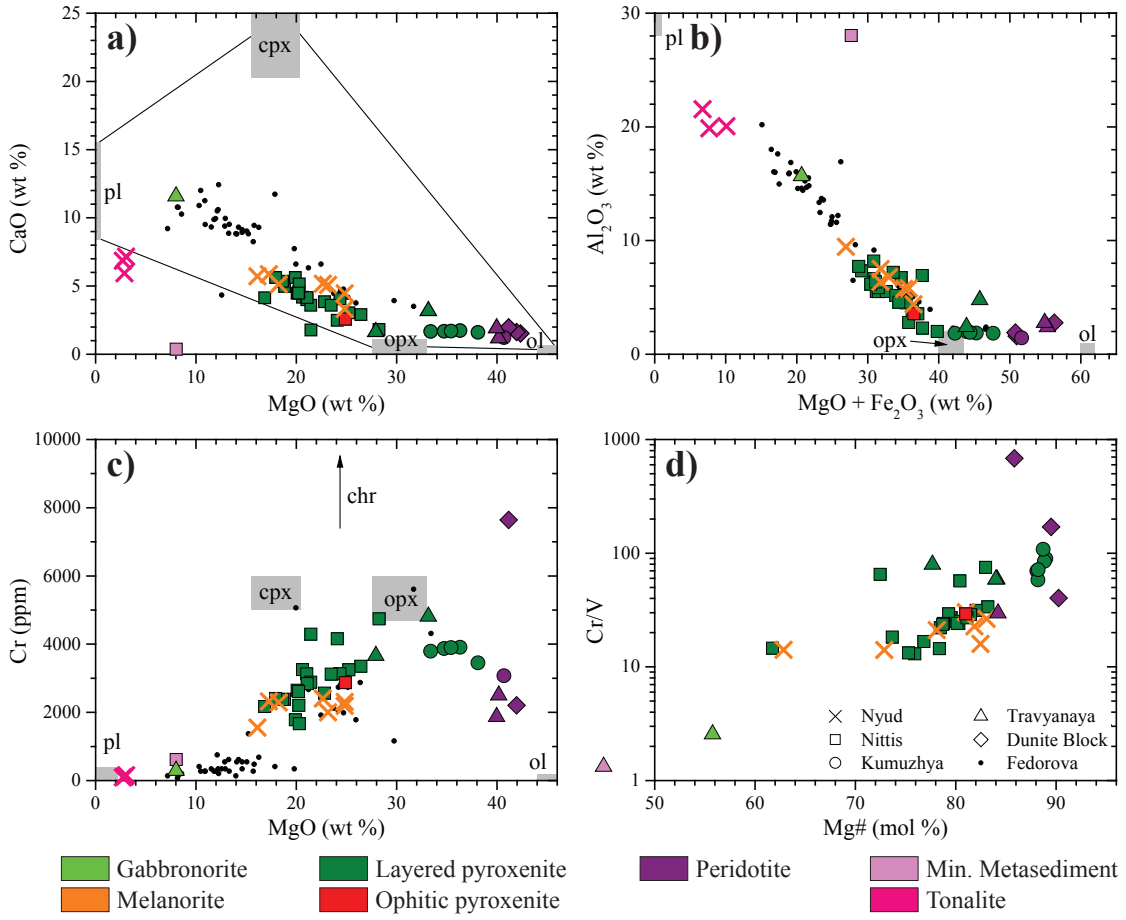

Fig. 43. Lithophile element variation of lithologies from the Dunite Block, the NKT Massif and the Nyud intrusion. a) CaO vs. MgO. b) Al_2O_3 vs. MgO + Fe_2O_3. c) Cr vs. MgO. d) Cr/V vs. Mg#. Data from the Fedorova intrusion were taken from Schissel et al. (2002). Abbreviations: ol = olivine; opx = orthopyroxene; cpx = clinopyroxene; pl = plagioclase; chr = chromite.

ever, the latter have consistently higher CaO concentration due to slightly higher modal abundances of clinopyroxene (Fig. 43 a, b). Lithologies similar to those from Travyanaya or the Dunite Block with $>$ 34 wt % MgO seem to be absent in the Fedorova-Pana intrusion. A broadly positive correlation between whole rock Mg# and Cr/V ratios is evident among the analysed chromite-poor lithologies, allowing for a comparison of the different intrusions with respect to the degree of fractionation (Fig. 43 d).

In terms of primitive mantle-normalised incompatible trace element patterns, most mafic-ultramafic samples have fractionated patterns with strongly negative Nb-Ta and minor Ti anomalies (Fig. 44 a - e). Moreover, many of them feature

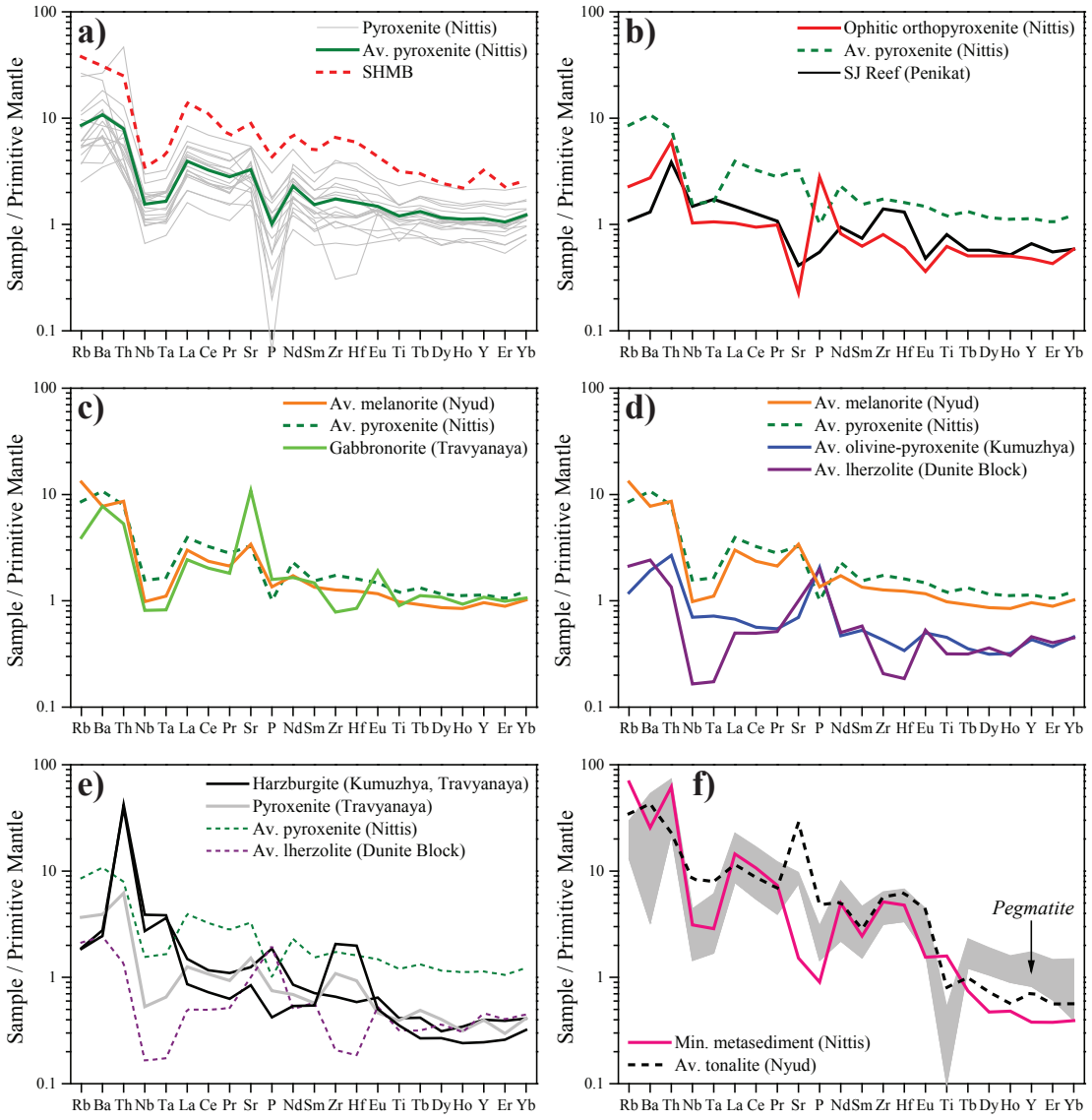

Fig. 44. Primitive mantle-normalised multi-element variation diagram of Monchegorsk lithologies analysed for this study. Normalisation values were taken from McDonough & Sun (1995). Data for the siliceous high-Mg basalts (SHMB) and the SJ Reef were taken from Guo et al. (2013) and Maier et al. (in review), respectively.

minor positive Zr-Hf and variable P anomalies. Only samples from the lowermost part of Nittis and a distinctly ophitic orthopyroxenite, associated with the mineralised zone, are characterised by relatively unfractionated incompatible trace elements with strongly positive Zr-Hf anomalies, whereas the Nb-Ta anomaly in these rocks is rather subtle to absent (Fig. 44 b). These compositions are remarkably similar to rocks from the Sompujärvi (SJ) Reef in the Penikat intrusion (Maier et al., in

review). The melanorites from Nyud, however, show a strong overlap with orthopyroxenites from Nittis and the mineralised gabbronorite from Travyanaya (Fig. 44 c). Olivine-rich lithologies, such as olivine-orthopyroxenite from Kumuzhya and lherzolite from the Dunite Block, have generally lower total incompatible trace element concentrations and are distinct from the Nittis orthopyroxenites as well as Nyud melanorites (Fig. 44 d). In contrast, harzburgite from Kumuzhya and Travyanaya plot between orthopyroxenites from Nittis and lherzolites from the Dunite Block, reflecting slight differences in modal olivine/pyroxene ratios (Fig. 44 e). The mineralised metasediment and tonalite from Nittis and Nyud, respectively, both have a typical upper crustal incompatible trace element pattern with a strong enrichment in light rare earth elements (REE) relative to heavy REE (Fig. 44 f). Felsic pegmatite from the intrusion contact shows extremely negative Ti anomalies in comparison to the associated basement lithologies.

Stratigraphic variations in lithophile element geochemistry

Downhole geochemical data along a composite profile across the peripheral portion of the Nittis intrusion show a distinct upward increase in whole rock MgO concentrations and Cr/V ratios, whereas Al_2O_3 contents decrease significantly (Fig. 45). La/Nb ratios mostly range from 2 to 3; however, close to the basal contact, the ratio increases gradually towards the pegmatite. The only exception is an ophitic orthopyroxenite sample with exceptionally high Cr/V and low La/Nb ratios.

6.3.4 Chalcophile element geochemistry

Magmatic sulfides are generally assumed to be the primary host for chalcophile metals in layered intrusions. The analysed sample set from the Dunite Block, the NKT Massif and the Nyud intrusion shows a broadly positive correlation between chalcophile metals and S, confirming sulfide as the main control on chalcophile metal abundances (Fig. 46 a - e). Variations in correlation between Ni and S can be partly attributed to Ni hosted in olivine, whereas elevated Ir concentrations result from high modal abundances of chromite (i.e., Dunite Block). The correlation between Cu, Pt, Pd and S, however, becomes notably poorer in samples with less than 1,000 ppm

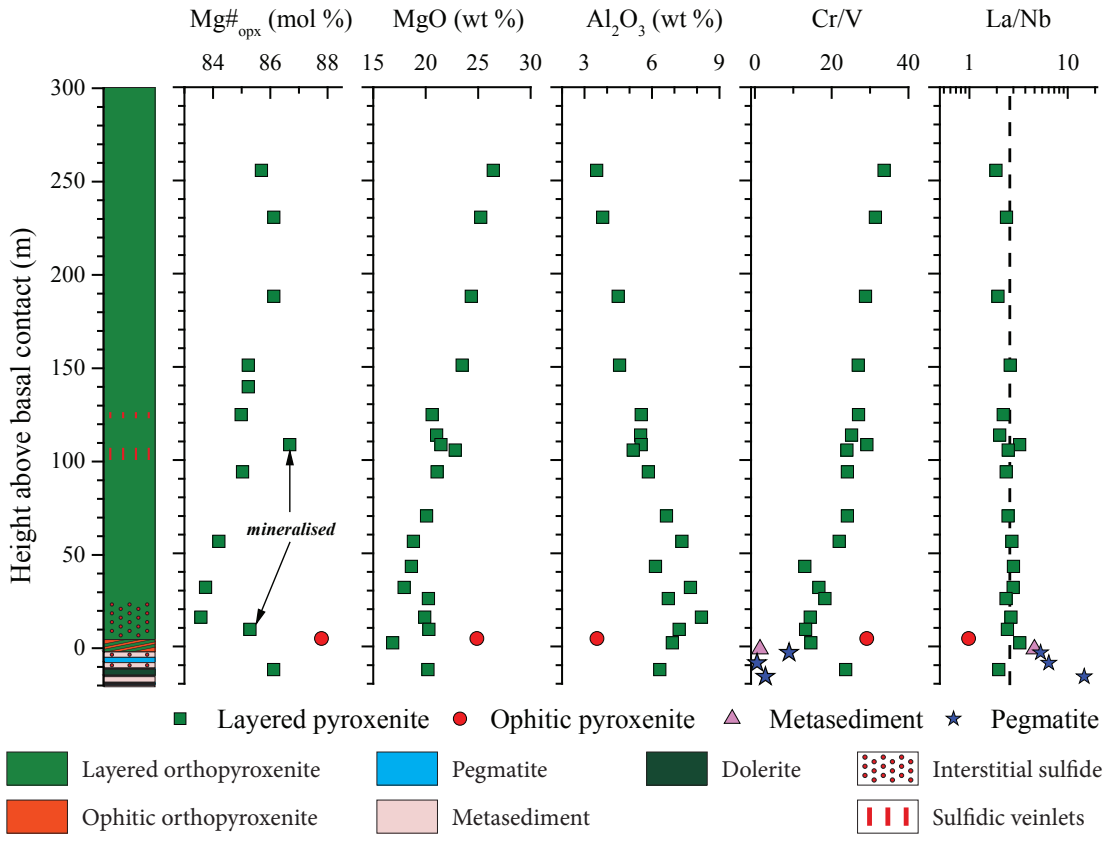

Fig. 45. Compositional variation of lithophile elements and orthopyroxene compositions across the Nittis intrusion. Note that orthopyroxene from the mineralised orthopyroxenite has slightly higher Mg# due to subsolidus re-equilibration with sulfide.

S, which is also evident in the negative correlation between Cu/S, Pt/S and S in this sample subset (Fig. 46 f, g). The positive correlation between Pt and Pd as well as Ir and Pd suggests limited mobility of the PGE as Pd may behave in a mobile way, while Pt and Ir are generally regarded as immobile elements (Fig. 46 h, i). A plot of Pd/Pt vs. Pd/Ir, however, shows that both Pd and Pt as well as Pd and Ir are fractionated (Fig. 46 j). Variations in Pd/Ir ratios can be explained by a combination of chromite crystallisation and *monosulfide solid solution* (mss) fractionation, whereas changes in Pd/Pt ratios are difficult to account for (Fig. 47). Notably, a group of samples plots away from the general trend; they are characterised by anomalously high PPGE (Pd, Pt, Rh) and low IPGE (Ir, Os, Ru), resulting in elevated PPGE to IPGE ratios (Fig. 46 e, i, k). All of these samples represent sulfide veins of variable thickness cross-cutting the layered succession containing interstitial

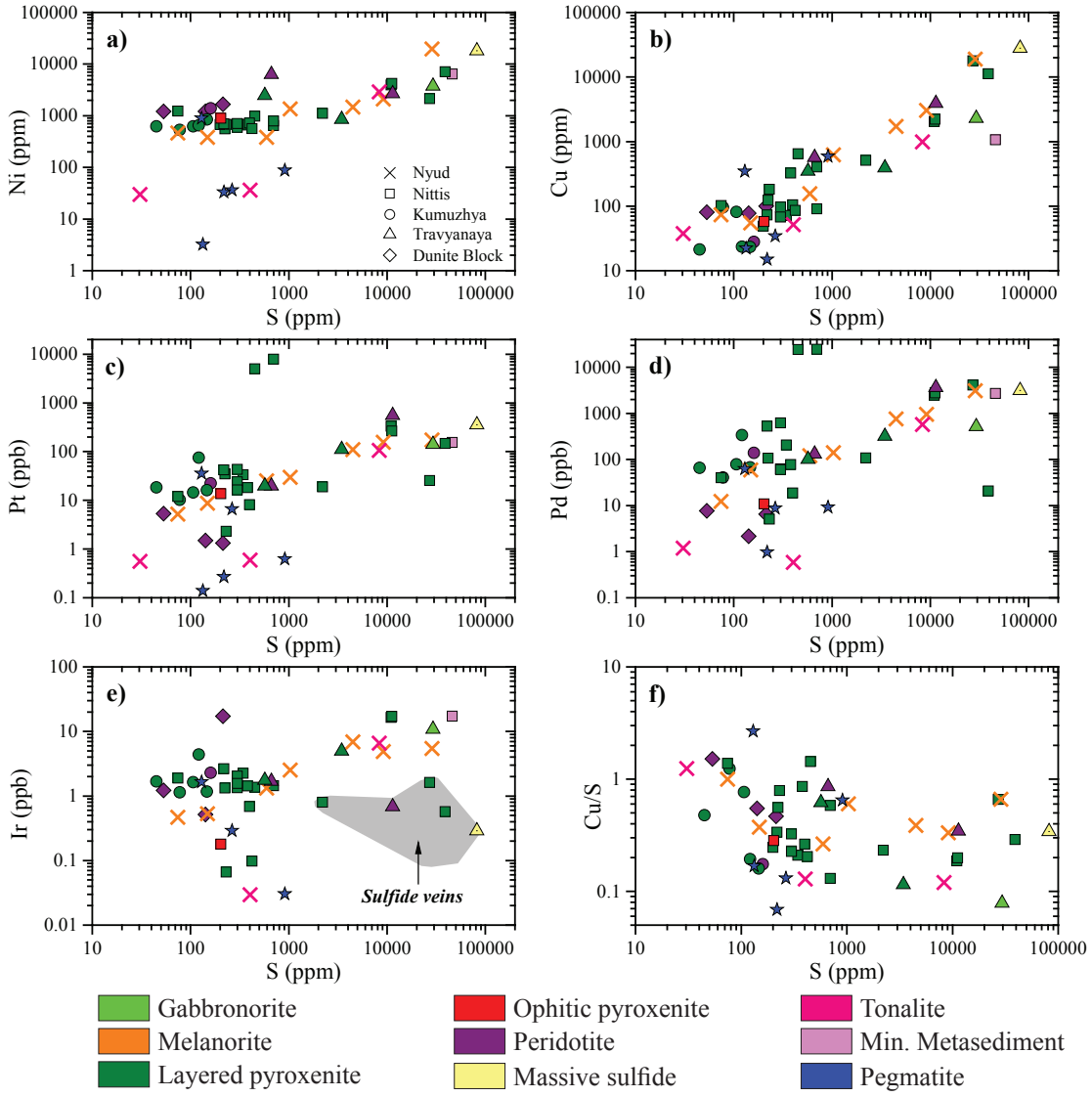

Fig. 46. Binary variation diagram of chalcophile elements. a) Ni vs. S. b) Cu vs. S. c) Pt vs. S. d) Pd vs. S. e) Ir vs. S. f) Cu/S vs. S. g) Pt/S vs. S. h) Pd vs. Pt. i) Ir vs. Pd. j) Pd/Pt vs. Pd/Ir. k) Pd/Rh vs. S. Note that sulfide veins plot in a distinct field away from the samples containing interstitial sulfide.

sulfides.

Drill core profiles, intersecting the mineralised contact of the Nittis and Nyud intrusions, show that significant sulfide accumulation (up to 5 wt % S) is exclusively associated with the basal contact zone of each intrusion (Fig. 48 a, b). These zones are characterised by elevated base metal concentrations, reaching up to 2 wt % Cu and Ni each, and 0.15 wt % Co, whereas precious metal concentrations may be as

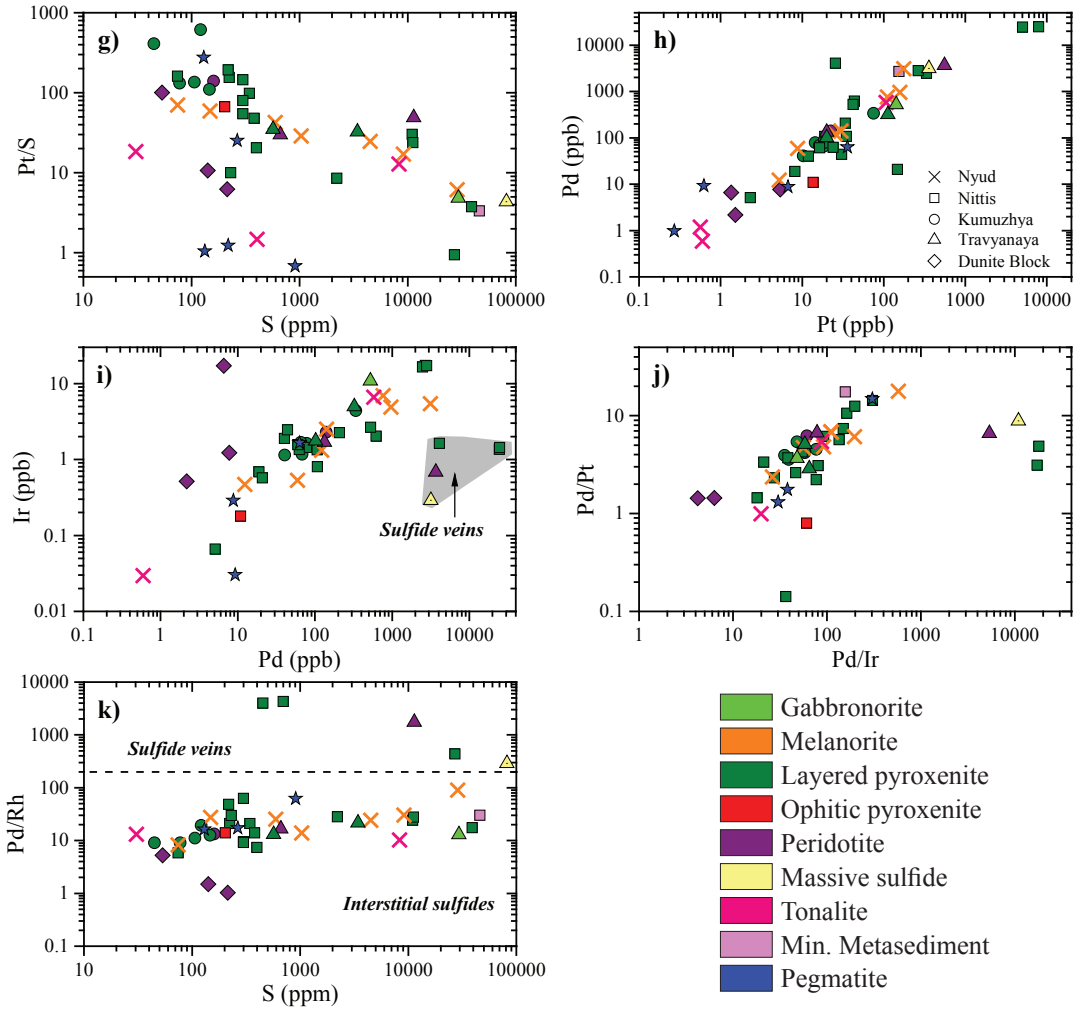

Fig. 46 (cont.)

high as 3.3 ppm Pt + Pd. Moreover, basement lithologies at both intrusions are mineralised in spatial proximity to the mafic-ultramafic rocks. Another remarkable zone of mineralisation was intersected some 100 m above the basal contact of Nittis. The mineralisation is hosted in several thin sulfidic veinlets, cross-cutting the orthopyroxenitic cumulate over a vertical thickness of about 3 m, and reaches up to 32.8 ppm Pt + Pd (Fig. 37 d). Sulfur concentrations are relatively low across the mineralised interval, which is why the mineralisation is difficult to distinguish macroscopically.

All rocks from the NKT Massif and the Nyud intrusion have > 20 ppb Pt + Pd, indicating that they crystallised from a magma, which was saturated in sulfide (Fig.

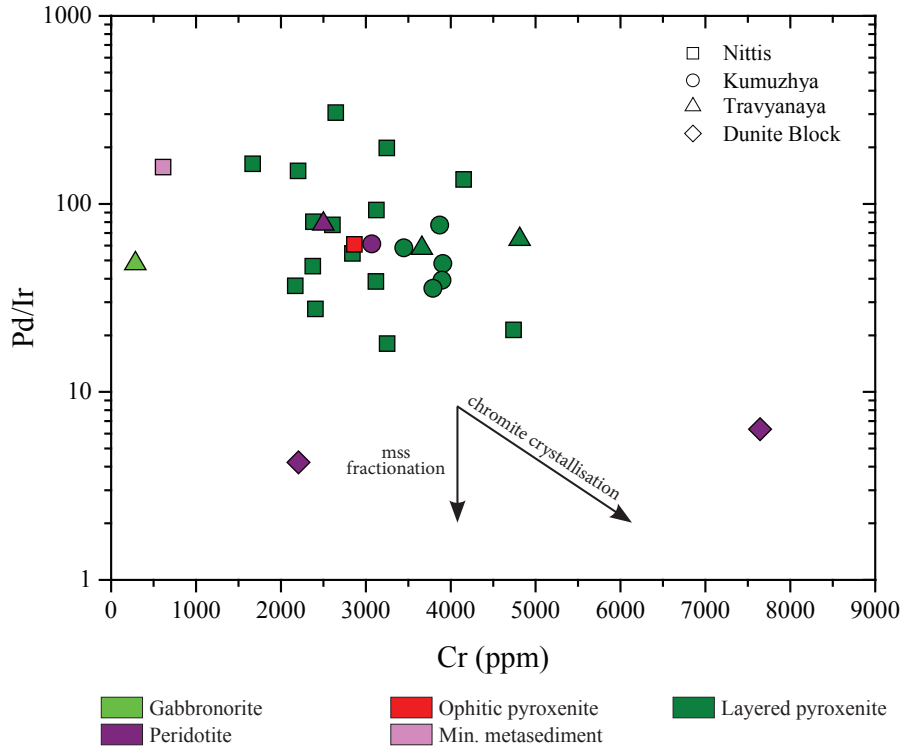

Fig. 47. Binary variation diagram of Pd/Ir ratios against whole rock Cr concentrations. Note the negative correlation. Abbreviations: mss = monosulfide solid solution.

46 c, d, 48). In addition, Cu/Pd ratios in the mafic-ultramafic rocks are generally below the primitive mantle value, reflecting the presence of cumulus sulfide (Fig. 48). In contrast, samples from the Dunite Block have < 15 ppb Pt + Pd, which is consistent with a crystallisation from a sulfide-undersaturated magma (Fig. 46 h).

This is particularly evident in primitive mantle-normalised chalcophile element patterns of the analysed samples as chromite-poor lherzolite from the Dunite Block has generally low PGE concentrations and almost flat patterns with Pd/Ir ratios below 6, supporting a lack of cumulus sulfide, whereas harzburgite from Travyanaya has higher PGE concentrations and features an enrichment in PPGE relative to IPGE with positive Pd as well as Rh anomalies and a high Pd/Ir ratio of more than 75 (Figs. 46 j, 49 a). Chromite-rich dunite from the Dunite Block exhibits a strong enrichment in IPGE relative to PPGE, which reflects the presence of IPGE-rich cumulus chromite (e.g., Capobianco & Drake 1990). All other lithologies from Travyanaya, ranging from websterite to orthopyroxenite and gabbronorite, have re-

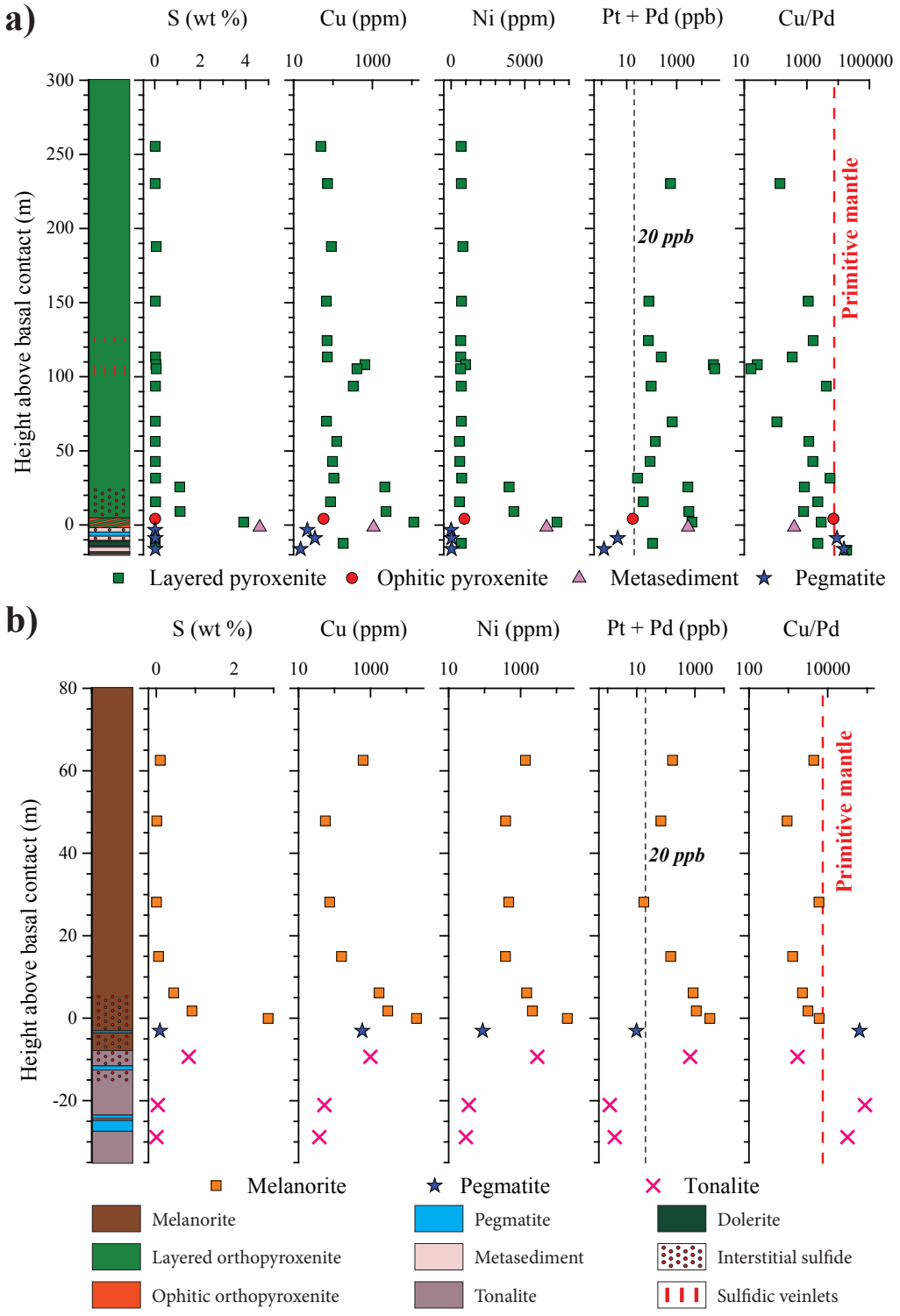

Fig. 48. Downhole chalcophile element geochemistry for drill holes, intersecting the basal mineralised contact at (a) Nittis and (b) Nyud. The primitive mantle value was taken from Barnes & Maier (1999).

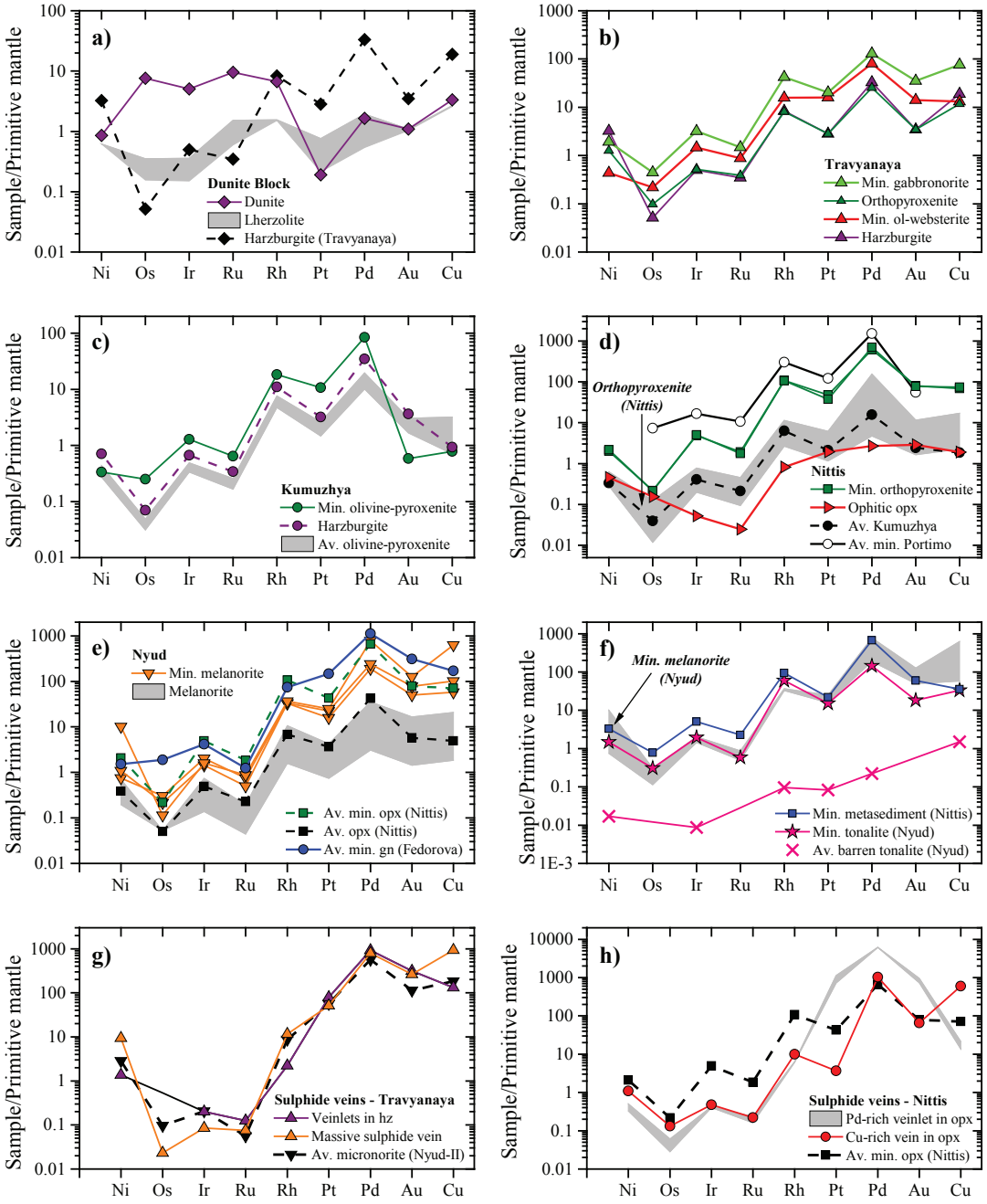

Fig. 49. Primitive mantle-normalised chalcophile element pattern of lithologies from the Dunite Block, the NKT Massif and the Nyud intrusion. a) Dunite Block. b) Travyanaya. c) Kumuzhya. d) Nittis. e) Nyud. f) Basement lithologies. g) Sulfide veins at Travyanaya. h) Sulfide veins at Nittis. Abbreviations: gn = gabbronorite; opx = orthopyroxenite; hz = harzburgite; min = mineralised; ol = olivine. Data for the Portimo Complex and the Fedorova intrusion were taken from Iljina et al. (1992) and Groshev et al. (unpublished data), respectively. Normalisation factors were taken from Barnes & Maier (1999).

markably similar patterns with Pd/Ir ratios from 48 to 65 and positive Pd as well as Rh anomalies (Fig. 49 b). Kumuzhya, Nittis and Nyud lithologies also show positive Pd and Rh anomalies and relatively high Pd/Ir ratios of more than 20 (Fig. 49 c, d, e). Only the ophitic orthopyroxenite from Nittis has a different pattern lacking distinct anomalies. It is worth noting that the positive Pd and Rh anomalies are characteristic of many other Fennoscandian intrusions of similar age, such as the Portimo Complex, and also in parts of the Great Dyke of Zimbabwe and the Muskox intrusion in Canada (Barnes & Francis 1995, Iljina et al. 1992, Maier et al. 2015). The mineralised metasediment from Nittis as well as the mineralised tonalite from Nyud show similar chalcophile element patterns to the mineralised melanorite and orthopyroxenite from the respective intrusions, which suggests a common origin of the sulfide mineralisation (Fig. 49 f). Notably, the mineralised tonalite is also distinct in its pattern from the barren one, despite similar lithophile element chemistry.

In contrast to the interstitial PGE-Ni-Cu mineralisation, characterised by Pd/Ir ratios, ranging from 20 to 600, and strongly positive Pd as well as Rh anomalies, sulfide veins from Travyanaya and Nittis have completely different patterns with much higher Pd/Ir ratios, starting above 2,500 and reaching up to 18,000 (Fig. 49 g, h). Additionally, the positive Rh anomalies are not as pronounced and may also be absent in the most fractionated samples. These veins strongly resemble massive sulfide mineralisation associated with micronorites from Nyud (Fig. 49 g).

6.4 Discussion

6.4.1 Emplacement mode: liquid or crystal-mush?

Many layered intrusions and mafic sills are characterised by a basal compositional reversal, in which whole rock and mineral compositions become progressively more primitive towards the centre of the intrusion or sill. A number of studies have shown that these basal reversals provide valuable insight into the processes associated with the emplacement of mafic-ultramafic intrusions (e.g., Alapieti 1982, Campbell & Kelly 1978, Lightfoot et al. 1984, Page 1979). Key features of the basal reversal at Nittis are an upward increase in the Mg# of orthopyroxene, whole rock MgO concentrations and Cr/V ratios, which are mirrored by decreasing Al_2O_3 concentrations. Moreover, La/Nb ratios remain relatively consistent across the pyroxenitic part of the profile (Fig. 45). Several models for the origin of these reversals have been proposed, ranging from the crystallisation of compositionally diverse liquids as a result of *in situ* contamination or magma stratification to the crystallisation of crystal-liquid mixtures, affected by crystal settling, flow differentiation, convection and variable amounts of trapped liquid (see Latypov 2003, for a review).

Key features of the basal reversal at Nittis are an upward increase in the Mg# of orthopyroxene, whole rock MgO concentrations and Cr/V ratios, which are mirrored by decreasing Al_2O_3 concentrations. Moreover, La/Nb ratios remain relatively consistent across the pyroxenitic part of the profile (Fig. 45).

In situ contamination of a crystal-poor parental magma with the immediate host metasediments would have considerably affected the incompatible trace element signature of the magma, especially close to the intrusion contact, where the degree of contamination would have been the highest. The near-constant La/Nb ratios across most of Nittis, however, argue strongly against *in situ* contamination as the principle mechanism for the development of a basal reversal. Only sample 79-145, which is in direct contact with the host metasediment, has a slightly elevated La/Nb ratio, indicating that the extent of *in situ* contamination is confined to the immediate surroundings. This is further supported by Bekker et al. (2016), who noted a slightly stronger mass-independent fractionation of sulfur isotopes in NKT Massif samples

from the intrusion contact relative to those from the intrusion centre.

Additionally, the highly elongated crystal shape of orthopyroxene, defining the typical mineral lamination of the Nittis pyroxenites, is unlikely to have formed *in situ* during the crystallisation of a liquid (Fig. 41 a). The upward increase in whole rock MgO concentrations together with the antithetical behaviour of Al_2O_3 reveal a distinct shift in modal mineralogy with stratigraphic height. As orthopyroxene is the only cumulus phase, the Al_2O_3 concentrations, reflecting the abundance of interstitial plagioclase, can be used as a proxy for the amount of trapped liquid (Fig. 45). The highest Al_2O_3 concentrations and therefore amount of trapped liquid occur at the basal contact of the intrusion and subsequently decrease towards the top of the succession. It is difficult to explain these features with the crystallisation of a crystal-poor liquid as this would produce distinct variations in the grain size of orthopyroxene and plagioclase as a function of cooling rate. Orthopyroxene in the layered orthopyroxenite, however, does not show any systematic changes in grain size from the intrusion contact to the centre and plagioclase remains an interstitial phase. Moreover, the ubiquitous presence of sulfide-saturated lithologies and the homogeneous large-scale distribution of cumulus sulfide in peridotites, pyroxenites and norites is also inconsistent with an initially crystal-poor magma chamber as gravity-driven sulfide settling would be expected under these conditions.

The basal reversal can thus be explained by a decreasing trapped liquid component away from the intrusion contact, whereby original liquidus compositions of orthopyroxene were modified by reaction with trapped liquid (e.g., Barnes 1986a). This may not only affect major elements, but also trace elements, such as Cr and V. The extent of the modification depends on the amount of trapped liquid as indicated by the negative correlation between the Mg# of orthopyroxene as well as the Cr/V ratios and the whole rock Al_2O_3 concentrations – the higher the amount of trapped liquid, the higher the extent of modification.

Thus, the geochemistry of the basal reversal helps to constrain the emplacement mode of the NKT Massif. Our data are consistent with a model in which the intrusion was emplaced as a crystal mush with relatively high amounts of suspended cumulus orthopyroxene. Close to the intrusion margins, elevated cooling rates hin-

dered effective and thorough gravitational settling of orthopyroxene, resulting in high amounts of trapped liquid. As cooling rates generally decrease away from the intrusion contact, the amount of interstitial liquid trapped in the cumulate was also lower, as evidenced by a smaller trapped liquid shift (Fig. 45).

6.4.2 Genetic aspects of contact-style PGE-Ni-Cu mineralisation at Monchegorsk

Cross-cutting relationships in drill core together with relative abundance and geochemical data indicate that the earliest pulse of magma, intruding relatively cold basement lithologies underlying the Monchegorsk area, was volumetrically insignificant, yet important for the formation of sulfide mineralisation. It is represented by the ophitic orthopyroxenite, which has the most primitive composition of all Nittis lithologies and seems to have crystallised from a sulfide-undersaturated magma with a distinct La/Nb ratio close to that of the primitive mantle (Fig. 45). Even though the first pulse of magma did not contribute any sulfides, it introduced considerable heat into the basement, resulting in an increased ambient temperature (Fig. 50 a). The second phase of magmatism was much more significant in terms of volume and caused intense brecciation of the ophitic orthopyroxenite. The ubiquitous presence of sulfide-saturated rocks across the NKT Massif and the Nyud intrusion requires an early sulfide saturation event, prior to final emplacement, most likely in a staging magma chamber (Fig. 50 b). After reaching sulfide saturation, the sulfide droplets were enriched in PGE, while interacting with the magma, and eventually settled to the base of the staging chamber together with crystallising olivine and orthopyroxene. This proto-cumulate, consisting of cumulus olivine, orthopyroxene, liquid sulfide and residual silicate melt, was episodically remobilised and crudely density-sorted within the crystal mushes as it was transported into higher crustal levels. Upon final emplacement of these large volumes of crystal mush, the preheated basement underwent not only partial melting, as reflected in the frequent occurrence of felsic pegmatite, but also devolatilisation, which led to the local addition of water and potentially carbon dioxide to the magma (Fig. 50 c).

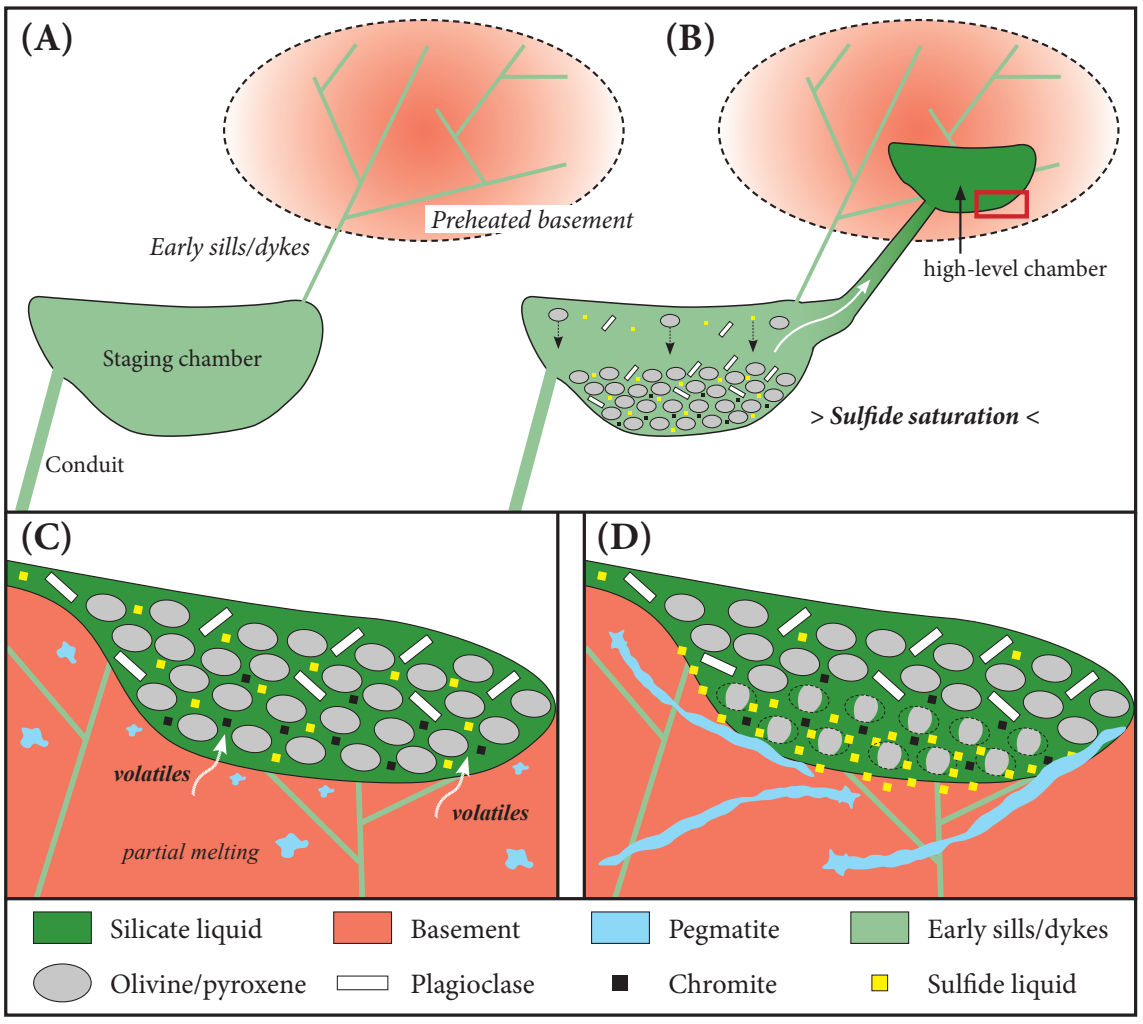

Fig. 50. Schematic model for the formation of contact-style sulfide mineralisation in the Monchegorsk Complex. Note that the partial melting of the basement in c) relies on the preheating of the basement through the intrusion of early sills and dykes. See text for explanation.

The effect of this is twofold: (1) the added volatiles act as fluxes, thus lowering the melting point of the cumulus minerals, which results in local small-scale dissolution of these cumulus phases within the crystal mush, and (2) it reduces the viscosity of the interstitial melt. Although Mg-rich orthopyroxene has a high liquidus temperature, thermodynamic considerations suggest that the melting temperature of cumulus orthopyroxene can be readily suppressed to less than 1,100 °C in the presence of plagioclase and water.

On the one hand, local melting of cumulus phases results in an enhanced porosity of the crystal mush in the vicinity of the lower contact, promoting preferential

sulfide liquid collection at the base of the intrusion. On the other hand, the local decrease in magma viscosity facilitates the gravitational settling of sulfide droplets. Together with the basement preheating and the associated lower cooling rate, these factors lead to a relatively efficient accumulation of sulfide, especially in the centre of the intrusion, where permeability can be maintained the longest due to slower cooling relative to more peripheral parts (Fig. 50 d). In some places, the settling sulfide liquid also percolated into the basement as reflected by the mineralised basement lithologies at Nittis and Nyud (Fig. 49 f). The migration of sulfide liquid has also been observed in many other intrusions, such as the Portimo Complex, where the mineralisation extends for several tens of metres into the basement (Iljina et al. 1992). Despite generally low modal sulfide abundances of up to 5 vol % in these basement lithologies, the sulfide liquid may have percolated into the footwall through an interconnected sulfide network, which may develop at even lower sulfide abundances (Godel 2013).

Constraining the composition of the parental magma is rather difficult as chilled margins have not been observed in the Monchegorsk Complex. The Mg# of the parental magma, however, can be calculated with the Mg-Fe olivine-liquid partition coefficient of 0.30, using the most primitive olivine composition from the NKT Massif (Roeder & Emslie 1970). Forsterite contents reach up to 87.2 mol % in olivine from the NKT Massif, which corresponds to a parental magma with Mg# = 67.1 mol %. This composition is similar to siliceous high-Mg basalts (SHMB) that are considered to represent the parental magma for other Paleoproterozoic intrusions, such as the Portimo Complex (Saini-Eidukat et al. 1997). Moreover, Paleoproterozoic picrites in northern Finland, analysed by Hanski et al. (2001a), have a similar Mg#, averaging at 66.7 mol % (n = 3).

The poor correlation between Cu, Pt, Pd and S in samples with relatively low S concentrations has been observed in many intrusions, similar to samples from this study with less than l,000 ppm S (Fig. 46 b, c, d, f, g), which is generally attributed to late magmatic or hydrothermal S loss (e.g., Cawthorn & Meyer 1993, Maier & Barnes 1996). In contrast, the positive correlation between Pt and Pd as well as Ir and Pd suggests limited mobility of the PGE as Pd may behave mobile, while Pt

and Ir are generally regarded as immobile elements (Fig. 46 h, i).

Therefore, assuming a picritic parental magma with 498 ppm Ni, 86 ppm Cu, 9.54 ppb Pd and 0.76 ppb Ir (see Barnes & Lightfoot 2005), the chalcophile element chemistry of the contact-style mineralisation can be explained by sulfide segregation at R factors between 1,000 and 10,000 with limited fractional crystallisation of the sulfide liquid (Fig. 51). It is worth noting that the *monosulfide solid solution* (mss) is

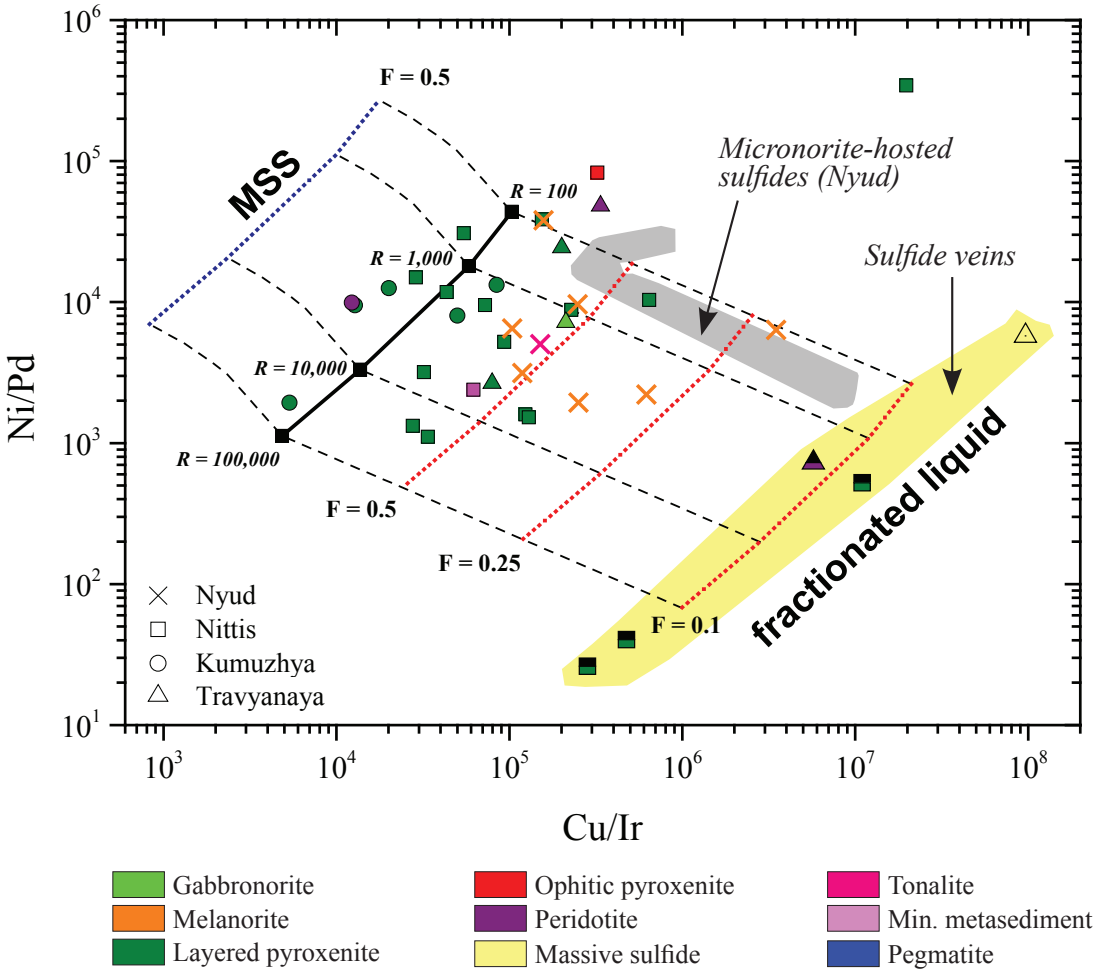

Fig. 51. Binary ratio plot of Ni/Pd vs. Cu/Ir. The black solid line shows model sulfide compositions at different R factors. The black dashed lines represent model compositions of *monosulfide solid solution* (mss), crystallising from sulfide liquids undergoing fractionation, and residual liquid. The dotted lines show different end-member mss (blue) and residual sulfide liquid (red) compositions, assuming different degrees of fractionation (F = fraction of residual liquid). Sulfide melt/silicate melt D values: 30,000 for the PGE, 1,000 for Cu and 500 for Ni. Mss/sulfide melt D values as summarised in Maier & Barnes (1999). Half-filled symbols represent samples, containing vein-hosted sulfide.

rather under-represented in the dataset, possibly indicating further mss-rich sulfide mineralisation at depth.

6.4.3 Thermal modelling of basement preheating

Distinct geochemical and textural characteristics of the intersected ophitic orthopyroxenite, together with complex cross-cutting relationships at the base of Nittis, indicate that this rock type may represent a volumetrically minor first pulse of magma, intruding into the crust. This pulse may have introduced significant heat into the basement, allowing for relatively slow cooling of the second major intrusive event, which led to effective sulfide collection at the base of the complex. This hypothesis can be tested numerically, assuming conductive heat transfer by using the explicit finite difference method. Discretisation of Newton's one-dimensional heat diffusion equation yields:

$$T_i^{n+1} = T_i^n + \kappa \Delta t \left(\frac{T_{i+1}^n - 2T_i^n + T_{i-1}^n}{\Delta x^2} \right)$$

The intention of the model is to evaluate two possibilities:

(1) Intrusion of a 1500-m-thick crystal mush into preheated basement

(2) Intrusion of a 1500-m-thick crystal mush into cold basement

The preheating of the basement was modelled assuming the intrusion of multiple sills with an average thickness of 50 m and a spacing of 250 m from approximately 2 to 4 km depth, as shown in Figure 52 a. The intruding sills were assumed to have a temperature of 1200 °C (e.g., Huppert et al. 1985). The model shows that these thin sills cool relatively quickly, reaching less than 800 °C after 10 years; however, basement temperatures in excess of 700 °C are only attained in close vicinity of the sills ($<$ 5 m). Nevertheless, these sills are capable of raising the average basement temperature from less than 120 °C to more than 350 °C across the intruded basement thickness.

In a second step, it was assumed that the main pulse of magma, which produced the NKT Massif, was emplaced with a temperature of 1200 °C into preheated

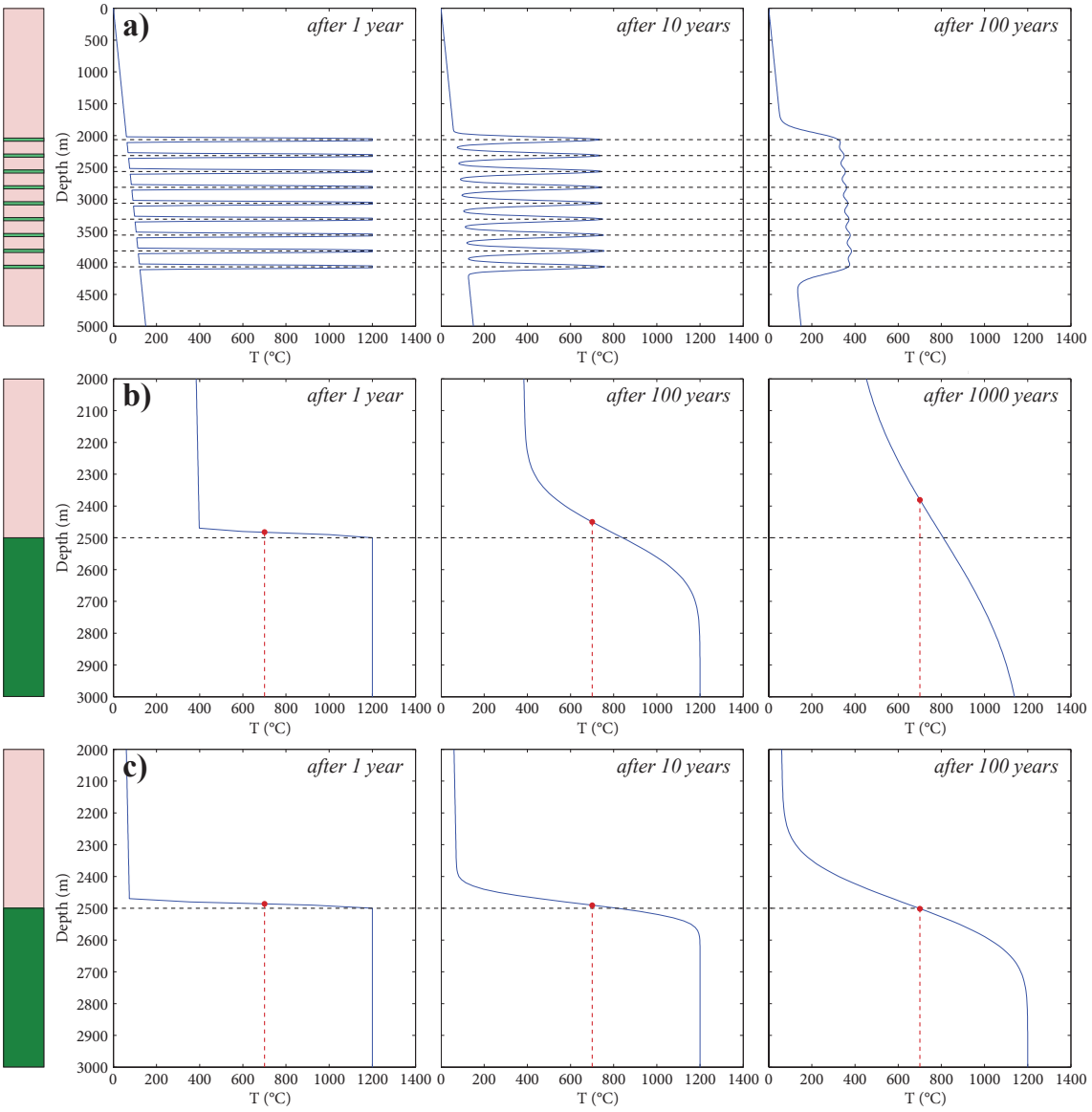

Fig. 52. Temperature-depth profile for different modelled intrusion emplacement scenarios. a) Preheating of the basement by multiple sills with a thickness of 50 m and a spacing of 250 m. b) Emplacement of a 1.5-km-thick crystal mush into preheated basement at a depth of 2.5 km. c) Emplacement of a 1.5-km-thick crystal mush at a depth of 2.5 km into cold basement. Note that significant partial melting of the basement (> 700 °C) is only feasible in a preheated basement. See text for further explanation. Green = mafic-ultramafic rocks; pink = basement.

basement at a depth of 2.5 km, as shown in Figure 52 b. The frequent occurrence of felsic pegmatite close to the intrusion contact strongly suggests partial melting of the immediate basement, but dehydration melting requires temperature in excess of 700 °C (e.g., Singh & Johannes 1996). The model indicates that this temperature is

reached up to 50 m away from the intrusion contact after 100 years and even 120 m away after 1000 years. Therefore, dehydration melting may also affect distal regions of the basement, given that the latter is preheated.

Alternatively, it may be assumed that the main pulse of magma was emplaced into cold basement, while all other variables remained unchanged. In this case, a geothermal gradient of 30 K/km was used for the basement temperature profile. The thermal modelling in Figure 52 c illustrates that basement temperatures in excess of 700 °C can only be attained directly at the intrusion contact upon emplacement. As a consequence, only insignificant volumes of pegmatite would be produced at the contact, which cannot account for the high abundance of pegmatite observed in drill core. Afterwards, temperatures gradually decrease from 700 °C, indicating much higher cooling rates compared to the emplacement into a preheated basement.

Thermal modelling shows that the early intrusion of relatively thin sills may lead to a thorough preheating of cold basement to temperatures of ca. 350 °C. Subsequent intrusions can then cause partial melting of the latter to produce the abundant pegmatite, which would not have been feasible without preheating the basement.

6.4.4 Comparison of Nittis with the Finnish Portimo and Penikat intrusions

The Paleoproterozoic Portimo Complex in northern Finland is not only broadly coeval with the Monchegorsk Complex, but it also hosts several sizeable examples of contact-style sulfide mineralisation related to the basal contact of the intrusion (e.g., Iljina 1994).

The Suhanko-Konttijärvi intrusion in the southern part of the Portimo Complex includes a succession of orthopyroxene-rich cumulates in its lower portion (e.g., Ahmavaara), which reaches up to 150 m in thickness with abundant floor rock xenoliths (Iljina et al. 1992). However, the modal proportion of plagioclase is much higher at this stratigraphic level compared to the Nittis intrusion. Another important stratigraphic difference is the presence of a relatively thick marginal zone at Portimo. This

zone is entirely missing at Nittis and Nyud, the latter being characterised by a relatively thin basal contaminated zone of approximately 20 m, comprising tonalite and pegmatite that give way to melanorite. The basal portion of the Narkaus intrusion in the northern part of the Portimo Complex consists of an about 80-m-thick orthopyroxenite, similar to Nittis, but it also hosts a massive chromite layer, which does not occur at Nittis. Therefore, a direct correlation with Paleoproterozoic Finnish intrusions proves to be inexpedient. In fact, the orthopyroxenitic body at Nittis is much thicker than in any of the Finnish intrusions, which suggests that the total volume of magma may have been significantly larger in the Monchegorsk Complex.

Another richly mineralised Paleoproterozoic intrusion in northern Finland is the Penikat intrusion, hosting at least seven PGE-enriched horizons (Alapieti & Halkoaho 1995). Notably, most samples from Penikat are characterised by relatively strong negative Nb-Ta anomalies similar to the Monchegorsk Complex (Maier et al., in review); however, the exceptionally primitive SJ Reef at Penikat as well as the most primitive ophitic orthopyroxenite from Nittis lack this feature (Fig. 44 b), which may indicate that the parental magma to the most primitive rocks at both intrusions may not have necessarily featured a negative Nb-Ta anomaly. This is particularly important with respect to magma derivation as negative Nb-Ta anomalies are consistent with either melting of asthenospheric mantle followed by crustal contamination or melting of the sub-continental lithospheric mantle (SCLM) (e.g., Amelin & Semenov 1996, Hanski et al. 2001b, Huhma et al. 1990, Puchtel et al. 1997, Yang et al. 2016). Since both alternatives have been considered as a possible source for the 2.5 to 2.44 Ga magmatism across the Fennoscandian Shield, the lack of negative Nb-Ta anomalies in some of the most primitive lithologies from the Monchegorsk Complex and the Penikat intrusion suggests that the widespread Nb-Ta depletion may not be a primary feature, inherited from the source region, but resulted from crustal contamination of asthenospheric mantle melt. This model would be consistent with recent Os, Nd, and Sr isotope data from Yang et al. (2016), which also argue for a mantle plume rather than an SCLM source.

6.4.5 Origin of cross-cutting massive sulfide veins

The ubiquitous cross-cutting massive sulfide veins associated with the NKT Massif seem to postdate the solidification of the host cumulates based on the sharp contact relationships between the two. Detailed element mapping of the vein contact reveals a 1 to 2-mm-thick alteration halo, with localised sulfide infiltration into the host rock, possibly reflecting small-scale partial melting (Fig. 40 d). Mantle-normalised chalcophile element patterns also suggest a different origin of these veins in comparison to the interstitial sulfide mineralisation concentrated at the basal contact of the intrusion (Fig. 49 g, h). The extremely high Pd/Ir ratios of up to 15,000 strongly resemble Cu-rich veins at Noril'sk, Cape Smith, Sudbury and PGE-rich sulfide veins at Kilvenjärvi (Portimo Complex), representing highly fractionated sulfide liquid (e.g., Andersen et al. 2006, Barnes & Lightfoot 2005, Duran et al. 2017, Li et al. 1992). Modelling of sulfide segregation from an undepleted picrite at different R factors together with variable degrees of sulfide liquid fractionation provides further insight into the formation and origin of these veins.

Our chalcophile element data indicate that the veins represent highly fractionated sulfide liquid (melt fraction F $\approx$ 10 %) at different R factors, ranging from less than 100 to more than 100,000 (Fig. 51). Furthermore, massive sulfide mineralisation associated with micronorites cross-cutting the Nyud intrusion has largely similar chalcophile element patterns that lack the positive Rh anomaly typical of interstitial sulfide mineralisation in the mafic-ultramafic cumulates of the Monchegorsk Complex (Fig. 49 g). Hence, these sulfide veins do not seem to be directly related to the formation of the contact-style PGE-Ni-Cu mineralisation intersected at the base of Nittis and Nyud.

6.4.6 Positive Rh anomaly

One of the key questions regarding PGE mineralisation in the Monchegorsk Complex is the origin of the positive Rh anomaly in the primitive mantle-normalised PGE patterns (Fig. 49) as most large layered intrusions, such as the Bushveld Complex or the Great Dyke, do not show this distinctive feature (cf. Barnes & Maier

2002, Oberthür 2002). The only other intrusion that features such an anomaly is the Muskox Intrusion in Canada (Barnes & Francis 1995).

It is widely recognised that many primary magmas may be characterised by Pd/Pt ratios that are higher than those of the primitive mantle, which can be explained by a more compatible behaviour of Pt relative to Pd during partial melting (e.g., Barnes & Picard 1993). The most primitive rocks from the Monchegorsk Complex are peridotites from the Dunite Block with Pd/Pt > 1.4, which is significantly higher than the primitive mantle ratio of 0.57 (Barnes & Maier 1999). Therefore, it seems likely that differences in the partition coefficients between Pt and Pd during mantle melting contributed to the fractionation of the two elements to a certain degree.

The overall increase in Pd/Pt ratios from about 1 to more than 10 across the Monchegorsk Complex, however, requires an additional fractionation process that is unrelated to magma generation (Fig. 46 j). Based on the occurrence of Pt-Fe alloys in chromitites from Alaskan-type complexes (Nixon et al. 1990), it was suggested that Pt may behave in a compatible manner during fractionation as a result of Pt-Fe alloy formation, which was potentially induced by chromite crystallisation (Peck & Keays 1990, Barnes & Francis 1995).

This process may be a feasible explanation for the strong fractionation of Pt relative to Pd in the Monchegorsk lithologies, which means that the positive Rh anomaly is caused by a depletion in Pt. Detailed studies on the mineralogy of the PGE in the Monchegorsk Complex, however, show that the number of Pt-Fe alloys is rather insignificant in the ultramafic portion of the complex. Therefore, it remains questionable, whether the Pt depletion resulted from the crystallisation of these alloys. In contrast, Grokhovskaya et al. (2003) reported that hollingworthite ((Rh,Pt,Pd)AsS), as they main host for Rh, was present throughout the complex, which may indicate that the parental magma may have been unusually rich in Rh.

6.4.7 Note on the Dunite Block and its relation to the Monchegorsk Complex

The Dunite Block is generally considered to be a tectonically uplifted ultramafic block, which represents the lowermost portion of the Monchegorsk Complex (e.g., Chistyakova et al. 2015, Smolkin et al. 2004). It hosts the most primitive lithologies in the Monchegorsk area dominated by dunite and lherzolite with highly magnesian olivine, reaching forsterite contents of up to 91.6 mol %. Subsolidus re-equilibration between olivine and chromite, however, may have affected olivine compositions to a certain degree, even though analyses were primarily conducted on olivine cores (e.g., Ozawa 1984). The corresponding parental magma would have most likely been a liquid of komatiitic composition with Mg# $\approx$ 77, possibly similar to broadly coeval komatiites from the Central Lapland Greenstone Belt described by Hanski et al. (2001a). As a consequence, the SHMB, considered to be the parental magma for most Paleoproterozoic layered intrusions in the Fennoscandian Shield, including the NKT Massif, would merely represent a fractionation product of a komatiite. Alternatively, the Dunite Block crystallised from a distinct batch of magma, but the close temporal and spatial relationship between the Dunite Block and the other parts of the Monchepluton strongly suggests a common origin.

Another important difference between the Dunite Block and the NKT Massif is the mineral chemistry of the ultramafic cumulates: orthopyroxene from the Dunite Block has considerably lower Cr concentrations than orthopyroxene from Travyanaya (3000 ppm vs. 5000 ppm Cr) at similar Mg# (Fig. 42); the latter being inconsistent with fractional crystallisation of a komatiitic parental magma. However, Cr concentrations of orthopyroxene are not only controlled by the parental magma composition, but also by the oxygen fugacity, as magma oxidation results in a higher partition coefficient for Cr between orthopyroxene and melt (Barnes 1986b). In addition, all NKT Massif lithologies are saturated in sulfide, whereas none of the analysed Dunite Block samples contain cumulus sulfide.

These characteristics can only be explained, if sulfide saturation occurred after the crystallisation of the cumulus minerals that were later emplaced as the Dunite

Block. Therefore, it is likely that highly magnesian cumulus phases were crystallising from a sulfide-undersaturated magma, while it was undergoing progressive contamination with basement lithologies. This eventually led to sulfide saturation along with an increase in the oxygen fugacity of the magma, which increased the partition coefficient for Cr between orthopyroxene and melt, and produced Cr-rich orthopyroxene. Subsequently, the overlying portions of the complex crystallised from a sulfide-saturated magma. The model, however, implies that the SHMB only represents a fractionation product of a contaminated komatiitic parental magma. Ultimately, the Dunite Block, as an early magmatic phase, may have also contributed to the preheating of the basement, thus facilitating the formation of contact-style mineralisation.

6.5 Summary and implications for exploration

Our study highlights key processes that lead to the formation of contact-style sulfide mineralisation, based on the geology and geochemistry of the Monchegorsk Complex. The chalcophile element chemistry indicates that sulfide saturation occurred relatively early, possibly in a staging chamber, prior to the final emplacement of the complex as all lithologies contain cumulus sulfide. Therefore, the critical control on the formation of a sizeable deposit is the efficient collection of sulfide in distinct zones of a layered intrusion, i.e. along the basal intrusion contact.

The frequent brecciation of mafic-ultramafic rocks, basement lithologies and felsic pegmatite, especially in the contact zone of the intrusion, suggests a multi-stage emplacement of the complex. Our thermal modelling shows that the early intrusion of sills may lead to a thorough preheating of the cold basement to temperatures of ca. 350 °C.

The basement preheating does not only facilitate the assimilation of (S-rich) basement lithologies to trigger sulfide saturation, but it also affects cooling rates, which directly control the duration of potential sulfide accumulation through gravitational settling, especially in the centre of the intrusion, where permeability can be maintained the longest due to slower cooling relative to more peripheral parts.

Moreover, dehydration melting of the basement introduces water and carbon dioxide into the magma, resulting in local melting of cumulus phases, which increases the porosity of the cumulate or crystal mush towards the base. This interstitial space may then be filled with sulfide liquid. In addition, the volatiles may also reduce the viscosity of the interstitial melt, facilitating sulfide settling. The lack of preheating considerably reduces the degree and extent of potential interaction between the magma and the basement, which leads to an inefficient collection of sulfide liquid at the base of the complex.

As a consequence, layered intrusions, comprising two or more temporally related, but distinct injections or pulses of magma, should be prospective with respect to contact-style sulfide mineralisation. Notably, the richest contact-style PGE deposits in the northern limb of the Bushveld Complex are located in areas where the Lower Zone is present (see McDonald et al. 2017, for a detailed geological map of the northern limb); the same applies to the Portimo Complex, where the presence of earlier Portimo Dykes seems to correlate with higher grade mineralization (see Iljina & Lee 2005). Moreover, Groshev et al. (2009) suggested that the 300-m-thick mineralised zone at the base of the Fedorova intrusion was emplaced after the formation of the more than 4-km-thick mafic-ultramafic main body of the layered intrusion.

Chapter 7

Petrogenetic processes associated with the formation of reef-style PGE mineralisation in the Monchegorsk Complex

Abstract

The Paleoproterozoic Monchegorsk Complex in NW Russia represents one of the largest known layered intrusions in Europe and hosts several examples of broadly stratiform PGE mineralisation at different stratigraphic levels of the intrusion.

The Sopcha Reef occurs in the ultramafic lower portion of the complex and comprises an up to 6-m-thick succession of layered, mineralised dunite, harzburgite and olivine-orthopyroxenite, with peak grades of 3.4 ppm Pt + Pd and 1.1 wt % Ni. Another PGE occurrence is hosted by the leucogabbronoritic to anorthositic Vuruchuaivench intrusion, which represents the mafic upper portion of the Monchegorsk Complex. The disseminated sulfide mineralisation reaches up to 7.3 ppm Pt + Pd and is concentrated in several lenticular bodies over a strike length of ca. 5 km, rather than in a laterally continuous reef as previously suggested. Moreover, our work identified a previously unreported minor enrichment in precious metals of up to 0.2 ppm Pt + Pd in leucogabbroic rocks of the Monchetundra intrusion, which is part of the more than 60-km-long mafic Main Ridge.

Detailed lithophile and chalcophile element data, coupled with mineral chemistry, indicate that the PGE mineralisation at Sopcha and Vuruchuaivench does not represent classic reef-style mineralisation, which is commonly narrow and marked by a sharp increase in Cu/Pd ratios, reflecting the *in situ* sulfide saturation within a large magma chamber. Instead, it is more likely that the Sopcha Reef was emplaced as a crustally contaminated and sulfide-saturated, olivine-rich crystal mush that was sourced from a deeper chamber. The Sopcha mineralisation is characterised by Pd/Pt > 5 and Pd/Ir > 55, similar to contact-style mineralisation elsewhere in the complex, possibly suggesting a common origin of the sulfides. The mineralised Vuruchuaivench lithologies have similar Pd/Pt ratios, but much higher Pd/Ir ratios of up to 600, whereas the unmineralised host rocks, below as well as above the mineralisation, have Pd/Ir < 100 and Pd/Pt < 2. These data indicate that the PGE-rich sulfides did not segregate *in situ* from the same magma that crystallised the host leucogabbronorites and anorthosites at Vuruchuaivench. Considering R factor and sulfide fractionation modelling results, we suggest that the mineralised

Vuruchuaivench lithologies represent a sill-like intrusion of gabbroic crystal mushes, which have entrained fractionated sulfide liquid that is related to an earlier sulfide saturation event.

The mineralised leucogabbroic rocks of the Monchetundra intrusion are characterised by a sharp increase in Cu/Pd ratios, which is consistent with a classic PGE reef model, in which sulfide saturation was triggered *in situ* by extensive fractionation and possibly affected the entire magma chamber. The potential of this mineralisation style elsewhere in the Main Ridge remains to be evaluated.

7.1 Introduction

The Paleoproterozoic Monchegorsk Complex, located in the central part of the Kola Peninsula in Arctic Russia, represents one of the most richly mineralised layered mafic-ultramafic intrusions in Europe with respect to PGE, Ni, Cu and Cr. The complex hosts a remarkable range of deposit types, including dunite-hosted chromite seams, contact-style PGE-Ni-Cu mineralisation, massive Ni-Cu sulfide mineralisation, cutting across the layered succession in steeply dipping veins and in lens-like micronorite-hosted bodies (Chashchin et al. 1999, Karykowski et al. 2016, Kozlov 1973, Sharkov & Chistyakov 2012). In addition, disseminated PGE-rich sulfide mineralisation occurs at two distinct stratigraphic levels: (1) the *Sopcha Reef*, hosted by interlayered peridotite and orthopyroxenite in the lower portion of the intrusion and (2) the *Vuruchuaivench Reef*, together with a previously unknown horizon of PGE enrichment in the Monchetundra intrusion, all of which are associated with interlayered leucogabbronorite and anorthosite in the upper portion of the complex (cf. section 2.2.4).

The Sopcha Reef was initially discovered in the 1930s with a confirmed strike length of about 2 km and a true thickness of 4 to 6 m with up to 0.6 wt % Ni, 0.3 wt % Cu and 8 ppm Pt + Pd (Grokhovskaya et al. 2003, Smolkin & Neradovsky 2006). In contrast, the Vuruchuaivench Reef can be traced for up to 5 km and measures 83.6 Mt of category C_1 + C_2 mineral reserves with 0.3 wt % Ni, 0.2 wt % Cu, 1.3 ppm Pt + Pd + Au (Petrov et al. 2016). The origin of the PGE mineralisation, however, remains poorly understood due to the complex nature of layering at Sopcha and the relatively strong alteration of the Vuruchuaivench lithologies.

As most of the world's PGE resource is hosted in reefs, such as the famous Merensky Reef in the Bushveld Complex of South Africa (e.g., Cawthorn 2010), it is of particular importance to understand their origin and the mechanisms, leading to the concentration of the economically important PGE. The formation of PGE reefs is a much-debated issue in the scientific community with petrogenetic models ranging from extensive magma fractionation to episodic pressure changes, crustal contamination and magma addition (e.g., Cameron 1980, Campbell et al. 1983,

Cawthorn 2005, Haughton et al. 1974, Lee & Butcher 1990).

In this study, we present comprehensive whole rock lithophile and chalcophile element geochemistry of the mineralised intrusions, particularly focusing on the mineralised reef intervals. Moreover, detailed compositional data of rock-forming minerals along a vertical profile across the ultramafic Sopcha Reef provide further insight into the origin of the reef mineralisation. This helps to improve our current understanding of the formation of these economically significant deposits, not only in the Monchegorsk Complex, but potentially also elsewhere in the world.

7.2 Nature of reef-style mineralisation

7.2.1 Sopcha intrusion

The geology and lithostratigraphy of the Sopcha intrusion is briefly summarised in section 2.2.2. The architecture of the mineralised Sopcha Reef is highly complex as several mineralogically and texturally distinct rock types are present in a section of about 5 m in thickness. The base of the reef interval is defined by an approximately 0.6-m-thick dunite, which is rarely exposed due to intense weathering (Fig. 53 a). It is overlain by some 1.5 m of weakly layered harzburgite, followed by a 3-m-thick succession of strongly layered olivine-orthopyroxenite at the top of the reef (Fig. 53 b). Contact relationships between these lithologies are generally gradational, although field exposures of the reef horizon are commonly characterised by distinct colour changes from light to dark brown, but this merely reflects the modal abundance of sulfide, rather than the rock type.

Much of the complexity in the reef interval is caused by a cross-cutting orthopyroxenite breccia that occurs just below the reef dunite as well as in the upper part of the reef olivine-orthopyroxenite (Fig. 53 c). It reaches a thickness of up to 0.8 m and contains abundant autoliths from the immediate ultramafic host rocks set in an orthopyroxenitic matrix: dunitic autoliths at the base of the reef and more orthopyroxene-rich autoliths at the top of the reef. The orthopyroxenite breccia has generally sharp undulating contacts and is discontinuous along strike. Historic mining of the overlying mineralised reef horizon led to the exposure of the salient green orthopyroxenite breccia over large areas, especially in the north-western part of the Sopcha intrusion.

Locally, the stratigraphy of the reef interval may be even more complex due the occurrence of autoliths in the orthopyroxenitic footwall of the orthopyroxenite breccia (Fig. 53 d). These autoliths are also composed of orthopyroxenite with variable amounts of olivine, but slight mineralogical differences between the autolith and its host rock resulted in distinct visual appearances on weathered surfaces, which cannot be distinguished in fresh exposures.

The sulfide mineralisation is concentrated directly above the basal dunite and

comprises finely disseminated pyrrhotite, pentlandite and minor chalcopyrite with an average composition of 0.4 wt % Ni, 0.2 wt % Cu and 1.6 ppm Pt + Pd (Dokuchaeva

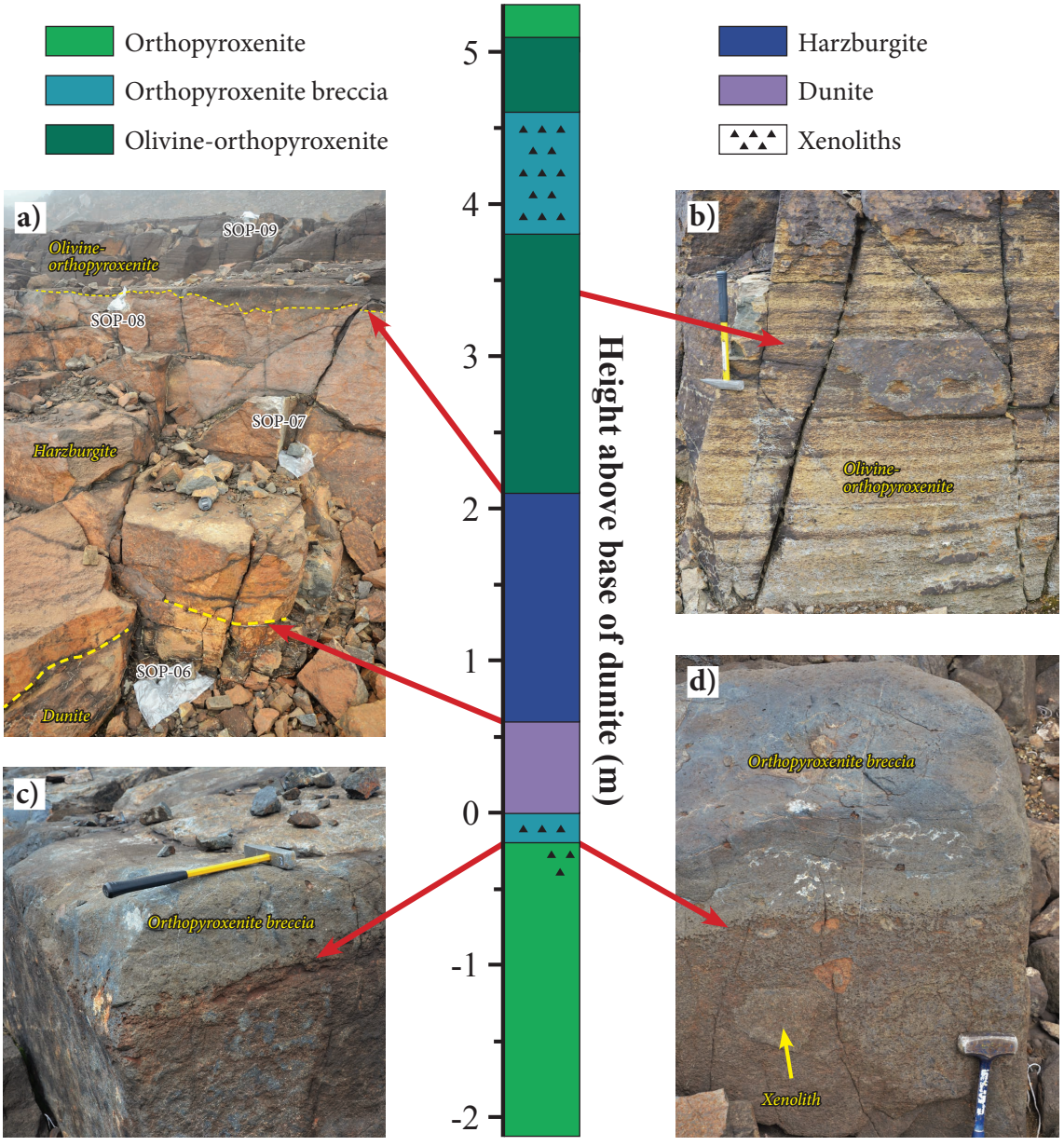

Fig. 53. Simplified stratigraphic log of the Sopcha Reef together with field photographs of key exposures. a) Lower portion of the Sopcha Reef profile. The harzburgite and the overlying olivine-orthopyroxenite samples have 1.3 and 1.4 ppm Pt + Pd, respectively (sample 15SOP-08, 09). The lens cap in the centre of the image is ca. 5 cm across. The sample numbers correspond to those in the stratigraphic column in Figs. 59, 64. b) Strongly layered olivine-orthopyroxenite with up to 1.2 ppm Pt + Pd (sample 15SOP-09). c) Sharp contact between green orthopyroxenite breccia and the underlying host orthopyroxenite. d) Abundant orthopyroxenitic autoliths in host orthopyroxenites. See text for explanation.

& Yakovlev 1994, Grokhovskaya et al. 2003).

For this study, a detailed profile across the Sopcha Reef was sampled in outcrop in the north-western part of the Sopcha intrusion (Figs. 7, 53). To ensure full coverage of the *Pyroxenite Zone*, especially below and above the reef interval, drill cores 1403 and 1408 were additionally sampled (Fig. 9 E-F). Orthopyroxene

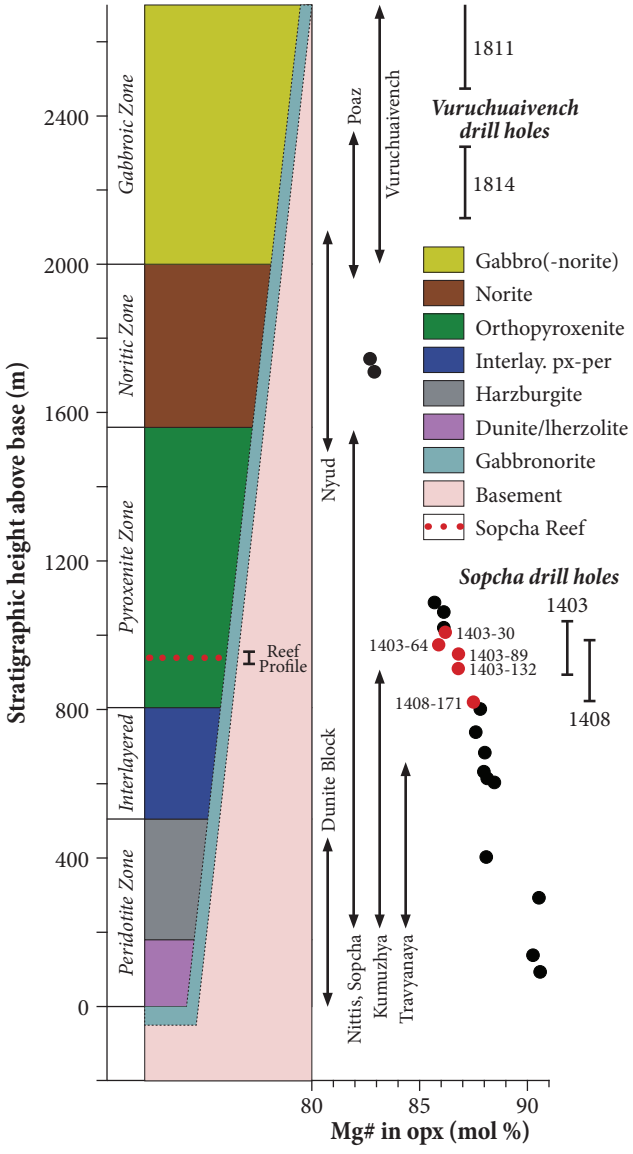

Fig. 54. Simplified stratigraphic column across the Monchepluton. The position of the Sopcha drill holes 1403 and 1408, used for this study, was determined based on the Mg# of orthopyroxene from Sopcha (red circles) relative to the Mg# of orthopyroxene from the Dunite Block, the NKT Massif and Nyud (black circles). Data for the latter were taken from Chapter 6. Abbreviations: interlay. = interlayered; px = pyroxenite; per = peridotite.

compositions across the Sopcha intrusion indicate that the Sopcha Reef is located in the lowermost quarter of the *Pyroxenite Zone*, stratigraphically transitional between the Kumuzhya and Nittis intrusions of the NKT Massif (Figs. 7, 54).

7.2.2 Vuruchuaivench intrusion

As summarised in section 2.2.2, the lower part of the Vuruchuaivench intrusion consists predominantly of massive gabbronorite, whereas the upper part is dominated by layered gabbronorite, reaching a total thickness of up to 700 m (Pripachkin & Rundkvist 2008). Moreover, these authors argued that the contact between the upper and lower part is defined by a fine-grained gabbro, which they interpreted as a chill zone. The drill cores used for this study, however, did not intersect the chill zone. All sampled rock types were generally massive in terms of texture and a ca. 10-m-thick anorthositic interval was observed in drill core 1811, representing the upper part of the Vuruchuaivench intrusion (Fig. 9 I-J). Further, interlayering between anorthosite and leucogabbronorite is evident in field exposures (Fig. 55 a). Sulfide mineralisation at Vuruchuaivench is not restricted to a particular rock type, but is concentrated in several lens-like leucogabbronoritic to anorthositic bodies in the upper part of the intrusion (Fig. 7). There is a strong correlation between the occurrence of anorthosite and sulfide mineralisation, but leucogabbronoritic drill

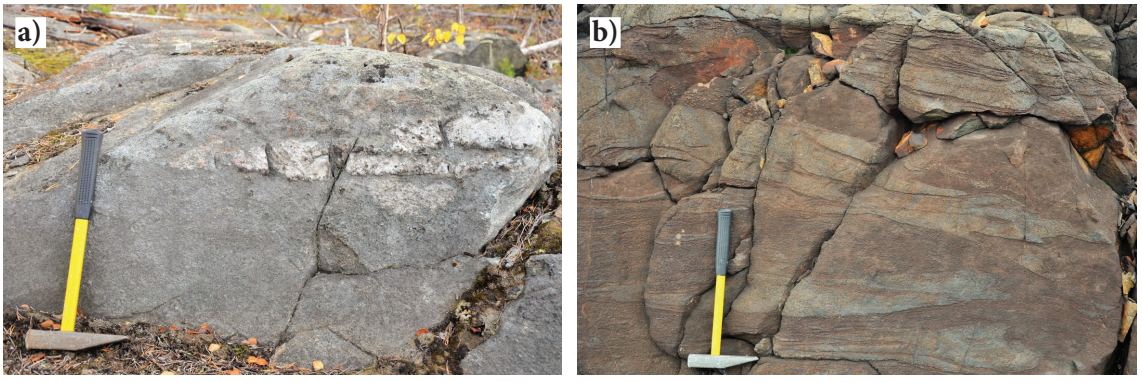

Fig. 55. Field exposures in the Monchegorsk Complex. a) Mineralised anorthosite in leucogabbronorite at Vuruchuaivench. The anorthosite layer has 7.3 ppm Pt + Pd (sample 15VURU-3). b) Complex interlayering between greenish orthopyroxenite breccia and distinctly brownish mineralised olivine-orthopyroxenite at Sopcha; the latter has 3.4 ppm Pt + Pd (sample 15SOP-16).

core samples are also mineralised. The mineralised bodies have variable thicknesses, ranging from 1 to 25 m, with peak grades of up to 10 ppm Pt + Pd (Grebnev et al. 2014, Pripachkin & Rundkvist 2008). Sulfides account for 1 to 3 vol % of the mineral mode and are comprised of finely disseminated chalcopyrite, pyrrhotite, pentlandite and locally millerite (Grokhovskaya et al. 2000).

A representative sample set from Vuruchuaivench was collected from drill cores 1811, 1814 and 1843, as well as from two different field exposures, located close to the drill sites (samples 15VURU-2, -3).

7.2.3 Monchetundra intrusion

The available information on the Monchetundra intrusion is summarised in section 2.2.2. The stratigraphy of the intrusion is poorly established, since the lowermost portion is not exposed, and only known from a single 2.5-km-deep drill hole (M1), described in Sharkov & Chistyakov (2012) (Fig. 7). Core-logging showed that the lowermost portion of the Monchetundra intrusion is characterised by complex interlayering between typical gabbronorite from Monchetundra, orthopyroxenite and minor chromite-rich dunite (Sharkov & Chistyakov 2012). The ultramafic units are considered to represent fragments of Monchepluton lithologies (Sharkov & Chistyakov 2014). In addition, mapping in the area indicates that the exposed basal portion of the Monchetundra intrusion is composed of layered medium-grained gabbronorite, which gives way to massive coarse-grained leucogabbronorite and anorthosite further up-section. Therefore, the total thickness of the Monchetundra intrusion is difficult to constrain, but the exposed portion has a true thickness of more than 1,500 m, assuming a 40°-dip of the magmatic layering. In addition, drill hole M1 indicates that the mafic intrusion continues at depth for more than 1,000 m (Smolkin & Neradovsky 2006). Sulfide mineralisation has only been documented in the outcropping contact zone between the mafic Monchetundra intrusion and the ultramafic Monchepluton, which is interpreted to reflect hydrothermal activity associated with the Monchetundra Fault (Grokhovskaya et al. 2009).

The Monchetundra sample set, used for this study, was collected from a traverse across the exposed portion of the intrusion: the profile starts in layered gab-

bronorites, located some 60 m below the drill site of M1, and continues for more than 1,400 m to the top of Monchetundra (Fig. 7).

7.3 Results

7.3.1 Petrography

Most orthopyroxenites from the Sopcha intrusion are relatively unaltered, whereas olivine-rich lithologies, such as dunite and harzburgite, show significantly stronger alteration, especially associated with olivine. The weakly layered dunite from the reef interval is the most altered rock type in the Sopcha sample set. It is an adcumulate, consisting of 96 vol % olivine, 2 vol % orthopyroxene, minor clinopyroxene and accessory chromite (Fig. 56 a). Subhedral olivine occurs as strongly fractured crystals of up to 15 mm in diameter, whereas ortho- and clinopyroxene are interstitial to olivine. The harzburgite is also an adcumulate, which is texturally similar to the dunite. It contains 72 to 75 vol % olivine, 18 to 22 vol % orthopyroxene, 4 to 5 vol % clinopyroxene, $<$ 2 vol % sulfide and accessory chromite. Olivine and orthopyroxene occur as subhedral phases, reaching up to 2.5 mm in diameter, with interstitial clinopyroxene. The olivine-orthopyroxenite is an orthocumulate, consisting of 12 to 34 vol % olivine, 64 to 84 vol % orthopyroxene and up to 3 vol % clinopyroxene with accessory chromite and sulfide (Fig. 57 a). Orthopyroxene is present as elongated crystals of up to 3 mm, or as tabular grains of up to 2 mm, with interstitial olivine, ranging from 0.5 to 1 mm across (Fig. 56 b). Chromite and sulfide show a strong spatial association with olivine. The orthopyroxenite is also an adcumulate with $>$ 90 vol % orthopyroxene, $<$ 8 vol % olivine, minor clinopyroxene and accessory chromite (Fig. 56 c). Orthopyroxene commonly forms subhedral tabular grains, reaching up to 2 mm across. Olivine and clinopyroxene occur interstitial to orthopyroxene. In the studied Sopcha Reef profile, the reef lithologies are bound by a weakly layered orthopyroxenite breccia, which is essentially similar to the orthopyroxenite, although it contains abundant dunitic autoliths (Fig. 57 b). Sulfides in the mineralised Sopcha rocks are spatially associated with interstitial olivine and occur as small blebs of up to 0.7 mm across, comprising pyrrhotite, chalcopyrite, pentlandite and minor covellite; the latter commonly surrounding chalcopyrite (Fig. 57 a).

Rocks from the Vuruchuaivench intrusion comprise strongly altered, medium-

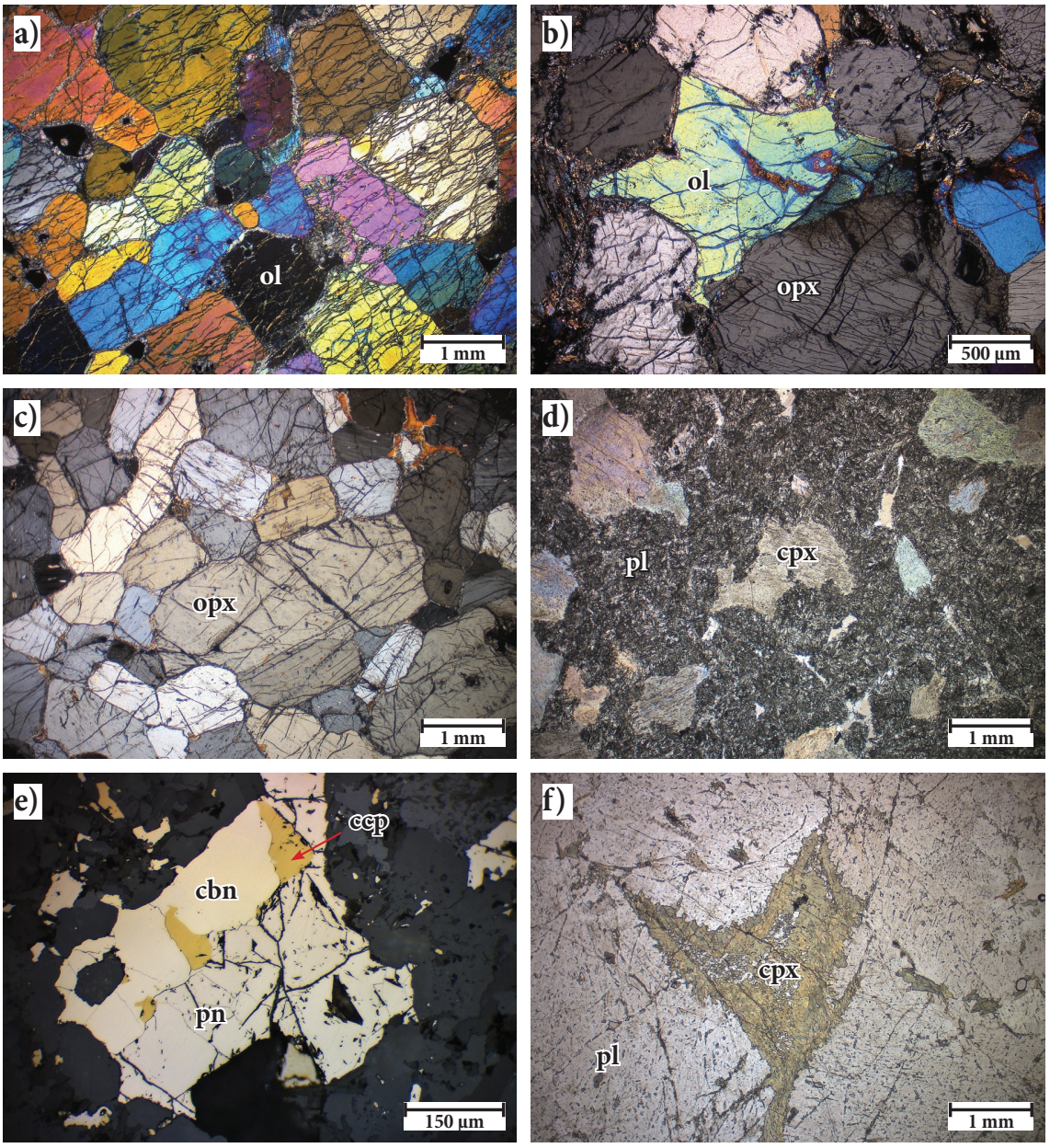

Fig. 56. Photomicrographs of major rock types at Sopcha, Vuruchuaivench and Monchetundra. a) Weakly layered dunite from the Sopcha Reef; crossed polarised light (XPL) (sample 15SOP-06). b) Interstitial olivine in orthopyroxenite from the Sopcha Reef; XPL; sample 15SOP-16. c) Orthopyroxenite from Sopcha, located some 70 m above the reef; XPL; sample 15SOP-18. d) Strongly altered leucogabbronorite from Vuruchuaivench; plane polarized light (PPL); sample 1814-021. e) Typical sulfide assemblage in mineralized Vuruchuaivench gabbronorites and anorthosites; reflected light; sample 15VURU-3. f) Altered leucogabbronorite from Monchetundra; PPL; sample 15MT-05. Abbreviations: ol = olivine; opx = orthopyroxene; cpx = clinopyroxene; pl = plagioclase; cbn = cubanite; ccp = chalcopyrite; pn = pentlandite.

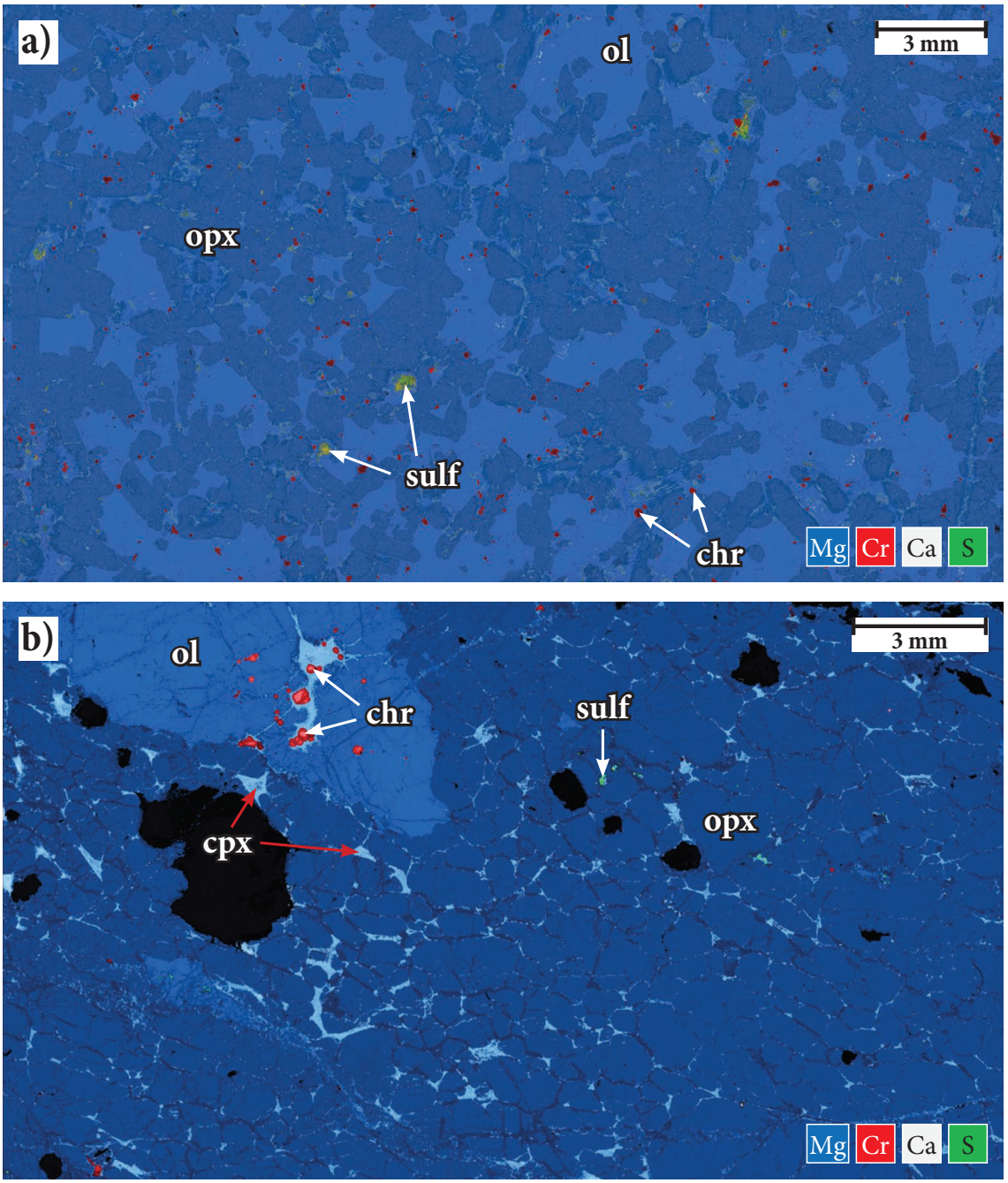

Fig. 57. Elemental maps of typical Sopcha Reef lithologies. a) Mineralised olivine-orthopyroxenite, located about 2.6 m above the base of the reef. Note that olivine occurs interstitial to orthopyroxene (sample 15SOP-09). b) Orthopyroxenite breccia, located just below the base of the reef. Note the dunitic autolith in the upper left corner (sample 15SOP-05). Abbreviations: ol =olivine; opx = orthopyroxene; cpx = clinopyroxene; chr = chromite; sulf = sulfide.

grained leucogabbronorites and anorthosites. They originally contained 65 to 95 vol % plagioclase and 5 to 35 vol % interstitial pyroxene, but plagioclase is completely replaced by amphibole and epidote-group minerals, whereas pyroxene is pervasively altered; no relict plagioclase and pyroxene are preserved (Fig. 56 d). Plagioclase occurred as subhedral tabular crystals of up to 10 mm in diameter, whereas pyroxene was present as an interstitial phase. Sulfides are generally finely disseminated and reach up to 200 µm across, accounting for approximately 0.5 vol % of the mineral mode. The mineralogy is dominated by pyrrhotite, chalcopyrite, cubanite and pentlandite with minor pyrite (Fig. 56 e).

The medium- to coarse-grained (leuco-)gabbronorites and anorthosites from the Monchetundra intrusions are largely similar to those from the Vuruchuaivench intrusion. The samples originally contained 50 to 95 vol % plagioclase with 5 to 50 vol % ortho- and clinopyroxene. Pyroxene was present as relatively large anhedral crystals interstitial to plagioclase, reaching about 20 mm across (Fig. 56 f). Typically, plagioclase from Monchetundra is characterised by abundant acicular inclusions of amphibole and minor apatite, whereas pyroxenes are entirely altered to chlorite and amphibole. Sulfides were only observed in sample 15MT-07, which hosts finely disseminated chalcopyrite, accounting for < 0.1 vol % of the mineral mode.

7.3.2 Mineral chemistry

The mineral chemistry of olivine, ortho- and clinopyroxene was determined in 17 ultramafic samples from the Sopcha intrusion. Primary rock-forming minerals in Monchetundra and Vuruchuaivench samples were not preserved due to pervasive alteration. The full dataset of mineral compositions is shown in Appendix D.

Peridotites from the mineralised reef section, comprising dunite and harzburgite, have orthopyroxene with a narrow range in Mg# (100 x molar Mg/(Mg+Fe)) from 88.0 to 88.2 and Cr concentrations range from 3,900 to 4,100 ppm (Fig. 58). The analysed orthopyroxenites have slightly less magnesian orthopyroxene with Mg#, varying from 85.9 to 88.3 with 3,600 to 4,500 ppm Cr. The Mg# of orthopyroxene from the orthopyroxenite breccias ranges from 88.1 to 88.5 and reaches up to 4,600 ppm Cr. Olivines from the orthopyroxenites have the most magnesian compositions with forsterite contents, ranging from Fo_{84} to Fo_{87}, whereas olivines from the

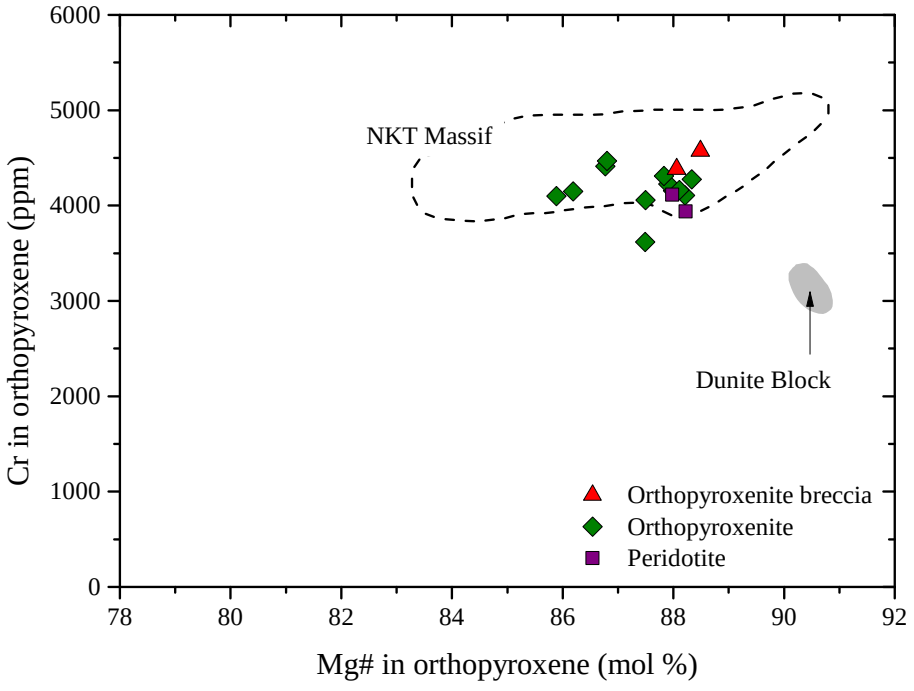

Fig. 58. Plot of Cr concentrations vs. Mg# in orthopyroxene from the Sopcha intrusion. Data for the Dunite Block and the NKT Massif were taken from Chapter 6.

peridotites and orthopyroxenite breccias reach Fo_{86} at most.

The stratigraphic variation in mineral chemistry across the reef section at Sopcha shows a distinct increase in the forsterite content of olivine from $Fo_{84.8}$ below the peridotitic interval to $Fo_{86.0}$ in the lowermost reef dunite (Fig. 59). Subsequently, forsterite contents decrease gradually across the reef to $Fo_{85.1}$ in the olivine-orthopyroxenite. The overlying orthopyroxenite breccia as well as the orthopyroxenite have slightly more magnesian olivine with $Fo_{85.9}$ and $Fo_{86.0}$, respectively. The uppermost orthopyroxenite, approximately 5 m above the reef, has the lowest forsterite contents with $Fo_{84.3}$. In contrast, the Mg# of orthopyroxene shows only limited variation across the reef section with Mg# $\approx$ 88; only the uppermost orthopyroxenite has slightly less magnesian orthopyroxene with Mg# = 86.6. Chromium concentrations in orthopyroxene are rather erratic across the reef section, and cover a relatively wide range from 3,900 to 4,600 ppm. The higher modal abundance of chromite in olivine-rich lithologies, however, may affect Cr concentrations in orthopyroxene.

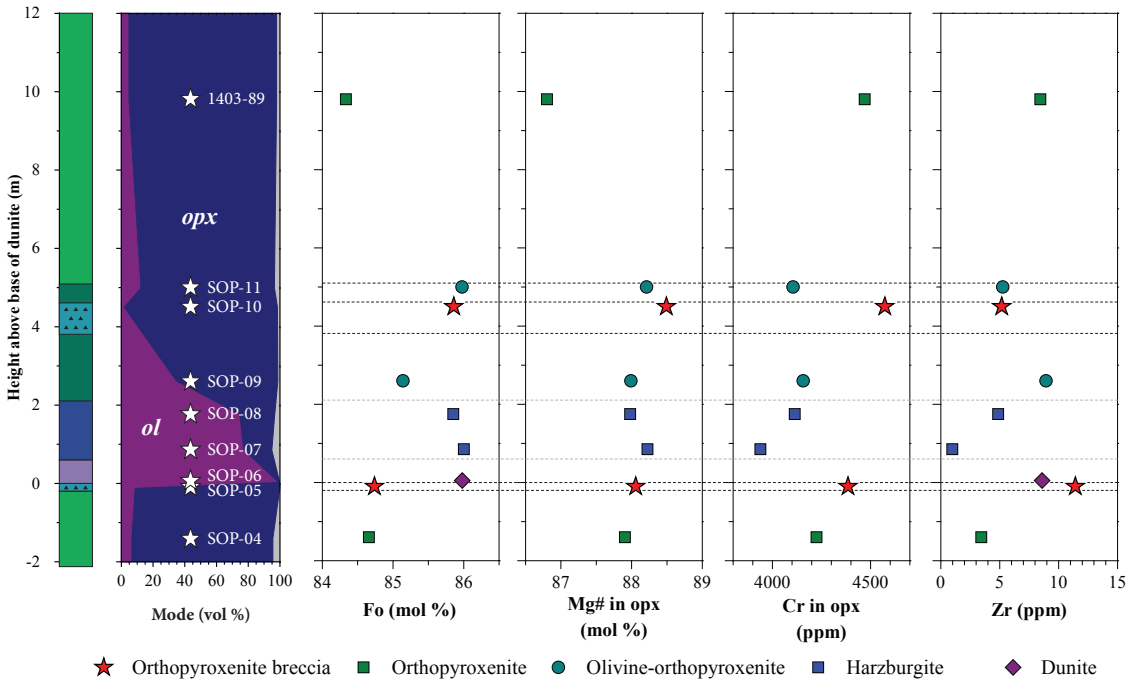

Fig. 59. Stratigraphic variation of mineral compositions and whole rock Zr concentrations across the Sopcha Reef. Clinopyroxene is shown in grey in the stratigraphic column. See Figure 53 for lithology key. Abbreviations: ol = olivine; opx = orthopyroxene; Fo = forsterite.

7.3.3 Lithophile element geochemistry

Major and trace element concentrations were determined in a set of 55 samples, covering the mafic Monchetundra and Vuruchuaivench intrusions as well as the ultramafic Sopcha intrusion. An overview of average whole rock compositions of the major rock types is shown in Table 7 and the full dataset is available in Appendix E.

Anorthosites and leucogabbronorites from Monchetundra are characterised by 0.5 to 8.4 wt % MgO, 10.6 to 12.7 wt % CaO and 14.7 to 26.0 wt % Al_2O_3. The same rock types from Vuruchuaivench have a comparable major element composition with 0.2 to 10.7 wt % MgO, 7.3 to 13.6 wt % CaO and 15.3 to 25.1 wt % Al_2O_3. Only a

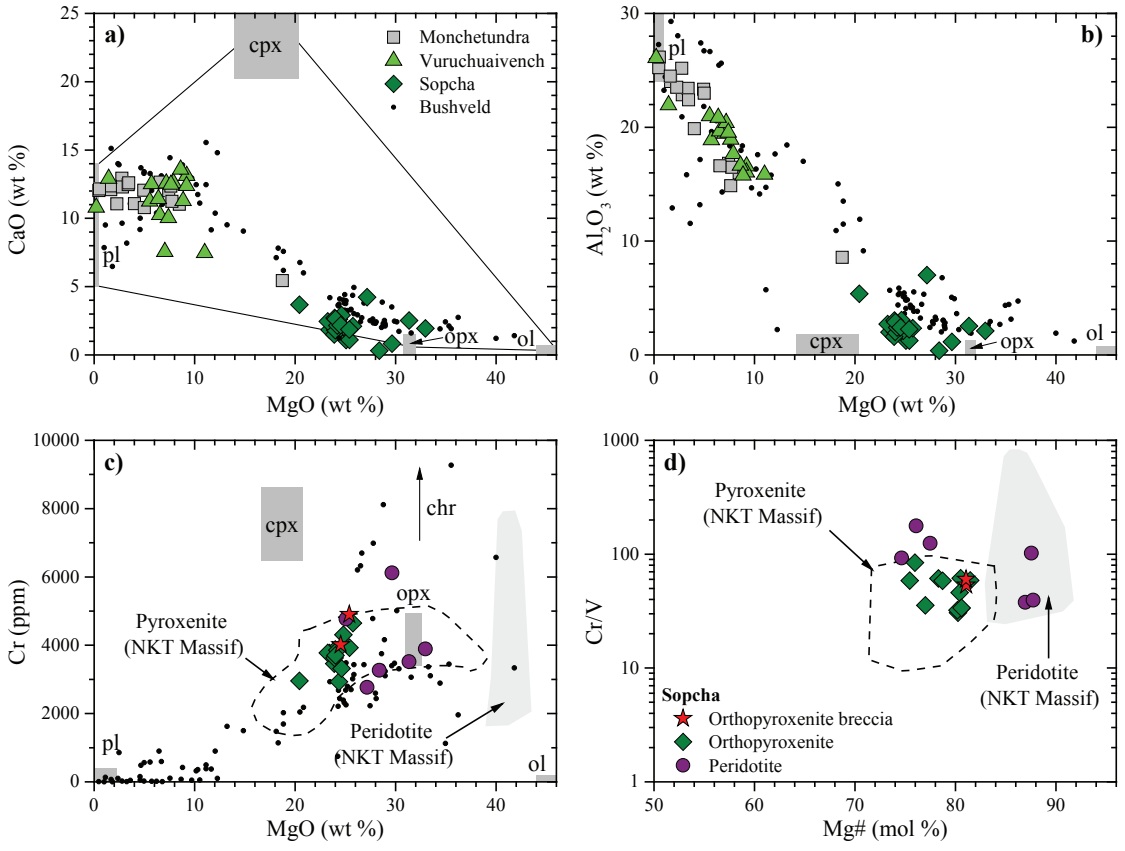

Fig. 60. Lithophile element variation of Monchetundra, Vuruchuaivench and Sopcha lithologies. a) CaO vs. MgO. b) Al_2O_3 vs. MgO. c) Cr vs. MgO. d) Cr/V vs. Mg#. Data from the NKT Massif were taken from Chapter 6. Data for the Bushveld Complex were taken from Maier et al. (2013). Abbreviations: ol = olivine; opx = orthopyroxene; cpx = clinopyroxene; pl = plagioclase; chr = chromite.

Table 7. Average whole rock geochemistry of major rock types from the Monchetundra, Vuruchuaivench and Sopcha intrusions

Rock type	av. AN	av. LGN	av. LGN	av. OPX BRC	av. OPX	av. OL-OPX	av. HZ
Intrusion	MT	MT	VURU	Sopcha	Sopcha	Sopcha	Sopcha
n	12	5	15	2	11	2	5
SiO_2 (wt %)	51.97	52.94	52.79	57.43	57.23	56.98	51.50
TiO_2	0.34	0.22	0.19	0.10	0.11	0.06	0.07
Al_2O_3	23.43	16.06	18.25	2.29	2.70	1.61	2.79
Fe_2O_{3T}	5.57	8.33	5.91	11.39	12.00	14.32	11.90
MnO	0.08	0.15	0.10	0.20	0.20	0.21	0.19
MgO	2.72	7.52	7.17	24.45	23.53	24.14	28.85
CaO	11.89	11.79	11.22	1.98	2.38	1.45	2.10
Na_2O	2.89	2.23	2.08	0.06	0.14	0.04	1.22
K_2O	0.26	0.16	0.35	0.01	0.02	bdl	0.02
P_2O_5	0.05	0.02	0.02	bdl	0.01	bdl	0.02
LOI	0.4	0.4	1.7	0.8	0.7	0.8	0.7
Total	99.58	99.81	99.78	98.74	99.05	99.61	99.37
Sc (ppm)	15	39	23	30	28	22	22
V	103	132	103	82	90	55	55
Cr	28	19	167	4365	3617	3803	4149
Co	23.8	38.9	37.6	84.4	115.3	136.5	93.6
Ni	64.8	120.5	420.9	1192.4	2053.9	3029.1	2946.5
Cu	78.7	115.0	356.1	352.8	456.8	649.0	561.9
Zn	29	53	43	65	66	60	69
Rb	4.7	2.2	9.3	0.7	0.8	0.4	0.7
Sr	292.9	223.6	312.7	2.9	14.4	3.8	21.1
Y	8.0	6.5	4.7	1.4	1.6	0.9	1.3
Zr	38.4	19.8	28.7	8.3	11.5	7.1	3.6
Nb	1.5	0.5	1.0	0.5	0.3	0.3	0.3
Cs	0.2	0.1	0.2	0.0	0.0	0.0	0.0
Ba	91	57	105	4	10	5	9
La	3.9	1.7	3.0	0.3	0.5	0.1	0.3
Ce	8.2	3.6	6.1	0.7	0.9	0.3	0.6
Pr	1.1	0.5	0.8	0.1	0.1	0.0	0.1
Nd	4.5	2.4	3.2	0.5	0.5	0.2	0.4
Sm	1.1	0.7	0.8	0.1	0.1	0.1	0.1
Eu	0.5	0.3	0.4	0.0	0.0	0.0	0.1
Gd	1.1	0.8	0.7	0.1	0.2	0.1	0.1
Tb	0.2	0.1	0.1	0.0	0.0	0.0	0.0
Dy	1.3	1.0	0.8	0.2	0.2	0.1	0.2
Ho	0.2	0.2	0.2	0.0	0.0	0.0	0.0
Er	0.8	0.6	0.5	0.2	0.2	0.1	0.1
Tm	0.1	0.1	0.1	0.0	0.0	0.0	0.0
Yb	0.8	0.7	0.5	0.2	0.2	0.1	0.2
Lu	0.1	0.1	0.1	0.0	0.0	0.0	0.0
Hf	0.9	0.5	0.4	0.2	0.2	0.2	0.1
Ta	0.1	0.0	0.1	0.0	0.0	0.0	0.0
Th	0.5	1.0	0.52	0.3	0.2	0.1	0.4
U	0.1	0.1	0.1	0.0	0.0	0.0	0.0
S	64	63	243	231	2554	1692	1281
Os (ppb)	bdl	bdl	1.3	0.3	0.6	1.9	0.8
Ir	0.06	0.38	0.32	2.26	5.97	18.23	5.99
Ru	0.34	0.12	0.60	1.44	3.30	9.52	3.24
Rh	0.17	0.99	2.34	8.93	25.66	80.39	21.49
Pt	1.6	41.2	18.9	30.2	66.7	230.0	59.9
Pd	1.9	11.6	104.9	171.5	404.6	1208.5	330.8
Au	2.9	8.1	3.7	14.6	21.0	22.9	14.7

AN = anorthosite; LGN = leucogabbronorite; OPX = orthopyroxenite; BRC = breccia; HZ = harzburgite; OL = olivine; MT = Monchetundra; VURU = Vuruchuaivench

single norite sample from the lowermost portion of the Monchetundra intrusion has somewhat higher MgO concentrations of 18.3 wt % (Fig. 60 a, b). In comparison, Sopcha lithologies range from 20.0 to 32.4 wt % MgO, whereas CaO and Al_2O_3 concentrations reach up to 4.2 wt % and 7.0 wt %, respectively. The main control on major and minor element concentrations of these rocks is the variation in modal abundances of olivine, plagioclase, orthopyroxene and clinopyroxene. Most of the

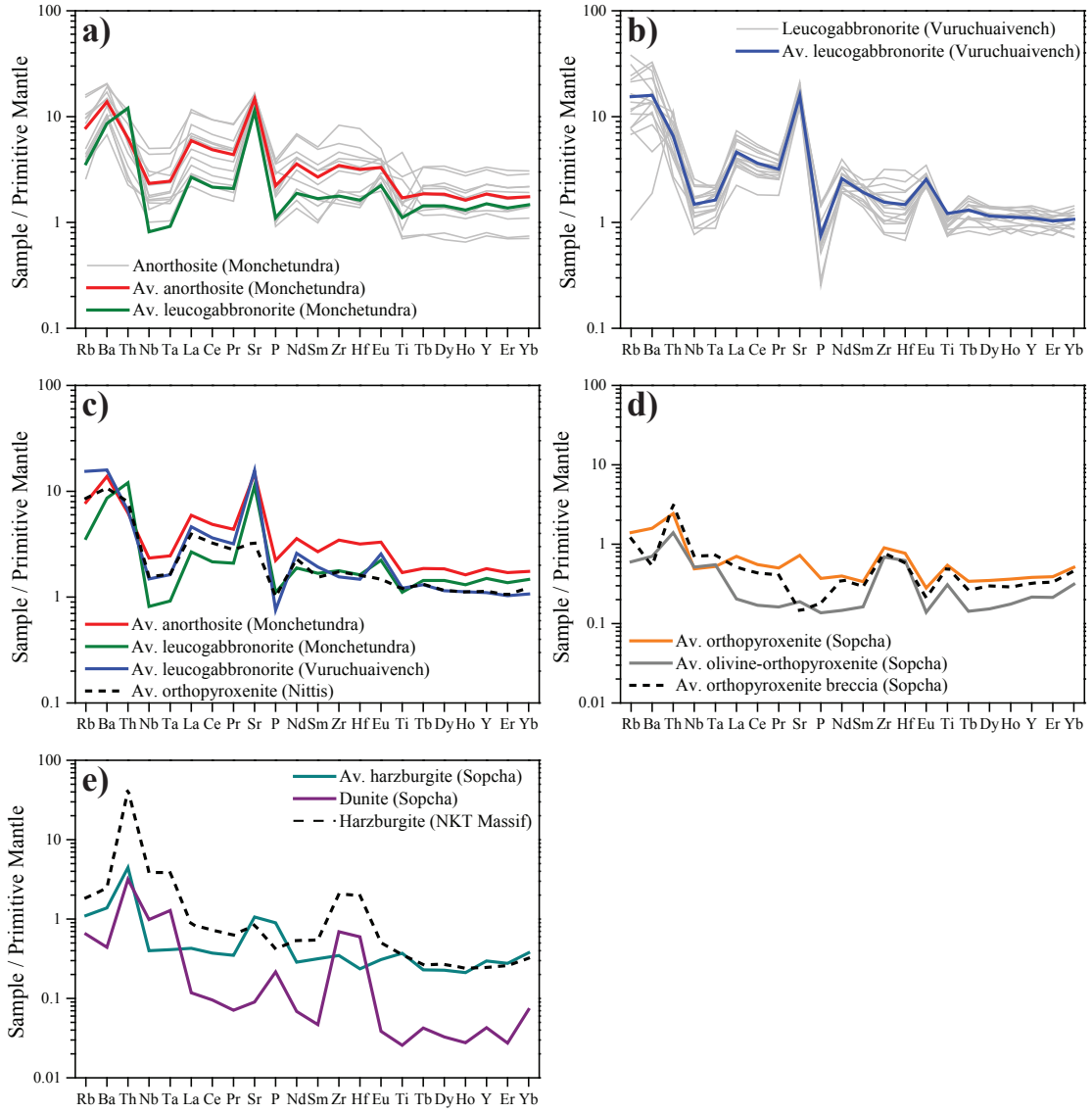

Fig. 61. Primitive mantle-normalised incompatible trace element diagram for Monchetundra, Vuruchuaivench and Sopcha lithologies. Normalisation values were taken from McDonough & Sun (1995). Data for the NKT Massif were taken from Chapter 6. Note the change in scale in d) and e).

Monchetundra and Vuruchuaivench samples plot on a tie-line between plagioclase and orthopyroxene with variable amounts of clinopyroxene. These two intrusions show a considerable overlap in major elements, which is consistent with their largely similar mineralogy.

The Sopcha sample set includes peridotites (dunite, harzburgite), orthopyroxenites and orthopyroxenite breccias. These are characterised by a relatively wide range in Cr concentrations from 2,800 to 6,000 ppm, which reflects the modal abundance of chromite (Fig. 60 c). Notably, none of the analysed peridotites from Sopcha reach MgO concentrations as high as those in peridotites from the NKT Massif (cf. Chapter 6), although this may be attributed to the relatively strong alteration of the Sopcha peridotites. The orthopyroxenites, however, plot well within the pyroxenite field from the NKT Massif; also in terms of Mg# and Cr/V ratios (Fig. 60 d). In contrast, only a subgroup of Sopcha peridotites have similar Mg# and Cr/V ratios to peridotites from the NKT Massif, whereas the other samples have slightly higher Cr/V ratios compared to orthopyroxenites with a similar Mg#.

Mantle-normalised incompatible trace element patterns for anorthosites and leucogabbronorites from Monchetundra and Vuruchuaivench are broadly parallel to each other and show a marked enrichment in large ion lithophile elements (LILE), negative Nb-Ta and Ti anomalies and a positive Sr anomaly (Fig. 61 a, b, c). Leucogabbronorites from Vuruchuaivench have a stronger depletion in P relative to those from Monchetundra and the negative Ti anomaly is not as pronounced. Sopcha lithologies are characterised by considerably lower total trace element concentrations. The incompatible trace element patterns show variably enriched LILE, together with largely positive Zr-Hf anomalies (Fig. 61 d, e). The Nb-Ta anomalies are not as strongly developed as in the Monchetundra and Vuruchuaivench samples, whereas Sr is variably enriched or depleted relative to the other lithophile elements.

7.3.4 Chalcophile element geochemistry

The chalcophile element data for Monchetundra, Vuruchuaivench and Sopcha lithologies show a broadly positive correlation between Cu and S; only two samples plot away from the general trend towards lower Cu/S ratios (Fig. 62 a). Together with the broadly positive correlation between Pt and S (Fig. 62 b), this suggests

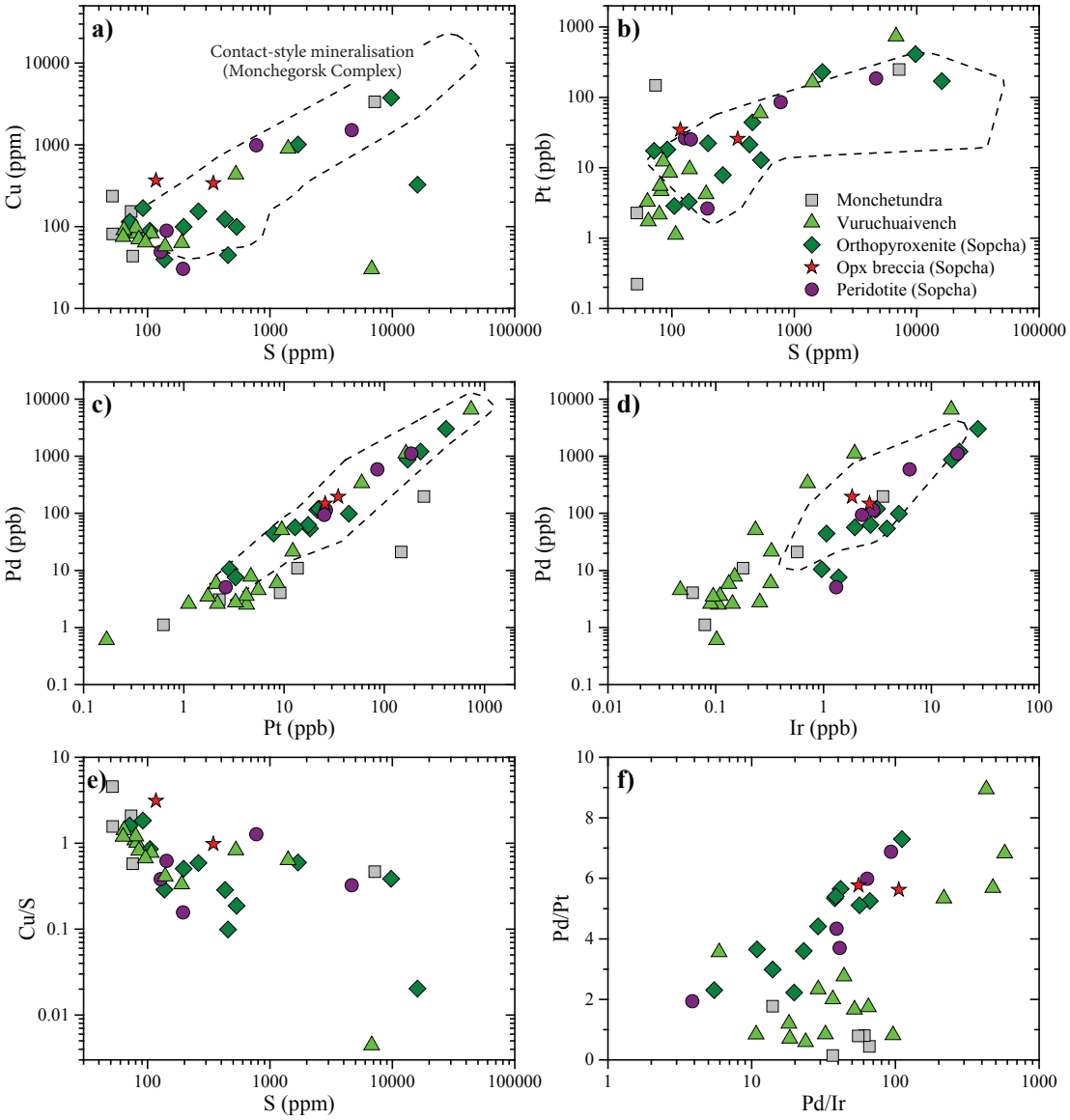

Fig. 62. Binary variation diagram of chalcophile elements. a) Cu vs. S. b) Pt vs. S. c) Pd vs. Pt. d) Pd vs. Ir. e) Cu/S vs. S. f) Pd/Pt vs. Pd/Ir. Data for contact-style mineralisation in Monchegorsk Complex were taken from Chapter 6.

a concentration of chalcophile metals by magmatic sulfides, as observed in most mafic-ultramafic systems. Moreover, the well-defined correlation between Pd and Pt as well as Pd and Ir is consistent with limited mobility of the PGE, as Pd may be mobile under certain conditions, whereas Pt and Ir are generally considered as immobile elements (Fig. 62 c, d). It is worth noting, however, that the correlation between the chalcophile metals and S becomes poorer in samples with less than 1000 ppm S. Additionally, the negative correlation between Cu/S and S as well as the unrealistically high Cu/S ratios (> 0.5) in this sample subset suggest late magmatic or hydrothermal S loss (Fig. 62 e) (e.g., Cawthorn & Meyer 1993, Maier & Barnes 1996). Notably, the Vuruchuaivench sample set defines two distinct trends in terms of Pd/Pt ratios: the unmineralised samples and the mafic Monchetundra lithologies have relatively low Pd/Pt of < 2, whereas the mineralised Vuruchuaivench rocks are characterised by distinctly higher Pd/Pt ratios that are in the range of those for ultramafic samples from Sopcha (Fig. 62 f). In contrast, Pd/Ir ratios of mineralised Vuruchuaivench lithologies are generally higher compared to those from Monchetundra and Sopcha. Moreover, the Sopcha dataset shows a fractionation of Pt and Pd as well as Pd and Ir, similar to contact-style mineralisation elsewhere in the complex (cf. section 6.3.4). The change in Pd/Ir ratios can be attributed to chromite crystallisation and *monosulfide solid solution* (mss) fractionation, whereas the variation in Pd/Pt ratios is difficult to explain.

Chalcophile metal patterns

Primitive mantle-normalised chalcophile element patterns of unmineralised Monchetundra and Vuruchuaivench lithologies are relatively fractionated with Pd/Ir ratios, ranging from 10 to 100. They show a weak positive Rh anomalies and average Pd/Pt ratios are less than 2 (Fig. 63 a, b). In contrast, the mineralised leucogabbronorite from Monchetundra has a much lower Pd/Pt ratio of about 0.1 with a distinct positive Au anomaly, whereas the Pd/Ir ratio of 37 is broadly similar to that of the unmineralised lithologies. The mineralised Vuruchuaivench samples, however, are characterised by positive Rh anomalies, considerably higher Pd/Ir ratios, ranging from 155 to 600, and Pd/Pt ratios mostly above 5. A comparison between relatively

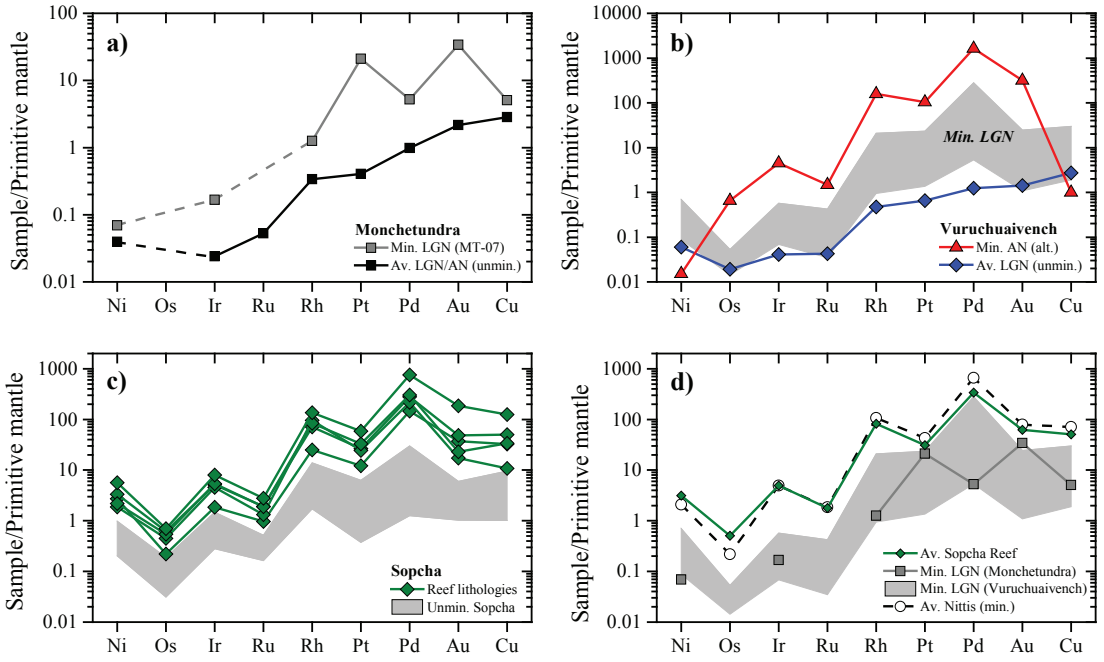

Fig. 63. Primitive mantle-normalised chalcophile element pattern for samples analysed in this study. a) Monchetundra. b) Vuruchuaivench. c) Sopcha. d) Comparison of different mineralisation styles in the Monchegorsk Complex. Data for contact-style mineralisation at Nittis were taken from Chapter 6. Normalisation factors were taken from Barnes & Maier (1999). Abbreviations: AN = anorthosite; LGN = leucogabbronorite; min. = mineralised; unmin. = unmineralised; alt. = altered; av. = average.

fresh and strongly altered, mineralised lithologies from Vuruchuaivench shows that the main difference is a significant depletion in Ni and Cu, whereas the PGE concentrations remain largely unaffected (Fig. 63 b). Chalcophile element patterns for mineralised and unmineralised Sopcha rocks are generally parallel to each other with distinct positive Rh anomalies, relatively fractionated Pd/Ir ratios of up to 110 and Pd/Pt ratios, ranging from 2 to 6 (Figs. 62 f, 63 c). It is worth noting that the mineralised Vuruchuaivench samples have a distinct chalcophile element signature from the unmineralised ones, and that the former strongly resemble Sopcha Reef samples (Fig. 63 d). Moreover, the sulfide mineralisation at Sopcha shares many similarities with contact-style mineralisation elsewhere in the Monchegorsk Complex (cf. Chapter 6).

Sopcha Reef

The mineralised Sopcha lithologies were sampled in outcrop and represent the lower part of the *Pyroxenite Zone* (Fig. 54). Detailed descriptions of the mineralised zone and contact relationships can be found in section 7.2.1. The base of the mineralised interval at Sopcha is marked by a significant increase in whole rock Cr/V ratios from about 60 in the footwall orthopyroxenite to almost 180 in the lowermost reef dunite (Fig. 64). Sulfur and Cu concentrations increase only marginally, whereas Ni and precious metal concentrations triple across the lower reef contact, reaching up to 0.65 wt % and 1.5 ppm Pt + Pd + Au at relatively low S contents of less than 0.5 wt % in the central portion of studied reef section. The only mineralised rock types in the Sopcha Reef include the lowermost peridotites and olivine-orthopyroxenites, which are located above the basal orthopyroxenite breccia. Notably, Cr/V ratios show a gradual upward decrease across the reef interval, which continues into the overlying unmineralised, olivine-poor lithologies.

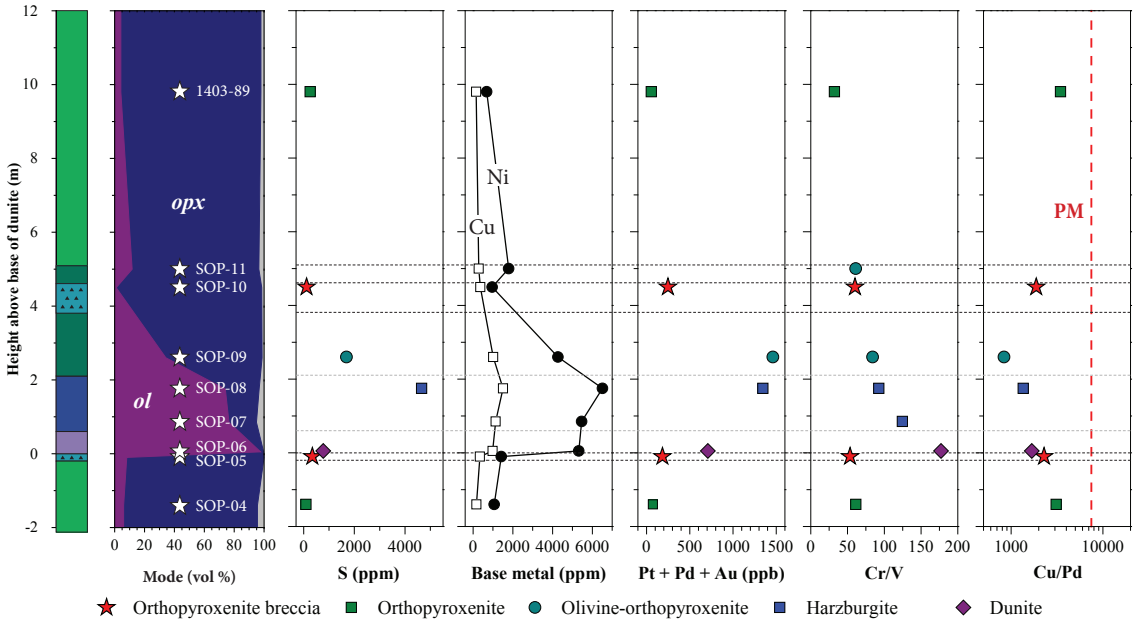

Fig. 64. Stratigraphic variation of S, Cu, Ni and precious metals together with whole rock Cr/V and Cu/Pd ratios across the Sopcha Reef. The mineral modes were calculated from phase images based on elemental mapping. Note the marked increase in Cr/V ratios at the base of the mineralised section. Clinopyroxene is shown in grey in the stratigraphic column. The primitive mantle (PM) value was taken from Barnes & Maier (1999). See Figure 53 for lithology key. Abbreviations: ol = olivine; opx = orthopyroxene.

Vuruchuaivench Reef

The PGE mineralisation at Vuruchuaivench, as intersected by drill hole 1811, is hosted in a relatively monotonous succession of leucogabbronorite, representing the uppermost *Gabbroic Zone* of the Monchegorsk Complex (Fig. 54). The mineralised interval is characterised by generally low chalcophile element concentrations of up to 190 ppm S, 160 ppm Ni, 100 ppm Cu and 15 ppb Pt + Pd + Au (Fig. 65). Only the approximately 4.5-m-thick mineralised interval shows a significant enrichment in base and precious metals with ca. 780 ppm Ni, 900 ppm Cu and 1.3 ppm Pt + Pd + Au at relatively low S contents of 0.14 wt %. Notably, Cu/Pd ratios are higher than the primitive mantle value and remain constant below and above the mineralised interval, as do the PGE concentrations.

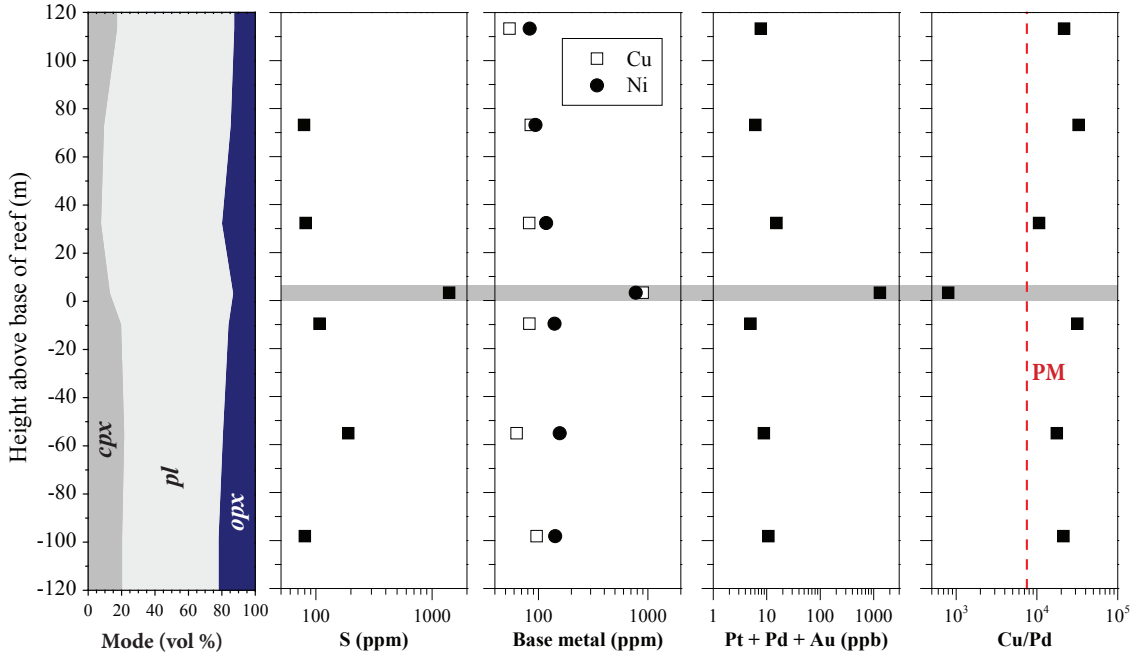

Fig. 65. Downhole chalcophile element geochemistry for drill hole 1811, intersecting the mineralised interval at Vuruchuaivench, together with mineral modes calculated according to the CIPW norm. Note the uniform Cu/Pd ratios below and above the mineralised zone. The primitive mantle (PM) value was taken from Barnes & Maier (1999). Abbreviations: cpx = clinopyroxene; pl = plagioclase; opx = orthopyroxene.

PGE enrichment at Monchetundra

The analysed Monchetundra lithologies predominantly comprise anorthosites and leucogabbronorites that overlie the Vuruchuainvech intrusion. Sulfur concentrations are mostly below the limit of detection, although a few samples reach up to 75 ppm (Fig. 66). Nickel and Cu concentrations are also generally low with less than 250 ppm, each. The lower portion of the profile (< 150 m) is characterised by elevated PGE concentrations, ranging from 6 to 200 ppb Pt + Pd + Au. In contrast, all samples above 150 m have less than 2 ppb Pt + Pd + Au. This transition is also reflected in a sharp increase in Cu/Pd ratios from about 7,300 to more than 75,000.

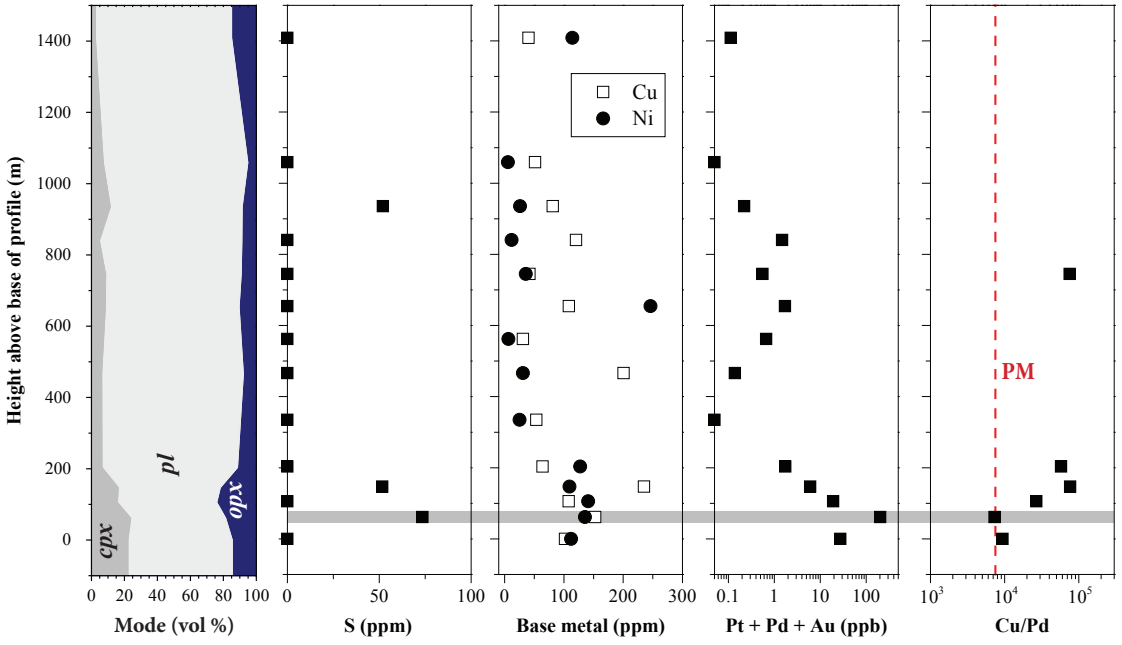

Fig. 66. Chalcophile element geochemistry profile across the exposed portion of the Monchetundra intrusion, together with mineral modes calculated according to the CIPW norm. Note the shift in Cu/Pd ratios above the PGE-enriched interval. The primitive mantle (PM) value was taken from Barnes & Maier (1999). Abbreviations: cpx = clinopyroxene; pl = plagioclase; opx = orthopyroxene.

7.4 Discussion

The architecture and emplacement history of the Monchegorsk Complex is a much-debated issue, especially because geochronological data suggest that the complex has been emplaced continuously over a period spanning more than 60 m.y. (cf. section 2.2.3). Moreover, tectonic movement along the Monchetundra Fault caused widespread alteration and dismemberment of the complex, which added to the architectural and geological complexity in the Monchegorsk area.

On the basis of the ubiquitous presence of cumulus sulfide and the pronounced mineral lamination in the ultramafic cumulates of the Monchepluton, the intrusion was likely emplaced as a series of sulfide-saturated pulses of crystal mushes, sourced from a staging chamber at depth (Fig. 67 a), as discussed in more detail in Chapter 6. The origin of the overlying mafic succession, however, remains poorly understood. The following sections on genetic aspects of the different styles of PGE mineralisation provide further insight into the emplacement history of the Monchegorsk Complex and highlight key processes, leading to precious metal enrichment in layered intrusions.

7.4.1 Origin of the Sopcha Reef

The formation of reef-style mineralisation remains one of the most important, unresolved issues in the study of mineral deposits associated with layered intrusions. Although most models envisage sulfide saturation in a silicate magma as the principal ore-forming process, the trigger for this is not always clear. Several mechanisms have been proposed for the supersaturation in sulfide melt: (1) magma addition and mixing (e.g., Cameron 1980, Campbell et al. 1983), (2) crustal contamination in a staging chamber and sulfide entrainment (Lee & Butcher 1990), (3) episodic pressure changes (Cawthorn 2005), and (4) extensive magma fractionation (Haughton et al. 1974).

In contrast, Boudreau & McCallum (1992) suggested that PGE in layered intrusions were concentrated by chloride-rich, aqueous fluids, migrating upwards through the underlying cumulates. In connection to this model, Sharkov & Bogatikov (1998)

suggested that the olivine-rich lithologies of the Sopcha Reef crystallised from a distinct injection of fluid- and PGE-rich melt into the solidifying Sopcha intrusion.

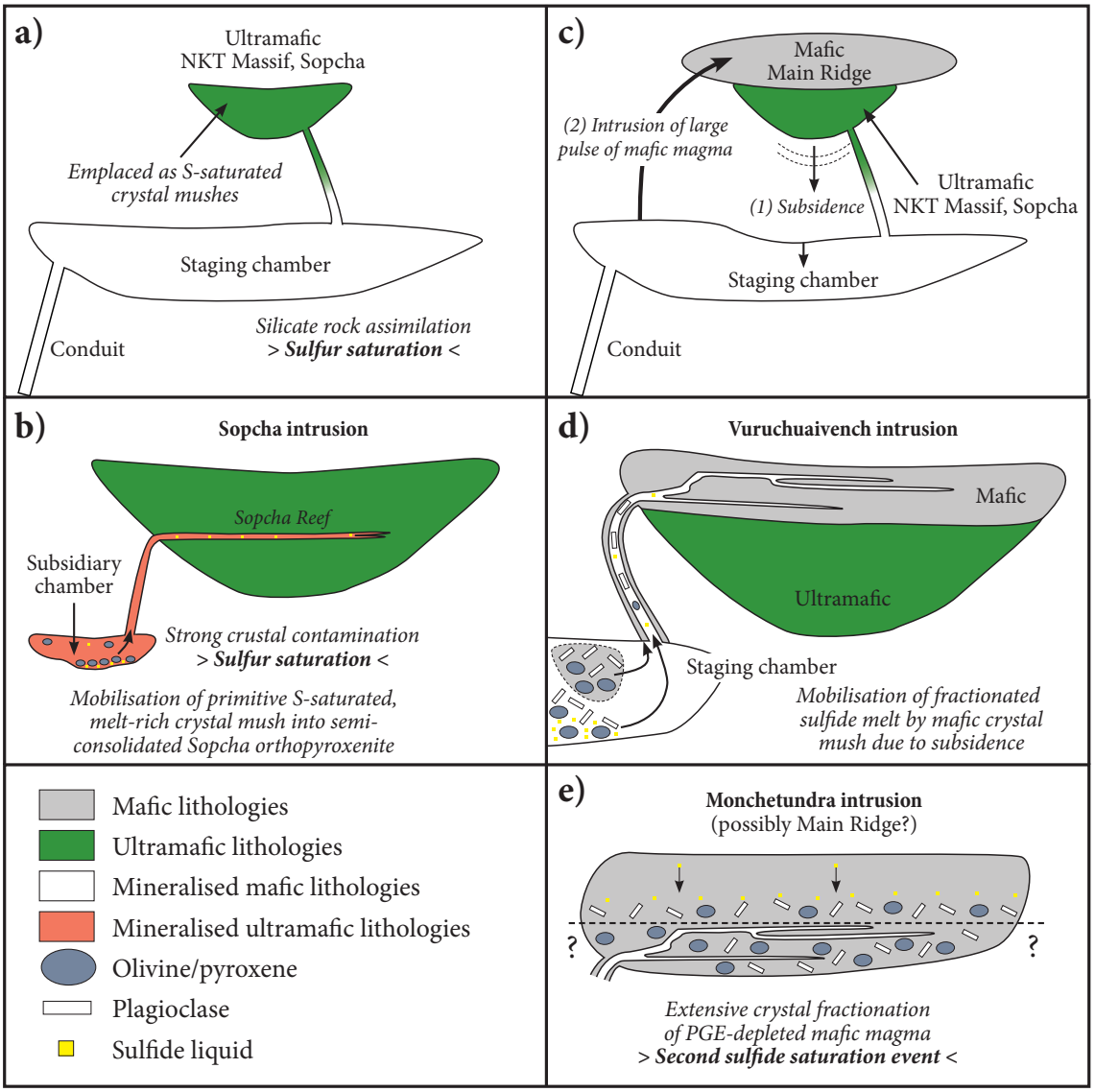

Fig. 67. Schematic model for the emplacement of the Monchegorsk Complex and the formation of different styles of PGE mineralisation. a) Emplacement of the ultramafic NKT Massif and the Sopcha intrusion as sulfide-saturated crystal mushes, sourced from a staging chamber. b) Formation of the Sopcha Reef. c) Crustal loading led to subsidence and the collapse of the staging chamber, which triggered the intrusion of a large batch of crystal-charged magma on top of the ultramafic sequence. d) Formation of the PGE mineralisation, hosted by the Vuruchuaivench intrusion. Note that fractionated sulfide melt was entrained relatively late in the formation of the mafic sequence. e) Formation of the putative PGE reef in the lower portion of the Monchetundra intrusion. The relationship between the Vuruchuaivench intrusion and the Monchetundra intrusion is not clear; however, it is likely that Vuruchuaivench represents the lower portion of the Monchetundra intrusion.

Due to its high density, this relatively small melt batch accumulated at the top of the crystallising cumulate pile, displacing the resident magma column. After the crystallisation of the mineralised olivine-rich Sopcha Reef, the initial crystallisation sequence resumed.

Our data show that most of the analysed samples from the Sopcha intrusion have $>$ 50 ppb Pt + Pd with Cu/Pd ratios below the primitive mantle level, which indicates that these rocks contain a cumulus sulfide component (Figs. 62, 64), similar to other ultramafic cumulates in the Monchegorsk Complex (cf. Chapter 6). The chalcophile element pattern for the Sopcha Reef is also almost identical to that of contact-style mineralisation elsewhere in the complex (Fig. 63 d). In the past, variations in element ratios, such as Cu/Pd, have proven successful in delineating the transitions from sulfide-undersaturated to sulfide-saturated conditions in layered intrusions, which results from the extremely high partition coefficients of Pd into the sulfide liquid relative to Cu (e.g., Barnes et al. 1993). Consequently, reef-style mineralisation is generally marked by a shift in Cu/Pd ratios at the stratigraphic level of mineralisation. The lack of distinct shifts in Cu/Pd ratios, below and above the Sopcha Reef, is in agreement with the proposed model by Sharkov & Bogatikov (1998), as the reef does not mark a transition from sulfide-undersaturated to sulfide-saturated conditions (Fig. 64). Therefore, *in situ* sulfide saturation is unlikely to have produced the observed chalcophile element signature of the reef (Smolkin & Neradovsky 2006). Further, the sharp increase in Cr/V ratios and forsterite contents at the base of the mineralised interval suggests an influx of primitive magma at the level of the Sopcha Reef. It is important to note that only the lower half of the mineralised reef interval is composed of peridotite, and that modal abundances of olivine, together with its forsterite content, gradually decrease with height (Fig. 59). Elemental mapping of thin sections also shows a strong spatial correlation between olivine, chromite and sulfide (Fig. 57 a). Moreover, olivine occurs interstitial to orthopyroxene in harzburgite and olivine-orthopyroxenite from the reef interval.

These observations suggest a strong genetic link between the sulfide mineralisation and the influx of primitive magma in the Sopcha Reef. The proposed closed system crystallisation of a distinct layer of melt to produce the reef is inconsistent

with our geochemical data, as Zr concentrations across the mineralised interval are mostly below 10 ppm (Fig. 59), whereas broadly coeval komatiite and picrites from northern Finland have > 30 ppm Zr (Hanski et al. 2001a). Therefore, these rocks clearly represent cumulates rather than melts.

Due to the stratigraphic complexity of the reef horizon, it is difficult to present an unambiguous genetic model for the reef; however, based on the local occurrence of orthopyroxenitic autoliths in typical Sopcha orthopyroxenites, underlying the mineralised reef lithologies (Fig. 53 d), we suggest that this stratigraphic level marks a significant change in the emplacement mode of the Sopcha intrusion, predating the actual formation of the reef (Fig. 68 a).

The abundance of autoliths from the immediate host orthopyroxenites indicates that normal fractional crystallisation was interrupted, possibly by the intrusion of an unmineralised orthopyroxenitic crystal mush along the boundary between largely solidified Sopcha cumulates and the overlying cumulus crystal pile (Fig. 68 b). This resulted in the erosion of the solid Sopcha cumulates to produce the locally autolith-rich orthopyroxenite, underlying the reef horizon (Fig. 53 d). After the consolidation of the autolith-rich crystal mush, a subsequent mineralised crystal mush may have intruded on top of the autolith-rich orthopyroxenite. This mush was probably melt-rich and contained cumulus olivine and chromite as well as sulfide melt. Presumably, it was sourced from a small subsidiary staging chamber that has undergone a different contamination history than the main staging chamber, from which most other Sopcha lithologies originated (Fig. 67 b). This is supported by an anomalously low Nd isotope composition of εNd(t = 2500 Ma) $\approx$ - 6.1 for the Sopcha Reef, whereas most other samples from the Monchegorsk Complex are characterised by εNd(t = 2500 Ma) values ranging from - 3 to + 1 (Bayanova et al. 2009, Chashchin et al. 2016, Yang et al. 2016). Upon final emplacement of the mineralised crystal-charged magma, cumulus olivine, chromite and sulfide liquid were concentrated at the bottom of the mush. Afterwards, the pre-existing cumulus orthopyroxene from the semi-consolidated host orthopyroxenites slightly subsided into the mush, which explains the constant orthopyroxene compositions below, within and above the reef, whereas olivine compositions vary (Fig. 59, 68 c). The primitive interstitial melt,

with the liquidus phases olivine and chromite, subsequently underwent fractional crystallisation, as indicated by the upward decrease in forsterite contents and Cr/V ratios across the mineralised interval. The generally low Zr concentrations and the lack of evolved mineral phases in the reef lithologies suggest that the interstitial melt was removed from the cumulate relatively early, possibly as a consequence of compaction (e.g., Boorman et al. 2004, Meurer & Boudreau 1996). This would also

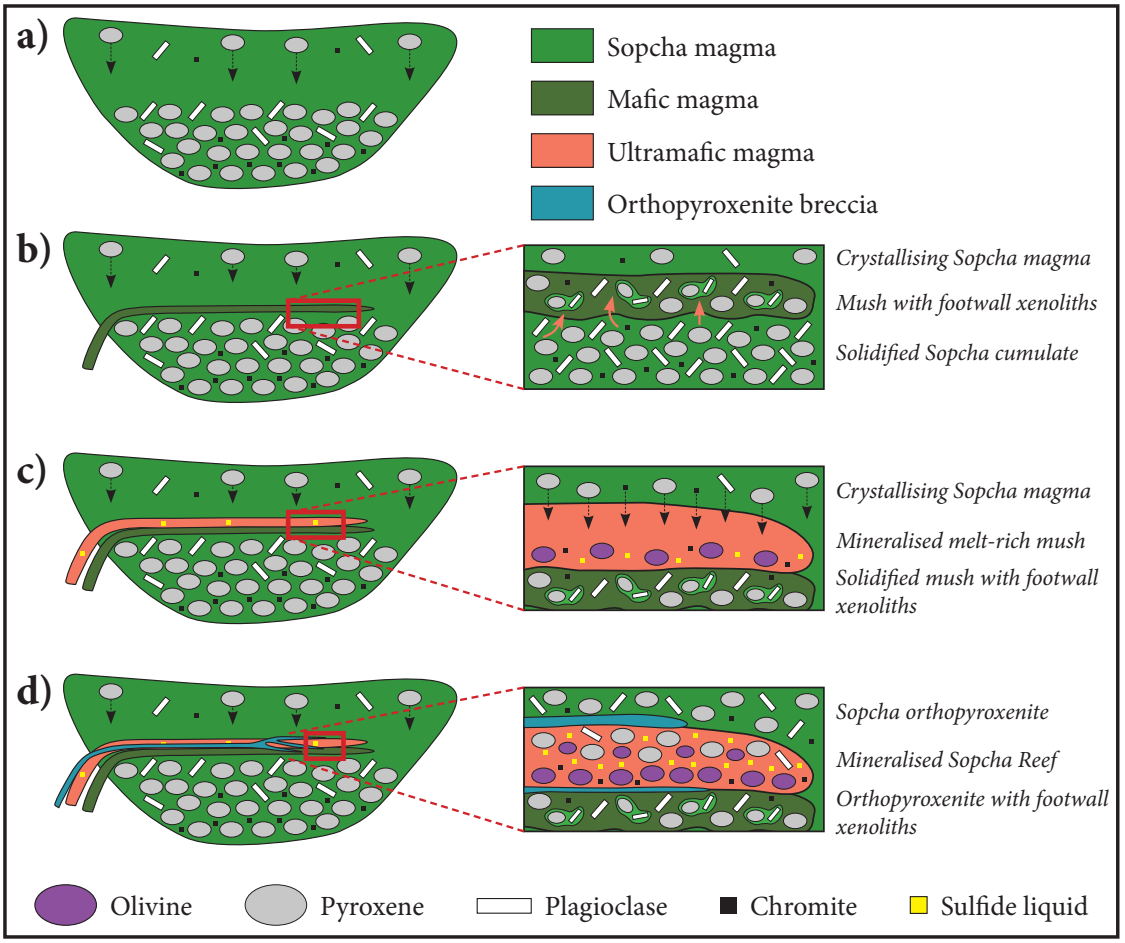

Fig. 68. Schematic emplacement model for the Sopcha Reef. a) Crystallisation of typical Sopcha cumulates. b) Intrusion of mafic crystal mush along the boundary between largely solidified Sopcha cumulates and the overlying crystal pile. Note that the intruding crystal mush eroded fragments from the footwall. c) Intrusion of an ultramafic, melt-rich crystal mush, containing cumulus olivine and chromite as well as sulfide melt. The overlying cumulus orthopyroxene crystals from the semi-consolidated hanging wall slightly subsided into the melt-rich mush. Sulfides and olivine crystallised interstitial to these cumulus orthopyroxene crystals. d) The orthopyroxenite breccia also intruded as a crystal mush, locally eroding the lowermost reef dunite. The distinct change in rock type at the base of the reef (orthopyroxenite to dunite) may have acted as a mechanical discontinuity, which was exploited by the intruding crystal mush. See section 7.4.1 for further explanation.

be consistent with the relatively low sulfide abundance in the lowermost dunite (Fig. 64).

The disseminated PGE-rich sulfide mineralisation is essentially controlled by the distribution of the primitive interstitial melt. The chalcophile element profile across the reef shows that sulfides preferentially collected on top of the lowermost dunite with decreasing modal abundances towards the top of the reef. The sulfide compositions can be modelled, using a PGE-undepleted picritic parental magma with 498 ppm Ni, 86 ppm Cu, 9.54 ppb Pd and 0.76 ppb Ir (see Barnes & Lightfoot 2005), which equilibrated with sulfide melt at R factors, ranging from 1,000 to 10,000 with limited sulfide liquid fractionation, similar to contact-style mineralisation elsewhere in the Monchegorsk Complex (Fig. 69). Notably, many of the orthopyroxenite

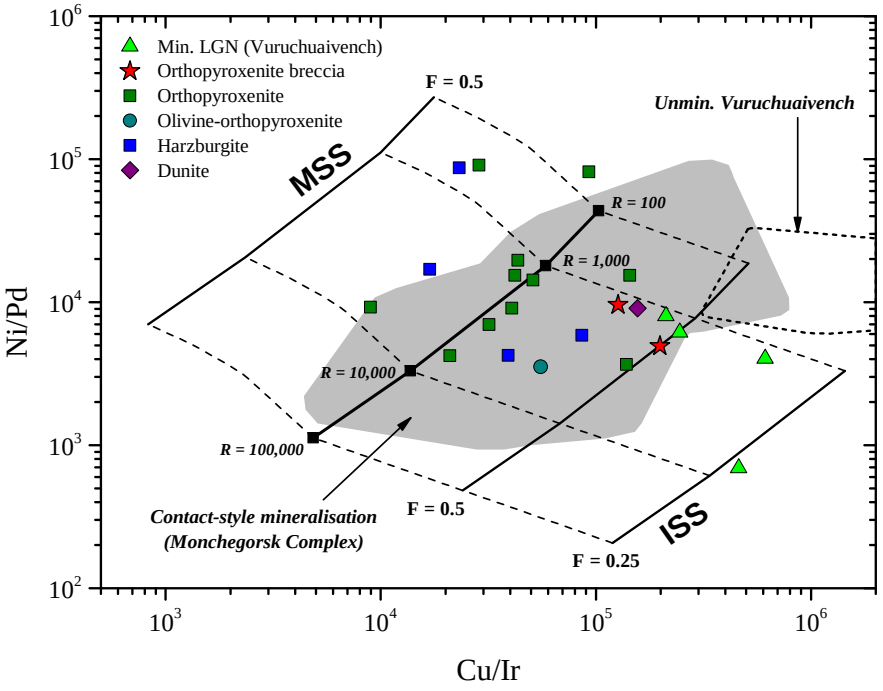

Fig. 69. Binary ratio plot of Ni/Pd vs. Cu/Ir. The dashed lines represent model compositions of *monosulfide solid solution* (mss), crystallising from sulfide liquids undergoing fractionation, and residual liquid. The solid lines show different end-member mss and residual sulfide liquid compositions, assuming different degrees of fractionation (F = fraction of residual liquid). Sulfide melt/silicate melt D values: 30,000 for the PGE, 1,000 for Cu and 500 for Ni. Mss/sulfide melt D values as summarised in Maier & Barnes (1999). Data for contact-style mineralisation in the Monchegorsk Complex were taken from Chapter 6.

samples from Sopcha plot close to the R factor model line, confirming the validity of the boundary conditions.

The positive correlation between sulfur and the PGE further suggests the concentration of chalcophile metals by sulfide liquid, rather than a fluid-induced PGE concentration, as proposed by Sharkov & Bogatikov (1998). The exact mechanism, leading to sulfide saturation, is generally difficult to constrain; however, multiple sulfur isotope data for the Sopcha Reef indicate that sulfide saturation was triggered by silicate assimilation rather than the addition of external sulfur (Bekker et al. 2016). The strongly negative Nd isotope composition of the Sopcha Reef is also consistent with this model (Chashchin et al. 2016).

Although the cross-cutting orthopyroxenite breccia is not mineralised, it provides valuable insight into the complex mechanisms, leading to the pronounced igneous layering in the Sopcha Reef. Most importantly, the presence of dunitic autoliths in the orthopyroxenite breccia indicates that the latter postdates the emplacement of the mineralised, olivine-rich Sopcha Reef lithologies (Fig. 57 b). In the studied profile, the breccia occurs as two distinct layers with sharp undulating contacts to the adjacent reef (Figs. 53 c, 63). Some 200 m further west, however, the orthopyroxenite breccia bifurcates into several sub-layers that interfinger with the mineralised reef lithologies (Fig. 55 b). These observations are consistent with a sill-like emplacement of the orthopyroxenite breccia as a crystal mush into the semi-consolidated Sopcha Reef. In particular, the distinct change in rock type at the base of the reef may have represented a mechanical discontinuity, which was exploited by the orthopyroxenite breccia (Fig. 68 d). Therefore, several lines of evidence suggest that layering at Sopcha resulted from a sill-like emplacement of multiple crystal mushes, some which contained sulfide melt.

7.4.2 Genetic aspects of the Vuruchuaivench intrusion

The formation of the Vuruchuaivench intrusion and its relation to the Monchepluton remains somewhat debatable, as the contact zone between the leucogabbroic to anorthositic Vuruchuaivench intrusion and the underlying cumulates is not exposed. Historic drilling, however, indicates that the intrusion overlies pyroxenitic

and gabbronoritic rocks of the Nyud and Poaz intrusions (Pripachkin et al. 2005, Sharkov & Chistyakov 2012). This is further supported by generally parallel incompatible trace element patterns for these lithologies (Fig. 61 c). Therefore, it is reasonable to assume that the Vuruchuaivench intrusion represents the upper portion of the Moncheplutón. Furthermore, the incompatible trace element patterns for Vuruchuaivench and Monchetundra gabbronorites and anorthosites are almost identical, which suggests a common origin of these intrusions. Since the latter constitutes one of the three blocks of the ca. 60-km-long Main Ridge, the Vuruchuaivench intrusion can also be considered to represent part of this voluminous intrusive event, which marks a major influx of mafic magma into the crust. Moreover, field evidence from the Moncheplutón indicates that these relatively coarse-grained leucogabbronoritic to anorthositic lithologies, typical of the Main Ridge, postdate the ultramafic orthopyroxene-dominated lithologies of the Moncheplutón, as documented in great detail by Pripachkin et al. (2016). Similar cross-cutting relationships were also observed in the northern Bushveld Complex, where the voluminous, mafic Main Zone intruded into more ultramafic, already solidified, rocks of the Platreef (e.g., Holwell & McDonald 2006). Equally, the Mafic Sequence of the Great Dyke has also been suggested to postdate the Ultramafic Sequence on the basis of field relationships (Maier et al. 2015). Thus, it appears that there is a close genetic link between the emplacement of a relatively small ultramafic sequence and the subsequent intrusion of a voluminous mafic domain in many large layered complexes.

We suggest that the emplacement of the dense ultramafic Moncheplutón at a relatively high crustal level caused structural instability of the deeper staging chamber, resulting in its collapse (Fig. 67 c). This led to a major expulsion of relatively fractionated, PGE-depleted, crystal-rich magma from the staging chamber, which was emplaced on top of the ultramafic lithologies, to produce the unlayered mafic Main Ridge intrusion, including the Vuruchuaivench intrusion. A largely similar model has also been suggested for the Mafic Sequence of the Great Dyke (Maier et al. 2015).

7.4.3 Formation of PGE mineralisation in the Vuruchuaivench intrusion

The sulfide-poor PGE mineralisation at Vuruchuaivench is considered to represent a classic PGE reef in the upper portion of a layered intrusion, similar to the Skaergaard intrusion in Greenland (Andersen et al. 1998) and the Sonju Lake intrusion in the USA (Miller et al. 2002). Grebnev et al. (2014) suggested that the PGE mineralisation formed as a reef, in response to extensive fractionation in a large magma chamber. A number of observations, however, seem to be inconsistent with an *in situ* origin of the mineralisation. As opposed to most other PGE reefs, the mineralised interval at Vuruchuaivench is highly erratic along strike in terms of host lithology, thickness and grade (Fig. 9 I-J). The mineralisation is laterally discontinuous and hosted in several lenticular, leucogabbronoritic to anorthositic bodies, ranging from 1 to 25 m in thickness with up to 10 ppm Pt + Pd (Grebnev et al. 2014, Pripachkin & Rundkvist 2008). In many mafic-ultramafic intrusions, PGE reefs are associated with a sharp increase in Cu/Pd ratios (e.g., Barnes et al. 1993, Karykowski et al. 2017, Miller et al. 2002). These systematic shifts in Cu/Pd ratios do not occur in the Vuruchuaivench intrusion (Fig. 65). In fact, lithologies above and below the mineralised interval have generally less than 15 ppb Pt + Pd with Cu/Pd ratios well above the primitive mantle level, indicating that these rocks crystallised from a PGE-depleted, sulfide-undersaturated magma. Moreover, chalcophile element patterns for unmineralised and mineralised Vuruchuaivench lithologies differ considerably in their characteristics, especially with respect to Pd/Pt and Pd/Ir ratios (Figs. 62 f, 63 b). The unmineralised lithologies have relatively low Pd/Pt and Pd/Ir ratios of < 2 and < 100, respectively, whereas the mineralised ones have much higher Pd/Pt ratios of > 5 and Pd/Ir ratios reach up to 600.

Therefore, it is unlikely that sulfide saturation and chalcophile metal concentration occurred *in situ* in a large magma chamber, e.g., the presently-exposed Vuruchuaivench intrusion. Instead, the similarities in the chalcophile element geochemistry between the Vuruchuaivench mineralisation and the Sopcha Reef as well as the contact-style mineralisation elsewhere in the Monchegorsk Complex (Fig. 63 d),

indicate that the sulfides initially segregated from a more primitive magma, possibly in a staging chamber at a deeper stratigraphic level (cf. Chapter 6).

To test this hypothesis, we modelled the PGE mineralisation at Vuruchuaivench, assuming a PGE-undepleted picritic parental magma (see above for details). Our calculations show that the sulfide compositions are consistent with sulfide segregation at R factors, ranging from 1,000 to 10,000, with subsequent sulfide liquid fractionation to reach Pd/Ir ratios of up to 600 (Fig. 69). It could also be argued that the sulfides segregated from a PGE-depleted basaltic or picritic parental magma, as indicated by the high Cu/Pd ratios of the S-poor rocks from Vuruchuaivench. This, however, would require unrealistically high R factors in excess of 100,000 to account for the high PGE concentrations of the sulfides. In contrast, most of the unmineralised lithologies from Vuruchuaivench cannot be modelled from a PGE-undepleted picritic magma, but require a PGE-depleted parental magma, which is consistent with the different chalcophile element signatures, in particular, the contrasting Pd/Pt ratios of the mineralised and unmineralised lithologies (Figs. 62 f, 63 b).

Hence, we suggest that sulfide saturation was reached relatively early in a PGE-undepleted picritic magma, possibly in response to silicate assimilation, as suggested by Bekker et al. (2016). The sulfide droplets subsequently extracted PGE from the magma and collected in structural traps in the staging chamber or possibly in a conduit. Following further fractionation of the magma and the emplacement of the sulfide-saturated ultramafic portions of the Monchegorsk Complex (cf. Chapter 6), the resident PGE-depleted and sulfide-undersaturated mafic magma was mobilised from the staging chamber and emplaced at Vuruchuaivench to produce the unmineralised lithologies (Fig. 67 d). The last pulses of magma, however, entrained small amounts of relatively fractionated sulfide melt and intruded as sills into the barren Vuruchuaivench leucogabbronorites and anorthosites to form the discontinuous PGE mineralisation, as opposed to a laterally extensive PGE reef. Based on the mineralogical diversity of the mineralised rock types, these influxes of magma were crystal mushes that ranged in composition from mafic to anorthositic. Notably, the marked difference in Pd/Pt ratios between mineralised and unmineralised Vuruchu-

aivench lithologies provides further evidence for the proposed entrainment model. Many layered intrusions, such as the Bushveld Complex and the Great Dyke, show a systematic decrease in Pd/Pt ratios with stratigraphic height: high Pd/Pt ratios are characteristic of early-formed sulfides, hosted in the most primitive portions of a layered complex (Maier & Barnes 1999, Naldrett & Wilson 1990).

7.4.4 An undiscovered PGE reef in the Monchetundra intrusion?

Most of the leucogabbronorites and anorthosites from the Monchetundra intrusion have PGE concentrations, ranging from below the limit of detection to about 1 ppb Pt + Pd, with exceptionally high Cu/Pd ratios of more than 50,000 (Fig. 66). A small group of samples, however, is characterised by higher PGE concentrations, ranging from 5 to 169 ppb Pt + Pd, and Cu/Pd ratios around 8,000. All of these samples are located at the bottom of the analysed profile across the exposed portion of the Monchetundra intrusion. Therefore, it is possible that the sharp increase in Cu/Pd ratios marks the stratigraphic level at which sulfide melt saturation was reached (Fig. 67 e). Due to the small number of samples from this interval, it is difficult to determine, whether the parental magma was fertile with respect to PGE, as sampling was not designed to discover this potential PGE reef, although the ubiquitous presence of cumulus sulfide in all ultramafic rocks from the Monchegorsk Complex suggests that the parental magma was already PGE-depleted, when the mafic Monchetundra intrusion crystallised. A feasible mechanism to trigger sulfide saturation at this stratigraphic level may have been extensive fractional crystallisation, similar to reef formation in the Skaergaard intrusion in Greenland and the Sonju Lake intrusion in the USA (Andersen et al. 1998, Miller et al. 2002). Considering that the Monchetundra intrusion merely represents a small part of the more than 60-km-long Main Ridge, further detailed work is required to establish the extent and potential of the mineralised interval along strike. On the basis of the slightly more primitive nature of the Vuruchuaivench cumulates, it is possible that Vuruchuaivench-style PGE mineralisation may also be present at depth, not only at

Monchetundra, but also elsewhere in the Main Ridge.

7.5 Summary

The results of this study demonstrate that disseminated PGE-rich sulfide mineralisation, concentrated in somewhat laterally extensive layers, may have quite different origins, even in a single complex. The PGE mineralisation at Vuruchuaivench has been traditionally classified as *reef-style mineralisation*; however, our detailed geological and geochemical work showed that the sulfides are not concentrated in a distinct, laterally extensive layer, but in several lenticular bodies. Moreover, the PGE-rich sulfides did not segregate from the same magma that crystallised the barren host leucogabbronorites and anorthosites. Hence, the Vuruchuaivench mineralisation shares very few characteristics with classic PGE reefs in the upper portions of layered intrusions, such as in the Skaergaard and the Sonju Lake intrusions (Andersen et al. 1998, Miller et al. 2002). It is more likely that the mineralised interval represents a sill-like intrusion of gabbroic crystal mushes that have entrained relatively fractionated sulfide liquid, possibly from a staging chamber at a deeper level.

Compared with this, the Sopcha Reef is ultramafic in composition and also located in the ultramafic portion of the complex, similar to the Main Sulfide Zone (MSZ) in the Great Dyke of Zimbabwe (e.g., Wilson et al. 1989). The mineralisation at Sopcha is closely associated with crustally contaminated layered olivine-rich lithologies, hosted by a thick succession of orthopyroxenite. As opposed to the MSZ, which is considered to have formed through sulfide segregation in response to silicate fractionation (Maier et al. 2015), the Sopcha Reef likely intruded as a sulfide-saturated crystal mush, triggered by silicate assimilation. In contrast, the geochemical characteristics of PGE mineralisation in the Monchetundra intrusion are consistent with extensive silicate fractionation. The mineralised interval is characterised by a sharp increase in Cu/Pd ratios, which is typical of classic PGE reefs. Due to the sulfide-rich nature of all other rocks in the Monchegorsk Complex, it is likely that the parental magma for the Monchetundra intrusion has undergone previous sulfide extraction, indicating that precious metal concentrations can be expected to be relatively low.

Ultimately, the Monchegorsk Complex presents a prime object of study for reef-

style PGE mineralisation in layered intrusions. Each PGE reef is characterised by a distinct set of geological and geochemical features, from which a petrogenetic model can be deduced. Hence, the formation mechanism has important implications for the continuity of the PGE mineralisation: a sill-like intrusion of a sulfide-saturated crystal mush, sourced from a staging chamber, does not necessarily form laterally extensive layers, whereas sulfide saturation as a consequence of extensive silicate fractionation commonly affects the entire magma chamber, leading to laterally continuous reefs.

Chapter 8

Synthesis

8.1 Introduction

This chapter aims to synthesise the findings of the preceding chapters in relation to the aims of the project. The formation of a cumulate can be subdivided into two principal stages: (1) the cumulus stage, in which a framework of cumulus minerals is assembled to form a proto-cumulate and (2) the postcumulus stage, in which different intercumulus processes lead to the solidification of the proto-cumulate. Evidence from the Bushveld and Monchegorsk complexes will be subsequently summarised and synthesised with respect to the formation of layered intrusions and their mineralisation. Lastly, implications for exploration will be briefly outlined.

8.2 Petrogenetic processes associated with the formation of layered intrusions

The distribution and geometry of the Lower Zone of the Bushveld Complex is highly variable and the zone is characterised by pronounced, yet laterally discontinuous layering on different scales (cf. Chapter 5). Together with the observed contact relationships between rock types, the ubiquitous lack of large-scale fractionation in the Mg# of orthopyroxene, the variable Sr isotope compositions and the erratic Pd/Pt ratios, these observations strongly argue against a simple *in situ* fractional crystallisation model. It is more likely that the Lower Zone was emplaced as a sill complex, as these contrasting geochemical characteristics are difficult to account for in a large Bushveld magma chamber, as previously suggested (e.g., Eales & Cawthorn 1996). These sills most likely represented crystal mushes that were episodically fed from a sub-Bushveld staging chamber, and variably contaminated, while passing through the crust before their final emplacement in the Lower Zone.

Further support for the importance of crystal mushes in the formation of layered intrusions is provided by the Monchegorsk Complex. Commonly occurring basal reversals in the Mg# of orthopyroxene, whole rock MgO concentrations and Cr/V ratios, which are mirrored by decreasing Al_2O_3 concentrations, are difficult to explain by an *in situ* crystallisation of the succession (cf. Chapter 6). *In situ* con-

tamination of a crystal-poor magma with host metasediments would have strongly affected the trace element signature of the magma; however, La/Nb ratios across the basal reversal are nearly constant. In addition, *in situ* crystallisation would have produced lithologies with varying grain sizes, especially at the intrusion contact, which is not observed. Thus, it is more likely that elevated cooling rates close to the intrusion margins hindered effective and thorough settling of orthopyroxene, resulting in high amounts of trapped liquid. As cooling rates generally decrease away from the intrusion contact, the amount of interstitial liquid trapped in the cumulate was also lower, as evidenced by a smaller trapped liquid shift towards the top. Hence, these reversals are consistent with the emplacement of a crystal mush, carrying considerable amounts of suspended cumulus orthopyroxene.

Furthermore, broadly stratiform mineralisation in the Vuruchuaivench and Sopcha intrusions of the Monchegorsk Complex lacks distinct shifts in Cu/Pd ratios across the mineralised intervals, which is inconsistent with an *in situ* crystallisation, as lithologies above and below the mineralisation do not record a transition from sulfide-undersaturated to sulfide-saturated conditions (cf. Chapter 7). Cross-cutting relationships in the Sopcha Reef and the development of several orthopyroxenite breccias above and below the reef, together with the intricate bifurcation of layers, suggest a sill-like emplacement of several crystal mushes at the level of the "reef".

Therefore, this process appears to be of major importance in the formation of ultramafic portions of layered intrusions, as it is capable of producing not only the observed (dis-)continuous layering and bifurcation of layers on the macroscopic scale, but also the diverse smaller-scale isotopic and geochemical characteristics, such as the lack of fractionation, basal reversals and variable Sr_i ratios.

In contrast, *in situ* Sr isotope data of plagioclase from the Main and Upper Critical zones of the Bushveld Complex indicate that magma mixing also plays an important role in the formation of layered intrusions (cf. Chapter 4). Cumulus plagioclase from the Main Zone records a gradual upward decrease in Sr_i ratios, which suggests an incremental addition of a less radiogenic magma to the resident, more radiogenic Main Zone magma. It is unlikely that the mixing occurred in a sub-Bushveld staging chamber, prior to the final emplacement of the zone, as this

would require that the distinct trend in the isotope composition of the Main Zone was preserved during the intrusion of the crystal mush (e.g., Maier & Barnes 1998). Conversely, the Upper Critical Zone is characterised by an upward increase in Sr_i ratios, indicating that the zone crystallised from a Critical Zone magma mixed with progressively increasing proportions of Main Zone magma; the co-accumulation of plagioclase from two distinct reservoirs could not account for the observed *in situ* Sr isotope variation (e.g., Yang et al. 2013, Seabrook et al. 2005).

Following the sill-like emplacement or the *in situ* crystallisation of cumulus minerals to form a proto-cumulate, intercumulus processes controlled the subsequent solidification of the proto-cumulate. The Sr isotope variation in most analysed ultramafic lithologies from the Bushveld Complex indicates that more than one isotopically and geochemically distinct batch of melt affected the intercumulus mineralogy (cf. Chapter 4). Moreover, the complex zonation patterns of interstitial plagioclase, with respect to mineral chemistry and isotope composition, cannot be explained by a simple closed system fractionation model of trapped liquid (cf. Chapter 5). Together with the non-cotectic interstitial mineral modes in a number of Lower Zone samples, this suggests that residual melt must have escaped during the solidification of the cumulate, which is consistent with the migration of interstitial melt at different stages of fractionation as a consequence of displacement by convecting interstitial liquids and compaction. This has important implications for high-precision dating of layered intrusions, because late-stage minerals, such as zircon, rarely crystallise from trapped liquid that was initially in equilibrium with the cumulate. Therefore, dating of interstitial zircon from cumulates is unlikely to record the actual timing of emplacement, but merely the crystallisation of a later episode of residual melt that migrated through the cumulate.

Lastly, decoupling of Sr isotope compositions and fractionation indices, such as Mg# of orthopyroxene, anorthite content or trace element ratios across the Lower and Main zones indicate that bulk assimilation of crustal lithologies cannot be the main control on the variation in isotopic signatures of the different magmas (cf. Chapter 4). It is conceivable, however, that some magma batches interacted with a fluid derived from the up to 2-km-thick dolomitic footwall, which caused a major shift

in Sr isotope composition, without significantly affecting the degree of fractionation or the trace element signature. This interaction could be also considered as a possible mechanism to create space in the crust, since the devolatilisation and dissociation of chemical sediments is directly linked to volume loss.

8.3 Origin of PGE mineralisation in layered intrusions

The chalcophile element geochemistry of the analysed samples from the lower portion of the Monchegorsk Complex (Monchepluton) shows that most lithologies contain cumulus sulfide, which indicates that sulfide saturation occurred relatively early (cf. Chapters 6, 7). Moreover, mineralisation occurs at different stratigraphic levels and in different parts of the complex, irrespective of the rock type and the position relative to the intrusion contact. The only difference between mineralised and unmineralised parts of the Monchepluton is the modal abundance of sulfide. Therefore, the critical control on the formation of PGE deposits is the efficiency of sulfide accumulation in distinct zones of a layered intrusion, preferentially at the basal intrusion contact. However, broadly stratiform PGE mineralisation in the central portion of the Sopcha intrusion is also similar in composition to contact-style mineralisation elsewhere in the complex, suggesting a common origin of the sulfides.

It is difficult to explain these geochemical characteristics with a model, in which sulfide saturation was triggered *in situ* as a result of local sulfide addition from an external source or extensive fractionation. It is thus likely that the saturation in sulfide liquid occurred in a staging chamber at depth together with the concurrent crystallisation of cumulus olivine and orthopyroxene. This proto-cumulate, consisting of cumulus silicate minerals, liquid sulfide and residual silicate melt, was episodically remobilised and crudely density-sorted within crystal mushes as they were transported into higher crustal levels, such as the Sopcha Reef.

Additionally, evidence from the mineralised interval of the Vuruchuaivench intrusion indicates that sulfide entrainment can also be an important process in the formation of somewhat laterally extensive PGE mineralisation in the upper portions

of layered intrusions. In this case, it is likely that an unmineralised gabbroic crystal mush entrained relatively fractionated sulfide melt, which had initially segregated from a more primitive magma, possibly in a staging chamber at depth.

Regarding contact-style mineralisation in the Monchegorsk Complex, thermal modelling results indicate that effective sulfide concentration at the base of the intrusion requires elevated basement temperatures of > 350 °C. This preheating of the basement can be achieved through a multi-stage emplacement of the complex, which is manifested in the frequent brecciation of mafic-ultramafic rocks, basement lithologies and felsic pegmatite and the presence of the sulfide-undersaturated lowermost portion of the Monchegorsk Complex, predating the emplacement of the main layered succession (see section 6.4.3 for further details). Upon final emplacement of the sulfide-charged crystal mushes, the underlying basement underwent devolatilisation, which led to the local addition of water and other volatiles to the magma. This resulted in a decrease in the melting temperature of the magma and caused local partial melting of cumulus silicate minerals within the crystal mush, together with a reduction in magma viscosity, which locally enhanced the porosity of the crystal mush, thus promoting gravitational sulfide liquid concentration at the base of the intrusion.

Although most types of sulfide mineralisation in the Monchegorsk Complex are related to sulfide entrainment in crystal mushes, the origin of a previously unreported occurrence of PGE mineralisation in the upper portion of the complex, overlying the Vuruchuaivench intrusion is different. Mineralised leucogabbroic rocks of the Monchetundra intrusion are associated with a sharp increase in Cu/Pd ratios, which is consistent with a classic PGE reef model, in which sulfide saturation was triggered *in situ* by extensive silicate fractionation. Another potential mechanism for the introduction of interstitial sulfide mineralisation into a cumulate is melt migration, as suggested for the Lower Zone of the Bushveld Complex (cf. Chapter 5). It is conceivable that sulfide-saturated crystal mushes do not only form discrete sills (e.g., Platreef), but also interact with the existing cumulate (e.g., Hayes et al. 2017), i.e., the liquid components of a mush are not withheld from further migration. Subsequently, these liquids crystallise in zones of low flow velocity.

8.4 Towards a petrogenetic model for layered intrusions

In the following section, the findings of this study will be synthesised into a broader petrogenetic model for layered intrusions, focusing on how different emplacement processes affect the development of distinct styles of mineralisation.

Evidence from the Bushveld and Monchegorsk complexes suggests that the emplacement of the lower, ultramafic portions of layered intrusions is generally associated with the intrusion of crystal mushes as multiple sills that are fed from potentially different staging chambers at depth to form an initially unconsolidated, strongly layered cumulate. The intrusion of the first sills into cold basement lithologies will lead to a significant preheating of the latter (Fig. 70 a). If these early, primitive magmas reach sulfide saturation prior to their final emplacement into cold basement, the physical concentration of sulfide along the basal contact of the sill will be relatively poor, resulting in dispersed, low grade sulfide mineralisation of little economic importance. In contrast, subsequent sulfide-saturated sills that intrude preheated basement lithologies can interact with the host rocks, which will enhance the collection of sulfide liquid at the base of the intrusion to form *contact-style* sulfide mineralisation (Fig. 70 b).

Furthermore, the occurrence of broadly stratiform sulfide mineralisation in the central portion of the ultramafic succession at Monchegorsk ("Sopcha Reef") and the 90-cm-thick mineralised noritic interval in the Lower Zone of the Bushveld Complex show that these sulfide-saturated crystal mushes can also intrude the unconsolidated ultramafic cumulate at different stratigraphic levels to form mineralised sills that cannot be necessarily traced across the entire complex (Fig. 70 c).

Moreover, the Sr isotope composition of interstitial plagioclase from the ultramafic portion of the Bushveld Complex indicate that more than one isotopically and geochemically distinct batch of melt affected the intercumulus mineralogy, which suggests that residual melt can escape during the solidification of the cumulate as a consequence of displacement by convecting interstitial liquids and compaction. This has important implications for dating ultramafic cumulates from layered intrusions

as it is unlikely that interstitial zircon records the actual timing of emplacement of an ultramafic rock.

The formation of the largely unlayered mafic portion of layered intrusions, however, appears to be controlled by mixing of relatively crystal-poor magmas and *in situ* crystallisation (Fig. 70 d). A potential reason for this could be that the emplacement of the dense ultramafic portion at a higher crustal level caused structural instability of the deeper staging chamber, which resulted in its collapse and the expulsion of large volumes of crystal-poor mafic magma. Similar to the Sopcha Reef, the broadly stratiform sulfide mineralisation at Vuruchuaivench demonstrates that preformed sulfides can also be entrained by relatively fractionated magmas and be emplaced as sills in the upper portions of layered intrusions (Fig. 70 e). Upon further fractionation of the mafic magma, sulfide saturation can be reached once again in response to extensive fractionation, resulting in the formation of a depleted PGE reef *sensu stricto*, such as the one observed in the uppermost portion of the Monchegorsk Complex at Monchetundra. If sulfide saturation was not reached early on in the evolution of the complex, these classic reefs could also occur at lower stratigraphic levels, showing significantly higher PGE concentrations.

Ultimately, petrogenetic processes associated with the formation of layered intrusions can be highly diverse. This study shows that a single process cannot account for all the described features in the Bushveld and Monchegorsk complexes. Instead, a combination of processes is necessary to explain the different types of layering and mineralisation even in a single complex. These include the intrusion of crystal mushes, magma mixing and melt percolation. It appears that the emplacement of the lower portions of layered intrusions is commonly related to the intrusion of crystal mushes, whereas the upper portions may also crystallise *in situ* from crystal-poor magmas (e.g., Main Zone in the Bushveld Complex and Monchetundra in the Monchegorsk Complex).

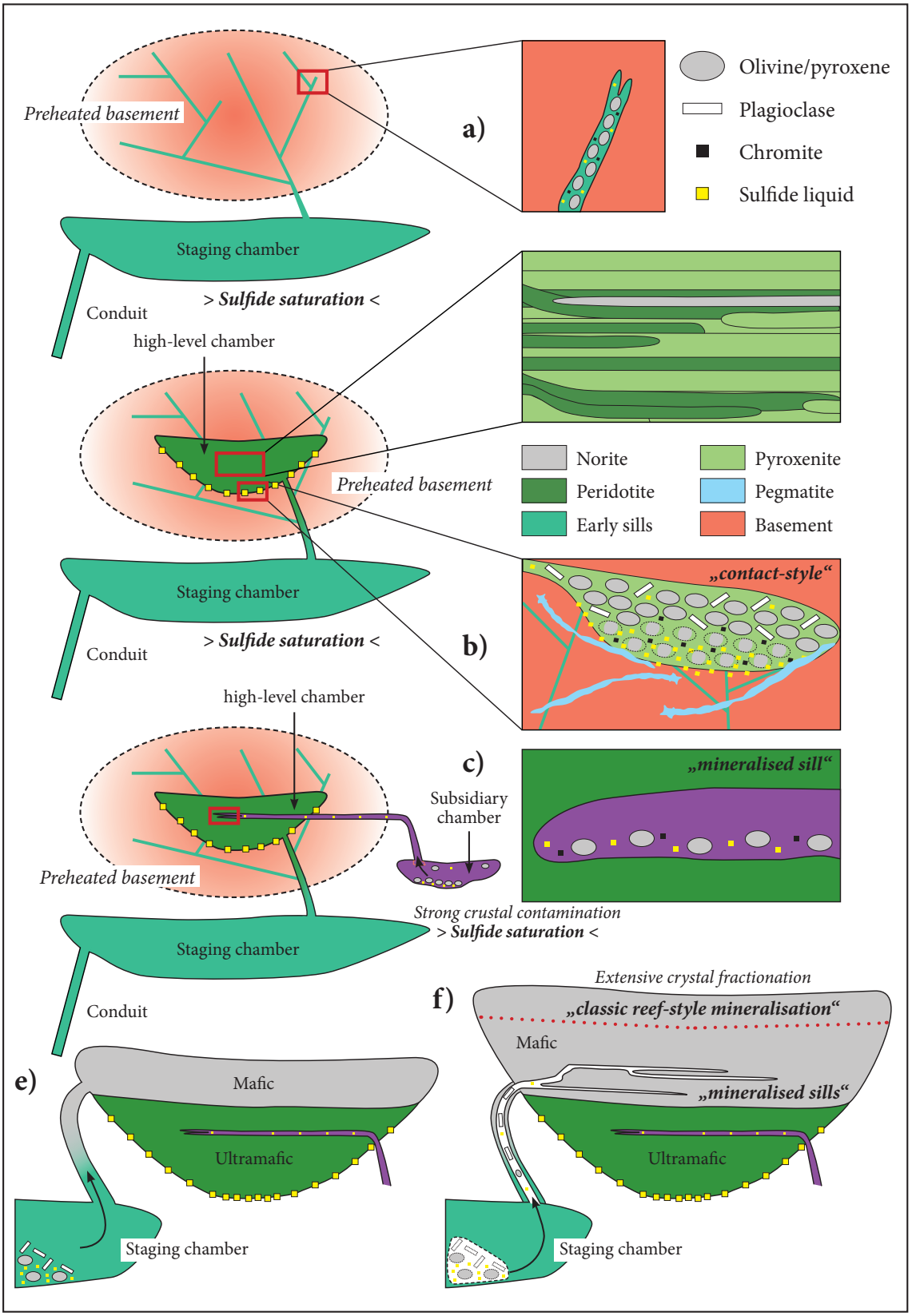

Fig. 70. Conceptual petrogenetic model for the emplacement of layered intrusions and the distribution of different styles of sulfide mineralisation.

8.5 Implications for exploration

This study indicates that the preheating of the basement plays a critical role in the formation of contact-style sulfide mineralisation in the Monchegorsk Complex. Moreover, it appears that this process also controls sulfide concentration in other layered intrusions: the richest contact-style PGE deposits in the northern limb of the Bushveld Complex are located in areas, where the Lower Zone is present (see McDonald et al. 2017, for a detailed geological map of the northern limb); the same applies to the Portimo Complex, where the presence of earlier Portimo Dykes seems to correlate with higher grade mineralisation (see Iljina & Lee 2005). Groshev et al. (2009) also suggested that the 300-m-thick mineralised zone at the base of the Fedorova intrusion was emplaced after the formation of the more than 4-km-thick mafic-ultramafic main body of the layered intrusion.

Therefore, one of the most important criteria for targeting contact-style mineralisation in layered intrusions is a multi-stage emplacement history. Apart from enhancing the sulfide concentration at the base of an intrusion, it may also facilitate silicate assimilation by subsequent magma pulses, which may trigger sulfide saturation. Hence, layered intrusions that are comprised of two or more temporally related, but distinct injections or pulses of magma, should thus be regarded as prospective.

Furthermore, it is important to characterise reef-style mineralisation, as the origin of a PGE reef has important implications for the continuity of the PGE mineralisation: a sill-like intrusion of a sulfide-saturated crystal mush, sourced from a staging chamber, does not necessarily form laterally extensive layers, whereas *in situ* sulfide saturation as a consequence of extensive silicate fractionation commonly affects the entire magma chamber, leading to laterally continuous reefs.

8.6 Future direction of research

One of the most important question that this study raises is the capability of dolomite-derived fluids to change the isotope composition of a mafic-ultramafic magma. Although it is well-known that thermal treatment of carbonate lithologies leads to the release of volatiles and a loss of volume (e.g., Olszak-Humienik & Jablon-

ski 2014), the chemical composition of these volatiles remains unclear. Therefore, a better geochemical and and isotopic whole rock characterisation of the Malmani Subgroup dolomite is needed. Especially quantifying the fractionation of Sr isotopes during thermal decomposition of dolomite should establish whether the released fluids are capable of changing the Sr isotope composition of the magma, while the latter passes through an extensive carbonate platform. In this case, the whole rock Sr isotope composition and the total Sr concentration of dolomite should be analysed at different temperatures to track the degree of isotope fractionation.

Moreover, the migration of interstitial melts in Lower Zone cumulates from the Bushveld Complex suggests that sulfide liquid could be moved through an intercumulus network to form PGE reefs, such as the Merensky Reef. In addition, melt migration has the potential to obscure zircon-based intrusion ages of ultramafic cumulates. Both these hypotheses could be tested with detailed *in situ* Pb isotope work on the main rock-forming silicates as well as sulfide and zircon. If all of these minerals had the same Pb isotope composition, it would be unlikely that melt migration was a significant ore-forming process. In contrast, isotope disequilibrium between these minerals would suggest that sulfides as well as zircon did not crystallise in equilibrium with the main rock-forming silicates, which would provide strong evidence against the *in situ* formation of PGE reefs.

In order to further constrain the timing and duration of magmatism associated with the Monchegorsk Complex, high-precision age dating of samples with a known provenance is needed. Modern CA-ID-TIMS U-Pb zircon age dating of lithologies from the Monchepluton as well as the Main Ridge should establish whether magmatism in the Monchegorsk area lasted for more than 60 m.y. as suggested by Bayanova et al. (2009). In connection to this, the massive sulfide veins and the thin PGE-rich veinlets that cross-cut the layered ultramafic Sopcha intrusion and the NKT Massif could also be dated, using the Pt-Os isotope system, to constrain their formation in relation to the crystallisation age of the host cumulates (e.g., Walker et al. 1997).

Furthermore, the 2.5-km-deep drill hole M1, intersecting the lower portion of the mafic Main Ridge intrusion, should be revisited (Sharkov & Chistyakov 2012), once made available by Norilsk Nickel, to examine whether mineralised sills, similar

to those at Vuruchuaivench, are also present in the lower portion of the Main Ridge. Detailed and careful core-logging should establish the presence of finely disseminated sulfide mineralisation in leucogabbronorite and anorthosite. These intervals should be analysed in terms of geochemistry and compared with the available data from the Vuruchuaivench intrusion.

Bibliography

Alapieti, T. T. (1982), 'The Koillismaa layered igneous complex, Finland: Its structure, mineralogy and geochemistry, with emphasis on the distribution of chromium', *Bulletin of the Geological Survey of Finland* **319**.

Alapieti, T. T., Filen, B. A., Lahtinen, J. J., Lavrov, M. M., Smolkin, V. F. & Voitsekhovsky, S. N. (1990), 'Early Proterozoic layered intrusions in the northeastern part of the Fennoscandian Shield', *Mineralogy and Petrology* **42**(1), 1–22.

Alapieti, T. T. & Halkoaho, T. A. A. (1995), 'Cryptic variation of augite in the Penikat Layered Intrusion, Northern Finland, with reference to megacyclic units and PGE-enriched zones', *Mineralogy and Petrology* **54**(1), 11–24.

Alapieti, T. T. & Lahtinen, J. J. (1986), 'Stratigraphy, petrology, and platinum-group element mineralization of the early Proterozoic Penikat layered intrusion, northern Finland', *Economic Geology* **81**(5), 1126–1136.

Amelin, Y. V., Heaman, L. M. & Semenov, V. S. (1995), 'U-Pb geochronology of layered mafic intrusions in the eastern Baltic Shield: implications for the timing and duration of Paleoproterozoic continental rifting', *Precambrian Research* **75**(1), 31–46.

Amelin, Y. V. & Semenov, V. S. (1996), 'Nd and Sr isotopic geochemistry of mafic layered intrusions in the eastern Baltic shield: implications for the evolution of Paleoproterozoic continental mafic magmas', *Contributions to Mineralogy and Petrology* **124**(3), 255–272.

Andersen, J. C. O., Rasmussen, H., Nielsen, T. F. D. & Ronsbo, J. G. (1998), 'The Triple Group and the Platinova gold and palladium reefs in the Skaergaard Intrusion; stratigraphic and petrographic relations', *Economic Geology* **93**(4), 488–509.

Andersen, J. C. O., Thalhammer, O. A. R. & Schoenberg, R. (2006), 'Platinum-group element and Re-Os isotope variations of the high-grade Kilvenjärvi platinum-group element deposit, Portimo Layered Igneous Complex, Finland', *Economic Geology* **101**(1), 159–177.

Anketell, J. M., Cegla, J. & Dzulynski, S. (1970), 'On the deformational structures in systems with reversed density gradients', *Rocznik Polskiego Towarzystwa Geologicznego* **40**(1), 3–29.

Armitage, P. E. B., McDonald, I., Edwards, S. J. & Manby, G. M. (2002), 'Platinum-group element mineralization in the Platreef and calc-silicate footwall at Sandsloot, Potgietersrus District, South Africa', *Applied Earth Science* **111**(1), 36–45.

Ashwal, L. D., Webb, S. J. & Knoper, M. W. (2005), 'Magmatic stratigraphy in the Bushveld Northern Lobe: continuous geophysical and mineralogical data from the 2950 m Bellevue drillcore', *South African Journal of Geology* **108**(2), 199–232.

Balashov, Y. A., Bayanova, T. B. & Mitrofanov, F. P. (1993), 'Isotope data on the age and genesis of layered basic-ultrabasic intrusions in the Kola Peninsula and northern Karelia, northeastern Baltic Shield', *Precambrian Research* **64**(1), 197–205.

Ballhaus, C. G., Cornelius, M. & Stumpfl, E. F. (1988), 'The Upper Critical Zone of the Bushveld Complex and the origin of Merensky-type ores; a discussion', *Economic Geology* **83**(5), 1082–1085.

Barkov, A. Y., Pakhomovskii, Y. A., Trofimov, N. N. & Lavrov, M. M. (1994), 'Loveringite: a first occurrence in Russia from the Burakovsky layered intrusion, Karelia', *Neues Jahrbuch für Mineralogie* **3**, 101–111.

Barkov, A. Y., Saychenko, Y. E., Men'shikov, Y. P. & Barkova, L. P. (1996), 'Loveringite from the Last-Yavr mafic-ultramafic intrusion, Kola Peninsula; a second occurrence in Russia', *Norsk Geologisk Tidsskrift* **76**(2), 115–120.

Barnes, S. J. (1986a), 'The effect of trapped liquid crystallization on cumulus mineral compositions in layered intrusions', *Contributions to Mineralogy and Petrology* **93**(4), 524–531.

Barnes, S. J. (1986b), 'The distribution of chromium among orthopyroxene, spinel and silicate liquid at atmospheric pressure', *Geochimica et Cosmochimica Acta* **50**(9), 1889–1909.

Barnes, S.-J., Couture, J. F., Sawyer, E. W. & Bouchaib, C. (1993), 'Nickel-copper occurrences in the Belleterre-Angliers Belt of the Pontiac Subprovince and the use of Cu-Pd ratios in interpreting platinum-group element distributions', *Economic Geology* **88**(6), 1402–1418.

Barnes, S.-J. & Francis, D. (1995), 'The distribution of platinum-group elements, nickel, copper, and gold in the Muskox layered intrusion, Northwest Territories, Canada', *Economic Geology* **90**(1), 135–154.

Barnes, S.-J. & Lightfoot, P. C. (2005), Formation of magmatic nickel-sulfide ore deposits and processes affecting their copper and platinum-group element contents, *in* J. W. Hedenquist, J. F. H. Thompson, R. J. Goldfarb & J. P. Richards, eds, 'Economic Geology 100th Anniversary Volume', pp. 179–213.

Barnes, S.-J. & Maier, W. D. (1999), The fractionation of Ni, Cu and the noble metals in silicate and sulphide liquids, *in* R. R. Keays, C. M. Lesher, P. C. Lightfoot & C. E. G. Farrow, eds, 'Dynamic processes in magmatic ore deposits and their application in mineral exploration, Short Course Notes', Vol. 13, Geological Association of Canada, pp. 69–106.

Barnes, S.-J. & Maier, W. D. (2002), Platinum-group element distributions in the Rustenburg layered suite of the Bushveld Complex, South Africa, *in* L. J. Cabri,

ed., 'Geology, geochemistry, mineralogy and mineral beneficiation of platinum-group elements', Vol. 54, Canadian Institute of Mining, Metallurgy and Petroleum, Montreal, pp. 431–458.

Barnes, S.-J., Maier, W. D. & Ashwal, L. D. (2004), 'Platinum-group element distribution in the Main Zone and Upper Zone of the Bushveld Complex, South Africa', *Chemical Geology* **208**(1), 293–317.

Barnes, S.-J., Maier, W. D. & Curl, E. A. (2010), 'Composition of the marginal rocks and sills of the Rustenburg Layered Suite, Bushveld Complex, South Africa: implications for the formation of the platinum-group element deposits', *Economic Geology* **105**(8), 1491–1511.

Barnes, S.-J. & Picard, C. (1993), 'The behaviour of platinum-group elements during partial melting, crystal fractionation, and sulphide segregation: an example from the Cape Smith Fold Belt, northern Quebec', *Geochimica et Cosmochimica Acta* **57**(1), 79–87.

Bayanova, T. B., Ludden, J. & Mitrofanov, F. P. (2009), 'Timing and duration of Palaeoproterozoic events producing ore-bearing layered intrusions of the Baltic Shield: metallogenic, petrological and geodynamic implications', *Geological Society, London, Special Publications* **323**(1), 165–198.

Bayanova, T. B. & Mitrofanov, F. P. (2005), Layered Proterozoic PGE intrusions in Kola region: new isotope data, *in* T. O. Törmänen & T. T. Alapieti, eds, 'Proceedings of the 10th International Platinum Symposium: Platinum-group elements – from genesis to beneficiation and environmental impact', Geological Survey of Finland, Espoo, Finland, pp. 289–291.

Bayanova, T. B., Nerovich, L. I., Mitrofanov, F. P., Zhavkov, V. A. & Serov, P. A. (2010), 'The Monchetundra Basic Massif of the Kola region: New geological and isotope geochronological data', *Doklady Earth Sciences* **431**(1), 288–293.

Bédard, J. H., Kerr, R. C. & Hallworth, M. A. (1992), 'Porous sidewall and sloping floor crystallization experiments using a reactive mush: Implications for the self-

channelization of residual melts in cumulates', *Earth and Planetary Science Letters* **111**(2), 319–329.

Bédard, L. P., Savard, D. & Barnes, S.-J. (2008), 'Total sulfur concentration in geological reference materials by elemental infrared analyser', *Geostandards and Geoanalytical Research* **32**(2), 203–208.

Bekker, A., Grokhovskaya, T. L., Hiebert, R., Sharkov, E. V., Bui, T. H., Stadnek, K. R., Chashchin, V. V. & Wing, B. A. (2016), 'Multiple sulfur isotope and mineralogical constraints on the genesis of Ni-Cu-PGE magmatic sulfide mineralization of the Monchegorsk Igneous Complex, Kola Peninsula, Russia', *Mineralium Deposita* **51**(8), 1035–1053.

Bekker, A., Kaufman, A. J., Karhu, J. A., Beukes, N. J., Swart, Q. D., Coetzee, L. L. & Eriksson, K. A. (2001), 'Chemostratigraphy of the Paleoproterozoic Duitschland Formation, South Africa: implications for coupled climate change and carbon cycling', *American Journal of Science* **301**(3), 261–285.

Beukes, N. J. (1973), 'Precambrian iron-formations of southern africa', *Economic Geology* **68**(7), 960–1004.

Beukes, N. J. (1987), 'Facies relations, depositional environments and diagenesis in a major early Proterozoic stromatolitic carbonate platform to basinal sequence, Campbellrand Subgroup, Transvaal Supergroup, Southern Africa', *Sedimentary Geology* **54**(1-2), 179–546.

Bleeker, W. & Ernst, R. E. (2006), Short-lived mantle generated magmatic events and their dyke swarms: the key unlocking Earth's paleogeographic record back to 2.6 Ga, *in* E. J. Hanski, S. Mertanen, O. T. Rämö & J. I. Vuollo, eds, 'Dyke Swarms - Time Markers of Crustal Evolution', Taylor and Francis, pp. 3–26.

Boorman, S., Boudreau, A. & Kruger, F. J. (2004), 'The Lower Zone–Critical Zone Transition of the Bushveld Complex: a Quantitative Textural Study', *Journal of Petrology* **45**(6), 1209–1235.

Boudreau, A. E. (1999), 'PELE—a version of the MELTS software program for the PC platform', *Computers & Geosciences* **25**(2), 201–203.

Boudreau, A. E., Mathez, E. A. & McCallum, I. S. (1986*a*), 'Halogen geochemistry of the stillwater and bushveld complexes: evidence for transport of the platinum-group elements by cl-rich fluids', *Journal of Petrology* **27**(4), 967–986.

Boudreau, A. E., Mathez, E. A. & McCallum, I. S. (1986*b*), 'Halogen geochemistry of the Stillwater and Bushveld Complexes: evidence for transport of the platinum-group elements by Cl-rich fluids', *Journal of Petrology* **27**(4), 967–986.

Boudreau, A. E. & McCallum, I. S. (1992), 'Concentration of platinum-group elements by magmatic fluids in layered intrusions', *Economic Geology* **87**(7), 1830–1848.

Bruno, A. (2016), *The Nature of Soviet Power*, Cambridge University Press, 305p.

Buchanan, D. L. (1977), 'Cryptic variation in minerals from the Bushveld Complex rocks in the Bethal area', *Transactions of the Geological Society of South Africa* **80**, 49–52.

Buchanan, D. L. (1988), *Platinum-group element exploration*, Developments in Economic Geology, Elsevier.

Buchanan, D. L., Nolan, J., Suddaby, P., Rouse, J. E., Viljoen, M. J. & Davenport, J. W. J. (1981), 'The genesis of sulfide mineralization in a portion of the Potgietersrus Limb of the Bushveld Complex', *Economic Geology* **76**(3), 568–579.

Buchanan, P., Reimold, W., Koeberl, C. & Kruger, F. (2002), 'Geochemistry of intermediate to siliceous volcanic rocks of the Rooiberg Group, Bushveld Magmatic Province, South Africa', *Contributions to Mineralogy and Petrology* **144**(2), 131–143.

Button, A. (1973a), 'Algal stromatolites of the early Proterozoic Wolkberg Group, Transvaal sequence', *Journal of Sedimentary Research* **43**(1), 160–167.

Button, A. (1973b), A regional study of the stratigraphy and development of the Transvaal Basin in the eastern and northeastern Transvaal, PhD thesis, University of the Witwatersrand, 704p.

Button, A., Pretorius, D. A., Jansen, H., Stocklmayer, V., Hunter, D. R., Wilson, J. F., Wilson, A. H., Vermaak, C. F., Lee, C. A. & Stagman, J. G. (1981), Chapter 9: The cratonic environment, *in* D. R. Hunter, ed., 'Precambrian of the Southern Hemisphere', Amsterdam, The Netherlands, pp. 501–628.

Cameron, E. N. (1978*a*), 'An unusual titanium-rich oxide mineral from the eastern Bushveld Complex', *American Mineralogist* **63**, 37–39.

Cameron, E. N. (1978*b*), 'The Lower Zone of the eastern Bushveld Complex in the Olifants River Trough', *Journal of Petrology* **19**(3), 437–462.

Cameron, E. N. (1979), 'Titanium-bearing oxide minerals of the Critical Zone of the Eastern Bushveld Complex', *American Mineralogist* **64**(1), 140–150.

Cameron, E. N. (1980), 'Evolution of the Lower Critical Zone, central sector, eastern Bushveld Complex, and its chromite deposits', *Economic Geology* **75**(6), 845–871.

Campbell, I. H. (1978), 'Some problems with the cumulus theory', *Lithos* **11**(4), 311–323.

Campbell, I. H. & Kelly, P. R. (1978), 'The geochemistry of loveringite, a uranium-rare-earth-bearing accessory phase from the Jimberlana Intrusion of Western Australia', *Mineralogical Magazine* **42**(322), 187–193.

Campbell, I. H., Naldrett, A. J. & Barnes, S. J. (1983), 'A model for the origin of the platinum-rich sulfide horizons in the Bushveld and Stillwater complexes', *Journal of Petrology* **24**(2), 133–165.

Capobianco, C. J. & Drake, M. J. (1990), 'Partitioning of ruthenium, rhodium, and palladium between spinel and silicate melt and implications for platinum group element fractionation trends', *Geochimica et Cosmochimica Acta* **54**(3), 869–874.

Carr, H. W., Groves, D. I. & Cawthorn, R. G. (1994), 'The importance of synmagmatic deformation in the formation of Merensky Reef potholes in the Bushveld Complex', *Economic Geology* **89**(6), 1398–1410.

Carr, H. W., Kruger, F. J., Groves, D. I. & Cawthorn, R. G. (1999), 'The petrogenesis of Merensky Reef potholes at the Western Platinum Mine, Bushveld Complex: Sr-isotopic evidence for synmagmatic deformation', *Mineralium Deposita* **34**(4), 335–347.

Cawthorn, R. G. (2005), 'Pressure fluctuations and the formation of the PGE-rich Merensky and chromitite reefs, Bushveld Complex', *Mineralium Deposita* **40**(2), 231–235.

Cawthorn, R. G. (2007), 'Cr and Sr: Keys to parental magmas and processes in the Bushveld Complex, South Africa', *Lithos* **95**(3), 381–398.

Cawthorn, R. G. (2010), 'The Platinum Group Element Deposits of the Bushveld Complex in South Africa', *Platinum Metals Review* **54**(4), 205–215.

Cawthorn, R. G. (2015), The Bushveld Complex, South Africa, *in* B. Charlier, O. Namur, R. Latypov & C. Tegner, eds, 'Layered Intrusions', Springer Netherlands, pp. 517–587.

Cawthorn, R. G. & Barry, S. D. (1992), 'The role of intercumulus residua in the formation of pegmatoid associated with the UG2 chromitite, Bushveld Complex', *Australian Journal of Earth Sciences* **39**(3), 263–276.

Cawthorn, R. G., Davies, G., Clubley-Armstrong, A. & McCarthy, T. S. (1981), 'Sills associated with the Bushveld Complex, South Africa: an estimate of the parental magma composition', *Lithos* **14**(1), 1–16.

Cawthorn, R. G., Eales, H. V., Walraven, F., Uken, R. & Watkeys, M. K. (2006), The Bushveld Complex, *in* M. R. Johnson, C. R. Anhaeusser & R. J. Thomas, eds, 'The Geology of South Africa', Geological Society of South Africa, Johannesburg, pp. 261–281.

Cawthorn, R. G., Merkle, R. K. W. & Viljoen, M. J. (2002), Platinum-group element deposits in the Bushveld Complex, South Africa, *in* L. J. Cabri, ed., 'Geology, geochemistry, mineralogy and mineral beneficiation of platinum-group elements', Vol. 54, Canadian Institute of Mining, Metallurgy and Petroleum, Montreal, pp. 389–430.

Cawthorn, R. G. & Meyer, F. M. (1993), 'Petrochemistry of the Okiep copper district basic intrusive bodies, northwestern Cape Province, South Africa', *Economic Geology* **88**(3), 590–605.

Cawthorn, R. G., Meyer, P. S. & Kruger, F. J. (1991), 'Major addition of magma at the Pyroxenite Marker in the western Bushveld Complex, South Africa', *Journal of Petrology* **32**(4), 739–763.

Cawthorn, R. G. & Molyneux, T. G. (1986), Vanadiferous magnetite deposits of the Bushveld Complex, *in* C. R. Anhaeusser & S. Maske, eds, 'Mineral deposits of Southern Africa', Geological Society of South Africa, Johannesburg, pp. 1251–1266.

Cawthorn, R. G. & Webb, S. J. (2001), 'Connectivity between the western and eastern limbs of the Bushveld Complex', *Tectonophysics* **330**(3), 195–209.

Chadwick, J. P., Troll, V. R., Ginibre, C., Morgan, D., Gertisser, R., Waight, T. E. & Davidson, J. P. (2007), 'Carbonate assimilation at Merapi Volcano, Java, Indonesia: Insights from crystal isotope stratigraphy', *Journal of Petrology* **48**(9), 1793–1812.

Charlier, B. L. A., Bachmann, O., Davidson, J. P., Dungan, M. A. & Morgan, D. J. (2007), 'The upper crustal evolution of a large silicic magma body: Evidence from crystal-scale Rb–Sr isotopic heterogeneities in the Fish Canyon magmatic system, Colorado', *Journal of Petrology* **48**(10), 1875–1894.

Charlier, B. L. A., Ginibre, C., Morgan, D., Nowell, G. M., Pearson, D. G., Davidson, J. P. & Ottley, C. J. (2006), 'Methods for the microsampling and high-precision

analysis of strontium and rubidium isotopes at single crystal scale for petrological and geochronological applications', *Chemical Geology* **232**(3), 114–133.

Chashchin, V. V., Bayanova, T. B., Mitrofanov, F. P. & Serov, P. A. (2016), 'Low-Sulfide PGE ores in Paleoproterozoic Monchegorsk pluton and massifs of its southern framing, Kola Peninsula, Russia: Geological characteristic and isotopic geochronological evidence of polychronous ore–magmatic systems', *Geology of Ore Deposits* **58**(1), 37–57.

Chashchin, V. V., Bayanova, T. B., Yelizarova, I. R. & Serov, P. A. (2012), 'The Volchetundrovsky Massif of the autonomous anorthosite complex of the Main Range, the Kola Peninsula: Geological, petrogeochemical, and isotope-geochronological studies', *Petrology* **20**(5), 467–490.

Chashchin, V. V., Galkin, A. S., Ozeryanskii, V. V. & Dedyukhin, A. N. (1999), 'Sopcha lake chromite deposit and its platinum potential, Monchegorsk pluton, Kola Peninsula (Russia)', *Geology of Ore Deposits* **41**(6), 460–468.

Chashchin, V. V. & Mitrofanov, F. P. (2014), 'The Paleoproterozoic Imandra-Varzuga rifting structure (Kola Peninsula): intrusive magmatism and mineral-ageny', *Geodynamics & Tectonophysics* **5**(1), 231–256.

Chashchin, V. V. & Petrov, S. V. (2013), 'Low-sulfide PGE ore in the Volchetundra gabbro-anorthosite pluton, Kola Peninsula, Russia', *Geology of Ore Deposits* **55**(5), 357–382.

Chistyakova, S., Latypov, R. & Zaccarini, F. (2015), 'Chromitite dykes in the Monchegorsk Layered Intrusion, Russia: In situ crystallization from chromite-saturated magma flowing in conduits', *Journal of Petrology* **56**(12), 2395–2424.

Chutas, N. I., Bates, E., Prevec, S. A., Coleman, D. S. & Boudreau, A. E. (2012), 'Sr and Pb isotopic disequilibrium between coexisting plagioclase and orthopyroxene in the Bushveld Complex, South Africa: microdrilling and progressive leaching evidence for sub-liquidus contamination within a crystal mush', *Contributions to Mineralogy and Petrology* **163**(4), 653–668.

Clarke, B., Uken, R. & Reinhardt, J. (2009), 'Structural and compositional constraints on the emplacement of the Bushveld Complex, South Africa', *Lithos* **111**(1), 21–36.

Clendenin, C. W. (1989), Tectonic influence on the evolution of the early Proterozoic Transvaal Sea, southern Africa, PhD thesis, University of the Witwatersrand, 367p.

Coertze, F. J. & Schumann, F. W. (1962), 'The basic portion and associated minerals of the Bushveld igneous Complex north of Pilanesberg', *Geological Survey of South Africa Bulletin* **38**, 48.

Cole, J., Finn, C. A. & Webb, S. J. (2013), 'Overview of the magnetic signatures of the Palaeoproterozoic Rustenburg layered suite, Bushveld complex, South Africa', *Precambrian Research* **236**, 193–213.

Cousins, C. A. (1969), 'The Merensky Reef of the Bushveld Igneous Complex', *Economic Geology Monograph* **4**, 239–251.

Cousins, C. A. & Feringa, G. (1964), The chromite deposits of the western belt of the Bushveld Complex, *in* S. H. Haughton, ed., 'The geology of some ore deposits in Southern Africa', Vol. 2, Geological Society of South Africa, Johannesburg, pp. 183–202.

Crowson, P. C. F. (2001), *Mineral handbook 2000-2001*, Mining Journal Books, Edenbridge.

Cruden, A. R. (1998), 'On the emplacement of tabular granites', *Journal of the Geological Society* **155**(5), 853–862.

Davidson, J. P., Morgan, D. J., Charlier, B. L. A., Harlou, R. & Hora, J. M. (2007), 'Microsampling and isotopic analysis of igneous rocks: Implications for the study of magmatic systems', *Annual Review of Earth and Planetary Sciences* **35**(1), 273–311.

Davidson, J. P., Tepley III, F. J. & Knesel, K. M. (1998), 'Crystal isotope stratigraphy; a method for constraining magma differentiation pathways', *Eos* **79**, 185–189.

Davies, G., Cawthorn, R. G., Barton, J. M. & Morton, M. (1980), 'Parental magma to the Bushveld Complex', *Nature* **287**(5777), 33–35.

De Klerk, W. J. (1982), The geology, geochemistry and silicate mineralogy of the Upper Critical Zone of the North-western Bushveld Complex, at Rustenburg Platinum Mines, Union section, MSc thesis, Rhodes University, 210p.

De Klerk, W. J. (1991), Petrogenesis of the Upper Critical Zone in the western Bushveld Complex with emphasis on the UG1 Footwall and Bastard units, PhD thesis, Rhodes University, 424p.

de Villiers, J. S. (1970), 'The structure and petrology of the mafic rocks of the Bushveld Complex south of Potgietersrus', *Geological Survey of South Africa Special Publication* **1**, 23–35.

Dedeev, A. V., Khashkovskaya, T. N. & Galkin, A. S. (2002), PGE mineralization of the Monchegorsk layered mafic–ultramafic intrusion of the Kola Peninsula, *in* L. J. Cabri, ed., 'Geology, geochemistry, mineralogy and mineral beneficiation of platinum-group elements', Vol. 54, Canadian Institute of Mining, Metallurgy and Petroleum, Montreal, pp. 569–577.

Dedeev, A. V. & Kozyrev, S. M. (2000), *The geological, mineralogical and analytical studies of the igneous rocks and sulphide ores of the NKT Massif: Report on Contract 325n*, Institute Gipronickel, 88p.

Dokuchaeva, V. S. & Yakovlev, N. Y. (1994), Monchegorsk Pluton, *in* F. P. Mitrofanov & M. Torokhov, eds, 'Kola Belt of Layered Intrusions. Guide to Pre-Symposium Field Trip', 7th International Platinum Symposium, KSC RAS, pp. 71–104.

Duran, C. J., Barnes, S.-J., Pleše, P., Kudrna Prašek, M. K., Zientek, M. L. & Pagé, P. (2017), 'Fractional crystallization-induced variations in sulfides from the

Noril'sk-Talnakh mining district (polar Siberia, Russia)', *Ore Geology Reviews* **90**, 326–351.

Eales, H. V. (2002), 'Caveats in defining the magmas parental to the mafic rocks of the Bushveld Complex, and the manner of their emplacement: review and commentary', *Mineralogical Magazine* **66**(6), 815–832.

Eales, H. V. & Cawthorn, R. G. (1996), The Bushveld Complex, *in* R. G. Cawthorn, ed., 'Developments in Petrology', Vol. 15, Elsevier, pp. 181–229.

Eales, H. V., De Klerk, W. J., Butcher, A. R. & Kruger, F. J. (1990a), 'The cyclic unit beneath the UG1 chromitite (UG1FW unit) at RPM Union Section platinum mine - Rosetta stone of the Bushveld Upper Critical Zone', *Mineralogical Magazine* **54**, 23–43.

Eales, H. V., De Klerk, W. J. & Teigler, B. (1990b), 'Evidence for magma mixing processes within the Critical and Lower Zones of the northwestern Bushveld Complex, South Africa', *Chemical Geology* **88**(3), 261–278.

Eales, H. V., Marsh, J. S., Mitchell, A. A., De Klerk, W. J., Kruger, F. J. & Field, M. (1986), 'Some geochemical constraints upon models for the crystallization of the Upper Critical Zone–Main Zone interval, northwestern Bushveld Complex', *Mineralogical Magazine* **50**(358), 567–582.

Elburg, M., Vroon, P., van der Wagt, B. & Tchalikian, A. (2005), 'Sr and Pb isotopic composition of five USGS glasses (BHVO-2G, BIR-1G, BCR-2G, TB-1G, NKT-1G)', *Chemical Geology* **223**(4), 196–207.

Els, B. G., Van den Berg, W. A. & Mayer, J. J. (1995), 'The Black Reef Quartzite Formation in the western Transvaal: sedimentological and economic aspects, and significance for basin evolution', *Mineralium Deposita* **30**(2), 112–123.

Emeleus, C. H. (1986), The Rhum layered complex, inner Hebrides, Scotland, *in* I. Parsons, ed., 'Origins of igneous layering', Springer Science+Business Media Dordrecht, pp. 263–286.

Engelbrecht, J. P. (1985), 'The chromites of the Bushveld Complex in the Nietverdiend area', *Economic Geology* **80**(4), 896–910.

Eriksson, K. A., McCarthy, T. S. & Truswell, J. F. (1975), 'Limestone formation and dolomitization in a lower Proterozoic succession from South Africa', *Journal of Sedimentary Research* **45**(3).

Eriksson, P. G. & Altermann, W. (1998), 'An overview of the geology of the Transvaal Supergroup dolomites (South Africa)', *Environmental Geology* **36**(1-2), 179–188.

Eriksson, P. G., Altermann, W. & Hartzer, F. J. (2006), The Transvaal Supergroup and its precursors, *in* M. R. Johnson, C. R. Anhaeusser & R. J. Thomas, eds, 'The Geology of South Africa', Geological Society of South Africa, Johannesburg, pp. 237–260.

Eriksson, P. G., Schreiber, U. M. & Van der Neut, M. (1991), 'A review of the sedimentology of the Early Proterozoic Pretoria Group, Transvaal Sequence, South Africa: implications for tectonic setting', *Journal of African Earth Sciences (and the Middle East)* **13**(1), 107–119.

Eriksson, P. G., Schweitzer, J. K., Bosch, P. J. A., Schereiber, U. M., Van Deventer, J. L. & Hatton, C. J. (1993), 'The Transvaal sequence: an overview', *Journal of African Earth Sciences (and the Middle East)* **16**(1-2), 25–51.

Eurasia Mining PLC (2010), Licence Extension and Drilling Update. New Announcement RNS Number : 0197Y.

Eurasia Mining PLC (2017), Russian Subsoil Agency Approves Maiden Reserves. New Announcement RNS Number : 6202G.

Faure, G. (1986), *Principles of Isotope Geology*, John Wiley & Sons.

Gagnevin, D., Daly, J. S., Poli, G. & Morgan, D. (2005), 'Microchemical and Sr isotopic investigation of zoned K-feldspar megacrysts: Insights into the petrogenesis of a granitic system and disequilibrium crystal growth', *Journal of Petrology* **46**(8).

Gain, S. B. (1985), 'The geologic setting of the platiniferous UG-2 chromitite layer on the farm Maandagshoek, eastern Bushveld Complex', *Economic Geology* **80**(4), 925–943.

Gain, S. B. & Mostert, A. B. (1982), 'The geological setting of the platinoid and base metal sulfide mineralization in the Platreef of the Bushveld Complex in Drenthe, North of Potgietersrus', *Economic Geology* **77**(6), 1395–1404.

Ganino, C., Arndt, N. T., Chauvel, C., Jean, A. & Athurion, C. (2013a), 'Melting of carbonate wall rocks and formation of the heterogeneous aureole of the Panzhihua intrusion, China', *Geoscience Frontiers* **4**(5), 535–546.

Ganino, C., Arndt, N. T., Zhou, M.-F., Gaillard, F. & Chauvel, C. (2008), 'Interaction of magma with sedimentary wall rock and magnetite ore genesis in the Panzhihua mafic intrusion, SW China', *Mineralium Deposita* **43**(6), 677–694.

Ganino, C., Harris, C., Arndt, N. T., Prevec, S. A. & Howarth, G. H. (2013b), 'Assimilation of carbonate country rock by the parent magma of the Panzhihua Fe-Ti-V deposit (SW China): Evidence from stable isotopes', *Geoscience Frontiers* **4**(5), 547–554.

Gao, J.-F., Zhou, M.-F., Robinson, P. T., Wang, C. Y., Zhao, J.-H. & Malpas, J. (2015), 'Magma mixing recorded by Sr isotopes of plagioclase from dacites of the Quaternary Tengchong volcanic field, SE Tibetan Plateau', *Journal of Asian Earth Sciences* **98**, 1–17.

Gatehouse, B. M., Grey, I. E., Campbell, I. H. & Kelly, P. (1978), 'The crystal structure of loveringite - a new member of the crichtonite group', *American Mineralogist* **63**, 28–36.

Ginibre, C. & Davidson, J. P. (2014), 'Sr isotope zoning in plagioclase from Parinacota Volcano (Northern Chile): Quantifying magma mixing and crustal contamination', *Journal of Petrology* **55**(6), 1203–1238.

Godel, B. (2013), 'High-resolution X-ray computed tomography and its application to ore deposits: From data acquisition to quantitative three-dimensional

measurements with case studies from Ni-Cu-PGE deposits', *Economic Geology* **108**(8), 2005–2019.

Godel, B., Barnes, S.-J. & Maier, W. D. (2011), 'Parental magma composition inferred from trace element in cumulus and intercumulus silicate minerals: An example from the Lower and Lower Critical Zones of the Bushveld Complex, South-Africa', *Lithos* **125**(1), 537–552.

Good, N. & De Wit, M. J. (1997), 'The Thabazimbi-Murchison lineament of the Kaapvaal craton, South Africa: 2700 Ma of episodic deformation', *Journal of the Geological Society* **154**(1), 93–97.

Grebnev, R. A., Rundkvist, T. V. & Pripachkin, P. V. (2014), 'Geochemistry of mafic rocks of the PGE-bearing Vurechuaivench Massif (Monchegorsk Complex, Kola region)', *Geochemistry International* **52**(9), 726–739.

Grokhovskaya, T. L., Bakaev, G. F., Shelepina, E. P., Lapina, M. I., Laputina, I. P. & Muravitskaya, G. N. (2000), 'PGE mineralization in the Vuruchuaivench gabbronorite massif, Monchegorsk pluton (Kola Peninsula, Russia)', *Geology of Ore Deposits* **42**(2), 133–146.

Grokhovskaya, T. L., Bakaev, G. F., Sholokhnev, V. V., Lapina, M. I., Muravitskaya, G. N. & Voitekhovich, V. S. (2003), 'The PGE ore mineralization in the Monchegorsk magmatic layered complex (Kola Peninsula, Russia)', *Geology of Ore Deposits* **45**(4), 287–308.

Grokhovskaya, T. L., Lapina, M. I. & Mokhov, A. V. (2009), 'Assemblages and genesis of platinum-group minerals in low-sulfide ores of the Monchetundra deposit, Kola Peninsula, Russia', *Geology of Ore Deposits* **51**(6), 467–485.

Groshev, N. Y., Nitkina, E. A. & Mitrofanov, F. P. (2009), 'Two-phase mechanism of the formation of platinum-metal basites of the Fedorova Tundra intrusion on the Kola Peninsula: New data on geology and isotope geochronology', *Doklady Earth Sciences* **427**(2), 1012–1016.

Groves, D. I., Ho, S. E., Rock, N. M., Barley, M. E. & Muggeridge, M. T. (1987), 'Archean cratons, diamond and platinum: Evidence for coupled long-lived crust-mantle systems', *Geology* **15**(9), 801–805.

Guo, F., Maier, W. D., Vuollo, J. I., Lahaye, Y., Huhma, H., O'Brien, H. & Junttila, H. (2013), Geochemistry of the ca. 2.45 ga mafic dykes in northern finland: constraints on the origin of PGE mineralization in coeval layered intrusions, *in* 'Proceedings of the 12th SGA Biennial Meeting', pp. 997–1000.

Hall, A. L. (1932), 'The Bushveld Igneous Complex of the central Transvaal', *Memoirs of the Geological Survey of South Africa* **28**, 530.

Hanski, E., Huhma, H., Rastas, P. & Kamenetsky, V. S. (2001a), 'The Palaeoproterozoic komatiite–picrite association of Finnish Lapland', *Journal of Petrology* **42**(5), 855–876.

Hanski, E., Walker, R. J., Huhma, H. & Suominen, I. (2001b), 'The Os and Nd isotopic systematics of c. 2.44 Ga Akanvaara and Koitelainen mafic layered intrusions in northern Finland', *Precambrian Research* **109**(1), 73–102.

Harmer, R. E., Auret, J. M. & Eglington, B. M. (1995), 'Lead isotope variations within the Bushveld Complex, Southern Africa: a reconnaissance study', *Journal of African Earth Sciences* **21**(4), 595–606.

Harmer, R. E. & Sharpe, M. R. (1985), 'Field relations and strontium isotope systematics of the marginal rocks of the eastern Bushveld Complex', *Economic Geology* **80**(4), 813–837.

Hart, R. J., Andreoli, M. A. G., Tredoux, M. & de Wit, M. J. (1990), 'Geochemistry across an exposed section of Archaean crust at Vredefort, South Africa: with implications for mid-crustal discontinuities', *Chemical Geology* **82**, 21–50.

Hart, R. J., Welke, H. J. & Nicolaysen, L. O. (1981), 'Geochronology of the deep profile through Archean basement at Vredefort, with implications for early crustal evolution', *Journal of Geophysical Research: Solid Earth* **86**(B11), 10663–10680.

Haughton, D. R., Roeder, P. L. & Skinner, B. J. (1974), 'Solubility of sulfur in mafic magmas', *Economic Geology* **69**(4), 451–467.

Hawkesworth, C. J., Gallagher, K., Hergt, J. M. & McDermott, F. (1993), 'Mantle and slab contribution in arc magmas', *Annual Review of Earth and Planetary Sciences* **21**, 175–204.

Hayes, B., Ashwal, L. D., Webb, S. J. & Bybee, G. M. (2017), 'Large-scale magmatic layering in the Main Zone of the Bushveld Complex and episodic downward magma infiltration', *Contributions to Mineralogy and Petrology* **172**(2-3), 13.

Hiemstra, S. A. (1985), 'The distribution of some platinum-group elements in the UG-2 chromitite layer of the Bushveld Complex', *Economic Geology* **80**(4), 944–957.

Hiemstra, S. A. (1986), 'The distribution of chalcophile and platinum-group elements in the UG-2 chromitite layer of the Bushveld Complex', *Economic Geology* **81**(5), 1080–1086.

Hölttä, P., Balagansky, V., Garde, A. A., Mertanen, S., Peltonen, P., Slabunov, A., Sorjonen-Ward, P. & Whitehouse, M. (2008), 'Archean of Greenland and Fennoscandia', *Episodes* **31**(1), 13–19.

Holwell, D. A., Armitage, P. E. B. & McDonald, I. (2005), 'Observations on the relationship between the Platreef and its hangingwall', *Applied Earth Science* **114**(4), 199–207.

Holwell, D. A., Boyce, A. J. & McDonald, I. (2007), 'Sulfur isotope variations within the Platreef Ni-Cu-PGE deposit: genetic implications for the origin of sulfide mineralization', *Economic Geology* **102**(6), 1091–1110.

Holwell, D. A., Jones, A., Smith, J. W. & Boyce, A. J. (2013), 'New mineralogical and isotopic constraints on Main Zone-hosted PGE mineralisation at Moorddrift, northern Bushveld Complex', *Mineralium Deposita* **48**(6), 675–686.

Holwell, D. A. & Jordaan, A. (2006), 'Three-dimensional mapping of the Platreef at the Zwartfontein South mine: implications for the timing of magmatic events in the northern limb of the Bushveld Complex, South Africa', *Applied Earth Science* **115**(2), 41–48.

Holwell, D. A., Keays, R. R., Firth, E. A. & Findlay, J. (2014), 'Geochemistry and mineralogy of platinum-group element mineralization in the River Valley Intrusion, Ontario, Canada: A model for early-stage sulfur saturation and multistage emplacement and the implications for "contact-type" Ni-Cu-PGE sulfide mineralization', *Economic Geology* **109**(3), 689–712.

Holwell, D. A. & McDonald, I. (2006), 'Petrology, geochemistry and the mechanisms determining the distribution of platinum-group element and base metal sulphide mineralisation in the Platreef at Overysel, northern Bushveld Complex, South Africa', *Mineralium Deposita* **41**(6), 575–598.

Holwell, D. A. & McDonald, I. (2007), 'Distribution of platinum-group elements in the Platreef at Overysel, northern Bushveld Complex: a combined PGM and LA-ICP-MS study', *Contributions to Mineralogy and Petrology* **154**(2), 171–190.

Holwell, D. A., McDonald, I. & Butler, I. B. (2011), 'Precious metal enrichment in the Platreef, Bushveld Complex, South Africa: evidence from homogenized magmatic sulfide melt inclusions', *Contributions to Mineralogy and Petrology* **161**(6), 1011–1026.

Holzer, L., Barton, J., Paya, B. & Kramers, J. D. (1999), 'Tectonothermal history of the western part of the Limpopo Belt: tectonic models and new perspectives', *Journal of African Earth Sciences* **28**(2), 383–402.

Hoogewerff, J. A., Van Bergen, M. J., Vroon, P. Z., Hertogen, J., Wordel, R., Sneyers, A., Nasution, A., Varekamp, J. C., Moens, H. L. E. & Mouchel, D. (1997), 'U-series, Sr-Nd-Pb isotope and trace-element systematics across an active island arc-continent collision zone: Implications for element transfer at the slab-wedge interface', *Geochimica et Cosmochimica Acta* **61**(5), 1057–1072.

Huhma, H., Cliff, R. A., Perttunen, V. & Sakko, M. (1990), 'Sm-Nd and Pb isotopic study of mafic rocks associated with early Proterozoic continental rifting: the Peröpohja schist belt in northern Finland', *Contributions to Mineralogy and Petrology* **104**(3), 369–379.

Huhtelin, T. (2015), The Kemi Chromite Deposit, *in* W. D. Maier, H. Lahtinen, Raimo & H. O'Brien, eds, 'Mineral Deposits of Finland', Elsevier, pp. 165–178.

Hulbert, L. J. (1983), A petrological investigation of the Rustenburg Layered Suite and associated mineralization south of Potgietersrus, PhD thesis, University of Pretoria, 514p.

Huppert, H. E., Stephen, R. & Sparks, J. (1985), 'Cooling and contamination of mafic and ultramafic magmas during ascent through continental crust', *Earth and Planetary Science Letters* **74**(4), 371–386.

Huthmann, F. M., Yudovskaya, M. A., Frei, D. & Kinnaird, J. A. (2016), 'Geochronological evidence for an extension of the Northern Lobe of the Bushveld Complex, Limpopo Province, South Africa', *Precambrian Research* **280**, 61–75.

Huthmann, F. M., Yudovskaya, M. A., Kinnaird, J. A., McCreesh, M. & McDonald, I. (2018), 'Geochemistry and PGE of the lower mineralized Zone of the Waterberg Project, South Africa', *Ore Geology Reviews* **92**, 161–185.

Iljina, M. J. (1994), The Portimo layered igneous complex: with emphasis on diverse sulphide and platinum-group element deposits, PhD thesis, Oulu University, 158p.

Iljina, M. J., Alapieti, T. T. & McElduff, B. M. (1992), 'Platinum-group element mineralization in the Suhanko-Konttijärvi intrusion, Finland', *Australian Journal of Earth Sciences* **39**(3), 303–313.

Iljina, M. J. & Lee, C. A. (2005), 'PGE deposits in the marginal series of layered intrusions', *Exploration for platinum group element deposits. Mineralog Assoc Can Short Course Series* **35**, 75–96.

Irvine, T. N. (1980), Magmatic infiltration metasomatism, double-diffusive fractional crystallization, and adcumulus growth in the Muskox intrusion and other layered intrusions, *in* R. B. Hargraves, ed., 'Physics of Magmatic Processes', Princeton University Press, Princeton, NJ, pp. 325–384.

Irvine, T. N., Andersen, J. C. O. & Brooks, C. K. (1998), 'Included blocks (and blocks within blocks) in the Skaergaard intrusion: Geologic relations and the origins of rhythmic modally graded layers', *Geological Society of America Bulletin* **110**(11), 1398–1447.

Jerram, D. A., Cheadle, M. J. & Philpotts, A. R. (2003), 'Quantifying the building blocks of igneous rocks: Are clustered crystal frameworks the foundation?', *Journal of Petrology* **44**(11), 2033–2051.

Junge, M., Oberthür, T. & Melcher, F. (2014), 'Cryptic Variation of Chromite Chemistry, Platinum Group Element and Platinum Group Mineral Distribution in the Ug-2 Chromitite: An Example from the Karee Mine, Western Bushveld Complex, South Africa', *Economic Geology* **109**(3), 795–810.

Karykowski, B. T. & Maier, W. D. (2017), 'Microtextural characterisation of the Lower Zone in the western limb of the Bushveld Complex, South Africa: evidence for extensive melt migration within a sill complex', *Contributions to Mineralogy and Petrology* **172**(8), 60.

Karykowski, B. T., Maier, W. D., Pripachkin, P. V. & Groshev, N. Y. (2016), 'The Monchegorsk Layered Complex – a natural laboratory for mineral deposit types associated with layered intrusions', *Applied Earth Science* **125**(2), 87–87.

Karykowski, B. T., Polito, P. A., Maier, W. D., Gutzmer, J. & Krause, J. (2017), 'New insights into the petrogenesis of the Jameson Range layered intrusion and associated Fe-Ti-P-V-PGE-Au mineralisation, West Musgrave Province, Western Australia', *Mineralium Deposita* **52**(2), 233–255.

Kinloch, E. D. (1982), 'Regional trends in the platinum-group mineralogy of the Crit-

ical Zone of the Bushveld Complex, South Africa', *Economic Geology* **77**(6), 1328–1347.

Kinnaird, J. A. (2005), 'Geochemical evidence for multiphase emplacement in the southern Platreef', *Applied Earth Science* **114**(4), 225–242.

Kinnaird, J. A., Hutchinson, D., Schurmann, L., Nex, P. A. M. & de Lange, R. (2005), 'Petrology and mineralisation of the southern Platreef: northern limb of the Bushveld Complex, South Africa', *Mineralium Deposita* **40**(5), 576–597.

Kinnaird, J. A., Yudovskaya, M., McCreesh, M., Huthmann, F. & Botha, T. J. (2017), 'The Waterberg Platinum Group Element Deposit: Atypical Mineralization in Mafic-Ultramafic Rocks of the Bushveld Complex, South Africa', *Economic Geology* **112**(6), 1367–1394.

Klemm, D. D., Ketterer, S., Reichhardt, F., Steindl, J. & Weber-Diefenbach, K. (1985), 'Implication of vertical and lateral compositional variations across the Pyroxene Marker and its associated rocks in the upper part of the Main Zone in the eastern Bushveld Complex', *Economic Geology* **80**(4), 1007–1015.

Konnikov, E. G. & Orsoev, D. A. (1991), 'Nature of the rhythmically layered horizon of the Sopcha Massif, Monchegorsk Pluton', *Doklady Akademii Nauk SSSR* **320**(3), 696–699.

Kozlov, E. K. (1973), *Natural rock series of nickel-bearing intrusions and their metallogeny*, Nauka, 288p (in Russian).

Kozlov, M. V., Zvereva, E. L. & Zverev, V. E. (2009), Methodology of the research and description of polluters, *in* 'Impacts of Point Polluters on Terrestrial Biota', number 15 *in* 'Environmental Pollution', Springer Netherlands, pp. 15–106.

Kruger, F. J. (1990), 'The stratigraphy of the Bushveld Complex; a reappraisal and the relocation of the Main Zone boundaries', *South African Journal of Geology* **93**(2), 376–381.

Kruger, F. J. (1992), 'The origin of the Merensky cyclic unit: Sr-isotopic and mineralogical evidence for an alternative orthomagmatic model', *Australian Journal of Earth Sciences* **39**(3), 255–261.

Kruger, F. J. (1994), 'The Sr-isotopic stratigraphy of the western Bushveld Complex', *South African Journal of Geology* **97**(4), 393–398.

Kruger, F. J. (2005), 'Filling the Bushveld Complex magma chamber: lateral expansion, roof and floor interaction, magmatic unconformities, and the formation of giant chromitite, PGE and Ti-V-magnetitite deposits', *Mineralium Deposita* **40**(5), 451–472.

Kruger, F. J., Cawthorn, R. G. & Walsh, K. L. (1987), 'Strontium isotopic evidence against magma addition in the Upper Zone of the Bushveld Complex', *Earth and Planetary Science Letters* **84**(1), 51–58.

Kruger, F. J. & Marsh, J. S. (1982), 'Significance of $^{87}Sr/^{86}Sr$ ratios in the Merensky cyclic unit of the Bushveld Complex', *Nature* **298**(5869), 53–55.

Kruger, F. J. & Mitchell, A. A. (1985), 'Discontinuities and variations of Sr-isotope systematics in the Main Zone of the Bushveld Complex, and their relevance to PGE mineralization', *Canadian Mineralogist* **23**, 306–306.

Lahtinen, R., Garde, A. A. & Melezhik, V. A. (2008), 'Paleoproterozoic evolution of Fennoscandia and Greenland', *Episodes* **31**(1), 20–28.

Latypov, R. (2003), 'The origin of marginal compositional reversals in basic-ultrabasic sills and layered intrusions by Soret fractionation', *Journal of Petrology* **44**(9), 1579–1618.

Latypov, R., Chistyakova, S., Barnes, S. J. & Hunt, E. J. (2017), 'Origin of platinum deposits in layered intrusions by in situ crystallization: evidence from undercutting Merensky Reef of the Bushveld Complex', *Journal of Petrology* **58**(4), 715–761.

Latypov, R., Chistyakova, S., Page, A. & Hornsey, R. (2015), 'Field Evidence for the In Situ Crystallization of the Merensky Reef', *Journal of Petrology* **56**(12), 2341–2372.

Lee, C. A. (1996), A review of mineralization in the Bushveld Complex and some other layered intrusions, *in* R. G. Cawthorn, ed., 'Developments in Petrology', Vol. 15, Elsevier, pp. 103–145.

Lee, C. A. & Butcher, A. R. (1990), 'Cyclicity in the Sr isotope stratigraphy through the Merensky and Bastard Reef units, Atok section, eastern Bushveld Complex', *Economic Geology* **85**(4), 877–883.

Lee, C. A. & Tredoux, M. (1986), 'Platinum-group element abundances in the Lower and the Lower Critical Zones of the eastern Bushveld Complex', *Economic Geology* **81**(5), 1087–1095.

Lenhardt, N., Eriksson, P. G., Catuneanu, O. & Bumby, A. J. (2012), 'Nature of and controls on volcanism in the ca. 2.32–2.06 Ga Pretoria Group, Transvaal Supergroup, Kaapvaal Craton, South Africa', *Precambrian Research* **214**, 106–123.

Letts, S. A., Torsvik, T. H., Webb, S. J. & Ashwal, L. D. (2009), 'Palaeomagnetism of the 2054 Ma Bushveld Complex (South Africa): implications for emplacement and cooling', *Geophysical Journal International* **179**(2), 850–872.

Li, C., Naldrett, A. J., Coats, C. J. A. & Johannessen, P. (1992), 'Platinum, palladium, gold, copper-rich stringers at the Strathcona Mine, Sudbury; their enrichment by fractionation of a sulfide liquid', *Economic Geology* **87**(6), 1584–1598.

Lightfoot, P. C., Naldrett, A. J. & Hawkesworth, C. J. (1984), 'The geology and geochemistry of the Waterfall Gorge section of the Insizwa Complex with particular reference to the origin of the nickel sulfide deposits', *Economic Geology* **79**(8), 1857–1879.

Liu, P.-P., Zhou, M.-F., Wang, C. Y., Xing, C.-M. & Gao, J.-F. (2014), 'Open magma chamber processes in the formation of the Permian Baima mafic–ultramafic layered intrusion, SW China', *Lithos* **184–187**, 194–208.

Long, G. L. & Winefordner, J. D. (1983), 'Limit of detection. A closer look at the IUPAC definition', *Analytical Chemistry* **55**(7), 712A–724A.

Lorand, J. P., Cottin, J.-Y. & Parodi, G. C. (1987), 'Occurrence and petrological significance of loveringite in the Western Laouni layered complex, southern Hoggar, Algeria', *Canadian Mineralogist* **25**, 683–693.

Lundgaard, K. L. & Tegner, C. (2004), 'Partitioning of ferric and ferrous iron between plagioclase and silicate melt', *Contributions to Mineralogy and Petrology* **147**(4), 470–483.

Maier, W. D., Arndt, N. T. & Curl, E. A. (2000), 'Progressive crustal contamination of the Bushveld Complex: evidence from Nd isotopic analyses of the cumulate rocks', *Contributions to Mineralogy and Petrology* **140**(3), 316–327.

Maier, W. D. & Barnes, S.-J. (1996), 'Unusually high concentrations of magnetite at Caraíba and other Cu-sulfide deposits in the Curaçá valley, Bahia, Brazil', *Canadian Mineralogist* **34**(4), 717–731.

Maier, W. D. & Barnes, S.-J. (1998), 'Concentrations of rare earth elements in silicate rocks of the Lower, Critical and Main Zones of the Bushveld Complex', *Chemical Geology* **150**(1), 85–103.

Maier, W. D. & Barnes, S.-J. (1999), 'Platinum-group elements in silicate rocks of the Lower, Critical and Main Zones at Union Section, Western Bushveld Complex', *Journal of Petrology* **40**(11), 1647–1671.

Maier, W. D. & Barnes, S.-J. (2008), 'Platinum-group elements in the UG1 and UG2 chromitites, and the Bastard reef, at Impala platinum mine, western Bushveld Complex, South Africa: Evidence for late magmatic cumulate instability and reef constitution', *South African Journal of Geology* **111**(2-3), 159–176.

Maier, W. D. & Barnes, S.-J. (2010), 'The petrogenesis of platinum-group element reefs in the Upper Main Zone of the Northern Lobe of the Bushveld Complex on the farm Moorddrift, South Africa', *Economic Geology* **105**(4), 841–854.

Maier, W. D., Barnes, S.-J. & Groves, D. I. (2013), 'The Bushveld Complex, South Africa: formation of platinum–palladium, chrome- and vanadium-rich layers via

hydrodynamic sorting of a mobilized cumulate slurry in a large, relatively slowly cooling, subsiding magma chamber', *Mineralium Deposita* **48**(1), 1–56.

Maier, W. D., Barnes, S.-J. & Karykowski, B. T. (2016a), 'A chilled margin of komatiite and Mg-rich basaltic andesite in the western Bushveld Complex, South Africa', *Contributions to Mineralogy and Petrology* **171**(6), 57.

Maier, W. D., Barnes, S.-J. & Van der Merwe, M. J. (2001), 'Platinum-group elements in the Pyroxenite Marker, Bushveld Complex: implications for the formation of the Main Zone', *South African Journal of Geology* **104**(4), 301–308.

Maier, W. D., de Klerk, L., Blaine, J., Manyeruke, T., Barnes, S.-J., Stevens, M. V. A. & Mavrogenes, J. A. (2008), 'Petrogenesis of contact-style PGE mineralization in the northern lobe of the Bushveld Complex: comparison of data from the farms Rooipoort, Townlands, Drenthe and Nonnenwerth', *Mineralium Deposita* **43**(3), 255–280.

Maier, W. D. & Eales, H. V. (1997), 'Correlation within the UG2-Merensky Reef interval of the Western Bushveld Complex, based on geochemical, mineralogical and petrological data', *Bulletin of the Geological Survey of South Africa* **120**.

Maier, W. D., Karykowski, B. T. & Yang, S.-H. (2016b), 'Formation of transgressive anorthosite seams in the Bushveld Complex via tectonically induced mobilisation of plagioclase-rich crystal mushes', *Geoscience Frontiers* **7**(6), 875–889.

Maier, W. D., Määttää, S., Yang, S.-H., Oberthür, T., Lahaye, Y., Huhma, H. & Barnes, S.-J. (2015), 'Composition of the ultramafic–mafic contact interval of the Great Dyke of Zimbabwe at Ngezi mine: Comparisons to the Bushveld Complex and implications for the origin of the PGE reefs', *Lithos* **238**, 207–222.

Mangwegape, M., Roelofse, F., Mock, T. & Carlson, R. W. (2016), 'The Sr-isotopic stratigraphy of the Northern Limb of the Bushveld Complex, South Africa', *Journal of African Earth Sciences* **113**, 95–100.

Mank, A. J. G. & Mason, P. R. D. (1999), 'A critical assessment of laser ablation ICP-MS as an analytical tool for depth analysis in silica-based glass samples', *Journal of Analytical Atomic Spectrometry* **14**(8), 1143–1153.

Manyeruke, T. D., Maier, W. D. & Barnes, S.-J. (2005), 'Major and trace element geochemistry of the Platreef on the farm Townlands, northern Bushveld Complex', *South African Journal of Geology* **108**(3), 381–396.

Mathez, E. A. (1995), 'Magmatic metasomatism and formation of the Merensky Reef, Bushveld Complex', *Contributions to Mineralogy and Petrology* **119**(2), 277–286.

Mathez, E. A., Hunter, R. H. & Kinzler, R. (1997), 'Petrologic evolution of partially molten cumulate: the Atok section of the Bushveld Complex', *Contributions to Mineralogy and Petrology* **129**(1), 20–34.

Mathez, E. A. & Kent, A. J. R. (2007), 'Variable initial Pb isotopic compositions of rocks associated with the UG2 chromitite, eastern Bushveld Complex', *Geochimica et Cosmochimica Acta* **71**(22), 5514–5527.

Mathez, E. A. & Mey, J. L. (2005), 'Character of the UG2 chromitite and host rocks and petrogenesis of its pegmatoidal footwall, northeastern Bushveld Complex', *Economic Geology* **100**(8), 1617–1630.

Mathez, E. A. & Waight, T. E. (2003), 'Lead isotopic disequilibrium between sulfide and plagioclase in the bushveld complex and the chemical evolution of large layered intrusions', *Geochimica et Cosmochimica Acta* **67**(10), 1875–1888.

McCouri, S. & Vearncombe, J. R. (1987), 'Shear zones bounding the central zone of the Limpopo mobile belt, southern Africa', *Journal of Structural Geology* **9**(2), 127–137.

McDonald, I., Harmer, R. E., Holwell, D. A., Hughes, H. S. R. & Boyce, A. J. (2017), 'Cu-Ni-PGE mineralisation at the Aurora Project and potential for a new PGE province in the Northern Bushveld Main Zone', *Ore Geology Reviews* **80**, 1135–1159.

McDonald, I. & Holwell, D. A. (2007), 'Did lower zone magma conduits store PGE-rich sulphides that were later supplied to the Platreef?', *South African Journal of Geology* **110**(4), 611–616.

McDonald, I. & Holwell, D. A. (2011), 'Geology of the Northern Bushveld Complex and the setting and genesis of the Platreef Ni-Cu-PGE deposit', *Reviews in Economic Geology* **17**, 297–327.

McDonald, I., Holwell, D. A. & Armitage, P. E. B. (2005), 'Geochemistry and mineralogy of the Platreef and "Critical Zone" of the northern lobe of the Bushveld Complex, South Africa: implications for Bushveld stratigraphy and the development of PGE mineralisation', *Mineralium Deposita* **40**(5), 526–549.

McDonald, I. & Viljoen, K. S. (2006), 'Platinum-group element geochemistry of mantle eclogites: a reconnaissance study of xenoliths from the Orapa kimberlite, Botswana', *Applied Earth Science* **115**(3), 81–93.

McDonough, W. F. & Sun, S.-s. (1995), 'The composition of the Earth', *Chemical Geology* **120**(3), 223–253.

Melezhik, V. A. & Sturt, B. A. (1994), 'General geology and evolutionary history of the early proterozoic Polmak-Pasvik-Pechenga-Imandra/Varzuga-Ust'Ponoy greenstone belt in the northeastern Baltic Shield', *Earth-Science Reviews* **36**(3), 205–241.

Merensky, H. (1925), 'The platinum occurrence on the properties of Potgietersrus Platinums Limited Report to the Directors', *London and Rhodesia Mining and Land Company Limited, Johannesburg* .

Meurer, W. P. & Boudreau, A. E. (1996), 'Compaction of density-stratified cumulates: effect on trapped-liquid distribution', *The Journal of Geology* **104**(1), 115–120.

Meurer, W. P. & Meurer, M. E. S. (2006), 'Using apatite to dispel the "trapped liquid" concept and to understand the loss of interstitial liquid by compaction in

mafic cumulates: an example from the Stillwater Complex, Montana', *Contributions to Mineralogy and Petrology* **151**(2), 187–201.

Miller, J. D., Green, J. C., Severson, M. J., Chandler, V. W., Hauck, S. A., Peterson, D. M. & Wahl, T. E. (2002), 'Geology and mineral potential of the Duluth Complex and related rocks of northeastern Minnesota', *Minnesota Geological Survey Report of Investigations* **58**, 207.

Mitchell, A. A. (1986), The petrology, mineralogy and geochemistry of the Main Zone of the Bushveld Complex at Rustenburg Platinum Mines, Union Section, Phd thesis, Rhodes University, 254p.

Mitchell, A. A. (1990), 'The stratigraphy, petrography and mineralogy of the Main Zone of the northwestern Bushveld Complex', *South African Journal of Geology* **93**(5), 818–831.

Mitrofanov, F. P., Balagansky, V. V., Balashov Y. A., Gannibal, L. F., Dokuchaeva, V. S., Nerovich, K. I., Radchenko, M. K. & Ryungenen, G. I. (1995), 'U-Pb age of gabbro-anorthosite massifs in the Lapland Granulite belt', *Norges Geologiske Undersokelse Special Paper* **7**, 179–183.

Müller, W., Aerden, D. & Halliday, A. N. (2000), 'Isotopic dating of strain fringe increments: Duration and rates of deformation in shear zones', *Science* **288**(5474), 2195–2198.

Müller, W., Kelley, S. P. & Villa, I. M. (2002), 'Dating fault-generated pseudotachylytes: comparison of $^{40}Ar/^{39}Ar$ stepwise-heating, laser-ablation and Rb–Sr microsampling analyses', *Contributions to Mineralogy and Petrology* **144**(1), 57–77.

Molyneux, T. G. (1970), A geological investigation of the Bushveld Complex in Sekhukhuneland and part of the Steelpoort Valley, eastern Transvaal, with particular reference to the oxide minerals, DSc thesis, University of Pretoria, 250p.

Mondal, S. K. & Mathez, E. A. (2006), 'Origin of the UG2 chromitite layer, Bushveld Complex', *Journal of Petrology* **48**(3), 495–510.

Mungall, J. E., Kamo, S. L. & McQuade, S. (2016), 'U–Pb geochronology documents out-of-sequence emplacement of ultramafic layers in the Bushveld Igneous Complex of South Africa', *Nature Communications* **7**, 13385.

Mungall, J. E. & Naldrett, A. J. (2008), 'Ore deposits of the platinum-group elements', *Elements* **4**(4), 253–258.

Mutanen, T. (1997), *Geology and ore petrology of the Akanvaara and Koitelainen mafic layered intrusions and the Keivitsa-Satovaara layered complex, northern Finland*, Vol. 395, Geological Survey of Finland.

Naldrett, A. J. (1989), 'Stratiform PGE deposits in layered intrusions', *Reviews in Economic Geology* **4**, 135–166.

Naldrett, A. J. (2004), *Magmatic Sulfide Deposits: Geology, Geochemistry and Exploration*, Springer Berlin Heidelberg.

Naldrett, A. J. (2011), 'Fundamentals of magmatic sulfide deposits', *Reviews in Economic Geology* **17**, 1–50.

Naldrett, A. J., Gasparrini, E. C., Barnes, S. J., Von Gruenewaldt, G. & Sharpe, M. R. (1986), 'The Upper Critical Zone of the Bushveld Complex and the origin of Merensky-type ores', *Economic Geology* **81**(5), 1105–1117.

Naldrett, A. J., Kinnaird, J., Wilson, A. H. & Chunnett, G. (2008), 'Concentration of PGE in the Earth's Crust with Special Reference to the Bushveld Complex', *Earth Science Frontiers* **15**(5), 264–297.

Naldrett, A. J. & Wilson, A. H. (1990), 'Horizontal and vertical variations in noble-metal distribution in the Great Dyke of Zimbabwe: A model for the origin of the PGE mineralization by fractional segregation of sulfide', *Chemical Geology* **88**(3-4), 279–300.

Naldrett, A. J., Wilson, A., Kinnaird, J. & Chunnett, G. (2009), 'PGE tenor and metal ratios within and below the Merensky Reef, Bushveld Complex: implications for its genesis', *Journal of Petrology* **50**(4), 625–659.

Naslund, H. R. & McBirney, A. R. (1996), Mechanisms of formation of igneous layering, *in* R. G. Cawthorn, ed., 'Developments in Petrology', Vol. 15, Elsevier, pp. 1–43.

Nebel, O., Scherer, E. E. & Mezger, K. (2011), 'Evaluation of the ^{87}Rb decay constant by age comparison against the U-Pb system', *Earth and Planetary Science Letters* **301**(1), 1–8.

Nex, P. A. M. (2005), 'The structural setting of mineralisation on Tweefontein Hill, northern limb of the Bushveld Complex, South Africa', *Applied Earth Science: Transactions of the Institution of Mining & Metallurgy, Section B* **114**(4), 243–251.

Nicholson, D. M. & Mathez, E. A. (1991), 'Petrogenesis of the Merensky Reef in the Rustenburg section of the Bushveld Complex', *Contributions to Mineralogy and Petrology* **107**(3), 293–309.

Nixon, G. T., Cabri, L. J. & Gilles Laflamme, J. (1990), 'Platinum-group-element mineralization in lode and placer deposits associated with the Tulameen alaskan-type complex, British Columbia', *The Canadian Mineralogist* **28**(3), 503–535.

Oberthür, T. (2002), Platinum-group element mineralization of the Great Dyke, Zimbabwe, *in* L. J. Cabri, ed., 'Geology, geochemistry, mineralogy and mineral beneficiation of platinum-group elements', Vol. 54, Canadian Institute of Mining, Metallurgy and Petroleum, Montreal, pp. 483–506.

Olszak-Humienik, M. & Jablonski, M. (2014), 'Thermal behavior of natural dolomite', *Journal of Thermal Analysis and Calorimetry* **119**(3), 2239–2248.

Ozawa, K. (1984), 'Olivine-spinel geospeedometry: Analysis of diffusion-controlled Mg-Fe^{2+} exchange', *Geochimica et Cosmochimica Acta* **48**(12), 2597–2611.

Page, N. J. (1979), 'Stillwater Complex, Montana: Structure, mineralogy, and petrology of the Basal Zone with emphasis on the occurrence of sulfides', *Geological Survey Professional Paper* **1038**.

Pechersky, D. M., Lyubushin, A. A. & Zakharov, V. S. (2004), 'Continuous record of geomagnetic field variations during cooling of the Monchegorsk, Kivakka and Bushveld Early Proterozoic layered intrusions', *Russian Journal of Earth Sciences* **6**(6), 391–456.

Peck, D. C. & Keays, R. R. (1990), 'Insights into the behavior of precious metals in primitive, S-undersaturated magmas; evidence from the Heazlewood River complex, Tasmania', *The Canadian Mineralogist* **28**(3), 553–577.

Peck, D. C., Keays, R. R., James, R. S., Chubb, P. T. & Reeves, S. J. (2001), 'Controls on the formation of contact-type platinum-group element mineralization in the East Bull Lake intrusion', *Economic Geology* **96**(3), 559–581.

Penberthy, C. J. & Merkle, R. K. W. (1999), 'Lateral variations in the platinum-group element content and mineralogy of the UG2 chromitite layer, Bushveld Complex', *South African Journal of Geology* **102**(3).

Penniston-Dorland, S. C., Wing, B. A., Nex, P. A. M., Kinnaird, J. A., Farquhar, J., Brown, M. & Sharman, E. R. (2008), 'Multiple sulfur isotopes reveal a magmatic origin for the Platreef platinum group element deposit, Bushveld Complex, South Africa', *Geology* **36**(12), 979–982.

Petrov, O. V., Morozov, A. F., Shatov, V. V., Molchanov, A. V., Terekhov, A. V., Lukyanova, L. I., Artem'ev, D. S., Belova, V. N. & Khalenev, V. O. (2016), Chapter 9: Russia, *in* R. Boyd, T. Bjerkgard, B. Nordahl & H. Schiellerup, eds, 'Mineral Resources in the Arctic', NGU - Geological Survey of Norway, p. 484.

Phinney, W. C. (1992), 'Partition coefficients for iron between plagioclase and basalt as a function of oxygen fugacity: Implications for Archean and lunar anorthosites', *Geochimica et Cosmochimica Acta* **56**(5), 1885–1895.

Piccoli, P. M. & Candela, P. A. (2002), 'Apatite in Igneous Systems', *Reviews in Mineralogy and Geochemistry* **48**(1), 255–292.

Prevec, S. A., Ashwal, L. D. & Mkaza, M. S. (2005), 'Mineral disequilibrium in the Merensky Reef, western Bushveld Complex, South Africa: new Sm–Nd isotopic evidence', *Contributions to Mineralogy and Petrology* **149**(3), 306–315.

Pripachkin, P. V., Kostenko, L. & Rundkvist, T. V. (2005), The localization of PGE-mineralization in the Vurechuaivench Member of the 2.5 Ga Monchegorsk Mafic Layered Complex (Kola Peninsula, Russia) based on cumulus stratigraphy, *in* T. O. Törmänen & T. T. Alapieti, eds, 'Proceedings of the 10th International Platinum Symposium: Platinum-group elements – from genesis to beneficiation and environmental impact', Geological Survey of Finland, Espoo, Finland, pp. 369–372.

Pripachkin, P. V. & Rundkvist, T. V. (2008), 'Geology and platinum potential of the southwestern part of the foothills Vuruchuaivench massif (Monchegorsk Complex, Kola Peninsula)', *Rudy i Metally* **5**, 61–68.

Pripachkin, P. V., Rundkvist, T. V., Miroshnikova, Y. A., Chernyavsky, A. V. & Borisenko, E. S. (2016), 'Geological structure and ore mineralization of the South Sopchinsky and Gabbro-10 massifs and the Moroshkovoe Lake target, Monchegorsk area, Kola Peninsula, Russia', *Mineralium Deposita* **51**(8), 973–992.

Pronost, J., Harris, C. & Pin, C. (2008), 'Relationship between footwall composition, crustal contamination, and fluid–rock interaction in the Platreef, Bushveld Complex, South Africa', *Mineralium Deposita* **43**(8), 825–848.

Puchtel, I. S., Haase, K. M., Hofmann, A. W., Chauvel, C., Kulikov, V. S., Garbe-Schönberg, C. D. & Nemchin, A. A. (1997), 'Petrology and geochemistry of crustally contaminated komatiitic basalts from the Vetreny Belt, southeastern Baltic Shield: Evidence for an early Proterozoic mantle plume beneath rifted Archean continental lithosphere', *Geochimica et Cosmochimica Acta* **61**(6), 1205–1222.

Ramos, F. C., Wolff, J. A. & Tollstrup, D. L. (2004), 'Measuring $^{87}Sr/^{86}Sr$ variations in minerals and groundmass from basalts using LA-MC-ICPMS', *Chemical Geology* **211**(1), 135–158.

Ramos, F. C., Wolff, J. A. & Tollstrup, D. L. (2005), 'Sr isotope disequilibrium in Columbia River flood basalts: Evidence for rapid shallow-level open-system processes', *Geology* **33**(6), 457–460.

Rankenburg, K., Lassiter, J. C. & Brey, G. (2004), 'Origin of megacrysts in volcanic rocks of the Cameroon volcanic chain – constraints on magma genesis and crustal contamination', *Contributions to Mineralogy and Petrology* **147**(2), 129–144.

Reid, D. L. & Basson, I. J. (2002), 'Iron-rich ultramafic pegmatite replacement bodies within the Upper Critical Zone, Rustenburg Layered Suite, Northam Platinum Mine, South Africa', *Mineralogical Magazine* **66**(6), 895–914.

Richardson, S. H. & Shirey, S. B. (2008), 'Continental mantle signature of Bushveld magmas and coeval diamonds', *Nature* **453**(7197), 910–913.

Roberts, M. D., Reid, D. L., Miller, J. A., Basson, I. J., Roberts, M. & Smith, D. (2007), 'The Merensky Cyclic Unit and its impact on footwall cumulates below Normal and Regional Pothole reef types in the Western Bushveld Complex', *Mineralium Deposita* **42**(3), 271–292.

Roeder, P. L. & Emslie, R. F. (1970), 'Olivine-liquid equilibrium', *Contributions to Mineralogy and Petrology* **29**(4), 275–289.

Roelofse, F. (2010), Constraints on the magmatic evolution of the Lower Main Zone and Platreef on the northern limb of the Bushveld Complex as inferred from the Moordkopje drill core, PhD thesis, University of Witwatersrand, 155p.

Roelofse, F. & Ashwal, L. D. (2012), 'The lower Main Zone in the northern limb of the Bushveld Complex - a >1.3 km thick sequence of intruded and variably contaminated crystal mushes', *Journal of Petrology* **53**(7), 1449–1476.

Roelofse, F., Ashwal, L. D. & Romer, R. L. (2015), 'Multiple, isotopically heterogeneous plagioclase populations in the Bushveld Complex suggest mush intrusion', *Chemie der Erde - Geochemistry* **75**(3), 357–364.

Rundkvist, D. V. & Sokolova, V. N. (1978), 'Ore zoning in the Monchegorsk Cu-Ni deposit', *Zapisky Vsesoyuznogo Mineralogicheskogo Obshchestva* **2**(6), 633–649.

Rundkvist, T. V., Bayanova, T. B., Sergeev, S. A., Pripachkin, P. V. & Grebnev, R. A. (2014), 'The Paleoproterozoic Vurechuaivench layered Pt-bearing pluton, Kola Peninsula: New results of the U-Pb (ID-TIMS, SHRIMP) dating of baddeleytte and zircon', *Doklady Earth Sciences* **454**(1), 1–6.

Rundqvist, D. V. & Mitrofanov, F. P. (1993), The Eastern Baltic Shield, *in* 'Precambrian Geology of the USSR', Vol. 9 of *Developments in Precambrian Geology*, Elsevier, pp. 25–123.

Saini-Eidukat, B., Alapieti, T. T., Thalhammer, O. A. R. & Iljina, M. J. (1997), Siliceous, high-magnesian parental magma compositions of the PGE-rich Early Proterozoic layered intrusion belt of northern Finland, *in* P. Rongfu, ed., 'Proceedings of the 30th International Geological Congress', Vol. 9, VSP, pp. 177–197.

Savard, D., Barnes, S.-J. & Meisel, T. (2010), 'Comparison between nickel-sulfur fire assay Te Co-precipitation and isotope dilution with high-pressure asher acid digestion for the determination of platinum-group elements, rhenium and gold', *Geostandards and Geoanalytical Research* **34**(3), 281–291.

Schissel, D., Tsvetkov, A. A., Mitrofanov, F. P. & Korchagin, A. U. (2002), 'Basal platinum-group element mineralization in the Federov Pansky layered mafic intrusion, Kola Peninsula, Russia', *Economic Geology* **97**(8), 1657–1677.

Schoenberg, R., Kruger, F. J., Nägler, T. F., Meisel, T. & Kramers, J. D. (1999), 'PGE enrichment in chromitite layers and the Merensky Reef of the western Bushveld Complex; a Re–Os and Rb–Sr isotope study', *Earth and Planetary Science Letters* **172**(1), 49–64.

Schouwstra, R. P., Kinloch, E. D. & Lee, C. A. (2000), 'A short geological review of the Bushveld Complex', *Platinum Metals Review* **44**(1), 33–39.

Scoates, J. S. & Friedman, R. M. (2008), 'Precise age of the platiniferous Merensky Reef, Bushveld Complex, South Africa, by the U-Pb zircon chemical abrasion ID-TIMS technique', *Economic Geology* **103**(3), 465–471.

Scoates, J. S. & Wall, C. J. (2015), Geochronology of Layered Intrusions, *in* B. Charlier, O. Namur, R. Latypov & C. Tegner, eds, 'Layered Intrusions', Springer Netherlands, pp. 3–74.

Scoon, R. N. & Mitchell, A. A. (2004), 'Petrogenesis of discordant magnesian dunite pipes from the central sector of the eastern Bushveld Complex with emphasis on the Winnaarshoek Pipe and disruption of the Merensky Reef', *Economic Geology* **99**(3), 517–541.

Scoon, R. N. & Mitchell, A. A. (2012), 'The Upper Zone of the Bushveld Complex at Roossenekal, South Africa: Geochemical stratigraphy and evidence of multiple episodes of magma replenishment', *South African Journal of Geology* **115**(4), 515–534.

Scoon, R. N. & Teigler, B. (1995), 'A new LG-6 chromite reserve at Eerste Geluk in the boundary zone between the central and southern sectors of the eastern Bushveld Complex', *Economic Geology* **90**(4), 969–982.

Seabrook, C. L. (2005), The Upper Critical and Lower Main Zones of the eastern Bushveld Complex, PhD thesis, University of Witwatersrand, 211p.

Seabrook, C. L., Cawthorn, R. G. & Kruger, F. J. (2005), 'The Merensky Reef, Bushveld Complex: mixing of minerals not mixing of magmas', *Economic Geology* **100**(6), 1191–1206.

Serov, P. A., Nitkina, E. A., Bayanova, T. B. & Mitrofanov, F. P. (2007), 'Comparison of new U-Pb and Sm-Nd isotope data on rocks of the early barren phase and basal ore-bearing rocks in the PGE-bearing Fedorovo-Pana layered massif, Kola Peninsula', *Doklady Earth Sciences* **416**(1), 1125–1127.

Sharkov, E. V. & Bogatikov, O. A. (1998), 'Concentration mechanisms of the platinum-group elements in layered intrusions of the Kola-Karelia region', *Geology of Ore Deposits* **40**, 372–390.

Sharkov, E. V. & Chistyakov, A. V. (2012), 'The Early Paleoproterozoic Monchegorsk layered mafite-ultramafite massif in the Kola Peninsula: Geology, petrology, and ore potential', *Petrology* **20**(7), 607–639.

Sharkov, E. V. & Chistyakov, A. V. (2014), 'Geological and petrological aspects of Ni-Cu-PGE mineralization in the early Paleoproterozoic Monchegorsk layered mafic-ultramafic complex, Kola Peninsula', *Geology of Ore Deposits* **56**(3), 147–168.

Sharman, E. R., Penniston-Dorland, S. C., Kinnaird, J. A., Nex, P. A. M., Brown, M. & Wing, B. A. (2013), 'Primary origin of marginal Ni-Cu-(PGE) mineralization in layered intrusions: Δ 33 S evidence from the Platreef, Bushveld, South Africa', *Economic Geology* **108**(2), 365–377.

Sharman-Harris, E. R., Kinnaird, J. A., Harris, C. & Horstmann, U. E. (2005), 'A new look at sulphide mineralisation of the northern limb, Bushveld Complex: a stable isotope study', *Applied Earth Science* **114**(4), 252–263.

Sharpe, M. R. (1981), 'The chronology of magma influxes to the eastern compartment of the Bushveld Complex as exemplified by its marginal border groups', *Journal of the Geological Society* **138**(3), 307–326.

Sharpe, M. R. (1985), 'Strontium isotope evidence for preserved density stratification in the Main Zone of the Bushveld Complex, South Africa', *Nature* **316**(6024), 119–126.

Silver, P. G., Fouch, M. J., Gao, S. S. & Schmitz, M. (2004), 'Seismic anisotropy, mantle fabric, and the magmatic evolution of Precambrian southern Africa', *South African Journal of Geology* **107**(1-2), 45–58.

Singh, J. & Johannes, W. (1996), 'Dehydration melting of tonalites. Part I. Beginning of melting', *Contributions to Mineralogy and Petrology* **125**(1), 16–25.

Smith, J. W., Holwell, D. A., McDonald, I. & Boyce, A. J. (2016), 'The application of S isotopes and S/Se ratios in determining ore-forming processes of magmatic Ni–Cu–PGE sulfide deposits: A cautionary case study from the northern Bushveld Complex', *Ore Geology Reviews* **73**, 148–174.

Smolkin, V. F., Fedotov, Z. A., Orsoev, D. A. & Ohnenstetter, D. (2004), Ore-bearing layered Monchepluton, *in* F. P. Mitrofanov & V. F. Smolkin, eds, 'Layered intrusions of the Monchegorsk ore region: petrology, mineralization, isotopy, deep structure', Vol. 1, KSC RAS, Apatity, pp. 36–75.

Smolkin, V. F. & Neradovsky, Y. N. (2006), The Monchegorsk ore district, Kola Peninsula, *in* V. F. Smolkin, ed., 'Field trip guidebook to the 12th IAGOD Symposium "Understanding the genesis of ore deposits to meet the demands of the 21st century"', "Science and Our Future" Foundation, pp. 13–40.

Spandler, C. & Pirard, C. (2013), 'Element recycling from subducting slabs to arc crust: A review', *Lithos* **170-171**, 208–223.

Swart, Q. D. (1999), Carbonate rocks of the Paleoproterozoic Pretoria and Postmasburg Groups, Transvaal Supergroup, MSc thesis, Rand Afrikaans University, 126p.

Tait, S. & Jaupart, C. (1992), 'Compositional convection in a reactive crystalline mush and melt differentiation', *Journal of Geophysical Research: Solid Earth* **97**, 6735–6756.

Tanner, D., Mavrogenes, J. A., Arculus, R. J. & Jenner, F. E. (2014), 'Trace Element Stratigraphy of the Bellevue Core, Northern Bushveld: Multiple Magma Injections Obscured by Diffusive Processes', *Journal of Petrology* **55**(5), 859–882.

Tarkian, M. & Mutanen, T. (1987), 'Loveringite from the Koitelainen layered intrusion, northern Finland', *Mineralogy and Petrology* **37**(1), 37–50.

Tegner, C., Cawthorn, R. G. & Kruger, F. J. (2006), 'Cyclicity in the Main and Upper Zones of the Bushveld Complex, South Africa: Crystallization from a Zoned Magma Sheet', *Journal of Petrology* **47**(11), 2257–2279.

Teigler, B. (1990), Mineralogy, petrology and geochemistry of the Lower and Lower Critical Zones, northwestern Bushveld Complex, PhD thesis, Rhodes University, 247p.

Teigler, B. & Eales, H. V. (1996), 'The Lower and Critical Zones of the western limb of the Bushveld Complex as intersected by the Nooitgedacht boreholes', *Bulletin of the Geological Survey of South Africa* **111**.

Tepley, F. J. & Davidson, J. P. (2003), 'Mineral-scale Sr-isotope constraints on magma evolution and chamber dynamics in the Rum layered intrusion, Scotland', *Contributions to Mineralogy and Petrology* **145**(5), 628–641.

Tollari, N., Baker, D. R. & Barnes, S.-J. (2008), 'Experimental effects of pressure and fluorine on apatite saturation in mafic magmas, with reference to layered intrusions and massif anorthosites', *Contributions to Mineralogy and Petrology* **156**(2), 161–175.

van der Merwe, M. J. (1976), 'The layered sequence of the Potgietersrus limb of the Bushveld Complex', *Economic Geology* **71**(7), 1337–1351.

VanTongeren, J. A. & Mathez, E. A. (2013), 'Incoming magma vomposition and style of recharge below the Pyroxenite Marker, eastern Bushveld Complex, South Africa', *Journal of Petrology* **54**(8), 1585–1605.

Veizer, J., Clayton, R. N. & Hinton, R. W. (1992), 'Geochemistry of precambrian carbonates: IV. Early paleoproterozoic (2.25 ± 0.25 Ga) seawater', *Geochimica et Cosmochimica Acta* **56**(3), 875–885.

Vermaak, C. F. (1976), 'The Merensky Reef; thoughts on its environment and genesis', *Economic Geology* **71**(7), 1270–1298.

Vermaak, C. F. (1985), 'The UG2 layer - South Africa's slumbering chromitite giant', *Chromium Review* **1**(5), 9–22.

Vermaak, C. F. (1995), *Platinum-group metals: a global perspective*, Mintek, 247p.

Vermaak, C. F. & Hendriks, L. P. (1976), 'A review of the mineralogy of the Merensky Reef, with specific reference to new data on the precious metal mineralogy', *Economic Geology* **71**(7), 1244–1269.

Viljoen, M. J. (1999), 'The nature and origin of the Merensky Reef of the western Bushveld Complex based on geological facies and geological data', *South African Journal of Geology* **102**(3).

Vogel, D. C., Vuollo, J. I., Alapieti, T. T. & James, R. S. (1998), 'Tectonic, stratigraphic, and geochemical comparisons between ca. 2500-2440 Ma mafic igneous events in the Canadian and Fennoscandian Shields', *Precambrian Research* **92**(2), 89–116.

von Gruenewaldt, G. (1971), A petrological and mineralogical investigation of the rocks of the Bushveld Igneous Complex in the Tauteshoogte-Roossenekal area of the eastern Transvaal, DSc thesis, University of Pretoria, 198p.

von Gruenewaldt, G. (1973), 'The Main and Upper zones of the Bushveld Complex in the Roossenekal area, Eastern Transvaal', *Transactions of the Geological Society of South Africa* **76**, 207–227.

Von Gruenewaldt, G., Hatton, C. J. & Merkle, R. K. W. (1986), 'Platinum-group element-chromitite associations in the Bushveld Complex', *Economic Geology* **81**(5), 1067–1079.

Von Gruenewaldt, G., Hulbert, L. J. & Naldrett, A. J. (1989), 'Contrasting platinum-group element concentration patterns in cumulates of the Bushveld Complex', *Mineralium deposita* **24**(3), 219–229.

Voordouw, R. J., Gutzmer, J. & Beukes, N. J. (2010), 'Zoning of platinum group mineral assemblages in the UG2 chromitite determined through in situ SEM-EDS-based image analysis', *Mineralium Deposita* **45**(2), 147–159.

Vrevskii, A. B., Bogomolov, E. S., Zinger, T. F. & Sergeev, S. A. (2010), 'Polychronic sources and isotopic age of the volcanogenic complex (Arvarench Unit) of the

Imandra-Varzuga structure, Kola Peninsula', *Doklady Earth Sciences* **431**(1), 386–389.

Vroon, P. Z., van der Wagt, B., Koornneef, J. M. & Davies, G. R. (2008), 'Problems in obtaining precise and accurate Sr isotope analysis from geological materials using laser ablation MC-ICPMS', *Analytical and Bioanalytical Chemistry* **390**(2), 465–476.

Wager, L. R. (1960), 'The major element variation of the Layered Series of the Skaergaard Intrusion and a re-estimation of the average composition of the hidden Layered Series and of the successive residual magmas', *Journal of Petrology* **1**(3), 364–398.

Wager, L. R. & Brown, G. M. (1967), *Layered igneous rocks*, WH Freeman, 588p.

Waight, T., Baker, J. & Peate, D. (2002), 'Sr isotope ratio measurements by double-focusing MC-ICPMS: techniques, observations and pitfalls', *International Journal of Mass Spectrometry* **221**(3), 229–244.

Walker, R. J., Morgan, J. W., Beary, E. S., Smoliar, M. I., Czamanske, G. K. & Horan, M. F. (1997), 'Applications of the ^{190}Pt-^{186}Os isotope system to geochemistry and cosmochemistry', *Geochimica et Cosmochimica Acta* **61**(22), 4799–4807.

Wall, C. J. (2016), Establishing the age and duration of magmatism in large open-system layered intrusions from the high-precision geochronology of the Neoarchean Stillwater Complex and Paleoproterozoic Bushveld Complex, PhD thesis, University of British Columbia, 525p.

Walraven, F. (1997), *Geochronology of the Rooiberg Group, Transvaal Supergroup, South Africa*, Vol. 316, Economic Geology Research Unit, University of the Witwatersrand.

Walraven, F. & Hattingh, E. (1993), 'Geochronology of the Nebo Granite, Bushveld Complex', *South African Journal of Geology* **96**(1-2), 31–41.

Walraven, F. & Martini, J. (1995), 'Zircon Pb-evaporation age determinations for the Oak Tree Formation, Chuniespoort Group, Transvaal Sequence; implications for Transvaal-Griqualand West basin correlations', *South African Journal of Geology* **98**(1), 58–67.

Webb, S. J., Cawthorn, R. G., Nguuri, T. & James, D. (2004), 'Gravity modeling of Bushveld Complex connectivity supported by Southern African seismic experiment results', *South African Journal of Geology* **107**(1-2), 207–218.

Webster, J. D. & Piccoli, P. M. (2015), 'Magmatic apatite: a powerful, yet deceptive, mineral', *Elements* **11**(3), 177–182.

Wei, X., Xu, Y.-G., Zhang, C.-L., Zhao, J.-X. & Feng, Y.-X. (2014), 'Petrology and Sr–Nd isotopic disequilibrium of the Xiaohaizi Intrusion, NW China: Genesis of layered intrusions in the Tarim Large Igneous Province', *Journal of Petrology* **55**(12), 2567–2598.

Wenzel, T., Baumgartner, L. P., Brügmann, G. E., Konnikov, E. G. & Kislov, E. V. (2002), 'Partial melting and assimilation of dolomitic xenoliths by mafic magma: the Ioko-Dovyren Intrusion (North Baikal Region, Russia)', *Journal of Petrology* **43**(11), 2049–2074.

Willmore, C. C., Boudreau, A. E. & Kruger, F. J. (2000), 'The Halogen Geochemistry of the Bushveld Complex, Republic of South Africa: Implications for Chalcophile Element Distribution in the Lower and Critical Zones', *Journal of Petrology* **41**(10), 1517–1539.

Wilson, A. H. (2012), 'A chill sequence to the Bushveld Complex: Insight into the first stage of emplacement and implications for the parental magmas', *Journal of Petrology* **53**(6), 1123–1168.

Wilson, A. H. (2015), 'The earliest stages of emplacement of the eastern Bushveld Complex: Development of the Lower Zone, Marginal Zone and Basal Ultramafic Sequence', *Journal of Petrology* **56**(2), 347–388.

Wilson, A. H. & Chunnett, G. (2006), 'Trace element and platinum-group element distributions and the genesis of the Merensky Reef, western Bushveld Complex, South Africa', *Journal of Petrology* **47**(12), 2369–2403.

Wilson, A. H., Naldrett, A. J. & Tredoux, M. (1989), 'Distribution and controls of platinum-group element and base metal mineralization in the Darwendale subchamber of the Great Dyke, Zimbabwe', *Geology* **17**(7), 649–652.

Wilson, J. R., Cawthorn, R. G., Kruger, F. J. & Grundvig, S. (1994), 'Intrusive origin for the unconformable Upper Zone in the Northern Gap, western Bushveld Complex', *South African Journal of Geology* **97**(4), 462–472.

Yakovlev, Y. N., Dokuchaeva, V. S. & Sviyageninov, F. I. (1999), The Monchegorsk district - Ore resource base of the non-ferrous and platinum metals industry in the XXI century, *in* 'The Platinum of Russia', Vol. 3, Closed Joint-Stock Company, Moscow, pp. 161–172.

Yang, S.-H., Hanski, E., Li, C., Maier, W. D., Huhma, H., Mokrushin, A. V., Latypov, R., Lahaye, Y., O'Brien, H. & Qu, W.-J. (2016), 'Mantle source of the 2.44–2.50-Ga mantle plume-related magmatism in the Fennoscandian Shield: evidence from Os, Nd, and Sr isotope compositions of the Monchepluton and Kemi intrusions', *Mineralium Deposita* **51**(8), 1055–1073.

Yang, S.-H., Maier, W. D., Lahaye, Y. & O'Brien, H. (2013), 'Strontium isotope disequilibrium of plagioclase in the Upper Critical Zone of the Bushveld Complex: evidence for mixing of crystal slurries', *Contributions to Mineralogy and Petrology* **166**(4), 959–974.

Yudovskaya, M. A., Kinnaird, J. A., Sobolev, A. V., Kuzmin, D. V., McDonald, I. & Wilson, A. H. (2013), 'Petrogenesis of the Lower Zone olivine-rich cumulates beneath the Platreef and their correlation with recognized occurrences in the Bushveld Complex', *Economic Geology* **108**(8), 1923–1952.

Zagorodny, V. G., Predovsky, A. A., Basalaev, A. A., Batieva, I. D., Borisov, A. Y., Vetrin, V. R., Voloshina, Z. M., Dokuchaeva, V. S., Zhangurov, A. A. & Kozlova,

N. E. (1982), *The Imandra-Varzuga Zone of the Karelides (Geology, geochemistry, history of development)*, Nauka, 280p (in Russian).

Zeh, A., Ovtcharova, M., Wilson, A. H. & Schaltegger, U. (2015), 'The Bushveld Complex was emplaced and cooled in less than one million years – results of zirconology, and geotectonic implications', *Earth and Planetary Science Letters* **418**, 103–114.

Zientek, M. L. (2012), Magmatic ore deposits in layered intrusions - descriptive model for reef-type PGE and contact-type Cu-Ni-PGE deposits, Open-File Report 2012-1010, US Geological Survey, 48p.

Appendix

A Sample list: Monchegorsk Complex

Table A.1. Monchegorsk sample list. WR = whole rock

No.	Sample No.	Intrusion	Sample type	Drill hole	Depth (m)	Rock type	WR	PGE
1	15DB-1	Dunite Block	Outcrop	-	-	CHR	X	
2	15DB-4	Dunite Block	Outcrop	-	-	DUN	X	X
3	15DB-2	Dunite Block	Outcrop	-	-	LH	X	X
4	15DB-3	Dunite Block	Outcrop	-	-	LH	X	X
5	15KMAS-1	Kumuzhya	Outcrop	-	-	HZ	X	X
6	15KMAS-2	Kumuzhya	Outcrop	-	-	OL-OPX	X	X
7	15KMAS-5	Kumuzhya	Outcrop	-	-	OL-OPX	X	X
8	15KMAS-6	Kumuzhya	Outcrop	-	-	OL-OPX	X	X
9	15KMAS-3	Kumuzhya	Outcrop	-	-	OL-OPX	X	X
10	15KMAS-7	Kumuzhya	Outcrop	-	-	OL-OPX	X	X
11	753-184	Monchetundra	Drill core	753	184.0	NO	X	X
12	15MT-03	Monchetundra	Outcrop	-	-	AN	X	X
13	15MT-05	Monchetundra	Outcrop	-	-	AN	X	X
14	15MT-08	Monchetundra	Outcrop	-	-	AN	X	X
15	15MT-09	Monchetundra	Outcrop	-	-	AN	X	X
16	15MT-10	Monchetundra	Outcrop	-	-	AN	X	X
17	15MT-11	Monchetundra	Outcrop	-	-	AN	X	X
18	15MT-12	Monchetundra	Outcrop	-	-	AN	X	X
19	15MT-13	Monchetundra	Outcrop	-	-	AN	X	X
20	15MT-14	Monchetundra	Outcrop	-	-	AN	X	X
21	15MT-16	Monchetundra	Outcrop	-	-	AN	X	X
22	15MT-18	Monchetundra	Outcrop	-	-	AN	X	X
23	15MT-19	Monchetundra	Outcrop	-	-	AN	X	X
24	15MT-01	Monchetundra	Outcrop	-	-	LGN	X	X
25	15MT-02	Monchetundra	Outcrop	-	-	LGN	X	X
26	15MT-04	Monchetundra	Outcrop	-	-	LGN	X	X
27	15MT-06	Monchetundra	Outcrop	-	-	LGN	X	X
28	15MT-07	Monchetundra	Outcrop	-	-	LGN	X	X
29	79-023	Nittis	Drill core	MT79	23.3	OPX	X	X
30	79-034	Nittis	Drill core	MT79	34.2	OPX	X	X
31	79-039	Nittis	Drill core	MT79	39.4	OPX	X	X
32	79-042	Nittis	Drill core	MT79	42.3	OPX	X	X
33	79-054	Nittis	Drill core	MT79	54.0	OPX	X	X
34	79-077	Nittis	Drill core	MT79	78.0	OPX	X	X
35	79-091	Nittis	Drill core	MT79	91.3	OPX	X	X
36	79-104	Nittis	Drill core	MT79	104.8	OPX	X	X
37	79-115	Nittis	Drill core	MT79	116.0	OPX	X	X
38	79-121	Nittis	Drill core	MT79	122.0	OPX	X	X
39	79-131	Nittis	Drill core	MT79	131.9	OPX	X	X
40	79-138	Nittis	Drill core	MT79	138.5	OPX	X	X
41	79-143	Nittis	Drill core	MT79	143.4	Oph. OPX	X	X
42	79-145	Nittis	Drill core	MT79	145.8	OPX	X	X
43	79-147	Nittis	Drill core	MT79	147.7	PEGM	X	X
44	79-149	Nittis	Drill core	MT79	149.0	METASED	X	X
45	79-150	Nittis	Drill core	MT79	150.9	PEGM	X	X
46	79-156	Nittis	Drill core	MT79	156.6	PEGM	X	X
47	79-159	Nittis	Drill core	MT79	159.7	DOL	X	X

Table A.1 (cont.)

No.	Sample No.	Intrusion	Sample type	Drill hole	Depth (m)	Rock type	WR	PGE
48	79-160	Nittis	Drill core	MT79	160.1	OPX	X	X
49	79-163	Nittis	Drill core	MT79	163.8	PEGM	X	X
50	79-164	Nittis	Drill core	MT79	164.6	DOL	X	X
51	94-013	Nittis	Drill core	MT94	13.7	OPX	X	
52	94-038	Nittis	Drill core	MT94	38.8	OPX	X	X
53	94-081	Nittis	Drill core	MT94	81.2	OPX	X	
54	94-118	Nittis	Drill core	MT94	118.1	OPX	X	X
55	15NMAS-01	Nittis	Outcrop	-	-	OPX	X	X
56	15NMAS-02	Nittis	Outcrop	-	-	OPX	X	X
57	15NMAS-03	Nittis	Outcrop	-	-	OPX	X	X
58	1815-011	Nyud	Drill core	1815	12.0	MNO	X	X
59	1815-026	Nyud	Drill core	1815	26.6	MNO	X	X
60	1815-046	Nyud	Drill core	1815	46.4	MNO	X	X
61	1815-059	Nyud	Drill core	1815	59.5	MNO	X	X
62	1815-068	Nyud	Drill core	1815	68.4	MNO	X	X
63	1815-072	Nyud	Drill core	1815	72.7	MNO	X	X
64	1815-074	Nyud	Drill core	1815	74.6	MNO	X	X
65	1815-077	Nyud	Drill core	1815	77.6	PEGM	X	X
66	1815-083	Nyud	Drill core	1815	83.9	TON	X	X
67	1815-095	Nyud	Drill core	1815	95.5	TON	X	X
68	1815-103	Nyud	Drill core	1815	103.3	TON	X	X
69	1403-030	Sopcha	Drill core	1403	30.0	OPX	X	X
70	1403-042	Sopcha	Drill core	1403	42.7	HZ	X	X
71	1403-064	Sopcha	Drill core	1403	64.6	OPX	X	X
72	1403-089	Sopcha	Drill core	1403	89.4	OPX	X	X
73	1403-132	Sopcha	Drill core	1403	132.6	OPX	X	X
74	1403-141	Sopcha	Drill core	1403	141.4	HZ	X	X
75	1408-171	Sopcha	Drill core	1408	171.4	OPX	X	X
76	15SOP-06	Sopcha	Outcrop	-	-	DUN	X	X
77	15SOP-07	Sopcha	Outcrop	-	-	HZ	X	
78	15SOP-08	Sopcha	Outcrop	-	-	HZ	X	X
79	16SOP-1	Sopcha	Outcrop	-	-	HZ	X	X
80	15SOP-09	Sopcha	Outcrop	-	-	OL-OPX	X	X
81	15SOP-11	Sopcha	Outcrop	-	-	OL-OPX	X	
82	15SOP-04	Sopcha	Outcrop	-	-	OPX	X	X
83	15SOP-15	Sopcha	Outcrop	-	-	OPX	X	X
84	15SOP-16	Sopcha	Outcrop	-	-	OPX	X	X
85	15SOP-17	Sopcha	Outcrop	-	-	OPX	X	X
86	15SOP-18	Sopcha	Outcrop	-	-	OPX	X	X
87	15SOP-01	Sopcha	Outcrop	-	-	OPX	X	X
88	15SOP-05	Sopcha	Outcrop	-	-	OPX BRC	X	X
89	15SOP-10	Sopcha	Outcrop	-	-	OPX BRC	X	X
90	15TMAS-4	Travyanaya	Outcrop	-	-	DOL	X	X
91	15TMAS-9	Travyanaya	Outcrop	-	-	HZ	X	X
92	15TMAS-5	Travyanaya	Outcrop	-	-	HZ	X	X
93	15TMAS-6	Travyanaya	Outcrop	-	-	MS	X	X
94	15TMAS-7	Travyanaya	Outcrop	-	-	OL-WEB	X	X

Table A.1 (cont.)

No.	Sample No.	Intrusion	Sample type	Drill hole	Depth (m)	Rock type	WR	PGE
95	15TMAS-1	Travyanaya	Outcrop	-	-	Oph. GN	X	X
96	15TMAS-8	Travyanaya	Outcrop	-	-	OPX	X	X
97	1811-062	Vuruchuaivench	Drill core	1811	62.6	LGN	X	X
98	1811-102	Vuruchuaivench	Drill core	1811	102.8	LGN	X	X
99	1811-143	Vuruchuaivench	Drill core	1811	143.6	LGN	X	X
100	1811-172	Vuruchuaivench	Drill core	1811	172.7	LGN	X	X
101	1811-185	Vuruchuaivench	Drill core	1811	185.6	LGN	X	X
102	1811-231	Vuruchuaivench	Drill core	1811	231.2	LGN	X	X
103	1811-274	Vuruchuaivench	Drill core	1811	274.1	LGN	X	X
104	1814-021	Vuruchuaivench	Drill core	1814	21.9	LGN	X	X
105	1814-055	Vuruchuaivench	Drill core	1814	55.6	LGN	X	X
106	1814-091	Vuruchuaivench	Drill core	1814	91.1	LGN	X	X
107	1814-118	Vuruchuaivench	Drill core	1814	118.9	LGN	X	X
108	1843-118	Vuruchuaivench	Drill core	1843	118.6	LGN	X	X
109	1843-169	Vuruchuaivench	Drill core	1843	169.9	LGN	X	X
110	1843-203	Vuruchuaivench	Drill core	1843	203.8	LGN	X	X
111	15VURU-3	Vuruchuaivench	Outcrop	-	-	AN	X	X
112	15VURU-2	Vuruchuaivench	Outcrop	-	-	LGN	X	X

CHR = chromitite; DUN = dunite; LH = lherzolite; HZ = harzburgite; OL-WEB = olivine-websterite; OL-OPX = olivine-orthopyroxenite; OPX = orthopyroxenite; MNO = melanorite; GN = gabbronorite LGN = leucogabbronorite; AN = anorthosite; DOL = dolerite; MS = massive sulfide; PEGM = pegmatite; TON = tonalite; METASED = metasediment; BRC = breccia; oph = ophitic

B Sample location: Monchegorsk Complex

Table B.1. Monchegorsk outcrop sample locations

No.	Sample No.	Intrusion	UTM Zone	Easting	Northing	Elevation (m)	Latitude	Longitude
1	15DB-1	Dunite Block	36 W	490243	7532023	254	67.9026	32.7676
2	15DB-2	Dunite Block	36 W	490243	7532023	254	67.9026	32.7676
3	15DB-3	Dunite Block	36 W	490243	7532023	254	67.9026	32.7676
4	15DB-4	Dunite Block	36 W	490243	7532023	254	67.9026	32.7676
5	15KMAS-1	Kumuzhya	36 W	491617	7535767	207	67.9362	32.8000
6	15KMAS-2	Kumuzhya	36 W	491587	7535729	213	67.9359	32.7993
7	15KMAS-3	Kumuzhya	36 W	491545	7535688	225	67.9355	32.7983
8	15KMAS-5	Kumuzhya	36 W	491472	7535552	261	67.9343	32.7966
9	15KMAS-6	Kumuzhya	36 W	491412	7535402	300	67.9329	32.7952
10	15KMAS-7	Kumuzhya	36 W	491226	7535224	330	67.9313	32.7907
11	15MT-01	Monchetundra	36 W	488947	7529858	339	67.8831	32.7369
12	15MT-02	Monchetundra	36 W	488947	7529858	339	67.8831	32.7369
13	15MT-03	Monchetundra	36 W	488947	7529858	339	67.8831	32.7369
14	15MT-04	Monchetundra	36 W	488978	7529711	346	67.8818	32.7377
15	15MT-05	Monchetundra	36 W	488863	7529243	442	67.8776	32.7350
16	15MT-06	Monchetundra	36 W	489062	7529948	307	67.8839	32.7397
17	15MT-07	Monchetundra	36 W	489024	7529868	327	67.8832	32.7388
18	15MT-08	Monchetundra	36 W	488730	7529904	369	67.8835	32.7318
19	15MT-09	Monchetundra	36 W	488435	7529676	431	67.8815	32.7248
20	15MT-10	Monchetundra	36 W	488333	7529616	465	67.8809	32.7223
21	15MT-11	Monchetundra	36 W	488220	7529573	493	67.8805	32.7197
22	15MT-12	Monchetundra	36 W	488133	7529504	522	67.8799	32.7176
23	15MT-13	Monchetundra	36 W	488030	7529464	553	67.8796	32.7151
24	15MT-14	Monchetundra	36 W	487926	7529452	586	67.8794	32.7127
25	15MT-16	Monchetundra	36 W	487781	7529430	615	67.8792	32.7092
26	15MT-18	Monchetundra	36 W	487366	7529416	693	67.8791	32.6994
27	15MT-19	Monchetundra	36 W	487267	7529456	709	67.8795	32.6970
28	15NMAS-01	Nittis	36 W	490429	7533981	245	67.9202	32.7718
29	15NMAS-02	Nittis	36 W	490429	7533981	245	67.9202	32.7718
30	15NMAS-03	Nittis	36 W	490429	7533981	245	67.9202	32.7718
31	15SOP-01	Sopcha	36 W	494547	7531335	232	67.8965	32.8701
32	15SOP-04	Sopcha	36 W	491855	7530721	339	67.8910	32.8061
33	15SOP-05	Sopcha	36 W	491857	7530723	339	67.8910	32.8061
34	15SOP-06	Sopcha	36 W	491859	7530715	339	67.8909	32.8062
35	15SOP-07	Sopcha	36 W	491858	7530715	340	67.8909	32.8061
36	15SOP-08	Sopcha	36 W	491859	7530714	341	67.8909	32.8062
37	15SOP-09	Sopcha	36 W	491861	7530713	343	67.8909	32.8062
38	15SOP-10	Sopcha	36 W	491867	7530703	348	67.8908	32.8064
39	15SOP-11	Sopcha	36 W	491875	7530703	347	67.8908	32.8066
40	15SOP-15	Sopcha	36 W	491788	7530684	338	67.8906	32.8045
41	15SOP-16	Sopcha	36 W	491686	7530651	326	67.8903	32.8021
42	15SOP-17	Sopcha	36 W	491686	7530651	326	67.8903	32.8021
43	15SOP-18	Sopcha	36 W	491826	7530433	400	67.8884	32.8054
44	16SOP-1	Sopcha	36 W	494547	7531335	232	67.8965	32.8701
45	15TMAS-1	Travyanaya	36 W	491695	7536500	197	67.9428	32.8018
46	15TMAS-4	Travyanaya	36 W	491695	7536500	197	67.9428	32.8018
47	15TMAS-5	Travyanaya	36 W	491695	7536500	197	67.9428	32.8018
48	15TMAS-6	Travyanaya	36 W	491695	7536500	197	67.9428	32.8018
49	15TMAS-7	Travyanaya	36 W	491695	7536500	197	67.9428	32.8018
50	15TMAS-8	Travyanaya	36 W	491692	7536421	195	67.9421	32.8018
51	15TMAS-9	Travyanaya	36 W	491692	7536421	195	67.9421	32.8018
52	15VURU-2	Vuruchuaivench	36 W	498121	7528862	165	67.8744	32.9553
53	15VURU-3	Vuruchuaivench	36 W	498003	7528812	156	67.8740	32.9525

Table B.2. Location of Monchegorsk drill holes used for this study

Drill hole	Intrusion	UTM Zone	Easting	Northing	Latitude	Longitude	End of hole (m)
753	Monchetundra	36 W	489963	7528961	67.8751	32.7612	1274.0
MT79	Nittis	36 W	489068	7533591	67.9166	32.7394	166.2
MT94	Nittis	36 W	489088	7533196	67.9131	32.7400	121.4
1815	Nyud	36 W	496157	7530079	67.8853	32.9085	103.6
1403	Sopcha	36 W	492546	7530211	67.8864	32.8226	147.2
1408	Sopcha	36 W	492539	7529940	67.8840	32.8224	171.3
1811	Vuruchuaivench	36 W	498675	7528384	67.8701	32.9685	280.4
1814	Vuruchuaivench	36 W	497523	7528509	67.8712	32.9411	200.0
1843	Vuruchuaivench	36 W	499357	7529452	67.8797	32.9847	205.5

C *In situ* Sr isotope data

Table C.1. *In situ* Sr isotope composition, anorthite content and FeO concentrations of plagioclase in relation to stratigraphic height, Union Section, western Bushveld Complex. Initial $^{87}Sr/^{86}Sr_i$ is recalculated to 2,055 Ma (Zeh et al. 2015)

Sample	Height (m)	Unit	Rock	Texture	Position	$^{87}Rb/^{86}Sr$	$^{87}Sr/^{86}Sr$	1σ	$^{87}Sr/^{86}Sr_i$	2σ	An	FeO (wt %)
351.70A	6049	UZ	Mt	Eu	Core	0.00396	0.70791	0.00009	0.70780	0.00017	48.7	0.27
351.70A	6049	UZ	Mt	Eu	Rim	0.00338	0.70765	0.00004	0.70755	0.00009	48.2	0.30
351.70A	6049	UZ	Mt	Eu	Core	0.00437	0.70789	0.00004	0.70777	0.00008	47.0	0.37
351.70A	6049	UZ	Mt	Sub	Core	0.00373	0.70795	0.00003	0.70784	0.00007	50.1	0.37
351.70A	6049	UZ	Mt	Sub	Rim	0.00405	0.70826	0.00004	0.70814	0.00008	49.3	0.33
351.70A	6049	UZ	Mt	Eu	Core	0.00675	0.70752	0.00004	0.70732	0.00009	46.4	
351.70A	6049	UZ	Mt	Eu	Rim	0.00329	0.70758	0.00004	0.70748	0.00008	49.5	0.38
351.70A	6049	UZ	Mt	Sub	Core	0.00181	0.70764	0.00005	0.70758	0.00009	47.5	0.30
351.70A	6049	UZ	Mt	Sub	Rim	0.00132	0.70739	0.00004	0.70735	0.00007	48.5	0.24
351.70A	6049	UZ	Mt	Sub	Rim	0.00362	0.70765	0.00004	0.70754	0.00009	49.1	0.51
351.70A	6049	UZ	Mt	Sub	Core	0.00489	0.70795	0.00006	0.70780	0.00012	48.8	
351.70A	6049	UZ	Mt	An	Rim	0.00200	0.70850	0.00006	0.70844	0.00013	48.0	0.39
351.70A	6049	UZ	Mt	An	Rim	0.00296	0.70740	0.00007	0.70731	0.00014	50.4	0.39
351.70A	6049	UZ	Mt	An	Core	0.00444	0.70733	0.00008	0.70720	0.00016	50.2	0.37
351.70A	6049	UZ	Mt	Sub	Core	0.00708	0.70767	0.00006	0.70746	0.00013	49.8	0.39
351.70A	6049	UZ	Mt	Sub	Rim	0.00420	0.70688	0.00006	0.70675	0.00012	48.5	0.36
351.70A	6049	UZ	Mt	Sub	Rim	0.00273	0.70724	0.00006	0.70717	0.00013	50.3	0.38
351.70A	6049	UZ	Mt	Sub	Rim	0.01239	0.70792	0.00007	0.70756	0.00014	48.8	0.39
351.70A	6049	UZ	Mt	Sub	Core	0.01890	0.70827	0.00005	0.70772	0.00015	50.2	0.36
351.70A	6049	UZ	Mt	Sub	Core	0.00613	0.70814	0.00005	0.70796	0.00011	48.6	0.43
351.70A	6049	UZ	Mt	Sub	Rim	0.00625	0.70772	0.00006	0.70754	0.00013	49.9	0.39
559	5842	UZ	Mt-G	Sub	Rim	0.00318	0.70753	0.00006	0.70744	0.00012	49.3	0.32
559	5842	UZ	Mt-G	Sub	Rim	0.00314	0.70719	0.00006	0.70710	0.00012	49.8	0.47
559	5842	UZ	Mt-G	Sub	Core	0.00663	0.70720	0.00006	0.70701	0.00012	49.0	0.34
559	5842	UZ	Mt-G	An	Rim	0.00108	0.70745	0.00005	0.70742	0.00010	48.8	0.27
559	5842	UZ	Mt-G	An	Core	0.00296	0.70756	0.00006	0.70747	0.00011	48.1	0.32
559	5842	UZ	Mt-G	An	Rim	0.00262	0.70764	0.00006	0.70757	0.00013	48.3	0.33
559	5842	UZ	Mt-G	An	Rim	0.00275	0.70753	0.00005	0.70745	0.00011	47.9	0.31
559	5842	UZ	Mt-G	Eu	Rim	0.00239	0.70749	0.00007	0.70742	0.00014	48.8	0.28
559	5842	UZ	Mt-G	Eu	Core	0.00213	0.70751	0.00005	0.70745	0.00010	51.8	0.34
559	5842	UZ	Mt-G	Eu	Rim	0.00167	0.70767	0.00006	0.70762	0.00011	53.4	0.38
559	5842	UZ	Mt-G	Sub	Core	0.00088	0.70743	0.00005	0.70741	0.00010	52.5	0.62
559	5842	UZ	Mt-G	Sub	Rim	0.00295	0.70768	0.00005	0.70760	0.00011	48.6	0.34
559	5842	UZ	Mt-G	Sub	Core	0.00306	0.70782	0.00005	0.70773	0.00010	48.8	0.32
559	5842	UZ	Mt-G	Sub	Core	0.00218	0.70748	0.00006	0.70742	0.00012	49.8	0.37
559	5842	UZ	Mt-G	Sub	Rim	0.00227	0.70761	0.00005	0.70754	0.00011	51.7	0.46
644.8	5756	UZ	Mt	Sub	Rim	0.00501	0.70707	0.00006	0.70692	0.00012	53.9	0.32
644.8	5756	UZ	Mt	Sub	Rim	0.00536	0.70733	0.00006	0.70718	0.00012	57.3	0.33
644.8	5756	UZ	Mt	Sub	Core	0.00324	0.70713	0.00006	0.70704	0.00012	57.6	0.36
644.8	5756	UZ	Mt	Sub	Rim	0.00183	0.70744	0.00007	0.70739	0.00014	58.6	0.43
644.8	5756	UZ	Mt	Sub	Rim	0.00525	0.70722	0.00006	0.70707	0.00012	57.5	0.44
644.8	5756	UZ	Mt	Sub	Core	0.00362	0.70721	0.00006	0.70710	0.00012	58.7	0.42
644.8	5756	UZ	Mt	Sub	Rim	0.00181	0.70772	0.00006	0.70767	0.00013	55.9	0.35
644.8	5756	UZ	Mt	Sub	Rim	0.00281	0.70725	0.00006	0.70717	0.00013	55.5	0.42
644.8	5756	UZ	Mt	Eu	Core	0.00354	0.70735	0.00005	0.70725	0.00011	56.6	0.31
644.8	5756	UZ	Mt	Eu	Rim	0.00239	0.70753	0.00006	0.70746	0.00013	55.0	0.37
644.8	5756	UZ	Mt	Eu	Rim	0.00236	0.70751	0.00006	0.70744	0.00013	55.1	0.31
644.8	5756	UZ	Mt	An	Rim	0.00151	0.70689	0.00007	0.70685	0.00015	56.8	0.35
644.8	5756	UZ	Mt	An	Rim	0.00086	0.70760	0.00007	0.70758	0.00014	57.1	0.30
644.8	5756	UZ	Mt	An	Rim	0.00138	0.70757	0.00006	0.70753	0.00013	56.9	0.32

Table C.1 (cont.)

Sample	Height (m)	Unit	Rock	Texture	Position	$^{87}Rb/^{86}Sr$	$^{87}Sr/^{86}Sr$	1σ	$^{87}Sr/^{86}Sr_i$	2σ	An	FeO (wt %)
806.02	5595	UZ	Mt-G	Sub	Core	0.01263	0.70754	0.00006	0.70717	0.00012	51.4	0.37
806.02	5595	UZ	Mt-G	Sub	Rim	0.02274	0.70820	0.00006	0.70754	0.00015	51.4	0.32
806.02	5595	UZ	Mt-G	Sub	Rim	0.01209	0.70743	0.00005	0.70708	0.00011	51.3	0.37
806.02	5595	UZ	Mt-G	Sub	Core	0.01026	0.70773	0.00006	0.70743	0.00012	51.6	0.35
806.02	5595	UZ	Mt-G	Sub	Rim	0.00449	0.70776	0.00006	0.70763	0.00012	52.9	0.37
806.02	5595	UZ	Mt-G	An	Rim	0.01053	0.70790	0.00007	0.70760	0.00015	52.8	0.47
806.02	5595	UZ	Mt-G	An	Core	0.01496	0.70788	0.00006	0.70745	0.00012	51.7	0.31
806.02	5595	UZ	Mt-G	An	Rim	0.00512	0.70796	0.00007	0.70781	0.00014	52.7	0.35
806.02	5595	UZ	Mt-G	Sub	Core	0.01119	0.70789	0.00007	0.70756	0.00014	50.8	0.37
806.02	5595	UZ	Mt-G	Sub	Rim	0.00350	0.70791	0.00007	0.70781	0.00014	52.5	0.34
806.02	5595	UZ	Mt-G	Sub	Rim	0.00270	0.70787	0.00007	0.70779	0.00015	52.4	0.32
806.02	5595	UZ	Mt-G	An	Rim	0.00392	0.70779	0.00007	0.70767	0.00014	51.2	0.34
806.02	5595	UZ	Mt-G	Sub	Core	0.00715	0.70743	0.00008	0.70722	0.00015	52.2	0.38
806.02	5595	UZ	Mt-G	Sub	Core	0.00830	0.70800	0.00008	0.70776	0.00016	51.1	0.36
806.02	5595	UZ	Mt-G	Sub	Core	0.00956	0.70718	0.00007	0.70690	0.00015	51.8	0.35
806.02	5595	UZ	Mt-G	Sub	Rim	0.00413	0.70751	0.00007	0.70739	0.00015	53.1	0.34
1049.26b	5352	UZ	Mt-G	Sub	Rim	0.01020	0.70759	0.00008	0.70730	0.00018	57.7	0.39
1049.26b	5352	UZ	Mt-G	Eu	Rim	0.00706	0.70761	0.00008	0.70740	0.00017	59.3	0.38
1049.26b	5352	UZ	Mt-G	Eu	Core	0.00656	0.70805	0.00009	0.70786	0.00018	61.8	0.42
1049.26b	5352	UZ	Mt-G	Eu	Rim	0.00769	0.70784	0.00007	0.70762	0.00015	58.1	0.40
1049.26b	5352	UZ	Mt-G	Eu	Core	0.00826	0.70794	0.00009	0.70770	0.00019	59.5	0.44
1049.26b	5352	UZ	Mt-G	Eu	Core	0.02234	0.70751	0.00009	0.70686	0.00020	59.9	0.44
1049.26b	5352	UZ	Mt-G	Eu	Core	0.00678	0.70801	0.00009	0.70781	0.00019	59.9	0.44
1049.26b	5352	UZ	Mt-G	Eu	Rim	0.00587	0.70761	0.00009	0.70744	0.00018	60.1	0.41
1049.26b	5352	UZ	Mt-G	An	Rim	0.00753	0.70733	0.00007	0.70711	0.00014	58.0	0.44
1049.26b	5352	UZ	Mt-G	An	Rim	0.00710	0.70764	0.00007	0.70744	0.00015	57.2	0.40
1049.26b	5352	UZ	Mt-G	An	Rim	0.00672	0.70751	0.00009	0.70732	0.00019	59.6	0.34
1049.26b	5352	UZ	Mt-G			0.00888	0.70737	0.00007	0.70711	0.00014	59.5	0.42
1144.8	5256	UZ	Mt-G	Eu	Core	0.00096	0.70710	0.00007	0.70707	0.00014	60.2	0.36
1144.8	5256	UZ	Mt-G	Eu	Rim	0.00092	0.70767	0.00007	0.70764	0.00014	60.5	0.44
1144.8	5256	UZ	Mt-G	Eu	Core	0.00093	0.70719	0.00007	0.70716	0.00013	60.6	
1144.8	5256	UZ	Mt-G	Eu	Core	0.00304	0.70684	0.00007	0.70675	0.00013	60.1	0.42
1144.8	5256	UZ	Mt-G	Eu	Core	0.00373	0.70807	0.00007	0.70796	0.00014	59.6	0.40
1144.8	5256	UZ	Mt-G	Sub	Core	0.00211	0.70739	0.00007	0.70733	0.00013	61.2	0.38
1144.8	5256	UZ	Mt-G	Sub	Rim	0.00354	0.70829	0.00006	0.70818	0.00013	60.4	0.40
1144.8	5256	UZ	Mt-G	Sub	Core	0.00287	0.70728	0.00007	0.70720	0.00014	59.2	0.34
1144.8	5256	UZ	Mt-G	Eu	Core	0.00397	0.70734	0.00008	0.70722	0.00015	58.2	0.38
1144.8	5256	UZ	Mt-G			0.00283	0.70723	0.00008	0.70714	0.00015	58.0	0.36
1144.8	5256	UZ	Mt-G			0.00100	0.70762	0.00006	0.70759	0.00012	59.6	0.63
1144.8	5256	UZ	Mt-G			0.00287	0.70752	0.00007	0.70744	0.00014	58.4	0.39
1279.93	5121	UZ	Mt-G	An	Rim	0.00653	0.70732	0.00008	0.70713	0.00016	58.7	0.44
1279.93	5121	UZ	Mt-G	An	Core	0.00632	0.70740	0.00006	0.70722	0.00013	59.4	0.41
1279.93	5121	UZ	Mt-G	An	Core	0.00557	0.70771	0.00007	0.70755	0.00015	58.1	0.40
1279.93	5121	UZ	Mt-G	An	Rim	0.00397	0.70779	0.00007	0.70768	0.00014	58.4	0.43
1279.93	5121	UZ	Mt-G	An	Rim	0.00296	0.70744	0.00007	0.70736	0.00013	61.4	0.46
1279.93	5121	UZ	Mt-G	An	Core	0.00578	0.70694	0.00007	0.70677	0.00014	58.7	0.44
1279.93	5121	UZ	Mt-G	Eu	Rim	0.00893	0.70752	0.00006	0.70726	0.00013	57.3	0.45
1279.93	5121	UZ	Mt-G	Eu	Core	0.01318	0.70788	0.00006	0.70749	0.00014	57.4	0.48
1279.93	5121	UZ	Mt-G	Eu	Rim	0.00481	0.70784	0.00006	0.70770	0.00012	58.0	0.41
1279.93	5121	UZ	Mt-G	Eu	Rim	0.00428	0.70707	0.00006	0.70695	0.00013	58.7	0.50

Table C.1 (cont.)

Sample	Height (m)	Unit	Rock	Texture	Position	$^{87}Rb/^{86}Sr$	$^{87}Sr/^{86}Sr$	1σ	$^{87}Sr/^{86}Sr_i$	2σ	An	FeO (wt %)
1279.93	5121	UZ	Mt-G	Eu	Core	0.00683	0.70761	0.00006	0.70741	0.00012	57.0	0.48
1279.93	5121	UZ	Mt-G	Eu	Rim	0.00879	0.70754	0.00006	0.70728	0.00012	57.9	0.44
1279.93	5121	UZ	Mt-G	Sub	Core	0.00825	0.70761	0.00006	0.70737	0.00013	58.1	0.47
1279.93	5121	UZ	Mt-G	Sub	Core	0.00726	0.70802	0.00006	0.70781	0.00013	57.8	0.38
1279.93	5121	UZ	Mt-G	Sub	Rim	0.00150	0.70674	0.00006	0.70670	0.00012	60.9	0.43
1279.93	5121	UZ	Mt-G	An	Core	0.00624	0.70724	0.00007	0.70706	0.00015	58.4	0.40
1404.35	4996	UZ	Mt-G	Eu	Core	0.01777	0.70798	0.00004	0.70747	0.00009	56.2	0.40
1404.35	4996	UZ	Mt-G	Eu	Rim	0.01238	0.70773	0.00004	0.70737	0.00009	56.6	0.40
1404.35	4996	UZ	Mt-G	Sub	Rim	0.01011	0.70740	0.00005	0.70710	0.00010	56.5	0.42
1404.35	4996	UZ	Mt-G	Eu	Rim	0.00972	0.70741	0.00004	0.70712	0.00009	55.9	0.40
1404.35	4996	UZ	Mt-G	Eu	Rim	0.00991	0.70748	0.00004	0.70719	0.00009	56.0	0.40
1404.35	4996	UZ	Mt-G	Sub	Core	0.00246	0.70750	0.00004	0.70743	0.00008	56.7	0.36
1404.35	4996	UZ	Mt-G	An	Core	0.00383	0.70772	0.00004	0.70761	0.00009	59.4	0.34
1404.35	4996	UZ	Mt-G	Sub	Core	0.01383	0.70784	0.00004	0.70744	0.00009	60.0	0.36
1404.35	4996	UZ	Mt-G			0.01095	0.70762	0.00005	0.70730	0.00010	56.9	0.38
1404.35	4996	UZ	Mt-G	Sub	Core	0.01279	0.70785	0.00004	0.70747	0.00009	57.4	0.39
1404.35	4996	UZ	Mt-G	Sub	Core	0.01429	0.70738	0.00005	0.70697	0.00010	56.2	0.38
1404.35	4996	UZ	Mt-G	Sub	Core	0.00954	0.70741	0.00004	0.70714	0.00009	60.1	0.41
1745.45A	4655	UZ	G	An	Core	0.00554	0.70787	0.00004	0.70771	0.00009	58.4	0.51
1745.45A	4655	UZ	G	An	Core	0.00448	0.70810	0.00004	0.70797	0.00009	58.4	0.48
1745.45A	4655	UZ	G	An	Core	0.00499	0.70760	0.00004	0.70746	0.00009	58.0	0.40
1745.45A	4655	UZ	G	Sub	Rim	0.00468	0.70758	0.00004	0.70745	0.00009	56.2	0.43
1745.45A	4655	UZ	G	Sub	Rim	0.00357	0.70755	0.00004	0.70745	0.00008	57.9	0.44
1745.45A	4655	UZ	G	Sub	Core	0.00523	0.70784	0.00004	0.70769	0.00008	56.4	0.37
1745.45A	4655	UZ	G	Sub	Rim	0.00322	0.70749	0.00004	0.70739	0.00009	57.1	0.47
1745.45A	4655	UZ	G	Sub	Core	0.00310	0.70787	0.00005	0.70778	0.00009	56.4	0.44
1745.45A	4655	UZ	G	Sub	Rim	0.00338	0.70763	0.00004	0.70753	0.00008	56.0	0.36
1745.45A	4655	UZ	G	Sub	Core	0.00601	0.70759	0.00004	0.70742	0.00009	58.2	0.65
1745.45A	4655	UZ	G	Eu	Rim	0.00622	0.70744	0.00005	0.70726	0.00009	56.8	0.48
1745.45A	4655	UZ	G			0.00550	0.70764	0.00005	0.70748	0.00010	57.5	0.56
1967.1	4434	UZ	G	Sub	Core	0.00641	0.70767	0.00005	0.70748	0.00009	63.2	0.57
1967.1	4434	UZ	G	Sub	Core	0.00415	0.70763	0.00005	0.70751	0.00010	63.7	0.57
1967.1	4434	UZ	G	Sub	Rim	0.00625	0.70754	0.00005	0.70736	0.00009	62.1	0.55
1967.1	4434	UZ	G	Sub	Rim	0.00512	0.70773	0.00005	0.70758	0.00010	63.2	0.52
1967.1	4434	UZ	G	Sub	Core	0.00653	0.70760	0.00004	0.70741	0.00009	61.5	0.57
1967.1	4434	UZ	G	An	Rim	0.00724	0.70780	0.00005	0.70759	0.00009	63.8	0.61
1967.1	4434	UZ	G	An	Core	0.00694	0.70733	0.00005	0.70713	0.00009	61.9	0.52
1967.1	4434	UZ	G	An	Rim	0.00660	0.70760	0.00004	0.70740	0.00009	62.6	0.48
1967.1	4434	UZ	G	Sub	Core	0.00697	0.70739	0.00005	0.70719	0.00009	62.3	0.48
1967.1	4434	UZ	G	Sub	Core	0.01257	0.70756	0.00005	0.70720	0.00011	58.9	0.48
1967.1	4434	UZ	G	Sub	Core	0.00992	0.70782	0.00005	0.70753	0.00012	60.0	0.51
1967.1	4434	UZ	G	An	Core	0.00742	0.70750	0.00005	0.70729	0.00009	61.9	0.51
1967.1	4434	UZ	G	An	Rim	0.00690	0.70790	0.00004	0.70769	0.00008	62.2	0.50
1967.1	4434	UZ	G	An	Core	0.00705	0.70776	0.00004	0.70755	0.00009	62.7	0.61
1967.1	4434	UZ	G	An	Core	0.00600	0.70750	0.00005	0.70732	0.00010	66.0	0.60
1967.1	4434	UZ	G			0.00612	0.70812	0.00005	0.70795	0.00009	65.1	0.58
A1	4032	MZ	GN	An	Rim	0.00824	0.70857	0.00004	0.70833	0.00009	59.8	0.28
A1	4032	MZ	GN	An	Rim	0.00969	0.70895	0.00004	0.70867	0.00009	58.0	0.27
A1	4032	MZ	GN	An	Rim	0.00917	0.70839	0.00004	0.70812	0.00009	56.9	0.26
A1	4032	MZ	GN	An	Rim	0.01208	0.70845	0.00005	0.70810	0.00009	58.1	0.24

Table C.1 (cont.)

Sample	Height (m)	Unit	Rock	Texture	Position	$^{87}Rb/^{86}Sr$	$^{87}Sr/^{86}Sr$	1σ	$^{87}Sr/^{86}Sr_i$	2σ	An	FeO (wt %)
A1	4032	MZ	GN	An	Core	0.01070	0.70867	0.00005	0.70835	0.00011	57.1	0.27
A1	4032	MZ	GN	An	Rim	0.01135	0.70866	0.00005	0.70833	0.00009	59.1	0.29
A1	4032	MZ	GN	An	Core	0.01045	0.70863	0.00004	0.70833	0.00008	58.6	0.29
A1	4032	MZ	GN	An	Core	0.01362	0.70872	0.00006	0.70833	0.00013	60.3	0.31
A1	4032	MZ	GN	An	Rim	0.01152	0.70889	0.00004	0.70856	0.00009	58.0	0.32
A1	4032	MZ	GN	An	Core	0.01016	0.70898	0.00005	0.70868	0.00010	59.8	0.26
A1	4032	MZ	GN	An	Rim	0.00943	0.70887	0.00004	0.70859	0.00008	57.3	0.27
A1	4032	MZ	GN	An	Rim	0.01028	0.70870	0.00004	0.70840	0.00008	56.8	0.28
A1	4032	MZ	GN	An	Rim	0.00943	0.70891	0.00004	0.70864	0.00008	58.5	0.25
A1	4032	MZ	GN	An	Rim	0.01006	0.70868	0.00004	0.70839	0.00009	59.3	0.28
A1	4032	MZ	GN	An	Rim	0.00882	0.70846	0.00004	0.70821	0.00008	57.5	0.29
A1	4032	MZ	GN	An	Rim	0.00797	0.70850	0.00004	0.70827	0.00009	57.4	0.24
A35	3826	MZ	GN	Sub	Rim	0.01016	0.70862	0.00004	0.70832	0.00009	58.6	0.31
A35	3826	MZ	GN	Sub	Rim	0.00694	0.70853	0.00012	0.70833	0.00024	58.8	0.31
A35	3826	MZ	GN	An	Rim	0.01040	0.70884	0.00004	0.70854	0.00009	57.5	0.33
A35	3826	MZ	GN	Sub	Rim	0.00907	0.70878	0.00005	0.70851	0.00010		
A35	3826	MZ	GN	Sub	Rim	0.01020	0.70853	0.00004	0.70823	0.00009		
A35	3826	MZ	GN	An	Core	0.01071	0.70927	0.00005	0.70896	0.00009	58.1	0.30
A35	3826	MZ	GN	Sub	Rim	0.00886	0.70859	0.00004	0.70833	0.00009	59.0	0.30
A35	3826	MZ	GN	Sub	Rim	0.00862	0.70902	0.00004	0.70877	0.00009	57.8	0.30
A35	3826	MZ	GN	An	Core	0.01265	0.70919	0.00005	0.70882	0.00010	57.9	0.33
A35	3826	MZ	GN	An	Rim	0.01195	0.70907	0.00005	0.70872	0.00010	58.4	0.33
A35	3826	MZ	GN	Sub	Rim	0.01199	0.70873	0.00005	0.70838	0.00009	58.2	0.32
A35	3826	MZ	GN	An	Rim	0.01023	0.70894	0.00005	0.70864	0.00011	59.5	0.34
A35	3826	MZ	GN	An	Core	0.01036	0.70865	0.00005	0.70835	0.00009	59.5	0.35
A35	3826	MZ	GN	An	Core	0.00797	0.70877	0.00005	0.70854	0.00010	58.0	0.32
A65	3633	MZ	GN	Sub	Rim	0.00477	0.70910	0.00005	0.70897	0.00010	58.6	0.20
A65	3633	MZ	GN	Sub	Core	0.00860	0.70903	0.00006	0.70878	0.00011	60.0	0.22
A65	3633	MZ	GN	Sub	Rim	0.00829	0.70869	0.00005	0.70844	0.00011	59.6	0.24
A65	3633	MZ	GN	Sub	Rim	0.00838	0.70849	0.00005	0.70825	0.00010	59.3	0.22
A65	3633	MZ	GN	Sub	Core	0.00776	0.70885	0.00006	0.70862	0.00012	61.1	0.23
A65	3633	MZ	GN	Sub	Core	0.00810	0.70883	0.00005	0.70860	0.00010	59.7	0.23
A65	3633	MZ	GN	Sub	Rim	0.00640	0.70874	0.00005	0.70855	0.00011	59.2	0.21
A65	3633	MZ	GN	Sub	Rim	0.00753	0.70875	0.00005	0.70853	0.00011	61.2	0.23
A65	3633	MZ	GN	Sub	Rim	0.00704	0.70895	0.00005	0.70875	0.00011	58.5	0.24
A65	3633	MZ	GN	Sub	Rim	0.00815	0.70890	0.00006	0.70866	0.00013	61.6	0.22
A65	3633	MZ	GN	Sub	Core	0.00784	0.70890	0.00006	0.70867	0.00011	59.0	0.22
A65	3633	MZ	GN	Sub	Rim	0.00821	0.70866	0.00005	0.70842	0.00010	58.9	0.23
A65	3633	MZ	GN	An	Rim	0.00829	0.70887	0.00005	0.70863	0.00010	57.6	0.20
A106	3426	MZ	GN	Eu	Rim	0.00412	0.70847	0.00006	0.70835	0.00012	63.2	0.21
A106	3426	MZ	GN	Eu	Rim	0.00252	0.70870	0.00005	0.70863	0.00011	63.6	0.23
A106	3426	MZ	GN	Sub	Core	0.00210	0.70852	0.00005	0.70846	0.00010	63.0	0.21
A106	3426	MZ	GN	Sub	Rim	0.00400	0.70867	0.00005	0.70855	0.00010	62.1	0.21
A106	3426	MZ	GN	Sub	Rim	0.00218	0.70884	0.00006	0.70878	0.00012	60.7	0.22
A106	3426	MZ	GN	Sub	Core	0.00433	0.70862	0.00005	0.70849	0.00011	62.8	0.24
A106	3426	MZ	GN	Sub	Rim	0.00303	0.70847	0.00006	0.70838	0.00011	63.4	0.22
A106	3426	MZ	GN	Eu	Core	0.00266	0.70902	0.00005	0.70895	0.00011	63.7	0.23
A106	3426	MZ	GN	Eu	Rim	0.00264	0.70878	0.00005	0.70871	0.00009	62.3	0.21
A106	3426	MZ	GN	Sub	Core	0.00479	0.70890	0.00006	0.70876	0.00011	62.9	0.23
A106	3426	MZ	GN	Sub	Core	0.00268	0.70875	0.00005	0.70867	0.00010	62.4	0.21

Table C.1 (cont.)

Sample	Height (m)	Unit	Rock	Texture	Position	$^{87}Rb/^{86}Sr$	$^{87}Sr/^{86}Sr$	1σ	$^{87}Sr/^{86}Sr_i$	2σ	An	FeO (wt %)
A106	3426	MZ	GN	An	Rim	0.00307	0.70873	0.00005	0.70864	0.00010	62.2	0.23
A106	3426	MZ	GN	Sub	Rim	0.00202	0.70867	0.00005	0.70861	0.00010	63.3	0.23
A106	3426	MZ	GN	An	Rim	0.00378	0.70862	0.00005	0.70851	0.00009	62.3	0.23
A141	3227	MZ	GN	Sub	Core	0.00679	0.70864	0.00005	0.70844	0.00010	64.4	0.27
A141	3227	MZ	GN	Eu	Rim	0.00888	0.70882	0.00006	0.70856	0.00012	61.6	0.28
A141	3227	MZ	GN	Sub	Core	0.00613	0.70918	0.00005	0.70900	0.00010	64.2	0.29
A141	3227	MZ	GN	An	Core	0.00534	0.70872	0.00005	0.70856	0.00010	63.6	0.27
A141	3227	MZ	GN	Eu	Rim	0.00931	0.70909	0.00006	0.70882	0.00013	64.4	0.34
A141	3227	MZ	GN	Eu	Core	0.01219	0.70882	0.00005	0.70847	0.00011	62.4	0.34
A141	3227	MZ	GN	Eu	Rim	0.00679	0.70869	0.00005	0.70849	0.00011	62.5	0.28
A141	3227	MZ	GN	Sub	Rim	0.00679	0.70860	0.00006	0.70840	0.00011	63.3	0.31
A141	3227	MZ	GN	Sub	Core	0.00974	0.70900	0.00005	0.70871	0.00011	63.4	0.35
A141	3227	MZ	GN	Sub	Core	0.00882	0.70913	0.00006	0.70887	0.00012	62.7	0.31
A141	3227	MZ	GN	Sub	Rim	0.00799	0.70930	0.00006	0.70907	0.00012	64.3	0.33
A141	3227	MZ	GN	Sub	Rim	0.00889	0.70892	0.00005	0.70866	0.00011	63.1	0.31
A141	3227	MZ	GN	Sub	Core	0.01011	0.70850	0.00006	0.70820	0.00012	62.4	0.32
A141	3227	MZ	GN	Sub	Core	0.01025	0.70934	0.00006	0.70904	0.00012	64.2	0.30
A141	3227	MZ	GN	Sub	Rim	0.00609	0.70912	0.00006	0.70895	0.00012	64.6	0.31
A141	3227	MZ	GN	Sub	Core	0.00774	0.70914	0.00005	0.70891	0.00010	62.5	0.31
A141	3227	MZ	GN	Sub	Rim	0.00771	0.70840	0.00006	0.70817	0.00012	64.3	0.33
A141	3227	MZ	GN	Sub	Rim	0.01110	0.70844	0.00006	0.70811	0.00013	65.1	0.33
A141	3227	MZ	GN	Sub	Core	0.00932	0.70893	0.00006	0.70866	0.00012	63.3	0.30
A168	2994	MZ	GN	Sub	Rim	0.00277	0.70868	0.00006	0.70860	0.00013	65.0	0.25
A168	2994	MZ	GN	Sub	Rim	0.00177	0.70896	0.00006	0.70891	0.00013	67.5	0.26
A168	2994	MZ	GN	An	Core	0.00410	0.70903	0.00006	0.70891	0.00013	66.2	0.29
A168	2994	MZ	GN	Sub	Core	0.00156	0.70862	0.00007	0.70857	0.00015	67.1	0.27
A168	2994	MZ	GN	Sub	Core	0.00210	0.70867	0.00005	0.70861	0.00011	70.8	0.29
A168	2994	MZ	GN	An	Core	0.00134	0.70911	0.00006	0.70908	0.00013	71.5	0.27
A168	2994	MZ	GN	Sub	Rim	0.00259	0.70892	0.00007	0.70885	0.00013	69.1	0.28
A168	2994	MZ	GN	Sub	Core	0.00339	0.70918	0.00006	0.70908	0.00012	66.6	0.27
A168	2994	MZ	GN	Sub	Rim	0.00291	0.70853	0.00006	0.70844	0.00013	67.3	0.29
A168	2994	MZ	GN	Sub	Rim	0.00350	0.70849	0.00006	0.70839	0.00012	66.2	0.25
A168	2994	MZ	GN	Sub	Core	0.00213	0.70899	0.00006	0.70893	0.00011	68.1	0.27
A168	2994	MZ	GN	Sub	Rim	0.00245	0.70909	0.00007	0.70902	0.00013	65.4	0.23
A168	2994	MZ	GN	Sub	Core	0.00294	0.70933	0.00006	0.70925	0.00013	69.9	0.28
A168	2994	MZ	GN	Sub	Rim	0.00184	0.70950	0.00006	0.70944	0.00013	70.1	0.26
A168	2994	MZ	GN	Sub	Rim	0.00343	0.70928	0.00007	0.70918	0.00014	66.9	0.25
A206	2822	MZ	GN	Eu	Rim	0.00549	0.70857	0.00007	0.70841	0.00014	67.4	0.35
A206	2822	MZ	GN	Eu	Rim	0.00440	0.70892	0.00007	0.70879	0.00015	67.2	0.27
A206	2822	MZ	GN	Sub	Core	0.00332	0.70902	0.00006	0.70892	0.00013	68.3	0.31
A206	2822	MZ	GN	An	Rim	0.00114	0.70904	0.00007	0.70901	0.00015	68.8	0.24
A206	2822	MZ	GN	An	Rim	0.00311	0.70917	0.00007	0.70908	0.00015	65.2	0.21
A206	2822	MZ	GN	Eu	Core	0.01361	0.70883	0.00007	0.70844	0.00014	64.2	0.36
A206	2822	MZ	GN	Eu	Rim	0.00489	0.70894	0.00006	0.70880	0.00013	65.4	0.35
A206	2822	MZ	GN	Eu	Rim	0.00893	0.70912	0.00006	0.70886	0.00013	65.8	0.41
A206	2822	MZ	GN	Sub	Rim	0.00311	0.70879	0.00006	0.70870	0.00011	69.1	0.35
A206	2822	MZ	GN	Sub	Rim	0.00317	0.70916	0.00006	0.70906	0.00013	70.2	0.23
A206	2822	MZ	GN	An	Rim	0.00671	0.70930	0.00007	0.70911	0.00014	67.2	0.35
A206	2822	MZ	GN	Sub	Core	0.00255	0.70915	0.00007	0.70908	0.00015	69.2	0.41
A206	2822	MZ	GN	An	Core	0.00272	0.70862	0.00008	0.70854	0.00016	64.3	0.30

Table C.1 (cont.)

Sample	Height (m)	Unit	Rock	Texture	Position	$^{87}Rb/^{86}Sr$	$^{87}Sr/^{86}Sr$	1σ	$^{87}Sr/^{86}Sr_i$	2σ	An	FeO (wt %)
A238	2620	MZ	GN	Sub	Rim	0.00150	0.70826	0.00005	0.70821	0.00011	63.8	0.23
A238	2620	MZ	GN	An	Rim	0.00208	0.70766	0.00006	0.70760	0.00012	58.6	0.26
A238	2620	MZ	GN	An	Core	0.00073	0.70768	0.00006	0.70766	0.00012	62.6	0.29
A238	2620	MZ	GN	An	Rim	0.00128	0.70767	0.00006	0.70764	0.00012	57.1	0.29
A238	2620	MZ	GN	An	Core	0.00170	0.70767	0.00005	0.70763	0.00010	62.3	0.35
A238	2620	MZ	GN	Sub	Rim	0.00323	0.70748	0.00006	0.70738	0.00012	56.5	0.29
A238	2620	MZ	GN	Sub	Rim	0.00303	0.70723	0.00006	0.70714	0.00013	63.4	0.29
A238	2620	MZ	GN	Sub	Rim	0.00247	0.70803	0.00006	0.70795	0.00012	55.4	0.25
A238	2620	MZ	GN	An	Rim	0.00113	0.70790	0.00006	0.70787	0.00011	58.3	0.25
A238	2620	MZ	GN	An	Core	0.00156	0.70776	0.00006	0.70772	0.00012	61.2	0.31
A238	2620	MZ	GN	An	Core	0.00177	0.70770	0.00006	0.70765	0.00012	62.2	0.32
A238	2620	MZ	GN	An	Rim	0.00125	0.70763	0.00006	0.70759	0.00011	54.5	0.28
A238	2620	MZ	GN	An	Core	0.00211	0.70796	0.00006	0.70790	0.00012	59.5	0.31
A238	2620	MZ	GN	Sub	Rim	0.00233	0.70785	0.00005	0.70779	0.00010	65.9	0.31
A238	2620	MZ	GN	An	Rim	0.00149	0.70746	0.00005	0.70742	0.00011	56.0	0.29
A271	2436	MZ	GN	Sub	Rim	0.00504	0.70938	0.00006	0.70923	0.00012	65.5	0.23
A271	2436	MZ	GN	Sub	Core	0.00287	0.70861	0.00006	0.70852	0.00012	65.4	0.25
A271	2436	MZ	GN	Eu	Core	0.00319	0.70891	0.00006	0.70882	0.00013	62.1	0.23
A271	2436	MZ	GN	Sub	Core	0.01039	0.70922	0.00006	0.70891	0.00012	64.1	0.27
A271	2436	MZ	GN	Sub	Rim	0.00550	0.70881	0.00006	0.70865	0.00012	63.9	0.24
A271	2436	MZ	GN	Sub	Rim	0.00545	0.70923	0.00007	0.70907	0.00014	68.5	0.27
A271	2436	MZ	GN	Sub	Core	0.00623	0.70962	0.00007	0.70944	0.00015	69.7	0.24
A271	2436	MZ	GN	Sub	Core	0.00591	0.70909	0.00007	0.70892	0.00013	69.6	0.30
A271	2436	MZ	GN	Sub	Rim	0.00418	0.70930	0.00007	0.70918	0.00015	69.5	0.24
A271	2436	MZ	GN	An	Core	0.00401	0.70908	0.00007	0.70897	0.00014	65.0	0.24
A271	2436	MZ	GN	Sub	Rim	0.00585	0.70989	0.00005	0.70972	0.00011	63.5	0.26
A271	2436	MZ	GN	Sub	Core	0.00534	0.70935	0.00007	0.70919	0.00015	65.3	0.27
A271	2436	MZ	GN	An	Rim	0.00499	0.70940	0.00007	0.70925	0.00014	64.5	0.24
A271	2436	MZ	GN	Sub	Core	0.00675	0.70900	0.00007	0.70880	0.00013	65.3	0.24
A297	2297	MZ	Px	An	Core	0.00328	0.70901	0.00008	0.70892	0.00017	62.8	0.23
A297	2297	MZ	Px	An	Core	0.00680	0.70912	0.00008	0.70892	0.00016	64.3	0.24
A297	2297	MZ	Px	An	Core	0.00952	0.70949	0.00008	0.70921	0.00017	65.1	0.22
A297	2297	MZ	Px	An	Core	0.00607	0.70896	0.00008	0.70879	0.00015	62.4	0.23
A297	2297	MZ	Px	An	Core	0.00361	0.70908	0.00008	0.70898	0.00016	63.7	0.30
A297	2297	MZ	Px	An	Core	0.00468	0.70900	0.00007	0.70887	0.00015	64.8	0.28
A297	2297	MZ	Px	An	Core	0.00312	0.70910	0.00008	0.70900	0.00016	63.0	0.29
A297	2297	MZ	Px	An	Core	0.00352	0.70946	0.00008	0.70936	0.00017	64.4	0.26
A297	2297	MZ	Px	An	Rim	0.00353	0.70903	0.00007	0.70893	0.00015	64.2	0.29
A297	2297	MZ	Px	An	Core	0.00318	0.70940	0.00008	0.70931	0.00017	63.5	0.22
A297	2297	MZ	Px	An	Core	0.00385	0.70860	0.00007	0.70849	0.00015	62.6	0.28
A297	2297	MZ	Px	An	Rim	0.00338	0.70898	0.00008	0.70888	0.00016	61.7	0.26
A297	2297	MZ	Px	An	Core	0.00309	0.70899	0.00008	0.70890	0.00017	63.8	0.21
NG3-146.5	1667	UCZ	Px	An	Core	0.01486	0.70623	0.00007	0.70580	0.00016	74.9	0.29
NG3-146.5	1667	UCZ	Px	An	Core	0.01237	0.70674	0.00007	0.70638	0.00015	73.4	0.30
NG3-146.5	1667	UCZ	Px	An	Rim	0.00945	0.70609	0.00007	0.70582	0.00015	75.7	0.29
NG3-146.5	1667	UCZ	Px	An	Rim	0.00977	0.70664	0.00007	0.70635	0.00014	75.6	0.28
NG3-146.5	1667	UCZ	Px	An	Core	0.00459	0.70606	0.00007	0.70593	0.00015	74.0	0.32
NG3-146.5	1667	UCZ	Px	An	Core	0.01362	0.70633	0.00007	0.70594	0.00015	74.7	0.30
NG3-146.5	1667	UCZ	Px	An	Incl	0.00820	0.70621	0.00007	0.70598	0.00013	74.1	0.30
NG3-146.5	1667	UCZ	Px	An	Rim	0.00910	0.70632	0.00007	0.70606	0.00014	76.4	0.30

Table C.1 (cont.)

Sample	Height (m)	Unit	Rock	Texture	Position	$^{87}Rb/^{86}Sr$	$^{87}Sr/^{86}Sr$	1σ	$^{87}Sr/^{86}Sr_i$	2σ	An	FeO (wt %)
NG3-146.5	1667	UCZ	Px	An	Core	0.01035	0.70587	0.00006	0.70557	0.00012	74.5	0.32
NG3-146.5	1667	UCZ	Px	An	Rim	0.00533	0.70657	0.00007	0.70641	0.00015	74.6	0.31
NG3-146.5	1667	UCZ	Px	An	Core	0.01053	0.70623	0.00007	0.70593	0.00013	75.0	0.31
NG3-146.5	1667	UCZ	Px	An	Core	0.01198	0.70693	0.00007	0.70658	0.00014	72.3	0.32
NG3-146.5	1667	UCZ	Px	An	Core	0.00730	0.70588	0.00009	0.70567	0.00018	70.1	0.27
NG3-146.5	1667	UCZ	Px	An	Core	0.00734	0.70636	0.00011	0.70614	0.00022	74.3	0.25
NG3-146.5	1667	UCZ	Px	An	Core	0.00718	0.70694	0.00010	0.70673	0.00021	75.7	0.25
NG3-156.16	1657	UCZ	A	Sub	Core	0.00680	0.70653	0.00006	0.70633	0.00012	75.4	0.20
NG3-156.16	1657	UCZ	A	Sub	Rim	0.00578	0.70618	0.00006	0.70601	0.00012	76.6	0.25
NG3-156.16	1657	UCZ	A	Eu	Core	0.00962	0.70637	0.00006	0.70609	0.00013	75.7	0.22
NG3-156.16	1657	UCZ	A	Sub	Core	0.00426	0.70581	0.00007	0.70568	0.00013	75.9	0.25
NG3-156.16	1657	UCZ	A	Sub	Core	0.00445	0.70648	0.00006	0.70635	0.00013	75.6	0.22
NG3-156.16	1657	UCZ	A	Sub	Core	0.00842	0.70654	0.00006	0.70629	0.00013	75.8	0.23
NG3-156.16	1657	UCZ	A	Sub	Core	0.00242	0.70665	0.00007	0.70658	0.00014	76.1	0.20
NG3-156.16	1657	UCZ	A	Sub	Rim	0.00737	0.70599	0.00006	0.70577	0.00012	75.9	0.21
NG3-156.16	1657	UCZ	A	Sub	Core	0.00860	0.70630	0.00006	0.70605	0.00012	75.9	0.20
NG3-156.16	1657	UCZ	A	Sub	Core	0.02123	0.70699	0.00007	0.70637	0.00018	74.0	0.22
NG3-156.16	1657	UCZ	A	Sub	Core	0.00299	0.70621	0.00006	0.70612	0.00013	76.0	0.19
NG3-156.16	1657	UCZ	A	Sub	Rim	0.00469	0.70645	0.00006	0.70631	0.00011	75.5	0.19
NG3-156.16	1657	UCZ	A			0.00826	0.70621	0.00006	0.70596	0.00013	75.6	0.21
NG3-156.16	1657	UCZ	A	Sub	Rim	0.00868	0.70675	0.00006	0.70649	0.00012	75.4	0.21
NG3-156.16	1657	UCZ	A	Sub	Rim	0.00709	0.70637	0.00007	0.70617	0.00014	78.9	0.22
NG3-175.56	1638	UCZ	N	An	Rim	0.00557	0.70642	0.00006	0.70626	0.00012	76.6	0.26
NG3-175.56	1638	UCZ	N	Sub	Rim	0.00488	0.70613	0.00006	0.70598	0.00011	78.0	0.24
NG3-175.56	1638	UCZ	N	An	Core	0.00617	0.70583	0.00005	0.70565	0.00011	77.5	0.28
NG3-175.56	1638	UCZ	N	An	Rim	0.00711	0.70600	0.00006	0.70580	0.00012	76.7	0.33
NG3-175.56	1638	UCZ	N	Sub	Core	0.00743	0.70588	0.00006	0.70566	0.00011	76.4	0.28
NG3-175.56	1638	UCZ	N	Sub	Core	0.00704	0.70648	0.00005	0.70628	0.00010	76.2	0.27
NG3-175.56	1638	UCZ	N	Sub	Rim	0.00457	0.70589	0.00006	0.70576	0.00011	77.0	0.29
NG3-175.56	1638	UCZ	N	Sub	Rim	0.00724	0.70649	0.00005	0.70627	0.00010	76.0	0.29
NG3-175.56	1638	UCZ	N	An	Core	0.00825	0.70661	0.00006	0.70637	0.00012	76.1	0.28
NG3-175.56	1638	UCZ	N	An	Rim	0.00854	0.70662	0.00006	0.70637	0.00012	75.9	0.29
NG3-175.56	1638	UCZ	N	An	Rim	0.00578	0.70665	0.00006	0.70648	0.00012	76.3	0.23
NG3-175.56	1638	UCZ	N	An	Rim	0.00790	0.70605	0.00006	0.70582	0.00013	75.4	0.28
NG3-175.56	1638	UCZ	N	An	Core	0.00868	0.70648	0.00006	0.70623	0.00013	75.3	0.28
NG3-175.56	1638	UCZ	N	An	Rim	0.00632	0.70626	0.00006	0.70608	0.00013	75.7	0.28
NG3-175.56	1638	UCZ	N	An	Core	0.00590	0.70642	0.00005	0.70625	0.00010	75.5	0.28
NG3-175.56	1638	UCZ	N	An	Rim	0.00644	0.70644	0.00007	0.70625	0.00014		
NG3-175.56	1638	UCZ	N	An	Rim	0.00528	0.70633	0.00006	0.70617	0.00013	77.8	0.28
NG3-212.93	1601	UCZ	A	Sub	Rim	0.00336	0.70571	0.00007	0.70561	0.00015	80.3	0.46
NG3-212.93	1601	UCZ	A	An	Rim	0.00240	0.70578	0.00007	0.70571	0.00014	81.3	0.46
NG3-212.93	1601	UCZ	A	An	Rim	0.00239	0.70576	0.00008	0.70569	0.00015	82.1	0.43
NG3-212.93	1601	UCZ	A	An	Rim	0.00181	0.70597	0.00007	0.70592	0.00015	81.9	0.58
NG3-212.93	1601	UCZ	A	Sub	Core	0.00279	0.70627	0.00008	0.70619	0.00016	80.3	0.45
NG3-212.93	1601	UCZ	A	An	Core	0.00227	0.70600	0.00008	0.70593	0.00016	81.1	0.43
NG3-212.93	1601	UCZ	A	Sub	Core	0.00307	0.70517	0.00007	0.70509	0.00014	79.9	0.34
NG3-212.93	1601	UCZ	A	An	Core	0.00264	0.70611	0.00007	0.70604	0.00014	80.6	0.37
NG3-212.93	1601	UCZ	A	An	Core	0.00268	0.70561	0.00007	0.70553	0.00014	81.4	0.47
NG3-212.93	1601	UCZ	A	An	Rim	0.00232	0.70613	0.00007	0.70606	0.00014	81.6	0.45
NG3-212.93	1601	UCZ	A	Sub	Rim	0.00275	0.70612	0.00007	0.70604	0.00014	80.5	0.48

Table C.1 (cont.)

Sample	Height (m)	Unit	Rock	Texture	Position	$^{87}Rb/^{86}Sr$	$^{87}Sr/^{86}Sr$	1σ	$^{87}Sr/^{86}Sr_i$	2σ	An	FeO (wt %)
NG3-212.93	1601	UCZ	A	Sub	Rim	0.00357	0.70590	0.00011	0.70580	0.00022	80.7	0.55
NG3-212.93	1601	UCZ	A	Sub	Core	0.00253	0.70548	0.00007	0.70541	0.00015	81.3	0.55
NG3-212.93	1601	UCZ	A	Sub	Rim	0.00252	0.70549	0.00006	0.70542	0.00013	82.8	0.67
NG3-212.93	1601	UCZ	A	An	Core	0.00313	0.70625	0.00007	0.70616	0.00014	81.4	0.55
NG1-163.27	1400	LCZ	Px	Sub	Core	0.00302	0.70558	0.00008	0.70550	0.00016	59.7	0.49
NG1-163.27	1400	LCZ	Px	An	Rim	0.00396	0.70589	0.00011	0.70577	0.00023	48.8	0.60
NG1-163.27	1400	LCZ	Px	An	Core	0.00162	0.70606	0.00006	0.70602	0.00013	61.7	0.59
NG1-163.27	1400	LCZ	Px	An	Rim	0.00070	0.70570	0.00006	0.70568	0.00012	68.9	0.60
NG1-163.27	1400	LCZ	Px	An	Core	0.00126	0.70572	0.00007	0.70568	0.00014	63.3	0.55
NG1-163.27	1400	LCZ	Px	An	Core	0.00099	0.70548	0.00007	0.70545	0.00014	68.2	0.58
NG1-163.27	1400	LCZ	Px	An	Rim	0.00030	0.70511	0.00006	0.70510	0.00013	72.2	0.64
NG1-163.27	1400	LCZ	Px	An	Rim	0.00049	0.70536	0.00007	0.70535	0.00014	66.8	0.57
NG1-163.27	1400	LCZ	Px			0.00068	0.70544	0.00007	0.70542	0.00014	66.4	0.62
NG1-163.27	1400	LCZ	Px	An	Core	0.00064	0.70556	0.00006	0.70554	0.00012	68.4	0.58
NG1-163.27	1400	LCZ	Px	An	Rim	0.00052	0.70511	0.00007	0.70509	0.00014	72.0	0.54
NG1-163.27	1400	LCZ	Px	An	Core	0.00093	0.70615	0.00007	0.70612	0.00015	67.4	0.43
NG1-163.27	1400	LCZ	Px	An	Core	0.00179	0.70544	0.00006	0.70538	0.00013	65.1	0.51
NG1-163.27	1400	LCZ	Px	An	Core	0.00017	0.70579	0.00006	0.70578	0.00012	73.6	0.53
NG1-163.27	1400	LCZ	Px	An	Rim	0.00092	0.70530	0.00006	0.70527	0.00013	68.3	0.52
NG1-327.45	1236	LCZ	Px	An	Rim	0.00226	0.70527	0.00010	0.70520	0.00020	68.2	0.43
NG1-327.45	1236	LCZ	Px	An	Rim	0.00133	0.70503	0.00013	0.70499	0.00027	68.4	0.57
NG1-327.45	1236	LCZ	Px	An	Core	0.00166	0.70566	0.00018	0.70561	0.00037	57.1	0.44
NG1-327.45	1236	LCZ	Px	An	Core	0.00580	0.70453	0.00012	0.70436	0.00025	56.6	0.47
NG1-327.45	1236	LCZ	Px	An	Core	0.00694	0.70566	0.00015	0.70546	0.00031	63.0	0.44
NG1-327.45	1236	LCZ	Px	An	Rim	0.00155	0.70405	0.00011	0.70401	0.00023	65.3	0.50
NG1-327.45	1236	LCZ	Px	An	Core	0.00133	0.70499	0.00013	0.70495	0.00026	63.1	0.43
NG1-327.45	1236	LCZ	Px	An	Rim	0.00247	0.70518	0.00014	0.70511	0.00027	62.1	0.58
NG1-327.45	1236	LCZ	Px	An	Rim	0.00086	0.70458	0.00012	0.70456	0.00025	60.0	0.72
NG1-327.45	1236	LCZ	Px	An	Core	0.00120	0.70523	0.00012	0.70519	0.00025	70.2	0.74
NG1-327.45	1236	LCZ	Px	An	Core	0.00150	0.70523	0.00010	0.70519	0.00020	66.9	0.76
NG1-327.45	1236	LCZ	Px	An	Rim	0.00453	0.70538	0.00011	0.70525	0.00022	59.3	0.60
NG1-327.45	1236	LCZ	Px	An	Rim	0.00190	0.70492	0.00013	0.70487	0.00025	58.4	0.40
NG1-327.45	1236	LCZ	Px	An	Rim	0.00182	0.70461	0.00012	0.70455	0.00024	60.0	0.53
NG1-575.35	988	LCZ	Px	An	Rim	0.00099	0.70469	0.00010	0.70466	0.00020	67.9	0.49
NG1-575.35	988	LCZ	Px	An	Core	0.00054	0.70588	0.00010	0.70586	0.00019	71.9	0.53
NG1-575.35	988	LCZ	Px	An	Core	0.00084	0.70527	0.00010	0.70525	0.00020	64.7	0.49
NG1-575.35	988	LCZ	Px	An	Core	0.00032	0.70544	0.00007	0.70543	0.00014	66.9	0.48
NG1-575.35	988	LCZ	Px	An	Rim	0.00039	0.70523	0.00005	0.70522	0.00011	66.7	0.48
NG1-575.35	988	LCZ	Px	An	Core	0.00027	0.70555	0.00006	0.70554	0.00012	68.6	0.48
NG1-575.35	988	LCZ	Px	An	Core	0.00183	0.70545	0.00007	0.70540	0.00015	61.7	0.41
NG1-575.35	988	LCZ	Px	An	Core	0.00201	0.70531	0.00007	0.70525	0.00014	62.5	0.44
NG1-575.35	988	LCZ	Px	An	Rim	0.00113	0.70497	0.00007	0.70493	0.00014	65.5	0.46
NG1-575.35	988	LCZ	Px	An	Core	0.00138	0.70508	0.00006	0.70504	0.00013	65.2	0.40
NG1-575.35	988	LCZ	Px	An	Core	0.00219	0.70575	0.00011	0.70568	0.00022	58.2	0.33
NG1-575.35	988	LCZ	Px	An	Rim	0.00148	0.70536	0.00007	0.70532	0.00015	58.1	0.39
NG1-575.35	988	LCZ	Px	An	Core	0.00251	0.70546	0.00012	0.70539	0.00024	51.1	0.43
NG1-575.35	988	LCZ	Px	An	Core	0.00181	0.70517	0.00008	0.70512	0.00016	64.6	0.37
NG1-575.35	988	LCZ	Px	An	Core	0.00136	0.70561	0.00008	0.70557	0.00017	64.6	0.34
NG1-575.35	988	LCZ	Px	An	Rim	0.00148	0.70584	0.00008	0.70580	0.00016	63.2	0.37
NG1-695.5	868	LCZ	Px	An	Rim	0.00057	0.70514	0.00006	0.70512	0.00012	67.7	0.34

Table C.1 (cont.)

Sample	Height (m)	Unit	Rock	Texture	Position	$^{87}Rb/^{86}Sr$	$^{87}Sr/^{86}Sr$	1σ	$^{87}Sr/^{86}Sr_i$	2σ	An	FeO (wt %)
NG1-695.5	868	LCZ	Px	An	Rim	0.00101	0.70514	0.00006	0.70511	0.00013	64.5	0.36
NG1-695.5	868	LCZ	Px	An	Core	0.00135	0.70542	0.00007	0.70538	0.00014	64.7	0.38
NG1-695.5	868	LCZ	Px	An	Rim	0.00116	0.70556	0.00006	0.70552	0.00012	64.5	0.35
NG1-695.5	868	LCZ	Px	An	Core	0.00086	0.70561	0.00006	0.70558	0.00012	61.3	0.29
NG1-695.5	868	LCZ	Px			0.00112	0.70561	0.00006	0.70557	0.00012	62.7	0.30
NG1-695.5	868	LCZ	Px	An	Core	0.00077	0.70508	0.00006	0.70506	0.00012	65.5	0.35
NG1-695.5	868	LCZ	Px	An	Core	0.00071	0.70578	0.00006	0.70576	0.00013	67.3	0.37
NG1-695.5	868	LCZ	Px	An	Core	0.00110	0.70523	0.00005	0.70520	0.00011	63.4	0.42
NG1-695.5	868	LCZ	Px	An	Core	0.00105	0.70550	0.00005	0.70547	0.00011	63.9	0.36
NG1-695.5	868	LCZ	Px	An	Rim	0.00085	0.70565	0.00007	0.70562	0.00014	64.0	0.34
NG1-695.5	868	LCZ	Px	An	Rim	0.00063	0.70537	0.00006	0.70536	0.00012	64.2	0.38
NG1-695.5	868	LCZ	Px	An	Core	0.00101	0.70560	0.00006	0.70557	0.00012	64.3	0.38
NG1-695.5	868	LCZ	Px	An	Core	0.00074	0.70516	0.00007	0.70514	0.00014	57.8	0.39
NG2-134.4	639	LZ	Dun	An	Rim	0.00044	0.70630	0.00009	0.70629	0.00017	69.3	0.60
NG2-134.4	639	LZ	Dun	An	Core	0.00071	0.70692	0.00007	0.70690	0.00013	70.3	0.55
NG2-134.4	639	LZ	Dun	An	Rim	0.00045	0.70732	0.00006	0.70731	0.00011	75.5	0.62
NG2-134.4	639	LZ	Dun	An	Core	0.00042	0.70735	0.00006	0.70733	0.00012	75.2	0.57
NG2-134.4	639	LZ	Dun	An	Rim	0.00034	0.70730	0.00006	0.70729	0.00012	78.3	0.65
NG2-134.4	639	LZ	Dun	An	Core	0.00095	0.70709	0.00006	0.70706	0.00012	73.1	0.58
NG2-134.4	639	LZ	Dun	An	Rim	0.00068	0.70741	0.00006	0.70739	0.00012	68.3	0.60
NG2-134.4	639	LZ	Dun	An	Rim	0.00048	0.70728	0.00006	0.70726	0.00011	55.1	0.44
NG2-134.4	639	LZ	Dun	An	Core	0.00095	0.70713	0.00005	0.70710	0.00011	69.3	0.47
NG2-134.4	639	LZ	Dun	An	Rim	0.00042	0.70722	0.00006	0.70720	0.00012	69.1	0.23
NG2-134.4	639	LZ	Dun	An	Rim	0.00040	0.70705	0.00005	0.70704	0.00010	77.8	0.42
NG2-134.4	639	LZ	Dun	An	Core	0.00109	0.70734	0.00006	0.70731	0.00011	71.5	0.57
NG2-134.4	639	LZ	Dun	An	Core	0.00057	0.70698	0.00006	0.70697	0.00012	68.4	0.18
NG2-134.4	639	LZ	Dun	An	Core	0.00070	0.70704	0.00005	0.70702	0.00010	63.1	0.30
NG2-134.4	639	LZ	Dun	An	Rim	0.00057	0.70698	0.00007	0.70696	0.00014	68.7	0.56
NG2-180.55	593	LZ	Px	An	Rim	0.00180	0.70661	0.00009	0.70655	0.00019	61.2	0.16
NG2-180.55	593	LZ	Px	An	Rim	0.00103	0.70697	0.00006	0.70694	0.00013	63.3	0.22
NG2-180.55	593	LZ	Px	An	Rim	0.00056	0.70749	0.00006	0.70748	0.00012	72.6	0.20
NG2-180.55	593	LZ	Px	An	Core	0.00090	0.70756	0.00006	0.70753	0.00012	64.1	0.18
NG2-180.55	593	LZ	Px	An	Rim	0.00063	0.70727	0.00007	0.70725	0.00013	71.8	0.21
NG2-180.55	593	LZ	Px	An	Rim	0.00159	0.70749	0.00007	0.70744	0.00014	58.3	0.24
NG2-180.55	593	LZ	Px	An	Core	0.00129	0.70771	0.00007	0.70768	0.00013	66.8	0.23
NG2-180.55	593	LZ	Px	An	Core	0.02429	0.70784	0.00008	0.70713	0.00019	67.4	0.31
NG2-180.55	593	LZ	Px	An	Rim	0.00103	0.70721	0.00009	0.70718	0.00019	63.8	0.28
NG2-180.55	593	LZ	Px	An	Rim	0.00171	0.70734	0.00010	0.70729	0.00020	65.3	0.24
NG2-180.55	593	LZ	Px	An	Rim	0.00143	0.70755	0.00010	0.70751	0.00020	65.1	0.20
NG2-180.55	593	LZ	Px	An	Core	0.00200	0.70704	0.00011	0.70698	0.00023	59.2	0.18
NG2-300	474	LZ	Px		Core	0.00203	0.70535	0.00007	0.70529	0.00014	83.6	0.30
NG2-300	474	LZ	Px		Rim	0.02899	0.70573	0.00007	0.70489	0.00017	83.2	0.33
NG2-300	474	LZ	Px		Core	0.00373	0.70556	0.00008	0.70545	0.00017	85.4	0.27
NG2-300	474	LZ	Px	An	Rim	0.00118	0.70571	0.00008	0.70568	0.00016	69.8	0.27
NG2-300	474	LZ	Px	An	Core	0.01172	0.70550	0.00009	0.70516	0.00021	76.7	0.24
NG2-300	474	LZ	Px	An	Rim	0.00432	0.70617	0.00008	0.70605	0.00017	69.4	0.31
NG2-300	474	LZ	Px	An	Rim	0.00174	0.70537	0.00008	0.70532	0.00017	84.1	0.28
NG2-300	474	LZ	Px	An	Core	0.01286	0.70611	0.00008	0.70573	0.00019	83.3	0.24
NG2-300	474	LZ	Px	Sub	Rim	0.00173	0.70608	0.00007	0.70603	0.00014	83.7	0.32
NG2-300	474	LZ	Px	Sub	Core	0.03164	0.70637	0.00007	0.70545	0.00018	84.4	0.31

Table C.1 (cont.)

Sample	Height (m)	Unit	Rock	Texture	Position	$^{87}Rb/^{86}Sr$	$^{87}Sr/^{86}Sr$	1σ	$^{87}Sr/^{86}Sr_i$	2σ	An	FeO (wt %)
NG2-300	474	LZ	Px	Sub	Core	0.00097	0.70552	0.00008	0.70549	0.00016	84.7	0.30
NG2-300	474	LZ	Px	Sub	Rim	0.00085	0.70579	0.00007	0.70577	0.00013	84.7	0.31
NG2-300	474	LZ	Px	Sub	Rim	0.00106	0.70587	0.00008	0.70584	0.00016	84.2	0.31
NG2-300	474	LZ	Px	Sub	Rim	0.00156	0.70612	0.00007	0.70608	0.00014	82.1	0.31
NG2-300	474	LZ	Px	Sub	Rim	0.00055	0.70540	0.00007	0.70538	0.00014	83.0	0.29
NG2-300	474	LZ	Px	Sub	Rim	0.00286	0.70598	0.00008	0.70590	0.00016	83.1	0.25
NG2-490.05	283	LZ	Hz	An	Core	0.00043	0.70503	0.00004	0.70502	0.00009	62.8	0.21
NG2-490.05	283	LZ	Hz	An	Rim	0.00023	0.70517	0.00004	0.70516	0.00008	69.4	0.21
NG2-490.05	283	LZ	Hz	An	Core	0.00477	0.70556	0.00004	0.70542	0.00009	75.5	0.22
NG2-490.05	283	LZ	Hz	An	Core	0.00108	0.70479	0.00005	0.70476	0.00010	69.6	0.21
NG2-490.05	283	LZ	Hz	An	Core	0.00055	0.70499	0.00005	0.70498	0.00011	67.2	0.19
NG2-490.05	283	LZ	Hz	An	Core	0.00381	0.70610	0.00005	0.70599	0.00010	53.2	0.19
NG2-490.05	283	LZ	Hz	An	Rim	0.00087	0.70515	0.00005	0.70512	0.00010	50.2	0.22
NG2-490.05	283	LZ	Hz	An	Core	0.00363	0.70603	0.00005	0.70593	0.00009	59.4	0.35
NG2-490.05	283	LZ	Hz	An	Rim	0.00153	0.70472	0.00007	0.70468	0.00015	68.0	0.20
NG2-490.05	283	LZ	Hz	An	Core	0.00045	0.70511	0.00006	0.70510	0.00012	64.9	0.19
NG2-626.17	147	LZ	Ol-Px	An	Rim	0.00053	0.70512	0.00007	0.70511	0.00014	67.2	0.24
NG2-626.17	147	LZ	Ol-Px	An	Core	0.00022	0.70428	0.00006	0.70427	0.00012	54.5	0.20
NG2-626.17	147	LZ	Ol-Px	An	Core	0.00046	0.70435	0.00007	0.70434	0.00014	51.1	0.19
NG2-626.17	147	LZ	Ol-Px	An	Rim	0.00056	0.70464	0.00007	0.70463	0.00014	54.9	0.20
NG2-626.17	147	LZ	Ol-Px	An	Core	0.00039	0.70488	0.00007	0.70486	0.00013	51.7	0.18
NG2-626.17	147	LZ	Ol-Px	An	Rim	0.00022	0.70440	0.00006	0.70440	0.00013	73.2	0.18
NG2-626.17	147	LZ	Ol-Px	An	Rim	0.00037	0.70443	0.00006	0.70442	0.00012	50.8	0.19
NG2-626.17	147	LZ	Ol-Px	An	Core	0.00041	0.70493	0.00007	0.70492	0.00013	53.9	0.19
NG2-626.17	147	LZ	Ol-Px	An	Core	0.00033	0.70485	0.00005	0.70484	0.00011	63.8	0.19
NG2-626.17	147	LZ	Ol-Px	An	Core	0.00027	0.70455	0.00007	0.70454	0.00013	68.9	0.21
NG2-626.17	147	LZ	Ol-Px	An	Core	0.00021	0.70462	0.00006	0.70461	0.00013	69.5	0.22
NG2-626.17	147	LZ	Ol-Px	An	Core	0.00017	0.70451	0.00007	0.70450	0.00014	66.0	0.20
NG2-626.17	147	LZ	Ol-Px	An	Rim	0.00022	0.70528	0.00007	0.70528	0.00013	64.2	0.26
NG2-664.35	109	LZ	Hz	An	Core	0.00113	0.70552	0.00007	0.70549	0.00014	53.6	0.19
NG2-664.35	109	LZ	Hz	An	Core	0.00092	0.70522	0.00008	0.70519	0.00016	49.7	0.18
NG2-664.35	109	LZ	Hz	An	Rim	0.00066	0.70510	0.00007	0.70508	0.00014	57.4	0.21
NG2-664.35	109	LZ	Hz	An	Core	0.00324	0.70541	0.00008	0.70531	0.00016	56.9	0.22
NG2-664.35	109	LZ	Hz	An	Core	0.00314	0.70509	0.00008	0.70500	0.00016	50.5	0.19
NG2-664.35	109	LZ	Hz	An	Core	0.00096	0.70546	0.00006	0.70543	0.00011	49.4	0.23
NG2-664.35	109	LZ	Hz	An	Core	0.00425	0.70586	0.00007	0.70574	0.00015	46.6	0.23
NG2-664.35	109	LZ	Hz	An	Rim	0.00079	0.70495	0.00008	0.70493	0.00016	39.5	0.24
NG2-664.35	109	LZ	Hz	An	Rim	0.00208	0.70526	0.00008	0.70520	0.00015	44.5	0.24
NG2-664.35	109	LZ	Hz	An	Rim	0.00145	0.70552	0.00007	0.70548	0.00015	49.2	0.28
NG2-664.35	109	LZ	Hz	An	Rim	0.00044	0.70539	0.00007	0.70538	0.00014	50.0	0.20
NG2-664.35	109	LZ	Hz	An	Core	0.01117	0.70561	0.00007	0.70528	0.00017	52.8	0.20
NG2-737	36	LZ	N	An	Core	0.00075	0.70421	0.00009	0.70418	0.00019	67.7	0.21
NG2-737	36	LZ	N	An	Rim	0.00057	0.70450	0.00009	0.70448	0.00019	74.1	0.24
NG2-737	36	LZ	N	An	Rim	0.00296	0.70455	0.00009	0.70446	0.00018	49.3	0.17
NG2-737	36	LZ	N	An	Core	0.00153	0.70495	0.00007	0.70491	0.00014	63.7	0.22
NG2-737	36	LZ	N	An	Rim	0.00047	0.70444	0.00006	0.70443	0.00012	69.8	0.21
NG2-737	36	LZ	N	An	Rim	0.00055	0.70464	0.00006	0.70463	0.00013	79.0	0.23
NG2-737	36	LZ	N	An	Core	0.00249	0.70465	0.00009	0.70458	0.00018	53.5	0.24
NG2-737	36	LZ	N	An	Rim	0.00115	0.70498	0.00010	0.70495	0.00021	60.3	0.22
NG2-737	36	LZ	N	An	Core	0.00273	0.70442	0.00009	0.70434	0.00018	65.6	0.21

Table C.1 (cont.)

Sample	Height (m)	Unit	Rock	Texture	Position	$^{87}Rb/^{86}Sr$	$^{87}Sr/^{86}Sr$	1σ	$^{87}Sr/^{86}Sr_i$	2σ	An	FeO (wt %)
NG2-737	36	LZ	N	An	Core	0.00071	0.70443	0.00006	0.70441	0.00013	75.2	0.24
NG2-737	36	LZ	N	An	Core	0.00267	0.70458	0.00007	0.70450	0.00014	46.5	0.20
NG2-737	36	LZ	N	An	Core	0.00203	0.70406	0.00009	0.70400	0.00018	49.1	0.20
NG2-737	36	LZ	N	An	Core	0.00148	0.70438	0.00009	0.70433	0.00018	65.8	0.23
NG2-737	36	LZ	N	An	Core	0.00132	0.70510	0.00010	0.70506	0.00020	53.2	0.20
NG2-762.27	11	LZ	GN	An	Rim	0.00047	0.70514	0.00005	0.70513	0.00010	69.5	0.27
NG2-762.27	11	LZ	GN	An	Core	0.00167	0.70457	0.00006	0.70452	0.00012	48.3	0.21
NG2-762.27	11	LZ	GN	An	Rim	0.00267	0.70494	0.00007	0.70486	0.00015	41.5	0.20
NG2-762.27	11	LZ	GN	An	Core	0.00202	0.70545	0.00006	0.70539	0.00013	38.5	0.32
NG2-762.27	11	LZ	GN	An	Core	0.00140	0.70486	0.00006	0.70482	0.00013	47.4	0.17
NG2-762.27	11	LZ	GN	An	Core	0.00124	0.70506	0.00007	0.70503	0.00014	47.7	0.20
NG2-762.27	11	LZ	GN	Sub	Core	0.00249	0.70466	0.00005	0.70458	0.00011	69.7	0.20
NG2-762.27	11	LZ	GN	Sub	Rim	0.00252	0.70517	0.00007	0.70510	0.00014	38.2	0.20
NG2-762.27	11	LZ	GN	An	Rim	0.00040	0.70462	0.00005	0.70461	0.00010	67.9	0.24
NG2-762.27	11	LZ	GN	Sub	Rim	0.00179	0.70470	0.00006	0.70465	0.00013	47.4	0.17
NG2-762.27	11	LZ	GN	An	Core	0.00262	0.70501	0.00006	0.70494	0.00012	68.7	0.21
NG2-762.27	11	LZ	GN	An	Rim	0.00161	0.70493	0.00006	0.70488	0.00012	66.9	0.18
NG2-762.27	11	LZ	GN	An	Rim	0.00136	0.70509	0.00007	0.70505	0.00014	50.6	0.16
NG2-772.98	0	LZ	GN	Sub	Core	0.00195	0.70448	0.00006	0.70443	0.00012	55.4	0.19
NG2-772.98	0	LZ	GN	An	Core	0.00248	0.70445	0.00008	0.70438	0.00015	70.3	0.29
NG2-772.98	0	LZ	GN	An	Rim	0.00141	0.70403	0.00008	0.70399	0.00017	62.8	0.28
NG2-772.98	0	LZ	GN	An	Rim	0.00260	0.70446	0.00008	0.70439	0.00016	69.6	0.33
NG2-772.98	0	LZ	GN	An	Rim	0.00310	0.70472	0.00009	0.70463	0.00019	53.5	0.25
NG2-772.98	0	LZ	GN	An	Rim	0.00459	0.70431	0.00009	0.70418	0.00018	58.3	0.29
NG2-772.98	0	LZ	GN	An	Rim	0.00185	0.70467	0.00009	0.70461	0.00018	66.9	0.21
NG2-772.98	0	LZ	GN	An	Rim	0.00153	0.70481	0.00008	0.70477	0.00015	55.2	0.25
NG2-772.98	0	LZ	GN	An	Rim	0.00137	0.70437	0.00008	0.70433	0.00017	67.3	0.30
NG2-772.98	0	LZ	GN	An	Rim	0.00184	0.70411	0.00009	0.70405	0.00018	58.1	0.28
NG2-772.98	0	LZ	GN	An	Rim	0.00328	0.70381	0.00010	0.70371	0.00021	51.9	0.18
NG2-772.98	0	LZ	GN	An	Rim	0.00246	0.70512	0.00010	0.70505	0.00020	46.0	0.28

UZ = Upper Zone, MZ = Main Zone, UCZ = Upper Critical Zone, LCZ = Lower Critical Zone, LZ = Lower Zone
Mt = magnetitite, Mt-G = magnetitite-gabbro, G = Gabbro, GN = gabbronorite, N = norite, A = anorthosite,
Px = pyroxenite, Ol-Px = olivine-pyroxenite, Hz = harzburgite, Dun = dunite
Eu = euhedral, Sub = subhedral, An = anhedral, Incl = inclusion

D Mineral chemistry

Table D.1. Mineral chemistry of olivine from the Monchegorsk Complex. Basis: 4 oxides

Sample No.	**15DB-1**	**15DB-1**	**15DB-1**	**15DB-1**	**15DB-1**	**15DB-1**	**15DB-2**	**15DB-2**	**15DB-2**	**15DB-2**
Intrusion	Dunite Block	Dunite Block	Dunite Block	Dunite Block	Dunite Block	Dunite Block	Dunite Block	Dunite Block	Dunite Block	Dunite Block
Sample Pt.	Ol 1	Ol 1	Ol 1	Ol 2	Ol 2	Ol 2	Ol 1	Ol 1	Ol 1	Ol 2
Rock type	CHR	CHR	CHR	CHR	CHR	CHR	LH	LH	LH	LH
SiO_2 (wt %)	41.28	41.35	41.38	41.75	41.62	41.54	40.56	40.44	40.55	40.35
FeO	5.78	5.93	5.84	5.19	5.23	5.06	10.83	10.90	10.94	10.83
MnO	0.12	0.12	0.11	0.11	0.09	0.12	0.17	0.19	0.20	0.20
MgO	52.32	52.60	52.80	53.49	53.33	53.41	48.69	48.27	48.65	48.34
NiO	0.62	0.62	0.63	0.66	0.65	0.62	0.45	0.40	0.39	0.40
Total	**100.12**	**100.62**	**100.76**	**101.20**	**100.92**	**100.75**	**100.70**	**100.20**	**100.73**	**100.12**
Si	0.99	0.99	0.99	0.99	0.99	0.99	0.99	1.00	0.99	0.99
Fe	0.12	0.12	0.12	0.10	0.10	0.10	0.22	0.22	0.22	0.22
Mn	0.00	0.00	0.00	0.00	0.00	0.00	0.00	0.00	0.00	0.00
Mg	1.88	1.88	1.89	1.90	1.90	1.90	1.78	1.77	1.78	1.78
Ni	0.01	0.01	0.01	0.01	0.01	0.01	0.01	0.01	0.01	0.01
Total	**3.01**	**3.01**	**3.01**	**3.01**	**3.01**	**3.01**	**3.01**	**3.00**	**3.01**	**3.01**
Mg#	94.2	94.1	94.2	94.8	94.8	95.0	88.9	88.8	88.8	88.8
Ni (ppm)	4872	4872	4951	5187	5108	4872	3536	3143	3065	3143

Sample No.	**15DB-2**	**15DB-2**	**15DB-3**	**15DB-3**	**15DB-3**	**15DB-3**	**15DB-3**	**15DB-3**	**15DB-4**	**15DB-4**
Intrusion	Dunite Block	Dunite Block	Dunite Block	Dunite Block	Dunite Block	Dunite Block	Dunite Block	Dunite Block	Dunite Block	Dunite Block
Sample Pt.	Ol 2	Ol 2	Ol 1	Ol 1	Ol 1	Ol 2	Ol 2	Ol 2	Ol 1	Ol 1
Rock type	LH	LH	LH	LH	LH	LH	LH	LH	DUN	DUN
SiO_2 (wt %)	40.36	40.65	40.77	40.65	40.54	40.76	40.85	40.76	41.05	41.20
FeO	11.05	11.02	10.57	10.55	10.58	10.57	10.62	10.71	8.40	8.28
MnO	0.17	0.19	0.20	0.20	0.20	0.18	0.18	0.18	0.17	0.17
MgO	48.34	48.60	48.26	48.92	48.46	49.07	49.11	49.00	50.76	50.89
NiO	0.41	0.40	0.40	0.45	0.44	0.43	0.45	0.41	0.46	0.48
Total	**100.33**	**100.86**	**100.20**	**100.77**	**100.22**	**101.01**	**101.21**	**101.06**	**100.84**	**101.02**
Si	0.99	0.99	1.00	0.99	1.00	0.99	0.99	0.99	0.99	0.99
Fe	0.23	0.23	0.22	0.22	0.22	0.22	0.22	0.22	0.17	0.17
Mn	0.00	0.00	0.00	0.00	0.00	0.00	0.00	0.00	0.00	0.00
Mg	1.77	1.77	1.77	1.78	1.78	1.78	1.78	1.78	1.83	1.83
Ni	0.01	0.01	0.01	0.01	0.01	0.01	0.01	0.01	0.01	0.01
Total	**3.01**	**3.01**	**3.00**	**3.01**	**3.00**	**3.01**	**3.01**	**3.01**	**3.01**	**3.01**
Mg#	88.6	88.7	89.1	89.2	89.1	89.2	89.2	89.1	91.5	91.6
Ni (ppm)	3222	3143	3143	3536	3458	3379	3536	3222	3615	3772

Sample No.	**15DB-4**	**15DB-4**	**15DB-4**	**15DB-4**	**15DB-4**	**15KMAS-1**	**15KMAS-1**	**15KMAS-1**	**15KMAS-1**	**15KMAS-1**
Intrusion	Dunite Block	Dunite Block	Dunite Block	Dunite Block	Dunite Block	Kumuzhya	Kumuzhya	Kumuzhya	Kumuzhya	Kumuzhya
Sample Pt.	Ol 1	Ol 2	Ol 2	Ol 2	Ol 2	Ol 1	Ol 1	Ol 2	Ol 2	Ol 3
Rock type	DUN	DUN	DUN	DUN	DUN	HZ	HZ	HZ	HZ	HZ
SiO_2 (wt %)	41.16	41.18	41.08	41.11	41.18	39.96	39.81	39.89	40.02	40.05
FeO	8.20	9.21	8.06	7.93	8.09	12.78	12.63	12.66	12.64	12.69
MnO	0.16	0.12	0.16	0.12	0.16	0.21	0.22	0.21	0.23	0.25
MgO	50.85	50.33	51.07	51.02	50.75	46.50	46.59	46.65	46.77	46.80
NiO	0.46	0.48	0.46	0.48	0.43	0.40	0.40	0.38	0.38	0.40
Total	**100.83**	**101.32**	**100.83**	**100.66**	**100.61**	**99.85**	**99.65**	**99.79**	**100.04**	**100.19**
Si	0.99	0.99	0.99	0.99	1.00	1.00	0.99	0.99	1.00	0.99
Fe	0.17	0.19	0.16	0.16	0.16	0.27	0.26	0.26	0.26	0.26
Mn	0.00	0.00	0.00	0.00	0.00	0.00	0.00	0.00	0.00	0.01
Mg	1.83	1.81	1.84	1.84	1.83	1.73	1.73	1.73	1.73	1.73
Ni	0.01	0.01	0.01	0.01	0.01	0.01	0.01	0.01	0.01	0.01
Total	**3.01**	**3.01**	**3.01**	**3.01**	**3.00**	**3.00**	**3.01**	**3.01**	**3.00**	**3.01**
Mg#	91.7	90.7	91.9	92.0	91.8	86.6	86.8	86.8	86.8	86.8
Ni (ppm)	3615	3772	3615	3772	3379	3143	3143	2986	2986	3143

CHR = chromitite; DUN = dunite; LH = lherzolite; HZ = harzburgite; OL-WEB = olivine-websterite;
OL-OPX = olivine-orthopyroxenite; OPX = orthopyroxenite; BRC = breccia; oph = ophitic

Table D.1 (cont.)

Sample No.	**15KMAS-1**	**15KMAS-1**	**15KMAS-1**	**15KMAS-1**	**15KMAS-2**	**15KMAS-2**	**15KMAS-2**	**15KMAS-2**	**15KMAS-2**	**15KMAS-2**
Intrusion	Kumuzhya	Kumuzhya	Kumuzhya	Kumuzhya	Kumuzhya	Kumuzhya	Kumuzhya	Kumuzhya	Kumuzhya	Kumuzhya
Sample Pt.	Ol 3	Ol 3	Ol 4	Ol 4	Ol 1	Ol 1	Ol 1	Ol 2	Ol 2	Ol 2
Rock type	HZ	HZ	HZ	HZ	OL-OPX	OL-OPX	OL-OPX	OL-OPX	OL-OPX	OL-OPX
SiO_2 (wt %)	39.76	39.82	39.99	40.02	39.83	39.80	39.65	40.05	40.01	39.91
FeO	12.50	12.55	12.68	12.74	12.63	12.72	12.60	12.82	12.75	12.56
MnO	0.22	0.20	0.21	0.20	0.20	0.21	0.21	0.20	0.18	0.20
MgO	46.67	46.78	46.79	46.79	46.60	46.60	46.35	46.74	46.91	46.70
NiO	0.38	0.41	0.42	0.38	0.43	0.44	0.44	0.42	0.44	0.42
Total	**99.53**	**99.76**	**100.09**	**100.13**	**99.69**	**99.77**	**99.25**	**100.23**	**100.29**	**99.79**
Si	0.99	0.99	0.99	0.99	0.99	0.99	0.99	0.99	0.99	0.99
Fe	0.26	0.26	0.26	0.26	0.26	0.27	0.26	0.27	0.26	0.26
Mn	0.00	0.00	0.00	0.00	0.00	0.00	0.00	0.00	0.00	0.00
Mg	1.74	1.74	1.73	1.73	1.73	1.73	1.73	1.73	1.74	1.74
Ni	0.01	0.01	0.01	0.01	0.01	0.01	0.01	0.01	0.01	0.01
Total	**3.01**	**3.01**	**3.01**	**3.01**	**3.01**	**3.01**	**3.01**	**3.01**	**3.01**	**3.01**
Mg#	86.9	86.9	86.8	86.8	86.8	86.7	86.8	86.7	86.8	86.9
Ni (ppm)	2986	3222	3301	2986	3379	3458	3458	3301	3458	3301

Sample No.	**15KMAS-2**	**15KMAS-2**	**15KMAS-3**	**15KMAS-3**	**15KMAS-3**	**15KMAS-3**	**15KMAS-3**	**15KMAS-3**	**15KMAS-3**	**15KMAS-3**
Intrusion	Kumuzhya	Kumuzhya	Kumuzhya	Kumuzhya	Kumuzhya	Kumuzhya	Kumuzhya	Kumuzhya	Kumuzhya	Kumuzhya
Sample Pt.	Ol 3	Ol 3	Ol 1	Ol 1	Ol 1	Ol 1	Ol 1	Ol 2	Ol 2	Ol 2
Rock type	OL-OPX	OL-OPX	OL-OPX	OL-OPX	OL-OPX	OL-OPX	OL-OPX	OL-OPX	OL-OPX	OL-OPX
SiO_2 (wt %)	40.52	40.33	40.18	40.16	40.18	40.08	40.10	40.36	40.48	40.30
FeO	12.74	12.72	13.05	12.92	12.87	12.85	13.00	12.90	12.97	12.96
MnO	0.19	0.21	0.20	0.21	0.20	0.19	0.22	0.20	0.19	0.20
MgO	47.27	47.02	46.90	46.76	46.70	46.63	46.56	46.94	46.97	46.97
NiO	0.40	0.43	0.44	0.42	0.46	0.42	0.42	0.38	0.41	0.39
Total	**101.12**	**100.71**	**100.77**	**100.47**	**100.41**	**100.17**	**100.30**	**100.78**	**101.02**	**100.82**
Si	1.00	1.00	0.99	1.00	1.00	1.00	1.00	1.00	1.00	1.00
Fe	0.26	0.26	0.27	0.27	0.27	0.27	0.27	0.27	0.27	0.27
Mn	0.00	0.00	0.00	0.00	0.00	0.00	0.00	0.00	0.00	0.00
Mg	1.73	1.73	1.73	1.73	1.73	1.73	1.72	1.73	1.73	1.73
Ni	0.01	0.01	0.01	0.01	0.01	0.01	0.01	0.01	0.01	0.01
Total	**3.00**	**3.00**	**3.01**	**3.00**	**3.00**	**3.00**	**3.00**	**3.00**	**3.00**	**3.00**
Mg#	86.9	86.8	86.5	86.6	86.6	86.6	86.5	86.6	86.6	86.6
Ni (ppm)	3143	3379	3458	3301	3615	3301	3301	2986	3222	3065

Sample No.	**15KMAS-4**	**15KMAS-4**	**15KMAS-4**	**15KMAS-4**	**15KMAS-4**	**15KMAS-4**	**15KMAS-4**	**15KMAS-5**	**15KMAS-5**	**15KMAS-5**
Intrusion	Kumuzhya	Kumuzhya	Kumuzhya	Kumuzhya	Kumuzhya	Kumuzhya	Kumuzhya	Kumuzhya	Kumuzhya	Kumuzhya
Sample Pt.	Ol 1	Ol 1	Ol 1	Ol 1	Ol 2	Ol 2	Ol 2	Ol 1	Ol 1	Ol 2
Rock type	OL-OPX	OL-OPX	OL-OPX	OL-OPX	OL-OPX	OL-OPX	OL-OPX	OL-OPX	OL-OPX	OL-OPX
SiO_2 (wt %)	40.01	40.06	39.94	39.92	40.15	40.05	40.16	40.12	40.08	40.05
FeO	12.97	12.82	12.97	12.94	13.05	12.96	13.06	12.91	12.71	12.91
MnO	0.22	0.20	0.21	0.21	0.21	0.21	0.20	0.22	0.21	0.20
MgO	46.50	46.57	46.59	46.67	46.56	46.54	46.70	46.79	46.86	46.58
NiO	0.43	0.42	0.42	0.46	0.44	0.46	0.44	0.40	0.39	0.41
Total	**100.13**	**100.07**	**100.13**	**100.20**	**100.41**	**100.22**	**100.56**	**100.44**	**100.25**	**100.15**
Si	1.00	1.00	0.99	0.99	1.00	1.00	1.00	0.99	0.99	1.00
Fe	0.27	0.27	0.27	0.27	0.27	0.27	0.27	0.27	0.26	0.27
Mn	0.00	0.00	0.00	0.00	0.00	0.00	0.00	0.00	0.00	0.00
Mg	1.73	1.73	1.73	1.73	1.72	1.73	1.73	1.73	1.73	1.73
Ni	0.01	0.01	0.01	0.01	0.01	0.01	0.01	0.01	0.01	0.01
Total	**3.00**	**3.00**	**3.01**	**3.01**	**3.00**	**3.00**	**3.00**	**3.01**	**3.01**	**3.00**
Mg#	86.5	86.6	86.5	86.5	86.4	86.5	86.4	86.6	86.8	86.5
Ni (ppm)	3379	3301	3301	3615	3458	3615	3458	3143	3065	3222

CHR = chromitite; DUN = dunite; LH = lherzolite; HZ = harzburgite; OL-WEB = olivine-websterite;
OL-OPX = olivine-orthopyroxenite; OPX = orthopyroxenite; BRC = breccia; oph = ophitic

Table D.1 (cont.)

Sample No.	**15KMAS-5**	**15KMAS-5**	**15KMAS-5**	**15KMAS-6**	**15KMAS-6**	**15KMAS-6**	**15KMAS-6**	**15KMAS-6**	**15KMAS-6**	**15KMAS-6**
Intrusion	Kumuzhya	Kumuzhya	Kumuzhya	Kumuzhya	Kumuzhya	Kumuzhya	Kumuzhya	Kumuzhya	Kumuzhya	Kumuzhya
Sample Pt.	Ol 2	Ol 2	Ol 2	Ol 1	Ol 1	Ol 1	Ol 2	Ol 2	Ol 2	Ol 2
Rock type	OL-OPX	OL-OPX	OL-OPX	OL-OPX	OL-OPX	OL-OPX	OL-OPX	OL-OPX	OL-OPX	OL-OPX
SiO_2 (wt %)	39.96	39.97	39.96	39.86	39.81	39.93	39.88	39.95	39.76	39.51
FeO	12.98	13.05	13.05	13.19	13.17	13.24	13.25	13.35	13.34	13.17
MnO	0.20	0.22	0.20	0.25	0.20	0.24	0.24	0.21	0.20	0.21
MgO	46.40	46.47	46.46	46.12	45.99	46.12	46.09	46.14	46.07	45.86
NiO	0.40	0.40	0.37	0.42	0.44	0.43	0.42	0.43	0.37	0.40
Total	**99.94**	**100.11**	**100.04**	**99.84**	**99.61**	**99.96**	**99.88**	**100.08**	**99.74**	**99.15**
Si	1.00	1.00	1.00	1.00	1.00	1.00	1.00	1.00	1.00	0.99
Fe	0.27	0.27	0.27	0.28	0.28	0.28	0.28	0.28	0.28	0.28
Mn	0.00	0.00	0.00	0.01	0.00	0.01	0.01	0.00	0.00	0.00
Mg	1.72	1.73	1.73	1.72	1.72	1.72	1.72	1.72	1.72	1.72
Ni	0.01	0.01	0.01	0.01	0.01	0.01	0.01	0.01	0.01	0.01
Total	**3.00**	**3.00**	**3.00**	**3.00**	**3.00**	**3.00**	**3.00**	**3.00**	**3.00**	**3.01**
Mg#	86.4	86.4	86.4	86.2	86.2	86.1	86.1	86.0	86.0	86.1
Ni (ppm)	3143	3143	2908	3301	3458	3379	3301	3379	2908	3143

Sample No.	**15KMAS-7**	**15KMAS-7**	**15KMAS-7**	**15KMAS-7**	**15KMAS-7**	**15KMAS-7**	**15KMAS-7**	**15KMAS-7**	**15NMAS-1**	**15NMAS-1**
Intrusion	Kumuzhya	Kumuzhya	Kumuzhya	Kumuzhya	Kumuzhya	Kumuzhya	Kumuzhya	Kumuzhya	Nittis	Nittis
Sample Pt.	Ol 1	Ol 1	Ol 1	Ol 2	Ol 2	Ol 2	Ol 2	Ol 3	Ol 1	Ol 1
Rock type	OL-OPX	OL-OPX	OL-OPX	OL-OPX	OL-OPX	OL-OPX	OL-OPX	OL-OPX	OPX	OPX
SiO_2 (wt %)	40.34	40.28	40.23	40.07	39.93	40.22	39.98	40.05	40.34	40.37
FeO	13.30	13.29	13.24	13.34	13.19	13.23	13.53	13.50	12.47	12.56
MnO	0.20	0.19	0.18	0.24	0.24	0.24	0.23	0.23	0.21	0.23
MgO	46.77	46.72	46.74	46.73	46.59	46.85	46.56	46.67	47.57	47.64
NiO	0.51	0.48	0.46	0.44	0.47	0.46	0.46	0.42	0.45	0.44
Total	**101.12**	**100.96**	**100.85**	**100.82**	**100.42**	**101.00**	**100.76**	**100.87**	**101.04**	**101.24**
Si	1.00	1.00	0.99	0.99	0.99	0.99	0.99	0.99	0.99	0.99
Fe	0.27	0.27	0.27	0.28	0.27	0.27	0.28	0.28	0.26	0.26
Mn	0.00	0.00	0.00	0.01	0.01	0.01	0.00	0.00	0.00	0.00
Mg	1.72	1.72	1.72	1.73	1.73	1.73	1.72	1.72	1.74	1.74
Ni	0.01	0.01	0.01	0.01	0.01	0.01	0.01	0.01	0.01	0.01
Total	**3.00**	**3.00**	**3.01**	**3.01**	**3.01**	**3.01**	**3.01**	**3.01**	**3.01**	**3.01**
Mg#	86.2	86.2	86.3	86.2	86.3	86.3	86.0	86.0	87.2	87.1
Ni (ppm)	4008	3772	3615	3458	3694	3615	3615	3301	3536	3458

Sample No.	**15NMAS-1**	**15NMAS-1**	**15NMAS-1**	**15NMAS-1**	**15NMAS-1**	**15NMAS-1**	**15NMAS-2**	**15NMAS-2**	**15NMAS-2**	**15NMAS-2**
Intrusion	Nittis	Nittis	Nittis	Nittis	Nittis	Nittis	Nittis	Nittis	Nittis	Nittis
Sample Pt.	Ol 2	Ol 2	Ol 2	Ol 3	Ol 3	Ol 3	Ol 1	Ol 1	Ol 2	Ol 2
Rock type	OPX	OPX	OPX	OPX	OPX	OPX	OPX	OPX	OPX	OPX
SiO_2 (wt %)	40.25	40.28	40.34	40.43	40.35	40.30	40.05	40.21	40.41	40.40
FeO	12.42	12.36	12.44	12.46	12.50	12.55	15.00	13.77	12.86	12.87
MnO	0.18	0.17	0.19	0.21	0.22	0.18	0.19	0.22	0.24	0.26
MgO	47.47	47.46	47.50	47.46	47.44	47.40	45.25	46.40	47.22	47.15
NiO	0.40	0.42	0.43	0.44	0.40	0.45	0.45	0.43	0.44	0.44
Total	**100.72**	**100.69**	**100.90**	**101.00**	**100.91**	**100.88**	**100.94**	**101.03**	**101.17**	**101.12**
Si	0.99	0.99	0.99	0.99	0.99	0.99	1.00	1.00	0.99	0.99
Fe	0.26	0.25	0.26	0.26	0.26	0.26	0.31	0.28	0.26	0.27
Mn	0.00	0.00	0.00	0.00	0.00	0.00	0.00	0.00	0.01	0.01
Mg	1.75	1.75	1.74	1.74	1.74	1.74	1.68	1.71	1.73	1.73
Ni	0.01	0.01	0.01	0.01	0.01	0.01	0.01	0.01	0.01	0.01
Total	**3.01**	**3.01**	**3.01**	**3.01**	**3.01**	**3.01**	**3.00**	**3.00**	**3.01**	**3.01**
Mg#	87.2	87.3	87.2	87.2	87.1	87.1	84.3	85.7	86.7	86.7
Ni (ppm)	3143	3301	3379	3458	3143	3536	3536	3379	3458	3458

CHR = chromitite; DUN = dunite; LH = lherzolite; HZ = harzburgite; OL-WEB = olivine-websterite;
OL-OPX = olivine-orthopyroxenite; OPX = orthopyroxenite; BRC = breccia; oph = ophitic

Table D.1 (cont.)

Sample No.	**15NMAS-2**	**15NMAS-2**	**15NMAS-2**	**15NMAS-2**	**79-054**	**79-054**	**79-054**	**79-054**	**79-115**	**79-115**
Intrusion	Nittis	Nittis	Nittis	Nittis	Nittis	Nittis	Nittis	Nittis	Nittis	Nittis
Sample Pt.	Ol 2	Ol 3	Ol 3	Ol 3	Ol 1	Ol 1	Ol 2	Ol 2	Ol 1	Ol 1
Rock type	OPX	OPX	OPX	OPX	OPX	OPX	OPX	OPX	OPX	OPX
SiO_2 (wt %)	40.43	40.09	40.23	40.29	40.15	40.22	39.83	39.83	39.23	39.87
FeO	12.99	14.52	13.39	13.58	13.33	13.03	15.40	15.35	18.42	17.26
MnO	0.21	0.20	0.21	0.20	0.17	0.15	0.26	0.25	0.25	0.22
MgO	47.12	45.91	46.79	46.61	46.76	46.88	45.00	45.07	43.53	43.96
NiO	0.41	0.41	0.47	0.41	0.47	0.45	0.39	0.39	0.37	0.41
Total	**101.16**	**101.13**	**101.09**	**101.09**	**100.88**	**100.73**	**100.89**	**100.89**	**101.80**	**101.73**
Si	1.00	0.99	0.99	1.00	0.99	0.99	0.99	0.99	0.99	1.00
Fe	0.27	0.30	0.28	0.28	0.28	0.27	0.32	0.32	0.39	0.36
Mn	0.00	0.00	0.00	0.00	0.00	0.00	0.01	0.01	0.01	0.00
Mg	1.73	1.70	1.72	1.72	1.72	1.73	1.68	1.68	1.63	1.64
Ni	0.01	0.01	0.01	0.01	0.01	0.01	0.01	0.01	0.01	0.01
Total	**3.00**	**3.01**	**3.01**	**3.00**	**3.01**	**3.01**	**3.01**	**3.01**	**3.01**	**3.00**
Mg#	86.6	84.9	86.2	86.0	86.2	86.5	83.9	84.0	80.8	81.9
Ni (ppm)	3222	3222	3694	3222	3700	3500	3100	3100	2900	3200

Sample No.	**79-115**	**79-115**	**79-143**	**79-143**	**79-143**	**79-143**	**79-143**	**79-143**	**79-143**	**79-143**
Intrusion	Nittis	Nittis	Nittis	Nittis	Nittis	Nittis	Nittis	Nittis	Nittis	Nittis
Sample Pt.	Ol 2	Ol 2	Ol 1	Ol 1	Ol 1	Ol 1	Ol 1	Ol 1	Ol 1	Ol 1
Rock type	OPX	OPX	Oph. OPX	Oph. OPX	Oph. OPX	Oph. OPX	Oph. OPX	Oph. OPX	Oph. OPX	Oph. OPX
SiO_2 (wt %)	39.85	39.90	39.95	39.92	39.67	40.04	39.91	40.00	39.96	39.85
FeO	17.38	17.24	15.59	15.29	14.95	15.63	15.22	15.11	15.28	15.66
MnO	0.25	0.26	0.25	0.22	0.21	0.23	0.20	0.22	0.21	0.22
MgO	43.86	43.99	44.73	45.16	43.96	45.07	45.09	45.42	45.26	45.05
NiO	0.41	0.37	0.39	0.44	0.56	0.43	0.47	0.42	0.44	0.45
Total	**101.75**	**101.75**	**100.91**	**101.03**	**99.35**	**101.40**	**100.89**	**101.17**	**101.15**	**101.23**
Si	1.00	1.00	1.00	0.99	1.00	1.00	1.00	0.99	0.99	0.99
Fe	0.36	0.36	0.33	0.32	0.32	0.32	0.32	0.31	0.32	0.33
Mn	0.01	0.01	0.01	0.00	0.00	0.00	0.00	0.00	0.00	0.00
Mg	1.63	1.64	1.67	1.68	1.66	1.67	1.68	1.68	1.68	1.67
Ni	0.01	0.01	0.01	0.01	0.01	0.01	0.01	0.01	0.01	0.01
Total	**3.00**	**3.00**	**3.00**	**3.01**	**3.00**	**3.00**	**3.00**	**3.01**	**3.01**	**3.01**
Mg#	81.8	82.0	83.6	84.0	84.0	83.7	84.1	84.3	84.1	83.7
Ni (ppm)	3200	2900	3065	3458	4401	3379	3694	3301	3458	3536

Sample No.	**79-143**	**79-143**	**79-143**	**79-143**	**1403-030**	**1403-030**	**1403-030**	**1403-030**	**1403-089**	**1403-089**
Intrusion	Nittis	Nittis	Nittis	Nittis	Sopcha	Sopcha	Sopcha	Sopcha	Sopcha	Sopcha
Sample Pt.	Ol 1	Ol 2	Ol 2	Ol 2	Ol 1	Ol 1	Ol 2	Ol 2	Ol 1	Ol 1
Rock type	Oph. OPX	Oph. OPX	Oph. OPX	Oph. OPX	OPX	OPX	OPX	OPX	OPX	OPX
SiO_2 (wt %)	39.91	39.97	40.06	40.04	39.90	39.81	39.96	39.98	40.11	39.83
FeO	15.50	15.59	15.44	15.48	15.25	15.12	15.10	14.92	14.88	15.76
MnO	0.20	0.20	0.19	0.23	0.25	0.25	0.22	0.21	0.22	0.21
MgO	45.03	44.95	45.18	44.99	45.27	45.19	45.34	45.53	45.35	44.80
NiO	0.39	0.43	0.43	0.41	0.39	0.39	0.38	0.41	0.27	0.24
Total	**101.03**	**101.14**	**101.30**	**101.15**	**101.05**	**100.75**	**101.00**	**101.05**	**100.83**	**100.84**
Si	1.00	1.00	1.00	1.00	0.99	0.99	1.00	0.99	1.00	1.00
Fe	0.32	0.32	0.32	0.32	0.32	0.32	0.31	0.31	0.31	0.33
Mn	0.00	0.00	0.00	0.00	0.01	0.01	0.00	0.00	0.00	0.00
Mg	1.67	1.67	1.67	1.67	1.68	1.68	1.68	1.69	1.68	1.67
Ni	0.01	0.01	0.01	0.01	0.01	0.01	0.01	0.01	0.01	0.00
Total	**3.00**	**3.00**	**3.00**	**3.00**	**3.01**	**3.01**	**3.00**	**3.01**	**3.00**	**3.00**
Mg#	83.8	83.7	83.9	83.8	84.1	84.2	84.3	84.5	84.5	83.5
Ni (ppm)	3065	3379	3379	3222	3100	3100	3000	3200	2100	1900

CHR = chromitite; DUN = dunite; LH = lherzolite; HZ = harzburgite; OL-WEB = olivine-websterite;
OL-OPX = olivine-orthopyroxenite; OPX = orthopyroxenite; BRC = breccia; oph = ophitic

Table D.1 (cont.)

Sample No.	**1403-089**	**1403-089**	**1403-089**	**1403-132**	**1403-132**	**1403-132**	**1403-132**	**1403-132**	**1403-132**	**1403-132**
Intrusion	Sopcha	Sopcha	Sopcha	Sopcha	Sopcha	Sopcha	Sopcha	Sopcha	Sopcha	Sopcha
Sample Pt.	Ol 2	Ol 2	Ol 2	Ol 1	Ol 1	Ol 2	Ol 2	Ol 2	Ol 3	Ol 3
Rock type	OPX	OPX	OPX	OPX	OPX	OPX	OPX	OPX	OPX	OPX
SiO_2 (wt %)	40.02	40.20	39.98	40.11	40.24	39.94	39.66	39.77	39.75	39.79
FeO	15.01	14.78	14.67	15.76	14.97	16.02	15.27	14.97	14.28	14.40
MnO	0.21	0.19	0.21	0.22	0.23	0.25	0.25	0.21	0.21	0.22
MgO	45.37	45.73	45.53	45.07	45.72	44.75	45.02	45.22	45.63	45.37
NiO	0.33	0.33	0.34	0.36	0.34	0.37	0.36	0.38	0.34	0.34
Total	**100.94**	**101.24**	**100.73**	**101.52**	**101.51**	**101.32**	**100.55**	**100.55**	**100.21**	**100.12**
Si	1.00	1.00	1.00	1.00	1.00	1.00	0.99	0.99	0.99	1.00
Fe	0.31	0.31	0.31	0.33	0.31	0.33	0.32	0.31	0.30	0.30
Mn	0.00	0.00	0.00	0.00	0.00	0.01	0.01	0.00	0.00	0.00
Mg	1.68	1.69	1.69	1.67	1.69	1.66	1.68	1.69	1.70	1.69
Ni	0.01	0.01	0.01	0.01	0.01	0.01	0.01	0.01	0.01	0.01
Total	**3.00**	**3.00**	**3.00**	**3.00**	**3.00**	**3.00**	**3.01**	**3.01**	**3.01**	**3.00**
Mg#	84.3	84.7	84.7	83.6	84.5	83.3	84.0	84.3	85.1	84.9
Ni (ppm)	2600	2600	2700	2800	2700	2900	2800	3000	2700	2700

Sample No.	**1403-132**	**1408-171**	**1408-171**	**1408-171**	**1408-171**	**1408-171**	**1408-171**	**15SOP-04**	**15SOP-04**	**15SOP-04**
Intrusion	Sopcha	Sopcha	Sopcha	Sopcha	Sopcha	Sopcha	Sopcha	Sopcha	Sopcha	Sopcha
Sample Pt.	Ol 3	Ol 1	Ol 1	Ol 2	Ol 2	Ol 2	Ol 3	Ol 1	Ol 1	Ol 1
Rock type	OPX	OPX	OPX	OPX	OPX	OPX	OPX	OPX	OPX	OPX
SiO_2 (wt %)	39.90	40.23	40.31	40.12	40.18	40.12	40.09	39.59	39.59	39.55
FeO	14.16	13.67	13.96	14.54	14.25	13.97	14.52	16.20	15.98	15.89
MnO	0.21	0.21	0.22	0.20	0.24	0.19	0.25	0.27	0.27	0.28
MgO	45.60	46.53	46.45	45.53	46.51	46.35	46.07	44.12	44.15	44.36
NiO	0.31	0.30	0.32	0.34	0.34	0.35	0.30	0.60	0.56	0.52
Total	**100.17**	**100.94**	**101.26**	**100.73**	**101.52**	**100.98**	**101.23**	**100.78**	**100.55**	**100.60**
Si	1.00	1.00	1.00	1.00	0.99	0.99	0.99	0.99	1.00	0.99
Fe	0.30	0.28	0.29	0.30	0.29	0.29	0.30	0.34	0.34	0.33
Mn	0.00	0.00	0.00	0.00	0.01	0.00	0.01	0.01	0.01	0.01
Mg	1.70	1.72	1.71	1.69	1.71	1.71	1.70	1.65	1.66	1.66
Ni	0.01	0.01	0.01	0.01	0.01	0.01	0.01	0.01	0.01	0.01
Total	**3.00**	**3.00**	**3.00**	**3.00**	**3.01**	**3.01**	**3.01**	**3.01**	**3.00**	**3.01**
Mg#	85.2	85.9	85.6	84.8	85.3	85.5	85.0	82.9	83.1	83.3
Ni (ppm)	2400	2358	2515	2672	2672	2750	2358	4715	4401	4086

Sample No.	**15SOP-04**	**15SOP-04**	**15SOP-04**	**15SOP-04**	**15SOP-04**	**15SOP-04**	**15SOP-04**	**15SOP-04**	**15SOP-04**	**15SOP-04**
Intrusion	Sopcha	Sopcha	Sopcha	Sopcha	Sopcha	Sopcha	Sopcha	Sopcha	Sopcha	Sopcha
Sample Pt.	Ol 1	Ol 2	Ol 2	Ol 2	Ol 3	Ol 3	Ol 4	Ol 4	Ol 5	Ol 5
Rock type	OPX	OPX	OPX	OPX	OPX	OPX	OPX	OPX	OPX	OPX
SiO_2 (wt %)	39.81	40.28	40.14	40.47	39.79	39.91	39.76	39.86	40.28	40.53
FeO	15.55	13.39	13.47	13.34	14.83	14.67	15.52	15.29	13.62	13.69
MnO	0.26	0.20	0.19	0.21	0.27	0.29	0.26	0.27	0.22	0.22
MgO	44.81	46.92	46.73	47.05	45.46	45.78	44.93	45.29	46.66	46.80
NiO	0.47	0.44	0.39	0.37	0.43	0.42	0.52	0.44	0.42	0.43
Total	**100.90**	**101.23**	**100.92**	**101.44**	**100.78**	**101.07**	**100.99**	**101.15**	**101.20**	**101.67**
Si	1.00	0.99	0.99	0.99	0.99	0.99	0.99	0.99	0.99	1.00
Fe	0.33	0.28	0.28	0.27	0.31	0.30	0.32	0.32	0.28	0.28
Mn	0.01	0.00	0.00	0.00	0.01	0.01	0.01	0.01	0.00	0.00
Mg	1.67	1.72	1.72	1.72	1.69	1.70	1.67	1.68	1.72	1.71
Ni	0.01	0.01	0.01	0.01	0.01	0.01	0.01	0.01	0.01	0.01
Total	**3.00**	**3.01**	**3.01**	**3.01**	**3.01**	**3.01**	**3.01**	**3.01**	**3.01**	**3.00**
Mg#	83.7	86.2	86.1	86.3	84.5	84.8	83.8	84.1	85.9	85.9
Ni (ppm)	3694	3458	3065	2908	3379	3301	4086	3458	3301	3379

CHR = chromitite; DUN = dunite; LH = lherzolite; HZ = harzburgite; OL-WEB = olivine-websterite;
OL-OPX = olivine-orthopyroxenite; OPX = orthopyroxenite; BRC = breccia; oph = ophitic

Table D.1 (cont.)

Sample No.	**15SOP-05**	**15SOP-05**	**15SOP-05**	**15SOP-05**	**15SOP-05**	**15SOP-05**	**15SOP-05**	**15SOP-05**	**15SOP-05**	**15SOP-06**
Intrusion	Sopcha	Sopcha	Sopcha	Sopcha	Sopcha	Sopcha	Sopcha	Sopcha	Sopcha	Sopcha
Sample Pt.	Ol 1	Ol 1	Ol 1	Ol 1	Ol 2	Ol 2	Ol 2	Ol 2	Ol 2	Ol 1
Rock type	OPX BRC	OPX BRC	OPX BRC	OPX BRC	OPX BRC	OPX BRC	OPX BRC	OPX BRC	OPX BRC	DUN
SiO_2 (wt %)	40.04	39.66	40.05	39.90	40.22	40.08	39.55	40.29	40.17	40.32
FeO	15.89	15.91	16.01	16.07	13.67	13.92	13.35	13.33	13.44	13.58
MnO	0.31	0.34	0.32	0.35	0.25	0.29	0.22	0.20	0.22	0.24
MgO	44.81	44.54	44.65	44.43	45.83	46.28	45.81	46.85	46.73	46.87
NiO	0.52	0.51	0.60	0.46	0.39	0.38	0.40	0.37	0.39	0.46
Total	**101.57**	**100.96**	**101.63**	**101.21**	**100.36**	**100.95**	**99.33**	**101.04**	**100.95**	**101.47**
Si	1.00	0.99	1.00	1.00	1.00	0.99	0.99	0.99	0.99	0.99
Fe	0.33	0.33	0.33	0.34	0.28	0.29	0.28	0.28	0.28	0.28
Mn	0.01	0.01	0.01	0.01	0.01	0.01	0.00	0.00	0.00	0.01
Mg	1.66	1.66	1.66	1.65	1.70	1.71	1.72	1.72	1.72	1.72
Ni	0.01	0.01	0.01	0.01	0.01	0.01	0.01	0.01	0.01	0.01
Total	**3.00**	**3.01**	**3.00**	**3.00**	**3.00**	**3.01**	**3.01**	**3.01**	**3.01**	**3.01**
Mg#	83.4	83.3	83.3	83.1	85.7	85.6	86.0	86.2	86.1	86.0
Ni (ppm)	4086	4008	4715	3615	3065	2986	3143	2908	3065	3615

Sample No.	**15SOP-06**	**15SOP-06**	**15SOP-06**	**15SOP-06**	**15SOP-06**	**15SOP-06**	**15SOP-06**	**15SOP-06**	**15SOP-07**	**15SOP-07**
Intrusion	Sopcha	Sopcha	Sopcha	Sopcha	Sopcha	Sopcha	Sopcha	Sopcha	Sopcha	Sopcha
Sample Pt.	Ol 1	Ol 1	Ol 1	Ol 2	Ol 2	Ol 2	Ol 3	Ol 3	Ol 1	Ol 1
Rock type	DUN	DUN	DUN	DUN	DUN	DUN	DUN	DUN	HZ	HZ
SiO_2 (wt %)	40.29	40.33	40.30	40.19	40.26	40.23	40.44	40.16	39.90	40.05
FeO	13.57	13.47	13.37	13.58	13.70	13.68	13.69	13.73	13.60	13.74
MnO	0.23	0.23	0.21	0.18	0.22	0.21	0.24	0.25	0.24	0.24
MgO	46.69	46.85	47.03	46.85	46.81	46.81	46.26	46.77	46.49	46.20
NiO	0.47	0.44	0.42	0.46	0.44	0.42	0.43	0.44	0.43	0.42
Total	**101.25**	**101.32**	**101.33**	**101.26**	**101.43**	**101.35**	**101.06**	**101.35**	**100.66**	**100.65**
Si	0.99	0.99	0.99	0.99	0.99	0.99	1.00	0.99	0.99	0.99
Fe	0.28	0.28	0.28	0.28	0.28	0.28	0.28	0.28	0.28	0.29
Mn	0.00	0.00	0.00	0.00	0.00	0.00	0.01	0.01	0.01	0.01
Mg	1.72	1.72	1.73	1.72	1.72	1.72	1.70	1.72	1.72	1.71
Ni	0.01	0.01	0.01	0.01	0.01	0.01	0.01	0.01	0.01	0.01
Total	**3.01**	**3.01**	**3.01**	**3.01**	**3.01**	**3.01**	**3.00**	**3.01**	**3.01**	**3.01**
Mg#	86.0	86.1	86.2	86.0	85.9	85.9	85.8	85.9	85.9	85.7
Ni (ppm)	3694	3458	3301	3615	3458	3301	3379	3458	3379	3301

Sample No.	**15SOP-07**	**15SOP-07**	**15SOP-07**	**15SOP-07**	**15SOP-08**	**15SOP-08**	**15SOP-08**	**15SOP-08**	**15SOP-08**	**15SOP-08**
Intrusion	Sopcha	Sopcha	Sopcha	Sopcha	Sopcha	Sopcha	Sopcha	Sopcha	Sopcha	Sopcha
Sample Pt.	Ol 2	Ol 2	Ol 3	Ol 3	Ol 3	Ol 4	Ol 4	Ol 4	Ol 4	Ol 5
Rock type	HZ	HZ	HZ	HZ	HZ	HZ	HZ	HZ	HZ	HZ
SiO_2 (wt %)	39.90	40.07	40.13	40.10	39.80	39.74	39.98	39.91	39.63	39.86
FeO	13.43	13.49	13.31	13.37	13.39	13.82	13.64	13.46	13.87	13.32
MnO	0.23	0.22	0.20	0.23	0.21	0.20	0.22	0.20	0.22	0.23
MgO	46.30	46.55	46.83	46.56	46.08	45.96	45.78	46.31	45.75	46.30
NiO	0.44	0.43	0.47	0.41	0.42	0.44	0.42	0.42	0.35	0.39
Total	**100.30**	**100.76**	**100.94**	**100.67**	**99.90**	**100.16**	**100.04**	**100.30**	**99.82**	**100.10**
Si	0.99	0.99	0.99	0.99	0.99	0.99	1.00	0.99	0.99	0.99
Fe	0.28	0.28	0.28	0.28	0.28	0.29	0.28	0.28	0.29	0.28
Mn	0.00	0.00	0.00	0.00	0.00	0.00	0.00	0.00	0.00	0.00
Mg	1.72	1.72	1.73	1.72	1.72	1.71	1.70	1.72	1.71	1.72
Ni	0.01	0.01	0.01	0.01	0.01	0.01	0.01	0.01	0.01	0.01
Total	**3.01**	**3.01**	**3.01**	**3.01**	**3.01**	**3.01**	**3.00**	**3.01**	**3.01**	**3.01**
Mg#	86.0	86.0	86.3	86.1	86.0	85.6	85.7	86.0	85.5	86.1
Ni (ppm)	3458	3379	3694	3222	3301	3458	3301	3301	2750	3065

CHR = chromitite; DUN = dunite; LH = lherzolite; HZ = harzburgite; OL-WEB = olivine-websterite;
OL-OPX = olivine-orthopyroxenite; OPX = orthopyroxenite; BRC = breccia; oph = ophitic

Table D.1 (cont.)

Sample No.	**15SOP-08**	**15SOP-08**	**15SOP-09**	**15SOP-09**	**15SOP-09**	**15SOP-09**	**15SOP-09**	**15SOP-09**	**15SOP-09**	**15SOP-09**
Intrusion	Sopcha	Sopcha	Sopcha	Sopcha	Sopcha	Sopcha	Sopcha	Sopcha	Sopcha	Sopcha
Sample Pt.	Ol 5	Ol 5	Ol 1	Ol 1	Ol 1	Ol 1	Ol 2	Ol 2	Ol 2	Ol 3
Rock type	HZ	HZ	OL-OPX	OL-OPX	OL-OPX	OL-OPX	OL-OPX	OL-OPX	OL-OPX	OL-OPX
SiO_2 (wt %)	39.77	39.94	39.86	39.92	39.84	39.88	40.13	40.09	40.03	40.13
FeO	13.33	13.43	14.91	14.91	14.89	15.07	13.83	13.57	13.66	13.81
MnO	0.20	0.23	0.28	0.26	0.27	0.27	0.25	0.23	0.20	0.22
MgO	46.05	46.32	45.27	45.21	45.46	45.09	46.32	46.53	46.48	46.50
NiO	0.38	0.37	0.44	0.41	0.41	0.42	0.40	0.43	0.42	0.41
Total	**99.73**	**100.29**	**100.76**	**100.71**	**100.87**	**100.73**	**100.93**	**100.85**	**100.79**	**101.07**
Si	1.00	0.99	0.99	1.00	0.99	1.00	0.99	0.99	0.99	0.99
Fe	0.28	0.28	0.31	0.31	0.31	0.31	0.29	0.28	0.28	0.29
Mn	0.00	0.00	0.01	0.01	0.01	0.01	0.01	0.00	0.00	0.00
Mg	1.72	1.72	1.68	1.68	1.69	1.68	1.71	1.72	1.72	1.72
Ni	0.01	0.01	0.01	0.01	0.01	0.01	0.01	0.01	0.01	0.01
Total	**3.00**	**3.01**	**3.01**	**3.00**	**3.01**	**3.00**	**3.01**	**3.01**	**3.01**	**3.01**
Mg#	86.0	86.0	84.4	84.4	84.5	84.2	85.7	85.9	85.8	85.7
Ni (ppm)	2986	2908	3458	3222	3222	3301	3143	3379	3301	3222

Sample No.	**15SOP-09**	**15SOP-10**	**15SOP-10**	**15SOP-10**	**15SOP-10**	**15SOP-11**	**15SOP-11**	**15SOP-11**	**15SOP-11**	**15SOP-11**
Intrusion	Sopcha	Sopcha	Sopcha	Sopcha	Sopcha	Sopcha	Sopcha	Sopcha	Sopcha	Sopcha
Sample Pt.	Ol 3	Ol 1	Ol 2	Ol 3	Ol 3	Ol 3	Ol 4	Ol 4	Ol 4	Ol 5
Rock type	OL-OPX	OPX BRC	OPX BRC	OPX BRC	OPX BRC	OL-OPX	OL-OPX	OL-OPX	OL-OPX	OL-OPX
SiO_2 (wt %)	40.14	40.16	40.20	40.33	40.17	40.27	40.30	40.30	40.28	40.28
FeO	13.91	14.01	13.55	13.69	13.62	13.58	13.58	13.52	13.49	13.78
MnO	0.20	0.24	0.24	0.25	0.21	0.21	0.22	0.23	0.20	0.21
MgO	46.44	46.66	47.02	46.13	47.06	46.91	46.88	46.96	46.93	46.67
NiO	0.40	0.39	0.39	0.35	0.37	0.38	0.35	0.34	0.37	0.38
Total	**101.09**	**101.46**	**101.40**	**100.75**	**101.43**	**101.35**	**101.33**	**101.35**	**101.27**	**101.32**
Si	0.99	0.99	0.99	1.00	0.99	0.99	0.99	0.99	0.99	0.99
Fe	0.29	0.29	0.28	0.28	0.28	0.28	0.28	0.28	0.28	0.28
Mn	0.00	0.01	0.01	0.01	0.00	0.00	0.00	0.00	0.00	0.00
Mg	1.71	1.72	1.73	1.70	1.73	1.72	1.72	1.72	1.72	1.72
Ni	0.01	0.01	0.01	0.01	0.01	0.01	0.01	0.01	0.01	0.01
Total	**3.01**	**3.01**	**3.01**	**3.00**	**3.01**	**3.01**	**3.01**	**3.01**	**3.01**	**3.01**
Mg#	85.6	85.6	86.1	85.7	86.0	86.0	86.0	86.1	86.1	85.8
Ni (ppm)	3143	3065	3065	2750	2908	2986	2750	2672	2908	2986

Sample No.	**15SOP-11**	**15SOP-11**	**15SOP-11**	**15SOP-15**	**15SOP-15**	**15SOP-15**	**15SOP-15**	**15SOP-15**	**15SOP-16**	**15SOP-16**
Intrusion	Sopcha	Sopcha	Sopcha	Sopcha	Sopcha	Sopcha	Sopcha	Sopcha	Sopcha	Sopcha
Sample Pt.	Ol 5	Ol 5	Ol 5	Ol 1	Ol 1	Ol 2	Ol 2	Ol 2	Ol 1	Ol 1
Rock type	OL-OPX	OL-OPX	OL-OPX	OPX	OPX	OPX	OPX	OPX	OPX	OPX
SiO_2 (wt %)	40.31	40.19	40.37	39.93	39.93	40.04	39.89	39.96	40.27	40.18
FeO	13.68	13.65	13.64	15.19	15.17	14.38	14.77	14.80	13.75	13.75
MnO	0.24	0.22	0.21	0.36	0.36	0.30	0.36	0.31	0.23	0.22
MgO	46.72	46.65	46.85	45.12	45.29	45.84	45.39	45.54	46.69	46.46
NiO	0.38	0.38	0.35	0.39	0.40	0.40	0.41	0.37	0.41	0.42
Total	**101.33**	**101.09**	**101.42**	**100.99**	**101.15**	**100.96**	**100.82**	**100.98**	**101.35**	**101.03**
Si	0.99	0.99	0.99	1.00	0.99	0.99	0.99	0.99	0.99	0.99
Fe	0.28	0.28	0.28	0.32	0.32	0.30	0.31	0.31	0.28	0.28
Mn	0.01	0.00	0.00	0.01	0.01	0.01	0.01	0.01	0.00	0.00
Mg	1.72	1.72	1.72	1.68	1.68	1.70	1.69	1.69	1.72	1.71
Ni	0.01	0.01	0.01	0.01	0.01	0.01	0.01	0.01	0.01	0.01
Total	**3.01**	**3.01**	**3.01**	**3.00**	**3.01**	**3.01**	**3.01**	**3.01**	**3.01**	**3.01**
Mg#	85.9	85.9	86.0	84.1	84.2	85.0	84.6	84.6	85.8	85.8
Ni (ppm)	2986	2986	2750	3065	3143	3143	3222	2908	3222	3301

CHR = chromitite; DUN = dunite; LH = lherzolite; HZ = harzburgite; OL-WEB = olivine-websterite;
OL-OPX = olivine-orthopyroxenite; OPX = orthopyroxenite; BRC = breccia; oph = ophitic

Table D.1 (cont.)

Sample No.	**15SOP-16**	**15SOP-16**	**15SOP-16**	**15SOP-16**	**15SOP-16**	**15SOP-17**	**15SOP-17**	**15SOP-17**	**15SOP-17**	**15TMAS-5**
Intrusion	Sopcha	Sopcha	Sopcha	Sopcha	Sopcha	Sopcha	Sopcha	Sopcha	Sopcha	Travyanaya
Sample Pt.	Ol 1	Ol 2	Ol 2	Ol 2	Ol 2	Ol 1	Ol 1	Ol 2	Ol 2	Ol 1
Rock type	OPX	OPX	OPX	OPX	OPX	OPX	OPX	OPX	OPX	HZ
SiO_2 (wt %)	40.18	40.30	40.12	40.16	40.20	39.91	39.96	40.00	39.92	39.77
FeO	13.75	13.69	13.64	13.68	13.71	13.00	13.00	13.09	12.76	14.47
MnO	0.24	0.20	0.24	0.26	0.22	0.23	0.19	0.20	0.23	0.26
MgO	46.74	46.16	46.20	46.50	46.54	46.38	46.42	46.35	46.57	45.52
NiO	0.45	0.44	0.42	0.44	0.41	0.41	0.40	0.39	0.42	0.39
Total	**101.36**	**100.79**	**100.62**	**101.04**	**101.08**	**99.93**	**99.97**	**100.03**	**99.90**	**100.42**
Si	0.99	1.00	1.00	0.99	0.99	1.00	1.00	1.00	1.00	0.99
Fe	0.28	0.28	0.28	0.28	0.28	0.27	0.27	0.27	0.27	0.30
Mn	0.01	0.00	0.01	0.01	0.00	0.00	0.00	0.00	0.00	0.01
Mg	1.72	1.71	1.71	1.72	1.72	1.72	1.72	1.72	1.73	1.70
Ni	0.01	0.01	0.01	0.01	0.01	0.01	0.01	0.01	0.01	0.01
Total	**3.01**	**3.00**	**3.00**	**3.01**	**3.01**	**3.00**	**3.00**	**3.00**	**3.00**	**3.01**
Mg#	85.8	85.7	85.8	85.8	85.8	86.4	86.4	86.3	86.7	84.9
Ni (ppm)	3536	3458	3301	3458	3222	3222	3143	3065	3301	3100

Sample No.	**15TMAS-5**	**15TMAS-5**	**15TMAS-5**	**15TMAS-5**	**15TMAS-5**	**15TMAS-5**	**15TMAS-5**	**15TMAS-7**	**15TMAS-7**	**15TMAS-7**
Intrusion	Travyanaya	Travyanaya	Travyanaya	Travyanaya	Travyanaya	Travyanaya	Travyanaya	Travyanaya	Travyanaya	Travyanaya
Sample Pt.	Ol 2	Ol 3	Ol 3	Ol 4	Ol 4	Ol 5	Ol 5	Ol 1	Ol 1	Ol 1
Rock type	HZ	HZ	HZ	HZ	HZ	HZ	HZ	OL-WEB	OL-WEB	OL-WEB
SiO_2 (wt %)	39.79	39.81	39.77	39.77	40.39	40.26	40.37	40.05	40.05	40.09
FeO	13.41	14.32	14.34	12.08	12.75	13.25	13.11	13.50	12.96	13.12
MnO	0.22	0.25	0.27	0.21	0.26	0.23	0.26	0.27	0.27	0.30
MgO	46.15	45.74	45.75	45.98	47.29	46.88	47.11	46.22	46.61	46.66
NiO	0.41	0.43	0.37	0.43	0.37	0.36	0.41	0.41	0.41	0.41
Total	**99.97**	**100.55**	**100.51**	**98.47**	**101.06**	**100.98**	**101.26**	**100.44**	**100.30**	**100.58**
Si	0.99	0.99	0.99	1.00	0.99	0.99	0.99	1.00	1.00	0.99
Fe	0.28	0.30	0.30	0.25	0.26	0.27	0.27	0.28	0.27	0.27
Mn	0.00	0.01	0.01	0.00	0.01	0.00	0.01	0.01	0.01	0.01
Mg	1.72	1.70	1.70	1.73	1.74	1.73	1.73	1.71	1.73	1.73
Ni	0.01	0.01	0.01	0.01	0.01	0.01	0.01	0.01	0.01	0.01
Total	**3.01**	**3.01**	**3.01**	**3.00**	**3.01**	**3.01**	**3.01**	**3.00**	**3.00**	**3.01**
Mg#	86.0	85.1	85.0	87.2	86.9	86.3	86.5	85.9	86.5	86.4
Ni (ppm)	3200	3400	2900	3400	2900	2800	3200	3200	3200	3200

Sample No.	**15TMAS-7**	**15TMAS-7**	**15TMAS-7**	**15TMAS-7**	**15TMAS-7**
Intrusion	Travyanaya	Travyanaya	Travyanaya	Travyanaya	Travyanaya
Sample Pt.	Ol 2	Ol 2	Ol 2	Ol 3	Ol 3
Rock type	OL-WEB	OL-WEB	OL-WEB	OL-WEB	OL-WEB
SiO_2 (wt %)	39.96	39.81	39.66	39.83	39.92
FeO	13.46	13.74	15.43	14.68	13.86
MnO	0.30	0.30	0.26	0.27	0.26
MgO	46.20	45.88	44.72	45.20	46.10
NiO	0.41	0.41	0.27	0.27	0.25
Total	**100.32**	**100.14**	**100.34**	**100.26**	**100.39**
Si	1.00	0.99	1.00	1.00	0.99
Fe	0.28	0.29	0.32	0.31	0.29
Mn	0.01	0.01	0.01	0.01	0.01
Mg	1.72	1.71	1.67	1.69	1.71
Ni	0.01	0.01	0.01	0.01	0.01
Total	**3.00**	**3.01**	**3.00**	**3.00**	**3.01**
Mg#	86.0	85.6	83.8	84.6	85.6
Ni (ppm)	3200	3200	2100	2100	2000

CHR = chromitite; DUN = dunite; LH = lherzolite; HZ = harzburgite; OL-WEB = olivine-websterite; OL-OPX = olivine-orthopyroxenite; OPX = orthopyroxenite; BRC = breccia; oph = ophitic

Table D.2. Mineral chemistry of orthopyroxene from the Monchegorsk Complex. Basis: 6 oxides

Sample No.	**15DB-1**	**15DB-1**	**15DB-1**	**15DB-1**	**15DB-1**	**15DB-2**	**15DB-2**	**15DB-2**	**15DB-2**	**15DB-2**
Intrusion	Dunite Block	Dunite Block	Dunite Block	Dunite Block	Dunite Block	Dunite Block	Dunite Block	Dunite Block	Dunite Block	Dunite Block
Sample Pt.	Opx 1	Opx 2	Opx 2	Opx 2	Opx 2	Opx 1	Opx 1	Opx 1	Opx 2	Opx 2
Rock type	CHR	CHR	CHR	CHR	CHR	LH	LH	LH	LH	LH
SiO_2 (wt %)	57.65	57.35	58.09	58.44	58.23	56.77	56.83	56.38	56.08	56.68
TiO_2	0.08	0.08	0.09	0.10	0.09	0.14	0.16	0.15	0.22	0.24
Al_2O_3	1.07	0.83	0.80	0.77	0.81	1.23	1.28	1.30	1.31	1.30
Cr_2O_3	0.51	0.48	0.47	0.53	0.67	0.48	0.47	0.46	0.52	0.47
FeO	3.94	3.89	3.82	3.08	3.89	7.11	7.20	7.09	7.19	7.15
MnO	0.11	0.13	0.10	0.11	0.12	0.21	0.17	0.19	0.21	0.20
MgO	36.20	36.26	36.42	37.25	36.27	32.98	33.49	33.08	32.91	33.16
CaO	1.35	1.07	1.13	0.87	1.17	1.86	1.33	1.43	1.59	1.60
NiO	0.18	0.18	0.18	0.20	0.17	0.14	0.15	0.17	0.15	0.17
Total	**101.09**	**100.27**	**101.10**	**101.35**	**101.42**	**100.92**	**101.08**	**100.25**	**100.18**	**100.97**
Si	1.96	1.96	1.97	1.97	1.97	1.96	1.96	1.96	1.95	1.95
Al^{IV}	0.03	0.02	0.02	0.02	0.02	0.04	0.04	0.04	0.04	0.04
Al^{VI}	0.01	0.01	0.01	0.01	0.01	0.01	0.01	0.01	0.02	0.01
Fe^{3+}	0.04	0.04	0.03	0.03	0.02	0.02	0.02	0.02	0.03	0.02
Cr	0.01	0.01	0.01	0.01	0.02	0.01	0.01	0.01	0.01	0.01
Ti	0.00	0.00	0.00	0.00	0.00	0.00	0.00	0.00	0.01	0.01
Fe^{2+}	0.07	0.07	0.08	0.06	0.09	0.19	0.18	0.19	0.18	0.19
Mn	0.00	0.00	0.00	0.00	0.00	0.01	0.00	0.01	0.01	0.01
Mg	1.83	1.85	1.84	1.87	1.83	1.70	1.72	1.71	1.71	1.70
Ca	0.05	0.04	0.04	0.03	0.04	0.07	0.05	0.05	0.06	0.06
Ni	0.00	0.00	0.00	0.01	0.00	0.00	0.00	0.00	0.00	0.00
Total	**4.01**	**4.01**	**4.01**	**4.01**	**4.01**	**4.01**	**4.01**	**4.01**	**4.01**	**4.01**
Wo	2.5	2.0	2.1	1.6	2.1	3.5	2.5	2.7	3.0	3.0
Fs	5.6	5.5	5.4	4.3	5.5	10.4	10.4	10.4	10.5	10.4
En	91.8	92.3	92.4	93.9	92.2	85.8	86.8	86.6	86.2	86.3
Mg#	96.3	96.5	95.7	96.9	95.2	90.1	90.4	90.2	90.5	90.2

Sample No.	**15DB-2**	**15DB-3**	**15DB-3**	**15DB-3**	**15DB-3**	**15DB-3**	**15KMAS-1**	**15KMAS-1**	**15KMAS-1**	**15KMAS-1**
Intrusion	Dunite Block	Dunite Block	Dunite Block	Dunite Block	Dunite Block	Dunite Block	Kumuzhya	Kumuzhya	Kumuzhya	Kumuzhya
Sample Pt.	Opx 2	Opx 1	Opx 1	Opx 1	Opx 2	Opx 2	Opx 1	Opx 1	Opx 2	Opx 2
Rock type	LH	LH	LH	LH	LH	LH	HZ	HZ	HZ	HZ
SiO_2 (wt %)	56.41	56.94	57.02	56.98	56.82	56.91	56.22	56.12	56.00	55.88
TiO_2	0.29	0.16	0.11	0.12	0.11	0.09	0.09	0.07	0.09	0.09
Al_2O_3	1.20	1.22	1.25	1.22	1.37	1.18	1.65	1.73	1.73	1.83
Cr_2O_3	0.44	0.42	0.47	0.40	0.49	0.40	0.66	0.67	0.63	0.74
FeO	7.16	7.06	6.96	7.01	6.98	7.02	8.24	8.20	8.17	8.15
MnO	0.21	0.20	0.19	0.19	0.19	0.19	0.19	0.20	0.17	0.22
MgO	33.14	33.66	33.54	33.50	33.42	33.66	32.18	32.05	32.07	32.08
CaO	1.48	1.31	1.50	1.36	1.46	1.39	1.68	1.77	1.58	1.56
NiO	0.15	0.15	0.18	0.17	0.15	0.16	0.17	0.14	0.14	0.14
Total	**100.48**	**101.12**	**101.22**	**100.95**	**100.99**	**101.00**	**101.08**	**100.95**	**100.58**	**100.69**
Si	1.95	1.96	1.96	1.96	1.96	1.96	1.95	1.95	1.95	1.94
Al^{IV}	0.04	0.04	0.04	0.04	0.04	0.03	0.05	0.05	0.05	0.05
Al^{VI}	0.01	0.01	0.01	0.01	0.02	0.01	0.02	0.02	0.02	0.02
Fe^{3+}	0.02	0.02	0.02	0.02	0.02	0.03	0.02	0.02	0.02	0.02
Cr	0.01	0.01	0.01	0.01	0.01	0.01	0.02	0.02	0.02	0.02
Ti	0.01	0.00	0.00	0.00	0.00	0.00	0.00	0.00	0.00	0.00
Fe^{2+}	0.18	0.18	0.18	0.18	0.18	0.17	0.21	0.22	0.22	0.21
Mn	0.01	0.01	0.01	0.01	0.01	0.01	0.01	0.01	0.01	0.01
Mg	1.71	1.72	1.72	1.72	1.71	1.73	1.66	1.66	1.66	1.66
Ca	0.05	0.05	0.06	0.05	0.05	0.05	0.06	0.07	0.06	0.06
Ni	0.00	0.00	0.00	0.00	0.00	0.00	0.00	0.00	0.00	0.00
Total	**4.01**	**4.01**	**4.01**	**4.01**	**4.01**	**4.01**	**4.01**	**4.01**	**4.01**	**4.01**
Wo	2.8	2.4	2.8	2.5	2.7	2.6	3.2	3.3	3.0	3.0
Fs	10.5	10.2	10.1	10.2	10.2	10.2	12.1	12.1	12.1	12.0
En	86.5	87.1	86.8	87.0	86.8	87.0	84.4	84.3	84.7	84.7
Mg#	90.3	90.7	90.6	90.3	90.5	90.9	88.5	88.5	88.4	88.6

CHR = chromitite; LH = lherzolite; HZ = harzburgite; OL-WEB = olivine-websterite; OL-OPX = olivine-orthopyroxenite;
OPX = orthopyroxenite; MNO = melanorite; BRC = breccia; oph = ophitic; xeno = xenolith

Table D.2 (cont.)

Sample No.	**15KMAS-1**	**15KMAS-1**	**15KMAS-1**	**15KMAS-2**	**15KMAS-2**	**15KMAS-2**	**15KMAS-2**	**15KMAS-2**	**15KMAS-3**	**15KMAS-3**
Intrusion	Kumuzhya	Kumuzhya	Kumuzhya	Kumuzhya	Kumuzhya	Kumuzhya	Kumuzhya	Kumuzhya	Kumuzhya	Kumuzhya
Sample Pt.	Opx 2	Opx 3	Opx 3	Opx 1	Opx 1	Opx 2	Opx 2	Opx 2	Opx 1	Opx 1
Rock type	HZ	HZ	HZ	OL-OPX	OL-OPX	OL-OPX	OL-OPX	OL-OPX	OL-OPX	OL-OPX
SiO_2 (wt %)	55.84	55.84	55.86	55.77	55.85	55.60	55.52	55.25	56.03	56.15
TiO_2	0.12	0.13	0.10	0.11	0.09	0.08	0.09	0.11	0.15	0.08
Al_2O_3	1.59	1.54	1.70	1.72	1.73	1.60	1.50	1.67	1.69	1.65
Cr_2O_3	0.55	0.54	0.60	0.61	0.63	0.60	0.67	0.59	0.63	0.62
FeO	8.10	8.27	8.08	8.08	8.21	8.10	8.09	8.59	8.46	8.23
MnO	0.19	0.19	0.21	0.21	0.21	0.20	0.19	0.21	0.21	0.19
MgO	31.73	31.89	31.76	31.64	31.80	31.80	31.80	31.21	32.17	31.89
CaO	1.99	1.71	1.96	2.00	1.77	1.62	1.55	1.71	1.45	1.84
NiO	0.14	0.17	0.16	0.13	0.11	0.15	0.10	0.16	0.17	0.15
Total	**100.25**	**100.28**	**100.43**	**100.27**	**100.40**	**99.75**	**99.51**	**99.50**	**100.96**	**100.80**
Si	1.95	1.95	1.95	1.95	1.95	1.95	1.95	1.95	1.94	1.95
Al^{IV}	0.05	0.05	0.05	0.05	0.05	0.05	0.04	0.05	0.05	0.05
Al^{VI}	0.02	0.02	0.02	0.02	0.02	0.02	0.02	0.02	0.02	0.02
Fe^{3+}	0.02	0.02	0.02	0.02	0.02	0.02	0.02	0.02	0.03	0.02
Cr	0.02	0.01	0.02	0.02	0.02	0.02	0.02	0.02	0.02	0.02
Ti	0.00	0.00	0.00	0.00	0.00	0.00	0.00	0.00	0.00	0.00
Fe^{2+}	0.22	0.22	0.22	0.22	0.22	0.22	0.22	0.23	0.22	0.22
Mn	0.01	0.01	0.01	0.01	0.01	0.01	0.01	0.01	0.01	0.01
Mg	1.65	1.66	1.65	1.65	1.65	1.66	1.67	1.64	1.66	1.65
Ca	0.07	0.06	0.07	0.07	0.07	0.06	0.06	0.06	0.05	0.07
Ni	0.00	0.00	0.00	0.00	0.00	0.00	0.00	0.00	0.00	0.00
Total	**4.01**	**4.01**	**4.01**	**4.01**	**4.01**	**4.01**	**4.01**	**4.01**	**4.01**	**4.01**
Wo	3.8	3.2	3.7	3.8	3.4	3.1	3.0	3.3	2.7	3.5
Fs	12.0	12.2	12.0	12.0	12.2	12.1	12.1	12.9	12.4	12.2
En	83.9	84.2	84.0	83.9	84.2	84.5	84.7	83.5	84.5	84.1
Mg#	88.4	88.4	88.5	88.3	88.2	88.4	88.3	87.5	88.4	88.1

Sample No.	**15KMAS-3**	**15KMAS-3**	**15KMAS-3**	**15KMAS-3**	**15KMAS-3**	**15KMAS-3**	**15KMAS-3**	**15KMAS-4**	**15KMAS-4**	**15KMAS-4**
Intrusion	Kumuzhya	Kumuzhya	Kumuzhya	Kumuzhya	Kumuzhya	Kumuzhya	Kumuzhya	Kumuzhya	Kumuzhya	Kumuzhya
Sample Pt.	Opx 1	Opx 2	Opx 2	Opx 2	Opx 3	Opx 3	Opx 3	Opx 1	Opx 1	Opx 1
Rock type	OL-OPX	OL-OPX	OL-OPX	OL-OPX	OL-OPX	OL-OPX	OL-OPX	OL-OPX	OL-OPX	OL-OPX
SiO_2 (wt %)	56.04	56.39	56.27	56.25	56.20	56.00	55.69	55.86	55.65	55.41
TiO_2	0.16	0.14	0.12	0.09	0.08	0.10	0.14	0.12	0.17	0.16
Al_2O_3	1.61	1.55	1.64	1.71	1.69	1.67	2.30	1.64	1.70	1.76
Cr_2O_3	0.55	0.54	0.64	0.61	0.65	0.63	0.71	0.56	0.61	0.63
FeO	8.54	8.33	8.41	8.26	8.20	8.17	8.47	8.14	8.36	8.35
MnO	0.22	0.24	0.20	0.23	0.20	0.20	0.20	0.21	0.19	0.20
MgO	32.02	31.87	31.85	31.78	31.96	31.76	32.15	31.84	32.25	31.51
CaO	1.46	1.82	1.93	1.93	1.66	1.86	0.99	1.61	1.05	1.88
NiO	0.15	0.13	0.14	0.16	0.16	0.13	0.14	0.15	0.16	0.14
Total	**100.75**	**101.01**	**101.20**	**101.02**	**100.80**	**100.52**	**100.79**	**100.13**	**100.14**	**100.04**
Si	1.95	1.95	1.95	1.95	1.95	1.95	1.93	1.95	1.94	1.94
Al^{IV}	0.05	0.05	0.05	0.05	0.05	0.05	0.07	0.05	0.05	0.05
Al^{VI}	0.02	0.02	0.02	0.02	0.02	0.02	0.03	0.02	0.02	0.02
Fe^{3+}	0.02	0.01	0.02	0.01	0.01	0.01	0.02	0.01	0.02	0.03
Cr	0.02	0.01	0.02	0.02	0.02	0.02	0.02	0.02	0.02	0.02
Ti	0.00	0.00	0.00	0.00	0.00	0.00	0.00	0.00	0.00	0.00
Fe^{2+}	0.23	0.23	0.23	0.23	0.23	0.22	0.23	0.23	0.22	0.22
Mn	0.01	0.01	0.01	0.01	0.01	0.01	0.01	0.01	0.01	0.01
Mg	1.66	1.65	1.64	1.64	1.65	1.65	1.66	1.66	1.68	1.65
Ca	0.05	0.07	0.07	0.07	0.06	0.07	0.04	0.06	0.04	0.07
Ni	0.00	0.00	0.00	0.00	0.00	0.00	0.00	0.00	0.00	0.00
Total	**4.01**	**4.00**	**4.01**	**4.00**	**4.00**	**4.00**	**4.01**	**4.00**	**4.01**	**4.01**
Wo	2.8	3.4	3.6	3.7	3.2	3.5	1.9	3.1	2.0	3.6
Fs	12.6	12.3	12.4	12.2	12.1	12.1	12.6	12.1	12.4	12.4
En	84.3	83.9	83.7	83.8	84.4	84.0	85.2	84.5	85.3	83.7
Mg#	87.9	87.6	87.9	87.9	87.9	88.0	88.0	88.0	88.5	88.3

CHR = chromitite; LH = lherzolite; HZ = harzburgite; OL-WEB = olivine-websterite; OL-OPX = olivine-orthopyroxenite;
OPX = orthopyroxenite; MNO = melanorite; BRC = breccia; oph = ophitic; xeno = xenolith

Table D.2 (cont.)

Sample No.	**15KMAS-4**	**15KMAS-4**	**15KMAS-4**	**15KMAS-4**	**15KMAS-4**	**15KMAS-4**	**15KMAS-5**	**15KMAS-5**	**15KMAS-5**	**15KMAS-5**
Intrusion	Kumuzhya	Kumuzhya	Kumuzhya	Kumuzhya	Kumuzhya	Kumuzhya	Kumuzhya	Kumuzhya	Kumuzhya	Kumuzhya
Sample Pt.	Opx 2	Opx 2	Opx 2	Opx 3	Opx 3	Opx 3	Opx 1	Opx 1	Opx 1	Opx 1
Rock type	OL-OPX	OL-OPX	OL-OPX	OL-OPX	OL-OPX	OL-OPX	OL-OPX	OL-OPX	OL-OPX	OL-OPX
SiO_2 (wt %)	56.23	55.75	55.91	55.44	55.94	55.55	55.65	55.73	55.66	55.93
TiO_2	0.15	0.10	0.14	0.10	0.10	0.14	0.08	0.06	0.07	0.15
Al_2O_3	1.28	1.58	1.54	1.95	1.75	1.88	1.71	1.60	1.56	1.61
Cr_2O_3	0.44	0.59	0.53	0.69	0.66	0.66	0.60	0.65	0.66	0.61
FeO	8.27	8.20	8.30	8.66	8.41	8.24	8.18	8.08	8.09	8.41
MnO	0.22	0.22	0.24	0.19	0.21	0.20	0.20	0.19	0.18	0.22
MgO	32.17	31.53	31.83	32.27	32.02	31.47	31.54	31.41	31.74	31.89
CaO	1.51	1.96	1.62	0.65	1.32	2.01	1.81	2.08	1.63	1.61
NiO	0.16	0.14	0.14	0.14	0.14	0.16	0.13	0.16	0.13	0.12
Total	**100.43**	**100.07**	**100.25**	**100.09**	**100.55**	**100.31**	**99.90**	**99.96**	**99.72**	**100.55**
Si	1.96	1.95	1.95	1.94	1.95	1.94	1.95	1.95	1.95	1.95
Al^{IV}	0.04	0.05	0.05	0.06	0.05	0.06	0.05	0.05	0.05	0.05
Al^{VI}	0.01	0.02	0.02	0.02	0.02	0.02	0.02	0.02	0.02	0.02
Fe^{3+}	0.02	0.02	0.01	0.03	0.02	0.02	0.01	0.01	0.01	0.02
Cr	0.01	0.02	0.01	0.02	0.02	0.02	0.02	0.02	0.02	0.02
Ti	0.00	0.00	0.00	0.00	0.00	0.00	0.00	0.00	0.00	0.00
Fe^{2+}	0.22	0.22	0.23	0.22	0.23	0.22	0.23	0.23	0.22	0.23
Mn	0.01	0.01	0.01	0.01	0.01	0.01	0.01	0.01	0.01	0.01
Mg	1.67	1.65	1.66	1.68	1.66	1.64	1.65	1.64	1.66	1.66
Ca	0.06	0.07	0.06	0.02	0.05	0.08	0.07	0.08	0.06	0.06
Ni	0.00	0.00	0.00	0.00	0.00	0.00	0.00	0.00	0.00	0.00
Total	**4.01**	**4.00**	**4.00**	**4.01**	**4.00**	**4.01**	**4.00**	**4.00**	**4.00**	**4.01**
Wo	2.9	3.7	3.1	1.2	2.5	3.8	3.5	4.0	3.1	3.1
Fs	12.2	12.2	12.3	12.9	12.5	12.3	12.2	12.1	12.1	12.4
En	84.6	83.7	84.3	85.6	84.7	83.6	84.0	83.7	84.5	84.2
Mg#	88.2	88.0	87.9	88.2	87.9	88.2	87.9	87.9	88.1	88.0

Sample No.	**15KMAS-5**	**15KMAS-5**	**15KMAS-5**	**15KMAS-5**	**15KMAS-6**	**15KMAS-6**	**15KMAS-6**	**15KMAS-6**	**15KMAS-6**	**15KMAS-6**
Intrusion	Kumuzhya	Kumuzhya	Kumuzhya	Kumuzhya	Kumuzhya	Kumuzhya	Kumuzhya	Kumuzhya	Kumuzhya	Kumuzhya
Sample Pt.	Opx 2	Opx 2	Opx 2	Opx 2	Opx 1	Opx 1	Opx 1	Opx 1	Opx 1	Opx 1
Rock type	OL-OPX	OL-OPX	OL-OPX	OL-OPX	OL-OPX	OL-OPX	OL-OPX	OL-OPX	OL-OPX	OL-OPX
SiO_2 (wt %)	55.71	55.37	55.60	55.58	55.92	55.97	55.96	55.35	55.31	55.47
TiO_2	0.09	0.10	0.12	0.10	0.09	0.15	0.09	0.10	0.15	0.08
Al_2O_3	1.66	1.67	1.65	1.68	1.62	1.60	1.52	1.67	1.62	1.73
Cr_2O_3	0.58	0.60	0.55	0.61	0.67	0.68	0.58	0.59	0.60	0.59
FeO	8.29	8.08	8.21	8.24	8.52	8.59	8.46	8.48	8.44	8.44
MnO	0.20	0.18	0.21	0.21	0.21	0.23	0.20	0.21	0.24	0.21
MgO	31.80	31.29	31.59	31.44	31.62	32.26	31.54	31.15	31.33	31.42
CaO	1.59	2.08	1.78	1.96	1.74	0.86	1.77	1.93	1.77	1.70
NiO	0.16	0.15	0.11	0.12	0.13	0.20	0.16	0.13	0.15	0.14
Total	**100.08**	**99.52**	**99.82**	**99.94**	**100.52**	**100.54**	**100.28**	**99.61**	**99.61**	**99.78**
Si	1.95	1.95	1.95	1.95	1.95	1.95	1.96	1.95	1.95	1.95
Al^{IV}	0.05	0.05	0.05	0.05	0.05	0.05	0.04	0.05	0.05	0.05
Al^{VI}	0.02	0.02	0.02	0.02	0.02	0.02	0.02	0.02	0.02	0.02
Fe^{3+}	0.02	0.02	0.02	0.02	0.01	0.02	0.01	0.02	0.02	0.02
Cr	0.02	0.02	0.02	0.02	0.02	0.02	0.02	0.02	0.02	0.02
Ti	0.00	0.00	0.00	0.00	0.00	0.00	0.00	0.00	0.00	0.00
Fe^{2+}	0.22	0.22	0.22	0.22	0.23	0.23	0.24	0.23	0.23	0.23
Mn	0.01	0.01	0.01	0.01	0.01	0.01	0.01	0.01	0.01	0.01
Mg	1.66	1.64	1.65	1.64	1.64	1.67	1.64	1.64	1.64	1.65
Ca	0.06	0.08	0.07	0.07	0.07	0.03	0.07	0.07	0.07	0.06
Ni	0.00	0.00	0.00	0.00	0.00	0.01	0.00	0.00	0.00	0.00
Total	**4.01**	**4.01**	**4.00**	**4.01**	**4.00**	**4.01**	**4.00**	**4.01**	**4.01**	**4.01**
Wo	3.0	4.0	3.4	3.7	3.3	1.6	3.4	3.7	3.4	3.3
Fs	12.3	12.1	12.2	12.3	12.6	12.7	12.6	12.7	12.6	12.6
En	84.4	83.6	84.0	83.7	83.7	85.3	83.7	83.3	83.6	83.8
Mg#	88.2	88.1	88.0	88.0	87.6	87.8	87.4	87.5	87.8	87.7

CHR = chromitite; LH = lherzolite; HZ = harzburgite; OL-WEB = olivine-websterite; OL-OPX = olivine-orthopyroxenite;
OPX = orthopyroxenite; MNO = melanorite; BRC = breccia; oph = ophitic; xeno = xenolith

Table D.2 (cont.)

Sample No.	**15KMAS-6**	**15KMAS-6**	**15KMAS-6**	**15KMAS-7**	**15KMAS-7**	**15KMAS-7**	**15KMAS-7**	**15KMAS-7**	**15KMAS-7**	**15KMAS-7**
Intrusion	Kumuzhya	Kumuzhya	Kumuzhya	Kumuzhya	Kumuzhya	Kumuzhya	Kumuzhya	Kumuzhya	Kumuzhya	Kumuzhya
Sample Pt.	Opx 2	Opx 2	Opx 2	Opx 1	Opx 1	Opx 1	Opx 2	Opx 2	Opx 2	Opx 2
Rock type	OL-OPX	OL-OPX	OL-OPX	OL-OPX	OL-OPX	OL-OPX	OL-OPX	OL-OPX	OL-OPX	OL-OPX
SiO_2 (wt %)	55.57	55.60	55.64	56.08	56.14	56.16	56.39	56.22	56.50	56.46
TiO_2	0.11	0.09	0.13	0.11	0.09	0.06	0.08	0.06	0.08	0.08
Al_2O_3	1.63	1.57	1.62	1.76	1.73	1.62	1.59	1.63	1.51	1.50
Cr_2O_3	0.63	0.58	0.62	0.67	0.67	0.62	0.70	0.68	0.69	0.67
FeO	8.27	8.54	8.32	8.58	8.53	8.45	8.38	8.29	8.37	8.33
MnO	0.19	0.21	0.18	0.20	0.19	0.20	0.20	0.17	0.21	0.18
MgO	31.29	31.60	31.43	31.88	31.74	31.63	32.15	31.84	32.22	32.26
CaO	1.82	1.65	1.76	1.60	1.79	1.95	1.54	1.74	1.53	1.55
NiO	0.13	0.17	0.20	0.18	0.17	0.17	0.13	0.17	0.14	0.16
Total	**99.64**	**100.01**	**99.90**	**101.06**	**101.05**	**100.86**	**101.16**	**100.80**	**101.25**	**101.19**
Si	1.95	1.95	1.95	1.95	1.95	1.95	1.95	1.95	1.95	1.95
Al^{IV}	0.05	0.05	0.05	0.05	0.05	0.05	0.05	0.05	0.04	0.04
Al^{VI}	0.02	0.02	0.02	0.02	0.02	0.02	0.02	0.02	0.02	0.02
Fe^{3+}	0.00	0.02	0.01	0.02	0.02	0.01	0.01	0.01	0.01	0.02
Cr	0.02	0.02	0.02	0.02	0.02	0.02	0.02	0.02	0.02	0.02
Ti	0.00	0.00	0.00	0.00	0.00	0.00	0.00	0.00	0.00	0.00
Fe^{2+}	0.24	0.23	0.23	0.23	0.23	0.23	0.23	0.23	0.23	0.22
Mn	0.01	0.01	0.01	0.01	0.01	0.01	0.01	0.01	0.01	0.01
Mg	1.64	1.65	1.64	1.65	1.64	1.64	1.66	1.65	1.66	1.66
Ca	0.07	0.06	0.07	0.06	0.07	0.07	0.06	0.06	0.06	0.06
Ni	0.00	0.00	0.01	0.01	0.00	0.00	0.00	0.00	0.00	0.00
Total	**4.00**	**4.01**	**4.00**	**4.01**	**4.00**	**4.00**	**4.00**	**4.00**	**4.00**	**4.01**
Wo	3.5	3.1	3.4	3.0	3.4	3.7	2.9	3.3	2.9	2.9
Fs	12.4	12.7	12.4	12.7	12.6	12.5	12.3	12.3	12.3	12.2
En	83.8	83.9	83.9	84.0	83.7	83.5	84.5	84.2	84.5	84.6
Mg#	87.3	87.9	87.5	87.8	87.7	87.6	87.9	87.7	87.9	88.1

Sample No.	**15KMAS-7**	**15KMAS-7**	**15NMAS-1**	**15NMAS-1**	**15NMAS-1**	**15NMAS-1**	**15NMAS-1**	**15NMAS-1**	**15NMAS-1**	**15NMAS-1**
Intrusion	Kumuzhya	Kumuzhya	Nittis	Nittis	Nittis	Nittis	Nittis	Nittis	Nittis	Nittis
Sample Pt.	Opx 4	Opx 4	Opx 1	Opx 1	Opx 1	Opx 2	Opx 2	Opx 2	Opx 3	Opx 3
Rock type	OL-OPX	OL-OPX	OPX	OPX	OPX	OPX	OPX	OPX	OPX	OPX
SiO_2 (wt %)	56.11	55.95	56.10	56.19	56.16	56.03	56.07	56.21	56.15	56.50
TiO_2	0.08	0.08	0.11	0.09	0.09	0.08	0.13	0.11	0.13	0.10
Al_2O_3	1.68	1.77	1.82	1.77	1.89	1.81	1.61	1.69	1.57	1.49
Cr_2O_3	0.68	0.67	0.70	0.71	0.71	0.69	0.61	0.61	0.58	0.58
FeO	8.43	8.37	8.02	8.06	8.03	8.01	7.95	8.04	8.13	8.22
MnO	0.21	0.23	0.22	0.20	0.21	0.19	0.18	0.23	0.18	0.21
MgO	31.87	31.66	32.36	32.25	32.08	32.17	31.87	32.28	32.42	32.97
CaO	1.66	1.76	1.60	1.61	1.81	1.69	2.12	1.68	1.59	0.92
NiO	0.14	0.16	0.16	0.16	0.11	0.17	0.11	0.16	0.14	0.14
Total	**100.86**	**100.65**	**101.09**	**101.04**	**101.09**	**100.84**	**100.65**	**101.01**	**100.89**	**101.13**
Si	1.95	1.95	1.94	1.95	1.94	1.94	1.95	1.95	1.95	1.95
Al^{IV}	0.05	0.05	0.05	0.05	0.06	0.05	0.05	0.05	0.05	0.04
Al^{VI}	0.02	0.02	0.02	0.02	0.02	0.02	0.02	0.02	0.02	0.02
Fe^{3+}	0.02	0.01	0.03	0.02	0.02	0.02	0.02	0.02	0.03	0.03
Cr	0.02	0.02	0.02	0.02	0.02	0.02	0.02	0.02	0.02	0.02
Ti	0.00	0.00	0.00	0.00	0.00	0.00	0.00	0.00	0.00	0.00
Fe^{2+}	0.23	0.23	0.20	0.21	0.21	0.21	0.21	0.21	0.21	0.21
Mn	0.01	0.01	0.01	0.01	0.01	0.01	0.01	0.01	0.01	0.01
Mg	1.65	1.64	1.67	1.66	1.66	1.66	1.65	1.67	1.68	1.70
Ca	0.06	0.07	0.06	0.06	0.07	0.06	0.08	0.06	0.06	0.03
Ni	0.00	0.00	0.00	0.00	0.00	0.00	0.00	0.00	0.00	0.00
Total	**4.01**	**4.00**	**4.01**	**4.01**	**4.01**	**4.01**	**4.01**	**4.01**	**4.01**	**4.01**
Wo	3.1	3.4	3.0	3.0	3.4	3.2	4.0	3.2	3.0	1.7
Fs	12.5	12.4	11.8	11.9	11.8	11.8	11.7	11.8	11.9	12.0
En	84.1	83.9	84.9	84.8	84.4	84.7	84.0	84.7	84.8	86.0
Mg#	87.8	87.7	89.1	88.7	88.5	88.9	88.6	88.9	89.1	88.9

CHR = chromitite; LH = lherzolite; HZ = harzburgite; OL-WEB = olivine-websterite; OL-OPX = olivine-orthopyroxenite;
OPX = orthopyroxenite; MNO = melanorite; BRC = breccia; oph = ophitic; xeno = xenolith

Table D.2 (cont.)

Sample No.	**15NMAS-2**	**15NMAS-2**	**15NMAS-2**	**15NMAS-2**	**15NMAS-2**	**15NMAS-2**	**15NMAS-2**	**15NMAS-2**	**15NMAS-2**	**79-008**
Intrusion	Nittis	Nittis	Nittis	Nittis	Nittis	Nittis	Nittis	Nittis	Nittis	Nittis
Sample Pt.	Opx 1	Opx 1	Opx 1	Opx 2	Opx 2	Opx 2	Opx 3	Opx 3	Opx 3	Opx 1
Rock type	OPX	OPX	OPX	OPX	OPX	OPX	OPX	OPX	OPX	OPX
SiO_2 (wt %)	56.10	56.11	56.04	55.89	56.05	55.99	56.27	56.05	56.16	55.21
TiO_2	0.10	0.18	0.07	0.11	0.07	0.08	0.09	0.09	0.09	0.15
Al_2O_3	1.67	1.70	1.71	1.78	1.73	1.53	1.55	1.56	1.51	1.74
Cr_2O_3	0.57	0.57	0.61	0.68	0.68	0.59	0.65	0.68	0.65	0.60
FeO	8.29	8.40	8.41	8.01	8.25	8.25	8.26	8.14	8.28	9.46
MnO	0.21	0.22	0.19	0.21	0.21	0.21	0.24	0.20	0.19	0.22
MgO	31.89	31.96	32.04	31.11	32.10	32.31	32.12	31.94	32.05	30.36
CaO	1.75	1.68	1.48	2.46	1.35	1.46	1.55	1.75	1.60	2.18
NiO	0.15	0.14	0.14	0.15	0.13	0.15	0.17	0.16	0.14	0.13
Total	**100.73**	**100.96**	**100.69**	**100.40**	**100.57**	**100.57**	**100.90**	**100.57**	**100.67**	**100.05**
Si	1.95	1.95	1.95	1.95	1.95	1.95	1.95	1.95	1.95	1.95
Al^{IV}	0.05	0.05	0.05	0.05	0.05	0.05	0.05	0.05	0.04	0.05
Al^{VI}	0.02	0.02	0.02	0.02	0.02	0.02	0.02	0.02	0.02	0.02
Fe^{3+}	0.02	0.02	0.02	0.00	0.01	0.03	0.02	0.02	0.02	0.02
Cr	0.02	0.02	0.02	0.02	0.02	0.02	0.02	0.02	0.02	0.02
Ti	0.00	0.00	0.00	0.00	0.00	0.00	0.00	0.00	0.00	0.00
Fe^{2+}	0.22	0.23	0.22	0.23	0.23	0.21	0.22	0.22	0.22	0.26
Mn	0.01	0.01	0.01	0.01	0.01	0.01	0.01	0.01	0.01	0.01
Mg	1.65	1.65	1.66	1.62	1.66	1.68	1.66	1.66	1.66	1.60
Ca	0.07	0.06	0.06	0.09	0.05	0.05	0.06	0.07	0.06	0.08
Ni	0.00	0.00	0.00	0.00	0.00	0.00	0.00	0.00	0.00	0.00
Total	**4.01**	**4.01**	**4.01**	**4.00**	**4.00**	**4.01**	**4.00**	**4.01**	**4.01**	**4.01**
Wo	3.3	3.2	2.8	4.7	2.6	2.8	2.9	3.3	3.0	4.2
Fs	12.2	12.4	12.4	12.0	12.2	12.1	12.2	12.0	12.2	14.2
En	84.1	84.1	84.5	83.0	84.9	84.8	84.5	84.3	84.5	81.3
Mg#	88.1	88.0	88.1	87.4	88.0	88.9	88.1	88.3	88.1	85.9

Sample No.	**79-008**	**79-008**	**79-008**	**79-008**	**79-008**	**79-008**	**79-008**	**79-008**	**79-008**	**79-008**
Intrusion	Nittis	Nittis	Nittis	Nittis	Nittis	Nittis	Nittis	Nittis	Nittis	Nittis
Sample Pt.	Opx 1	Opx 1	Opx 1	Opx 1	Opx 2	Opx 2	Opx 2	Opx 2	Opx 2	Opx 2
Rock type	OPX	OPX	OPX	OPX	OPX	OPX	OPX	OPX	OPX	OPX
SiO_2 (wt %)	55.00	55.80	55.71	55.62	55.77	55.60	55.84	55.97	56.13	55.98
TiO_2	0.18	0.08	0.08	0.08	0.20	0.10	0.19	0.14	0.09	0.15
Al_2O_3	1.70	1.69	1.65	1.66	1.34	1.51	1.55	1.58	1.54	1.63
Cr_2O_3	0.54	0.65	0.66	0.65	0.51	0.60	0.59	0.61	0.56	0.58
FeO	9.40	9.50	9.98	9.58	10.16	9.97	9.24	9.55	9.71	9.88
MnO	0.25	0.24	0.24	0.24	0.21	0.23	0.23	0.23	0.21	0.25
MgO	30.15	30.58	31.19	30.58	30.96	30.53	30.89	31.53	31.62	31.58
CaO	1.01	1.92	1.02	2.34	1.55	2.18	2.11	1.39	0.89	0.72
NiO	0.15	0.15	0.14	0.13	0.14	0.17	0.17	0.14	0.18	0.18
Total	**98.38**	**100.61**	**100.67**	**100.88**	**100.84**	**100.89**	**100.81**	**101.14**	**100.93**	**100.95**
Si	1.96	1.95	1.95	1.95	1.95	1.95	1.95	1.95	1.95	1.95
Al^{IV}	0.04	0.05	0.05	0.05	0.04	0.04	0.05	0.05	0.05	0.05
Al^{VI}	0.03	0.02	0.02	0.02	0.02	0.02	0.02	0.02	0.02	0.02
Fe^{3+}	0.00	0.00	0.02	0.03	0.02	0.03	0.01	0.02	0.01	0.01
Cr	0.02	0.02	0.02	0.02	0.01	0.02	0.02	0.02	0.02	0.02
Ti	0.00	0.00	0.00	0.00	0.01	0.00	0.00	0.00	0.00	0.00
Fe^{2+}	0.28	0.28	0.27	0.25	0.27	0.26	0.26	0.25	0.27	0.27
Mn	0.01	0.01	0.01	0.01	0.01	0.01	0.01	0.01	0.01	0.01
Mg	1.60	1.60	1.63	1.60	1.62	1.59	1.61	1.64	1.64	1.64
Ca	0.04	0.07	0.04	0.09	0.06	0.08	0.08	0.05	0.03	0.03
Ni	0.00	0.00	0.00	0.00	0.00	0.00	0.00	0.00	0.01	0.01
Total	**3.99**	**4.00**	**4.01**	**4.01**	**4.01**	**4.01**	**4.00**	**4.01**	**4.00**	**4.00**
Wo	2.0	3.7	1.9	4.5	2.9	4.1	4.0	2.6	1.7	1.4
Fs	14.5	14.2	14.8	14.2	15.0	14.8	13.7	14.1	14.4	14.7
En	83.1	81.7	82.8	81.0	81.7	80.7	81.9	83.0	83.6	83.6
Mg#	85.1	85.2	85.6	86.3	85.5	85.9	86.3	86.6	85.8	85.7

CHR = chromitite; LH = lherzolite; HZ = harzburgite; OL-WEB = olivine-websterite; OL-OPX = olivine-orthopyroxenite;
OPX = orthopyroxenite; MNO = melanorite; BRC = breccia; oph = ophitic; xeno = xenolith

Table D.2 (cont.)

Sample No.	**79-008**	**79-008**	**79-008**	**79-008**	**79-008**	**79-008**	**79-023**	**79-023**	**79-023**	**79-023**
Intrusion	Nittis	Nittis	Nittis	Nittis	Nittis	Nittis	Nittis	Nittis	Nittis	Nittis
Sample Pt.	Opx 3	Opx 3	Opx 3	Opx 4	Opx 4	Opx 4	Opx 1	Opx 1	Opx 1	Opx 2
Rock type	OPX	OPX	OPX	OPX	OPX	OPX	OPX	OPX	OPX	OPX
SiO_2 (wt %)	55.11	55.43	55.30	55.81	55.15	55.81	55.64	55.28	55.04	55.51
TiO_2	0.08	0.15	0.12	0.17	0.15	0.07	0.07	0.12	0.12	0.10
Al_2O_3	1.57	1.68	1.72	1.44	1.76	1.59	2.27	2.06	2.02	1.68
Cr_2O_3	0.64	0.56	0.60	0.57	0.70	0.64	0.51	0.60	0.88	0.60
FeO	10.43	10.47	10.43	10.61	10.20	9.66	11.04	10.41	9.91	10.50
MnO	0.23	0.21	0.22	0.26	0.22	0.21	0.19	0.21	0.19	0.23
MgO	30.71	30.66	30.61	31.16	29.50	30.35	31.11	30.20	29.00	30.38
CaO	1.11	1.20	1.22	0.85	2.90	2.32	0.64	2.03	3.60	1.71
NiO	0.13	0.14	0.15	0.15	0.11	0.11	0.13	0.17	0.15	0.15
Total	**100.01**	**100.50**	**100.37**	**101.02**	**100.69**	**100.76**	**101.60**	**101.06**	**100.91**	**100.86**
Si	1.95	1.95	1.95	1.95	1.94	1.95	1.93	1.94	1.94	1.95
Al^{IV}	0.05	0.05	0.05	0.04	0.05	0.05	0.07	0.06	0.06	0.05
Al^{VI}	0.02	0.02	0.02	0.02	0.02	0.02	0.03	0.02	0.02	0.02
Fe^{3+}	0.03	0.02	0.02	0.02	0.02	0.01	0.03	0.03	0.02	0.02
Cr	0.02	0.02	0.02	0.02	0.02	0.02	0.01	0.02	0.02	0.02
Ti	0.00	0.00	0.00	0.00	0.00	0.00	0.00	0.00	0.00	0.00
Fe^{2+}	0.28	0.29	0.29	0.29	0.28	0.28	0.29	0.27	0.27	0.29
Mn	0.01	0.01	0.01	0.01	0.01	0.01	0.01	0.01	0.01	0.01
Mg	1.62	1.61	1.61	1.62	1.55	1.58	1.61	1.58	1.52	1.59
Ca	0.04	0.05	0.05	0.03	0.11	0.09	0.02	0.08	0.14	0.06
Ni	0.00	0.00	0.00	0.00	0.00	0.00	0.00	0.00	0.00	0.00
Total	**4.01**	**4.01**	**4.01**	**4.01**	**4.01**	**4.00**	**4.01**	**4.01**	**4.01**	**4.01**
Wo	2.1	2.3	2.3	1.6	5.6	4.4	1.2	3.9	6.9	3.3
Fs	15.6	15.6	15.6	15.7	15.3	14.4	16.3	15.5	14.9	15.6
En	81.9	81.7	81.7	82.3	78.8	80.8	82.2	80.3	77.9	80.8
Mg#	85.3	84.7	84.9	85.0	84.8	85.2	84.8	85.2	84.8	84.8

Sample No.	**79-023**	**79-023**	**79-023**	**79-023**	**79-039**	**79-039**	**79-039**	**79-039**	**79-039**	**79-039**
Intrusion	Nittis	Nittis	Nittis	Nittis	Nittis	Nittis	Nittis	Nittis	Nittis	Nittis
Sample Pt.	Opx 2	Opx 2	Opx 3	Opx 3	Opx 1	Opx 1	Opx 1	Opx 2	Opx 2	Opx 2
Rock type	OPX	OPX	OPX	OPX	OPX	OPX	OPX	OPX	OPX	OPX
SiO_2 (wt %)	55.49	55.68	55.73	55.15	56.07	56.01	55.60	56.22	56.11	56.01
TiO_2	0.17	0.18	0.08	0.08	0.10	0.08	0.13	0.10	0.08	0.12
Al_2O_3	1.59	1.40	1.64	1.76	1.70	1.83	2.00	1.62	1.68	1.78
Cr_2O_3	0.61	0.47	0.53	0.75	0.60	0.69	0.67	0.54	0.66	0.56
FeO	10.61	10.76	10.14	9.73	9.52	9.21	9.28	9.19	9.21	9.31
MnO	0.25	0.22	0.18	0.19	0.23	0.23	0.22	0.19	0.23	0.23
MgO	30.28	31.04	31.47	29.91	32.05	31.54	31.14	31.42	31.13	31.28
CaO	1.76	0.94	0.62	2.49	1.02	1.75	2.10	1.90	2.03	1.89
NiO	0.15	0.13	0.14	0.15	0.17	0.17	0.15	0.14	0.13	0.15
Total	**100.91**	**100.81**	**100.53**	**100.21**	**101.47**	**101.51**	**101.30**	**101.33**	**101.26**	**101.32**
Si	1.95	1.95	1.95	1.95	1.94	1.94	1.93	1.95	1.95	1.95
Al^{IV}	0.05	0.04	0.05	0.05	0.05	0.05	0.06	0.05	0.05	0.05
Al^{VI}	0.02	0.02	0.02	0.02	0.02	0.02	0.02	0.02	0.02	0.02
Fe^{3+}	0.02	0.03	0.02	0.02	0.04	0.03	0.04	0.02	0.01	0.02
Cr	0.02	0.01	0.01	0.02	0.02	0.02	0.02	0.01	0.02	0.02
Ti	0.00	0.00	0.00	0.00	0.00	0.00	0.00	0.00	0.00	0.00
Fe^{2+}	0.29	0.29	0.28	0.27	0.24	0.24	0.23	0.25	0.25	0.25
Mn	0.01	0.01	0.01	0.01	0.01	0.01	0.01	0.01	0.01	0.01
Mg	1.58	1.62	1.64	1.57	1.66	1.63	1.62	1.63	1.61	1.62
Ca	0.07	0.04	0.02	0.09	0.04	0.06	0.08	0.07	0.08	0.07
Ni	0.00	0.00	0.00	0.00	0.00	0.00	0.00	0.00	0.00	0.00
Total	**4.01**	**4.01**	**4.01**	**4.01**	**4.01**	**4.01**	**4.01**	**4.01**	**4.00**	**4.01**
Wo	3.4	1.8	1.2	4.8	1.9	3.3	4.0	3.6	3.8	3.6
Fs	15.8	15.9	15.1	14.6	13.9	13.5	13.7	13.5	13.6	13.7
En	80.5	82.0	83.5	80.3	83.8	82.8	82.0	82.6	82.2	82.3
Mg#	84.6	84.9	85.5	85.4	87.4	87.3	87.4	86.8	86.4	86.8

CHR = chromitite; LH = lherzolite; HZ = harzburgite; OL-WEB = olivine-websterite; OL-OPX = olivine-orthopyroxenite;
OPX = orthopyroxenite; MNO = melanorite; BRC = breccia; oph = ophitic; xeno = xenolith

Table D.2 (cont.)

Sample No.	**79-039**	**79-039**	**79-039**	**79-054**	**79-054**	**79-054**	**79-054**	**79-054**	**79-064**	**79-064**
Intrusion	Nittis	Nittis	Nittis	Nittis	Nittis	Nittis	Nittis	Nittis	Nittis	Nittis
Sample Pt.	Opx 3	Opx 3	Opx 3	Opx 1	Opx 2	Opx 2	Opx 2	Opx 3	Opx 1	Opx 1
Rock type	OPX	OPX	OPX	OPX	OPX	OPX	OPX	OPX	OPX	OPX
SiO_2 (wt %)	55.37	55.32	55.22	56.09	55.43	55.66	55.77	55.26	56.09	56.16
TiO_2	0.13	0.12	0.10	0.12	0.17	0.15	0.07	0.10	0.09	0.10
Al_2O_3	1.83	1.83	2.00	1.57	1.97	1.91	1.87	1.91	1.58	1.60
Cr_2O_3	0.67	0.70	0.79	0.61	0.54	0.56	0.66	0.67	0.64	0.60
FeO	9.97	9.83	10.29	10.38	10.19	10.29	10.18	10.20	8.91	8.89
MnO	0.25	0.23	0.25	0.19	0.21	0.22	0.23	0.23	0.22	0.18
MgO	30.88	30.74	31.24	30.16	29.96	30.81	31.26	30.59	31.52	31.56
CaO	1.50	1.68	0.73	2.06	2.57	1.61	1.01	1.32	1.82	1.63
NiO	0.15	0.17	0.18	0.15	0.13	0.15	0.15	0.15	0.16	0.18
Total	**100.75**	**100.62**	**100.79**	**101.34**	**101.16**	**101.36**	**101.19**	**100.43**	**101.03**	**100.90**
Si	1.94	1.94	1.93	1.96	1.94	1.94	1.94	1.94	1.95	1.95
Al^{IV}	0.05	0.05	0.06	0.04	0.06	0.06	0.06	0.06	0.05	0.05
Al^{VI}	0.02	0.02	0.02	0.02	0.02	0.02	0.02	0.02	0.02	0.02
Fe^{3+}	0.03	0.03	0.04	0.00	0.02	0.03	0.02	0.02	0.02	0.01
Cr	0.02	0.02	0.02	0.02	0.01	0.02	0.02	0.02	0.02	0.02
Ti	0.00	0.00	0.00	0.00	0.00	0.00	0.00	0.00	0.00	0.00
Fe^{2+}	0.26	0.26	0.26	0.30	0.27	0.27	0.27	0.28	0.24	0.25
Mn	0.01	0.01	0.01	0.01	0.01	0.01	0.01	0.01	0.01	0.01
Mg	1.61	1.61	1.63	1.57	1.56	1.60	1.62	1.60	1.63	1.64
Ca	0.06	0.06	0.03	0.08	0.10	0.06	0.04	0.05	0.07	0.06
Ni	0.00	0.00	0.01	0.00	0.00	0.00	0.00	0.00	0.00	0.01
Total	**4.01**	**4.01**	**4.01**	**4.00**	**4.01**	**4.01**	**4.01**	**4.01**	**4.01**	**4.00**
Wo	2.9	3.2	1.4	3.9	4.9	3.1	1.9	2.5	3.4	3.1
Fs	14.8	14.6	15.3	15.5	15.2	15.2	15.1	15.3	13.2	13.2
En	82.0	81.8	83.0	80.3	79.6	81.4	82.7	81.8	83.1	83.5
Mg#	86.0	86.0	86.0	83.8	85.1	85.5	85.7	85.1	87.2	86.8

Sample No.	**79-064**	**79-064**	**79-064**	**79-064**	**79-064**	**79-064**	**79-064**	**79-064**	**79-091**	**79-091**
Intrusion	Nittis	Nittis	Nittis	Nittis	Nittis	Nittis	Nittis	Nittis	Nittis	Nittis
Sample Pt.	Opx 1	Opx 1	Opx 2	Opx 2	Opx 2	Opx 2	Opx 3	Opx 4	Opx 1	Opx 1
Rock type	OPX	OPX	OPX	OPX	OPX	OPX	OPX	OPX	OPX	OPX
SiO_2 (wt %)	56.62	56.18	55.99	56.10	55.64	55.97	55.86	56.09	55.49	55.53
TiO_2	0.04	0.08	0.08	0.10	0.10	0.10	0.09	0.07	0.17	0.10
Al_2O_3	1.09	1.47	1.66	1.66	1.71	1.68	1.70	1.47	1.78	1.66
Cr_2O_3	0.45	0.62	0.67	0.66	0.70	0.67	0.74	0.59	0.54	0.60
FeO	8.74	8.82	8.71	8.91	8.39	8.58	9.16	8.92	11.01	11.00
MnO	0.22	0.21	0.21	0.19	0.21	0.18	0.24	0.21	0.23	0.23
MgO	32.14	31.83	31.75	31.63	31.09	31.64	31.09	32.07	30.54	30.21
CaO	1.49	1.50	1.44	1.69	2.22	1.88	1.87	1.03	1.08	1.54
NiO	0.14	0.15	0.12	0.15	0.15	0.14	0.15	0.15	0.14	0.15
Total	**100.93**	**100.86**	**100.63**	**101.09**	**100.21**	**100.84**	**100.90**	**100.60**	**100.98**	**101.03**
Si	1.97	1.95	1.95	1.95	1.95	1.95	1.95	1.95	1.94	1.95
Al^{IV}	0.03	0.04	0.05	0.05	0.05	0.05	0.05	0.04	0.05	0.05
Al^{VI}	0.01	0.02	0.02	0.02	0.02	0.02	0.02	0.02	0.02	0.02
Fe^{3+}	0.02	0.02	0.01	0.02	0.01	0.02	0.01	0.02	0.02	0.02
Cr	0.01	0.02	0.02	0.02	0.02	0.02	0.02	0.02	0.01	0.02
Ti	0.00	0.00	0.00	0.00	0.00	0.00	0.00	0.00	0.00	0.00
Fe^{2+}	0.24	0.24	0.24	0.24	0.23	0.23	0.25	0.24	0.30	0.30
Mn	0.01	0.01	0.01	0.01	0.01	0.01	0.01	0.01	0.01	0.01
Mg	1.66	1.65	1.65	1.64	1.62	1.64	1.62	1.67	1.60	1.58
Ca	0.06	0.06	0.05	0.06	0.08	0.07	0.07	0.04	0.04	0.06
Ni	0.00	0.00	0.00	0.00	0.00	0.00	0.00	0.00	0.00	0.00
Total	**4.01**	**4.01**	**4.00**	**4.01**	**4.00**	**4.01**	**4.00**	**4.01**	**4.01**	**4.01**
Wo	2.8	2.8	2.7	3.2	4.3	3.6	3.6	2.0	2.1	2.9
Fs	12.8	13.0	12.9	13.2	12.5	12.7	13.6	13.2	16.4	16.4
En	84.1	83.8	84.0	83.4	82.9	83.5	82.5	84.6	81.2	80.3
Mg#	87.5	87.3	87.3	87.2	87.4	87.7	86.5	87.4	84.1	84.0

CHR = chromitite; LH = lherzolite; HZ = harzburgite; OL-WEB = olivine-websterite; OL-OPX = olivine-orthopyroxenite;
OPX = orthopyroxenite; MNO = melanorite; BRC = breccia; oph = ophitic; xeno = xenolith

Table D.2 (cont.)

Sample No.	**79-091**	**79-091**	**79-091**	**79-091**	**79-091**	**79-091**	**79-115**	**79-115**	**79-115**	**79-115**
Intrusion	Nittis	Nittis	Nittis	Nittis	Nittis	Nittis	Nittis	Nittis	Nittis	Nittis
Sample Pt.	Opx 2	Opx 2	Opx 2	Opx 3	Opx 3	Opx 3	Opx 1	Opx 1	Opx 2	Opx 2
Rock type	OPX	OPX	OPX	OPX	OPX	OPX	OPX	OPX	OPX	OPX
SiO_2 (wt %)	55.43	55.53	55.11	55.34	55.49	55.68	54.87	55.11	55.41	55.26
TiO_2	0.12	0.15	0.10	0.10	0.08	0.10	0.28	0.18	0.08	0.08
Al_2O_3	1.83	1.74	1.98	1.74	1.72	1.85	1.55	1.70	1.76	1.83
Cr_2O_3	0.66	0.48	0.73	0.72	0.69	0.69	0.29	0.37	0.73	0.82
FeO	10.77	11.40	10.51	10.67	11.01	10.52	12.96	12.16	10.00	10.37
MnO	0.21	0.25	0.21	0.23	0.22	0.23	0.28	0.25	0.18	0.22
MgO	30.23	30.81	29.57	29.86	30.41	30.61	29.23	29.20	30.53	30.20
CaO	1.69	0.62	2.24	2.13	1.26	1.44	0.92	1.64	1.64	1.86
NiO	0.15	0.14	0.15	0.15	0.15	0.10	0.14	0.15	0.14	0.09
Total	**101.08**	**101.11**	**100.60**	**100.94**	**101.04**	**101.23**	**100.53**	**100.75**	**100.46**	**100.72**
Si	1.94	1.94	1.94	1.94	1.95	1.94	1.95	1.95	1.95	1.94
Al^{IV}	0.05	0.05	0.06	0.05	0.05	0.05	0.05	0.05	0.05	0.05
Al^{VI}	0.02	0.02	0.02	0.02	0.02	0.02	0.02	0.02	0.02	0.02
Fe^{3+}	0.02	0.03	0.01	0.02	0.02	0.02	0.02	0.02	0.01	0.02
Cr	0.02	0.01	0.02	0.02	0.02	0.02	0.01	0.01	0.02	0.02
Ti	0.00	0.00	0.00	0.00	0.00	0.00	0.01	0.00	0.00	0.00
Fe^{2+}	0.29	0.31	0.30	0.29	0.30	0.29	0.36	0.34	0.28	0.28
Mn	0.01	0.01	0.01	0.01	0.01	0.01	0.01	0.01	0.01	0.01
Mg	1.58	1.61	1.55	1.56	1.59	1.59	1.55	1.54	1.60	1.58
Ca	0.06	0.02	0.08	0.08	0.05	0.05	0.04	0.06	0.06	0.07
Ni	0.00	0.00	0.00	0.00	0.00	0.00	0.00	0.00	0.00	0.00
Total	**4.01**	**4.01**	**4.00**	**4.01**	**4.01**	**4.01**	**4.01**	**4.01**	**4.00**	**4.01**
Wo	3.2	1.2	4.3	4.1	2.4	2.7	1.8	3.2	3.1	3.6
Fs	16.0	16.9	15.8	15.9	16.4	15.6	19.4	18.2	15.0	15.5
En	80.4	81.6	79.5	79.6	80.9	81.3	78.4	78.2	81.6	80.6
Mg#	84.4	84.1	84.0	84.3	84.1	84.6	81.1	81.9	85.2	84.9

Sample No.	**79-115**	**79-115**	**79-115**	**79-115**	**79-115**	**79-115**	**79-131**	**79-131**	**79-131**	**79-131**
Intrusion	Nittis	Nittis	Nittis	Nittis	Nittis	Nittis	Nittis	Nittis	Nittis	Nittis
Sample Pt.	Opx 3	Opx 3	Opx 4	Opx 4	Opx 4	Opx 5	Opx 1	Opx 2	Opx 2	Opx 3
Rock type	OPX	OPX	OPX	OPX	OPX	OPX	OPX	OPX	OPX	OPX
SiO_2 (wt %)	55.23	56.07	55.56	55.90	55.26	55.90	55.81	56.00	55.45	55.68
TiO_2	0.08	0.07	0.08	0.08	0.08	0.08	0.10	0.10	0.10	0.08
Al_2O_3	1.74	1.28	1.68	1.32	1.57	1.76	1.80	1.30	1.78	1.89
Cr_2O_3	0.61	0.50	0.72	0.54	0.60	0.75	0.76	0.57	0.70	0.64
FeO	11.69	10.73	11.19	11.19	11.24	9.69	10.67	12.39	11.81	10.59
MnO	0.25	0.25	0.21	0.23	0.25	0.19	0.23	0.27	0.26	0.21
MgO	29.75	30.51	29.88	30.23	29.96	31.36	30.00	29.83	28.89	30.23
CaO	1.50	1.76	1.80	1.51	1.40	1.43	2.06	1.20	2.38	1.64
NiO	0.17	0.13	0.14	0.17	0.14	0.17	0.10	0.13	0.14	0.14
Total	**101.02**	**101.29**	**101.26**	**101.17**	**100.50**	**101.31**	**101.52**	**101.80**	**101.50**	**101.10**
Si	1.94	1.96	1.95	1.96	1.95	1.94	1.95	1.96	1.95	1.95
Al^{IV}	0.05	0.04	0.05	0.04	0.05	0.05	0.05	0.04	0.05	0.05
Al^{VI}	0.02	0.02	0.02	0.02	0.02	0.02	0.02	0.02	0.02	0.03
Fe^{3+}	0.03	0.02	0.02	0.01	0.02	0.02	0.01	0.01	0.01	0.01
Cr	0.02	0.01	0.02	0.01	0.02	0.02	0.02	0.02	0.02	0.02
Ti	0.00	0.00	0.00	0.00	0.00	0.00	0.00	0.00	0.00	0.00
Fe^{2+}	0.32	0.29	0.31	0.31	0.31	0.26	0.30	0.35	0.34	0.30
Mn	0.01	0.01	0.01	0.01	0.01	0.01	0.01	0.01	0.01	0.01
Mg	1.56	1.59	1.56	1.58	1.58	1.63	1.56	1.56	1.51	1.58
Ca	0.06	0.07	0.07	0.06	0.05	0.05	0.08	0.05	0.09	0.06
Ni	0.00	0.00	0.00	0.00	0.00	0.00	0.00	0.00	0.00	0.00
Total	**4.01**	**4.01**	**4.01**	**4.00**	**4.01**	**4.01**	**4.00**	**4.00**	**4.00**	**4.00**
Wo	2.9	3.3	3.5	2.9	2.7	2.7	3.9	2.3	4.6	3.1
Fs	17.4	15.8	16.7	16.6	16.8	14.3	15.9	18.4	17.7	15.8
En	79.3	80.4	79.5	80.1	80.1	82.7	79.8	78.9	77.3	80.7
Mg#	83.2	84.4	83.4	83.5	83.5	86.4	83.7	81.7	81.8	83.9

CHR = chromitite; LH = lherzolite; HZ = harzburgite; OL-WEB = olivine-websterite; OL-OPX = olivine-orthopyroxenite;
OPX = orthopyroxenite; MNO = melanorite; BRC = breccia; oph = ophitic; xeno = xenolith

Table D.2 (cont.)

Sample No.	**79-131**	**79-131**	**79-131**	**79-138**	**79-138**	**79-138**	**79-138**	**79-138**	**79-138**	**79-138**
Intrusion	Nittis	Nittis	Nittis	Nittis	Nittis	Nittis	Nittis	Nittis	Nittis	Nittis
Sample Pt.	Opx 3	Opx 4	Opx 4	Opx 1	Opx 1	Opx 1	Opx 2	Opx 2	Opx 2	Opx 3
Rock type	OPX	OPX	OPX	OPX	OPX	OPX	OPX	OPX	OPX	OPX
SiO_2 (wt %)	55.60	55.88	55.41	55.11	54.72	54.98	55.34	55.62	54.91	51.92
TiO_2	0.17	0.12	0.10	0.07	0.10	0.10	0.08	0.00	0.10	0.10
Al_2O_3	1.81	1.98	1.93	1.72	1.66	1.81	1.85	1.10	1.95	2.63
Cr_2O_3	0.45	0.67	0.69	0.79	0.60	0.80	0.82	0.47	0.79	0.67
FeO	11.19	10.15	9.61	10.92	11.22	11.09	9.38	10.43	10.43	10.99
MnO	0.26	0.23	0.22	0.19	0.27	0.22	0.21	0.23	0.19	0.23
MgO	29.37	30.53	30.51	29.96	29.38	30.10	30.91	30.44	29.88	29.90
CaO	2.49	1.90	2.04	1.62	1.82	1.29	1.62	1.79	1.86	1.61
NiO	0.15	0.18	0.15	0.17	0.15	0.17	0.17	0.15	0.15	0.15
Total	**101.49**	**101.64**	**100.66**	**100.55**	**99.93**	**100.55**	**100.38**	**100.24**	**100.27**	**98.20**
Si	1.95	1.94	1.94	1.94	1.95	1.94	1.94	1.96	1.94	1.89
Al^{IV}	0.05	0.06	0.06	0.05	0.05	0.05	0.05	0.03	0.06	0.08
Al^{VI}	0.02	0.02	0.02	0.02	0.02	0.02	0.02	0.01	0.02	0.04
Fe^{3+}	0.01	0.01	0.02	0.02	0.02	0.03	0.02	0.03	0.02	0.14
Cr	0.01	0.02	0.02	0.02	0.02	0.02	0.02	0.01	0.02	0.02
Ti	0.00	0.00	0.00	0.00	0.00	0.00	0.00	0.00	0.00	0.00
Fe^{2+}	0.31	0.28	0.26	0.30	0.31	0.30	0.25	0.28	0.29	0.19
Mn	0.01	0.01	0.01	0.01	0.01	0.01	0.01	0.01	0.01	0.01
Mg	1.53	1.58	1.59	1.58	1.56	1.58	1.62	1.60	1.57	1.62
Ca	0.09	0.07	0.08	0.06	0.07	0.05	0.06	0.07	0.07	0.06
Ni	0.00	0.00	0.00	0.00	0.00	0.00	0.00	0.00	0.00	0.00
Total	**4.00**	**4.00**	**4.01**	**4.01**	**4.01**	**4.01**	**4.01**	**4.01**	**4.01**	**4.04**
Wo	4.8	3.6	3.9	3.1	3.5	2.5	3.1	3.4	3.6	3.1
Fs	16.7	15.1	14.4	16.4	16.9	16.6	14.0	15.5	15.7	16.3
En	78.2	80.9	81.4	80.2	79.1	80.6	82.5	80.7	80.4	80.2
Mg#	83.1	84.9	85.9	84.1	83.5	84.1	86.4	85.1	84.5	89.3

Sample No.	**79-143**	**79-143**	**79-143**	**79-143**	**79-143**	**79-143**	**79-143**	**79-143**	**79-147**	**79-147**
Intrusion	Nittis	Nittis	Nittis	Nittis	Nittis	Nittis	Nittis	Nittis	Nittis	Nittis
Sample Pt.	Opx 1	Opx 1	Opx 1	Opx 2	Opx 2	Opx 3	Opx 3	Opx 3	Opx 1	Opx 1
Rock type	Oph. OPX	Oph. OPX	Oph. OPX	Oph. OPX	Oph. OPX	Oph. OPX	Oph. OPX	Oph. OPX	OPX xeno	OPX xeno
SiO_2 (wt %)	56.39	56.27	56.38	56.22	56.40	56.42	56.03	56.30	54.90	54.79
TiO_2	0.08	0.11	0.09	0.06	0.09	0.10	0.09	0.07	0.15	0.15
Al_2O_3	1.62	1.71	1.68	1.55	1.57	1.62	1.62	1.60	1.51	1.78
Cr_2O_3	0.69	0.70	0.70	0.63	0.69	0.67	0.66	0.69	0.44	0.50
FeO	8.70	7.97	8.08	8.12	7.95	8.18	8.37	8.11	14.34	13.77
MnO	0.19	0.21	0.21	0.20	0.19	0.21	0.20	0.21	0.30	0.26
MgO	31.84	31.67	32.02	31.74	31.90	32.07	31.70	31.81	28.16	27.83
CaO	1.67	2.09	1.81	1.95	1.95	1.69	1.73	1.85	0.88	1.85
NiO	0.17	0.16	0.15	0.16	0.18	0.21	0.17	0.19	0.11	0.11
Total	**101.35**	**100.89**	**101.12**	**100.63**	**100.92**	**101.17**	**100.57**	**100.83**	**100.79**	**101.02**
Si	1.95	1.95	1.95	1.96	1.95	1.95	1.95	1.95	1.96	1.95
Al^{IV}	0.05	0.05	0.05	0.04	0.05	0.05	0.05	0.05	0.04	0.05
Al^{VI}	0.02	0.02	0.02	0.02	0.02	0.02	0.02	0.02	0.02	0.02
Fe^{3+}	0.01	0.00	0.01	0.01	0.00	0.01	0.01	0.01	0.01	0.01
Cr	0.02	0.02	0.02	0.02	0.02	0.02	0.02	0.02	0.01	0.01
Ti	0.00	0.00	0.00	0.00	0.00	0.00	0.00	0.00	0.00	0.00
Fe^{2+}	0.24	0.23	0.22	0.23	0.23	0.23	0.23	0.23	0.42	0.40
Mn	0.01	0.01	0.01	0.01	0.01	0.01	0.01	0.01	0.01	0.01
Mg	1.64	1.64	1.65	1.65	1.65	1.65	1.65	1.65	1.50	1.47
Ca	0.06	0.08	0.07	0.07	0.07	0.06	0.06	0.07	0.03	0.07
Ni	0.00	0.00	0.00	0.00	0.01	0.01	0.00	0.01	0.00	0.00
Total	**4.00**	**4.00**	**4.00**	**4.00**	**4.00**	**4.00**	**4.00**	**4.00**	**4.00**	**4.00**
Wo	3.2	4.0	3.4	3.7	3.7	3.2	3.3	3.5	1.7	3.6
Fs	12.8	11.8	11.9	12.0	11.8	12.1	12.4	12.0	21.7	20.8
En	83.7	83.9	84.3	84.0	84.2	84.4	84.0	84.1	76.1	75.2
Mg#	87.3	87.7	88.1	87.8	88.0	88.0	87.6	87.8	78.2	78.9

CHR = chromitite; LH = lherzolite; HZ = harzburgite; OL-WEB = olivine-websterite; OL-OPX = olivine-orthopyroxenite;
OPX = orthopyroxenite; MNO = melanorite; BRC = breccia; oph = ophitic; xeno = xenolith

Table D.2 (cont.)

Sample No.	**79-147**	**79-147**	**79-147**	**79-147**	**79-147**	**79-147**	**79-147**	**79-147**	**79-147**	**79-147**
Intrusion	Nittis	Nittis	Nittis	Nittis	Nittis	Nittis	Nittis	Nittis	Nittis	Nittis
Sample Pt.	Opx 1	Opx 1	Opx 2	Opx 2	Opx 2	Opx 2	Opx 3	Opx 3	Opx 3	Opx 3
Rock type	OPX xeno	OPX xeno	OPX xeno	OPX xeno	OPX xeno	OPX xeno	OPX xeno	OPX xeno	OPX xeno	OPX xeno
SiO_2 (wt %)	54.79	54.85	54.75	55.11	55.13	54.51	54.13	54.23	54.42	54.27
TiO_2	0.15	0.13	0.10	0.13	0.13	0.17	0.13	0.15	0.10	0.13
Al_2O_3	1.76	1.85	1.66	1.27	1.19	1.95	1.91	1.76	1.81	1.87
Cr_2O_3	0.51	0.44	0.44	0.32	0.35	0.50	0.47	0.42	0.42	0.45
FeO	13.98	13.84	14.70	14.60	14.95	14.63	13.62	13.29	13.75	13.37
MnO	0.27	0.27	0.26	0.27	0.30	0.28	0.28	0.27	0.28	0.26
MgO	28.22	28.47	28.06	28.24	28.01	27.78	28.27	27.54	28.04	27.83
CaO	1.12	1.02	0.76	0.74	0.81	0.81	0.76	2.00	1.02	1.72
NiO	0.09	0.11	0.11	0.11	0.10	0.13	0.13	0.10	0.11	0.08
Total	**100.89**	**101.00**	**100.84**	**100.80**	**100.97**	**100.75**	**99.70**	**99.77**	**99.98**	**99.98**
Si	1.95	1.95	1.95	1.96	1.96	1.95	1.94	1.95	1.95	1.95
Al^{IV}	0.05	0.05	0.05	0.04	0.04	0.05	0.06	0.05	0.05	0.05
Al^{VI}	0.02	0.02	0.02	0.02	0.01	0.03	0.02	0.02	0.03	0.02
Fe^{3+}	0.01	0.02	0.02	0.01	0.01	0.01	0.02	0.01	0.01	0.01
Cr	0.01	0.01	0.01	0.01	0.01	0.01	0.01	0.01	0.01	0.01
Ti	0.00	0.00	0.00	0.00	0.00	0.00	0.00	0.00	0.00	0.00
Fe^{2+}	0.40	0.39	0.42	0.43	0.44	0.43	0.39	0.39	0.40	0.39
Mn	0.01	0.01	0.01	0.01	0.01	0.01	0.01	0.01	0.01	0.01
Mg	1.50	1.51	1.49	1.50	1.49	1.48	1.51	1.48	1.50	1.49
Ca	0.04	0.04	0.03	0.03	0.03	0.03	0.03	0.08	0.04	0.07
Ni	0.00	0.00	0.00	0.00	0.00	0.00	0.00	0.00	0.00	0.00
Total	**4.00**	**4.01**	**4.00**	**4.00**	**4.00**	**4.00**	**4.01**	**4.00**	**4.00**	**4.00**
Wo	2.2	2.0	1.5	1.4	1.6	1.6	1.5	3.9	2.0	3.4
Fs	21.2	20.9	22.3	22.1	22.6	22.3	20.8	20.4	21.0	20.4
En	76.2	76.7	75.9	76.1	75.4	75.6	77.2	75.3	76.5	75.8
Mg#	78.8	79.3	77.9	77.8	77.3	77.5	79.4	79.1	78.8	79.4

Sample No.	**79-160**	**79-160**	**79-160**	**79-160**	**79-160**	**79-160**	**79-160**	**79-160**	**79-160**	**94-013**
Intrusion	Nittis	Nittis	Nittis	Nittis	Nittis	Nittis	Nittis	Nittis	Nittis	Nittis
Sample Pt.	Opx 1	Opx 1	Opx 2	Opx 3	Opx 3	Opx 3	Opx 4	Opx 4	Opx 4	Opx 1
Rock type	OPX	OPX	OPX	OPX	OPX	OPX	OPX	OPX	OPX	OPX
SiO_2 (wt %)	55.67	55.43	55.56	55.47	55.47	55.09	55.88	55.64	55.79	55.70
TiO_2	0.10	0.13	0.10	0.07	0.10	0.12	0.05	0.12	0.08	0.15
Al_2O_3	1.72	1.74	1.59	1.68	1.83	2.44	1.79	1.89	1.93	1.42
Cr_2O_3	0.66	0.56	0.70	0.66	0.60	0.73	0.73	0.69	0.82	0.60
FeO	9.76	9.76	10.63	10.30	10.42	10.48	8.93	8.88	9.19	9.44
MnO	0.23	0.21	0.22	0.22	0.23	0.19	0.21	0.21	0.19	0.22
MgO	31.26	30.41	30.20	30.79	30.56	30.93	31.66	30.66	31.46	30.18
CaO	1.30	2.34	1.62	1.47	1.60	1.02	1.62	2.90	1.67	2.66
NiO	0.14	0.17	0.13	0.19	0.14	0.15	0.19	0.14	0.14	0.15
Total	**100.84**	**100.74**	**100.74**	**100.86**	**100.96**	**101.15**	**101.06**	**101.12**	**101.26**	**100.52**
Si	1.94	1.94	1.95	1.94	1.94	1.92	1.94	1.94	1.94	1.96
Al^{IV}	0.05	0.05	0.05	0.05	0.05	0.07	0.05	0.06	0.06	0.04
Al^{VI}	0.02	0.02	0.02	0.02	0.02	0.03	0.02	0.02	0.02	0.02
Fe^{3+}	0.03	0.03	0.01	0.03	0.03	0.04	0.03	0.03	0.03	0.01
Cr	0.02	0.02	0.02	0.02	0.02	0.02	0.02	0.02	0.02	0.02
Ti	0.00	0.00	0.00	0.00	0.00	0.00	0.00	0.00	0.00	0.00
Fe^{2+}	0.26	0.26	0.30	0.27	0.28	0.27	0.23	0.23	0.24	0.27
Mn	0.01	0.01	0.01	0.01	0.01	0.01	0.01	0.01	0.01	0.01
Mg	1.63	1.59	1.58	1.61	1.60	1.61	1.64	1.59	1.63	1.58
Ca	0.05	0.09	0.06	0.06	0.06	0.04	0.06	0.11	0.06	0.10
Ni	0.00	0.00	0.00	0.01	0.00	0.00	0.01	0.00	0.00	0.00
Total	**4.01**	**4.01**	**4.00**	**4.01**	**4.01**	**4.01**	**4.01**	**4.01**	**4.01**	**4.00**
Wo	2.5	4.5	3.1	2.8	3.0	2.0	3.1	5.5	3.2	5.1
Fs	14.5	14.5	15.9	15.3	15.5	15.6	13.2	13.1	13.6	14.1
En	82.7	80.7	80.6	81.6	81.1	82.2	83.4	81.1	83.0	80.5
Mg#	86.3	86.0	84.0	85.7	85.1	85.7	87.7	87.4	87.2	85.4

CHR = chromitite; LH = lherzolite; HZ = harzburgite; OL-WEB = olivine-websterite; OL-OPX = olivine-orthopyroxenite;
OPX = orthopyroxenite; MNO = melanorite; BRC = breccia; oph = ophitic; xeno = xenolith

Table D.2 (cont.)

Sample No.	**94-013**	**94-013**	**94-013**	**94-013**	**94-013**	**94-038**	**94-038**	**94-038**	**94-038**	**94-038**
Intrusion	Nittis	Nittis	Nittis	Nittis	Nittis	Nittis	Nittis	Nittis	Nittis	Nittis
Sample Pt.	Opx 1	Opx 2	Opx 2	Opx 3	Opx 3	Opx 1	Opx 1	Opx 2	Opx 2	Opx 3
Rock type	OPX	OPX	OPX	OPX	OPX	OPX	OPX	OPX	OPX	OPX
SiO_2 (wt %)	55.88	55.77	56.05	55.51	55.70	56.15	56.05	55.00	56.03	55.94
TiO_2	0.17	0.12	0.28	0.12	0.25	0.17	0.12	0.10	0.15	0.23
Al_2O_3	1.44	1.78	1.11	1.74	1.25	1.49	1.51	1.78	1.36	1.53
Cr_2O_3	0.60	0.76	0.54	0.70	0.50	0.60	0.58	0.69	0.47	0.57
FeO	9.83	9.64	9.88	9.84	10.01	9.82	9.75	9.70	10.43	9.42
MnO	0.22	0.19	0.22	0.23	0.23	0.23	0.22	0.21	0.22	0.18
MgO	31.17	31.12	31.42	30.96	31.44	31.69	31.67	30.41	31.52	30.98
CaO	1.43	1.53	1.20	1.22	0.76	1.25	1.08	1.78	0.77	2.13
NiO	0.15	0.15	0.14	0.17	0.17	0.15	0.11	0.14	0.13	0.14
Total	**100.88**	**101.05**	**100.85**	**100.48**	**100.30**	**101.55**	**101.09**	**99.80**	**101.08**	**101.11**
Si	1.95	1.94	1.96	1.95	1.96	1.95	1.95	1.94	1.95	1.95
Al^{IV}	0.04	0.05	0.03	0.05	0.04	0.04	0.04	0.05	0.04	0.05
Al^{VI}	0.02	0.02	0.01	0.02	0.01	0.02	0.02	0.02	0.02	0.02
Fe^{3+}	0.02	0.02	0.02	0.01	0.02	0.03	0.02	0.02	0.02	0.02
Cr	0.02	0.02	0.01	0.02	0.01	0.02	0.02	0.02	0.01	0.02
Ti	0.00	0.00	0.01	0.00	0.01	0.00	0.00	0.00	0.00	0.01
Fe^{2+}	0.27	0.26	0.27	0.27	0.28	0.26	0.26	0.27	0.28	0.26
Mn	0.01	0.01	0.01	0.01	0.01	0.01	0.01	0.01	0.01	0.01
Mg	1.62	1.62	1.64	1.62	1.64	1.64	1.64	1.60	1.64	1.61
Ca	0.05	0.06	0.05	0.05	0.03	0.05	0.04	0.07	0.03	0.08
Ni	0.00	0.00	0.00	0.00	0.00	0.00	0.00	0.00	0.00	0.00
Total	**4.01**	**4.01**	**4.00**	**4.00**	**4.01**	**4.01**	**4.01**	**4.01**	**4.01**	**4.01**
Wo	2.7	2.9	2.3	2.3	1.4	2.3	2.0	3.4	1.5	4.0
Fs	14.6	14.3	14.6	14.7	14.9	14.4	14.4	14.6	15.4	13.9
En	82.4	82.5	82.8	82.6	83.3	82.9	83.3	81.7	82.9	81.8
Mg#	85.8	86.0	85.7	85.5	85.6	86.5	86.3	85.8	85.4	86.2

Sample No.	**94-038**	**94-038**	**94-038**	**94-038**	**94-081**	**94-081**	**94-081**	**94-081**	**94-081**	**94-118**
Intrusion	Nittis	Nittis	Nittis	Nittis	Nittis	Nittis	Nittis	Nittis	Nittis	Nittis
Sample Pt.	Opx 3	Opx 3	Opx 4	Opx 4	Opx 1	Opx 1	Opx 2	Opx 2	Opx 3	Opx 1
Rock type	OPX	OPX	OPX	OPX	OPX	OPX	OPX	OPX	OPX	OPX
SiO_2 (wt %)	55.47	55.17	55.38	55.26	55.38	55.02	55.36	55.70	55.70	54.81
TiO_2	0.12	0.12	0.23	0.13	0.20	0.17	0.10	0.12	0.10	0.25
Al_2O_3	1.55	1.70	1.44	1.70	1.49	1.95	1.61	1.80	1.83	1.25
Cr_2O_3	0.64	0.67	0.54	0.67	0.51	0.66	0.60	0.63	0.72	0.34
FeO	9.57	9.51	9.71	9.83	10.12	9.21	9.64	9.61	9.82	10.70
MnO	0.22	0.23	0.23	0.21	0.23	0.22	0.21	0.21	0.23	0.23
MgO	31.51	30.99	30.68	30.81	31.06	29.38	30.74	31.36	31.31	30.51
CaO	0.88	1.41	1.89	1.47	1.19	3.58	1.78	1.36	1.20	0.92
NiO	0.15	0.15	0.14	0.15	0.15	0.14	0.18	0.15	0.15	0.10
Total	**100.11**	**99.96**	**100.25**	**100.23**	**100.35**	**100.33**	**100.21**	**100.93**	**101.07**	**99.11**
Si	1.95	1.94	1.95	1.94	1.95	1.94	1.95	1.94	1.94	1.95
Al^{IV}	0.05	0.05	0.04	0.05	0.04	0.06	0.05	0.05	0.05	0.04
Al^{VI}	0.02	0.02	0.02	0.02	0.02	0.02	0.02	0.02	0.02	0.02
Fe^{3+}	0.02	0.03	0.02	0.02	0.03	0.02	0.02	0.03	0.02	0.03
Cr	0.02	0.02	0.02	0.02	0.01	0.02	0.02	0.02	0.02	0.01
Ti	0.00	0.00	0.01	0.00	0.01	0.00	0.00	0.00	0.00	0.01
Fe^{2+}	0.26	0.25	0.26	0.27	0.27	0.25	0.26	0.25	0.26	0.29
Mn	0.01	0.01	0.01	0.01	0.01	0.01	0.01	0.01	0.01	0.01
Mg	1.65	1.63	1.61	1.62	1.63	1.54	1.61	1.63	1.63	1.62
Ca	0.03	0.05	0.07	0.06	0.04	0.14	0.07	0.05	0.04	0.04
Ni	0.00	0.00	0.00	0.00	0.00	0.00	0.01	0.00	0.00	0.00
Total	**4.01**	**4.01**	**4.01**	**4.01**	**4.01**	**4.01**	**4.01**	**4.01**	**4.01**	**4.01**
Wo	1.7	2.7	3.6	2.8	2.3	6.9	3.4	2.6	2.3	1.8
Fs	14.2	14.2	14.5	14.7	15.0	13.9	14.4	14.2	14.5	16.1
En	83.7	82.7	81.6	82.2	82.4	78.9	81.9	82.9	82.8	81.8
Mg#	86.5	86.5	85.9	85.9	85.9	85.9	86.1	86.5	86.2	84.7

CHR = chromitite; LH = lherzolite; HZ = harzburgite; OL-WEB = olivine-websterite; OL-OPX = olivine-orthopyroxenite;
OPX = orthopyroxenite; MNO = melanorite; BRC = breccia; oph = ophitic; xeno = xenolith

Table D.2 (cont.)

Sample No.	**94-118**	**94-118**	**94-118**	**94-118**	**94-118**	**1815-011**	**1815-011**	**1815-011**	**1815-011**	**1815-011**
Intrusion	Nittis	Nittis	Nittis	Nittis	Nittis	Nyud	Nyud	Nyud	Nyud	Nyud
Sample Pt.	Opx 1	Opx 2	Opx 2	Opx 2	Opx 2	Opx 4	Opx 4	Opx 4	Opx 1	Opx 2
Rock type	OPX	OPX	OPX	OPX	OPX	MNO	MNO	MNO	MNO	MNO
SiO_2 (wt %)	55.45	55.85	55.36	56.07	55.56	55.51	55.49	55.53	56.05	56.03
TiO_2	0.20	0.12	0.30	0.30	0.10	0.13	0.20	0.12	0.10	0.12
Al_2O_3	1.36	1.61	1.47	1.11	1.55	1.49	1.28	1.68	1.30	1.27
Cr_2O_3	0.51	0.50	0.42	0.23	0.57	0.53	0.48	0.56	0.47	0.47
FeO	10.41	10.39	10.47	10.38	10.54	11.90	11.91	12.08	10.90	11.09
MnO	0.23	0.21	0.21	0.21	0.23	0.23	0.23	0.25	0.23	0.23
MgO	29.88	31.52	30.84	31.52	30.58	29.62	29.45	29.55	30.53	30.11
CaO	2.25	0.80	1.48	1.09	1.67	1.74	1.92	1.80	1.83	2.07
NiO	0.17	0.17	0.17	0.13	0.17	0.14	0.13	0.13	0.11	0.09
Total	**100.46**	**101.16**	**100.73**	**101.05**	**100.95**	**101.29**	**101.10**	**101.69**	**101.52**	**101.47**
Si	1.95	1.95	1.94	1.96	1.95	1.95	1.95	1.95	1.96	1.96
Al^{IV}	0.04	0.05	0.04	0.03	0.05	0.04	0.04	0.05	0.04	0.04
Al^{VI}	0.02	0.02	0.02	0.01	0.02	0.02	0.02	0.02	0.02	0.01
Fe^{3+}	0.01	0.03	0.04	0.03	0.03	0.02	0.02	0.03	0.03	0.02
Cr	0.01	0.01	0.01	0.01	0.02	0.01	0.01	0.02	0.01	0.01
Ti	0.01	0.00	0.01	0.01	0.00	0.00	0.01	0.00	0.00	0.00
Fe^{2+}	0.29	0.27	0.27	0.27	0.28	0.33	0.33	0.33	0.29	0.30
Mn	0.01	0.01	0.01	0.01	0.01	0.01	0.01	0.01	0.01	0.01
Mg	1.57	1.64	1.61	1.64	1.60	1.55	1.55	1.54	1.59	1.57
Ca	0.09	0.03	0.06	0.04	0.06	0.07	0.07	0.07	0.07	0.08
Ni	0.00	0.00	0.00	0.00	0.00	0.00	0.00	0.00	0.00	0.00
Total	**4.00**	**4.01**	**4.01**	**4.01**	**4.01**	**4.01**	**4.01**	**4.01**	**4.01**	**4.01**
Wo	4.3	1.5	2.8	2.1	3.2	3.3	3.7	3.4	3.5	3.9
Fs	15.6	15.3	15.5	15.2	15.6	17.7	17.7	17.9	16.0	16.4
En	79.8	82.9	81.4	82.4	80.9	78.6	78.3	78.3	80.2	79.4
Mg#	84.3	85.8	85.7	85.7	85.2	82.6	82.4	82.6	84.5	83.7

Sample No.	**1815-011**	**1815-011**	**1815-011**	**1815-046**	**1815-046**	**1815-046**	**1815-046**	**1815-046**	**1815-046**	**1815-046**
Intrusion	Nyud	Nyud	Nyud	Nyud	Nyud	Nyud	Nyud	Nyud	Nyud	Nyud
Sample Pt.	Opx 2	Opx 3	Opx 5	Opx 1	Opx 2	Opx 2	Opx 2	Opx 3	Opx 3	Opx 3
Rock type	MNO	MNO	MNO	MNO	MNO	MNO	MNO	MNO	MNO	MNO
SiO_2 (wt %)	55.38	54.91	55.30	55.21	55.58	55.32	55.41	55.36	54.91	54.98
TiO_2	0.10	0.13	0.12	0.12	0.17	0.13	0.12	0.12	0.10	0.10
Al_2O_3	1.34	1.53	1.40	2.00	1.45	1.78	1.81	1.57	1.64	1.66
Cr_2O_3	0.47	0.53	0.45	0.64	0.58	0.61	0.53	0.60	0.60	0.56
FeO	11.73	12.99	11.40	10.72	11.36	11.91	11.63	12.03	11.62	12.22
MnO	0.25	0.26	0.25	0.25	0.26	0.27	0.28	0.26	0.23	0.26
MgO	29.73	28.82	28.65	30.36	29.83	29.68	30.20	29.55	29.23	29.75
CaO	1.65	1.46	2.62	1.15	1.78	1.64	1.05	1.53	1.80	0.85
NiO	0.11	0.14	0.15	0.14	0.18	0.18	0.15	0.13	0.14	0.14
Total	**100.77**	**100.77**	**100.33**	**100.59**	**101.19**	**101.52**	**101.17**	**101.14**	**100.28**	**100.52**
Si	1.95	1.95	1.96	1.94	1.95	1.94	1.94	1.95	1.95	1.95
Al^{IV}	0.04	0.05	0.04	0.06	0.04	0.05	0.05	0.05	0.05	0.05
Al^{VI}	0.02	0.02	0.02	0.02	0.02	0.02	0.02	0.02	0.02	0.02
Fe^{3+}	0.03	0.03	0.00	0.02	0.02	0.03	0.03	0.02	0.02	0.03
Cr	0.01	0.01	0.01	0.02	0.02	0.02	0.01	0.02	0.02	0.02
Ti	0.00	0.00	0.00	0.00	0.00	0.00	0.00	0.00	0.00	0.00
Fe^{2+}	0.32	0.36	0.34	0.30	0.31	0.32	0.31	0.33	0.32	0.33
Mn	0.01	0.01	0.01	0.01	0.01	0.01	0.01	0.01	0.01	0.01
Mg	1.56	1.52	1.52	1.59	1.56	1.55	1.58	1.55	1.55	1.57
Ca	0.06	0.06	0.10	0.04	0.07	0.06	0.04	0.06	0.07	0.03
Ni	0.00	0.00	0.00	0.00	0.01	0.01	0.00	0.00	0.00	0.00
Total	**4.01**	**4.01**	**4.00**	**4.01**	**4.01**	**4.01**	**4.01**	**4.01**	**4.01**	**4.01**
Wo	3.2	2.8	5.1	2.2	3.4	3.1	2.0	2.9	3.5	1.6
Fs	17.5	19.5	17.2	16.1	16.9	17.7	17.3	17.9	17.5	18.3
En	79.0	77.3	77.3	81.3	79.3	78.8	80.3	78.7	78.7	79.7
Mg#	83.0	80.9	81.8	84.2	83.2	83.1	83.4	82.4	82.7	82.5

CHR = chromitite; LH = lherzolite; HZ = harzburgite; OL-WEB = olivine-websterite; OL-OPX = olivine-orthopyroxenite;
OPX = orthopyroxenite; MNO = melanorite; BRC = breccia; oph = ophitic; xeno = xenolith

Table D.2 (cont.)

Sample No.	**1815-046**	**1815-046**	**1815-046**	**1403-030**	**1403-030**	**1403-030**	**1403-030**	**1403-030**	**1403-030**	**1403-030**
Intrusion	Nyud	Nyud	Nyud	Sopcha	Sopcha	Sopcha	Sopcha	Sopcha	Sopcha	Sopcha
Sample Pt.	Opx 4	Opx 4	Opx 4	Opx 1	Opx 1	Opx 2	Opx 2	Opx 3	Opx 3	Opx 4
Rock type	MNO	MNO	MNO	OPX	OPX	OPX	OPX	OPX	OPX	OPX
SiO_2 (wt %)	55.36	55.49	55.15	56.09	55.83	55.62	55.83	55.73	55.60	55.73
TiO_2	0.10	0.25	0.13	0.18	0.20	0.20	0.13	0.15	0.17	0.13
Al_2O_3	1.42	1.27	1.83	1.64	1.70	1.85	1.64	1.83	1.66	1.83
Cr_2O_3	0.56	0.57	0.44	0.57	0.58	0.63	0.57	0.61	0.53	0.64
FeO	11.15	11.85	11.99	9.78	9.74	9.64	9.78	9.56	9.67	9.13
MnO	0.22	0.26	0.28	0.22	0.21	0.21	0.23	0.22	0.22	0.23
MgO	29.43	29.73	29.68	31.17	31.07	30.86	31.27	30.61	31.06	30.49
CaO	2.03	1.36	1.12	1.74	1.76	1.86	1.29	2.21	1.41	2.85
NiO	0.14	0.18	0.11	0.14	0.14	0.14	0.11	0.14	0.13	0.13
Total	**100.41**	**100.95**	**100.74**	**101.64**	**101.64**	**101.64**	**101.64**	**101.64**	**101.64**	**101.64**
Si	1.96	1.95	1.95	1.95	1.94	1.94	1.95	1.94	1.95	1.94
Al^{IV}	0.04	0.04	0.05	0.05	0.05	0.05	0.05	0.05	0.05	0.05
Al^{VI}	0.02	0.02	0.02	0.02	0.02	0.02	0.02	0.02	0.02	0.02
Fe^{3+}	0.01	0.01	0.02	0.02	0.02	0.02	0.02	0.02	0.02	0.02
Cr	0.02	0.02	0.01	0.02	0.02	0.02	0.02	0.02	0.01	0.02
Ti	0.00	0.01	0.00	0.00	0.01	0.01	0.00	0.00	0.00	0.00
Fe^{2+}	0.32	0.34	0.33	0.26	0.26	0.26	0.27	0.26	0.27	0.24
Mn	0.01	0.01	0.01	0.01	0.01	0.01	0.01	0.01	0.01	0.01
Mg	1.55	1.56	1.56	1.61	1.61	1.61	1.63	1.59	1.62	1.58
Ca	0.08	0.05	0.04	0.06	0.07	0.07	0.05	0.08	0.05	0.11
Ni	0.00	0.01	0.00	0.00	0.00	0.00	0.00	0.00	0.00	0.00
Total	**4.00**	**4.00**	**4.01**	**4.01**	**4.01**	**4.01**	**4.01**	**4.00**	**4.01**	**4.01**
Wo	3.9	2.6	2.2	3.3	3.3	3.5	2.4	4.2	2.7	5.4
Fs	16.8	17.7	18.0	14.4	14.4	14.3	14.5	14.2	14.4	13.5
En	79.0	79.3	79.4	82.0	82.0	81.8	82.7	81.2	82.6	80.7
Mg#	82.9	82.3	82.4	86.0	86.1	86.0	85.9	85.8	85.9	86.7

Sample No.	**1403-030**	**1403-030**	**1403-030**	**1403-064**	**1403-064**	**1403-064**	**1403-064**	**1403-064**	**1403-064**	**1403-064**
Intrusion	Sopcha	Sopcha	Sopcha	Sopcha	Sopcha	Sopcha	Sopcha	Sopcha	Sopcha	Sopcha
Sample Pt.	Opx 4	Opx 4	Opx 4	Opx 1	Opx 1	Opx 1	Opx 1	Opx 2	Opx 2	Opx 3
Rock type	OPX	OPX	OPX	OPX	OPX	OPX	OPX	OPX	OPX	OPX
SiO_2 (wt %)	55.83	55.73	55.21	55.38	54.93	55.38	55.28	55.68	55.58	55.58
TiO_2	0.15	0.12	0.15	0.13	0.18	0.20	0.10	0.18	0.13	0.08
Al_2O_3	1.64	1.93	1.89	1.89	1.95	1.74	1.80	1.68	1.87	1.85
Cr_2O_3	0.60	0.67	0.66	0.63	0.63	0.54	0.61	0.57	0.63	0.61
FeO	9.83	9.48	9.64	9.65	9.48	9.82	9.53	9.93	9.80	9.61
MnO	0.23	0.19	0.25	0.22	0.23	0.22	0.19	0.23	0.23	0.21
MgO	31.32	31.17	31.07	30.93	30.74	31.14	30.71	30.89	31.11	30.63
CaO	1.40	1.80	1.30	1.37	1.57	1.39	1.68	1.26	1.20	2.03
NiO	0.14	0.14	0.13	0.15	0.13	0.11	0.13	0.14	0.14	0.13
Total	**101.64**	**101.64**	**101.64**	**101.64**	**101.64**	**101.64**	**101.64**	**101.64**	**101.64**	**101.64**
Si	1.95	1.94	1.94	1.94	1.94	1.94	1.95	1.95	1.94	1.95
Al^{IV}	0.05	0.06	0.06	0.06	0.06	0.05	0.05	0.05	0.06	0.05
Al^{VI}	0.02	0.02	0.02	0.02	0.02	0.02	0.02	0.02	0.02	0.02
Fe^{3+}	0.03	0.03	0.03	0.02	0.02	0.03	0.02	0.01	0.02	0.02
Cr	0.02	0.02	0.02	0.02	0.02	0.01	0.02	0.02	0.02	0.02
Ti	0.00	0.00	0.00	0.00	0.00	0.01	0.00	0.00	0.00	0.00
Fe^{2+}	0.26	0.25	0.26	0.27	0.26	0.26	0.26	0.28	0.27	0.26
Mn	0.01	0.01	0.01	0.01	0.01	0.01	0.01	0.01	0.01	0.01
Mg	1.63	1.62	1.63	1.62	1.62	1.63	1.61	1.61	1.62	1.60
Ca	0.05	0.07	0.05	0.05	0.06	0.05	0.06	0.05	0.05	0.08
Ni	0.00	0.00	0.00	0.00	0.00	0.00	0.00	0.00	0.00	0.00
Total	**4.01**	**4.01**	**4.01**	**4.01**	**4.01**	**4.01**	**4.01**	**4.00**	**4.01**	**4.01**
Wo	2.6	3.4	2.5	2.6	3.0	2.6	3.2	2.4	2.3	3.9
Fs	14.5	14.0	14.4	14.4	14.2	14.5	14.3	14.8	14.6	14.3
En	82.5	82.3	82.8	82.6	82.4	82.5	82.2	82.4	82.7	81.5
Mg#	86.3	86.7	86.4	85.9	86.3	86.4	85.9	85.0	85.8	85.9

CHR = chromitite; LH = lherzolite; HZ = harzburgite; OL-WEB = olivine-websterite; OL-OPX = olivine-orthopyroxenite;
OPX = orthopyroxenite; MNO = melanorite; BRC = breccia; oph = ophitic; xeno = xenolith

Table D.2 (cont.)

Sample No.	**1403-064**	**1403-089**	**1403-089**	**1403-089**	**1403-089**	**1403-089**	**1403-089**	**1403-089**	**1403-089**	**1403-089**
Intrusion	Sopcha	Sopcha	Sopcha	Sopcha	Sopcha	Sopcha	Sopcha	Sopcha	Sopcha	Sopcha
Sample Pt.	Opx 3	Opx 1	Opx 1	Opx 1	Opx 2	Opx 2	Opx 2	Opx 3	Opx 4	Opx 4
Rock type	OPX	OPX	OPX	OPX	OPX	OPX	OPX	OPX	OPX	OPX
SiO_2 (wt %)	55.73	55.53	55.38	55.85	55.83	56.41	55.79	55.77	55.90	55.96
TiO_2	0.12	0.10	0.12	0.12	0.12	0.13	0.10	0.13	0.17	0.08
Al_2O_3	1.80	1.87	1.95	1.89	1.72	1.55	1.98	1.83	1.80	1.85
Cr_2O_3	0.57	0.67	0.72	0.70	0.60	0.57	0.70	0.67	0.61	0.66
FeO	9.83	9.37	9.28	8.92	8.94	8.88	8.77	8.98	9.62	9.56
MnO	0.21	0.23	0.22	0.18	0.22	0.21	0.21	0.19	0.22	0.21
MgO	31.12	30.84	30.54	30.88	31.31	32.32	31.16	30.79	31.31	31.19
CaO	1.43	2.08	2.49	2.55	2.04	1.16	2.35	2.43	1.53	1.62
NiO	0.11	0.10	0.08	0.11	0.13	0.14	0.11	0.10	0.13	0.11
Total	**101.64**	**101.64**	**101.64**	**101.64**	**101.64**	**101.64**	**101.64**	**101.64**	**101.64**	**101.64**
Si	1.95	1.94	1.94	1.94	1.95	1.95	1.94	1.94	1.94	1.95
Al^{IV}	0.05	0.06	0.06	0.06	0.05	0.05	0.06	0.05	0.05	0.05
Al^{VI}	0.02	0.02	0.02	0.02	0.02	0.02	0.02	0.02	0.02	0.02
Fe^{3+}	0.02	0.02	0.03	0.02	0.02	0.02	0.02	0.01	0.02	0.02
Cr	0.02	0.02	0.02	0.02	0.02	0.02	0.02	0.02	0.02	0.02
Ti	0.00	0.00	0.00	0.00	0.00	0.00	0.00	0.00	0.00	0.00
Fe^{2+}	0.27	0.25	0.25	0.24	0.24	0.23	0.23	0.25	0.26	0.26
Mn	0.01	0.01	0.01	0.01	0.01	0.01	0.01	0.01	0.01	0.01
Mg	1.62	1.61	1.59	1.60	1.63	1.67	1.61	1.60	1.62	1.62
Ca	0.05	0.08	0.09	0.09	0.08	0.04	0.09	0.09	0.06	0.06
Ni	0.00	0.00	0.00	0.00	0.00	0.00	0.00	0.00	0.00	0.00
Total	**4.01**	**4.01**	**4.01**	**4.01**	**4.01**	**4.01**	**4.01**	**4.00**	**4.01**	**4.01**
Wo	2.7	4.0	4.8	4.8	3.9	2.2	4.5	4.6	2.9	3.1
Fs	14.6	13.9	13.8	13.2	13.2	13.0	13.0	13.4	14.2	14.2
En	82.4	81.8	81.1	81.7	82.6	84.5	82.3	81.7	82.6	82.5
Mg#	85.9	86.6	86.7	86.9	87.4	87.7	87.5	86.6	86.3	86.1

Sample No.	**1403-089**	**1403-132**	**1403-132**	**1403-132**	**1403-132**	**1403-132**	**1403-132**	**1403-132**	**1403-132**	**1408-171**
Intrusion	Sopcha	Sopcha	Sopcha	Sopcha	Sopcha	Sopcha	Sopcha	Sopcha	Sopcha	Sopcha
Sample Pt.	Opx 4	Opx 1	Opx 1	Opx 1	Opx 1	Opx 2	Opx 2	Opx 3	Opx 3	Opx 1
Rock type	OPX	OPX	OPX	OPX	OPX	OPX	OPX	OPX	OPX	OPX
SiO_2 (wt %)	55.70	56.00	56.09	56.15	55.26	55.38	55.23	55.53	55.62	56.12
TiO_2	0.08	0.12	0.12	0.13	0.07	0.10	0.12	0.10	0.08	0.16
Al_2O_3	1.78	1.98	1.93	1.87	1.87	1.70	1.93	1.80	1.76	1.72
Cr_2O_3	0.63	0.70	0.67	0.61	0.66	0.60	0.66	0.61	0.64	0.64
FeO	9.44	8.93	9.20	9.08	8.95	9.10	9.16	8.98	9.01	8.92
MnO	0.21	0.18	0.19	0.22	0.19	0.19	0.22	0.22	0.19	0.21
MgO	31.16	31.04	31.34	31.26	30.94	31.06	30.96	30.86	31.29	32.02
CaO	1.54	2.45	1.85	1.99	1.89	1.74	1.82	2.00	1.47	1.45
NiO	0.13	0.11	0.14	0.10	0.15	0.13	0.13	0.10	0.13	0.12
Total	**101.64**	**101.64**	**101.64**	**101.64**	**101.64**	**101.64**	**101.64**	**101.64**	**101.64**	**101.64**
Si	1.95	1.94	1.94	1.95	1.94	1.95	1.94	1.95	1.95	1.94
Al^{IV}	0.05	0.06	0.06	0.05	0.06	0.05	0.06	0.05	0.05	0.05
Al^{VI}	0.02	0.02	0.02	0.02	0.02	0.02	0.02	0.02	0.02	0.02
Fe^{3+}	0.02	0.02	0.02	0.01	0.02	0.02	0.03	0.01	0.01	0.03
Cr	0.02	0.02	0.02	0.02	0.02	0.02	0.02	0.02	0.02	0.02
Ti	0.00	0.00	0.00	0.00	0.00	0.00	0.00	0.00	0.00	0.00
Fe^{2+}	0.26	0.24	0.25	0.25	0.24	0.25	0.24	0.25	0.25	0.23
Mn	0.01	0.01	0.01	0.01	0.01	0.01	0.01	0.01	0.01	0.01
Mg	1.62	1.60	1.62	1.61	1.62	1.63	1.62	1.61	1.63	1.65
Ca	0.06	0.09	0.07	0.07	0.07	0.07	0.07	0.08	0.06	0.05
Ni	0.00	0.00	0.00	0.00	0.00	0.00	0.00	0.00	0.00	0.00
Total	**4.01**	**4.01**	**4.01**	**4.00**	**4.01**	**4.01**	**4.01**	**4.00**	**4.00**	**4.01**
Wo	2.9	4.6	3.5	3.8	3.6	3.3	3.5	3.8	2.8	2.7
Fs	14.0	13.2	13.6	13.4	13.4	13.6	13.7	13.4	13.5	13.1
En	82.7	81.9	82.6	82.5	82.7	82.8	82.5	82.4	83.4	83.9
Mg#	86.3	87.0	86.7	86.5	87.1	86.8	87.0	86.5	86.7	87.8

CHR = chromitite; LH = lherzolite; HZ = harzburgite; OL-WEB = olivine-websterite; OL-OPX = olivine-orthopyroxenite;
OPX = orthopyroxenite; MNO = melanorite; BRC = breccia; oph = ophitic; xeno = xenolith

Table D.2 (cont.)

Sample No.	**1408-171**	**1408-171**	**1408-171**	**1408-171**	**1408-171**	**1408-171**	**15SOP-04**	**15SOP-04**	**15SOP-04**	**15SOP-04**
Intrusion	Sopcha	Sopcha	Sopcha	Sopcha	Sopcha	Sopcha	Sopcha	Sopcha	Sopcha	Sopcha
Sample Pt.	Opx 1	Opx 1	Opx 2	Opx 2	Opx 2	Opx 2	Opx 1	Opx 1	Opx 1	Opx 1
Rock type	OPX	OPX	OPX	OPX	OPX	OPX	OPX	OPX	OPX	OPX
SiO_2 (wt %)	56.09	56.14	55.94	56.28	56.32	56.26	55.98	55.91	56.06	56.08
TiO_2	0.13	0.15	0.16	0.19	0.12	0.18	0.09	0.08	0.11	0.08
Al_2O_3	1.55	1.62	1.72	1.71	1.58	1.61	1.69	1.72	1.72	1.71
Cr_2O_3	0.60	0.59	0.60	0.58	0.58	0.56	0.60	0.65	0.65	0.65
FeO	8.69	8.93	9.18	9.25	8.98	9.06	8.62	8.53	8.49	8.65
MnO	0.22	0.20	0.24	0.23	0.22	0.22	0.21	0.22	0.19	0.21
MgO	31.94	31.80	31.78	32.18	31.70	31.86	31.81	31.79	31.68	31.94
CaO	1.76	1.54	1.33	1.10	1.95	1.51	1.62	1.78	1.86	1.68
NiO	0.14	0.13	0.12	0.15	0.12	0.13	0.16	0.15	0.18	0.19
Total	**101.64**	**101.64**	**101.64**	**101.64**	**101.64**	**101.64**	**101.64**	**101.64**	**101.64**	**101.64**
Si	1.95	1.95	1.94	1.94	1.95	1.95	1.95	1.94	1.95	1.94
Al^{IV}	0.05	0.05	0.05	0.05	0.05	0.05	0.05	0.05	0.05	0.05
Al^{VI}	0.02	0.02	0.02	0.02	0.02	0.02	0.02	0.02	0.02	0.02
Fe^{3+}	0.03	0.02	0.02	0.03	0.03	0.02	0.02	0.03	0.02	0.03
Cr	0.02	0.02	0.02	0.02	0.02	0.02	0.02	0.02	0.02	0.02
Ti	0.00	0.00	0.00	0.00	0.00	0.00	0.00	0.00	0.00	0.00
Fe^{2+}	0.22	0.24	0.24	0.24	0.23	0.24	0.23	0.22	0.23	0.22
Mn	0.01	0.01	0.01	0.01	0.01	0.01	0.01	0.01	0.01	0.01
Mg	1.65	1.65	1.65	1.66	1.63	1.64	1.65	1.65	1.64	1.65
Ca	0.07	0.06	0.05	0.04	0.07	0.06	0.06	0.07	0.07	0.06
Ni	0.00	0.00	0.00	0.00	0.00	0.00	0.00	0.00	0.01	0.01
Total	**4.01**	**4.01**	**4.01**	**4.01**	**4.01**	**4.01**	**4.01**	**4.01**	**4.01**	**4.01**
Wo	3.3	2.9	2.5	2.1	3.7	2.8	3.1	3.4	3.5	3.2
Fs	12.7	13.2	13.5	13.5	13.1	13.3	12.7	12.6	12.6	12.7
En	83.6	83.6	83.6	84.1	82.9	83.5	83.9	83.7	83.6	83.8
Mg#	88.2	87.3	87.2	87.4	87.5	87.2	87.8	88.2	87.7	88.2

Sample No.	**15SOP-04**	**15SOP-04**	**15SOP-04**	**15SOP-04**	**15SOP-05**	**15SOP-05**	**15SOP-05**	**15SOP-05**	**15SOP-05**	**15SOP-05**
Intrusion	Sopcha	Sopcha	Sopcha	Sopcha	Sopcha	Sopcha	Sopcha	Sopcha	Sopcha	Sopcha
Sample Pt.	Opx 2	Opx 2	Opx 3	Opx 3	Opx 1	Opx 1	Opx 1	Opx 1	Opx 1	Opx 2
Rock type	OPX	OPX	OPX	OPX	OPX BRC	OPX BRC	OPX BRC	OPX BRC	OPX BRC	OPX BRC
SiO_2 (wt %)	55.80	55.81	55.88	55.93	56.09	55.99	56.19	55.98	55.81	56.12
TiO_2	0.09	0.10	0.12	0.14	0.13	0.08	0.12	0.12	0.07	0.07
Al_2O_3	1.70	1.72	1.76	1.73	1.59	1.72	1.68	1.76	1.76	1.72
Cr_2O_3	0.61	0.62	0.59	0.57	0.60	0.61	0.60	0.71	0.64	0.63
FeO	8.61	8.51	8.69	8.71	8.51	8.57	8.66	8.24	8.54	8.61
MnO	0.21	0.22	0.21	0.22	0.21	0.21	0.21	0.19	0.22	0.20
MgO	31.73	31.48	31.72	31.77	31.53	31.54	31.59	30.81	31.26	31.87
CaO	1.57	1.97	1.67	1.75	2.31	2.10	2.09	3.33	2.52	1.71
NiO	0.13	0.15	0.13	0.16	0.15	0.12	0.16	0.14	0.20	0.13
Total	**101.64**	**101.64**	**101.64**	**101.64**	**101.64**	**101.64**	**101.64**	**101.64**	**101.64**	**101.64**
Si	1.95	1.95	1.95	1.94	1.95	1.95	1.95	1.94	1.94	1.95
Al^{IV}	0.05	0.05	0.05	0.05	0.05	0.05	0.05	0.05	0.05	0.05
Al^{VI}	0.02	0.02	0.02	0.02	0.02	0.02	0.02	0.02	0.02	0.02
Fe^{3+}	0.02	0.02	0.02	0.03	0.02	0.02	0.02	0.02	0.03	0.02
Cr	0.02	0.02	0.02	0.02	0.02	0.02	0.02	0.02	0.02	0.02
Ti	0.00	0.00	0.00	0.00	0.00	0.00	0.00	0.00	0.00	0.00
Fe^{2+}	0.23	0.23	0.23	0.22	0.22	0.23	0.23	0.22	0.22	0.23
Mn	0.01	0.01	0.01	0.01	0.01	0.01	0.01	0.01	0.01	0.01
Mg	1.65	1.64	1.65	1.65	1.63	1.63	1.63	1.60	1.62	1.65
Ca	0.06	0.07	0.06	0.07	0.09	0.08	0.08	0.12	0.09	0.06
Ni	0.00	0.00	0.00	0.00	0.00	0.00	0.00	0.00	0.01	0.00
Total	**4.01**	**4.01**	**4.01**	**4.01**	**4.01**	**4.01**	**4.01**	**4.01**	**4.01**	**4.01**
Wo	3.0	3.7	3.2	3.3	4.4	4.0	3.9	6.3	4.8	3.2
Fs	12.8	12.6	12.8	12.8	12.5	12.6	12.7	12.2	12.6	12.7
En	83.9	83.3	83.7	83.5	82.8	83.1	83.0	81.2	82.3	83.8
Mg#	87.8	87.8	87.8	88.0	88.0	87.9	87.7	88.0	88.3	87.9

CHR = chromitite; LH = lherzolite; HZ = harzburgite; OL-WEB = olivine-websterite; OL-OPX = olivine-orthopyroxenite;
OPX = orthopyroxenite; MNO = melanorite; BRC = breccia; oph = ophitic; xeno = xenolith

Table D.2 (cont.)

Sample No.	**15SOP-05**	**15SOP-05**	**15SOP-05**	**15SOP-05**	**15SOP-05**	**15SOP-07**	**15SOP-07**	**15SOP-07**	**15SOP-07**	**15SOP-07**
Intrusion	Sopcha	Sopcha	Sopcha	Sopcha	Sopcha	Sopcha	Sopcha	Sopcha	Sopcha	Sopcha
Sample Pt.	Opx 2	Opx 2	Opx 3	Opx 3	Opx 3	Opx 1	Opx 1	Opx 1	Opx 1	Opx 2
Rock type	OPX BRC	OPX BRC	OPX BRC	OPX BRC	OPX BRC	HZ	HZ	HZ	HZ	HZ
SiO_2 (wt %)	56.08	55.97	56.32	56.49	56.30	55.65	55.78	55.54	55.77	55.83
TiO_2	0.08	0.07	0.07	0.08	0.06	0.10	0.07	0.06	0.10	0.09
Al_2O_3	1.86	1.77	1.54	1.55	1.55	1.85	1.78	1.80	1.74	1.63
Cr_2O_3	0.62	0.64	0.68	0.66	0.66	0.61	0.56	0.63	0.57	0.58
FeO	8.56	8.58	8.39	8.40	8.40	8.40	8.52	8.43	8.45	8.48
MnO	0.22	0.22	0.20	0.19	0.21	0.22	0.23	0.21	0.24	0.20
MgO	31.88	31.87	32.16	32.35	32.24	31.48	31.91	31.50	31.79	31.88
CaO	1.44	1.67	1.69	1.59	1.59	1.94	1.33	1.95	1.66	1.75
NiO	0.15	0.16	0.17	0.15	0.15	0.14	0.17	0.10	0.15	0.15
Total	**101.64**	**101.64**	**101.64**	**101.64**	**101.64**	**101.64**	**101.64**	**101.64**	**101.64**	**101.64**
Si	1.95	1.94	1.95	1.95	1.95	1.94	1.95	1.94	1.95	1.95
Al^{IV}	0.05	0.05	0.05	0.05	0.05	0.05	0.05	0.05	0.05	0.05
Al^{VI}	0.02	0.02	0.02	0.02	0.02	0.02	0.02	0.02	0.02	0.02
Fe^{3+}	0.01	0.03	0.02	0.02	0.03	0.02	0.02	0.03	0.02	0.03
Cr	0.02	0.02	0.02	0.02	0.02	0.02	0.02	0.02	0.02	0.02
Ti	0.00	0.00	0.00	0.00	0.00	0.00	0.00	0.00	0.00	0.00
Fe^{2+}	0.23	0.22	0.22	0.22	0.22	0.22	0.23	0.22	0.22	0.22
Mn	0.01	0.01	0.01	0.01	0.01	0.01	0.01	0.01	0.01	0.01
Mg	1.65	1.65	1.66	1.66	1.66	1.64	1.66	1.64	1.65	1.66
Ca	0.05	0.06	0.06	0.06	0.06	0.07	0.05	0.07	0.06	0.07
Ni	0.00	0.00	0.00	0.00	0.00	0.00	0.00	0.00	0.00	0.00
Total	**4.00**	**4.01**	**4.01**	**4.01**	**4.01**	**4.01**	**4.01**	**4.01**	**4.01**	**4.01**
Wo	2.7	3.2	3.2	3.0	3.0	3.7	2.5	3.7	3.2	3.3
Fs	12.7	12.6	12.3	12.3	12.3	12.5	12.6	12.5	12.5	12.5
En	84.3	83.9	84.2	84.5	84.4	83.5	84.5	83.5	84.0	83.9
Mg#	87.6	88.1	88.4	88.4	88.5	88.0	88.0	88.2	88.2	88.5

Sample No.	**15SOP-07**	**15SOP-07**	**15SOP-07**	**15SOP-08**	**15SOP-08**	**15SOP-08**	**15SOP-08**	**15SOP-08**	**15SOP-08**	**15SOP-08**
Intrusion	Sopcha	Sopcha	Sopcha	Sopcha	Sopcha	Sopcha	Sopcha	Sopcha	Sopcha	Sopcha
Sample Pt.	Opx 2	Opx 2	Opx 2	Opx 1	Opx 1	Opx 1	Opx 1	Opx 2	Opx 2	Opx 2
Rock type	HZ	HZ	HZ	HZ	HZ	HZ	HZ	HZ	HZ	HZ
SiO_2 (wt %)	55.80	55.89	55.77	55.65	55.68	55.53	55.56	55.61	55.40	55.46
TiO_2	0.10	0.08	0.07	0.10	0.08	0.09	0.10	0.09	0.07	0.07
Al_2O_3	1.71	1.66	1.69	1.78	1.76	1.85	1.76	1.64	1.65	1.73
Cr_2O_3	0.57	0.56	0.56	0.63	0.62	0.63	0.58	0.57	0.62	0.57
FeO	8.45	8.55	8.51	8.30	8.40	8.56	8.26	8.44	8.22	8.34
MnO	0.21	0.21	0.21	0.20	0.19	0.22	0.20	0.18	0.19	0.22
MgO	31.74	31.87	31.88	31.64	31.55	31.88	31.37	31.53	31.15	31.38
CaO	1.79	1.59	1.62	1.76	1.74	1.46	1.90	1.72	2.22	1.95
NiO	0.16	0.16	0.12	0.13	0.14	0.12	0.14	0.15	0.12	0.18
Total	**101.64**	**101.64**	**101.64**	**101.64**	**101.64**	**101.64**	**101.64**	**101.64**	**101.64**	**101.64**
Si	1.95	1.95	1.95	1.95	1.95	1.94	1.95	1.95	1.95	1.95
Al^{IV}	0.05	0.05	0.05	0.05	0.05	0.05	0.05	0.05	0.05	0.05
Al^{VI}	0.02	0.02	0.02	0.02	0.02	0.02	0.02	0.02	0.02	0.02
Fe^{3+}	0.03	0.03	0.03	0.02	0.02	0.03	0.01	0.02	0.02	0.02
Cr	0.02	0.02	0.02	0.02	0.02	0.02	0.02	0.02	0.02	0.02
Ti	0.00	0.00	0.00	0.00	0.00	0.00	0.00	0.00	0.00	0.00
Fe^{2+}	0.22	0.22	0.22	0.22	0.23	0.22	0.23	0.23	0.22	0.22
Mn	0.01	0.01	0.01	0.01	0.01	0.01	0.01	0.01	0.01	0.01
Mg	1.65	1.66	1.66	1.65	1.65	1.66	1.64	1.65	1.63	1.64
Ca	0.07	0.06	0.06	0.07	0.07	0.05	0.07	0.06	0.08	0.07
Ni	0.00	0.00	0.00	0.00	0.00	0.00	0.00	0.00	0.00	0.01
Total	**4.01**	**4.01**	**4.01**	**4.01**	**4.00**	**4.01**	**4.00**	**4.01**	**4.01**	**4.01**
Wo	3.4	3.0	3.1	3.4	3.3	2.8	3.6	3.3	4.3	3.7
Fs	12.5	12.6	12.6	12.3	12.5	12.7	12.3	12.6	12.3	12.4
En	83.8	84.1	84.1	84.0	83.9	84.2	83.7	83.9	83.2	83.5
Mg#	88.2	88.1	88.3	88.1	87.8	88.4	87.7	87.8	87.9	88.1

CHR = chromitite; LH = lherzolite; HZ = harzburgite; OL-WEB = olivine-websterite; OL-OPX = olivine-orthopyroxenite;
OPX = orthopyroxenite; MNO = melanorite; BRC = breccia; oph = ophitic; xeno = xenolith

Table D.2 (cont.)

Sample No.	**15SOP-08**	**15SOP-09**	**15SOP-09**	**15SOP-09**	**15SOP-09**	**15SOP-09**	**15SOP-09**	**15SOP-09**	**15SOP-09**	**15SOP-10**
Intrusion	Sopcha	Sopcha	Sopcha	Sopcha	Sopcha	Sopcha	Sopcha	Sopcha	Sopcha	Sopcha
Sample Pt.	Opx 2	Opx 1	Opx 1	Opx 1	Opx 1	Opx 2	Opx 2	Opx 2	Opx 2	Opx 1
Rock type	HZ	OL-OPX	OL-OPX	OL-OPX	OL-OPX	OL-OPX	OL-OPX	OL-OPX	OL-OPX	OPX BRC
SiO_2 (wt %)	55.45	56.01	56.03	56.03	56.15	56.04	55.94	55.93	55.95	56.12
TiO_2	0.09	0.07	0.09	0.07	0.08	0.09	0.12	0.13	0.08	0.07
Al_2O_3	1.75	1.67	1.67	1.70	1.66	1.72	1.85	1.64	1.70	1.59
Cr_2O_3	0.59	0.55	0.61	0.62	0.59	0.57	0.63	0.64	0.65	0.68
FeO	8.25	8.54	8.49	8.53	8.58	8.68	8.56	8.33	8.48	8.39
MnO	0.22	0.23	0.21	0.22	0.21	0.24	0.20	0.21	0.20	0.19
MgO	31.31	31.84	31.83	31.68	32.01	32.22	31.69	31.41	31.87	32.24
CaO	2.06	1.68	1.78	1.98	1.58	1.27	1.46	2.39	1.74	1.67
NiO	0.08	0.15	0.15	0.10	0.17	0.18	0.13	0.13	0.14	0.16
Total	**101.64**	**101.64**	**101.64**	**101.64**	**101.64**	**101.64**	**101.64**	**101.64**	**101.64**	**101.64**
Si	1.95	1.95	1.95	1.95	1.95	1.94	1.95	1.95	1.95	1.95
Al^{IV}	0.05	0.05	0.05	0.05	0.05	0.05	0.05	0.05	0.05	0.05
Al^{VI}	0.02	0.02	0.02	0.02	0.02	0.02	0.02	0.02	0.02	0.02
Fe^{3+}	0.02	0.02	0.02	0.02	0.02	0.03	0.01	0.02	0.03	0.03
Cr	0.02	0.02	0.02	0.02	0.02	0.02	0.02	0.02	0.02	0.02
Ti	0.00	0.00	0.00	0.00	0.00	0.00	0.00	0.00	0.00	0.00
Fe^{2+}	0.22	0.23	0.22	0.22	0.22	0.22	0.24	0.22	0.22	0.21
Mn	0.01	0.01	0.01	0.01	0.01	0.01	0.01	0.01	0.01	0.01
Mg	1.64	1.65	1.65	1.64	1.66	1.67	1.65	1.63	1.65	1.67
Ca	0.08	0.06	0.07	0.07	0.06	0.05	0.05	0.09	0.06	0.06
Ni	0.00	0.00	0.00	0.00	0.00	0.01	0.00	0.00	0.00	0.00
Total	**4.01**	**4.01**	**4.01**	**4.01**	**4.01**	**4.01**	**4.00**	**4.01**	**4.01**	**4.01**
Wo	3.9	3.2	3.4	3.7	3.0	2.4	2.8	4.5	3.3	3.1
Fs	12.3	12.6	12.5	12.6	12.6	12.7	12.7	12.3	12.5	12.3
En	83.4	83.9	83.8	83.4	84.1	84.5	84.2	82.9	83.9	84.3
Mg#	88.0	88.0	88.1	88.0	88.1	88.3	87.2	88.1	88.2	88.9

Sample No.	**15SOP-10**	**15SOP-10**	**15SOP-10**	**15SOP-10**	**15SOP-10**	**15SOP-10**	**15SOP-10**	**15SOP-10**	**15SOP-10**	**15SOP-10**
Intrusion	Sopcha	Sopcha	Sopcha	Sopcha	Sopcha	Sopcha	Sopcha	Sopcha	Sopcha	Sopcha
Sample Pt.	Opx 1	Opx 1	Opx 1	Opx 1	Opx 2	Opx 2	Opx 2	Opx 2	Opx 3	Opx 3
Rock type	OPX BRC	OPX BRC	OPX BRC	OPX BRC	OPX BRC	OPX BRC	OPX BRC	OPX BRC	OPX BRC	OPX BRC
SiO_2 (wt %)	56.28	56.15	56.19	56.18	56.12	56.12	55.93	56.13	56.29	56.28
TiO_2	0.06	0.07	0.10	0.09	0.08	0.09	0.09	0.07	0.08	0.00
Al_2O_3	1.56	1.51	1.60	1.58	1.58	1.57	1.58	1.55	1.52	1.57
Cr_2O_3	0.66	0.68	0.68	0.66	0.64	0.68	0.68	0.70	0.64	0.67
FeO	8.42	8.47	8.42	8.41	8.43	8.47	8.38	8.40	8.44	8.50
MnO	0.21	0.22	0.21	0.23	0.19	0.19	0.18	0.18	0.19	0.23
MgO	32.09	32.09	32.17	32.09	32.14	32.19	32.09	32.20	32.06	32.12
CaO	1.68	1.67	1.68	1.67	1.67	1.65	1.68	1.67	1.66	1.68
NiO	0.13	0.14	0.16	0.15	0.18	0.14	0.14	0.17	0.15	0.13
Total	**101.64**	**101.64**	**101.64**	**101.64**	**101.64**	**101.64**	**101.64**	**101.64**	**101.64**	**101.64**
Si	1.95	1.95	1.95	1.95	1.95	1.95	1.95	1.95	1.95	1.95
Al^{IV}	0.05	0.04	0.05	0.05	0.05	0.05	0.05	0.05	0.04	0.05
Al^{VI}	0.02	0.02	0.02	0.02	0.02	0.02	0.02	0.02	0.02	0.02
Fe^{3+}	0.02	0.03	0.03	0.03	0.03	0.03	0.03	0.03	0.02	0.03
Cr	0.02	0.02	0.02	0.02	0.02	0.02	0.02	0.02	0.02	0.02
Ti	0.00	0.00	0.00	0.00	0.00	0.00	0.00	0.00	0.00	0.00
Fe^{2+}	0.22	0.22	0.21	0.22	0.21	0.21	0.21	0.21	0.22	0.22
Mn	0.01	0.01	0.01	0.01	0.01	0.01	0.01	0.01	0.01	0.01
Mg	1.66	1.66	1.66	1.66	1.66	1.66	1.66	1.66	1.66	1.66
Ca	0.06	0.06	0.06	0.06	0.06	0.06	0.06	0.06	0.06	0.06
Ni	0.00	0.00	0.00	0.00	0.01	0.00	0.00	0.00	0.00	0.00
Total	**4.01**	**4.01**	**4.01**	**4.01**	**4.01**	**4.01**	**4.01**	**4.01**	**4.01**	**4.01**
Wo	3.2	3.1	3.2	3.1	3.1	3.1	3.2	3.1	3.1	3.2
Fs	12.4	12.4	12.3	12.3	12.4	12.4	12.3	12.3	12.4	12.4
En	84.2	84.1	84.2	84.2	84.2	84.2	84.3	84.3	84.2	84.1
Mg#	88.2	88.4	88.6	88.4	88.6	88.7	88.7	88.8	88.1	88.4

CHR = chromitite; LH = lherzolite; HZ = harzburgite; OL-WEB = olivine-websterite; OL-OPX = olivine-orthopyroxenite;
OPX = orthopyroxenite; MNO = melanorite; BRC = breccia; oph = ophitic; xeno = xenolith

Table D.2 (cont.)

Sample No.	**15SOP-10**	**15SOP-11**	**15SOP-11**	**15SOP-11**	**15SOP-11**	**15SOP-11**	**15SOP-11**	**15SOP-11**	**15SOP-11**	**15SOP-15**
Intrusion	Sopcha	Sopcha	Sopcha	Sopcha	Sopcha	Sopcha	Sopcha	Sopcha	Sopcha	Sopcha
Sample Pt.	Opx 3	Opx 1	Opx 1	Opx 1	Opx 1	Opx 2	Opx 2	Opx 2	Opx 2	Opx 1
Rock type	OPX BRC	OL-OPX	OL-OPX	OL-OPX	OL-OPX	OL-OPX	OL-OPX	OL-OPX	OL-OPX	OPX
SiO_2 (wt %)	56.28	56.00	56.21	56.08	56.03	56.13	56.05	56.16	56.19	56.24
TiO_2	0.09	0.10	0.07	0.06	0.10	0.11	0.07	0.07	0.07	0.07
Al_2O_3	1.56	1.73	1.68	1.76	1.80	1.85	1.88	1.85	1.73	1.70
Cr_2O_3	0.65	0.64	0.61	0.64	0.64	0.56	0.54	0.60	0.57	0.65
FeO	8.46	8.42	8.63	8.69	8.55	8.72	8.77	8.70	8.62	8.64
MnO	0.21	0.20	0.24	0.21	0.23	0.23	0.21	0.20	0.21	0.23
MgO	32.12	31.51	32.07	32.02	31.85	32.08	32.32	31.91	31.96	31.97
CaO	1.65	2.32	1.71	1.60	1.88	1.52	1.25	1.69	1.67	1.51
NiO	0.13	0.13	0.14	0.14	0.18	0.15	0.15	0.16	0.15	0.16
Total	**101.64**	**101.64**	**101.64**	**101.64**	**101.64**	**101.64**	**101.64**	**101.64**	**101.64**	**101.64**
Si	1.95	1.95	1.95	1.94	1.94	1.94	1.94	1.94	1.95	1.95
Al^{IV}	0.05	0.05	0.05	0.05	0.05	0.05	0.06	0.05	0.05	0.05
Al^{VI}	0.02	0.02	0.02	0.02	0.02	0.02	0.02	0.02	0.02	0.02
Fe^{3+}	0.02	0.02	0.03	0.03	0.03	0.03	0.04	0.03	0.02	0.02
Cr	0.02	0.02	0.02	0.02	0.02	0.02	0.01	0.02	0.02	0.02
Ti	0.00	0.00	0.00	0.00	0.00	0.00	0.00	0.00	0.00	0.00
Fe^{2+}	0.22	0.22	0.22	0.22	0.22	0.22	0.22	0.23	0.23	0.23
Mn	0.01	0.01	0.01	0.01	0.01	0.01	0.01	0.01	0.01	0.01
Mg	1.66	1.63	1.65	1.65	1.65	1.65	1.67	1.65	1.65	1.65
Ca	0.06	0.09	0.06	0.06	0.07	0.06	0.05	0.06	0.06	0.06
Ni	0.00	0.00	0.00	0.00	0.01	0.00	0.00	0.00	0.00	0.00
Total	**4.01**	**4.01**	**4.01**	**4.01**	**4.01**	**4.01**	**4.01**	**4.01**	**4.01**	**4.01**
Wo	3.1	4.4	3.2	3.0	3.5	2.9	2.3	3.2	3.1	2.9
Fs	12.4	12.4	12.6	12.7	12.6	12.8	12.8	12.8	12.7	12.7
En	84.2	82.9	83.8	83.9	83.6	84.0	84.5	83.7	83.9	84.1
Mg#	88.2	88.1	88.4	88.2	88.4	88.2	88.5	87.9	88.0	87.7

Sample No.	**15SOP-15**	**15SOP-15**	**15SOP-15**	**15SOP-15**	**15SOP-15**	**15SOP-15**	**15SOP-15**	**15SOP-15**	**15SOP-15**	**15SOP-16**
Intrusion	Sopcha	Sopcha	Sopcha	Sopcha	Sopcha	Sopcha	Sopcha	Sopcha	Sopcha	Sopcha
Sample Pt.	Opx 1	Opx 1	Opx 1	Opx 2	Opx 2	Opx 2	Opx 2	Opx 3	Opx 3	Opx 1
Rock type	OPX	OPX	OPX	OPX	OPX	OPX	OPX	OPX	OPX	OPX
SiO_2 (wt %)	56.33	55.94	56.14	56.13	56.16	56.09	56.05	56.24	56.21	56.24
TiO_2	0.08	0.08	0.09	0.09	0.08	0.08	0.07	0.09	0.08	0.05
Al_2O_3	1.64	1.77	1.72	1.70	1.71	1.76	1.70	1.84	1.67	1.63
Cr_2O_3	0.62	0.67	0.65	0.66	0.58	0.62	0.63	0.64	0.58	0.58
FeO	8.53	8.62	8.37	8.57	8.66	8.71	8.69	8.80	8.62	8.44
MnO	0.20	0.20	0.21	0.17	0.22	0.24	0.20	0.19	0.23	0.22
MgO	32.15	32.00	31.74	31.87	31.85	31.69	31.78	31.95	31.66	32.01
CaO	1.57	1.56	2.30	1.92	1.53	1.86	1.63	1.44	1.56	1.80
NiO	0.17	0.17	0.14	0.15	0.16	0.16	0.17	0.12	0.16	0.16
Total	**101.64**	**101.64**	**101.64**	**101.64**	**101.64**	**101.64**	**101.64**	**101.64**	**101.64**	**101.64**
Si	1.95	1.94	1.94	1.94	1.95	1.95	1.95	1.95	1.95	1.95
Al^{IV}	0.05	0.05	0.05	0.05	0.05	0.05	0.05	0.05	0.05	0.05
Al^{VI}	0.02	0.02	0.02	0.02	0.02	0.02	0.02	0.02	0.02	0.02
Fe^{3+}	0.02	0.03	0.03	0.03	0.02	0.02	0.02	0.02	0.00	0.03
Cr	0.02	0.02	0.02	0.02	0.02	0.02	0.02	0.02	0.02	0.02
Ti	0.00	0.00	0.00	0.00	0.00	0.00	0.00	0.00	0.00	0.00
Fe^{2+}	0.22	0.22	0.21	0.22	0.24	0.23	0.23	0.24	0.25	0.22
Mn	0.01	0.01	0.01	0.00	0.01	0.01	0.01	0.01	0.01	0.01
Mg	1.66	1.66	1.64	1.65	1.65	1.64	1.65	1.65	1.64	1.65
Ca	0.06	0.06	0.09	0.07	0.06	0.07	0.06	0.05	0.06	0.07
Ni	0.00	0.00	0.00	0.00	0.00	0.00	0.00	0.00	0.00	0.00
Total	**4.01**	**4.01**	**4.01**	**4.01**	**4.00**	**4.01**	**4.01**	**4.01**	**4.00**	**4.01**
Wo	3.0	2.9	4.3	3.6	2.9	3.5	3.1	2.7	3.0	3.4
Fs	12.5	12.7	12.3	12.6	12.8	12.8	12.8	13.0	12.8	12.4
En	84.2	84.1	83.1	83.6	84.0	83.3	83.8	84.0	83.9	83.9
Mg#	88.1	88.3	88.5	88.2	87.5	87.8	87.7	87.4	87.0	88.3

CHR = chromitite; LH = lherzolite; HZ = harzburgite; OL-WEB = olivine-websterite; OL-OPX = olivine-orthopyroxenite;
OPX = orthopyroxenite; MNO = melanorite; BRC = breccia; oph = ophitic; xeno = xenolith

Table D.2 (cont.)

Sample No.	**15SOP-16**	**15SOP-16**	**15SOP-16**	**15SOP-16**	**15SOP-16**	**15SOP-16**	**15SOP-17**	**15SOP-17**	**15SOP-17**	**15SOP-17**
Intrusion	Sopcha	Sopcha	Sopcha	Sopcha	Sopcha	Sopcha	Sopcha	Sopcha	Sopcha	Sopcha
Sample Pt.	Opx 1	Opx 1	Opx 2	Opx 2	Opx 3	Opx 3	Opx 1	Opx 1	Opx 1	Opx 2
Rock type	OPX	OPX	OPX	OPX	OPX	OPX	OPX	OPX	OPX	OPX
SiO_2 (wt %)	56.30	56.21	56.04	56.40	56.18	56.23	55.48	55.47	55.48	55.47
TiO_2	0.07	0.09	0.09	0.09	0.08	0.10	0.10	0.06	0.10	0.06
Al_2O_3	1.65	1.67	1.73	1.59	1.56	1.76	1.77	1.76	1.77	1.76
Cr_2O_3	0.57	0.59	0.62	0.63	0.61	0.66	0.65	0.65	0.65	0.65
FeO	8.40	8.42	8.40	8.25	8.20	8.32	8.42	8.24	8.42	8.24
MnO	0.20	0.21	0.20	0.21	0.22	0.19	0.19	0.18	0.19	0.18
MgO	31.92	32.02	31.77	32.04	32.03	32.01	31.80	31.45	31.80	31.45
CaO	1.81	1.72	1.80	1.71	1.80	1.71	1.44	1.98	1.44	1.98
NiO	0.16	0.13	0.17	0.15	0.13	0.13	0.16	0.14	0.16	0.14
Total	**101.64**	**101.64**	**101.64**	**101.64**	**101.64**	**101.64**	**101.64**	**101.64**	**101.64**	**101.64**
Si	1.95	1.95	1.95	1.95	1.95	1.95	1.94	1.95	1.94	1.95
Al^{IV}	0.05	0.05	0.05	0.05	0.05	0.05	0.05	0.05	0.05	0.05
Al^{VI}	0.02	0.02	0.02	0.02	0.02	0.02	0.02	0.02	0.02	0.02
Fe^{3+}	0.02	0.02	0.02	0.01	0.02	0.02	0.03	0.02	0.03	0.02
Cr	0.02	0.02	0.02	0.02	0.02	0.02	0.02	0.02	0.02	0.02
Ti	0.00	0.00	0.00	0.00	0.00	0.00	0.00	0.00	0.00	0.00
Fe^{2+}	0.23	0.22	0.23	0.23	0.22	0.22	0.22	0.22	0.22	0.22
Mn	0.01	0.01	0.01	0.01	0.01	0.01	0.01	0.01	0.01	0.01
Mg	1.65	1.65	1.65	1.65	1.66	1.65	1.66	1.64	1.66	1.64
Ca	0.07	0.06	0.07	0.06	0.07	0.06	0.05	0.07	0.05	0.07
Ni	0.00	0.00	0.00	0.00	0.00	0.00	0.00	0.00	0.00	0.00
Total	**4.01**	**4.01**	**4.01**	**4.00**	**4.01**	**4.01**	**4.01**	**4.01**	**4.01**	**4.01**
Wo	3.4	3.2	3.4	3.2	3.4	3.2	2.7	3.8	2.7	3.8
Fs	12.4	12.4	12.4	12.2	12.1	12.3	12.5	12.3	12.5	12.3
En	83.9	84.1	83.9	84.3	84.2	84.2	84.4	83.7	84.4	83.7
Mg#	88.0	88.2	87.9	87.9	88.4	88.0	88.3	88.3	88.3	88.3

Sample No.	**15SOP-17**	**15SOP-17**	**15SOP-17**	**15SOP-17**	**15SOP-17**	**15SOP-17**	**15SOP-18**	**15SOP-18**	**15SOP-18**	**15SOP-18**
Intrusion	Sopcha	Sopcha	Sopcha	Sopcha	Sopcha	Sopcha	Sopcha	Sopcha	Sopcha	Sopcha
Sample Pt.	Opx 2	Opx 2	Opx 3	Opx 3	Opx 4	Opx 4	Opx 1	Opx 1	Opx 1	Opx 2
Rock type	OPX	OPX	OPX	OPX	OPX	OPX	OPX	OPX	OPX	OPX
SiO_2 (wt %)	55.47	55.67	55.64	55.66	55.66	55.62	56.21	56.14	56.14	56.26
TiO_2	0.08	0.09	0.09	0.10	0.10	0.09	0.08	0.10	0.07	0.09
Al_2O_3	1.66	1.68	1.61	1.64	1.61	1.63	1.56	1.61	1.59	1.61
Cr_2O_3	0.60	0.63	0.62	0.60	0.60	0.60	0.52	0.58	0.53	0.53
FeO	8.25	8.23	8.19	8.12	8.25	8.26	8.98	8.95	9.06	9.10
MnO	0.24	0.19	0.20	0.20	0.20	0.20	0.21	0.23	0.23	0.21
MgO	31.67	31.81	31.68	31.67	31.77	31.68	31.85	31.74	31.87	31.63
CaO	1.66	1.75	1.81	1.90	1.70	1.73	1.69	1.94	1.52	1.89
NiO	0.14	0.16	0.14	0.13	0.16	0.18	0.14	0.15	0.14	0.14
Total	**101.64**	**101.64**	**101.64**	**101.64**	**101.64**	**101.64**	**101.64**	**101.64**	**101.64**	**101.64**
Si	1.95	1.95	1.95	1.95	1.95	1.95	1.95	1.95	1.95	1.95
Al^{IV}	0.05	0.05	0.05	0.05	0.05	0.05	0.05	0.05	0.05	0.05
Al^{VI}	0.02	0.02	0.02	0.02	0.02	0.02	0.02	0.02	0.02	0.02
Fe^{3+}	0.02	0.03	0.02	0.02	0.02	0.02	0.03	0.03	0.03	0.03
Cr	0.02	0.02	0.02	0.02	0.02	0.02	0.01	0.02	0.01	0.01
Ti	0.00	0.00	0.00	0.00	0.00	0.00	0.00	0.00	0.00	0.00
Fe^{2+}	0.22	0.21	0.22	0.22	0.22	0.22	0.23	0.22	0.23	0.24
Mn	0.01	0.01	0.01	0.01	0.01	0.01	0.01	0.01	0.01	0.01
Mg	1.66	1.66	1.65	1.65	1.66	1.65	1.65	1.64	1.65	1.63
Ca	0.06	0.07	0.07	0.07	0.06	0.06	0.06	0.07	0.06	0.07
Ni	0.00	0.00	0.00	0.00	0.00	0.01	0.00	0.00	0.00	0.00
Total	**4.01**	**4.01**	**4.01**	**4.01**	**4.01**	**4.01**	**4.01**	**4.01**	**4.01**	**4.01**
Wo	3.2	3.3	3.5	3.6	3.2	3.3	3.2	3.6	2.9	3.6
Fs	12.3	12.2	12.2	12.1	12.2	12.3	13.2	13.1	13.3	13.3
En	84.2	84.2	84.1	84.0	84.2	84.1	83.4	82.9	83.5	82.8
Mg#	88.4	88.5	88.3	88.4	88.4	88.3	87.7	87.9	87.6	87.3

CHR = chromitite; LH = lherzolite; HZ = harzburgite; OL-WEB = olivine-websterite; OL-OPX = olivine-orthopyroxenite;
OPX = orthopyroxenite; MNO = melanorite; BRC = breccia; oph = ophitic; xeno = xenolith

Table D.2 (cont.)

Sample No.	**15SOP-18**	**15SOP-18**	**15SOP-18**	**15TMAS-1**	**15TMAS-1**	**15TMAS-1**	**15TMAS-1**	**15TMAS-5**	**15TMAS-5**	**15TMAS-5**
Intrusion	Sopcha	Sopcha	Sopcha	Travyanaya	Travyanaya	Travyanaya	Travyanaya	Travyanaya	Travyanaya	Travyanaya
Sample Pt.	Opx 2	Opx 3	Opx 3	Opx 1	Opx 1	Opx 2	Opx 3	Opx 1	Opx 1	Opx 2
Rock type	OPX	OPX	OPX	Oph. GN	Oph. GN	Oph. GN	Oph. GN	HZ	HZ	HZ
SiO_2 (wt %)	56.28	56.25	56.28	54.15	53.95	54.17	53.08	56.01	55.77	56.05
TiO_2	0.09	0.08	0.10	0.12	0.27	0.18	0.15	0.08	0.10	0.05
Al_2O_3	1.60	1.63	1.60	1.32	1.49	1.45	1.97	1.51	1.74	1.59
Cr_2O_3	0.50	0.53	0.51	0.03	0.04	0.00	0.04	0.70	0.79	0.73
FeO	9.26	9.27	9.22	14.11	14.05	13.55	16.24	7.71	7.45	7.38
MnO	0.21	0.23	0.21	0.36	0.36	0.34	0.46	0.15	0.17	0.19
MgO	31.89	31.98	31.89	26.98	26.90	27.08	22.55	32.80	32.75	32.93
CaO	1.43	1.28	1.49	2.27	2.25	2.45	4.59	1.50	1.62	1.60
NiO	0.15	0.16	0.16	0.13	0.13	0.11	0.11	0.14	0.14	0.17
Total	**101.64**	**101.64**	**101.64**	**101.64**	**101.64**	**101.64**	**101.64**	**101.64**	**101.64**	**101.64**
Si	1.95	1.95	1.95	1.96	1.95	1.96	1.96	1.94	1.94	1.94
Al^{IV}	0.05	0.05	0.05	0.04	0.04	0.04	0.04	0.04	0.05	0.05
Al^{VI}	0.02	0.02	0.02	0.02	0.02	0.02	0.05	0.02	0.02	0.02
Fe^{3+}	0.03	0.03	0.03	0.02	0.02	0.01	0.00	0.04	0.04	0.04
Cr	0.01	0.01	0.01	0.00	0.00	0.00	0.00	0.02	0.02	0.02
Ti	0.00	0.00	0.00	0.00	0.01	0.00	0.00	0.00	0.00	0.00
Fe^{2+}	0.24	0.24	0.24	0.40	0.41	0.40	0.50	0.18	0.17	0.17
Mn	0.01	0.01	0.01	0.01	0.01	0.01	0.01	0.00	0.00	0.01
Mg	1.65	1.65	1.65	1.46	1.45	1.46	1.24	1.70	1.70	1.70
Ca	0.05	0.05	0.06	0.09	0.09	0.09	0.18	0.06	0.06	0.06
Ni	0.00	0.00	0.00	0.00	0.00	0.00	0.00	0.00	0.00	0.00
Total	**4.01**	**4.01**	**4.01**	**4.01**	**4.01**	**4.00**	**3.99**	**4.01**	**4.01**	**4.01**
Wo	2.7	2.4	2.8	4.4	4.4	4.8	9.4	2.8	3.1	3.0
Fs	13.6	13.6	13.5	21.5	21.5	20.7	25.9	11.3	10.9	10.8
En	83.4	83.7	83.4	73.5	73.5	73.9	64.0	85.7	85.8	85.9
Mg#	87.2	87.3	87.3	78.3	78.1	78.7	71.2	90.2	90.7	90.8

Sample No.	**15TMAS-5**	**15TMAS-7**	**15TMAS-7**	**15TMAS-7**	**15TMAS-7**	**15TMAS-7**	**15TMAS-7**
Intrusion	Travyanaya	Travyanaya	Travyanaya	Travyanaya	Travyanaya	Travyanaya	Travyanaya
Sample Pt.	Opx 2	Opx 1	Opx 2	Opx 2	Opx 3	Opx 3	Opx 3
Rock type	HZ	OL-WEB	OL-WEB	OL-WEB	OL-WEB	OL-WEB	OL-WEB
SiO_2 (wt %)	56.29	55.41	56.09	56.18	55.11	55.13	55.05
TiO_2	0.08	0.13	0.08	0.07	0.10	0.37	0.08
Al_2O_3	1.57	2.23	1.74	1.70	2.15	1.95	1.97
Cr_2O_3	0.72	0.88	0.73	0.73	0.70	0.53	0.70
FeO	7.59	7.40	7.62	7.54	9.30	9.49	9.40
MnO	0.18	0.21	0.21	0.18	0.22	0.23	0.22
MgO	33.03	31.21	32.63	32.67	30.63	30.48	30.51
CaO	1.54	2.87	1.62	1.68	2.10	2.25	2.14
NiO	0.11	0.10	0.11	0.10	0.15	0.11	0.14
Total	**101.64**	**101.64**	**101.64**	**101.64**	**101.64**	**101.64**	**101.64**
Si	1.94	1.93	1.94	1.94	1.93	1.93	1.94
Al^{IV}	0.05	0.07	0.05	0.05	0.06	0.06	0.06
Al^{VI}	0.02	0.03	0.02	0.02	0.03	0.02	0.02
Fe^{3+}	0.04	0.02	0.03	0.03	0.03	0.02	0.03
Cr	0.02	0.02	0.02	0.02	0.02	0.01	0.02
Ti	0.00	0.00	0.00	0.00	0.00	0.01	0.00
Fe^{2+}	0.18	0.20	0.19	0.19	0.24	0.25	0.25
Mn	0.01	0.01	0.01	0.01	0.01	0.01	0.01
Mg	1.70	1.62	1.68	1.69	1.60	1.59	1.60
Ca	0.06	0.11	0.06	0.06	0.08	0.08	0.08
Ni	0.00	0.00	0.00	0.00	0.00	0.00	0.00
Total	**4.01**	**4.01**	**4.01**	**4.01**	**4.01**	**4.01**	**4.01**
Wo	2.9	5.5	3.1	3.2	4.0	4.3	4.1
Fs	11.0	11.0	11.2	11.0	13.9	14.2	14.1
En	85.8	83.2	85.5	85.5	81.7	81.2	81.5
Mg#	90.5	89.2	89.9	89.9	86.8	86.2	86.6

CHR = chromitite; LH = lherzolite; HZ = harzburgite; OL-WEB = olivine-websterite; OL-OPX = olivine-orthopyroxenite; OPX = orthopyroxenite; MNO = melanorite; BRC = breccia; oph = ophitic; xeno = xenolith

Table D.3. Mineral chemistry of clinopyroxene from the Monchegorsk Complex. Basis: 6 oxides

Sample No.	**79-023**	**79-023**	**79-023**	**79-023**	**79-023**	**79-054**	**79-091**	**79-091**	**79-115**	**79-115**
Intrusion	Nittis	Nittis	Nittis	Nittis	Nittis	Nittis	Nittis	Nittis	Nittis	Nittis
Sample Pt.	Cpx 1	Cpx 2	Cpx 2	Cpx 3	Cpx 3	Cpx 1	Cpx 1	Cpx 2	Cpx 1	Cpx 2
Rock type	OPX	OPX	OPX	OPX	OPX	OPX	OPX	OPX	OPX	OPX
SiO_2 (wt %)	51.92	51.60	52.07	52.30	52.35	51.60	51.47	53.14	52.22	52.03
TiO_2	1.00	0.85	0.98	0.73	0.63	0.20	0.30	0.52	0.78	0.68
Al_2O_3	2.87	2.83	2.72	2.89	2.91	3.34	2.99	2.53	2.99	2.91
Cr_2O_3	0.82	0.77	0.86	0.92	0.94	1.87	0.92	0.57	0.47	0.53
FeO	5.09	5.11	4.61	4.71	4.82	6.55	6.07	7.86	6.42	6.05
MnO	0.13	0.15	0.13	0.14	0.17	0.18	0.14	0.22	0.13	0.15
MgO	16.25	16.66	16.20	16.13	16.27	19.25	16.65	19.30	16.45	15.52
CaO	20.65	20.44	21.63	21.72	21.44	16.64	19.57	15.36	19.46	21.30
Na_2O	0.47	0.43	0.46	0.50	0.50	0.40	0.46	0.38	0.55	0.57
NiO	0.11	0.09	0.10	0.11	0.10	0.10	0.09	0.13	0.10	0.08
Total	**99.32**	**98.95**	**99.76**	**100.16**	**100.12**	**100.14**	**98.66**	**100.01**	**99.57**	**99.81**
Si	1.92	1.91	1.91	1.92	1.92	1.88	1.91	1.94	1.92	1.92
Al^{IV}	0.08	0.08	0.08	0.08	0.08	0.10	0.09	0.06	0.08	0.08
Al^{VI}	0.04	0.04	0.04	0.04	0.04	0.05	0.05	0.04	0.05	0.05
Fe^{3+}	0.00	0.02	0.01	0.02	0.02	0.07	0.04	0.00	0.01	0.03
Cr	0.02	0.02	0.03	0.03	0.03	0.05	0.03	0.02	0.01	0.02
Ti	0.03	0.02	0.03	0.02	0.02	0.01	0.01	0.01	0.02	0.02
Fe^{2+}	0.16	0.13	0.13	0.12	0.13	0.12	0.15	0.24	0.19	0.15
Mn	0.00	0.00	0.00	0.00	0.01	0.01	0.00	0.01	0.00	0.00
Mg	0.89	0.92	0.89	0.88	0.89	1.05	0.92	1.05	0.90	0.85
Ca	0.82	0.81	0.85	0.85	0.84	0.65	0.78	0.60	0.77	0.84
Na	0.03	0.03	0.03	0.04	0.04	0.03	0.03	0.03	0.04	0.04
Ni	0.00	0.00	0.00	0.00	0.00	0.00	0.00	0.00	0.00	0.00
Total	**4.00**	**4.01**	**4.00**	**4.01**	**4.01**	**4.02**	**4.01**	**4.00**	**4.00**	**4.01**
Wo	43.6	42.8	45.2	45.3	44.7	34.2	41.1	31.7	41.0	44.6
Fs	8.4	8.3	7.5	7.7	7.8	10.4	9.9	12.6	10.5	9.9
En	47.8	48.6	47.1	46.8	47.2	55.1	48.7	55.3	48.2	45.3
Mg#	85.0	87.3	87.3	87.7	87.6	89.4	86.4	81.5	82.8	84.7

Sample No.	**79-131**	**79-131**	**79-131**	**79-131**	**79-160**	**79-160**	**79-160**	**79-160**	**79-160**	**79-160**
Intrusion	Nittis	Nittis	Nittis	Nittis	Nittis	Nittis	Nittis	Nittis	Nittis	Nittis
Sample Pt.	Cpx 1	Cpx 2	Cpx 2	Cpx 2	Cpx 1	Cpx 1	Cpx 2	Cpx 2	Cpx 3	Cpx 3
Rock type	OPX	OPX	OPX	OPX	OPX	OPX	OPX	OPX	OPX	OPX
SiO_2 (wt %)	54.10	53.59	53.52	53.46	52.71	52.61	52.67	52.56	53.14	53.23
TiO_2	0.22	0.42	0.38	0.38	0.30	0.30	0.32	0.30	0.22	0.22
Al_2O_3	1.80	2.42	2.42	2.51	3.14	3.17	3.06	3.19	2.51	2.59
Cr_2O_3	0.70	0.38	0.45	0.56	0.92	0.94	0.72	0.94	0.61	0.70
FeO	3.92	5.54	5.96	5.48	5.29	5.43	4.55	4.66	4.50	4.59
MnO	0.12	0.12	0.18	0.15	0.15	0.17	0.15	0.12	0.14	0.13
MgO	17.06	16.05	16.63	16.03	17.05	16.85	16.12	15.94	16.43	16.90
CaO	22.64	22.33	21.10	22.26	20.20	20.08	22.25	22.12	22.49	21.83
Na_2O	0.27	0.32	0.36	0.36	0.53	0.53	0.50	0.53	0.46	0.49
NiO	0.11	0.10	0.10	0.00	0.10	0.10	0.11	0.11	0.09	0.11
Total	**100.94**	**101.27**	**101.11**	**101.21**	**100.39**	**100.17**	**100.45**	**100.46**	**100.60**	**100.78**
Si	1.96	1.94	1.94	1.94	1.92	1.92	1.92	1.92	1.94	1.93
Al^{IV}	0.04	0.06	0.06	0.06	0.08	0.08	0.08	0.08	0.06	0.07
Al^{VI}	0.03	0.05	0.04	0.05	0.05	0.06	0.05	0.06	0.04	0.04
Fe^{3+}	0.00	0.00	0.01	0.00	0.03	0.02	0.03	0.03	0.04	0.04
Cr	0.02	0.01	0.01	0.02	0.03	0.03	0.02	0.03	0.02	0.02
Ti	0.01	0.01	0.01	0.01	0.01	0.01	0.01	0.01	0.01	0.01
Fe^{2+}	0.12	0.17	0.17	0.16	0.13	0.14	0.11	0.11	0.10	0.10
Mn	0.00	0.00	0.01	0.00	0.00	0.01	0.00	0.00	0.00	0.00
Mg	0.92	0.87	0.90	0.87	0.93	0.92	0.88	0.87	0.89	0.91
Ca	0.88	0.87	0.82	0.87	0.79	0.79	0.87	0.87	0.88	0.85
Na	0.02	0.02	0.03	0.03	0.04	0.04	0.04	0.04	0.03	0.03
Ni	0.00	0.00	0.00	0.00	0.00	0.00	0.00	0.00	0.00	0.00
Total	**4.00**	**4.00**	**4.00**	**4.00**	**4.01**	**4.01**	**4.01**	**4.01**	**4.01**	**4.01**
Wo	45.7	45.5	43.0	45.5	41.9	41.9	46.0	46.1	45.9	44.5
Fs	6.2	8.8	9.5	8.7	8.5	8.8	7.3	7.6	7.2	7.3
En	47.9	45.5	47.2	45.6	49.3	49.0	46.4	46.2	46.7	48.0
Mg#	88.6	83.8	83.9	84.3	87.5	86.5	89.3	88.5	89.9	90.3

OPX = orthopyroxenite; MNO = melanorite; GN = gabbronorite; HZ = harzburgite; oph = ophitic

Table D.3 (cont.)

Sample No.	**79-160**	**94-038**	**94-038**	**94-038**	**94-038**	**94-038**	**94-081**	**94-081**	**94-081**	**94-081**
Intrusion	Nittis	Nittis	Nittis	Nittis	Nittis	Nittis	Nittis	Nittis	Nittis	Nittis
Sample Pt.	Cpx 3	Cpx 1	Cpx 1	Cpx 1	Cpx 2	Cpx 2	Cpx 1	Cpx 1	Cpx 2	Cpx 3
Rock type	OPX	OPX	OPX	OPX	OPX	OPX	OPX	OPX	OPX	OPX
SiO_2 (wt %)	53.16	52.24	51.96	52.15	51.92	52.18	52.60	52.18	52.35	51.90
TiO_2	0.22	0.58	0.58	0.73	0.60	0.80	0.48	0.37	0.45	0.72
Al_2O_3	2.48	2.65	2.83	2.59	2.97	2.57	2.89	3.06	3.04	2.82
Cr_2O_3	0.66	1.13	1.18	1.01	1.23	0.99	0.98	1.10	1.13	0.98
FeO	4.55	3.98	4.09	4.64	4.18	4.18	5.34	4.32	4.79	4.48
MnO	0.15	0.10	0.12	0.13	0.12	0.12	0.15	0.12	0.14	0.12
MgO	16.48	16.32	16.18	17.25	16.35	16.33	18.24	15.97	16.81	16.48
CaO	22.33	21.97	21.86	20.27	21.77	21.97	18.92	21.83	20.09	21.30
Na_2O	0.49	0.39	0.43	0.44	0.42	0.46	0.42	0.50	0.49	0.44
NiO	0.11	0.09	0.09	0.09	0.09	0.09	0.15	0.11	0.13	0.11
Total	**100.64**	**99.44**	**99.33**	**99.31**	**99.64**	**99.68**	**100.18**	**99.55**	**99.41**	**99.34**
Si	1.94	1.92	1.92	1.92	1.91	1.92	1.92	1.92	1.92	1.91
Al^{IV}	0.06	0.08	0.08	0.08	0.09	0.08	0.08	0.08	0.08	0.08
Al^{VI}	0.04	0.04	0.04	0.04	0.04	0.04	0.04	0.05	0.05	0.04
Fe^{3+}	0.04	0.01	0.01	0.02	0.02	0.02	0.03	0.02	0.00	0.02
Cr	0.02	0.03	0.03	0.03	0.04	0.03	0.03	0.03	0.03	0.03
Ti	0.01	0.02	0.02	0.02	0.02	0.02	0.01	0.01	0.01	0.02
Fe^{2+}	0.10	0.12	0.11	0.12	0.11	0.11	0.13	0.12	0.15	0.12
Mn	0.00	0.00	0.00	0.00	0.00	0.00	0.00	0.00	0.00	0.00
Mg	0.89	0.89	0.89	0.95	0.90	0.89	0.99	0.88	0.92	0.91
Ca	0.87	0.87	0.86	0.80	0.86	0.86	0.74	0.86	0.79	0.84
Na	0.03	0.03	0.03	0.03	0.03	0.03	0.03	0.04	0.03	0.03
Ni	0.00	0.00	0.00	0.00	0.00	0.00	0.00	0.00	0.00	0.00
Total	**4.01**	**4.00**	**4.00**	**4.01**	**4.01**	**4.01**	**4.01**	**4.01**	**4.00**	**4.01**
Wo	45.6	45.9	45.9	42.2	45.5	45.7	38.9	45.9	42.4	44.5
Fs	7.2	6.5	6.7	7.5	6.8	6.8	8.6	7.1	7.9	7.3
En	46.9	47.4	47.3	50.0	47.5	47.3	52.3	46.8	49.4	48.0
Mg#	90.1	88.6	88.9	88.4	89.4	89.2	88.2	88.4	86.3	88.7

Sample No.	**94-081**	**94-118**	**94-118**	**94-118**	**94-118**	**1815-046**	**1815-046**	**1815-046**	**1815-046**	**1815-046**
Intrusion	Nittis	Nittis	Nittis	Nittis	Nittis	Nyud	Nyud	Nyud	Nyud	Nyud
Sample Pt.	Cpx 3	Cpx 1	Cpx 1	Cpx 1	Cpx 2	Cpx 1	Cpx 2	Cpx 2	Cpx 3	Cpx 4
Rock type	OPX	OPX	OPX	OPX	OPX	MNO	MNO	MNO	MNO	MNO
SiO_2 (wt %)	52.13	51.62	52.35	51.38	51.58	54.46	52.65	52.30	52.43	52.41
TiO_2	0.75	1.27	1.02	1.08	0.97	0.12	0.28	0.27	0.35	0.33
Al_2O_3	2.83	3.00	2.83	2.99	3.04	0.43	2.70	2.76	2.59	2.68
Cr_2O_3	0.92	0.77	0.70	0.85	0.82	0.19	1.05	0.92	0.77	0.80
FeO	4.39	4.88	5.31	4.77	4.75	3.80	4.90	5.11	6.56	5.36
MnO	0.12	0.13	0.12	0.10	0.12	0.13	0.14	0.13	0.17	0.18
MgO	16.30	15.85	17.23	15.64	15.67	16.53	15.87	15.77	17.11	15.99
CaO	21.65	21.39	19.88	21.67	21.35	24.04	22.08	21.90	18.58	21.63
Na_2O	0.47	0.63	0.57	0.57	0.57	0.23	0.38	0.34	0.30	0.32
NiO	0.14	0.11	0.11	0.09	0.10	0.09	0.10	0.13	0.10	0.10
Total	**99.70**	**99.66**	**100.12**	**99.14**	**98.96**	**100.02**	**100.15**	**99.62**	**98.97**	**99.82**
Si	1.92	1.90	1.91	1.90	1.91	1.99	1.93	1.93	1.94	1.93
Al^{IV}	0.08	0.09	0.08	0.09	0.09	0.01	0.07	0.07	0.06	0.07
Al^{VI}	0.04	0.04	0.04	0.04	0.04	0.01	0.05	0.05	0.05	0.04
Fe^{3+}	0.02	0.03	0.03	0.03	0.01	0.00	0.01	0.01	0.00	0.01
Cr	0.03	0.02	0.02	0.02	0.02	0.01	0.03	0.03	0.02	0.02
Ti	0.02	0.04	0.03	0.03	0.03	0.00	0.01	0.01	0.01	0.01
Fe^{2+}	0.12	0.12	0.14	0.12	0.14	0.11	0.14	0.15	0.20	0.15
Mn	0.00	0.00	0.00	0.00	0.00	0.00	0.00	0.00	0.01	0.01
Mg	0.89	0.87	0.94	0.86	0.87	0.90	0.87	0.87	0.94	0.88
Ca	0.85	0.84	0.78	0.86	0.85	0.94	0.87	0.86	0.74	0.85
Na	0.03	0.05	0.04	0.04	0.04	0.02	0.03	0.02	0.02	0.02
Ni	0.00	0.00	0.00	0.00	0.00	0.00	0.00	0.00	0.00	0.00
Total	**4.01**	**4.01**	**4.01**	**4.01**	**4.00**	**4.00**	**4.00**	**4.00**	**3.99**	**4.00**
Wo	45.2	45.2	41.3	45.9	45.5	48.0	45.9	45.7	39.0	44.9
Fs	7.1	8.0	8.6	7.9	7.9	5.9	7.9	8.3	10.7	8.7
En	47.4	46.6	49.9	46.1	46.4	45.9	45.9	45.8	50.0	46.1
Mg#	88.5	87.6	87.3	87.6	86.4	88.9	85.9	85.4	82.3	85.1

OPX = orthopyroxenite; MNO = melanorite; GN = gabbronorite; HZ = harzburgite; oph = ophitic

Table D.3 (cont.)

Sample No.	**1815-11**	**1815-11**	**1815-11**	**1403-030**	**1403-030**	**1403-030**	**1403-064**	**1403-064**	**1403-064**	**1403-064**
Intrusion	Nyud	Nyud	Nyud	Sopcha	Sopcha	Sopcha	Sopcha	Sopcha	Sopcha	Sopcha
Sample Pt.	Cpx 1	Cpx 1	Cpx 2	Cpx 1	Cpx 1	Cpx 2	Cpx 1	Cpx 1	Cpx 1	Cpx 2
Rock type	MNO	MNO	MNO	OPX	OPX	OPX	OPX	OPX	OPX	OPX
SiO_2 (wt %)	52.09	52.13	53.76	52.62	52.67	53.50	52.35	51.90	52.37	52.43
TiO_2	0.25	0.32	0.23	0.32	0.35	0.32	0.42	0.33	0.47	0.32
Al_2O_3	2.87	2.72	2.46	3.08	3.06	2.68	2.97	3.08	2.87	2.91
Cr_2O_3	1.07	0.98	0.79	1.27	1.21	0.96	1.18	1.14	1.05	1.04
FeO	5.03	5.25	7.37	4.70	5.12	6.78	4.18	4.25	4.86	5.87
MnO	0.13	0.15	0.19	0.14	0.17	0.18	0.12	0.13	0.15	0.15
MgO	15.65	16.02	20.36	16.60	17.64	20.63	16.18	16.10	17.18	19.00
CaO	21.65	21.37	14.51	20.89	19.25	14.85	21.69	21.03	19.91	16.65
Na_2O	0.44	0.40	0.28	0.54	0.54	0.42	0.50	0.53	0.47	0.42
NiO	0.13	0.11	0.10	0.11	0.11	0.09	0.09	0.09	0.09	0.11
Total	**99.31**	**99.46**	**100.06**	**100.27**	**100.13**	**100.41**	**99.67**	**98.57**	**99.43**	**98.90**
Si	1.93	1.93	1.95	1.92	1.92	1.93	1.92	1.92	1.92	1.93
Al^{IV}	0.07	0.07	0.05	0.08	0.08	0.07	0.08	0.08	0.08	0.07
Al^{VI}	0.05	0.04	0.05	0.05	0.05	0.04	0.05	0.06	0.05	0.05
Fe^{3+}	0.01	0.02	0.00	0.02	0.02	0.02	0.01	0.01	0.01	0.01
Cr	0.03	0.03	0.02	0.04	0.03	0.03	0.03	0.03	0.03	0.03
Ti	0.01	0.01	0.01	0.01	0.01	0.01	0.01	0.01	0.01	0.01
Fe^{2+}	0.14	0.14	0.22	0.13	0.13	0.19	0.12	0.13	0.14	0.17
Mn	0.00	0.00	0.01	0.00	0.01	0.01	0.00	0.00	0.00	0.00
Mg	0.86	0.88	1.10	0.90	0.96	1.11	0.89	0.89	0.94	1.04
Ca	0.86	0.85	0.56	0.82	0.75	0.57	0.85	0.84	0.78	0.65
Na	0.03	0.03	0.02	0.04	0.04	0.03	0.04	0.04	0.03	0.03
Ni	0.00	0.00	0.00	0.00	0.00	0.00	0.00	0.00	0.00	0.00
Total	**4.00**	**4.01**	**3.99**	**4.01**	**4.01**	**4.00**	**4.00**	**4.00**	**4.00**	**4.00**
Wo	45.6	44.6	29.8	43.7	40.2	30.3	45.6	44.9	41.7	34.8
Fs	8.3	8.5	11.8	7.7	8.3	10.8	6.9	7.1	7.9	9.6
En	45.9	46.6	58.1	48.4	51.2	58.6	47.4	47.8	50.1	55.3
Mg#	86.0	86.3	83.1	87.8	87.8	85.5	88.3	87.6	87.3	85.9

Sample No.	**1403-089**	**1403-089**	**1403-089**	**15TMAS-1**	**15TMAS-1**	**15TMAS-1**	**15TMAS-1**	**15TMAS-1**	**15TMAS-1**	**15TMAS-1**
Intrusion	Sopcha	Sopcha	Sopcha	Travyanaya	Travyanaya	Travyanaya	Travyanaya	Travyanaya	Travyanaya	Travyanaya
Sample Pt.	Cpx 2	Cpx 3	Cpx 4	Cpx 1	Cpx 1	Cpx 1	Cpx 2	Cpx 2	Cpx 2	Cpx 3
Rock type	OPX	OPX	OPX	Oph. GN	Oph. GN	Oph. GN	Oph. GN	Oph. GN	Oph. GN	Oph. GN
SiO_2 (wt %)	53.12	52.58	52.69	52.58	52.11	52.33	51.66	51.96	51.86	52.05
TiO_2	0.53	0.48	0.55	0.22	0.23	0.33	0.28	0.25	0.22	0.33
Al_2O_3	2.63	2.82	2.68	2.31	2.15	2.29	2.31	2.21	2.17	2.36
Cr_2O_3	0.96	1.02	1.08	0.07	0.06	0.10	0.07	0.09	0.18	0.00
FeO	5.31	3.87	4.73	8.85	8.47	9.39	6.92	7.47	6.69	8.17
MnO	0.14	0.13	0.10	0.26	0.27	0.28	0.19	0.25	0.19	0.25
MgO	18.11	17.46	17.11	16.93	17.01	16.58	15.65	17.00	16.25	16.60
CaO	19.16	19.52	20.44	17.62	17.55	18.08	20.79	19.41	20.37	18.48
Na_2O	0.42	0.51	0.46	0.34	0.28	0.28	0.32	0.26	0.31	0.35
NiO	0.10	0.10	0.08	0.08	0.08	0.10	0.09	0.08	0.10	0.10
Total	**100.48**	**98.50**	**99.93**	**99.25**	**98.22**	**99.77**	**98.30**	**98.97**	**98.34**	**98.70**
Si	1.93	1.94	1.93	1.95	1.95	1.94	1.94	1.93	1.94	1.94
Al^{IV}	0.07	0.06	0.07	0.05	0.05	0.06	0.06	0.07	0.06	0.06
Al^{VI}	0.04	0.06	0.04	0.05	0.05	0.04	0.04	0.03	0.04	0.05
Fe^{3+}	0.01	0.00	0.01	0.01	0.01	0.03	0.04	0.06	0.04	0.03
Cr	0.03	0.03	0.03	0.00	0.00	0.00	0.00	0.00	0.01	0.00
Ti	0.01	0.01	0.02	0.01	0.01	0.01	0.01	0.01	0.01	0.01
Fe^{2+}	0.15	0.12	0.14	0.26	0.25	0.26	0.18	0.18	0.17	0.23
Mn	0.00	0.00	0.00	0.01	0.01	0.01	0.01	0.01	0.01	0.01
Mg	0.98	0.96	0.93	0.94	0.95	0.92	0.88	0.94	0.91	0.92
Ca	0.74	0.77	0.80	0.70	0.70	0.72	0.84	0.77	0.82	0.74
Na	0.03	0.04	0.03	0.02	0.02	0.02	0.02	0.02	0.02	0.03
Ni	0.00	0.00	0.00	0.00	0.00	0.00	0.00	0.00	0.00	0.00
Total	**4.00**	**3.99**	**4.00**	**4.00**	**4.00**	**4.01**	**4.01**	**4.02**	**4.01**	**4.01**
Wo	39.4	41.6	42.6	36.5	36.5	37.1	43.2	39.6	42.1	38.4
Fs	8.5	6.4	7.7	14.3	13.7	15.0	11.2	11.8	10.8	13.2
En	51.8	51.8	49.6	48.8	49.3	47.4	45.3	48.2	46.8	48.0
Mg#	86.6	88.9	87.1	78.2	79.0	77.8	83.1	84.2	84.3	80.3

OPX = orthopyroxenite; MNO = melanorite; GN = gabbronorite; HZ = harzburgite; oph = ophitic

Table D.3 (cont.)

Sample No.	**15TMAS-1**	**15TMAS-1**	**15TMAS-5**	**15TMAS-5**	**15TMAS-5**	**15TMAS-5**	**15TMAS-5**
Intrusion	Travyanaya	Travyanaya	Travyanaya	Travyanaya	Travyanaya	Travyanaya	Travyanaya
Sample Pt.	Cpx 4	Cpx 4	Cpx 1	Cpx 1	Cpx 2	Cpx 2	Cpx 2
Rock type	Oph. GN	Oph. GN	HZ	HZ	HZ	HZ	HZ
SiO_2 (wt %)	51.84	52.01	51.90	52.65	52.16	52.54	52.41
TiO_2	0.35	0.30	0.58	0.57	0.43	0.48	0.52
Al_2O_3	2.19	2.17	3.50	3.34	3.34	3.33	3.42
Cr_2O_3	0.04	0.06	1.26	1.13	1.18	1.10	1.17
FeO	7.20	7.40	4.00	4.95	4.37	4.58	4.22
MnO	0.25	0.25	0.13	0.21	0.12	0.14	0.15
MgO	16.00	16.30	16.55	19.12	17.83	19.07	18.12
CaO	20.62	20.05	21.60	18.61	20.46	18.72	20.54
Na_2O	0.31	0.30	0.46	0.32	0.40	0.36	0.35
NiO	0.09	0.08	0.06	0.11	0.11	0.08	0.08
Total	**98.90**	**98.91**	**100.04**	**101.01**	**100.41**	**100.40**	**100.99**
Si	1.94	1.94	1.90	1.90	1.90	1.90	1.89
Al^{IV}	0.06	0.06	0.10	0.10	0.10	0.10	0.10
Al^{VI}	0.03	0.03	0.05	0.04	0.04	0.04	0.04
Fe^{3+}	0.05	0.04	0.03	0.04	0.05	0.04	0.05
Cr	0.00	0.00	0.04	0.03	0.03	0.03	0.03
Ti	0.01	0.01	0.02	0.02	0.01	0.01	0.01
Fe^{2+}	0.17	0.19	0.09	0.11	0.08	0.10	0.08
Mn	0.01	0.01	0.00	0.01	0.00	0.00	0.00
Mg	0.89	0.91	0.90	1.03	0.97	1.03	0.98
Ca	0.83	0.80	0.85	0.72	0.80	0.73	0.79
Na	0.02	0.02	0.03	0.02	0.03	0.03	0.02
Ni	0.00	0.00	0.00	0.00	0.00	0.00	0.00
Total	**4.02**	**4.01**	**4.01**	**4.01**	**4.02**	**4.01**	**4.02**
Wo	42.4	41.2	45.1	37.8	42.0	38.3	41.8
Fs	11.5	11.8	6.5	7.8	7.0	7.3	6.7
En	45.7	46.6	48.1	54.0	50.9	54.2	51.3
Mg#	83.7	82.9	90.5	90.2	92.3	91.0	92.4

OPX = orthopyroxenite; MNO = melanorite; GN = gabbronorite; HZ = harzburgite; oph = ophitic

Table D.4. Mineral chemistry of plagioclase from the Monchegorsk Complex. Basis: 8 oxides

Sample No.	**79-008**	**79-008**	**79-008**	**79-008**	**79-008**	**79-008**	**79-008**	**79-023**	**79-023**	**79-023**
Intrusion	Nittis	Nittis	Nittis	Nittis	Nittis	Nittis	Nittis	Nittis	Nittis	Nittis
Sample Pt.	Pl 1	Pl 2	Pl 2	Pl 2	Pl 3	Pl 4	Pl 4	Pl 1	Pl 2	Pl 2
Rock type	OPX	OPX	OPX	OPX	OPX	OPX	OPX	OPX	OPX	OPX
SiO_2 (wt %)	50.34	51.13	51.47	51.73	51.30	54.01	54.12	55.51	52.13	51.94
Al_2O_3	31.10	30.59	30.35	30.18	30.89	28.97	28.95	28.51	30.72	30.97
FeO	0.42	0.27	0.27	0.18	0.30	0.23	0.28	0.36	0.24	0.39
CaO	13.54	12.80	12.69	12.34	13.07	10.89	10.87	10.16	12.79	12.98
Na_2O	3.73	4.07	4.26	4.31	4.04	5.37	5.32	5.92	4.31	4.23
K_2O	0.05	0.08	0.04	0.04	0.04	0.06	0.05	0.04	0.00	0.00
Total	**99.19**	**98.95**	**99.07**	**98.77**	**99.64**	**99.52**	**99.60**	**100.50**	**100.20**	**100.51**
Si	2.31	2.35	2.36	2.37	2.34	2.45	2.45	2.49	2.36	2.35
Al	1.68	1.65	1.64	1.63	1.66	1.55	1.55	1.51	1.64	1.65
Fe	0.02	0.01	0.01	0.01	0.01	0.01	0.01	0.01	0.01	0.01
Ca	0.67	0.63	0.62	0.61	0.64	0.53	0.53	0.49	0.62	0.63
Na	0.33	0.36	0.38	0.38	0.36	0.47	0.47	0.51	0.38	0.37
K	0.00	0.00	0.00	0.00	0.00	0.00	0.00	0.00	0.00	0.00
Total	**5.01**	**5.01**	**5.01**	**5.00**	**5.01**	**5.01**	**5.01**	**5.02**	**5.01**	**5.01**
An	66.5	63.2	62.1	61.1	64.0	52.7	52.9	48.6	62.1	62.9
Ab	33.2	36.3	37.7	38.7	35.8	47.0	46.9	51.2	37.9	37.1
Or	0.3	0.5	0.2	0.2	0.2	0.3	0.3	0.2	0.0	0.0

Sample No.	**79-023**	**79-023**	**79-039**	**79-039**	**79-039**	**79-039**	**79-039**	**79-039**	**79-054**	**79-054**
Intrusion	Nittis	Nittis	Nittis	Nittis	Nittis	Nittis	Nittis	Nittis	Nittis	Nittis
Sample Pt.	Pl 3	Pl 3	Pl 1	Pl 2	Pl 2	Pl 2	Pl 3	Pl 3	Pl 1	Pl 2
Rock type	OPX	OPX	OPX	OPX	OPX	OPX	OPX	OPX	OPX	OPX
SiO_2 (wt %)	54.23	54.34	52.65	52.09	52.18	52.11	52.05	51.92	51.13	51.77
Al_2O_3	29.27	29.25	30.87	31.23	31.25	31.04	31.18	31.21	31.27	30.87
FeO	0.37	0.41	0.15	0.26	0.26	0.22	0.19	0.14	0.28	0.12
CaO	11.04	11.00	12.49	12.89	12.96	12.73	12.82	12.96	13.38	12.94
Na_2O	5.31	5.39	4.72	4.43	4.39	4.45	4.34	4.33	3.90	4.17
K_2O	0.04	0.00	0.04	0.05	0.05	0.04	0.05	0.04	0.04	0.00
Total	**100.26**	**100.39**	**100.93**	**100.95**	**101.09**	**100.59**	**100.62**	**100.60**	**99.99**	**99.87**
Si	2.44	2.45	2.37	2.34	2.35	2.35	2.35	2.34	2.33	2.35
Al	1.55	1.55	1.64	1.66	1.66	1.65	1.66	1.66	1.68	1.65
Fe	0.01	0.02	0.01	0.01	0.01	0.01	0.01	0.01	0.01	0.00
Ca	0.53	0.53	0.60	0.62	0.62	0.62	0.62	0.63	0.65	0.63
Na	0.46	0.47	0.41	0.39	0.38	0.39	0.38	0.38	0.34	0.37
K	0.00	0.00	0.00	0.00	0.00	0.00	0.00	0.00	0.00	0.00
Total	**5.01**	**5.01**	**5.02**	**5.02**	**5.02**	**5.02**	**5.01**	**5.02**	**5.01**	**5.01**
An	53.3	53.0	59.3	61.5	61.8	61.1	61.8	62.2	65.3	63.2
Ab	46.4	47.0	40.5	38.3	37.9	38.7	37.9	37.6	34.4	36.8
Or	0.2	0.0	0.2	0.3	0.3	0.2	0.3	0.2	0.2	0.0

Sample No.	**79-054**	**79-054**	**79-091**	**79-091**	**79-091**	**79-091**	**79-091**	**79-091**	**79-115**	**79-115**
Intrusion	Nittis	Nittis	Nittis	Nittis	Nittis	Nittis	Nittis	Nittis	Nittis	Nittis
Sample Pt.	Pl 2	Pl 3	Pl 1	Pl 1	Pl 2	Pl 2	Pl 3	Pl 3	Pl 1	Pl 1
Rock type	OPX	OPX	OPX	OPX	OPX	OPX	OPX	OPX	OPX	OPX
SiO_2 (wt %)	51.85	51.36	50.57	50.72	50.96	51.34	51.98	52.07	54.27	54.25
Al_2O_3	30.61	30.59	31.48	31.29	31.04	30.53	30.61	30.57	28.81	28.87
FeO	0.22	0.24	0.22	0.30	0.24	0.10	0.32	0.22	0.39	0.24
CaO	12.77	12.24	13.70	13.53	13.26	12.84	12.65	12.68	10.59	10.66
Na_2O	4.30	4.08	3.65	3.77	3.94	4.14	4.30	4.30	5.47	5.47
K_2O	0.00	0.27	0.02	0.02	0.04	0.00	0.04	0.04	0.06	0.07
Total	**99.76**	**98.79**	**99.64**	**99.64**	**99.48**	**98.96**	**99.90**	**99.87**	**99.60**	**99.57**
Si	2.36	2.36	2.31	2.32	2.33	2.35	2.36	2.36	2.46	2.46
Al	1.64	1.66	1.69	1.68	1.67	1.65	1.64	1.64	1.54	1.54
Fe	0.01	0.01	0.01	0.01	0.01	0.00	0.01	0.01	0.01	0.01
Ca	0.62	0.60	0.67	0.66	0.65	0.63	0.62	0.62	0.51	0.52
Na	0.38	0.36	0.32	0.33	0.35	0.37	0.38	0.38	0.48	0.48
K	0.00	0.02	0.00	0.00	0.00	0.00	0.00	0.00	0.00	0.00
Total	**5.01**	**5.00**	**5.01**	**5.01**	**5.01**	**5.01**	**5.01**	**5.01**	**5.01**	**5.01**
An	62.1	61.4	67.4	66.4	64.9	63.2	61.8	61.8	51.5	51.6
Ab	37.9	37.0	32.5	33.5	34.9	36.8	38.0	38.0	48.2	48.0
Or	0.0	1.6	0.1	0.1	0.2	0.0	0.2	0.2	0.3	0.4

OPX = orthopyroxenite; MNO = melanorite; BRC = breccia; oph = ophitic; xeno = xenolith

Table D.4 (cont.)

Sample No.	**79-115**	**79-115**	**79-115**	**79-115**	**79-115**	**79-115**	**79-115**	**79-115**	**79-131**	**79-131**
Intrusion	Nittis	Nittis	Nittis	Nittis	Nittis	Nittis	Nittis	Nittis	Nittis	Nittis
Sample Pt.	Pl 1	Pl 2	Pl 2	Pl 3	Pl 3	Pl 3	Pl 4	Pl 4	Pl 1	Pl 1
Rock type	OPX	OPX	OPX	OPX	OPX	OPX	OPX	OPX	OPX	OPX
SiO_2 (wt %)	54.40	53.89	54.06	52.11	51.19	51.66	54.23	53.35	51.83	54.19
Al_2O_3	28.76	29.06	28.89	30.69	32.61	30.72	29.00	29.33	31.31	29.68
FeO	0.37	0.27	0.17	0.24	0.22	0.12	0.14	0.44	0.09	0.09
CaO	10.52	10.89	10.79	12.66	13.21	12.76	10.80	11.28	13.29	11.36
Na_2O	5.58	5.30	5.41	4.34	3.92	4.29	5.39	5.14	4.19	5.19
K_2O	0.07	0.07	0.07	0.06	0.04	0.00	0.05	0.04	0.00	0.05
Total	**99.71**	**99.47**	**99.38**	**100.10**	**101.19**	**99.55**	**99.62**	**99.56**	**100.72**	**100.56**
Si	2.46	2.45	2.45	2.36	2.30	2.35	2.46	2.43	2.34	2.43
Al	1.53	1.55	1.55	1.64	1.73	1.65	1.55	1.57	1.66	1.57
Fe	0.01	0.01	0.01	0.01	0.01	0.00	0.01	0.02	0.00	0.00
Ca	0.51	0.53	0.52	0.61	0.64	0.62	0.52	0.55	0.64	0.55
Na	0.49	0.47	0.48	0.38	0.34	0.38	0.47	0.45	0.37	0.45
K	0.00	0.00	0.00	0.00	0.00	0.00	0.00	0.00	0.00	0.00
Total	**5.02**	**5.01**	**5.01**	**5.01**	**5.01**	**5.01**	**5.01**	**5.02**	**5.01**	**5.01**
An	50.8	53.0	52.2	61.5	64.9	62.2	52.4	54.7	63.7	54.6
Ab	48.8	46.6	47.4	38.1	34.9	37.8	47.3	45.1	36.3	45.1
Or	0.4	0.4	0.4	0.3	0.2	0.0	0.3	0.2	0.0	0.3

Sample No.	**79-131**	**79-131**	**79-131**	**79-131**	**79-131**	**79-138**	**79-138**	**79-138**	**79-138**	**79-138**
Intrusion	Nittis	Nittis	Nittis	Nittis	Nittis	Nittis	Nittis	Nittis	Nittis	Nittis
Sample Pt.	Pl 2	Pl 2	Pl 2	Pl 3	Pl 3	Pl 1	Pl 1	Pl 1	Pl 2	Pl 3
Rock type	OPX	OPX	OPX	OPX	OPX	OPX	OPX	OPX	OPX	OPX
SiO_2 (wt %)	52.00	52.73	52.37	51.88	51.98	51.58	51.32	51.34	53.20	51.04
Al_2O_3	30.91	30.99	30.69	31.48	31.06	30.48	30.61	30.67	29.23	30.89
FeO	0.14	0.08	0.14	0.19	0.14	0.21	0.14	0.21	0.15	0.17
CaO	12.84	12.76	12.68	13.31	13.03	12.69	12.82	12.83	11.28	13.11
Na_2O	4.27	4.46	4.45	4.11	4.19	4.27	4.19	4.12	5.04	4.03
K_2O	0.06	0.04	0.00	0.04	0.05	0.00	0.00	0.06	0.00	0.00
Total	**100.24**	**101.05**	**100.32**	**101.00**	**100.45**	**99.22**	**99.08**	**99.23**	**98.91**	**99.24**
Si	2.35	2.37	2.37	2.33	2.35	2.36	2.35	2.35	2.43	2.34
Al	1.65	1.64	1.63	1.67	1.65	1.64	1.65	1.65	1.57	1.67
Fe	0.01	0.00	0.01	0.01	0.01	0.01	0.01	0.01	0.01	0.01
Ca	0.62	0.61	0.61	0.64	0.63	0.62	0.63	0.63	0.55	0.64
Na	0.38	0.39	0.39	0.36	0.37	0.38	0.37	0.37	0.45	0.36
K	0.00	0.00	0.00	0.00	0.00	0.00	0.00	0.00	0.00	0.00
Total	**5.01**	**5.01**	**5.01**	**5.01**	**5.01**	**5.01**	**5.01**	**5.01**	**5.01**	**5.01**
An	62.2	61.1	61.2	64.0	63.0	62.1	62.8	63.0	55.3	64.3
Ab	37.4	38.7	38.8	35.8	36.7	37.9	37.2	36.7	44.7	35.7
Or	0.3	0.2	0.0	0.2	0.3	0.0	0.0	0.4	0.0	0.0

Sample No.	**79-138**	**79-147**	**79-147**	**79-147**	**79-147**	**79-160**	**79-160**	**79-160**	**79-160**	**79-160**
Intrusion	Nittis	Nittis	Nittis	Nittis	Nittis	Nittis	Nittis	Nittis	Nittis	Nittis
Sample Pt.	Pl 3	Pl 1	Pl 1	Pl 2	Pl 2	Pl 1	Pl 1	Pl 2	Pl 2	Pl 2
Rock type	OPX	OPX xeno	OPX xeno	OPX xeno	OPX xeno	OPX	OPX	OPX	OPX	OPX
SiO_2 (wt %)	51.90	47.88	48.28	49.25	49.16	51.96	51.66	51.22	50.89	51.52
Al_2O_3	30.44	32.82	32.50	31.91	32.10	30.65	30.97	31.50	31.38	31.16
FeO	0.18	0.14	0.05	0.09	0.22	0.21	0.17	0.13	0.32	0.22
CaO	12.54	15.52	15.15	14.36	14.68	12.86	13.00	13.67	13.57	13.35
Na_2O	4.34	2.70	2.84	3.24	3.22	4.45	4.29	3.94	3.96	4.08
K_2O	0.00	0.02	0.04	0.04	0.04	0.04	0.07	0.02	0.10	0.05
Total	**99.39**	**99.08**	**98.87**	**98.88**	**99.42**	**100.16**	**100.16**	**100.47**	**100.23**	**100.37**
Si	2.37	2.21	2.23	2.27	2.26	2.36	2.34	2.32	2.31	2.33
Al	1.64	1.79	1.77	1.73	1.74	1.64	1.66	1.68	1.68	1.66
Fe	0.01	0.01	0.00	0.00	0.01	0.01	0.01	0.00	0.01	0.01
Ca	0.61	0.77	0.75	0.71	0.72	0.62	0.63	0.66	0.66	0.65
Na	0.38	0.24	0.25	0.29	0.29	0.39	0.38	0.35	0.35	0.36
K	0.00	0.00	0.00	0.00	0.00	0.00	0.00	0.00	0.01	0.00
Total	**5.01**	**5.02**	**5.01**	**5.01**	**5.02**	**5.02**	**5.02**	**5.01**	**5.02**	**5.02**
An	61.5	76.0	74.5	70.9	71.4	61.4	62.4	65.7	65.1	64.2
Ab	38.5	23.9	25.3	28.9	28.4	38.4	37.2	34.2	34.4	35.5
Or	0.0	0.1	0.2	0.2	0.2	0.2	0.4	0.1	0.6	0.3

OPX = orthopyroxenite; MNO = melanorite; BRC = breccia; oph = ophitic; xeno = xenolith

Table D.4 (cont.)

Sample No.	**79-160**	**79-160**	**79-160**	**79-160**	**94-013**	**94-013**	**94-013**	**94-013**	**94-013**	**94-038**
Intrusion	Nittis	Nittis	Nittis	Nittis	Nittis	Nittis	Nittis	Nittis	Nittis	Nittis
Sample Pt.	Pl 3	Pl 3	Pl 4	Pl 4	Pl 1	Pl 2	Pl 2	Pl 2	Pl 3	Pl 1
Rock type	OPX	OPX	OPX	OPX	OPX	OPX	OPX	OPX	OPX	OPX
SiO_2 (wt %)	51.94	50.98	51.88	51.77	57.67	57.18	57.48	56.35	55.73	53.67
Al_2O_3	31.01	31.37	31.08	31.18	28.06	28.36	28.46	27.55	28.93	29.50
FeO	0.32	0.26	0.15	0.24	0.21	0.26	0.19	0.76	0.26	0.15
CaO	13.01	13.52	13.12	13.12	8.84	9.19	9.14	9.09	9.88	11.46
Na_2O	4.29	4.21	4.26	4.26	6.70	6.50	6.55	6.42	6.08	5.26
K_2O	0.04	0.07	0.06	0.04	0.04	0.04	0.04	0.00	0.05	0.07
Total	**100.61**	**100.40**	**100.56**	**100.61**	**101.52**	**101.53**	**101.85**	**100.17**	**100.92**	**100.11**
Si	2.35	2.31	2.34	2.34	2.55	2.53	2.53	2.53	2.49	2.43
Al	1.65	1.68	1.66	1.66	1.46	1.48	1.48	1.46	1.52	1.57
Fe	0.01	0.01	0.01	0.01	0.01	0.01	0.01	0.03	0.01	0.01
Ca	0.63	0.66	0.64	0.64	0.42	0.44	0.43	0.44	0.47	0.55
Na	0.38	0.37	0.37	0.37	0.57	0.56	0.56	0.56	0.53	0.46
K	0.00	0.00	0.00	0.00	0.00	0.00	0.00	0.00	0.00	0.00
Total	**5.02**	**5.03**	**5.02**	**5.02**	**5.01**	**5.01**	**5.01**	**5.02**	**5.02**	**5.02**
An	62.5	63.7	62.8	62.9	42.1	43.8	43.4	43.9	47.2	54.4
Ab	37.3	35.9	36.9	36.9	57.7	56.0	56.4	56.1	52.5	45.2
Or	0.2	0.4	0.3	0.2	0.2	0.2	0.2	0.0	0.3	0.4

Sample No.	**94-038**	**94-038**	**94-038**	**94-081**	**94-081**	**94-081**	**94-081**	**94-081**	**94-081**	**94-081**
Intrusion	Nittis	Nittis	Nittis	Nittis	Nittis	Nittis	Nittis	Nittis	Nittis	Nittis
Sample Pt.	Pl 2	Pl 3	Pl 3	Pl 1	Pl 1	Pl 1	Pl 2	Pl 2	Pl 2	Pl 2
Rock type	OPX	OPX	OPX	OPX	OPX	OPX	OPX	OPX	OPX	OPX
SiO_2 (wt %)	53.03	50.85	50.40	52.71	52.47	52.62	54.98	54.85	54.98	54.85
Al_2O_3	30.06	30.25	30.95	29.63	29.48	29.68	28.64	28.63	28.64	28.63
FeO	0.31	0.48	0.54	0.36	0.45	0.32	0.44	0.40	0.44	0.40
CaO	12.01	12.76	13.18	11.73	11.75	11.81	10.38	10.38	10.38	10.38
Na_2O	4.74	4.11	3.83	4.79	4.79	4.79	5.74	5.69	5.74	5.69
K_2O	0.00	0.00	0.00	0.08	0.04	0.05	0.05	0.06	0.05	0.06
Total	**100.15**	**98.45**	**98.90**	**99.29**	**98.98**	**99.27**	**100.23**	**100.00**	**100.23**	**100.00**
Si	2.40	2.35	2.32	2.40	2.40	2.40	2.48	2.47	2.48	2.47
Al	1.60	1.65	1.68	1.59	1.59	1.60	1.52	1.52	1.52	1.52
Fe	0.01	0.02	0.02	0.01	0.02	0.01	0.02	0.02	0.02	0.02
Ca	0.58	0.63	0.65	0.57	0.58	0.58	0.50	0.50	0.50	0.50
Na	0.42	0.37	0.34	0.42	0.42	0.42	0.50	0.50	0.50	0.50
K	0.00	0.00	0.00	0.00	0.00	0.00	0.00	0.00	0.00	0.00
Total	**5.01**	**5.01**	**5.01**	**5.01**	**5.01**	**5.01**	**5.02**	**5.01**	**5.02**	**5.01**
An	58.3	63.2	65.5	57.2	57.5	57.5	49.8	50.0	49.8	50.0
Ab	41.7	36.8	34.5	42.3	42.3	42.2	49.9	49.6	49.9	49.6
Or	0.0	0.0	0.0	0.5	0.2	0.3	0.3	0.3	0.3	0.3

Sample No.	**94-081**	**94-081**	**94-081**	**94-081**	**94-081**	**94-118**	**94-118**	**1815-011**	**1815-011**	**1815-011**
Intrusion	Nittis	Nittis	Nittis	Nittis	Nittis	Nittis	Nittis	Nyud	Nyud	Nyud
Sample Pt.	Pl 3	Pl 3	Pl 3	Pl 4	Pl 4	Pl 1	Pl 1	Pl 1	Pl 1	Pl 2
Rock type	OPX	OPX	OPX	OPX	OPX	OPX	OPX	MNO	MNO	MNO
SiO_2 (wt %)	52.71	52.71	52.71	52.47	52.62	57.63	57.27	51.02	50.89	51.02
Al_2O_3	30.04	29.63	30.04	29.48	29.68	26.89	26.93	30.99	30.78	30.80
FeO	0.51	0.36	0.51	0.45	0.32	0.23	0.22	0.35	0.42	0.31
CaO	11.94	11.73	11.94	11.75	11.81	8.30	8.48	13.24	13.03	13.14
Na_2O	4.68	4.79	4.68	4.79	4.79	6.94	6.83	3.88	3.88	3.99
K_2O	0.13	0.08	0.13	0.04	0.05	0.00	0.00	0.08	0.24	0.06
Total	**100.01**	**99.29**	**100.01**	**98.98**	**99.27**	**99.99**	**99.72**	**99.56**	**99.25**	**99.32**
Si	2.39	2.40	2.39	2.40	2.40	2.58	2.57	2.33	2.33	2.34
Al	1.61	1.59	1.61	1.59	1.60	1.42	1.43	1.67	1.66	1.66
Fe	0.02	0.01	0.02	0.02	0.01	0.01	0.01	0.01	0.02	0.01
Ca	0.58	0.57	0.58	0.58	0.58	0.40	0.41	0.65	0.64	0.64
Na	0.41	0.42	0.41	0.42	0.42	0.60	0.60	0.34	0.35	0.35
K	0.01	0.00	0.01	0.00	0.00	0.00	0.00	0.00	0.01	0.00
Total	**5.02**	**5.01**	**5.02**	**5.01**	**5.01**	**5.01**	**5.01**	**5.01**	**5.01**	**5.01**
An	58.1	57.2	58.1	57.5	57.5	39.8	40.7	65.0	64.0	64.3
Ab	41.2	42.3	41.2	42.3	42.2	60.2	59.3	34.5	34.5	35.3
Or	0.8	0.5	0.8	0.2	0.3	0.0	0.0	0.5	1.4	0.4

OPX = orthopyroxenite; MNO = melanorite; BRC = breccia; oph = ophitic; xeno = xenolith

Table D.4 (cont.)

Sample No.	**1815-011**	**1815-011**	**1815-011**	**1815-011**	**1815-046**	**1815-046**	**1815-046**	**1815-046**
Intrusion	Nyud	Nyud	Nyud	Nyud	Nyud	Nyud	Nyud	Nyud
Sample Pt.	Pl 2	Pl 3	Pl 4	Pl 4	Pl 1	Pl 1	Pl 1	Pl 2
Rock type	MNO	MNO	MNO	MNO	MNO	MNO	MNO	MNO
SiO_2 (wt %)	51.11	49.84	51.40	51.79	50.87	50.85	51.08	51.43
Al_2O_3	31.04	32.05	30.89	30.72	31.12	30.99	31.35	31.25
FeO	0.33	0.49	0.39	0.41	0.28	0.42	0.36	0.35
CaO	13.25	14.30	13.11	13.19	13.42	13.45	13.56	12.30
Na_2O	3.88	3.29	4.02	3.95	3.84	3.79	3.76	3.81
K_2O	0.06	0.10	0.00	0.27	0.04	0.05	0.13	0.76
Total	**99.68**	**100.06**	**99.81**	**100.33**	**99.57**	**99.54**	**100.24**	**99.90**
Si	2.33	2.27	2.34	2.35	2.32	2.33	2.32	2.34
Al	1.67	1.72	1.66	1.64	1.68	1.67	1.68	1.68
Fe	0.01	0.02	0.01	0.02	0.01	0.02	0.01	0.01
Ca	0.65	0.70	0.64	0.64	0.66	0.66	0.66	0.60
Na	0.34	0.29	0.35	0.35	0.34	0.34	0.33	0.34
K	0.00	0.01	0.00	0.02	0.00	0.00	0.01	0.04
Total	**5.01**	**5.01**	**5.01**	**5.01**	**5.01**	**5.01**	**5.01**	**5.01**
An	65.1	70.2	64.3	63.9	65.7	66.0	66.1	61.2
Ab	34.5	29.2	35.7	34.6	34.1	33.7	33.2	34.3
Or	0.4	0.6	0.0	1.5	0.2	0.3	0.8	4.5

OPX = orthopyroxenite; MNO = melanorite; BRC = breccia; oph = ophitic; xeno = xenolith

E Whole rock geochemical analyses

Table E.1. Whole rock geochemical data of Monchegorsk samples

Sample No.	**15DB-1**	**15DB-4**	**15DB-2**	**15DB-3**	**15KMAS-1**	**15KMAS-2**	**15KMAS-5**	**15KMAS-6**	**15KMAS-3**
Intrusion	Dunite Block	Dunite Block	Dunite Block	Dunite Block	Kumuzhya	Kumuzhya	Kumuzhya	Kumuzhya	Kumuzhya
Sample type	Outcrop	Outcrop	Outcrop	Outcrop	Outcrop	Outcrop	Outcrop	Outcrop	Outcrop
Rock type	CHR	DUN	LH	LH	HZ	OL-OPX	OL-OPX	OL-OPX	OL-OPX
SiO_2 (wt %)	17.48	30.74	39.68	39.15	44.60	48.87	47.52	47.48	49.60
TiO_2	0.20	0.08	0.06	0.07	0.07	0.10	0.09	0.09	0.09
Al_2O_3	10.98	2.36	1.56	1.77	1.40	1.83	1.85	1.96	1.88
Fe_2O_{3T}	22.15	11.87	8.82	8.92	10.78	8.80	9.53	9.25	8.79
MnO	0.22	0.12	0.13	0.14	0.17	0.17	0.17	0.17	0.17
MgO	22.38	36.07	40.97	38.11	39.97	35.67	38.03	34.68	34.69
CaO	0.05	1.29	1.59	1.83	1.20	1.70	1.59	1.67	1.66
Na_2O	5.38	2.60	4.80	2.48	0.00	0.98	0.97	4.49	1.00
K_2O	0.00	0.02	0.03	0.10	0.01	0.01	0.01	0.02	0.01
P_2O_5	0.05	0.04	0.04	0.04	0.01	0.05	0.04	0.04	0.04
LOI	0.9	6.1	3.1	5.6	0.2	0.1	0.0	0.1	0.1
Total	89.66	91.27	100.78	98.18	98.43	98.29	99.82	99.94	98.08
Sc (ppm)	6	8	10	11	14	19	18	19	20
V	340	78	36	38	37	43	43	72	38
Cr	143659	61744	2155	7077	3016	3837	3441	3865	3818
Co	66.4	48.4	119.3	36.9	49.1	38.3	42.3	88.5	38.2
Ni	833.8	1683.8	1217.2	1221.4	1393.4	628.7	854.6	657.8	624.9
Cu	105.3	100.3	77.8	80.9	28.1	81.7	23.5	23.5	21.5
Zn	983	95	72	54	74	80	68	71	55
Rb	0.5	0.6	1.0	1.5	1.1	0.8	0.8	0.6	0.8
Sr	5.9	12.6	21.9	17.9	16.8	11.4	17.9	16.4	13.6
Y	0.5	1.7	2.1	1.9	1.1	2.0	1.8	1.7	2.0
Zr	0.0	2.3	2.8	7.2	25.1	4.4	4.8	6.4	4.9
Nb	0.5	0.8	0.1	0.1	2.6	1.2	0.2	0.5	0.2
Cs	0.1	0.0	0.1	0.1	0.1	0.0	0.0	0.0	0.0
Ba	5	2	12	19	13	12	12	11	15
La	0.1	0.2	0.3	0.3	0.6	0.5	0.6	0.4	0.5
Ce	0.2	0.7	0.8	0.8	1.2	1.0	1.3	0.8	1.1
Pr	0.0	0.1	0.1	0.1	0.2	0.2	0.2	0.1	0.1
Nd	0.1	0.7	0.7	0.6	0.7	0.6	0.7	0.5	0.6
Sm	0.0	0.2	0.2	0.2	0.2	0.2	0.2	0.2	0.2
Eu	0.0	0.1	0.1	0.1	0.1	0.1	0.1	0.1	0.1
Gd	0.0	0.2	0.2	0.2	0.2	0.2	0.2	0.2	0.2
Tb	0.0	0.0	0.0	0.0	0.0	0.0	0.0	0.0	0.0
Dy	0.0	0.2	0.3	0.2	0.2	0.2	0.2	0.2	0.2
Ho	0.0	0.0	0.0	0.0	0.0	0.0	0.0	0.0	0.0
Er	0.0	0.1	0.2	0.2	0.1	0.2	0.2	0.1	0.2
Tm	0.0	0.0	0.0	0.0	0.0	0.0	0.0	0.0	0.0
Yb	0.1	0.1	0.2	0.2	0.1	0.2	0.2	0.2	0.2
Lu	0.0	0.0	0.0	0.0	0.0	0.0	0.0	0.0	0.0
Hf	0.0	0.0	0.0	0.1	0.6	0.1	0.1	0.1	0.1
Ta	0.0	0.1	0.0	0.0	0.1	0.1	0.0	0.0	0.0
Th	0.4	0.1	0.1	0.1	3.3	0.3	0.2	0.2	0.2
U	0.0	0.0	0.0	0.0	0.1	0.0	0.0	0.0	0.0
S	137	214	142	53	161	106	147	122	45
Os (ppb)	n.d.	25.9	0.5	1.2	0.2	0.1	0.1	0.9	0.2
Ir	n.d.	17.21	0.52	1.23	2.29	1.63	1.17	4.40	1.68
Ru	n.d.	47.87	2.99	7.67	1.71	1.17	0.99	3.23	1.30
Rh	n.d.	6.40	1.45	1.49	10.54	7.11	5.45	17.49	7.31
Pt	n.d.	1.3	1.5	5.4	22.5	14.5	16.3	75.1	18.4
Pd	n.d.	6.6	2.2	7.8	140.4	78.5	68.2	339.7	65.9
Au	n.d.	1.1	1.0	1.1	3.7	2.6	2.4	0.6	1.7

CHR = chromitite; DUN = dunite; LH = lherzolite; HZ = harzburgite; OL-WEB = olivine-websterite;
OL-OPX = olivine-orthopyroxenite; OPX = orthopyroxenite; NO = Norite; MNO = melanorite;
GN = gabbronorite; LGN = leucogabbronorite; AN = anorthosite; DOL = dolerite; MS = massive sulfide;
PEGM = pegmatite; TON = tonalite; METASED = metasediment; BRC = breccia; oph = ophitic

Table E.1 (cont.)

Sample No.	**15KMAS-7**	**753-184**	**15MT-03**	**15MT-05**	**15MT-08**	**15MT-09**	**15MT-10**	**15MT-11**	**15MT-12**
Intrusion	Kumuzhya	Monchetundra	Monchetundra	Monchetundra	Monchetundra	Monchetundra	Monchetundra	Monchetundra	Monchetundra
Sample type	Outcrop	Drill core	Outcrop	Outcrop	Outcrop	Outcrop	Outcrop	Outcrop	Outcrop
Rock type	OL-OPX	NO	AN	AN	AN	AN	AN	AN	AN
SiO_2 (wt %)	51.20	49.87	55.47	52.03	50.09	50.46	55.59	49.77	51.76
TiO_2	0.09	0.11	0.31	0.51	0.15	0.30	0.17	0.92	0.24
Al_2O_3	1.85	8.38	19.75	23.68	23.22	24.83	25.00	22.75	23.33
Fe_2O_{3T}	8.89	12.23	5.59	5.45	6.22	4.46	2.95	8.01	5.25
MnO	0.17	0.18	0.10	0.09	0.07	0.07	0.04	0.12	0.08
MgO	33.37	18.33	3.99	1.64	4.92	2.73	0.48	2.80	3.38
CaO	1.67	5.32	11.00	11.92	11.99	12.74	11.92	12.23	12.41
Na_2O	2.59	3.23	2.91	2.93	2.68	2.77	2.46	2.69	2.94
K_2O	0.05	0.21	0.20	0.29	0.16	0.19	0.41	0.22	0.21
P_2O_5	0.04	0.00	0.06	0.06	0.02	0.02	0.07	0.04	0.02
LOI	0.1	1.1	0.4	0.3	0.4	0.4	0.4	0.2	0.3
Total	99.97	98.99	99.81	98.91	99.88	98.96	99.51	99.78	99.89
Sc (ppm)	22	22	20	15	15	15	6	20	23
V	47	79	104	202	52	82	24	315	103
Cr	3788	483	23	29	46	32	42	20	54
Co	37.7	52.9	24.2	24.2	36.8	19.2	8.0	24.5	23.0
Ni	537.8	657.0	141.1	25.2	127.6	30.8	6.4	246.2	35.7
Cu	96.5	3348.4	108.2	53.6	64.1	200.6	31.0	108.3	41.9
Zn	60	107	34	25	13	13	47	39	18
Rb	0.5	4.3	5.9	1.6	2.2	2.7	5.2	3.0	2.4
Sr	10.2	46.5	330.1	269.7	286.9	300.9	318.1	261.8	267.9
Y	1.7	3.2	7.8	6.4	3.2	5.2	9.9	8.1	5.6
Zr	3.5	6.4	34.3	19.7	20.9	14.6	59.1	32.6	22.1
Nb	0.2	0.2	2.9	0.9	1.1	1.1	1.1	1.5	1.0
Cs	0.0	0.3	0.3	0.1	0.1	0.1	0.2	0.2	0.1
Ba	8	23	113	66	44	69	125	83	66
La	0.3	2.4	4.5	2.7	1.4	2.3	5.4	3.2	1.9
Ce	0.7	4.3	9.5	5.6	3.0	4.6	11.4	6.9	4.0
Pr	0.1	0.5	1.3	0.8	0.4	0.6	1.5	1.0	0.6
Nd	0.5	1.6	5.2	3.1	1.7	2.6	5.8	3.9	2.4
Sm	0.2	0.4	1.3	0.8	0.4	0.7	1.4	0.9	0.6
Eu	0.1	0.2	0.5	0.5	0.3	0.4	0.6	0.5	0.4
Gd	0.2	0.4	1.1	0.9	0.4	0.7	1.4	1.0	0.7
Tb	0.0	0.1	0.2	0.1	0.1	0.1	0.2	0.2	0.1
Dy	0.2	0.4	1.2	1.0	0.5	0.8	1.5	1.2	0.9
Ho	0.1	0.1	0.2	0.2	0.1	0.2	0.3	0.2	0.2
Er	0.2	0.3	0.7	0.6	0.3	0.5	0.9	0.7	0.6
Tm	0.0	0.1	0.1	0.1	0.0	0.1	0.2	0.1	0.1
Yb	0.2	0.4	0.8	0.6	0.3	0.5	1.0	0.8	0.6
Lu	0.1	0.1	0.1	0.1	0.1	0.1	0.2	0.1	0.1
Hf	0.1	0.1	0.9	0.4	0.5	0.4	1.2	0.8	0.5
Ta	0.0	0.0	0.2	0.1	0.1	0.1	0.1	0.1	0.1
Th	0.1	0.8	0.5	0.9	0.2	0.3	0.9	0.4	0.2
U	0.0	0.0	0.1	0.1	0.0	0.1	0.2	0.1	0.1
S	78	7189	b.d.l	b.d.l	b.d.l	b.d.l	b.d.l	b.d.l	b.d.l
Os (ppb)	0.1	1.4	b.d.l	b.d.l	b.d.l	b.d.l	b.d.l	b.d.l	b.d.l
Ir	1.14	3.56	0.06	0.10	0.08	b.d.l	b.d.l	b.d.l	b.d.l
Ru	0.83	2.82	b.d.l	0.25	0.42	b.d.l	b.d.l	b.d.l	b.d.l
Rh	4.51	15.63	0.20	b.d.l	0.21	b.d.l	b.d.l	b.d.l	b.d.l
Pt	10.3	249.0	9.2	b.d.l	0.6	0.1	0.7	0.4	b.d.l
Pd	40.6	196.4	4.0	b.d.l	1.1	b.d.l	b.d.l	b.d.l	0.6
Au	3.1	57.7	6.0	b.d.l	b.d.l	b.d.l	b.d.l	1.3	b.d.l

CHR = chromitite; DUN = dunite; LH = lherzolite; HZ = harzburgite; OL-WEB = olivine-websterite;
OL-OPX = olivine-orthopyroxenite; OPX = orthopyroxenite; NO = Norite; MNO = melanorite;
GN = gabbronorite; LGN = leucogabbronorite; AN = anorthosite; DOL = dolerite; MS = massive sulfide;
PEGM = pegmatite; TON = tonalite; METASED = metasediment; BRC = breccia; oph = ophitic

Table E.1 (cont.)

Sample No.	**15MT-13**	**15MT-14**	**15MT-16**	**15MT-18**	**15MT-19**	**15MT-01**	**15MT-02**	**15MT-04**	**15MT-06**
Intrusion	Monchetundra	Monchetundra	Monchetundra	Monchetundra	Monchetundra	Monchetundra	Monchetundra	Monchetundra	Monchetundra
Sample type	Outcrop	Outcrop	Outcrop	Outcrop	Outcrop	Outcrop	Outcrop	Outcrop	Outcrop
Rock type	AN	AN	AN	AN	AN	LGN	LGN	LGN	LGN
SiO_2 (wt %)	53.26	51.91	53.04	48.73	51.48	52.55	53.19	52.44	53.48
TiO_2	0.29	0.23	0.31	0.14	0.54	0.19	0.16	0.19	0.27
Al_2O_3	23.36	22.23	24.53	22.52	26.01	16.69	15.80	16.44	16.68
Fe_2O_{3T}	5.40	5.52	4.71	8.21	5.07	7.13	8.33	9.29	7.96
MnO	0.08	0.09	0.06	0.10	0.06	0.14	0.16	0.17	0.14
MgO	2.25	3.41	1.63	4.90	0.54	7.36	8.38	7.73	6.59
CaO	10.99	12.49	12.39	10.56	12.08	11.92	10.90	11.22	12.69
Na_2O	3.39	2.88	3.25	2.58	3.16	2.99	1.76	2.17	2.37
K_2O	0.25	0.37	0.21	0.18	0.43	0.15	0.18	0.13	0.20
P_2O_5	0.08	0.04	0.04	0.02	0.08	0.04	0.01	0.01	0.03
LOI	0.6	0.5	0.4	0.4	0.3	0.4	0.3	0.5	0.3
Total	99.93	99.63	100.61	98.31	99.73	99.56	99.21	100.28	100.67
Sc (ppm)	16	24	10	9	8	38	32	36	39
V	69	87	95	47	59	139	96	126	145
Cr	9	56	14	5	10	25	16	28	7
Co	23.8	24.1	20.6	44.6	12.1	22.0	45.6	40.3	37.8
Ni	11.8	26.1	5.7	114.4	6.6	85.3	160.2	109.6	112.1
Cu	120.5	81.3	51.4	40.3	43.4	30.5	54.6	235.2	101.9
Zn	15	35	54	22	30	56	46	71	56
Rb	5.8	9.2	6.3	2.5	9.7	1.5	2.6	2.8	2.9
Sr	321.9	274.6	317.4	244.8	320.8	288.2	148.8	190.0	263.0
Y	14.3	9.8	8.6	3.4	13.5	6.5	4.1	5.2	7.4
Zr	90.9	42.0	44.6	19.5	60.5	4.0	21.6	9.7	21.0
Nb	1.8	1.2	2.0	0.7	3.3	0.3	0.4	0.5	0.8
Cs	0.1	0.2	0.3	0.1	0.2	0.1	0.1	0.2	0.1
Ba	99	133	95	64	136	62	48	56	72
La	7.6	4.1	4.3	1.8	7.1	1.5	0.7	1.7	2.4
Ce	15.7	8.6	9.3	3.6	15.7	3.0	1.6	3.2	5.0
Pr	2.2	1.2	1.2	0.5	2.1	0.5	0.2	0.4	0.7
Nd	8.6	5.0	5.0	2.0	8.3	2.1	1.1	2.1	3.3
Sm	2.1	1.3	1.3	0.4	2.0	0.6	0.3	0.6	0.9
Eu	0.8	0.6	0.5	0.4	0.6	0.3	0.2	0.3	0.4
Gd	2.0	1.2	1.2	0.5	1.9	0.8	0.4	0.7	0.9
Tb	0.3	0.2	0.2	0.1	0.3	0.1	0.1	0.1	0.2
Dy	2.3	1.6	1.4	0.5	2.1	0.9	0.6	0.8	1.1
Ho	0.4	0.3	0.3	0.1	0.4	0.2	0.1	0.2	0.2
Er	1.4	0.9	0.8	0.3	1.2	0.5	0.4	0.5	0.7
Tm	0.2	0.2	0.1	0.1	0.2	0.1	0.1	0.1	0.1
Yb	1.4	1.0	0.8	0.3	1.3	0.6	0.4	0.6	0.7
Lu	0.2	0.2	0.1	0.1	0.2	0.1	0.1	0.1	0.1
Hf	2.2	0.9	1.1	0.4	1.4	0.1	0.5	0.3	0.5
Ta	0.1	0.1	0.1	0.0	0.2	0.0	0.0	0.0	0.0
Th	0.7	0.4	0.5	0.2	0.8	3.9	0.2	0.3	0.3
U	0.2	0.1	0.1	0.0	0.2	0.0	0.1	0.0	0.1
S	b.d.l	52	b.d.l	b.d.l	76	b.d.l	b.d.l	52	b.d.l
Os (ppb)	b.d.l	b.d.l	b.d.l	b.d.l	b.d.l	b.d.l	b.d.l	b.d.l	b.d.l
Ir	0.04	b.d.l	b.d.l	0.03	b.d.l	b.d.l	b.d.l	b.d.l	0.18
Ru	b.d.l	b.d.l	b.d.l	b.d.l	b.d.l	b.d.l	b.d.l	b.d.l	0.12
Rh	b.d.l	b.d.l	b.d.l	b.d.l	0.09	b.d.l	b.d.l	b.d.l	0.79
Pt	b.d.l	0.2	b.d.l	0.1	b.d.l	b.d.l	1.1	2.3	13.6
Pd	b.d.l	b.d.l	b.d.l	b.d.l	b.d.l	b.d.l	b.d.l	3.1	10.9
Au	1.5	b.d.l	b.d.l	b.d.l	b.d.l	1.0	1.7	0.7	2.9

CHR = chromitite; DUN = dunite; LH = lherzolite; HZ = harzburgite; OL-WEB = olivine-websterite;
OL-OPX = olivine-orthopyroxenite; OPX = orthopyroxenite; NO = Norite; MNO = melanorite;
GN = gabbronorite; LGN = leucogabbronorite; AN = anorthosite; DOL = dolerite; MS = massive sulfide;
PEGM = pegmatite; TON = tonalite; METASED = metasediment; BRC = breccia; oph = ophitic

Table E.1 (cont.)

Sample No.	**15MT-07**	**79-023**	**79-034**	**79-039**	**79-042**	**79-054**	**79-077**	**79-091**	**79-104**
Intrusion	Monchetundra	Nittis	Nittis	Nittis	Nittis	Nittis	Nittis	Nittis	Nittis
Sample type	Outcrop	Drill core	Drill core	Drill core	Drill core	Drill core	Drill core	Drill core	Drill core
Rock type	LGN	OPX	OPX	OPX	OPX	OPX	OPX	OPX	OPX
SiO_2 (wt %)	53.02	56.95	56.90	55.70	54.73	56.41	56.02	55.19	52.99
TiO_2	0.31	0.21	0.22	0.20	0.24	0.22	0.20	0.23	0.46
Al_2O_3	14.69	5.43	5.42	5.42	5.07	5.75	6.57	7.14	5.84
Fe_2O_{3T}	8.93	10.40	10.31	10.97	10.94	10.25	10.67	10.03	11.18
MnO	0.15	0.19	0.19	0.22	0.19	0.18	0.18	0.18	0.22
MgO	7.55	20.27	20.73	21.07	22.39	20.76	19.88	18.33	17.68
CaO	12.22	4.10	3.93	3.52	3.78	4.09	4.41	4.83	5.07
Na_2O	1.88	0.59	0.64	0.56	0.62	0.66	0.74	1.11	0.95
K_2O	0.13	0.12	0.12	0.56	0.15	0.13	0.23	0.25	0.40
P_2O_5	0.02	0.03	0.02	0.00	0.03	0.01	0.02	0.02	0.06
LOI	0.4	0.2	0.4	0.8	0.4	0.2	0.2	1.4	3.9
Total	99.33	98.49	98.86	99.02	98.58	98.71	99.12	98.68	98.71
Sc (ppm)	47	28	27	24	23	26	26	23	29
V	154	121	123	113	114	119	113	114	166
Cr	21	3196	3078	2834	2513	2799	2618	2320	2253
Co	49.1	67.0	74.3	62.9	58.0	73.4	73.2	61.7	66.2
Ni	135.6	660.7	661.6	990.4	648.6	690.0	691.2	560.4	597.1
Cu	152.8	70.5	72.0	648.6	407.1	328.1	68.8	124.5	97.4
Zn	37	79	70	107	76	63	68	96	86
Rb	1.0	3.2	3.2	15.8	3.3	2.7	4.9	6.5	7.0
Sr	228.1	55.9	59.7	40.0	55.2	67.1	75.8	103.0	108.2
Y	9.1	4.3	4.5	3.6	4.7	4.2	3.7	5.0	9.3
Zr	42.5	16.3	18.1	13.3	21.7	15.3	17.5	28.9	44.3
Nb	0.7	0.9	0.9	0.6	1.1	0.8	0.7	1.1	2.0
Cs	0.1	0.0	0.0	1.3	0.2	0.0	0.4	0.3	0.3
Ba	46	43	42	144	60	45	79	99	117
La	2.4	1.9	1.9	2.1	2.8	1.9	1.8	2.9	5.5
Ce	5.1	4.1	4.0	4.4	6.0	4.1	3.9	6.2	11.6
Pr	0.8	0.6	0.5	0.6	0.8	0.5	0.5	0.9	1.6
Nd	3.3	2.2	2.2	2.2	3.0	2.3	2.0	3.4	6.4
Sm	1.0	0.5	0.5	0.5	0.7	0.5	0.4	0.7	1.2
Eu	0.4	0.2	0.2	0.2	0.2	0.2	0.2	0.2	0.4
Gd	1.1	0.6	0.7	0.5	0.6	0.6	0.6	0.8	1.5
Tb	0.2	0.1	0.1	0.1	0.1	0.1	0.1	0.1	0.3
Dy	1.4	0.7	0.7	0.6	0.8	0.8	0.7	0.8	1.6
Ho	0.3	0.2	0.2	0.1	0.1	0.2	0.1	0.2	0.3
Er	0.8	0.4	0.4	0.3	0.4	0.4	0.4	0.5	0.9
Tm	0.1	0.1	0.1	0.1	0.1	0.1	0.1	0.1	0.1
Yb	0.9	0.5	0.5	0.4	0.4	0.6	0.5	0.6	1.0
Lu	0.1	0.1	0.1	0.1	0.1	0.1	0.1	0.1	0.1
Hf	0.9	0.3	0.3	0.3	0.5	0.3	0.3	0.6	1.1
Ta	0.0	0.1	0.1	0.0	0.1	0.0	0.0	0.1	0.1
Th	0.2	0.2	0.3	0.3	0.4	0.2	0.2	0.7	1.0
U	0.1	0.0	0.0	0.0	0.1	0.0	0.0	0.2	0.1
S	74	b.d.l.	344	453	700	381	300	224	300
Os (ppb)	b.d.l	0.4	0.2	0.2	0.1	0.1	0.0	b.d.l.	0.1
Ir	0.57	2.45	2.24	1.36	1.44	1.43	2.04	1.33	1.35
Ru	b.d.l	2.28	1.28	0.81	1.17	0.94	0.98	0.84	1.31
Rh	1.19	3.98	9.90	6.11	5.81	5.60	9.93	5.11	6.61
Pt	147.6	30.5	33.8	5050.4	7955.8	18.4	43.6	34.8	24.0
Pd	20.9	44.1	207.9	24545.2	24826.0	78.2	622.9	107.2	62.8
Au	34.1	5.3	4.4	963.9	728.3	3.2	11.6	8.2	5.1

CHR = chromitite; DUN = dunite; LH = lherzolite; HZ = harzburgite; OL-WEB = olivine-websterite;
OL-OPX = olivine-orthopyroxenite; OPX = orthopyroxenite; NO = Norite; MNO = melanorite;
GN = gabbronorite; LGN = leucogabbronorite; AN = anorthosite; DOL = dolerite; MS = massive sulfide;
PEGM = pegmatite; TON = tonalite; METASED = metasediment; BRC = breccia; oph = ophitic

Table E.1 (cont.)

Sample No.	**79-115**	**79-121**	**79-131**	**79-138**	**79-143**	**79-145**	**79-147**	**79-149**	**79-150**
Intrusion	Nittis	Nittis	Nittis	Nittis	Nittis	Nittis	Nittis	Nittis	Nittis
Sample type	Drill core	Drill core	Drill core	Drill core	Drill core	Drill core	Drill core	Drill core	Drill core
Rock type	OPX	OPX	OPX	OPX	Oph. OPX	OPX	PEGM	METASED	PEGM
SiO_2 (wt %)	56.04	50.85	52.75	50.63	54.94	47.86	55.73	40.50	72.97
TiO_2	0.30	0.29	0.31	0.30	0.13	0.14	0.20	0.32	0.02
Al_2O_3	7.70	6.49	8.06	6.98	3.44	6.59	7.57	26.81	16.29
Fe_2O_{3T}	10.76	13.93	10.77	12.86	11.25	19.85	13.65	18.81	0.18
MnO	0.19	0.19	0.20	0.17	0.19	0.21	0.20	0.06	0.00
MgO	17.91	19.56	19.58	19.68	24.06	16.07	16.63	7.69	0.08
CaO	5.60	4.43	5.52	4.98	2.49	3.95	3.48	0.35	2.69
Na_2O	1.04	0.59	0.92	0.76	0.14	0.54	0.79	0.27	4.08
K_2O	0.22	0.17	0.19	0.52	0.04	0.14	0.16	0.88	1.83
P_2O_5	0.04	0.00	0.04	0.01	0.01	0.00	0.06	0.00	0.07
LOI	0.3	2.2	0.5	1.8	1.7	1.9	0.6	4.5	1.0
Total	100.08	98.67	98.82	98.70	98.36	97.23	99.10	100.20	99.18
Sc (ppm)	28	23	23	22	21	36	31	17	0
V	137	123	126	123	104	145	134	476	3
Cr	2402	2127	1751	1615	2772	2069	1641	587	37
Co	96.0	156.7	59.2	150.8	72.0	1493.7	83.7	281.9	0.9
Ni	729.1	3950.3	568.0	4265.0	903.5	7186.2	898.0	6475.7	3.3
Cu	105.4	2055.3	86.4	2225.3	57.8	11286.3	348.8	1070.8	22.4
Zn	91	84	84	83	69	152	97	178	16
Rb	5.0	3.7	3.7	14.8	1.4	3.3	5.9	41.3	22.9
Sr	105.4	43.6	104.0	51.4	5.3	77.4	74.4	34.4	234.8
Y	6.7	5.5	6.5	7.2	2.0	4.4	7.4	1.7	5.3
Zr	32.4	22.8	26.9	41.0	11.0	6.0	14.7	56.3	49.3
Nb	1.3	1.2	1.3	1.6	0.7	0.6	0.6	2.0	1.0
Cs	0.1	0.2	0.2	0.8	0.0	0.2	0.5	3.0	0.1
Ba	76	43	75	177	18	34	69	163	259
La	3.6	2.8	3.4	3.9	0.7	2.1	5.3	9.4	5.1
Ce	7.8	5.9	7.6	8.8	1.6	4.1	10.3	17.9	9.1
Pr	1.0	0.8	1.0	1.2	0.3	0.5	1.2	1.9	1.0
Nd	4.2	3.2	3.9	4.6	1.0	1.8	4.7	6.2	2.7
Sm	0.8	0.7	0.9	1.0	0.3	0.4	0.9	1.0	0.6
Eu	0.3	0.2	0.3	0.4	0.1	0.2	0.2	0.2	1.1
Gd	1.1	0.8	0.9	1.0	0.3	0.5	1.0	0.7	0.7
Tb	0.2	0.1	0.2	0.2	0.1	0.1	0.2	0.1	0.1
Dy	1.1	0.9	1.0	1.1	0.3	0.6	1.2	0.3	0.9
Ho	0.2	0.2	0.2	0.2	0.1	0.2	0.2	0.1	0.2
Er	0.7	0.5	0.6	0.7	0.2	0.4	0.7	0.2	0.5
Tm	0.1	0.1	0.1	0.1	0.0	0.1	0.1	0.0	0.1
Yb	0.8	0.6	0.6	0.7	0.3	0.6	0.8	0.2	0.6
Lu	0.1	0.1	0.1	0.1	0.0	0.1	0.1	0.0	0.1
Hf	0.7	0.5	0.6	1.0	0.2	0.1	0.3	1.4	1.2
Ta	0.1	0.1	0.1	0.1	0.0	0.0	0.0	0.1	0.1
Th	0.4	0.4	0.7	3.7	0.5	0.5	1.1	4.9	1.8
U	0.1	0.0	0.1	0.1	0.0	0.1	0.3	0.4	1.0
S	399	11025	424	11182	204	39100	130	46100	133
Os (ppb)	0.1	0.7	b.d.l.	0.7	b.d.l.	b.d.l.	0.1	2.7	b.d.l.
Ir	0.68	16.56	0.10	17.17	0.18	0.57	1.66	17.26	b.d.l.
Ru	0.47	9.66	0.25	8.84	0.12	b.d.l.	1.19	11.43	b.d.l.
Rh	2.55	102.62	b.d.l.	101.56	0.79	1.19	3.87	90.23	b.d.l.
Pt	8.2	334.9	b.d.l.	265.5	13.6	147.6	35.9	154.4	0.1
Pd	18.9	2477.8	b.d.l.	2805.5	10.9	20.9	63.1	2706.4	b.d.l.
Au	4.2	80.6	b.d.l.	77.9	2.9	34.1	13.1	59.6	b.d.l.

CHR = chromitite; DUN = dunite; LH = lherzolite; HZ = harzburgite; OL-WEB = olivine-websterite;
OL-OPX = olivine-orthopyroxenite; OPX = orthopyroxenite; NO = Norite; MNO = melanorite;
GN = gabbronorite; LGN = leucogabbronorite; AN = anorthosite; DOL = dolerite; MS = massive sulfide;
PEGM = pegmatite; TON = tonalite; METASED = metasediment; BRC = breccia; oph = ophitic

Table E.1 (cont.)

Sample No.	**79-156**	**79-159**	**79-160**	**79-163**	**79-164**	**94-013**	**94-038**	**94-081**	**94-118**
Intrusion	Nittis	Nittis	Nittis	Nittis	Nittis	Nittis	Nittis	Nittis	Nittis
Sample type	Drill core	Drill core	Drill core	Drill core	Drill core	Drill core	Drill core	Drill core	Drill core
Rock type	PEGM	DOL	OPX	PEGM	DOL	OPX	OPX	OPX	OPX
SiO_2 (wt %)	74.97	51.51	56.63	79.68	58.75	54.94	55.40	54.21	55.30
TiO_2	0.24	1.34	0.23	0.05	1.01	0.17	0.15	0.19	0.27
Al_2O_3	13.95	14.74	6.35	12.36	16.77	3.50	3.76	4.43	4.49
Fe_2O_{3T}	1.51	15.12	10.89	0.51	10.10	10.50	10.88	10.86	10.72
MnO	0.02	0.21	0.19	0.00	0.17	0.18	0.18	0.20	0.18
MgO	0.42	5.30	20.20	0.31	3.57	26.09	24.92	23.96	23.10
CaO	1.96	8.70	4.48	1.68	3.99	2.87	3.00	3.99	3.53
Na_2O	4.62	2.48	0.73	3.22	3.53	0.35	0.35	0.43	0.58
K_2O	0.96	0.44	0.17	1.10	1.12	0.08	0.06	0.11	0.16
P_2O_5	0.03	0.18	0.02	0.06	0.14	0.02	0.01	0.01	0.03
LOI	1.1	0.0	0.4	0.6	0.1	0.2	0.1	0.2	0.2
Total	99.75	100.06	100.34	99.61	99.24	98.87	98.79	98.58	98.56
Sc (ppm)	3	37	25	0	25	26	25	24	27
V	26	289	117	4	203	111	111	107	124
Cr	21	64	2605	8	154	3309	3206	3080	3069
Co	2.2	44.7	63.4	1.7	34.0	72.2	70.2	70.4	74.2
Ni	36.5	44.9	683.5	33.4	70.3	681.1	698.6	797.2	712.9
Cu	34.7	69.2	182.9	15.1	76.6	49.4	73.4	91.1	68.0
Zn	24	117	86	10	38	59	65	65	86
Rb	22.7	6.7	3.6	18.2	26.6	2.3	1.5	2.2	5.8
Sr	151.3	343.2	71.7	191.1	279.0	30.0	33.8	44.7	49.2
Y	12.5	24.7	4.6	3.5	17.8	3.0	2.7	3.2	4.8
Zr	138.8	103.7	15.6	34.8	169.2	13.3	7.8	13.1	29.3
Nb	4.6	7.1	1.2	0.9	8.0	0.7	0.4	0.7	1.2
Cs	0.3	0.2	0.2	0.1	1.7	0.0	0.0	0.1	0.1
Ba	223	293	70	905	458	23	21	51	51
La	29.3	17.3	2.3	14.0	25.5	1.3	1.0	1.4	3.1
Ce	55.7	36.8	4.9	26.7	50.1	3.0	2.1	3.0	6.5
Pr	5.9	4.8	0.6	2.9	6.0	0.4	0.3	0.4	0.8
Nd	18.9	20.4	2.6	9.6	22.5	1.5	1.1	1.6	3.4
Sm	3.1	4.6	0.6	1.8	4.5	0.4	0.3	0.3	0.7
Eu	0.5	1.5	0.2	0.9	1.4	0.1	0.1	0.1	0.2
Gd	2.6	4.3	0.5	1.3	3.4	0.4	0.4	0.4	0.7
Tb	0.3	0.7	0.1	0.2	0.5	0.1	0.1	0.1	0.1
Dy	1.9	4.2	0.7	0.7	3.0	0.5	0.4	0.4	0.7
Ho	0.4	0.8	0.2	0.1	0.6	0.1	0.1	0.1	0.2
Er	1.1	2.3	0.4	0.3	1.6	0.3	0.2	0.3	0.4
Tm	0.2	0.4	0.1	0.0	0.2	0.0	0.0	0.0	0.1
Yb	1.1	2.3	0.5	0.2	1.5	0.3	0.3	0.4	0.5
Lu	0.2	0.3	0.1	0.0	0.2	0.0	0.0	0.0	0.1
Hf	4.1	2.2	0.3	0.9	3.8	0.3	0.2	0.3	0.5
Ta	0.4	0.4	0.1	0.1	0.4	0.0	0.0	0.0	0.1
Th	14.5	1.8	0.4	3.4	4.4	0.6	0.3	0.3	0.6
U	2.7	0.1	0.0	0.7	0.9	0.0	0.0	0.0	0.1
S	265	1273	231	219	1646	200	219	700	300
Os (ppb)	0.3	b.d.l.	b.d.l.	b.d.l.	b.d.l.	n.d.	0.3	n.d.	0.1
Ir	0.29	b.d.l.	0.07	b.d.l.	0.95	n.d.	2.66	n.d.	1.57
Ru	0.74	b.d.l.	b.d.l.	b.d.l.	0.49	n.d.	1.44	n.d.	0.97
Rh	0.51	b.d.l.	0.17	b.d.l.	2.19	n.d.	10.87	n.d.	6.64
Pt	6.7	0.2	2.3	0.3	5.4	n.d.	42.2	n.d.	16.3
Pd	8.8	b.d.l.	5.1	1.0	25.1	n.d.	526.3	n.d.	60.6
Au	3.0	0.5	11.2	0.5	2.6	n.d.	7.6	n.d.	4.2

CHR = chromitite; DUN = dunite; LH = lherzolite; HZ = harzburgite; OL-WEB = olivine-websterite;
OL-OPX = olivine-orthopyroxenite; OPX = orthopyroxenite; NO = Norite; MNO = melanorite;
GN = gabbronorite; LGN = leucogabbronorite; AN = anorthosite; DOL = dolerite; MS = massive sulfide;
PEGM = pegmatite; TON = tonalite; METASED = metasediment; BRC = breccia; oph = ophitic

Table E.1 (cont.)

Sample No.	**15NMAS-01**	**15NMAS-02**	**15NMAS-03**	**1815-011**	**1815-026**	**1815-046**	**1815-059**	**1815-068**	**1815-072**
Intrusion	Nittis	Nittis	Nittis	Nyud	Nyud	Nyud	Nyud	Nyud	Nyud
Sample type	Outcrop	Outcrop	Outcrop	Drill core	Drill core	Drill core	Drill core	Drill core	Drill core
Rock type	OPX	OPX	OPX	MNO	MNO	MNO	MNO	MNO	MNO
SiO_2 (wt %)	55.53	54.12	57.61	55.00	50.86	55.74	50.89	48.54	49.36
TiO_2	0.09	0.09	0.12	0.34	0.20	0.19	0.24	0.13	0.13
Al_2O_3	1.99	2.16	2.76	6.35	7.41	9.39	6.63	5.54	4.18
Fe_2O_{3T}	11.46	15.22	11.56	13.51	9.07	9.58	9.58	10.49	11.02
MnO	0.19	0.18	0.31	0.20	0.17	0.17	0.17	0.17	0.14
MgO	28.03	20.10	23.82	18.20	22.35	17.14	22.59	23.74	23.55
CaO	1.79	1.66	2.45	5.13	5.10	5.83	4.95	4.27	3.15
Na_2O	0.13	0.10	0.19	0.81	3.26	1.01	2.31	2.59	3.28
K_2O	0.02	0.03	0.04	0.18	0.26	0.18	0.14	0.17	0.05
P_2O_5	0.01	0.00	0.00	0.03	0.05	0.02	0.06	0.02	0.01
LOI	0.5	3.7	0.2	0.7	0.7	1.1	0.8	3.3	3.7
Total	99.72	97.36	99.08	100.41	99.47	100.39	98.34	98.92	98.59
Sc (ppm)	24	22	28	33	27	27	28	26	25
V	61	66	77	153	93	119	128	80	76
Cr	4704	4019	4105	2284	2373	2302	1952	2097	2187
Co	99.7	217.4	90.9	108.6	40.5	60.5	41.0	115.8	146.3
Ni	1239.0	2147.8	1116.1	1366.4	386.6	469.6	383.7	1477.3	2132.4
Cu	102.8	17890.0	515.5	624.7	55.5	74.2	157.2	1735.7	3046.3
Zn	48	121	270	92	55	57	70	85	84
Rb	0.7	1.0	1.4	7.0	5.6	5.1	4.2	9.3	1.6
Sr	7.3	5.0	14.2	75.0	109.2	128.8	90.1	30.3	16.8
Y	1.4	1.3	1.8	6.6	4.8	3.8	5.0	2.5	2.8
Zr	2.2	7.9	12.8	28.1	14.9	18.7	29.1	7.4	6.9
Nb	0.3	0.2	0.3	1.5	0.4	0.7	0.7	0.3	0.2
Cs	0.0	0.1	0.2	0.5	0.5	0.5	0.5	1.4	0.3
Ba	6	4	9	51	69	64	50	58	6
La	0.2	0.6	0.4	3.6	2.3	1.9	2.5	0.8	1.2
Ce	0.5	1.2	1.1	7.3	4.7	3.7	5.5	1.8	2.5
Pr	0.1	0.2	0.1	1.1	0.6	0.5	0.7	0.3	0.3
Nd	0.3	0.6	0.6	4.2	2.4	2.0	2.9	1.1	1.3
Sm	0.1	0.1	0.2	0.9	0.6	0.5	0.7	0.3	0.4
Eu	0.0	0.0	0.1	0.3	0.3	0.2	0.2	0.1	0.1
Gd	0.1	0.2	0.2	1.1	0.6	0.5	0.7	0.3	0.3
Tb	0.0	0.0	0.0	0.2	0.1	0.1	0.1	0.1	0.1
Dy	0.2	0.2	0.2	1.0	0.7	0.5	0.7	0.4	0.4
Ho	0.0	0.0	0.1	0.2	0.1	0.1	0.1	0.1	0.1
Er	0.1	0.1	0.2	0.6	0.4	0.4	0.5	0.2	0.3
Tm	0.0	0.0	0.0	0.1	0.1	0.0	0.1	0.1	0.0
Yb	0.2	0.2	0.2	0.7	0.5	0.4	0.5	0.3	0.3
Lu	0.0	0.0	0.0	0.1	0.1	0.1	0.1	0.0	0.0
Hf	0.0	0.2	0.3	0.7	0.4	0.4	0.5	0.2	0.1
Ta	0.0	0.0	0.0	0.1	0.0	0.0	0.0	0.0	0.0
Th	0.0	0.1	0.1	0.4	3.4	0.2	0.3	0.2	0.2
U	0.0	0.0	0.0	0.1	0.1	0.1	0.1	0.0	0.0
S	74	27200	2212	1035	148	74	594	4489	9146
Os (ppb)	0.3	0.4	0.2	0.2	b.d.l.	b.d.l.	b.d.l.	1.0	0.7
Ir	1.89	1.63	0.80	2.52	0.53	0.47	1.33	6.92	4.91
Ru	1.31	1.10	0.78	0.97	0.28	0.22	0.68	3.74	2.49
Rh	6.89	9.43	3.82	10.11	2.16	1.50	4.80	31.38	31.81
Pt	12.0	25.6	19.0	29.9	8.8	5.2	25.4	111.1	157.3
Pd	40.3	4108.5	107.8	141.4	59.5	12.4	122.0	762.5	963.7
Au	1.7	65.4	8.5	16.7	4.6	1.4	13.6	49.9	77.9

CHR = chromitite; DUN = dunite; LH = lherzolite; HZ = harzburgite; OL-WEB = olivine-websterite;
OL-OPX = olivine-orthopyroxenite; OPX = orthopyroxenite; NO = Norite; MNO = melanorite;
GN = gabbronorite; LGN = leucogabbronorite; AN = anorthosite; DOL = dolerite; MS = massive sulfide;
PEGM = pegmatite; TON = tonalite; METASED = metasediment; BRC = breccia; oph = ophitic

Table E.1 (cont.)

Sample No.	**1815-074**	**1815-077**	**1815-083**	**1815-095**	**1815-103**	**1403-030**	**1403-042**	**1403-064**	**1403-089**
Intrusion	Nyud	Nyud	Nyud	Nyud	Nyud	Sopcha	Sopcha	Sopcha	Sopcha
Sample type	Drill core	Drill core	Drill core	Drill core	Drill core	Drill core	Drill core	Drill core	Drill core
Rock type	MNO	PEGM	TON	TON	TON	OPX	HZ	OPX	OPX
SiO_2 (wt %)	49.02	64.34	59.43	62.53	58.92	56.97	50.09	55.95	57.56
TiO_2	0.15	0.11	0.08	0.12	0.29	0.14	0.13	0.11	0.14
Al_2O_3	5.40	18.71	19.50	20.84	19.31	2.57	2.52	3.00	3.01
Fe_2O_{3T}	17.86	1.02	6.85	3.75	4.85	11.77	9.31	11.61	11.69
MnO	0.25	0.05	0.04	0.05	0.06	0.21	0.18	0.20	0.21
MgO	15.15	0.76	2.95	2.78	2.64	23.97	31.10	24.14	23.75
CaO	5.37	2.64	6.96	5.74	6.67	2.57	2.50	2.85	2.68
Na_2O	0.20	9.52	0.73	0.23	3.73	0.15	3.31	0.14	0.16
K_2O	0.59	0.27	0.64	0.59	0.58	0.03	0.05	0.03	0.03
P_2O_5	0.00	0.09	0.04	0.09	0.17	0.01	0.04	0.01	0.00
LOI	2.7	2.2	1.4	1.6	1.2	0.2	0.0	0.6	0.2
Total	96.73	99.74	98.64	98.35	98.40	98.60	99.26	98.66	99.41
Sc (ppm)	24	1	5	7	7	26	28	27	29
V	110	5	31	37	61	104	88	108	121
Cr	1460	39	154	107	93	2882	3490	3253	3604
Co	567.5	14.3	127.3	17.6	21.2	87.4	31.7	74.2	89.8
Ni	19844.0	88.8	2920.0	36.4	30.2	909.1	440.3	686.0	683.0
Cu	18993.1	591.6	995.3	52.1	38.0	44.8	30.5	39.7	153.4
Zn	148	32	88	45	45	64	43	64	76
Rb	22.2	7.9	30.7	17.2	14.3	1.1	0.9	1.2	1.1
Sr	24.7	197.4	667.3	539.0	498.1	13.5	17.3	7.6	15.6
Y	3.3	8.6	2.0	2.5	4.8	2.2	2.6	1.9	2.2
Zr	10.6	61.7	35.6	109.7	74.3	8.6	4.7	7.3	8.5
Nb	0.8	5.2	1.0	14.0	1.6	0.3	0.4	0.3	0.2
Cs	2.4	0.3	1.7	0.6	1.0	0.0	0.0	0.0	0.0
Ba	60	21	195	294	342	13	11	10	11
La	1.3	10.8	4.3	3.5	14.7	0.6	0.6	0.5	0.8
Ce	2.0	21.9	8.1	6.8	28.8	1.3	1.4	0.8	1.4
Pr	0.2	2.6	1.0	0.8	3.4	0.2	0.2	0.1	0.2
Nd	1.2	9.5	3.5	3.3	12.1	0.7	0.8	0.4	0.7
Sm	0.3	2.0	0.7	0.6	2.1	0.2	0.3	0.1	0.2
Eu	0.1	0.3	0.7	0.6	0.7	0.0	0.1	0.1	0.1
Gd	0.4	1.8	0.5	0.5	1.7	0.3	0.2	0.2	0.3
Tb	0.1	0.3	0.0	0.1	0.2	0.1	0.0	0.0	0.1
Dy	0.5	1.6	0.3	0.3	0.8	0.3	0.3	0.3	0.3
Ho	0.1	0.3	0.0	0.1	0.2	0.1	0.1	0.1	0.1
Er	0.3	0.8	0.1	0.2	0.4	0.2	0.2	0.2	0.2
Tm	0.1	0.1	0.0	0.0	0.1	0.0	0.0	0.0	0.0
Yb	0.4	0.8	0.2	0.2	0.4	0.3	0.3	0.3	0.3
Lu	0.1	0.1	0.0	0.0	0.1	0.1	0.0	0.0	0.0
Hf	0.2	1.5	0.7	2.8	1.7	0.1	0.1	0.1	0.1
Ta	0.0	0.4	0.1	0.7	0.1	0.0	0.0	0.0	0.0
Th	0.1	3.8	1.0	1.9	2.5	0.1	0.6	0.1	0.1
U	0.1	4.6	1.0	1.2	0.5	0.0	0.0	0.0	0.0
S	28600	911	8302	403	30	453	195	137	261
Os (ppb)	0.4	b.d.l.	1.1	b.d.l.	b.d.l.	0.5	0.3	0.1	0.2
Ir	5.45	0.03	6.61	0.03	b.d.l.	4.99	1.31	1.38	1.07
Ru	4.37	b.d.l.	2.94	b.d.l.	b.d.l.	2.59	0.83	0.96	0.92
Rh	34.79	0.15	56.86	b.d.l.	0.09	13.26	1.64	1.78	2.29
Pt	175.7	0.6	106.9	0.6	0.6	44.2	2.6	3.3	7.8
Pd	3128.8	9.2	580.1	0.6	1.2	98.5	5.1	7.6	44.3
Au	127.0	2.2	18.3	b.d.l.	b.d.l.	6.0	1.4	2.9	2.5

CHR = chromitite; DUN = dunite; LH = lherzolite; HZ = harzburgite; OL-WEB = olivine-websterite;
OL-OPX = olivine-orthopyroxenite; OPX = orthopyroxenite; NO = Norite; MNO = melanorite;
GN = gabbronorite; LGN = leucogabbronorite; AN = anorthosite; DOL = dolerite; MS = massive sulfide;
PEGM = pegmatite; TON = tonalite; METASED = metasediment; BRC = breccia; oph = ophitic

Table E.1 (cont.)

Sample No.	**1403-132**	**1403-141**	**1408-171**	**15SOP-06**	**15SOP-07**	**15SOP-08**	**16SOP-1**	**15SOP-09**	**15SOP-11**
Intrusion	Sopcha	Sopcha	Sopcha	Sopcha	Sopcha	Sopcha	Sopcha	Sopcha	Sopcha
Sample type	Drill core	Drill core	Drill core	Outcrop	Outcrop	Outcrop	Outcrop	Outcrop	Outcrop
Rock type	OPX	HZ	OPX	DUN	HZ	HZ	HZ	OL-OPX	OL-OPX
SiO_2 (wt %)	59.15	52.27	57.22	52.10	49.84	54.22	51.09	55.28	58.68
TiO_2	0.11	0.08	0.12	0.01	0.04	0.05	0.08	0.04	0.08
Al_2O_3	2.41	2.07	2.83	0.37	1.13	1.23	7.01	1.25	1.97
Fe_2O_{3T}	11.60	9.16	11.33	17.52	16.82	16.65	7.58	15.87	12.77
MnO	0.21	0.18	0.20	0.21	0.21	0.21	0.16	0.21	0.21
MgO	24.18	32.34	23.56	27.96	29.04	24.59	27.17	25.15	23.13
CaO	2.15	1.90	2.59	0.31	0.81	1.07	4.22	1.10	1.81
Na_2O	0.07	0.08	0.20	0.02	0.03	0.03	2.64	0.04	0.04
K_2O	0.03	0.00	0.04	0.01	0.01	0.00	0.04	0.00	0.01
P_2O_5	0.01	0.00	0.01	0.00	0.01	0.00	0.04	0.00	0.00
LOI	0.4	0.8	0.2	1.6	1.6	0.7	0.4	1.0	0.6
Total	100.36	98.92	98.33	100.13	99.49	98.74	100.45	99.97	99.25
Sc (ppm)	28	26	28	6	14	18	24	19	25
V	117	33	73	18	50	41	64	44	67
Cr	3853	3820	3635	3220	5990	4678	2769	3884	3721
Co	80.8	38.0	88.6	190.8	183.0	181.7	33.5	168.6	104.4
Ni	839.7	1920.1	810.4	5317.0	5466.9	6509.0	396.4	4268.6	1789.5
Cu	99.7	49.0	99.6	983.6	1136.8	1504.4	89.0	1010.8	287.1
Zn	67	103	79	97	83	82	35	77	43
Rb	1.2	1.0	1.2	0.4	0.3	0.3	0.8	0.2	0.5
Sr	6.7	7.3	20.7	1.8	2.4	1.1	77.7	3.2	4.3
Y	1.6	1.5	1.9	0.2	0.5	0.7	1.0	0.7	1.2
Zr	9.8	4.5	16.3	8.6	1.0	4.9	3.0	8.9	5.3
Nb	0.3	0.3	0.9	0.6	0.1	0.3	0.2	0.4	0.3
Cs	0.0	0.1	0.0	0.0	0.0	0.0	0.1	0.0	0.0
Ba	8	8	20	3	3	1	23	2	7
La	0.4	0.4	0.7	0.1	0.1	0.0	0.3	0.0	0.2
Ce	0.8	0.9	1.4	0.2	0.2	0.1	0.6	0.1	0.5
Pr	0.1	0.1	0.2	0.0	0.0	0.0	0.1	0.0	0.1
Nd	0.4	0.5	0.7	0.1	0.1	0.1	0.3	0.1	0.3
Sm	0.1	0.2	0.2	0.0	0.0	0.0	0.1	0.0	0.1
Eu	0.0	0.1	0.1	0.0	0.0	0.0	0.1	0.0	0.0
Gd	0.2	0.2	0.2	0.0	0.0	0.0	0.1	0.0	0.1
Tb	0.0	0.0	0.0	0.0	0.0	0.0	0.0	0.0	0.0
Dy	0.2	0.2	0.3	0.0	0.1	0.1	0.1	0.1	0.1
Ho	0.1	0.0	0.1	0.0	0.0	0.0	0.0	0.0	0.0
Er	0.2	0.1	0.2	0.0	0.1	0.1	0.1	0.1	0.1
Tm	0.0	0.0	0.0	0.0	0.0	0.0	0.0	0.0	0.0
Yb	0.2	0.2	0.2	0.0	0.1	0.1	0.2	0.1	0.2
Lu	0.0	0.0	0.0	0.0	0.0	0.0	0.0	0.0	0.0
Hf	0.1	0.1	0.4	0.2	0.0	0.1	0.0	0.2	0.1
Ta	0.0	0.0	0.1	0.0	0.0	0.0	0.0	0.0	0.0
Th	0.0	0.9	1.0	0.3	0.1	0.0	0.1	0.2	0.0
U	0.0	0.0	0.0	0.0	0.0	0.0	0.0	0.0	0.0
S	197	128	534	773	n.d.	4657	143	1692	n.d.
Os (ppb)	0.6	0.4	0.3	0.8	n.d.	2.1	0.2	1.9	n.d.
Ir	3.13	2.90	1.95	6.29	n.d.	17.49	2.28	18.23	n.d.
Ru	2.15	1.68	1.44	4.85	n.d.	9.60	0.85	9.52	n.d.
Rh	10.09	10.33	5.09	23.72	n.d.	67.97	6.04	80.39	n.d.
Pt	22.3	26.1	12.8	85.3	n.d.	185.7	25.2	230.0	n.d.
Pd	120.4	113.2	56.6	586.7	n.d.	1111.5	93.2	1208.5	n.d.
Au	5.2	5.9	3.2	37.1	n.d.	48.4	2.9	22.9	n.d.

CHR = chromitite; DUN = dunite; LH = lherzolite; HZ = harzburgite; OL-WEB = olivine-websterite;
OL-OPX = olivine-orthopyroxenite; OPX = orthopyroxenite; NO = Norite; MNO = melanorite;
GN = gabbronorite; LGN = leucogabbronorite; AN = anorthosite; DOL = dolerite; MS = massive sulfide;
PEGM = pegmatite; TON = tonalite; METASED = metasediment; BRC = breccia; oph = ophitic

Table E.1 (cont.)

Sample No.	**15SOP-04**	**15SOP-15**	**15SOP-16**	**15SOP-17**	**15SOP-18**	**15SOP-01**	**15SOP-05**	**15SOP-10**	**15TMAS-4**
Intrusion	Sopcha	Sopcha	Sopcha	Sopcha	Sopcha	Sopcha	Sopcha	Sopcha	Travyanaya
Sample type	Outcrop	Outcrop	Outcrop	Outcrop	Outcrop	Outcrop	Outcrop	Outcrop	Outcrop
Rock type	OPX	OPX	OPX	OPX	OPX	OPX	OPX BRC	OPX BRC	DOL
SiO_2 (wt %)	57.90	56.46	55.56	57.55	59.12	56.10	57.58	57.28	50.87
TiO_2	0.09	0.10	0.07	0.08	0.13	0.12	0.10	0.10	2.30
Al_2O_3	2.10	2.29	1.55	1.98	2.68	5.24	2.37	2.21	10.60
Fe_2O_{3T}	11.81	11.42	15.06	12.65	11.18	11.87	11.14	11.63	19.04
MnO	0.21	0.20	0.18	0.18	0.20	0.19	0.20	0.20	0.20
MgO	24.46	25.19	23.20	23.45	23.01	19.93	23.93	24.96	2.78
CaO	1.99	2.05	1.45	1.77	2.43	3.58	2.13	1.83	6.81
Na_2O	0.07	0.07	0.02	0.04	0.16	0.44	0.06	0.06	4.64
K_2O	0.01	0.01	0.01	0.00	0.03	0.05	0.02	0.00	0.33
P_2O_5	0.01	0.01	0.00	0.00	0.01	0.01	0.01	0.00	0.07
LOI	0.4	1.6	1.0	0.8	0.1	2.5	1.2	0.5	0.2
Total	99.02	99.43	98.08	98.49	99.09	100.08	98.71	98.77	97.83
Sc (ppm)	30	29	23	27	34	29	29	31	29
V	77	79	63	64	91	89	79	85	303
Cr	4247	4548	3359	3786	3734	2882	3914	4816	84
Co	100.7	100.2	224.4	81.7	87.9	252.5	87.6	81.2	39.6
Ni	1064.8	966.1	11063.8	1034.1	850.1	3685.3	1422.1	962.8	209.1
Cu	168.2	114.6	3767.8	122.8	89.2	324.6	339.3	366.3	9874.8
Zn	56	67	101	39	48	69	85	46	180
Rb	0.4	0.6	0.4	0.3	1.0	0.7	1.0	0.4	5.6
Sr	2.5	4.2	1.0	0.6	11.0	74.7	3.7	2.0	160.0
Y	1.1	1.6	0.9	0.9	1.8	1.9	1.4	1.3	48.2
Zr	3.4	27.1	17.1	6.7	7.6	14.3	11.4	5.2	71.6
Nb	0.1	0.2	0.4	0.2	0.3	0.3	0.6	0.3	5.9
Cs	0.0	0.0	0.0	0.0	0.0	0.1	0.1	0.0	0.2
Ba	2	5	3	2	10	33	5	2	353
La	0.1	0.4	0.1	0.1	0.6	0.8	0.4	0.2	26.8
Ce	0.3	0.9	0.2	0.2	1.2	1.7	0.9	0.5	58.0
Pr	0.0	0.1	0.0	0.0	0.2	0.2	0.1	0.1	8.0
Nd	0.2	0.5	0.2	0.2	0.6	0.8	0.5	0.4	31.5
Sm	0.1	0.1	0.1	0.1	0.2	0.2	0.1	0.1	7.5
Eu	0.0	0.0	0.0	0.0	0.0	0.1	0.0	0.0	2.2
Gd	0.1	0.1	0.1	0.1	0.2	0.2	0.1	0.1	7.9
Tb	0.0	0.0	0.0	0.0	0.0	0.0	0.0	0.0	1.3
Dy	0.2	0.2	0.1	0.1	0.2	0.3	0.2	0.2	8.5
Ho	0.0	0.0	0.0	0.0	0.1	0.1	0.0	0.0	1.7
Er	0.1	0.2	0.1	0.1	0.2	0.2	0.1	0.1	4.9
Tm	0.0	0.0	0.0	0.0	0.0	0.0	0.0	0.0	0.9
Yb	0.2	0.2	0.1	0.2	0.3	0.2	0.2	0.2	5.2
Lu	0.0	0.0	0.0	0.0	0.0	0.0	0.0	0.0	0.7
Hf	0.0	0.5	0.3	0.1	0.2	0.4	0.2	0.1	1.5
Ta	0.0	0.0	0.0	0.0	0.0	0.0	0.0	0.0	0.5
Th	0.1	0.1	0.2	0.1	0.2	0.2	0.4	0.1	3.6
U	0.0	0.0	0.0	0.0	0.0	0.0	0.0	0.0	0.8
S	91	71	9789	430	104	16027	345	117	24600
Os (ppb)	0.4	0.6	2.4	0.2	0.2	1.5	0.3	0.2	b.d.l.
Ir	3.87	2.72	27.10	3.01	0.96	15.49	2.68	1.84	0.10
Ru	2.35	2.58	13.96	1.85	0.82	6.63	1.54	1.33	0.14
Rh	10.16	6.57	128.46	11.69	1.71	91.16	8.83	9.02	0.29
Pt	18.2	17.4	412.4	21.4	2.9	170.6	25.7	34.6	3.5
Pd	54.2	62.7	3009.5	114.2	10.4	872.1	148.3	194.6	15.0
Au	1.7	2.6	186.0	3.1	1.0	17.3	10.9	18.3	17.5

CHR = chromitite; DUN = dunite; LH = lherzolite; HZ = harzburgite; OL-WEB = olivine-websterite;
OL-OPX = olivine-orthopyroxenite; OPX = orthopyroxenite; NO = Norite; MNO = melanorite;
GN = gabbronorite; LGN = leucogabbronorite; AN = anorthosite; DOL = dolerite; MS = massive sulfide;
PEGM = pegmatite; TON = tonalite; METASED = metasediment; BRC = breccia; oph = ophitic

Table E.1 (cont.)

Sample No.	**15TMAS-9**	**15TMAS-5**	**15TMAS-6**	**15TMAS-7**	**15TMAS-1**	**15TMAS-8**	**1811-062**	**1811-102**	**1811-143**
Intrusion	Travyanaya	Travyanaya	Travyanaya	Travyanaya	Travyanaya	Travyanaya	Vuruchuaivench	Vuruchuaivench	Vuruchuaivench
Sample type	Outcrop	Outcrop	Outcrop	Outcrop	Outcrop	Outcrop	Drill core	Drill core	Drill core
Rock type	HZ	HZ	MS	OL-WEB	Oph. GN	OPX	LGN	LGN	LGN
SiO_2 (wt %)	35.75	39.06	42.98	44.37	49.34	49.74	53.43	51.67	53.04
TiO_2	0.08	0.17	0.24	0.20	0.18	0.08	0.21	0.22	0.23
Al_2O_3	2.36	2.73	9.70	4.67	15.60	2.33	18.62	20.37	19.29
Fe_2O_{3T}	14.93	14.71	22.96	12.33	12.62	15.48	5.69	5.30	6.17
MnO	0.15	0.19	0.15	0.15	0.14	0.20	0.10	0.09	0.11
MgO	39.60	39.35	9.54	32.46	7.98	27.02	5.64	5.38	6.43
CaO	1.17	1.88	3.02	3.10	11.52	1.59	12.34	10.92	10.08
Na_2O	4.45	0.21	2.35	0.43	1.99	0.27	2.15	2.57	2.19
K_2O	0.03	0.14	1.10	0.13	0.14	0.05	0.40	0.55	0.65
P_2O_5	0.04	0.00	0.01	0.02	0.01	0.02	0.03	0.03	0.03
LOI	1.1	1.3	3.2	2.2	1.3	2.8	1.3	1.5	2.2
Total	99.62	99.80	95.24	100.09	100.86	99.59	99.95	98.62	100.38
Sc (ppm)	8	10	19	17	33	11	18	17	17
V	41	53	161	95	124	50	92	95	96
Cr	2465	1838	1634	4710	286	3543	69	113	79
Co	61.4	143.2	394.2	121.0	222.9	159.0	21.4	24.3	29.6
Ni	6407.5	2689.0	18301.6	861.7	3776.4	2492.8	83.4	94.1	117.7
Cu	571.6	3933.5	28065.4	396.6	2307.6	352.8	54.6	85.4	82.6
Zn	81	211	352	174	130	154	32	43	45
Rb	1.1	2.8	26.1	2.9	2.4	2.2	8.2	12.8	14.7
Sr	24.8	29.5	187.5	53.7	221.2	30.2	357.2	334.7	320.2
Y	1.7	3.7	6.6	4.3	4.2	1.7	4.6	5.6	5.3
Zr	7.0	7.8	2.4	17.0	7.0	9.8	35.0	45.6	46.0
Nb	1.8	0.6	0.2	0.6	0.5	0.3	1.5	1.1	1.7
Cs	0.0	0.1	1.4	0.1	0.1	0.0	0.0	0.1	0.2
Ba	19	44	194	47	49	24	87	152	216
La	1.0	3.9	6.3	2.6	1.6	0.8	4.0	4.3	4.8
Ce	2.0	6.7	11.1	5.5	3.4	1.8	8.0	8.6	9.1
Pr	0.3	1.0	1.4	0.8	0.5	0.2	1.0	1.1	1.1
Nd	1.1	3.6	4.9	3.0	2.1	0.9	4.1	4.9	4.2
Sm	0.3	1.0	1.0	0.7	0.6	0.2	0.7	0.9	1.0
Eu	0.1	0.2	0.6	0.3	0.3	0.1	0.4	0.4	0.5
Gd	0.3	0.6	1.0	0.7	0.7	0.2	0.8	0.8	1.0
Tb	0.0	0.1	0.2	0.1	0.1	0.0	0.1	0.2	0.2
Dy	0.2	0.6	1.0	0.7	0.7	0.3	0.8	0.9	0.9
Ho	0.1	0.1	0.2	0.2	0.1	0.0	0.2	0.2	0.2
Er	0.2	0.4	0.6	0.5	0.4	0.1	0.5	0.6	0.5
Tm	0.0	0.1	0.1	0.1	0.1	0.0	0.1	0.1	0.1
Yb	0.2	0.4	0.8	0.5	0.5	0.2	0.6	0.5	0.5
Lu	0.0	0.1	0.1	0.1	0.1	0.0	0.1	0.1	0.1
Hf	0.2	0.3	0.1	0.4	0.2	0.3	0.5	0.6	0.7
Ta	0.1	0.0	0.0	0.1	0.0	0.0	0.1	0.1	0.1
Th	3.1	0.5	0.3	0.4	0.4	0.5	0.7	0.6	0.8
U	0.0	0.1	0.1	0.0	0.0	0.1	0.1	0.1	0.2
S	664	11366	81900	3440	29400	569	b.d.l	79	82
Os (ppb)	0.2	b.d.l.	0.1	0.7	1.5	0.3	0.1	b.d.l	7.6
Ir	1.70	0.69	0.29	4.99	10.89	1.76	0.11	0.14	0.15
Ru	1.75	0.63	0.38	4.42	7.41	1.96	0.29	0.19	b.d.l
Rh	7.97	2.12	11.00	15.02	40.52	7.76	0.36	0.11	0.19
Pt	19.9	557.6	359.0	112.6	142.5	20.0	4.2	2.2	4.7
Pd	133.1	3692.7	3179.5	323.4	524.0	102.1	2.5	2.6	7.8
Au	3.5	315.7	264.1	14.2	35.6	3.5	1.0	1.4	2.8

CHR = chromitite; DUN = dunite; LH = lherzolite; HZ = harzburgite; OL-WEB = olivine-websterite;
OL-OPX = olivine-orthopyroxenite; OPX = orthopyroxenite; NO = Norite; MNO = melanorite;
GN = gabbronorite; LGN = leucogabbronorite; AN = anorthosite; DOL = dolerite; MS = massive sulfide;
PEGM = pegmatite; TON = tonalite; METASED = metasediment; BRC = breccia; oph = ophitic

Table E.1 (cont.)

Sample No.	**1811-172**	**1811-185**	**1811-231**	**1811-274**	**1814-021**	**1814-055**	**1814-091**	**1814-118**	**1843-118**
Intrusion	Vuruchuaivench	Vuruchuaivench	Vuruchuaivench	Vuruchuaivench	Vuruchuaivench	Vuruchuaivench	Vuruchuaivench	Vuruchuaivench	Vuruchuaivench
Sample type	Drill core	Drill core	Drill core	Drill core	Drill core	Drill core	Drill core	Drill core	Drill core
Rock type	LGN	LGN	LGN	LGN	LGN	LGN	LGN	LGN	LGN
SiO_2 (wt %)	50.17	52.46	52.36	50.88	52.18	53.70	58.09	52.07	51.05
TiO_2	0.15	0.21	0.18	0.17	0.18	0.19	0.20	0.15	0.16
Al_2O_3	19.96	17.54	16.39	15.66	18.58	16.63	19.07	15.39	18.92
Fe_2O_{3T}	6.15	5.96	6.02	7.84	5.00	5.22	4.25	9.17	6.07
MnO	0.09	0.11	0.12	0.15	0.09	0.11	0.00	0.13	0.11
MgO	7.02	7.83	9.12	8.98	7.51	8.60	6.89	10.68	7.16
CaO	12.30	12.50	12.98	12.09	12.25	13.57	7.40	7.25	9.71
Na_2O	1.83	2.31	1.51	1.63	1.80	1.56	2.01	1.81	2.93
K_2O	0.22	0.32	0.20	0.23	0.58	0.30	0.12	0.32	0.70
P_2O_5	0.00	0.01	0.01	0.01	0.02	0.02	0.02	0.01	0.01
LOI	1.9	1.3	1.4	1.5	1.5	0.9	1.8	3.2	2.1
Total	99.82	100.60	100.30	99.13	99.66	100.77	99.89	100.28	98.92
Sc (ppm)	18	28	29	30	24	32	30	20	24
V	89	129	119	132	99	121	95	91	109
Cr	92	55	237	170	180	325	242	644	60
Co	26.6	37.5	36.4	39.5	27.8	34.3	44.4	63.2	29.2
Ni	776.6	140.3	156.4	142.3	142.4	57.9	312.1	1364.7	181.3
Cu	896.8	82.7	63.2	96.3	73.6	90.9	57.2	435.1	74.9
Zn	45	45	68	51	34	34	13	71	42
Rb	6.4	7.1	4.1	4.7	13.5	6.7	4.7	9.8	22.7
Sr	320.6	296.8	248.7	246.4	286.5	255.1	300.2	395.9	290.0
Y	4.0	5.9	4.9	4.1	4.5	5.0	5.7	3.5	4.4
Zr	20.6	58.0	21.5	20.9	29.0	24.7	19.9	16.9	14.4
Nb	0.8	0.9	0.8	0.5	0.9	1.1	1.4	0.6	0.9
Cs	0.0	0.1	0.1	0.2	0.1	0.1	0.1	0.2	0.2
Ba	69	92	55	73	201	110	89	92	178
La	2.3	2.8	2.2	1.5	2.9	2.6	3.0	2.4	2.6
Ce	4.8	6.1	4.5	3.0	5.6	5.8	6.1	4.7	5.2
Pr	0.7	0.9	0.6	0.5	0.8	0.8	0.8	0.7	0.7
Nd	2.7	3.6	2.6	2.4	2.8	2.9	3.3	2.4	3.0
Sm	0.6	0.8	0.7	0.6	0.9	0.9	0.8	0.6	0.8
Eu	0.3	0.3	0.4	0.3	0.3	0.4	0.4	0.4	0.4
Gd	0.7	0.8	0.7	0.5	0.8	0.8	0.8	0.4	0.5
Tb	0.1	0.1	0.1	0.1	0.1	0.1	0.1	0.1	0.1
Dy	0.7	0.9	0.7	0.6	0.8	0.9	0.8	0.5	0.7
Ho	0.1	0.2	0.2	0.1	0.2	0.2	0.2	0.1	0.2
Er	0.4	0.5	0.5	0.4	0.4	0.5	0.4	0.3	0.5
Tm	0.1	0.1	0.1	0.1	0.1	0.1	0.1	0.1	0.1
Yb	0.4	0.6	0.5	0.4	0.5	0.6	0.5	0.4	0.4
Lu	0.1	0.1	0.1	0.1	0.0	0.1	0.1	0.1	0.1
Hf	0.3	0.9	0.3	0.3	0.3	0.4	0.4	0.2	0.2
Ta	0.0	0.1	0.0	0.0	0.1	0.1	0.1	0.0	0.1
Th	0.4	0.3	0.4	0.2	0.6	0.4	0.5	0.9	0.2
U	0.1	0.1	0.0	0.0	0.1	0.1	0.1	0.1	0.0
S	1407	107	190	80	b.d.l	64	139	527	63
Os (ppb)	0.0	b.d.l	b.d.l	0.0	b.d.l	b.d.l	b.d.l	0.2	0.1
Ir	1.94	0.09	0.11	0.05	0.13	0.09	0.23	0.71	0.26
Ru	2.12	b.d.l	b.d.l	0.24	b.d.l	b.d.l	0.18	0.59	b.d.l
Rh	19.97	0.18	0.80	0.62	0.51	0.21	1.16	6.42	0.47
Pt	164.2	1.1	4.2	5.5	2.1	1.7	9.5	59.5	3.3
Pd	1120.5	2.6	3.6	4.5	5.8	3.5	50.7	338.3	2.8
Au	24.5	1.3	1.1	0.7	1.0	1.2	2.9	13.0	0.7

CHR = chromitite; DUN = dunite; LH = lherzolite; HZ = harzburgite; OL-WEB = olivine-websterite;
OL-OPX = olivine-orthopyroxenite; OPX = orthopyroxenite; NO = Norite; MNO = melanorite;
GN = gabbronorite; LGN = leucogabbronorite; AN = anorthosite; DOL = dolerite; MS = massive sulfide;
PEGM = pegmatite; TON = tonalite; METASED = metasediment; BRC = breccia; oph = ophitic

Table E.1 (cont.)

Sample No.	**1843-169**	**1843-203**	**15VURU-3**	**15VURU-2**
Intrusion	Vuruchuaivench	Vuruchuaivench	Vuruchuaivench	Vuruchuaivench
Sample type	Drill core	Drill core	Outcrop	Outcrop
Rock type	LGN	LGN	AN	LGN
SiO_2 (wt %)	53.77	53.19	54.66	53.78
TiO_2	0.23	0.15	0.15	0.22
Al_2O_3	15.27	20.69	25.13	21.41
Fe_2O_{3T}	6.32	4.46	1.40	5.06
MnO	0.12	0.09	0.03	0.07
MgO	8.58	6.35	0.21	1.42
CaO	10.91	11.34	10.39	12.60
Na_2O	1.47	2.43	2.58	2.99
K_2O	0.13	0.53	1.73	0.00
P_2O_5	0.01	0.01	0.06	0.02
LOI	2.2	1.6	1.9	1.0
Total	98.97	100.85	98.23	98.52
Sc (ppm)	31	18	2	9
V	138	88	22	54
Cr	114	87	55	37
Co	38.2	29.7	8.3	81.2
Ni	171.1	118.2	29.9	2455.6
Cu	69.7	64.0	30.1	3115.1
Zn	59	24	26	39
Rb	4.6	18.5	27.7	0.6
Sr	242.6	374.0	632.4	421.7
Y	6.2	3.2	3.4	4.1
Zr	32.8	21.4	29.8	23.4
Nb	1.2	0.6	0.9	0.7
Cs	0.0	1.2	0.2	0.0
Ba	31	115	637	12
La	3.2	2.5	4.3	3.8
Ce	6.9	5.2	8.3	7.6
Pr	0.9	0.7	1.0	1.0
Nd	3.6	2.4	3.7	3.6
Sm	0.9	0.8	0.7	0.8
Eu	0.4	0.4	0.5	0.4
Gd	0.8	0.7	0.7	0.8
Tb	0.2	0.1	0.1	0.1
Dy	1.0	0.6	0.5	0.7
Ho	0.2	0.1	0.1	0.1
Er	0.6	0.4	0.3	0.4
Tm	0.1	0.1	0.0	0.1
Yb	0.6	0.3	0.2	0.3
Lu	0.1	0.0	0.0	0.1
Hf	0.4	0.3	0.7	0.4
Ta	0.1	0.0	0.1	0.0
Th	0.6	0.4	0.5	0.9
U	0.1	0.1	0.1	0.3
S	85	96	6783	b.d.l
Os (ppb)	b.d.l	b.d.l	2.2	b.d.l
Ir	0.33	0.32	15.29	0.10
Ru	b.d.l	b.d.l	7.41	b.d.l
Rh	0.90	0.92	150.58	b.d.l
Pt	12.2	8.5	734.0	0.2
Pd	21.4	6.0	6563.4	0.6
Au	1.1	1.2	318.7	1.0

CHR = chromitite; DUN = dunite; LH = lherzolite; HZ = harzburgite; OL-WEB = olivine-websterite;
OL-OPX = olivine-orthopyroxenite; OPX = orthopyroxenite; NO = Norite; MNO = melanorite;
GN = gabbronorite; LGN = leucogabbronorite; AN = anorthosite; DOL = dolerite; MS = massive sulfide;
PEGM = pegmatite; TON = tonalite; METASED = metasediment; BRC = breccia; oph = ophitic

F Photomicrographs of Lower Zone samples

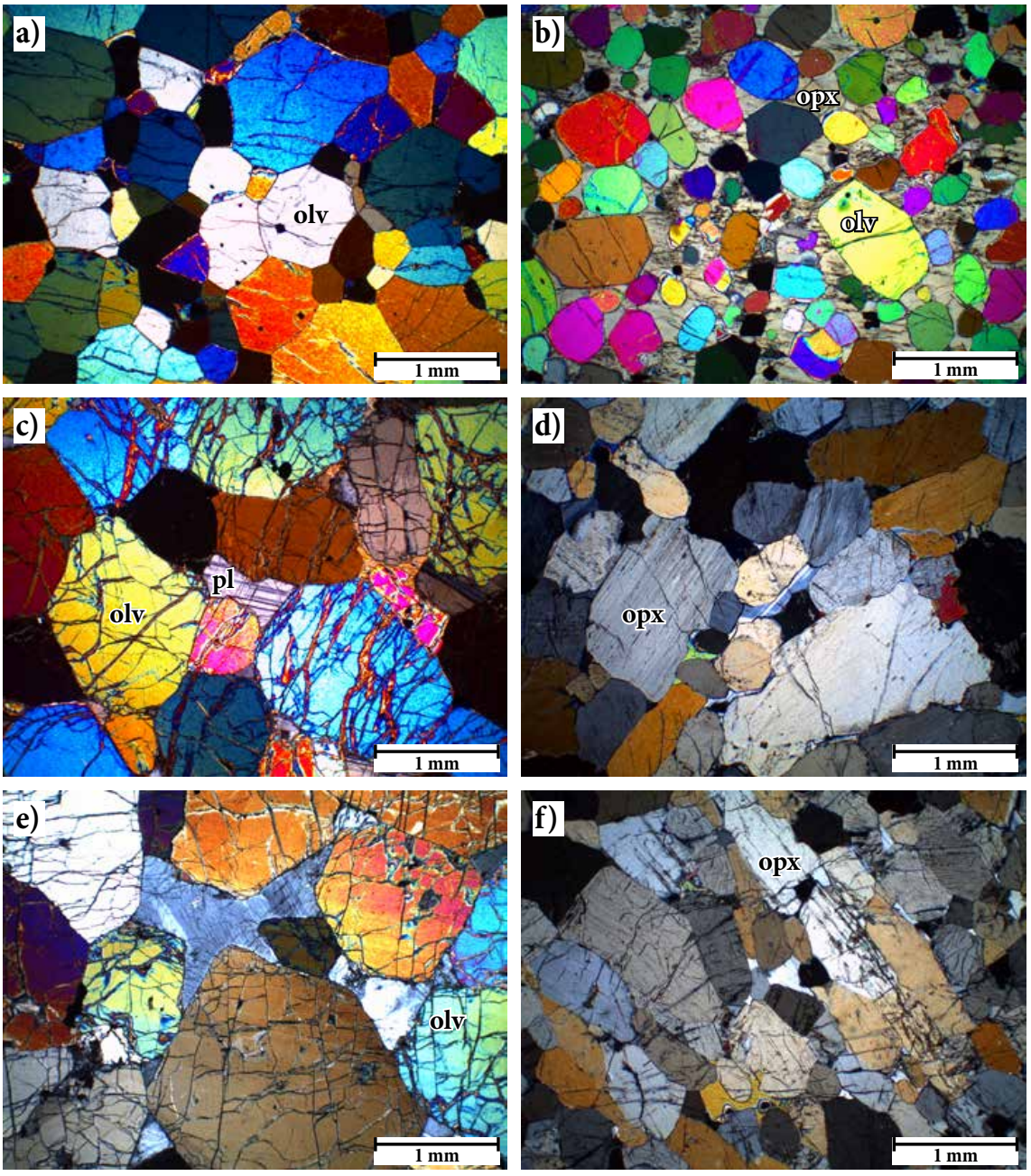

Fig. F.1. Photomicrographs of typical Lower Zone lithologies. a) Medium-grained dunite (NG1-773). b) Poikilitic harzburgite (NG1-793). c) Coarse-grained dunite (NG2-42). d) Medium-grained pyroxenite (NG2-91). e) Poikilitic harzburgite (NG2-143). f) Medium-grained pyroxenite (NG2-171). Abbreviations: olv = olivine; opx = orthopyroxene; pl = plagioclase.

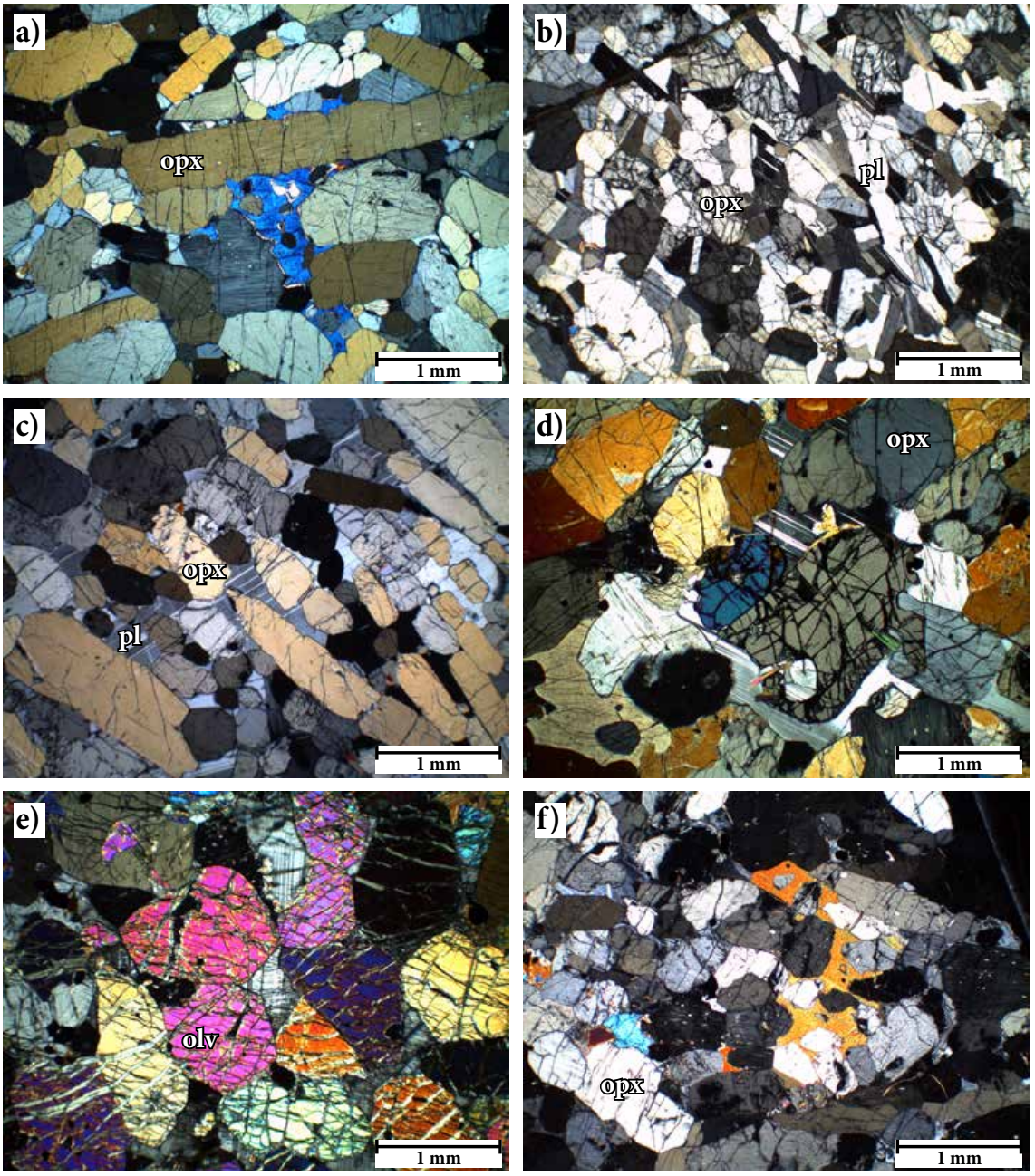

Fig. F.2. Photomicrographs of typical Lower Zone lithologies. a) Medium-grained pyroxenite (NG2-267). b) Medium-grained norite (NG2-298). c) Medium-grained pyroxenite (NG2-320). d) Medium-grained olivine-pyroxenite (NG2-418). e) Medium-grained dunite (NG2-449). f) Medium-grained pyroxenite (NG2-546). Abbreviations: olv = olivine; opx = orthopyroxene; pl = plagioclase.

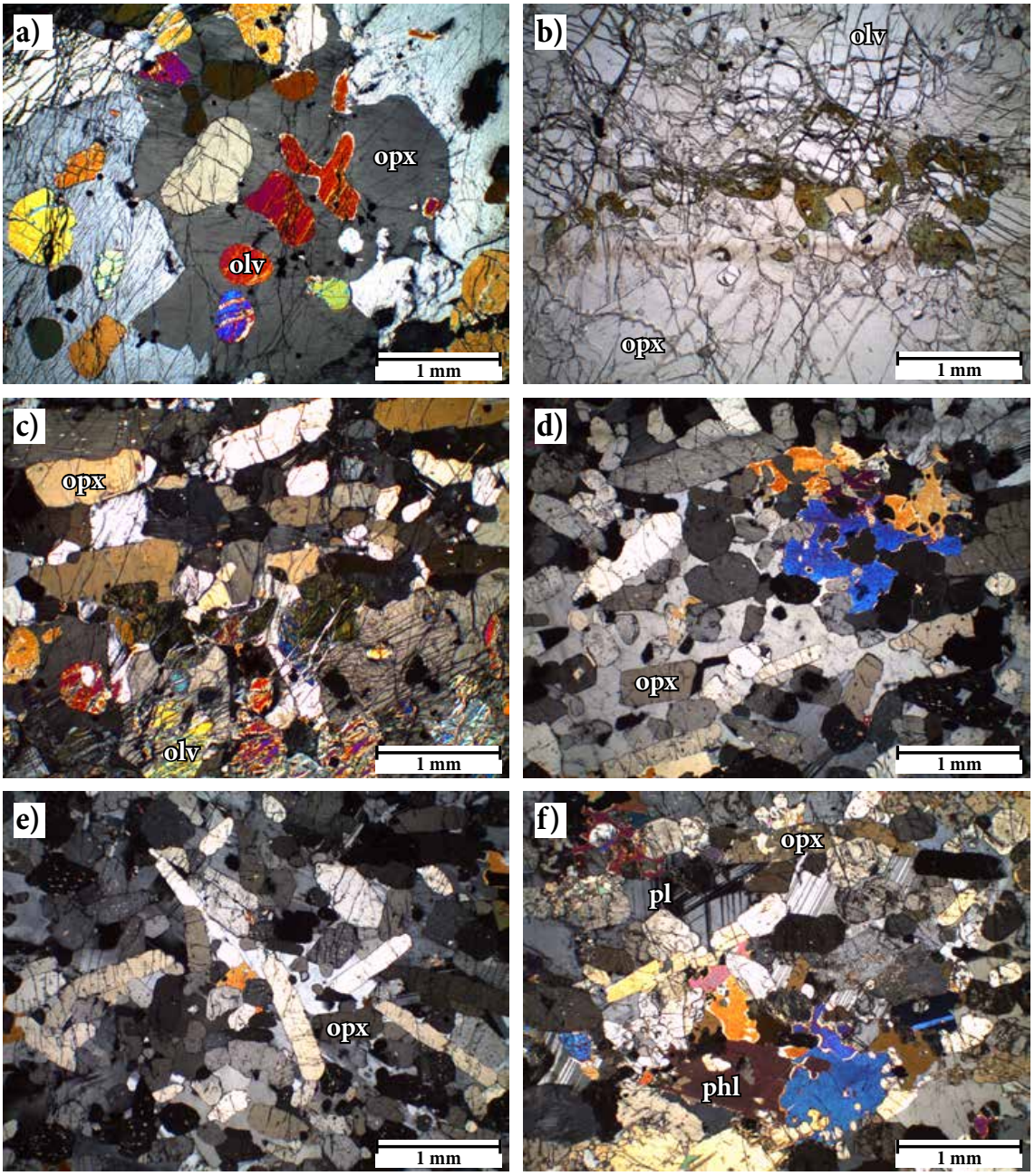

Fig. F.3. Photomicrographs of typical Lower Zone lithologies. a) Poikilitic harzburgite (NG2-640). b) Contact between pyroxenite and harzburgite. Note the altered olivine at the basal contact of the harzburgite (NG2-676). c) Contact between pyroxenite and harzburgite (NG2-702). d) Poikilitic pyroxenite (NG2-739). e) Fine-grained pyroxenite (NG2-748). f) Fine-grained melagabbronorite (NG2-762). Abbreviations: olv = olivine; opx = orthopyroxene; pl = plagioclase; phl = phlogopite.

G Element maps of Lower Zone samples

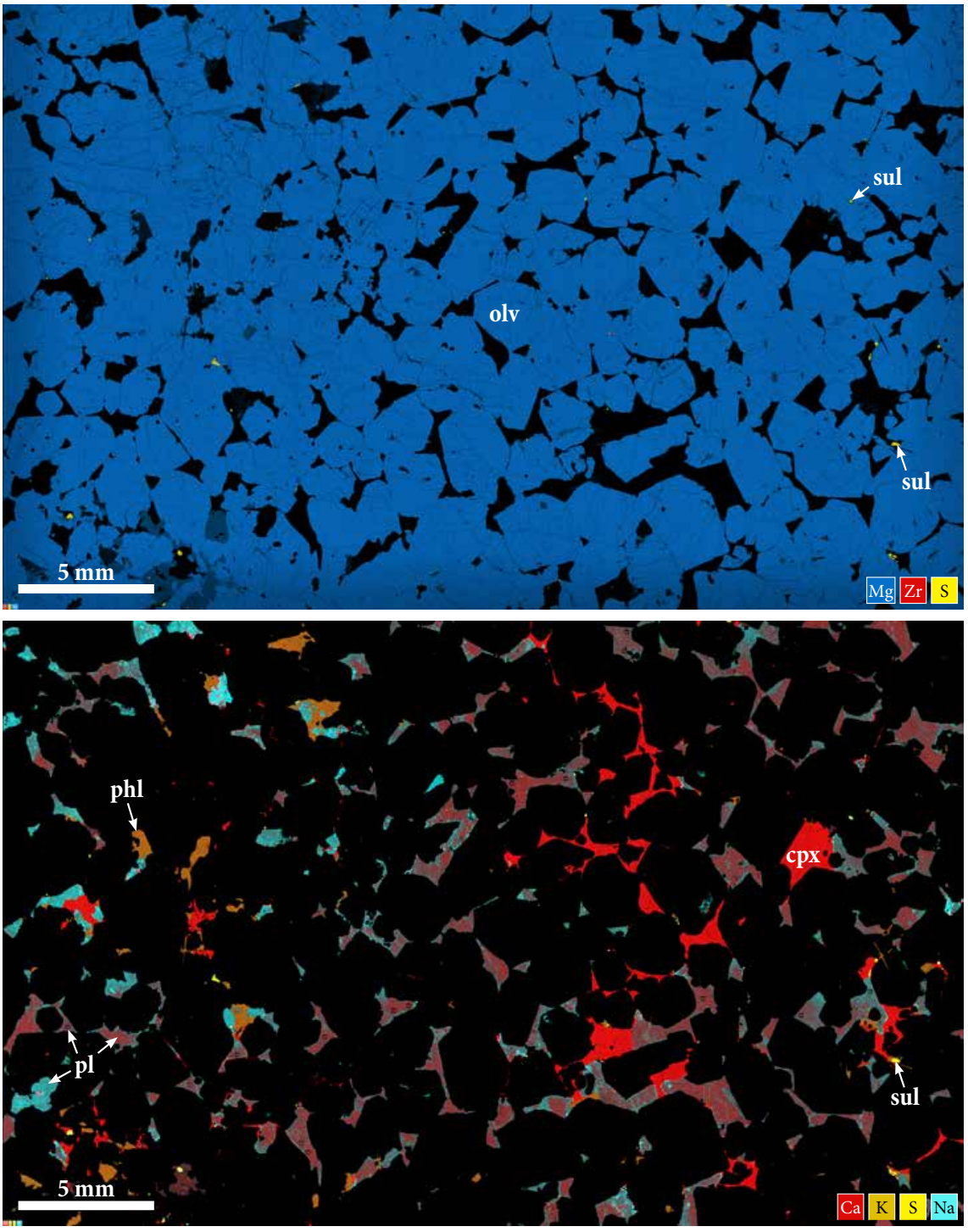

Fig. G.1. Elemental map of dunite sample NG2-134. Abbreviations: olv = olivine; sul = sulfide; cpx = clinopyroxene; pl = plagioclase; phl = phlogopite.

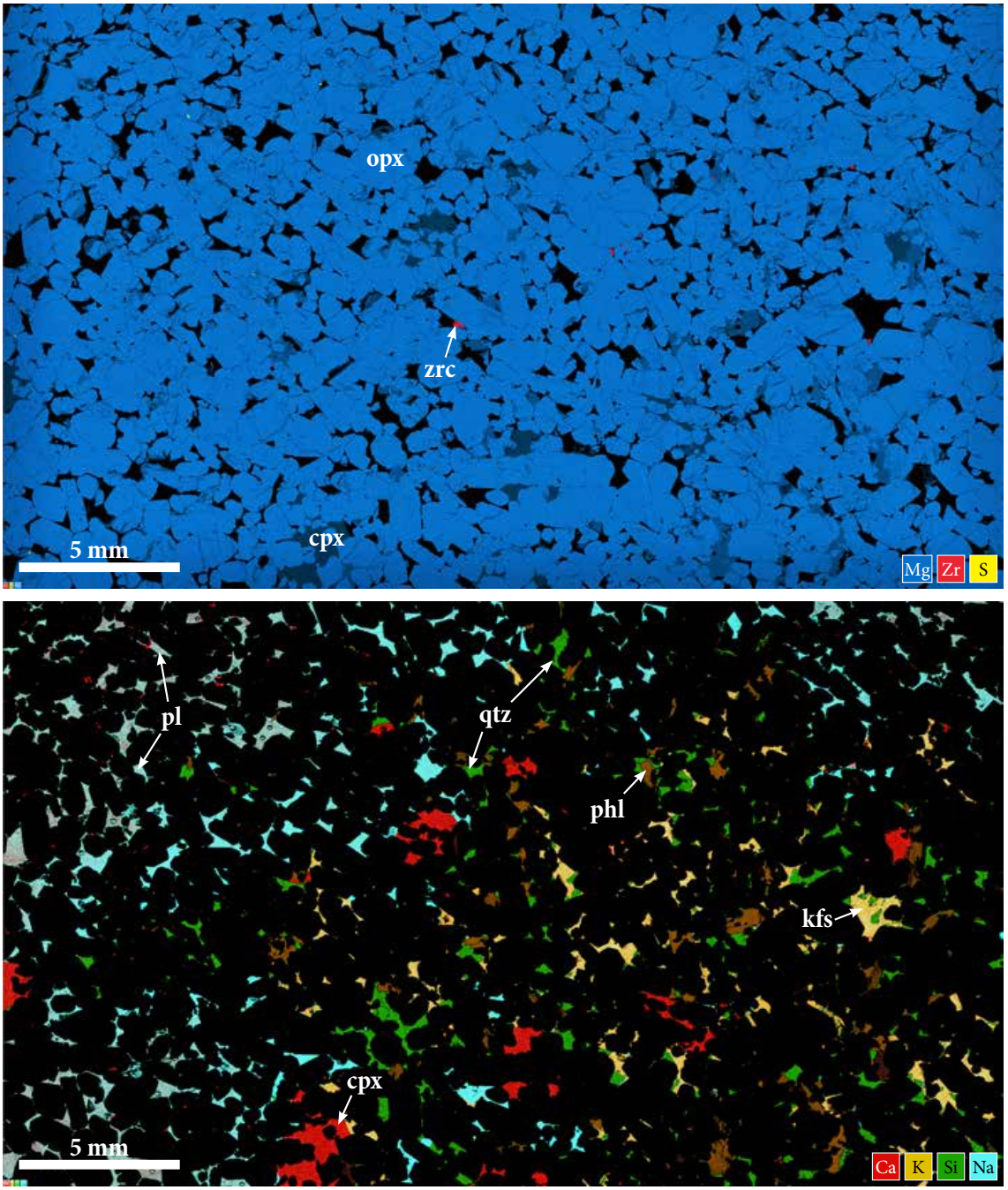

Fig. G.2. Elemental map of orthopyroxenite sample NG2-180. Abbreviations: opx = orthopyroxene; cpx = clinopyroxene; pl = plagioclase; qtz = quartz; phl = phlogopite; kfs = alkali feldspar.

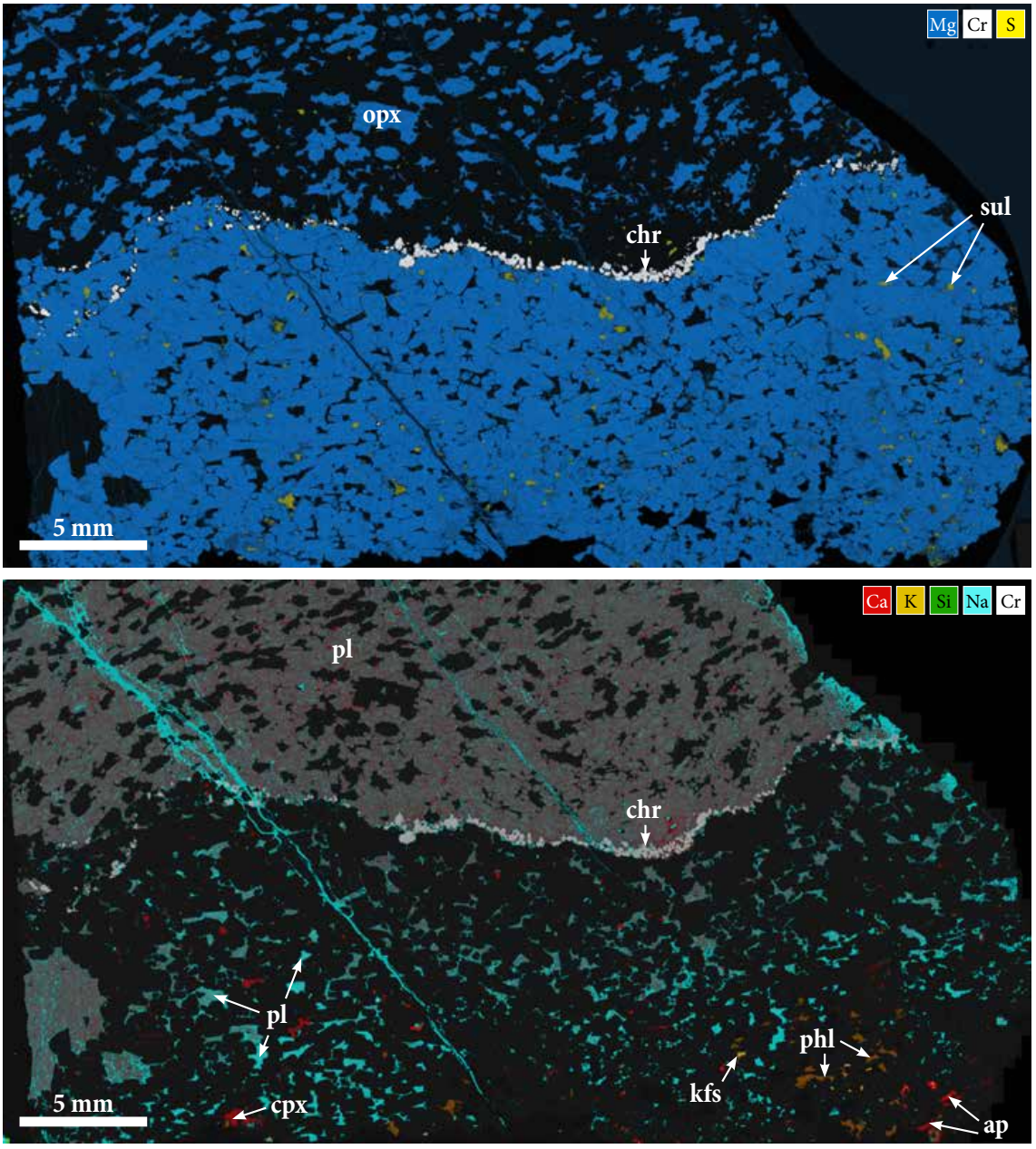

Fig. G.3. Elemental map of orthopyroxenite/leuconorite sample NG2-300. Abbreviations: opx = orthopyroxene; chr = chromite; cpx = clinopyroxene; pl = plagioclase; phl = phlogopite; kfs = alkali feldspar; ap = apatite.

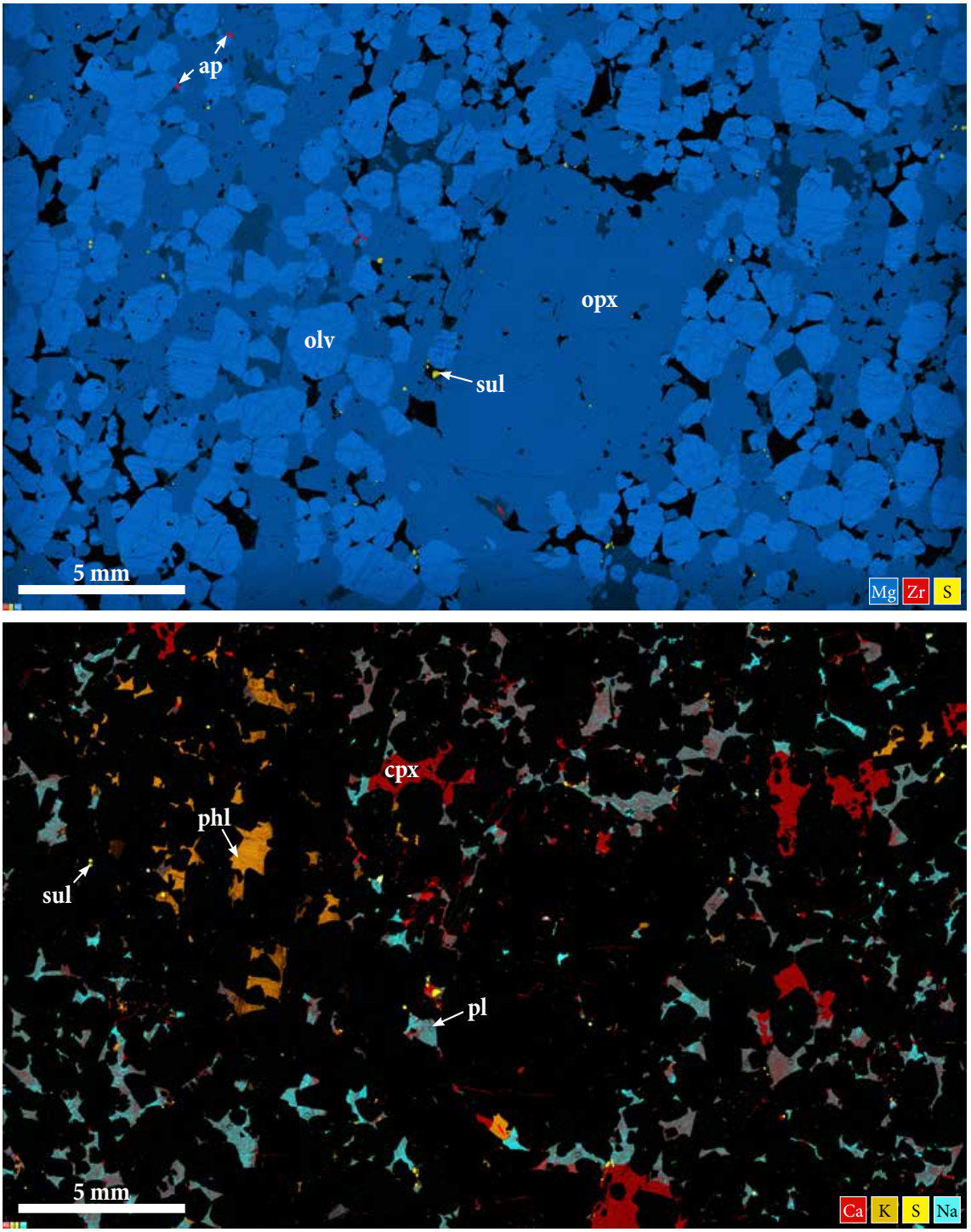

Fig. G.4. Elemental map of harzburgite sample NG2-490. Abbreviations: olv = olivine; opx= orthopyroxene; sul = sulfide; ap = apatite; cpx = clinopyroxene; pl = plagioclase; phl = phlogopite.

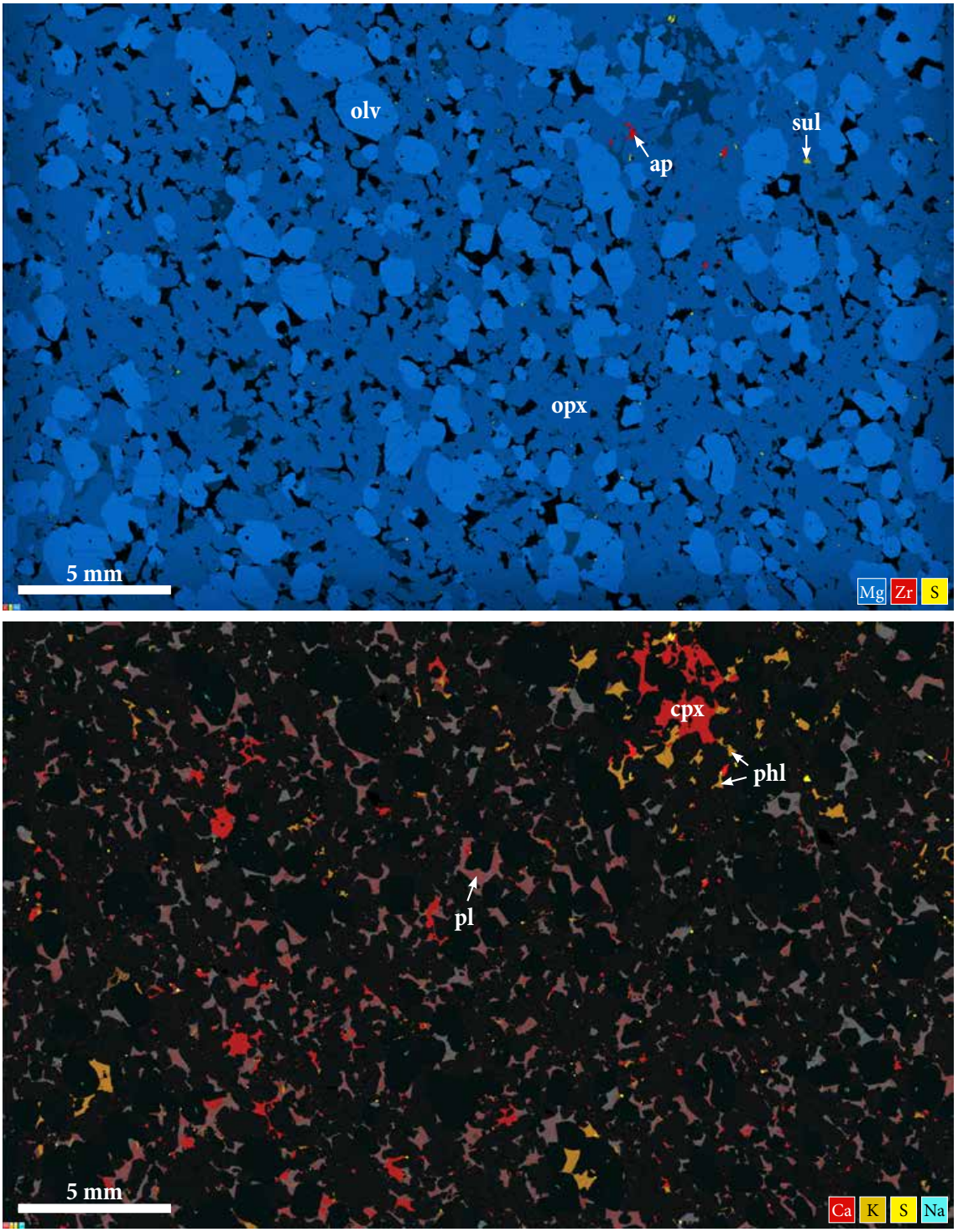

Fig. G.5. Elemental map of olivine-pyroxenite sample NG2-626. Abbreviations: olv = olivine; opx = orthopyroxene; sul = sulfide; ap = apatite; cpx = clinopyroxene; pl = plagioclase; phl = phlogopite.

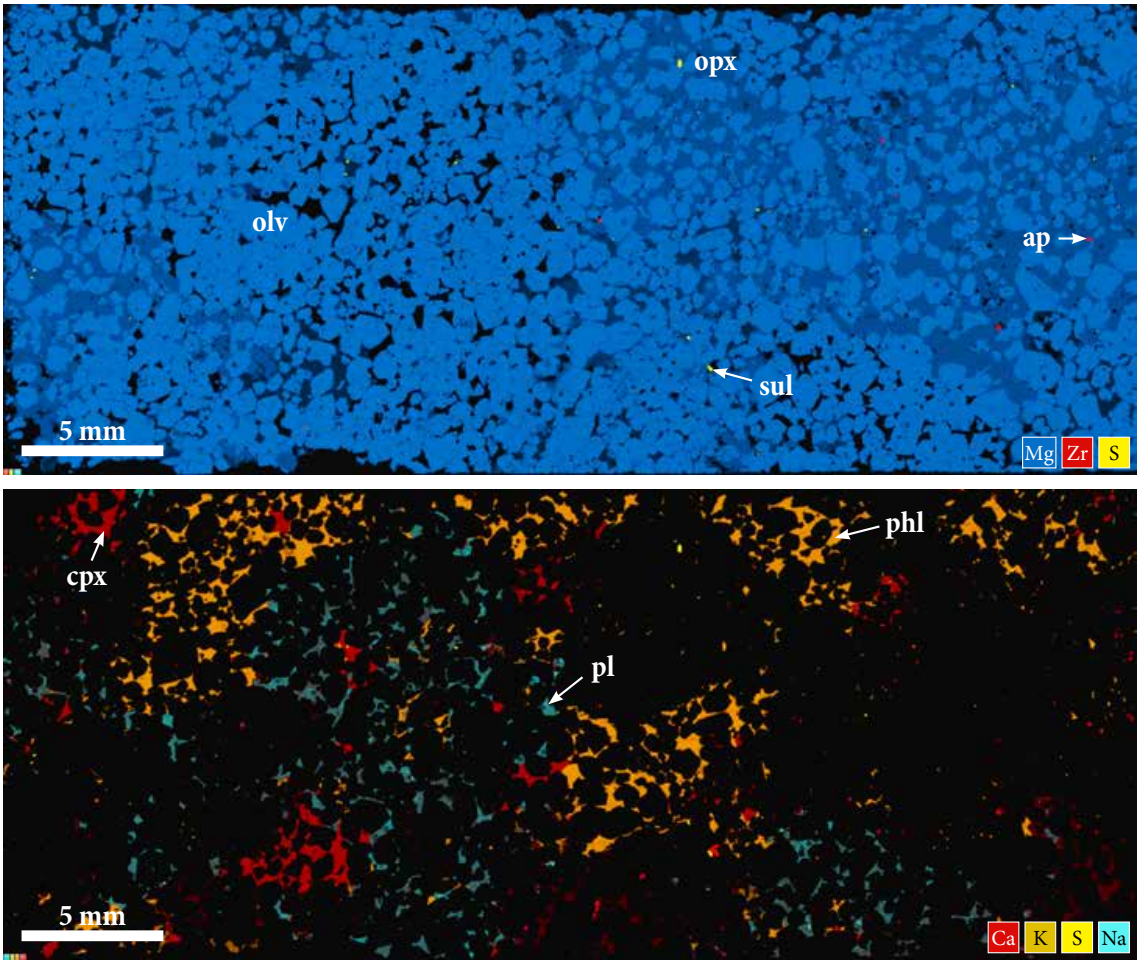

Fig. G.6. Elemental map of harzburgite sample NG2-664. Abbreviations: olv = olivine; opx = orthopyroxene; sul = sulfide; ap = apatite; cpx = clinopyroxene; pl = plagioclase; phl = phlogopite.

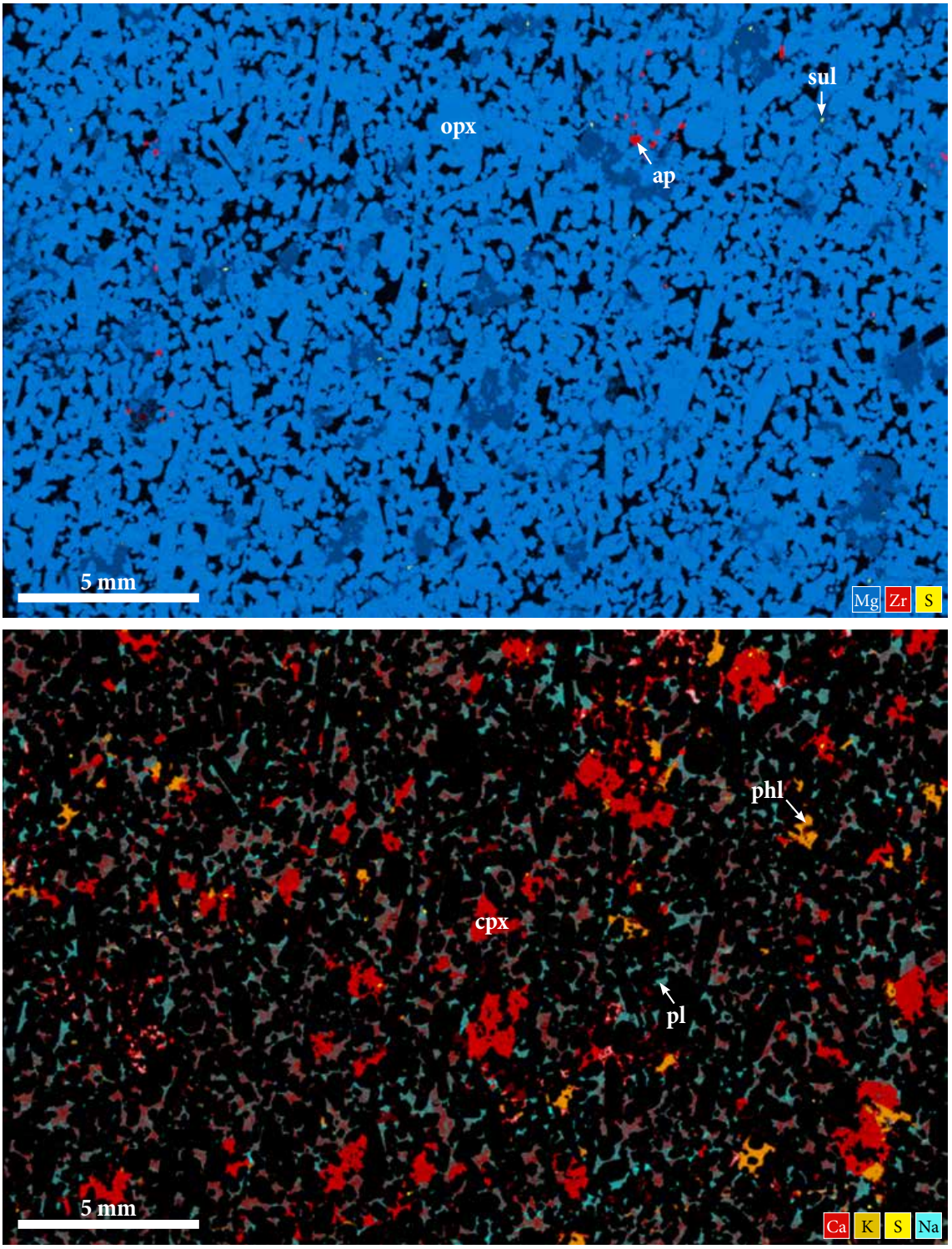

Fig. G.7. Elemental map of melanorite sample NG2-737. Abbreviations: opx = orthopyroxene; sul = sulfide; ap = apatite; cpx = clinopyroxene; pl = plagioclase; phl = phlogopite.

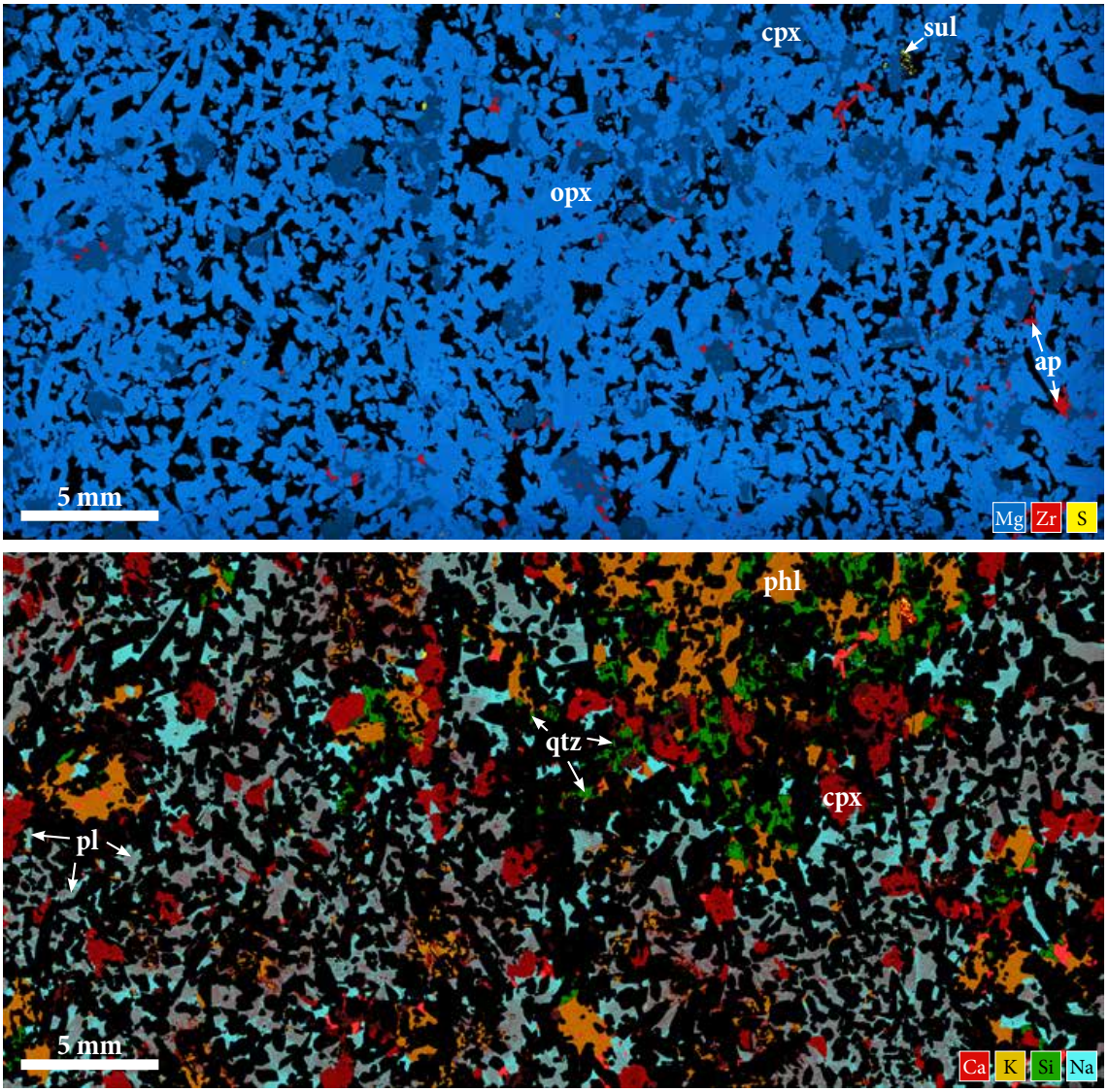

Fig. G.8. Elemental map of melagabbronorite sample NG2-762. Abbreviations: opx = orthopyroxene; cpx = clinopyroxene; sul = sulfide; ap = apatite; pl = plagioclase; qtz = quartz; phl = phlogopite.

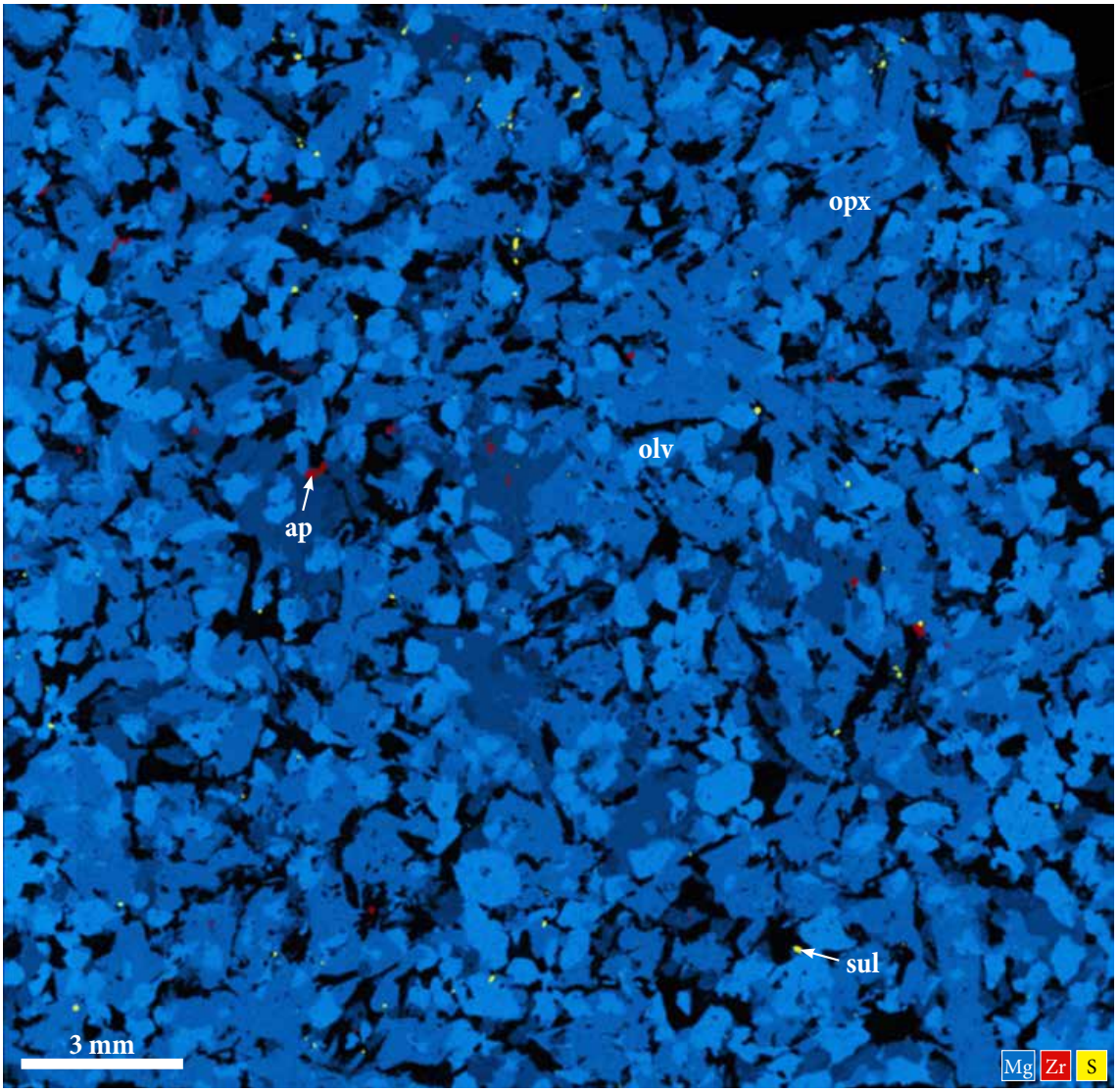

Fig. G.9. Elemental map of olivine-gabbronorite sample NG2-772. Abbreviations: olv = olivine; opx = orthopyroxene; sul = sulfide; ap = apatite.

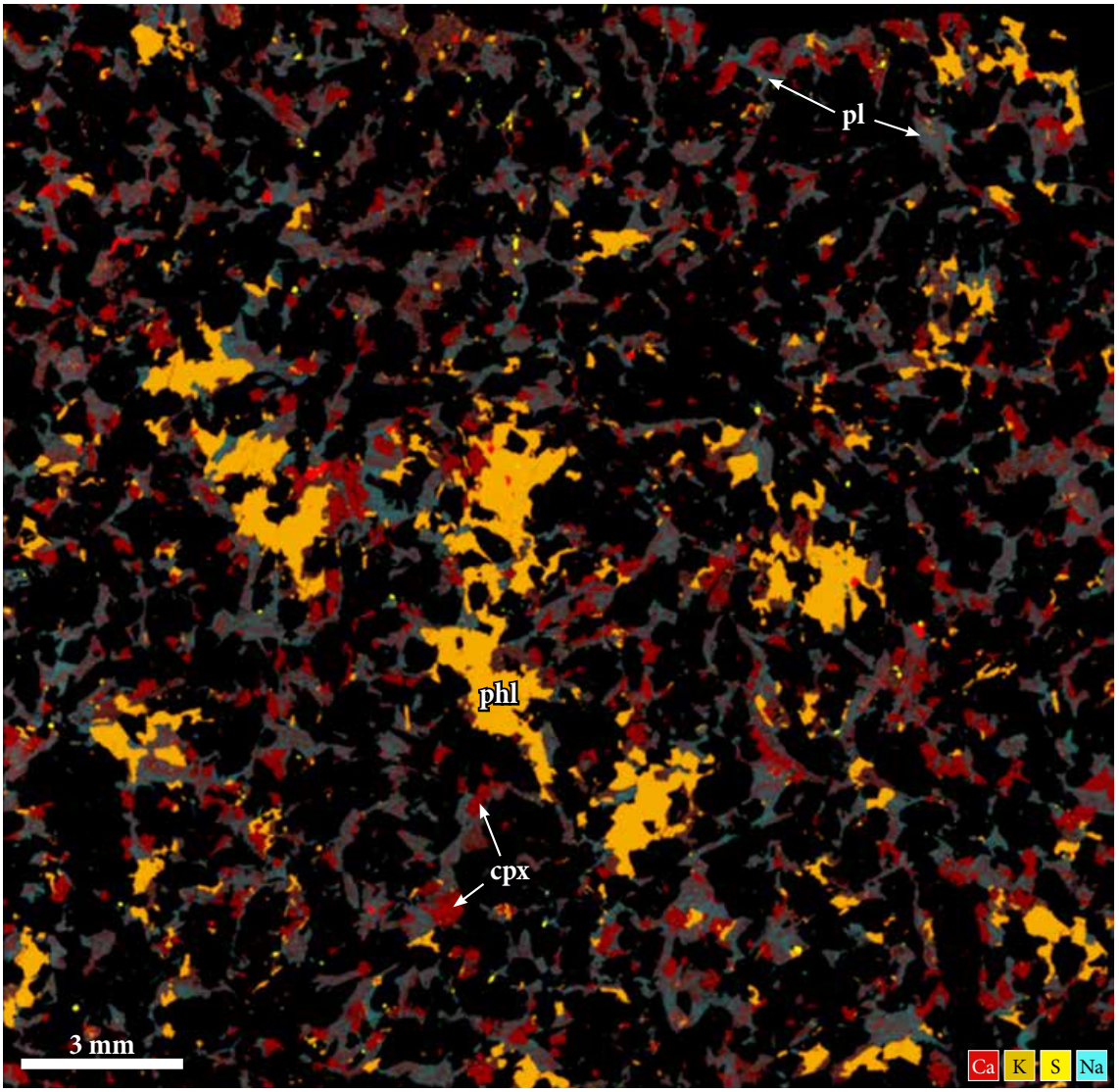

Fig. G.10. Elemental map of olivine-gabbronorite sample NG2-772. Abbreviations: cpx = clinopyroxene; pl = plagioclase; phl = phlogopite.

H Element map of Nittis sample 79-23

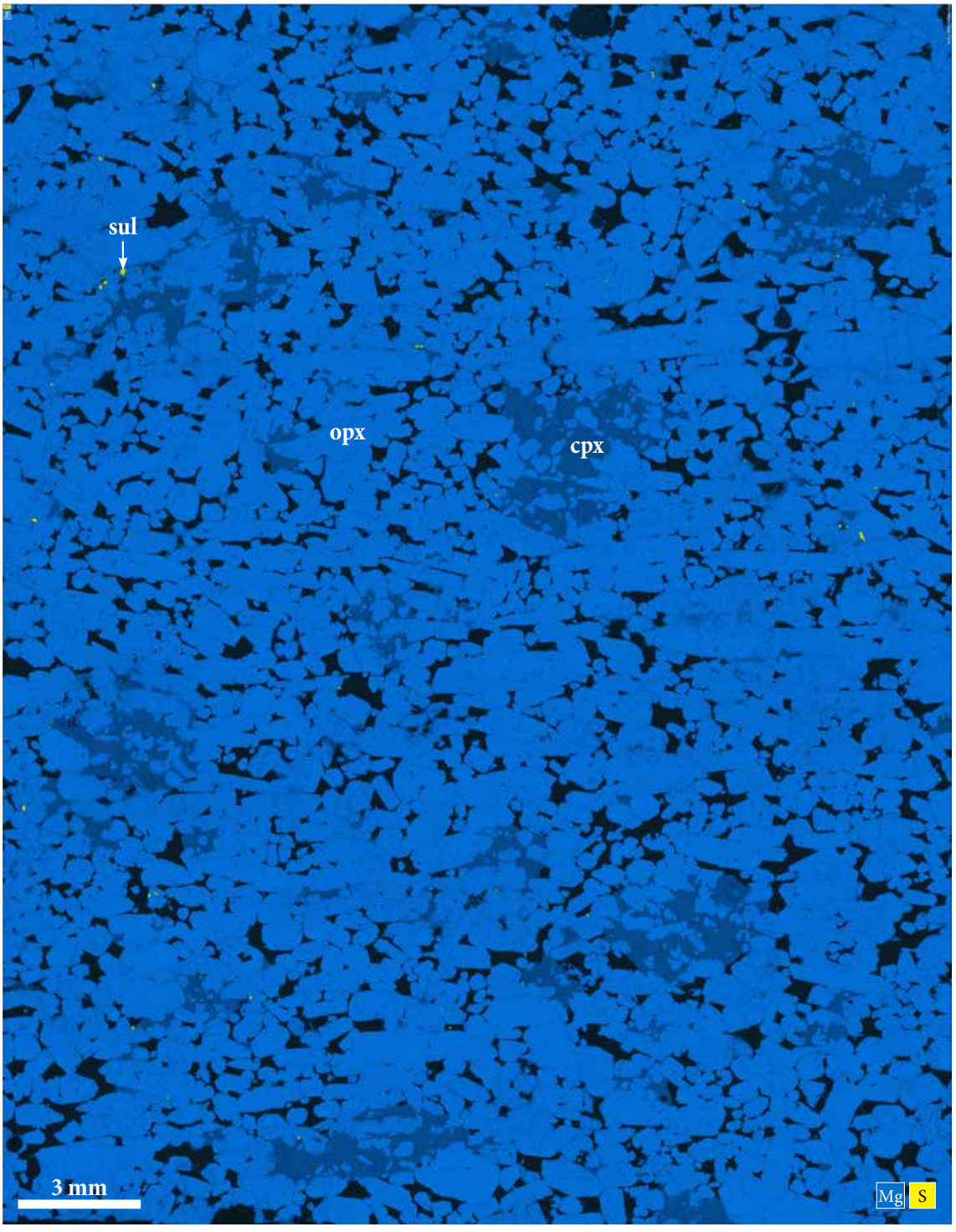

Fig. H.1. Elemental map of orthopyroxenite sample 79-23. Abbreviations: opx = orthopyroxene; cpx = clinopyroxene; sul = sulfide.

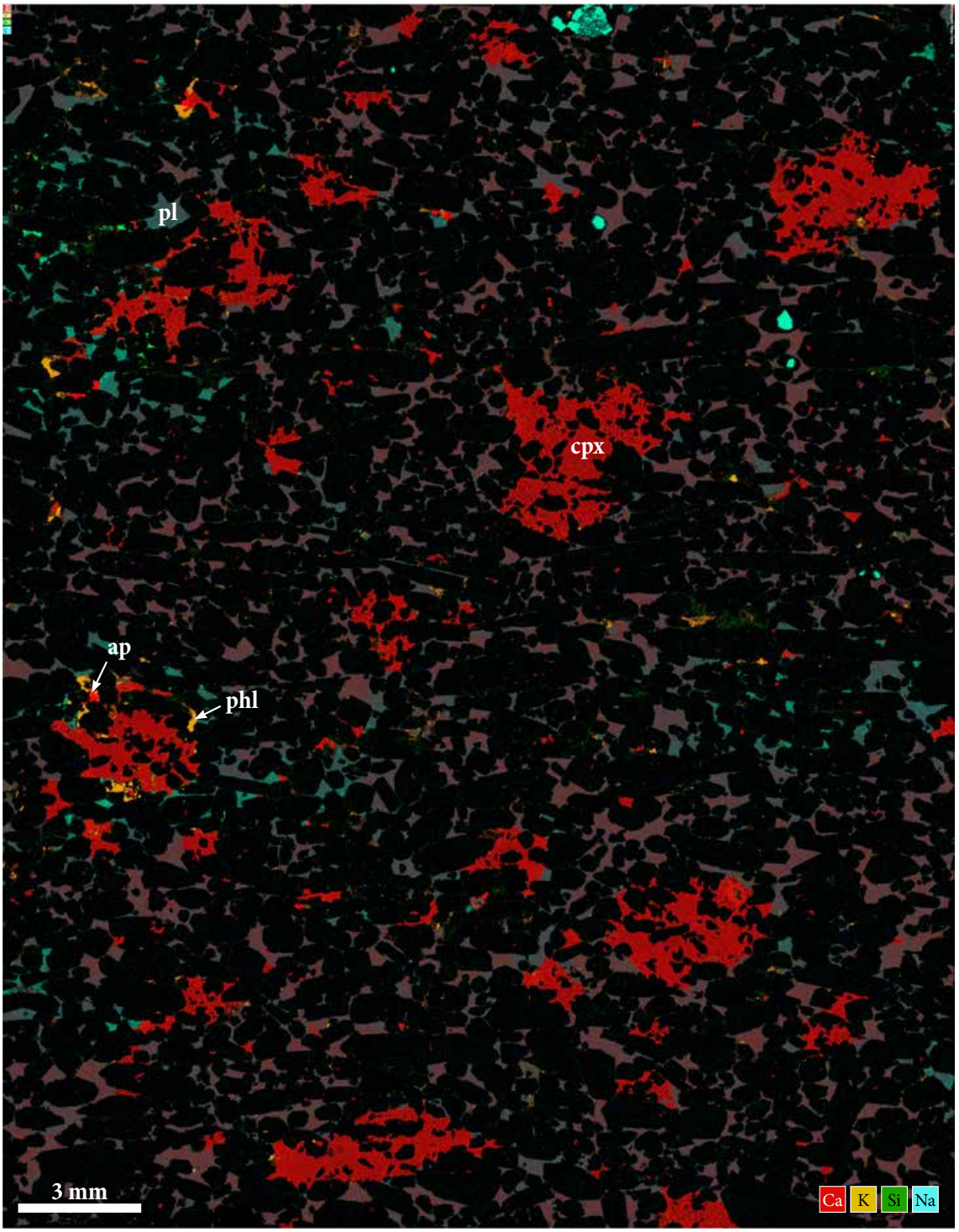

Fig. H.2. Elemental map of orthopyroxenite sample 79-23. Abbreviations: cpx = clinopyroxene; pl = plagioclase; phl = phlogopite; ap = apatite.